THE UNIVERSITY *of* EDINBURGH

Discrete Element Modelling of Iron Ore Pellets to Include the Effects of Moisture and Fines

by

John Paul Morrissey

A dissertation submitted in partial fulfilment
for the degree of
Doctor of Philosophy

in the

Institute for Infrastructure and Environment
School of Engineering
UNIVERSITY OF EDINBURGH

2013

Declaration of Authorship

This thesis entitled, "*Discrete Element Modelling of Iron Ore Pellets To Include The Effects Of Moisture And Fines*" is submitted to the University of Edinburgh for the degree of Doctor of Philosophy. The research work described and reported in this thesis has been completed solely by *John Paul Morrissey* under the supervision of *Prof. Jin Y. Ooi* and *Prof. Jian-Fei Chen*. I confirm that:

- Where I have consulted the published work of others, this is always clearly attributed. Where I have quoted from the work of others, the source is given.
- I have acknowledged all main sources of help.
- Where the thesis is based on work done by myself jointly with others, I have made clear exactly what was done by others and what I have contributed myself. This applies in the area of the parametric study where work on the subject of the development of adhesion and the relationship to the unloading/reloading stiffness has been carried out jointly with S.C. Thakur.

Publications based on this thesis:

Thakur, S.C., Morrissey, J.P., Sun, J., Chen, J-.F., & Ooi, J.Y. Micromechanical analysis of cohesive granular materials using discrete element method with an adhesive elasto-plastic contact model. *To be submitted for review, June 2013*.

Morrissey, J.P., Chen, J-.F., Ooi, J.Y., Tano, K.T., & Horrigmoe, G. (2012). An Experimental and DEM Study of the Behaviour of Iron Ore Fines. *7th International Conference for Conveying and Handling of Particulate Solids - CHoPS 2012* . Friedrichshafen, Germany.

Morrissey, J.P., Thakur, S.C., Sun, J., Chen, J-.F., & Ooi, J.Y. (2011). Modelling Cohesive-Frictional Particulate Solids For Bulk Handling Applications. In E. Oñate & D.R.J. Owen (Eds.), *II International Conference on Particle-based Methods - Fundamentals and Applications - PARTICLES 2011*.

Morrissey, J.P., Ooi, J.Y., Chen, J-.F. (2012). Modelling a cohesive granular material. *EDEM Academic Poster Contest - 3rd place*. DEM Solution Ltd., Edinburgh, Scotland.

Signed: _____

Date: _____

UNIVERSITY OF EDINBURGH

Abstract

Institute for Infrastructure and Environment
School of Engineering

Doctor of Philosophy

by John Paul Morrissey

Across industry the majority of raw materials handled are particulate in nature, ranging in size and properties from aggregates to powders. The stress regimes experienced by the granular solids vary and the exhibited bulk behaviours can be complex and unexpected. The prevalence of granular solids makes them an area of interest for industry and researchers alike as many challenges still remain, such as dealing with complex cohesive behaviour in materials, which often gives rise to handling difficulties.

Storage and transportation are an important part of the process chain for industries where particulate solids are commonplace. Failure to properly account for the cohesive nature of a particulate solid can be costly as it can easily lead to blockages in a silo such as ratholing or arching near the outlet during discharge. The cohesive strength of a bulk material depends on the consolidation stress it has experienced. As a result, the stress history in the material leading up to a handling scenario needs to be considered when evaluating its handling behaviour.

The Discrete Element Method (DEM) has been extensively used to simulate the behaviour of granular materials, however the majority of the focus has been on non-cohesive systems. For cohesive solids, it is crucial that the stress history dependent behaviour is adequately captured. Many of the contact models commonly used in DEM simulations to simulate cohesive granular materials such as the JKR model or liquid bridge models are elastic in nature and may not capture the stress history dependent behaviour observed in cohesive particulate solids.

A comprehensive study on the effect of cohesion arising from the addition of moisture on the behaviour of two types of LKAB iron ore fines (KPBO and KPRS) has been carried out. The addition of moisture to the sample has been found to have a significant effect on both kinds of fines. KPRS fines were found to have a much higher unconfined strength and flow function at higher moisture contents, and also show a greater increase in cohesion with the addition of moisture, while at moisture contents of less than 2% the KPBO fines demonstrate higher unconfined yield strength. The KPBO fines were also found to achieve a significantly looser initial packing at much lower moisture content when compared to the KPRS fines. The lateral pressure ratio has also been evaluated.

In this study a mesoscopic adhesive contact model that accounts for contact plasticity and stress history dependency in the bulk solid, the Edinburgh Elasto-Plastic Adhesion (EEPA) mode, has been presented and mathematically verified. A parametric study of the DEM contact model parameters was conducted to gain a deeper understating of the effect of input parameters on the simulated cohesive bulk behaviour.

The EEPA contact model has been used to predict an experimental flow function of KPRS iron ore fines. The contact model has demonstrated the ability to capture the stress history dependent behaviour that exists in cohesive granular solids. The DEM simulations provide a very close match to the experimental flow functions, with the predicted unconfined strengths found to be within the standard deviations of the experimental results. Investigations into the failure mode predicted by the DEM simulations show that the samples are failing from the development of shear planes similar to those observed experimentally.

The effect of increasing levels of adhesion has been explored for a flat bottomed silo where the level of adhesion has been varied. The DEM simulations were found to capture the major phenomena occurring in silo discharge including the various flow zones associated with a flat bottomed silo. Funnel flow, the effective transition and mass flow which are associated with a mixed flow pattern were observed in the model silo. The location of the effective transition height was identified: above this was mass flow. The velocity determined from the discharge rate was found to be in excellent agreement with the velocity profiles found in the zones of mass flow. A high velocity core flow zone was observed above the outlet where velocities were greater than 1.25 times the mass flow velocity, V_{MF}.

The level of adhesion in the silo was found to affect the discharge rate - a reduced flow rate was found until the eventual blockage of the silo at a high level of adhesion was found. As the level of adhesion increased the probability of arching also increased, and the formation of intermittent arching behaviour was noted in the cases with higher levels of adhesion in the system. The development of both temporary and permanent cohesive arches over the silo outlet were also observed with stopped flow from the silo.

Acknowledgements

I would like to take this opportunity to thank my supervisors Prof. Jin Ooi and Prof. Jian-Fei Chen, without whose excellent supervision, guidance, friendship and support I would not have been able to complete this dissertation. I would most likely be still lost in the woods, barking up the wrong tree ...

At this point I would also like to thank my friends and colleagues within the Silos & Granular Solids Research Group, Dr. Jin Sun for his expertise in DEM and all his help in the initial coding of the API; Dr. Carlos Labra for his implementation of the P4 post-processing toolbox; Dr. Zhijun Zhong for all his assistance in the laboratory and experimental set-up and to Dr. Nick Brown and Mr. Subhash Thakur for all their help and expertise in EDEM and experiments. I would also like to thank all of my friends within the institute for making those darks days brighter.

I'm also very grateful for the studentship provided to me by the British Engineering and Physical Sciences Research Council and my industrial sponsors DEM Solutions Ltd., and LKAB for making this project possible.

A special thank you also needs to be made to the school IT department for all their assistance, particularly any time I went looking for more storage.

And last, but not least, my parents who can finally say I'm something other than a student!! Without their patience,support and encouragement, none of this would have been possible.

Contents

List of Figures

List of Tables

Abbreviations

AFM	**A**tomic **F**orce **M**icroscopy
API	**A**pplication **P**rogramming **I**nterface
BSI	**B**ritish **S**tandards **I**nstitute
CAD	**C**omputer **A**ided **D**esign
CAE	**C**omputer **A**ided **E**ngineering
CFD	**C**omputational **F**luid **D**ynamics
CoV	**C**oefficient **o**f **V**ariance
DEDS	**D**iscrete **E**vent **D**ynamic **S**ystems
DEM	**D**iscrete **E**lement **M**ethod
EPT	**E**dinburgh **P**owder **T**ester
FEA	**F**inite **E**lement **A**nalysis
FEM	**F**inite **E**lement **M**ethod
GUI	**G**raphical **U**ser **I**nterface
LVDT	**L**inear **V**ariable **D**ifferential **T**ransformer
MFF	**M**aterial **F**low **F**unction
NFD	**N**ormal **F**orce **D**isplacement
NMRI	**N**uclear **M**agnetic **R**esonance **I**maging
PEPT	**P**ositron **E**mission **P**article **T**racking
PETP	**P**oly-**E**thylene **T**erephthalate **P**ellets
PIV	**P**article **I**mage **V**elocimetry
RDF	**R**adial **D**istribution **F**unction
RDP	**R**esponse **D**esirability **P**rofiling
REV	**R**epresentative **E**lementary **V**olume
RF	**R**ain-fall **F**illing method
SEM	**S**canning **E**lectron **M**icroscopy
TFD	**T**angential **F**orce **D**isplacement

Symbols

A	Hamaker constant	m
a	Contact patch radius	m
a_r	Aspect ratio	
c	Apparent cohesion	kPa
c	Beverloo constants	
d	Particle diameter	m
d_{10}	Particle diameter at 10$^{\text{th}}$ percentile	m
d_{30}	Particle diameter at 30$^{\text{th}}$ percentile	m
d_{60}	Particle diameter at 60$^{\text{th}}$ percentile	m
D	Diameter of outlet orifice	m
E_p	Particle Young's Modulus	Pa
e	Void ratio	
e_0	Initial void ratio	
e_r	Coefficient of restitution Particle-Particle	
e_w	Coefficient of restitutionParticle-Wall	
E_w	Geometry Young's Modulus	Pa
$\overrightarrow{F}$	Resultant force vector, the sum of all the contact forces	N
F_B	Measured force on the bottom platen	N
F_N	Normal component of the contact force	N
F_{Nd}	Normal damping force	N
F_{Nk1}	Normal spring force	N
F_T	Tangential component of the contact force	N
F_{Td}	Tangential damping force	N
f_t	Tangential spring force	N
F_{normal}	Normal force	-
F_s	Shear forces	N

F_T	Applied load at the top platen	N
F_{tan}	Tangential force	-
F_W	wall frictional force	-
Fr	Non dimensional rotational Froude number	
G	Shear modulus of the particle	-
g	Gravitational constant	-
	Gravity acceleration vector	-
h	Height of the granular material	-
	Time rate of change of the angular momentum	-
K	Lateral pressure ratio	-
K_{adh}	Geometric constant	-
k_1	Load dependant parameter relating	
	to loading stress path	-
k_n	Load dependant parameter relating	
	to unloading stress path	-
$K_{n,Hz}$	Hertz contact constant	-
Kn	Normal contact stiffness	-
Kt	Tangential contact stiffness	-
m	total mass of the particle	-
$m*$	Equivalent mass	-
	Resultant moment vector taken about the mass centre	-
M_s	Mass of solids	-
P	Normal pressure	-
	Inverse distance weighting factor	-
R	Confined compression cylinder radius	m
r	Radius of sphere	m
$r*$	Equivalent radius	-
$R_i.R_j$	Distance of the contact point from the centre of mass	-
T_{Ray}	Rayleigh time step	-
t	Thickness of the cylinder	-
tc	Computational time	-
T_{sim}	Simulation time	-
V_{Ray}	Rayleigh wave velocity	-
$V_{rel,N}$	Relative normal velocity	-
$V_{rel,T}$	Relative tangential velocity	-

V_s	Volume of the solids	m^3
	Acceleration vector of mass centre	-
W	Flow rate	kg/s
ω	angular frequency	rads^{-1}
d	Normal contact displacement (overlap)	-
bd	Damping ratio	-
g	Bulk of total - weight (c.f. p)	-
DdT	Incremental tangential displacement	-
DKT	Increment of the tangential spring force	-
ε_θ	Hoop strain of the cylinder at the measuring points	-
ε_a	Axial strain of sample of the cylinder at the measuring points	-
ε_v	Mean vertical strain	-
λ	Bulk loading parameter	-
μ_{mob}	Mobilised friction coefficient	-
μ	Coefficient of sliding friction (Particle-particle)	-
μ	Coefficient of sliding friction (Particle-Wall)	-
μ	Critical particle-wall friction for transition from slipping to avalanching motion	
	Bulk particle-particle coefficient of sliding friction	-
μ	Bulk particle to wall coefficient of sliding friction	-
μ	coefficient of rolling friction particle-particle	-
μ	coefficient of rolling friction Particle to wall	-
κ	Bulk unloading parameter	-
ρ	Bulk density	-
ρ_s	Density of solids	-
$\overline{\sigma}_h$	Mean horizontal stress	-
$\sigma_{h\prime}$	Effective horizontal pressure	-
σ_n	Normal stress on failure plane	-
$\overline{\sigma}_v$	Mean vertical stress	-
$\sigma_{v\prime}$	Effective vertical pressure	-
$\overline{\tau}$	Mean shear stress	-
τ_f	Limiting shear stress on failure plane	-
τ_w	Wall shear stress	-
ν	Poisson's ratio	

ν_b	Bulk Poisson's ratio	-
ν_{cyl}	Poisson's ratio of the cylinder	-
$\Phi_{p,bulk}$	Bulk particle friction angle	-
Φ_{pw}	Bulk particle to wall friction angle	-
$\overrightarrow{\omega}$	Angular velocity vector of the particle	-
$\dot{\overrightarrow{\omega}}$	Angular velocity vector of the mass centre	-
ω_i	Angular velocity vector	-

This thesis is dedicated to my Parents.
For their endless love, support and encouragement.

Chapter 1

Introduction

Bulk handling of powders and granular solids is common in many industries and often gives rise to handling difficulties especially when the material exhibits complex cohesive behaviour. For example, high storage stresses in a silo can lead to high cohesive strength of the stored solid, which may in turn cause problems such as ratholing or blockages arising from arching near the outlet during discharge. The cohesive strength of a bulk material depends on the consolidation stress it has experienced and as a result, the stress history in the material leading up to a handling scenario needs to be considered when evaluating its handling behaviour.

The discrete element method (DEM) has been extensively used to simulate the behaviour of granular materials. For cohesive solids, it is crucial that the stress history dependent behaviour is adequately captured. A number of contact models are available in several commercial DEM packages to simulate cohesive granular materials. These include models based on surface forces such as the JKR model [Johnson *et al.*, 1971] and DMT model [Derjaguin *et al.*, 1975] and capillary force models [Gröger *et al.*, 2003; Remy *et al.*, 2012]. However, it is still not clear whether DEM simulations with these contact models can adequately capture the stress history dependent behaviour observed in bulk solids.

The flowability of bulk solids, particularly fine-grained ones, is greatly affected by the adhesive forces that act between the particles. In moist bulk solids, the capillary forces and solid bridging tend to become the dominant adhesive force, while van der Waals forces become less influential as particle size increases past several microns. In the case of the iron ore fines; which are relatively large, dense particles, it is expected that the effect of moisture will be most significant factor. The flowability of bulk solids is usually

measured using the flow function, which is the relationship between the unconfined yield strength (σ_c) and the consolidation stress (σ_1).

1.1 Industry Background

The demand for world steel has continued to rise over the past decade, largely driven by the economic development of countries such as India and china. The industry now directly employs over 2 million people worldwide as global consumption has risen (see Figure 1.1) from 851 megatonnes in 2001 to 1157 megatonnes (MT) in 2011 [World Steel Association, 2012]. This increasing trend is expected to continue into 2013 and beyond.

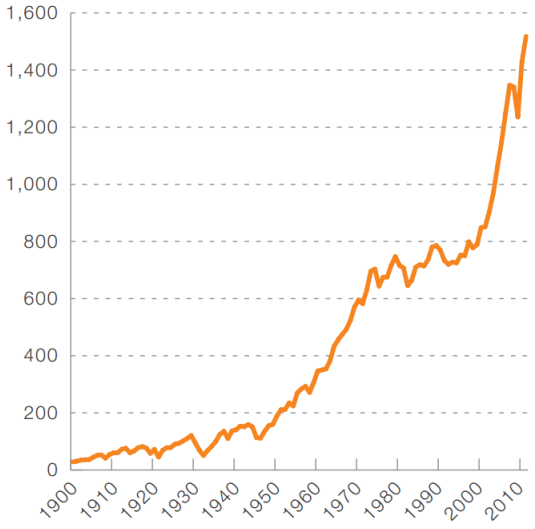

Figure 1.1: Crude Steel Production - From 1900 to present day (MT), after [World Steel Association, 2012]

Luossavaara-Kiirunavaara AB (LKAB) is the world's second largest producer of high quality iron ore pellets for use in the production of steel. Over the past decade their output has increased from 20 to 26 million tons of pellets produced per year and this growth is expected to continue with LKAB able to supply 35-40 million tons per year in the future [Luossavaara-Kiirunavaara AB, 2012*d*]. LKAB's mines are located in Kiruna and Malmberget in the northern part of Sweden, several hundred kilometres inside the Arctic Circle. The mines are the largest underground iron ore mines in the world and the Kiruna mine alone produces more than 75,000 tonnes of iron ore per day [Luossavaara-Kiirunavaara AB, 2012*c*].

1.2 Iron Ore Pellets

Iron ore pellets are approximately centimetre-sized spheres of iron ore that are used to feed blast furnaces in the steel production process. There are many reasons why pellets are favoured for used in the steel industry as opposed to other forms. The main advantages of pellets can be summarised as:

- Good bed permeability
- Excellent reducibility
- High strength
- Uniform composition
- Good resistance to disintegration in the blast furnace

Due to the spherical nature of pellets, which leads to the generation of open pores in the bed packing, they form a bed that has a uniform permeability leading to smooth operation of the furnace. The consistent shape and size, along with a relatively low angle of repose, gives minimal segregation and an even distribution of the charge in the furnace. Because of their high porosity (25 - 35%), pellets can be reduced considerably faster than hard burden sinter or hard natural ores, which can lead to energy and cost saving in the production process. The cold strength of pellets is very high, in the region of 150-250 kN/m^2 or more. This means that the pellets have sufficient structural strength to withstand the normal handling that occurs in the various transportation and handling steps between the pellet furnace and the blast furnace without significant breakage reducing handling losses. Unlike lump ores, pellets can have a controlled composition specified during concentration and pelletisation allowing for easier managing of the blast furnace. Finally, the high strength of the pellets also provides strong resistance to disintegration that can occur in a blast furnace due to the addition of burden. The main disadvantage of pellets is the extra cost required with the manufacture of pellets when compared to lump ores.

LKAB's pellets have an unusually high iron content; an iron content of close to 67%; and due to this have a lower environmental impact than competing pellets. Different additives are added in the manufacturing process to give certain characteristics to the pellets and the most common additives are bentonite, limestone, olivine and dolomite. Bentonite is added as a binding agent to help agglomerate the pellets, olivine is used to raise the pellet melting temperature while dolomite is added to prevent clumping in direct reduction plants. Limestone is added to help reduce the amount of slag formed [Luossavaara-Kiirunavaara AB, 2012*e*]. This leads to two main types of pellets being

produced: KPBO blast furnace (BF) pellets which are olivine fluxed for superior high temperature properties and KPRS direct reduction (DR) pellets which are dolomite fluxed and coated for optimal behaviour in the DR-shaft.

1.2.1 Pellet Manufacturing

The process of manufacturing iron ore pellets contains many stages from the initial extraction of the raw ore from the mine. A schematic of the mining process is given in Figure 1.2. The Kiruna mine operated by LKAB is the largest underground iron ore mine with the current operating depth now at more than 1000m below the surface. The key stages of underground mining can be broken into: construction of the network of tunnels, drilling and blasting of the ore body, removal from the face and transportation [1-4]. Some crushing of the extracted ore is carried out in the mine before [5] before removal to the surface for processing [6-8].

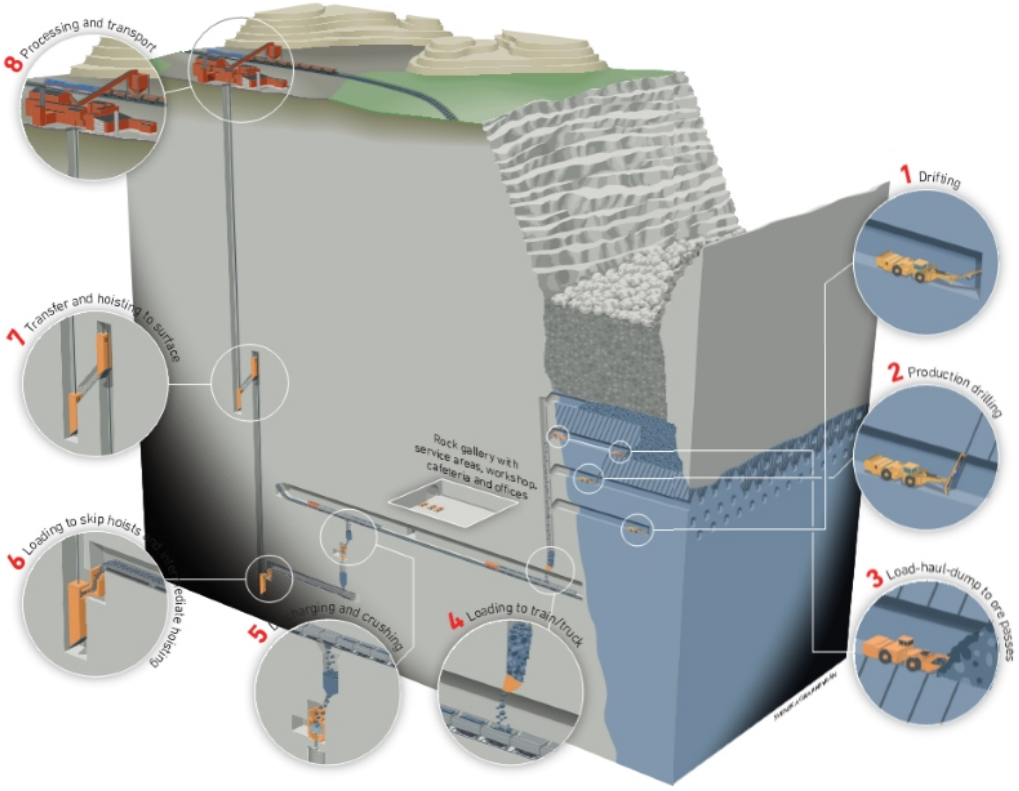

Figure 1.2: LKAB's mining process - An overview of the mining process, after Luossavaara-Kiirunavaara AB [2012*c*]

The mining and production process can be summarised by Figure 1.3, while the post-production process is depicted by Figure 1.4.

There are many challenges arising from the handling of very large and very fine materials in the initial production stage from raw material to final product, it is in the final

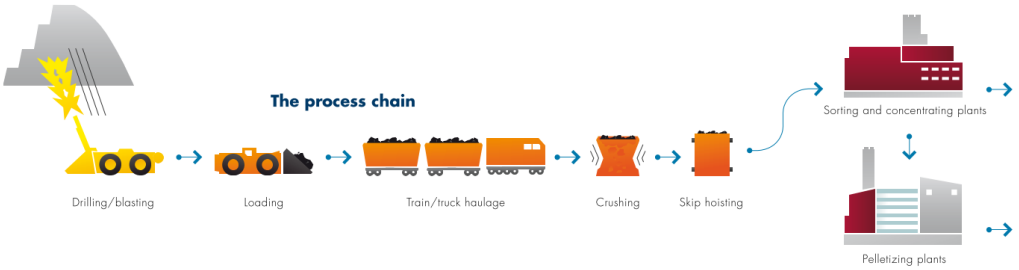

Figure 1.3: Manufacturing Process - From mine to pellets

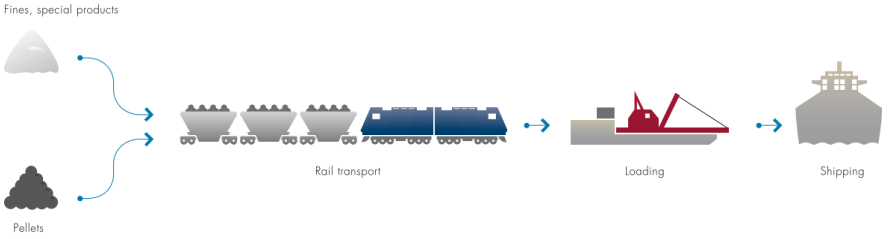

Figure 1.4: Handling and logistics - From product to customers

stage of product to customer that the work presented in this thesis will aim to improve on. This is discussed in more detail in the following section. However, it is important to note that the materials properties that effect the handelability of a material, such as size, shape, strength or susceptibility to moisture are inherited from the manufacturing process which creates the material initially.

1.2.2 Handling & Storage

For LKAB, storage and handling of the iron ore pellets are key areas which have to be considered when the production capacity has to be increased to meet demands without having a significant effect on the high quality pellets which customers have come to expect. LKAB's mines are located several hundred kilometres away from the ports from which they will be shipped, and as such, LKAB transports the pellets the several hundred kilometres from the mines to the harbour via its dedicated ore railway. Each ore train consists of 68 cars (almost 750m total length), with each one carrying approximately 100 tons of pellets through the mountainous, and often frozen, landscape to the harbour for dispatch to customers [Luossavaara-Kiirunavaara AB, 2009, 2011]. The storage of the pellets at the mines and harbours, and the transport between the locations can have a major impact on the quality of the pellets shipped to customers. In particular the silo filling and discharge process can have a significant effect on the quality of the end product. Large silos involve the dropping of pellets from large heights which can lead to fracture and attrition of pellets and thus increasing the amount of

fine material in the silo. The significant mass of the stored material exerts large pressures which may lead to the development of flow problems,particularly in the presence of cohesion, and further effect the quality of the final product.

LKAB has two main ports which it uses for the shipping of its pellets to customers: Luleå and Narvik. Narvik, which is LKAB's largest port has an operating capacity of 20 million tons per year following the competition of the SILA project in late 2009 [Luossavaara-Kiirunavaara AB, 2009, 2012*a*,*b*]. The SILA project constructed eleven underground silos in Narvik, with each silo having a diameter of 38m and a depth of 60m. An inner silo is employed in the design to reduce the stress acting on the pellets and the silos are filled and discharged through this inner silo. Each silo can hold approximately 110,000 tons of pellets or roughly equivalent to sixteen train loads. Above the silos, an enclosed train culvert allows the bottom emptying cars to quickly discharge the pellets in to the silos in just under 30 minutes while offering protection from the weather and reducing dust pollution. A schematic of the transportation and storage network at Narvik harbour is presented in Figure 1.5.

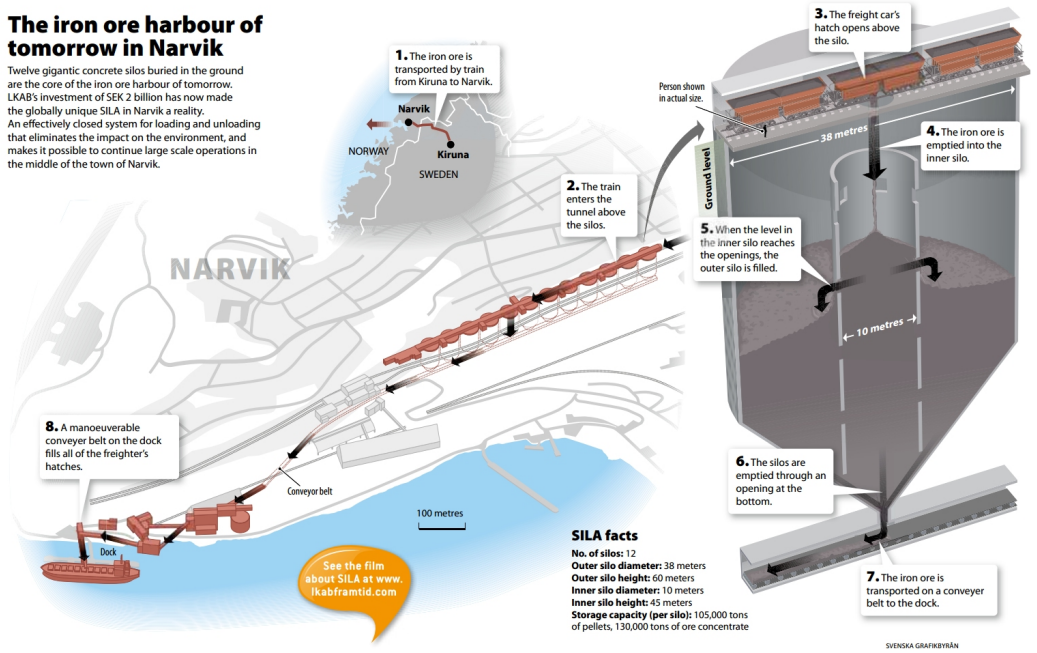

Figure 1.5: Narvik iron ore harbour - Overview of the SILA project, after [Luossavaara-Kiirunavaara AB, 2011]

The new design of silos are already showing an improvement of the quality in the pellets being shipped to customers and the impact of dust on the local environment has also been reduced. Plans are also being made for the addition of further overground silos to increase capacity.

1.3 Research Scope & Objectives

The main aim of the research is to develop an improved contact model to better capture the behaviour of cohesive granular solids, particularly iron ore fines, which are significantly affected by the presence of moisture. In order for numerical simulations to be successfully used for more efficient design and management of industrial equipment and structures, the transition from qualitative to quantitative prediction needs to be made. To help achieve this a secondary aim is to rigorously characterise the properties of the material that are required for calibration of a numerical model. A study of the effect of the parameters of the adhesive contact model is also carried out. In this study a particular focus is paid to the two types of iron ore fines: KPBO and KPRS, with the purpose of characterising the different materials types and assessing the distinct behaviour exhibited by the different fines.

Cohesive granular solids such as powders can have a very loose, highly porous structure under very low stresses. While it is possible to generate similar initial packing structures in a DEM simulation, it is not feasible to attempt to match all stress states. In this study, stress states larger than 5-10 kPa are of interest and as such all packing structures will aim to match the experimental results from this stress level. As hardware capabilities continue to improve and the price of computing power continues to decrease, the use of the normally computationally intensive discrete element method will become more common in both research and design. It is hoped that the work presented in this thesis will provide a valuable insight into simulation the complex behaviour of cohesive granular solids.

1.4 Thesis Structure

This dissertation is divided into nine chapters and a brief description of the content of each is outlined below.

Chapter 1 presents the background information and the scope and objectives of this research. A brief outline of the thesis is also presented.

Chapter 2 reviews the literature that is relevant to this topic. It focuses on the sources of adhesion that exist and how they have been implemented for DEM studies, studies on the experimental validation of DEM and a study of how DEM parameters affect the simulation results. The application of DEM to an industrial process, silo discharge is also reviewed.

Chapter 3 provides a more in-depth look at the Discrete Element Method. The DEM code used, EDEM is introduced along with it's capabilities. The DEM calculation method

is introduced and a review of the commonly used DEM contact models is carried out and the abilities of those models is summarised. DEM simulations with the JKR adhesion model are also presented.

Chapter 4 details the development of the Edinburgh Elasto-Plastic Adhesion (EEPA) contact model for DEM. The main characteristics and parameters are introduced followed by a detailed overview of the contact model calculation process. Verification of the implementation of the contact model is also presented.

Chapter 5 describes the laboratory experiments and measured bulk properties that have been used for calibration of the DEM contact model. An assessment of the distinct behaviour of the different types iron ore fines is made.

Chapter 6 presents a study on the effects of various DEM parameters on the cohesive characteristics of an assembly of particles under both confined consolidation and unconfined compression. The effect of the DEM model parameters on experimentally measured quantities such as the lateral pressure ratio and unconfined compression strength is considered.

Chapter 7 presents a simple calibration the Edinburgh Elasto-Plastic Adhesion (EEPA) model with measured values the iron ore fines.A comparison is made between the predicted DEM flow functions and those measured for the iron ore fines. Investigations in to the failure mode in the DEM simulations are also made.

Chapter 8 presents an exploratory study of the effects of adhesion on silo discharge using simple DEM models of a flat bottomed silo. The chapter also includes an assessment of the capability of the contact model to qualitatively predict the phenomena that are present in the discharge of a silo.

Chapter 9 summarises the main conclusions of the work, and also highlights areas that require further research in the future.

Chapter 2

Literature Review

Granular materials have become increasingly common materials that are encountered on a regular basis in all type of industry. More than 75% of materials handled in the raw state and almost half of all finished products are granular solids [Nedderman, 1992]. In order to store these granular materials storage structures such as hoppers, bins and silos are required. Silo discharge and flow problems have been studied for well over a century but more focus is required on dealing with and designing for cohesive solids. Failure to account for cohesion will may leads to flow problems and blockages which are a major concern for operators who want a low cost, efficient system.

This chapter presents a literature review of the main areas related to the research presented in this thesis. The topics of adhesive forces, silo pressure, silo flow, the discrete element method (DEM) and previous numerical studies will be introduced. While it is not possible to present an exhaustive review of adhesive forces and silo research, the aim of this chapter is present the salient work related to the topic of cohesive materials.

2.1 Mechanical Descriptors of Packing

In the formation of a granular packing a large number of factors are encountered. The packing structure can be quantitatively characterised through the measurement of certain parameter such a coordination number, void ratio and porosity, particle orientation or contact orientation.

2.1.1 Coordination Number

The coordination number is an indicator of the level of packing in an assembly and is the measurement of the contact density. It is defined as the number of contacts per particle

$$CN = \frac{2N_{c,p}}{N_p} \tag{2.1}$$

Where $N_{c,p}$ is the number of particle-particle contacts in and assembly and N_p is the number of particles in the assembly.

As the coordination number is related to the packing density it can be seen that a high coordination number related to a high density or low porosity. In the absence of particle crushing O' Sullivan *et al.* [2002] noted that the material bulk stiffness and strength are proportional to the number of contacts and coordination number. A similar relationship was also found by Thakur *et al.* [2013] for unconfined yield strength in the presence of adhesive forces.

It is worth noting that during shearing there may be some particles that only have one contact and these particles do not contribute anything to the stability or strength of the fabric. According to Thornton and Antony [2000] the mechanical coordination number can be defined by Equation (2.2).

$$CN_m = \frac{2N_{c,p} - N_1}{N_p - N_1 - N_0} \tag{2.2}$$

where N_1 and N_0 are the number of particles with zero or one contact respectively. The mechanical contact number CN_m should be ≥ 2.

2.1.2 Void Ratio & Porosity

The porosity, φ, and void ratio, e, of a particulate solid play an important role in defining the mechanical response under various loading conditions such as compression or direct shear. The void ratio, given by Equation (2.3), can be defined as the ratio of the volume of voids to the volume of solids.

$$e = \frac{V_v}{V_s} = \frac{V - V_s}{V_s} \tag{2.3}$$

Where V is the total volume of the sample, V_v is the volume of voids and V_s is the volume of the solids in the sample.

Porosity, defined by Equation (2.4), is another method of describing the packing of a granular solid and the value will always be between 0 and 1, unlike the void ratio which can increase significantly above 1. A porosity of 0.05 is typical of a rock while

it in not uncommon for highly cohesive powders to achieve a porosity of 0.7-0.8 in an uncompacted state.

$$\varphi = \frac{V - V_s}{V} = \frac{e}{1+e} \tag{2.4}$$

The porosity can also be related to the particle density and the bulk density by Equation (2.5) when the material is dry, or with negligible moisture content.

$$\varphi = 1 - \frac{\rho_{Bulk}}{\rho_{particle}} \tag{2.5}$$

The porosity of a packing when moisture content is included is given by Equation (2.6).

$$\varphi = 1 - \frac{\rho_{Bulk}}{\rho_{particle}\,(1-w)} \tag{2.6}$$

The packing can also be expressed in terms of the solid volume fraction (SF) which is a measure of the amount of solids in a volume rather than the amount of voids as described by the porosity. The solid volume fraction is related to the porosity by Equation (2.7).

$$SF = 1 - \varphi \tag{2.7}$$

2.1.3 Particle & Contact Orientation

Most granular materials exhibit anisotropic behaviour and this is either from the initial formation of the packing or the application of some loading condition to the sample. The anisotropy of a sample can be characterised through both the particle and contact orientations. Particle orientations and contact orientations, as defined in Figure 2.1 for clumped particles in contact, are typically displayed using polar plots [Geng *et al.*, 2001; Masson and Martinez, 2000; Thomas and Bray, 1999; Zhou and Ooi, 2009] but it also possible to display the particle orientations through stereographic projection [Ketterhagen, 2011].

For the construction of contact and particle orientation plots it is normal to use a band width of approximately 5 degrees which will give 72 distinct orientation bands. As each contact appears as a pair the orientation plots will have a symmetry to their appearance. Particle orientations can only be determined for non-spherical particles or clumps

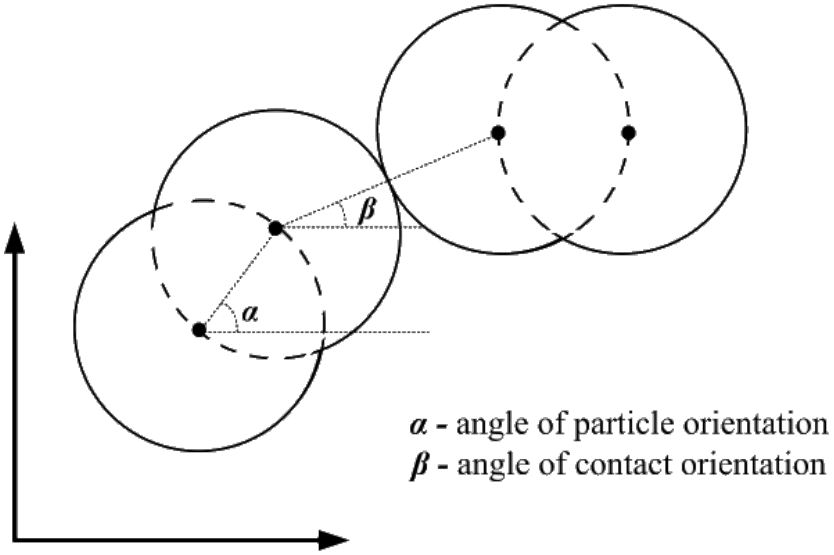

Figure 2.1: Orientation Definitions - Contact and particle orientation, after Zhou and Ooi [2009]

where a particle has a distinct shape upon which a distinct initial reference state can be defined. For spherical particles no distinct orientation can exist.

A spherical coordinate system (Figure 2.2) has been utilised in this study for the representation of the contact orientation. This allows the contact orientations to be represented by just two values: an elevation angle and an azimuth angle. In the spherical coordinate system the position of a point is defined by three parameters: the radial distance,r, of that point from a fixed origin, φ is its elevation angle measured from a fixed horizontal plane, and θ is the azimuth angle anti-clockwise from the positive xz-plane to a reference plane that passes through the origin and the point and is orthogonal to the horizontal plane. Azimuth angles of 0° and 180° represent the positive and negative x-direction and 90° and 270° represent the positive and negative y-direction. The elevation angle is presented in terms of its angle from the horizontal plane with +90° degrees representing upward contact orientation and -90° representing downwards.

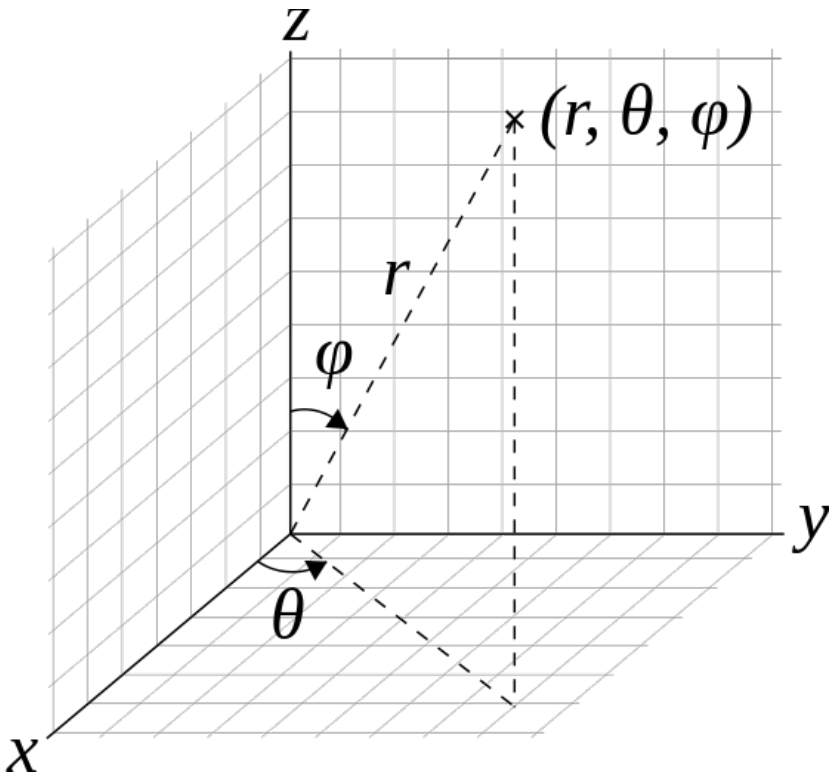

Figure 2.2: Spherical coordinate system - with radial distance, polar angle and azimuth angle

2.2 Attractive Forces

Adhesion forces, such as van der Waals' forces exist for all particles as they are an ever present force but the presences of these forces does not mean all materials are cohesive. Thus, according to the Cohesive Granular Bond number, which is the ratio of the inter-particle adhesive force to the particle weight, it is possible to divide granular materials in to two groups: cohesive and non-cohesive particles where cohesive particles are found to have a high bond number [Castellanos, 2005].

Parker and Taylor [1966] describe adhesion as the use of one material to bond two other materials together, while cohesion is termed as the bonding or joining of two of the same material. On a particulate level or atomic level adhesion is often described as the tendency of particles or surfaces of different material or elements to stick to one another whereas cohesion refers to the tendency of similar or identical particles/surfaces to stick to one another. However, in relation to the discrete element method, both terms have been freely used to refer to the attractive force that can form between particles. For this thesis adhesion will be used when referring to the inter-particle force whereas cohesion is restricted to use for the bulk material.

Adhesive forces are the forces that cause particles within both wet and dry granular materials to adhere together. The dependence of adhesive forces between particles on the external forces acting on the bulk solid is a characteristic of cohesive bulk solids [Schulze, 2008*a*]. As a result, when evaluating their behaviour the stress history is an important aspect and should be considered. Adhesion forces can act through two main binding mechanisms [Pietsch, 2002; Rumpf, 1962]: binding without a solid bridge or binding where a solid bridge is formed. Where a solid bridge does not form, short range forces such as molecular, electrostatic or magnetic forces can cause adhesion between particles.

Adhesive inter-particle forces can originate from several sources such as mechanical forces, solid bridges (including sintering and chemical bonding), intermolecular forces (which include van der Waals forces), electrostatic forces, magnetic forces, capillary forces and other forces. The total adhesion force acting between particles can normally be described a superposition of all interacting surface forces [equation 2.8].

$$F_A = F_{vdw} + F_{cap} + F_{es} + \dots \tag{2.8}$$

Adhesive forces are dependent on the separation distance of the particles, van der Waals forces decrease with increasing separation while liquid bridges will disappear when the separation is such that the liquid bridge ruptures. Van der Waals forces are large at small separation distances (or when in contact) but decrease rapidly with separation distance (Equation (2.9)) while liquid bridge forces and electrostatic forces do not decrease as rapidly with increasing separation distance [Schulze, 2008*a*]. Therefore at larger separation distances liquid bridges and electrostatic forces are the most likely source of cohesion. Also the effect of van der Waals forces diminishes for particles larger than a few hundred microns [Seville *et al.*, 2000]. While the van der Waals forces will increase with increasing radius for a smooth particle, the mass of the particle increases more quickly than the adhesive van der Waals force. This is demonstrated by Figure 2.3 [Seville *et al.*, 2000] where the weight of a given particle and the van der Waals force converge at approximately 1mm for the single asperity contact of a sphere. This has the effect of reducing the cohesive granular bond number by increasing particle mass.

Inter-particle forces are also dependent on the local radius of curvature; the strength will decrease with reducing size of asperities. During contact when the particle surface is rough, the contact is between the asperities on the surface rather than the particle itself, and thus, the local curvature of the asperities becomes the critical value in determining the adhesive force of the contact, as shown by Figure 2.4.

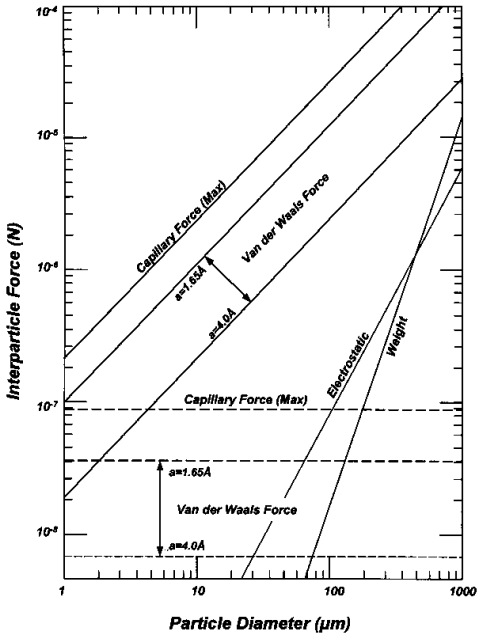

Fig. – Comparison of the magnitude of interparticle forces (dashed lines indicate asperity-to-plane contact). Theoretical interparticle forces for single-point contact between equal spheres (in air), with particle weight plotted for comparison [22].

van der Waals (i) $A = 6.5 \times 10^{-20}$ J (quarts)
(ii) values presented for interparticle separations of 1.65 Å and 4.0 Å
(iii) dashed lines assume asperity-to-plane contact with asperity radius 0.1 μm

Capillary (i) $\gamma = 72.8 \times 10^{-2}$ N m^{-1} (water)
(ii) values are maximum ($\beta \rightarrow 0$)
(iii) dashed lines indicate asperity contact as above

Electrostatic (i) maximum force (opposite sign)
(ii) $\varepsilon_r = 1$; $\varepsilon_0 = 8.9 \times 10^{-12}$ C^2 N^{-1} m^{-2}
(iii) charge density = 10 μC m^{-2}

Weight $\varrho_p = 3 \times 10^3$ kg m^{-3}

Figure 2.3: Comparison of the magnitude of inter-particle forces - Illustration of influence of size on inter-particle forces, after Seville *et al.* [2000]

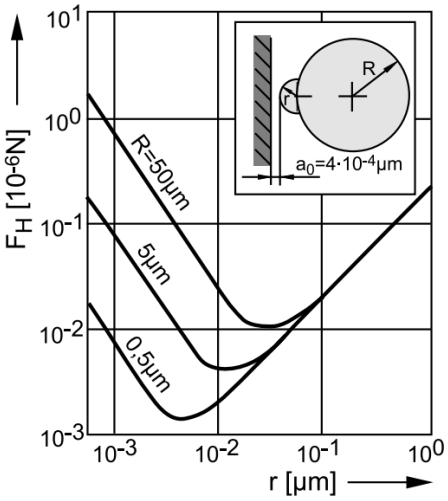

Figure 2.4: Influence of asperity on van der Waals forces - Illustration of influence of asperity size on inter-particle forces, after Schulze [2008*a*]

A comparison between the force calculated from the particle radius and the particle asperity radius is also made in Figure 2.3, where the asperity controlled values are plotted as dotted lines. As the particle radius increases, the asperity radius remains constant leading to a constant adhesion force with increasing particle radius. This suggest that a particle of 100μm should have a van der Waals force equal to it weight, and not a particle of 1mm radius as found when using the particle radius.

It is often noted that *"powders that pack well, flow well"*. In these cases the mass of the particles are larger than the attractive forces acting between them so a dense packing

is formed. This is the case for materials such as rice or coffee which are easily poured and considered non-cohesive. On the other hand materials like flour are very cohesive in nature and often having very loose packings with a solid fraction as low as 0.2-0.3. These materials have poor flowability characteristics due to the relatively high attractive forces in comparison to the particle weight.

2.2.1 Solid Bridges

Solid bridges are a common source of adhesion in many materials and can arise from many different situations such as:

- Sintering
- Partial melting
- Chemical reaction
- Hardening binders
- Recrystallization

If the temperature of a system rises above approximately two thirds of the melting temperature or above the softening temperature of the material sinter bridges can easily form. The strength of the sinter bridges will be depend on both the temperature reached and the pressure applied. Partial melting may occur when the rough peaks on the material surface at the contact point melt due to the heat caused by friction or pressure of the contact. This is more common in material with low melting or softening temperatures.

Chemical reactions often lead to the formation of solid bridges and depends on the materials involved and their reactivity. The presence of hardening binders may also lead to the formation of solid bridges. Both of these binding mechanisms are often activated by the presence or introduction of moisture to a system. Chemical adhesion occurs when atoms of two contacting (or extremely close) materials swap or share electrons. This process is knows as either ionic or covalent bonding. These bonds are much stronger than the third type of chemical bonds – hydrogen bonds. The chemical bonds that form are only effective over extremely small separation distances, in the range of one nanometre.

Recrystallization can occur as a result of temperature fluctuations, such as between day and night even within a sealed bulk solid. Materials such as salts are particularly susceptible to recrystallization even if there is only a small amount of moisture present. This is a time dependent process in which the bonds that form grow stronger with time.

2.2.2 Mechanical Adhesion

Mechanical adhesion refers to adhesion generated through the physical interlocking of the voids and/or pores of a material surface. Mechanical adhesion can occur on many length scales, from nano-scale surface roughness to particle interlocking. An excellent example of the concept of mechanical adhesion is Velcro®, where hooks on one piece interlock with loops on another to form a strong bond. While mechanical adhesion can contribute to the adhesive forces in granular materials, generally it is not a dominant source and as such, and will not be discussed further.

2.2.3 Electrostatic Adhesion

Electrostatic adhesion develops due to a difference in electro-negativity between two materials. As two surfaces come in contact, the transfer of electrons between the two materials creates positive and negative charges which lead to a strong adhesive bond forming from the oppositely charged materials. Electrostatic attractive forces are defined by Coulomb's law which was established in the late eighteenth century by the French physicist. A common example of electrostatics is in xerography (photocopying). However, the electrostatic force is negligible compared to van der Waals forces for fine dry neutral powders [Rietema, 1991]. More detailed discussion on the underlying mechanics is available [Burnham and Kulik, 1999; Israelachvili, 2011].

2.2.4 Van der Waals Forces

The van der Waals force is the sum of the attractive and/or repulsive forces that exist between molecules and was first identified by the Dutch scientist Johannes Diderik van der Waals. The force can be defined as:

> *The attractive or repulsive forces between molecular entities (or between groups within the same molecular entity) other than those due to bond formation or to the electrostatic interaction of ions or of ionic groups with one another or with neutral molecules.* [IUPAC, 2009].

The term includes forces arising from permanent dipole-dipole interactions (Keesom), permanent dipole-induced dipole (Debye) and London dispersion forces. Van der Waals forces are one of the most common sources of cohesion as they are an ever present force, unlike other forces such as chemical forces or magnetic forces. All three types of forces have the same separation distance dependency [Butt *et al.*, 2003]. The van der Waals force is a long range intermolecular force which can have a significant effect on microscopic bodies separated by a few nano-meters. The van der Waals force between

two particles is defined by Equation (2.9) [Israelachvili, 2011; Walton, 2008] where A is the Hamaker constant, R^* is the contact radius and s is the separation distance between the particles.

$$F_{vdw} = \frac{AR^*}{6s^2} \tag{2.9}$$

Generally the Hamaker constant [Hamaker, 1937] is in the order of 10^{-20}J for most materials, which means even for very small particles travelling with a relatively low velocity, the kinetic energy is significantly larger than the van der Waals binding energy [Herminghaus, 2005]. As can be seen from Equation (2.9) the van der Waals force is dependent on the inverse square of the separation distance between the two spheres. This means the force will drop by two orders of magnitude at 4nm separation and four orders of magnitude at 40nm [Walton, 2008]. It can be concluded that van der Waals forces can be neglected in granular bulk solids for particles sizes larger than a few hundred microns [Herminghaus, 2005; Seville *et al.*, 2000] due to the constraints of particle size and separation. For fine grained, dry bulk solids van der Waals forces tend to be dominant while for moist bulk solids liquid bridges and solid bridges between particles tend to be more important [Schulze, 2008*a*].

In DEM simulations for dry uncharged particles the van der Waals forces are accounted for by the widely accepted JKR and DMT models [Derjaguin *et al.*, 1975; Johnson *et al.*, 1971] for smooth spherical particles. However, the roughness of a particle surface is known to have an effect on the on the adhesion force generated during contact. On a rough surface the contact takes place places between the surface asperities and not the particles itself, which means a significantly smaller contact area [Butt, 2008; Castellanos, 2005; Li *et al.*, 2006; Prokopovich and Starov, 2011]. Contact models that account for van der Waals forces and asperities have been developed [Cooper *et al.*, 2000; Rabinovich *et al.*, 2000*a*,*b*]. Details of the commonly used JKR model are discussed in further detail in Chapter 3.

A more detailed discussion of van der Waals forces and interactions (either inter-molecular or inter-particle) and the underlying theory can be found in several books [Israelachvili, 2011; Parsegian, 2006] and journals [Castellanos, 2005; Li *et al.*, 2004].

2.2.5 Liquid bridges & Capillary Forces

The introduction of moisture into a granular material is known to change its behaviour significantly [Herminghaus, 2005; Mitarai and Nori, 2006; Nowak *et al.*, 2005]. The

smallest amount of moisture in the air may be enough to lead to the formation of individual liquid bridges between particles in the pendular state, which induces cohesion due to the surface tension of the liquid. As early as the 1920's capillary/liquid bridges [Fisher, 1926; Haines, 1925] were known to cause adhesive forces between particles. Liquid bridges between spherical objects have been studied by many, with most attention paid to contacts involving a single liquid bridge [Clark and Mason, 1967; Hotta *et al.*, 1974; Mason and Clark, 1965; Willett *et al.*, 2000].

The cohesive force of the liquid bridge is dependent on the volume of the bridge, and hence the amount of moisture present. There are four known states of liquid content [Mitarai and Nori, 2006] within granular materials (see Figure 2.5): Pendular (driest state), Funicular, Capillary and Slurry; with cohesion arising in the pendular, funicular and capillary states. At low moisture contents stable liquid bridges are only possible at small separation distances. The development of liquid clusters occurs in the funicular stage until all pores are full of water in the capillary stage. Liquid bridges cease to exist in wet granular materials when the material becomes saturated at which point there will no longer be adhesive interactions between particles.

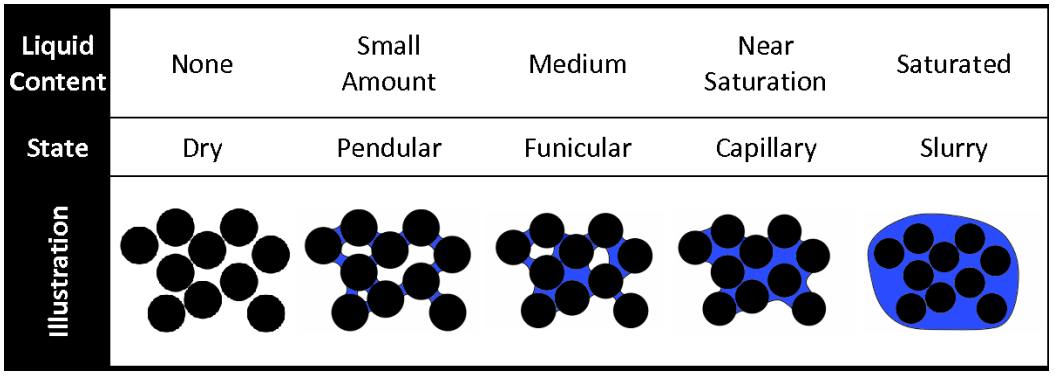

Figure 2.5: Liquid bridge regimes - Illustration of moisture content for various stages of capillarity

The capillary pressure is calculated from the Young-Laplace equation before the capillary force is given by Equation (2.10) [Butt and Kappl, 2009; Mitarai and Nori, 2006; van Honschoten *et al.*, 2010], where R is the radius of the sphere and $\theta_{1,2}$ are the contact angles at the surfaces.

$$F_{cap} = -2\pi R\gamma_L \left(\cos\theta_1 + \cos\theta_2\right) \tag{2.10}$$

The study of capillary forces has been mainly confined to liquid bridges within the pendular state [Adams *et al.*, 2002; Iveson *et al.*, 2001; Richefeu *et al.*, 2006*a*,*b*; Willett *et al.*, 2000], both in terms of experiments and numerical analysis, where the study

is generally in relation to two bodies. While it may be possible to examine capillary bridges in the pendular state for two particles [Fournier *et al.*, 2005] the study of funicular force in a random granular assembly is more difficult. Kohonen *et al.* [2004] have shown that the number of liquid bridges increase with increasing moisture content, reaching a stable level above a critical value.

The presence of liquid within a granular material is known to affect the tensile strength of the material [Pierrat and Caram, 1997], its flow properties [Samadani *et al.*, 2002; Tegzes *et al.*, 2003] and its agglomeration behaviour [Iveson *et al.*, 2001]. The presence of fines in the granular material and its interaction with both the particle and moisture also has to be accounted for. However, the relationship of the mechanical properties of wet granular material to its liquid content is not yet fully understood and still being investigated [Kohonen *et al.*, 2004; Mitarai and Nakanishi, 2009]. The addition of small amounts of moisture has been found to reduce segregation in some mixtures [Anand *et al.*, 2010; Chou *et al.*, 2010; Samadani and Kudrolli, 2000, 2001] due to the additional cohesion. However cohesion is not the only effect resulting from the presence of a liquid in granular materials. An obvious example is lubrication of friction between solids [Xu *et al.*, 2007].

Liquid bridge volumes need to be solved numerically and can be seen as too computationally intensive for DEM simulations. By using a toroidal approximation of the liquid bridge, the force can be calculated from either of two methods, the boundary method or gorge method [Hotta *et al.*, 1974]. Lian *et al.* [1993] showed that the difference between the numerical solution of the approximation and experimental results for the approximate gorge method was less than 10%. Details of implementation of capillary force models in DEM are presented in Chapter 3. A detailed review on the field of capillary forces and wet granular materials has previously been carried out by many authors [Butt and Kappl, 2009; Fournier *et al.*, 2005; Herminghaus, 2005; Iveson *et al.*, 2001; Kohonen *et al.*, 2004; Mitarai and Nori, 2006; Simons, 2007] and as such will not be presented in detail here.

2.2.6 Additional Forces

Other methods of inducing adhesive forces also exist such as magnetism, which will only affect magnetic materials such as metals. While magnetism may be used in some industrial process such a separation, it is unlikely to develop naturally.

2.3 Silo Flow

Silo wall pressures are normally calculated based on a differential force balance for a section of a silo. Janssen solved this problem by using the assumption that the vertical normal stress is proportional to the lateral normal stress [Janssen, 1895; Sperl, 2005]. For a circular silo of cross-sectional area A and with the boundary condition that the pressure is equal to zero at the free surface, Janssen's equation [Brown and Nielsen, 2004; Nedderman, 1992] can be written as :

$$q = \frac{\gamma R}{\mu K}\left[1 - \exp^{(-\mu K z/R)}\right] \tag{2.11}$$

where q is the vertical pressure, R is the hydraulic radius, μ is the coefficient of wall friction, γ is the bulk unit weight and K is the lateral pressure ratio. The hydraulic radius R is defined for a circular silo by Equation (2.12) and for a rectangular silo by Equation (2.13), where a and b are the dimensions of the silo base.

$$R = \frac{D}{4} \tag{2.12}$$

$$R = \frac{ab}{2\,(a+b)} \tag{2.13}$$

The horizontal wall pressure can then be calculated from Janssen's assumption that the horizontal pressure is related to the vertical pressure by the lateral pressure ratio. The horizontal wall pressure P_H can then be found from Equation (2.14).

$$P_H = Kq \tag{2.14}$$

For silos that are very tall the pressure is only a function of the diameter and not the height, which is the main reason many industrial silo will tend to be tall and slender.

2.3.1 Flow Pattern

Despite Janssen's early work it was more than half a century before the first scientific publications on bulk flow in silos appeared 1947 by Brown and Hawksley on cohesionless material during discharge [Brown and Nielsen, 2004]. Following work by Jenike [1964] in the 1960's, the flow pattern from silos was described as one of two distinct states: mass flow and funnel flow, which are so called based on the flow patterns they

exhibit, are show in Figure 2.6. In mass flow (Figure 2.6a), as the name suggest, the whole volume of the material flow as one, whereas in funnel flow (Figure 2.6b) only the central part of the silo has movement with large static zones to be found along wall and shallow inclined or flat bases. Following Jenike's work other researchers also proposed further procedures but Jenike's method remains the most widely used.

The distinct flow patterns have remained largely unchanged, although the funnel flow category has been sub-divided in to pipe flow and mixed flow [Rotter, 2001; Zhong *et al.*, 2001]. With pipe flow a channel exists all the way from the outlet to the free surface at the top off the material. In mixed flows there is mass flow up to an effective transition point where it switches to funnel flow.

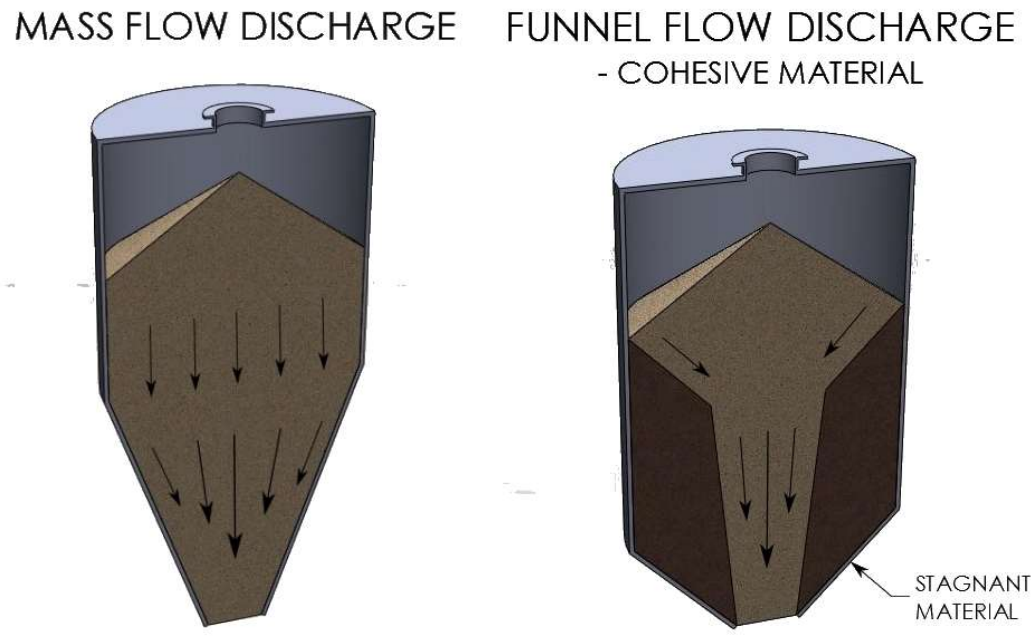

(a) Mass Flow **(b)** Funnel Flow

Figure 2.6: Typical silo flow patterns - Common flow modes during discharge [Jenike.com, 2013]

There are many types of problems in silo and hopper design that need to be considered:

- Incomplete emptying – Stagnant zones cause old material to get trapped in the silo and is not completely removed during discharge. Not acceptable for perishable goods
- Blockage – cohesion or mechanical arching around the outlet cause a blockage. Time consolidation and caking may also play a role here

- Slow Discharge – the material does not discharge at the required rate for the process
- Rat-holing – the core of the hopper/silo discharges leaving a hole through the stored material
- Segregation – the material is not mixed properly

Mass flow is usually the preferred discharge mode for a silo as it prevents many of the above problems. Generally a hopper of angle $> 30°$ is required for mass flow. In certain cases, it may be preferential to design for funnel flow, such as the additional capacity that can be achieved from lower hopper angles.In order to design for mass flow, a relationship between the hopper half angle, the wall friction angle and internal angle of friction in the solid was derived [Jenike, 1964]. While this gives a good prediction of when mass flow or funnel flow will occur, the definition of the funnel flow cannot be easily predicted. The latest Eurocode 1 [British Standards Institution, 2006] also derives a similar relationship for mass flow or funnel flow but does not take in to account the angle of internal friction of the solid.

The main remaining problem for mass flow silos is that of arching, which causes blockage. Mechanical arching can occur for coarse grained materials due to interlocking and wedging of particles. Normally this can be avoided by having a sufficiently large outlet, typically in the range of 6-10 particle diameters [Brown and Nielsen, 2004; Rotter, 2001; Schulze, 2008*a*]. While this is usually enough to prevent a stable arch forming, it can sometimes lead to pulsating flow where arches form and collapse. However for fine, cohesive particulate solids such as powders the arching is not related to the particle size and shape, but the adhesion between the particles, and therefore a sufficiently large outlet may not prevent cohesive arching.

2.3.2 Further Experimental Studies

Many factors are known to affect the type of flow achieved during discharge and include the filling method, the geometry of the silo and the flowability of the stored materials [Bradley *et al.*, 2000; Rotter, 2001; Sukumaran and Ashmawy, 2003; Vanel *et al.*, 2000; Zhong *et al.*, 2001]. However much of the work has been done for free-flowing, cohesionless materials [Nedderman *et al.*, 1982; Tüzün *et al.*, 1982; Vanel *et al.*, 2000]. Rose and Tanaka [1959] suggested that a cohesion term be included in the discharge rate correlation but did not specify at what porosity, which has a large influence on the level of cohesion generated, the cohesion factor should be measured.

Much work has been done in the study of silo discharge since the early work by Jenike. Discharge devices and flow promoters are often fitted to silo hoppers to improve flow patterns and discharge rates from them. These can be in the form of flow promoting inserts and feeders. A detailed discussion on these is presented elsewhere [Härtl, 2008; Härtl *et al.*, 2008; Schulze, 2008*a*; Tüzün and Nedderman, 1985*a*,*b*; Wójcik *et al.*, 2012; Yang and Hsiau, 2001]. The use of inserts has been shown to widen the flow channel and achieve mass flow in most cases. The wall normal stress distribution is often significantly affected by the inclusion of inserts in a silo, particularly in the hopper section where the presence of the insert has an effect.

A comprehensive overview of pressure and flow measurements is silos has previously been carried out by [Chen *et al.*, 1996; Ding, 2005; Härtl, 2008; Rotter *et al.*, 1995] and will not be discussed in detail here. The wall pressure developed in silos has been extensively covered [Chen *et al.*, 1998; Ooi *et al.*, 1996; Ooi and Rotter, 1990, 1991; Ooi and She, 1997; Rotter *et al.*, 1998; Sanad *et al.*, 2001] and also the relationship between wall pressure and flow patterns has also been investigated [Chen *et al.*, 2007; Ooi *et al.*, 1998; Sanad *et al.*, 2001]. Studies, both experimental and numerical, have also been carried out on the dynamic effects that lead to "silo music" or "honking" [Buick *et al.*, 2005; Muite *et al.*, 2004; Roberts and Wensrich, 2002; Schulze, 2008*b*; Wensrich, 2002, 2003; Wilde *et al.*, 2008, 2010].

2.3.3 Flow Rate

Flow rate is typically defined by Equation (2.15) as the mass which passes through a given opening per unit of time. The common unit is kgs^{-1}.

$$\dot{m} = \lim_{\Delta t \to 0} \frac{\Delta m}{\Delta t} \tag{2.15}$$

Over the year numerous attempts had been made at relating the discharge rate to the density of the system and the opening through which it flows. Early researchers found that the discharge rate varies with a raised power of the opening width, but there discrepancies in the values which covered a range of 2.8 – 3.1 [Brown and Richards, 1960; Franklin and Johanson, 1955]. This variation was resolved by Beverloo *et al.* [1961] where a linear relationship between the outlet width and a width$^{(5/2)}$. A modification to account for the layer of particles at the edges of the outlet where there is little or no flow was included and is known as the Beverloo constant, k. This relationship has become known as the Beverloo law and is one of the most frequently used correlations for particle discharge rates from hoppers. The degree of compaction during filling is

known to have little effect on the discharge rate [Huntington and Rooney, 1971].

2.3.3.1 Beverloo Equation

The Beverloo equation is used for types of funnel flow and was derived for a flat-bottomed cylindrical silo with cylindrical opening. The discharge rate $\dot{W}$ was found to vary linearly with the (corrected outlet width)$^{5/2}$.

$$\dot{W} = C\rho_b\sqrt{g}(W_o - kd)^{\frac{5}{2}} \tag{2.16}$$

where k is the Beverloo constant, d is the particle diameter, W_o is the opening width and ρ_b is the bulk density after filling. The constant C is empirically found to be in the range of 0.55 - 0.65. the Beverloo constant k is generally agreed to be a shape constant that varies somewhere between approximately 1.3 and 2.9 depending on both particle shape and hopper angle. An alternative is given for non-circular outlets by Equation (2.17), where the hydraulic diameter D_H, given by Equation (2.18), can be used instead.

$$\dot{W} = C\rho_b\sqrt{g}(D_H - kd)^{\frac{5}{2}} \tag{2.17}$$

$$D_H = \frac{4 \times Outlet\,Cross\,Sectional\,Area}{Outlet\,Perimeter} \tag{2.18}$$

The Beverloo equation has been modified to account for various hopper geometries and the discharge rate for rectangular openings and flat bottoms where $L \gg W_0$ was proposed by Myers and Sellers [1971] and is given by:

$$\dot{W} = 1.03\rho_{flow}\sqrt{g}\,(L - kd)\,(W_o - kd)^{\frac{3}{2}} \tag{2.19}$$

The effect of hopper angle was included by Brown and Richards [1965] and given by:

$$\dot{W} = \dot{W}_{flat-bottom}\frac{1 - \cos\frac{3}{2}\theta}{\sin\frac{5}{2}\theta} \tag{2.20}$$

where θ is the hopper angle from the vertical.

There is a general consensus that provided a hopper width, W is at least a minimum of $2.5W_0$ [Brown and Richards, 1960], the discharge rate is independent of hopper width.

At smaller values of W, larger discharge rates should be observed until $W = W_0$, at which point the whole mass accelerates with gravity [Nedderman *et al.*, 1982]. Particle diameter has been reported to have little effect on discharge rates provided that the opening diameter is sufficiently large in comparison to the particle diameter to prevent problems like arching. Orifices less than six times the particle diameter have been shown to produce inconsistent and intermittent discharge [Nedderman *et al.*, 1982]. Particle-Wall friction has also been reported to have little or no effect on the discharge rate, most likely due to the limited number of wall contacts in comparison to particle-particle friction, although it has been shown that there is a slight decrease in flow rate with increasing wall friction [Nguyen *et al.*, 1979].

2.4 The Discrete Element Method – A Brief Introduction

The literature on DEM has been covered extensively in the past by many researchers and this section serves only to introduce the method and provide the key elements to the method. A comprehensive review of the major applications and findings of DEM work in general has been compiled by Zhu *et al.* [2007, 2008]. A more detailed introduction to the workings of the DEM is presented in Chapter 3.

Since its development in the 1970's the Discrete Element Method (DEM) is today becoming a widely exploited method of dealing with engineering problems that deal with granular materials. The method was first developed for analysis of rock mechanics [Cundall and Strack, 1979] but has since been employed to look at problems ranging from powder flow to bulk solids handling in a variety of different industries. The primary virtues of DEM are to be found in its ability to handle wide ranging contact laws and material constitutive behaviours. Its flexibility also allows it to be coupled to computational fluid dynamics (CFD) solvers to simulate multi-phase flows. With the explosion in cheap computing power over the past two decades the amount of research in the DEM area has increased significantly in areas such as:

- Development of improved contact models
- Development of non-spherical particles
- Experimental validation of the DEM
- Increased used of coupling between DEM, FEM and CFD
- Large scale industrial applications – DEM can now be used to assess design for storage and handling systems

While output from DEM is normally local contact information, averaging methods allows for this to be transformed in to a continuum description for quantities such as density, velocity and stress.

However DEM's major flaw is its computational requirement which stems from being an explicit simulation method in which many timesteps are required to ensure numerical stability. The amount of simulation time required increases significantly with increasing number of particles. It is also difficult to incorporate crushing and pore-pressure within an assembly of particles.

2.5 DEM Studies

2.5.1 Shape Representation

Particle shape representation is an important component of any DEM simulation and it is necessary to study the effect of grain shape on the mechanical behaviour of a soil. The shear strength of a granular material is affected by the dilation and contraction properties of the material which are in turn dependant on the particle shape and size distribution. Another reason for capturing particle shape relates to breakage – while most DEM simulations do not account for breakage directly, where it is accounted for particles that are angular and irregular in shape are much more susceptible to breakage than spherical particles.

While Spherical particles are simple to implement for contact and force resolution, the spherical nature means that the particles are susceptible to large rotations and, as such, are not capable of reproducing the behaviour seen in irregular or angular particles and failure to incorporate a proper shape consideration can mean that an important characteristic of the material is missed. By restricting the rotation of particles through non-spherical shapes the shear strength of a materials is enhanced [Thomas and Bray, 1999]. It has been shown that in the in the case of spherical particles highly frictional material cannot be successfully modelled and the bulk friction generated saturates at lower friction angles of approximately 30 degrees for spherical particles [Härtl and Ooi, 2011; Katagiri *et al.*, 2010; Matsushima and Katagiri, 2009; Shimizu *et al.*, 2004]. The static and dynamic angles of friction have also been found to increase significantly in rotating drum simulations between spherical and non-spherical particles [Walton, 1994*a*; Walton and Braun, 1993]. The effect of particle shape on silo discharge is significant. They found that spherical particles always lead to a situation of mass flow, whereas by including some shape representation a resistance to flow was generated and lower discharge rates were achieved [Cleary and Sawley, 2002].

The effect of particle shape can be seen in many other different situations, such as where the interlocking effect of the non-spherical particles comes in to play. Shape has been used to simulate large angular railway ballast [Lim and McDowell, 2005; Lu and McDowell, 2006], agricultural grains [Abbaspour-Fard, 2004], soils [Ashmawy *et al.*, 2003; Kock and Huhn, 2007; Sallam and Ashmawy, 2009] and pharmaceuticals tablets [Ketterhagen, 2011; Song and Turton, 2007; Suzzi *et al.*, 2012].

There are many different methods of including particle shape but the [Favier *et al.*, 2001, 1999; Ferellec and McDowell, 2008, 2010; González-Montellano *et al.*, 2012*b*, 2011; Jensen *et al.*, 1999, 2001; Matsushima *et al.*, 2003] sometimes referred to as "clumps", ellipsoidal particles [Donev *et al.*, 2004, 2005; Lin and Ng, 1995; Ng, 2004; Ng and Lin, 1997; Ouadfel and Rothenburg, 1999; Wang *et al.*, 1999] or polygonal particles [Fu and Harvey, 2008; Peña *et al.*, 2008; Ramm *et al.*, 2010]. Multi-sphere particles are the commonly implemented method in commercial codes such as EDEM and PFC^{3D}. Generally speaking, if an ellipsoid is modelled using the multi-sphere approach, the results tend to converge as the number of spheres in the cluster increase and a high fidelity is achieved [Markauskas *et al.*, 2009]. Creating high fidelity representation of actual particles adds considerable computational cost from the increased number of spheres required to define the particle shape. It has been suggested that capturing the general particle with as few spheres as possible provides sufficiently accurate results without the need for computationally intensive high fidelity shapes [Chung, 2006; Härtl, 2008].

The effect of particle shape on the lateral pressure ratio and packing has been investigated [Wiącek *et al.*, 2012*a*,*b*]. As the particle shape was changed from spherical particles to overlapping paired particles with an aspect ratio of 1.6 it was seen that the porosity decreased while the stiffness of the assembly increased. A similar trend was noted for the lateral pressure ratio; as the aspect ratio increased from 1 to 1.6 the lateral pressure ratio was found to decreases significantly. This is partly due to the higher angle of friction found for non-spherical particles which arises from the greater particle interlocking and higher number of contacts.

2.5.2 Particle Friction

The effect of inter-particle friction has a significant effect on the mechanical response of a particulate system. While increasing inter-particle friction may increase the shear strength of the material in a similar manner to non-spherical particles, there are also other effect. Under axial compression the additional friction has the effect of increasing the stiffness of the assembly through a reduction in the freedom of movement and rotation [Sheng *et al.*, 2004].

2.5.3 Sample Size Effect

An important consideration for DEM simulations is that of sample size – how many particles is enough to be representative? Due to the high computation cost of DEM, it is always a consideration to make the simulation as small as possible without affecting the results. According to Eurocode 1 [British Standards Institution, 2006] the recommended diameter for the shear cell should be at least 20 times the size of the largest particle diameter, and for the determination of the lateral pressure ratio a specimen diameter (D) at least 5 times the diameter of the largest particle with a height in the range of 0.3-0.4D. These provide a guideline for what should be considered in a DEM simulation also. Masson and Martinez [2000] found that a Representative Elementary Volume (REV) of at least 7-8 particle diameters was sufficient for parameters such as porosity and coordination number while a REV size of at least 12 particle diameters should be used for the stress tensor. A study of the response of the load-displacement relationship for rapeseed samples of various thickness under uniaxial compression [Rusinek *et al.*, 2007] showed significant variations when the sample thickness was less than 11 particle diameters. More recently Wiącek *et al.* [2012*b*] investigated the effect of REV's for a uniaxial confined compression test of granular materials and found that provided the volume was approximately five particle or greater in dimension, there was little effect on the computed results.

A solution to avoid boundary effects is to use periodic boundaries in the DEM simulations which allows a sample to be considered without associated boundary effects of a geometry and has been employed by many researchers [Anand *et al.*, 2008; Cleary and Sawley, 2002; Martin *et al.*, 2003; Mehrotra *et al.*, 2009; O' Sullivan and Cui, 2009].

2.5.4 DEM Implementation of Adhesive Forces

DEM simulations based on van der Waals type forces have mainly been used to study the packing of nano-sized particles [Yang *et al.*, 2007, 2000, 2003*a*, 2008, 2006] where the packing structure was shown to become significantly looser as the particle size decreased and the cohesive granular bond number increased and is comparable with the experimental data [Feng and Yu, 1998]. Similar trends have also been noted with capillary force models [Gröger *et al.*, 2003; Xu *et al.*, 2004; Yang *et al.*, 2003*b*]. Dong *et al.* [2006] incorporated both liquid and van der Waals forces in a study on packing behaviour and the results show the dependence of packing structure on both liquid and van der Waals forces.

Another area where inter-particle forces have been used is that of powder compaction. Several different mechanisms exist within compaction, particle re-arrangement, plastic

deformation and breakage. Uniaxial tests and indentation tests using the JKR theory for inter-particle forces [Hassanpour and Ghadiri, 2004, 2007; Moreno-Atanasio *et al.*, 2005; Wang *et al.*, 2008] have been used to assess the flowability of powders at low consolidation pressures where the effect of the inter-particle forces on the initial packing plays a key role. While a qualitative match was found there was a large variation from the experimental values.

The compaction of powders for tableting has been studied [Mehrotra *et al.*, 2009] using a square well potential. The effect of adhesive inter-particle forces was found to cause longer filling times of the die and also larger forces were required during the compaction to the final density. A similar scheme [Baxter *et al.*, 2000] was used to study cohesive powder discharging under gravity for different conical hopper half-angles and for a number of different values of the square-well depth. The scheme was found to capture most of the essential mechanics of fine powder discharge from conical hoppers. The DEM scheme employed is based on the use of a square-well potential which attempts to account for the adhesion of particles from all electrostatic or van der Waals forces together as one force. The square well potential is a rough approximation of the Lennard-Jones potential [Jones, 1924] which is typically used to describe the repulsive and attractive forces on particles. Unlike the Lennard-Jones potential where the level of adhesion/repulsion is constantly varying with the separation distance, the square well method is an on/off solution where the adhesion force is a fixed value that is applied when the separation distance falls within a certain range.

Anand *et al.* [2009] implemented a capillary force model[Mikami *et al.*, 1998] to model discharge from a rectangular hopper [Anand *et al.*, 2008] and a reasonable match between the simulation data and modified Beverloo constant for cohesive discharge was observed. Gröger *et al.* [2003] used a capillary force model to carry out tensile tests on fine, granular materials and the model displayed a good general agreement for tensile tests in agglomerates which consisted of mono-sized spherical particles. They also found that the surface roughness is an important parameter that has a large influence on stresses in a wet granular system due to its pre-stretching of the liquid bridges. Remy *et al.* [2012] implemented the liquid bridge model proposed by Mikami *et al.* [1998] in EDEM through the extended API features to study the effect of wet particles in a bladed mixer. They found that a low moisture contents diffuse and convective motion was aided by the formation of small agglomerates while the opposite behaviour was observed at high moisture contents.

Tykhoniuk *et al.* [2007] conducted 2D and 3D DEM simulations of the Jenike shear cell and the biaxial box testers using a lumped parameter contact model to account for

the adhesive forces [Luding, 2008*b*]. A qualitative agreement was found between the simulations and experiments.

Grima and Wypych [2009, 2010] have used the linear cohesion model in the EDEM code to simulate discharge from a hopper and the resulting slump formation. For cohesive material it was found that following a calibration of parameters an accurate representation of the cohesive solid could be predicted by the DEM simulation.

2.5.5 Silo Flow & Discharge

While much of the initial computational work carried out to investigate silo pressure and flow was by the Finite Element Method (FEM) [Karlsson *et al.*, 1998; Ooi and Rotter, 1990; Ooi and She, 1997; Rotter *et al.*, 1998; Sanad *et al.*, 2001], due to improvements in computing DEM is becoming much more widely used as it becomes possible to simulate large scale systems on a desktop machine.

Masson and Martinez [2000] confirmed the efficiency of DEM for the simulation of quasi-static granular flow problems such as silos. They found the for a 2D flat bottomed silo that computed wall pressures at the end of filling are in agreement with experimental and FEM numerical results. They also found that microscopic parameters, namely friction coefficient and contact stiffness, appear to play a major role in the contact network connectivity, macroscopic porosity, stress anisotropy within the granular material and these appear to have a significant influence on flow and stresses during discharge.

Parisi *et al.* [2004] performed 3D DEM simulations of an industrial silo with 170,000 cohesionless particles using a layered method to deal with the large size of the simulation. The simulations investigated the presence of inserts and showed that inserts significantly effected flow patterns and lead to higher localized loads on and around the inserts. Goda and Ebert [2005] modelled the initial filling and discharge of various silo geometries (both flat bottom and inclined hoppers) with 40,000 cohesionless spherical particles. They found that pressure distributions calculated were in accordance with previous 2D simulations [Yang and Hsiau, 2001] and theoretical work.

Ketterhagen *et al.* [2007] presented a comprehensive validation study of discharge with a focus on segregation. 3D simulations were carried out of an experimental setup; derived from technical standards; at a 1:1 scale, with the number of particle varying depending on the particle size ratios used. They found a close match to the experimental result in most cases, with the discharge rate being slightly under predicted in some cases due to varying friction or fill in homogeneity. Particle parameters such as fines

mass-fraction and particle size range as well as hopper angle and shape were found to be significant factors that affect the flow pattern and discharge rate.

Parametric studies of the effect of various particle and hopper properties on silo discharge have been carried out [Anand *et al.*, 2008; Ketterhagen *et al.*, 2009] using 3D DEM simulations with cohesionless particles. At low values of particle-particle friction (0.05) the discharge rate and fill height are not independent and the rates increase with increasing fill height. The critical friction value was found to be approximately 0.2. Values below 0.2 were said to behave like fluids At high friction values (0.84) discharge rate remains constants regardless of fill height and is consistent with Janssen's theory. The effect of particle-wall friction has been found to be negligible when considering its effect on discharge rates and is due the significantly larger volume of particle-particle contacts (as opposed to particle wall contacts) which are more likely to affect the flow regime and discharge rate. The particle-particle friction coefficient was found to have a significant effect on the measured discharge rate, where the rate of discharge reduced with increasing friction. Until the hopper angle from vertical is greater than a critical angle there is little variation in the discharge rate of flow mode. Once the critical is passed the discharge rate increases rapidly and the flow mode begins to change from funnel flow to mass flow. The critical angle is the flow angle of the stagnant-flowing boundary inside the hopper [Anand *et al.*, 2008]. Hopper flows contain mainly long duration, highly frictional and sliding contacts between particles and as such the coefficient of restitution has negligible effect on the discharge rate [Anand *et al.*, 2008; Ristow, 1997]. The discharge rate also agreed well with predictions for the modified Beverloo equation for rectangular geometries.

Ketterhagen *et al.* [2009] found that mass-flow occurs for small hopper wall angles and small wall friction angles. As either or both of these angles increase, the flow transitions to the funnel-flow regime. The boundary between mass and funnel-flow is generally similar to that predicted by Jenike. In some cases particle rotation was also prevented, to effectively mimic the behaviour of non-spherical particles, and the observation of the agreement with the flow boundary showed improvements reinforcing that spherical particles and the unrealistically associated large particle rotations are generally not accurate models for most particulate materials [Ketterhagen *et al.*, 2009].

Balevičius *et al.* [2008, 2011*a*,*b*] have carried out various DEM and experimental studies to validate DEM simulations for silo discharge. They concluded that that the DEM analysis provides an accurate prediction of flow parameters provided the material parameters were carefully selected. Good agreement was found between the wall pressures measured and those computed by the numerical model and the main peaks of

the discharge overpressures were also captured. A close fit of Janssen's solution to the experimental observation was found, when Eurocode 1 values for K were adopted. Balevičius *et al.* [2012] have also carried out DEM simulations to quantify the effect of rolling friction on discharged from flat bottomed bins. They found that experimentally measured wall pressure values in the experiment were quite accurately matched by the numerical analysis, for both the filling and the discharge processes. The rolling friction coefficient was found to have a minimal effect on the wall pressure values, especially at filling. Rolling friction was found to have an effect on the velocity profiles - it was shown to reduce the horizontal velocity. The inclusion of rolling friction was also found to improve the correlation between the experimental and simulation result during the final part of discharge. Again the importance of non-sphericity is shown.

Tao *et al.* [2010] used multi-sphere DEM to simulate the discharge of corn grains from a rectangular hopper and found that a quantitative match was found to the experimental flow pattern demonstrated by Coetzee and Els [2009]. The effect of friction on discharge was also found to confirm the findings of Anand *et al.* [2008] with the result showing that discharge rate decreases with the increasing friction coefficient.

González-Montellano and co-workers have carried out numerous DEM studies on Silo filling and discharge. Numerical simulations of glass beads and maize grains were compared to experimental results on set-ups of equal dimensions [González-Montellano *et al.*, 2011]. Following calibration of the friction parameters which affected the initial density and discharge rate a close match to the experimental results was achieved. They found that en-masse filling leads to unrealistic wall pressure being developed [González-Montellano *et al.*, 2012*b*] and should be avoided in cases where the values of wall pressure are of particular interest. Progressive filling was shown to negate this effect by allowing the development of natural arching found in the real granular solids. They also presented a detailed study on the determination of parameters for calibrating DEM models from experiments [González-Montellano *et al.*, 2012*a*].

Anand *et al.* [2009] implemented a pendular liquid bridge model [Mikami *et al.*, 1998] to simulate discharge of a cohesive granular material from a rectangular hopper [Anand *et al.*, 2008]. The cohesive part of the model is a pendular bridge model with an additional viscous resistance force is included in the normal direction. No viscous resistance is included in the tangential direction as this has been shown to have a negligible effect [Hsiau and Yang, 2003]. In the simulation steel particles are assumed and a bond number of 1 is specified. Moisture content is set at 2%. It is assumed that every particle has a constant thickness of water around it. Liquid bridges between particles and geometry are treated the same as between particles. The effect of the changing bond number on

the hopper discharge rate is studied and a reasonable match between the simulation data and modified Beverloo constant for cohesive discharge where the basic discharge rate trend given in the Beverloo correlation is also valid in the presence of cohesion. A correlation similar to Beverloo's was also proposed for cohesive articles but was found to only provide an accurate estimate at a low bond number. The influence of the liquid content of the sample (1-23%) was found to have a much less significant effect than that of the Bond number. At low Bond numbers, the results were similar across all liquid content levels, while for high Bond numbers the discharge rate dropped as the liquid content increased [Anand *et al.*, 2009]. No change in flow regimes (from funnel to mass flow) were reported as a result of the additional cohesion. Xu *et al.* [2002] also found that the inclusion cohesion leads to significantly longer discharge times due to the formation of clusters.

A further study on segregation [Anand *et al.*, 2010] found that for Bond numbers equal to or greater than one, where the maximum cohesive force on a particle is greater than or equal to the particle's weight, there is significantly reduced and discharge segregation discharge. A Bond number greater than one was found to have little additional effect on segregation since the cohesive force on small particles is already sufficiently large to overcome the small particle's weight. However, Bond numbers greater than were found to have a significant influence on the discharge rate from the hopper, with the flow decreasing within increasing Bond number.

2.6 Numerical Studies & Validation

The use of computer aided design (CAD) and numerical simulations has been on the increase in recent years. While the Finite Element Method (FEM) has been rigorously verified and validated since its inception in the early 1960's the same cannot be said of the Discrete Element Method yet. Until recently the majority of discrete element simulations computations were assumed to be displaying the correct results without any detailed experimental validation. Even as late as the end of the 1990's confidence in DEM results was low. This was highlighted by a study by Holst *et al.* [1999], where a simple DEM problem of filling a hopper and predicting wall pressure was sent out to various groups to carry out the simulation and report back the results anonymously. The results highlighted the need for proper validation on a community basis – some simulations failed to even satisfy the basic vertical equilibrium. There is still a question today as to whether DEM can actually produce quantitative predictions of salient values rather than just qualitative representations of a system. To achieve quantitative predictions it is necessary to both calibrate and validate the DEM model and it is at this point that an important distinction needs to be drawn between calibration and validation.

Chung [2006] conducted a comparative study between physical experiments and simulated numerical experiments and found that DEM could produce quantitative predictions of dense quasi-static systems such as the confined compression test or rod penetration. A suite of benchmark tests was also suggested for verify the basic calculations of a DEM code [Chung, 2006; Chung and Ooi, 2011]. Basic verification of DEM codes is the first step towards validated quantitative predictions from DEM simulations.

In the case where spherical particles are used in simulations rolling friction is often implemented to incorporate resistance to rolling similar to that of the real particles trying to be simulated. Recent studies [Ai *et al.*, 2011; Wensrich and Katterfeld, 2012] have highlighted the suitability and applicability of the various rolling friction models and whether rolling friction is a suitable substitute for real shape.

O' Sullivan and Bray [2003] presented a simple validation study using a 2D model of rods with a hexagonal packing under a biaxial compression which was compared to experimental [O' Sullivan *et al.*, 2002] and theoretical predictions for the system. It was found that by accurately incorporating the inter-particle friction and quantitative match within 2° of the experimental result for the angle of mobilized friction. However real granular materials are three dimensional and validations should be considered on this level. O' Sullivan *et al.* [2004*a*], using assemblies of uniform spheres with face-centred cubic (FCC) packing and rhombic packing, studied the triaxial and plane strain compression. The DEM simulations explored the response and its sensitivity to the level of friction between both particles and boundaries. Provided that accurate particle size, boundary conditions and the correct level of friction were employed accurate predictions for the peak strength and mobilized could be made. Predicting the post peak behaviour however proved more challenging – FCC packings seem to underestimate the strain at which the load drop-off occurred, while rhombic packings over estimated it.

O' Sullivan *et al.* [2004*b*] examined direct shear tests on steel balls with a 3D DEM simulation and found the internal angle of friction was under predicted by approximately 4 degrees when compared to the experimental results. The response of the DEM simulations was also stiffer than the observed physical response. Yan and Ji [2010] showed that by utilising non-spherical clumps to represent limestone rubble a good match between the DEM simulation and the direct shear test could be found. Härtl and Ooi [2011] conducted a study comparing DEM simulations of a Jenike shear test using spherical and non-spherical particles with physical experiments. It was found that spherical particles alone could never produce a close match to the experimental result regardless of the level of friction applied in the simulation but with non-spherical

particles the correct level of bulk friction and a good quantitative prediction could be achieved from DEM simulations.

2.7 Summary

The literature related to the research presented in this thesis has been reviewed in this chapter. The common descriptors used for describing the fabric of the granular solid have been introduced as have the most common sources for adhesives forces in granular materials. Discharge from silos is a common industrial process and the theory behind the design of these structures is presented in terms of the flow patterns and discharge rates achieved. A brief introduction of DEM was also presented in this chapter but will dealt with more thoroughly in the following chapter. The use of DEM has become prevalent in recent years and a review of the use of DEM for modelling cohesion and silo related problems has been presented. Several key issues that are important for achieving satisfactory DEM predictions have been discussed.

One of the key points arising from the literature review is that while much work has been done to include the effects of adhesive forces into DEM simulations, much of this work has focused on fine powders in the range of several microns to several hundred microns were where van der Waals forces are significant for applications such as powder packing and compaction. For larger granular materials, the effect of van der Waals forces has been shown to be not as significant and simulation work has focused on liquid bridge model. It is also clear that for silo discharge that the majority of the studies, either experimental or numerical, have been focused on cohesionless materials. Further study in to the effect of cohesion on flow patterns and discharge rates is necessary.

Chapter 3

The Discrete Element Method

The following chapter will present an introduction to DEM and the contact models that are so crucial for modelling a materials. The intention of this chapter is not to provide a detailed autopsy of DEM or an exhaustive review of all contact models, but to focus on the more commonly used contact models and the strengths and weaknesses of each of model. DEM simulations with the JKR adhesion model are also presented.

3.1 DEM Background

The Discrete Element Method (DEM) is today becoming a widely exploited method of dealing with engineering problems that deal with granular materials the method was first developed for analysis of rock mechanics [Cundall and Strack, 1979] but has since been employed to look at problems ranging from powder flow to bulk solids handling in a variety of different industries. DEM is an explicit numerical method that looks at the interactions of all particles in a continuum. The particles are rigid but are subject to local deformation in places of contact and the resulting forces from particle overlap are calculated. The motion of the particles is modelled on a particle-by-particle basis, which makes the method computationally intensive. As each particle's behaviour is modelled at an individual level, it is important that a small enough timestep is chosen so that the reactions to the forces acting on a particular particle do not propagate any further than the particles immediate neighbour.

A key advantage of the method is that as the particles are modelled separately there is no need for a constitutive model to represent the bulk behaviour of the material. Also the DEM can provide valuable information and insight that is often not available from experimental setups. This is particularly the case when dealing with materials such as

powders, where the force network and packing structures can be visualised and analysed in great details, which is something not possible in a physical experiment where taking the necessary measurements is next to impossible. Unfortunately, DEM has its drawbacks as well, and the most obvious is a problem of scale. DEM is computationally intensive method and this has a large impact on the number of particle and size of a simulation that is feasible to run.

3.2 DEM Software Packages

There are many different DEM software packages available, with many of them being free open source codes that are continually being developed and new features being added.

3.2.1 EDEM Commercial Code

EDEM® is a state-of-the-art discrete element modelling software package for the simulation and analysis of granular solids systems. It implements a GUI based approach to creating models and analysing results to make the process of running DEM simulations more accessible. DEM codes have traditionally been text based and may have been seen as too complicated to be implemented by industry at large.

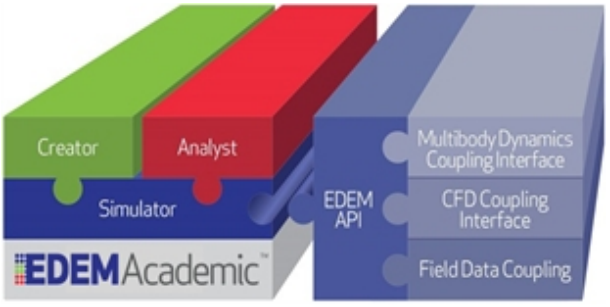

Figure 3.1: EDEM modules - An overview of the EDEM modules and interactions (DEM Solutions, 2013)

The EDEM® software package is divided in to three main sections - the creator, Simulator and Analyst (Figure 3.1). The creator module allows the user to quickly set up all the simulation parameters. EDEM® supports the use most common 3D CAD files which can be simply imported to create the geometry for the simulation. The Particle creator allows for analysis of non-spherical particles in a system, with complexly shaped particles generated from the placement of multiple spheres. Many particle generation methods are supported in the EDEM Particle Factory™ such as both static and dynamic creation of particles. Both normal and log-normal particle size distributions can also be generated. The Simulator module is a parallelised DEM Solver that also

allows real-time visualisation of the simulation, along with statistics for the simulation. The Analyst module is the post-processing environment. Within the Analyst module it is possible to playback the results of the simulation, where particles can be coloured and visualised by simulation properties such as force or velocity, with the option of creating videos. Results can also be exported for processing outside of EDEM®.

3.2.2 EDEM Application Programming Interface

The EDEM API also for customization and extension of the capabilities of EDEM. The API uses standard C++ scripting to allow user to add features as new contact models, additional particle body force models, custom particle, contact and simulation properties and custom particle factories. For example a custom particle factory may be used to implement a simple particle breakage model or generating non uniform particle flow rates. More details of the API and it capabilities can be found in the EDEM Programming guide DEM Solutions Ltd. [2010*a*, 2011*b*].

3.3 DEM Formulation

The discrete element method (DEM) was first developed as a tool for analysing quasi-static problems in densely packed granular materials. Interaction is modelled using the soft contact approach where rigid-shaped particles are allowed to overlap each other at the contact point with small overlaps, typically less than 1% of the particle diameter. The contact force is calculated according to the contact model as a function of the overlap.

3.3.1 Equations of Motion

The changes in positions and velocities of the particles due to the contact and gravitational forces are calculated from integration of Newton's motion equations. For particle *i* the translational motion equation is given by Equation (3.1).

$$m_i \frac{d^2}{dt^2} \boldsymbol{x_i} = \boldsymbol{f_i} + m_i \mathbf{g} \tag{3.1}$$

where m_i is the mass of the particle, t is time, $\boldsymbol{x_i}$ is its position, $\boldsymbol{f_i} = \sum_c \mathbf{f_i}^c$ is the force acting on the particle due to particle contacts and $\mathbf{g}$ is the acceleration due to gravity. The rotational motion equation for particle *i* is given by Equation (3.2).

$$I_i \frac{d}{dt} \boldsymbol{\omega_i} = \mathbf{T_i} \tag{3.2}$$

where I_i is the moment of inertia for particle i, ω_i is its angular velocity and T_i is the total torque acting on it, which is defined by Equation (3.4) where l_i is the branch vector of particle i, defined by Equation (3.3).

$$\mathbf{l_i} = \mathbf{r_i} - \mathbf{r_j} \tag{3.3}$$

$$\mathbf{T_i} = \sum_{i=1}^{N_c} \mathbf{l_i}^c \times \mathbf{f_i}^c \tag{3.4}$$

A more detailed discussion of the equation of motion for non-spherical will not be included here but can be found in the work of Chung [2006] and the PFC user manual [Itasca, 2003].

3.3.2 Contact Detection

Contact detection is one of the most time consuming parts of a DEM simulation. The amount of time used for this task is proportional to the number of particles in a system and therefore an efficient method of detecting particles in contact is required. It is very inefficient to simply loop through every individual particle and check the separation distance between two particles at every timestep, particularly for a large number of particles. To improve the efficiency through either reducing the number of times all particles are checked or by reducing the number of neighbours checked, three main types of contact detection schemes are used:

- Verlet Neighbour Lists
- Link/Grid Cells
- Lattices

Verlet neighbours list construct a list of particles within a certain search radius, typically 2-3 particle radii, and only this list is searched for contact, rather than every individual particle in the system. The neighbour list is not updated every timestep, but instead is updated every 20-50 timesteps or if displacements are large. Link or Grid cells divide the simulation domain into a number of equally sized cells which are larger than a couple of particle diameters. A list is maintained of all the particles in each cell, and their respective positions. Contacts are only checked for particles within the same cell and the neighbouring cells. The lattice method divides the simulation domain into a number of equally sized cells, where each one is the size of a particle (each cell can contain only one particle). If a polydisperse particle size distribution is being used the

cell size will be related to the size of the smallest particle. Each particle is indexed in relation to a grid point and a neighbour list is created for all cells within a particle diameter d. The contact detection method employed by the EDEM code is a hybrid between the lattice method and the link/grid cells method. The user specifies the size of the grid to be used with the recommended range being 2-3R, where R is the radius of the smallest particle. At a value of 2R this is the lattice method, while at values larger than 3-4R it become the link/grid cell method. Each cell is checked for more than one particle, and if found these are checked first for contacts [DEM Solutions Ltd., 2010*b*, 2011*d*]. The EDEM Simulator module is most efficient at a grid radius of 2R, but this can lead to large amounts of memory being used. If the memory use is greater than the available memory then EDEM will attempt to swap the memory to disk, which can be very time consuming. In this case the grid radius should be increased sufficiently to ensure that the memory use is within the available memory of the computer system being used.

3.3.3 Time Integration Scheme

The time integration scheme is the method in which the DEM code iterates through the timesteps of the simulations. It should be selected based on the trade of between performance and accuracy. When Cundall and Strack [1979] first detailed the distinct element method they proposed a computationally efficient, explicit central difference time integration scheme. Most DEM codes use this central-difference scheme or a slight variation of it. The Verlet equations used in DEM are a second order scheme (the accuracy is dependent on the square of the time increment) which are both accurate and stable provide a small enough time increment is utilised [O' Sullivan, 2011]. While the Verlet time Integration method is the most commonly used in DEM codes, other methods such as the predictor-gear method are also used. The predictor-corrector method is a multi-step method, in which information from previous timesteps may be used to predict the particle positions at $t + \Delta t$. Another timstep is then used to "correct" or refine the prediction. Cundall and Strack [1979] stated that a key DEM principle is that the timestep chosen is sufficiently small such that in a single timestep, disturbances from an individual particle cannot propagate further than their neighbour. If this is neglected it can lead to a significant instability in the system.

3.3.3.1 Simulation Timestep

A sufficiently small integration time step is required to ensure the stability of simulation by having a sufficient number of time steps within each collision. As a rule of thumb a timstep Δt that is approximately 1/50 of the contact time t_c, which is given

by Equation (3.5) and where ω is the particle angular velocity.

$$t_c = \frac{\pi}{\omega} \tag{3.5}$$

It has been suggested for the predictor-gear method that approximately 20-50 timesteps are required to accurately integrate the collision [Cleary, 2000]. For quasi-static simulations it has been suggested that the timestep used should be related to the Rayleigh timestep, which is the time taken by a shear wave to propagate through a solid. The Rayleigh timestep is calculated from Equation (3.6).

$$T_R = \left(\frac{\pi r_{min}}{0.1631v + 0.8766} \right) \sqrt{\frac{\rho}{G}} \tag{3.6}$$

This should be regarded as the upper limit for the timestep which is usually calculated as a percentage of the Rayleigh time step [DEM Solutions Ltd., 2010*b*, 2012; Rayleigh, 1885; Sheng *et al.*, 2004; Thornton and Randall, 1988], typically less than 20% for systems with a high coordination number.

A detailed study of the selection of a suitable timestep was carried out by O' Sullivan and Bray [2004] and it was suggested that a timestep of less than $0.3\sqrt{m/k}$ should be used for 2D uniform sized disks and a timestep of less than $0.17\sqrt{m/k}$ should be used in 3D simulations.

3.3.4 Energy Dissipation

DEM dissipates energy through two main methods - friction and damping. While friction is a real phenomenon experienced by particles, damping is an artificial numerical method applied to dissipate the collision energy in a system in a reasonable number of calculation timesteps in a simulation.

3.3.4.1 Viscous damping

Viscous damping is applied in the contact model through the implementation of dashpots in both the normal and tangential directions and the damping force is added to the contact force (example: see Figure 3.5). Viscous damping is characterised by the critical damping ratio. A critically damped system will dampen to zero at the quickest rate and is the transition between under-damped and over-damped systems. An over-damped system will display an exponentially decaying response while an under-damped system while have an oscillatory response. The coefficient of restitution is related to the damping coefficient, although this relationship can vary between contact models.

3.3.4.2 Global non-viscous damping

Global damping is applied to the entire system to dissipate energy by damping the motion of the particle. This is implemented through the addition of a damping term to the equations of motions. The key advantages of global damping are that only accelerating particles are damped, meaning no erroneous damping in a steady state. It also applies the same level to all parts of a system, so parts of the system with different natural frequencies are not affected adversely. Both viscous and non-viscous damping is available in the PFC code while only viscous damping is implemented in EDEM. By default PFC set the global damping to a value of 0.7 [Itasca, 2003].

3.3.5 Rolling Friction

Springs and dampers are used in the normal and tangential directions to describe the particle interactions in DEM contact models. Sliding occurs below the friction limit which is normally defined by Coulomb theory with Equation (3.7).

$$|F_s| = \mu F_N \tag{3.7}$$

Where μ is the coefficient of sliding friction. However this theory does not cover the effect of particle rotation, and as spherical particles are particularly susceptible to rolling [Bardet, 1994; Iwashita and Oda, 1998] an additional rolling friction model including torque is required to incorporate resistance to rolling. A detailed study of the different types of rolling friction models available has been carried out [Ai *et al.*, 2011] and further improvements proposed. Further studies on rolling friction have also been carried out [Wensrich and Katterfeld, 2012] in an attempt to relate the rolling friction coefficient to the eccentricity of contact. It is important to bear in mind that different contact models or DEM codes may use different rolling friction models, which may have a significant effect on simulation results. Comparing rolling friction coefficients between simulations may also be more difficult. The default EDEM rolling friction model [DEM Solutions Ltd., 2010*b*] is defined in Equation (3.8) by *Model A* in Ai *et al.* [2011]. The total applied torque, τ_i, is given by equation

$$\tau_i = \mu_r f_N R_i \omega_i \tag{3.8}$$

where μ_r is the coefficient of rolling friction, R_i is the distance from the contact point to the particle centre of mass and ω_i is the unit angular velocity vector of the object at the contact point and f_N is the normal force.

3.3.6 Periodic Boundaries

The particle behaviour at boundaries is described by the boundary conditions prescribed in the model setup. These are typically one of two kinds – solid geometry walls or periodic boundaries. Periodic boundaries are used to mimic very large systems without the burden of a hugely increased number of particles. This is achieved through the use of a periodic cell, which is surrounded by identical copies of itself. Therefore it can be considered that there is a copy of a particle repeated at a set interval in a prescribed direction – a particle may be repeated at intervals of length L_x in the x-direction and L_y in the y-direction. In the directions where periodic boundaries the simulated material is effectively infinitely long in that direction. Periodic boundaries can be explained by Figure 3.2, where the periodic cell setup is demonstrated on the left and how it appears in a simulation is shown to the right. For example, when particle *4* exits through the right hand boundary of the cell, it will re-appear on the left side. It is possible for a simulation to use periodic boundaries in one, two or all three directions.

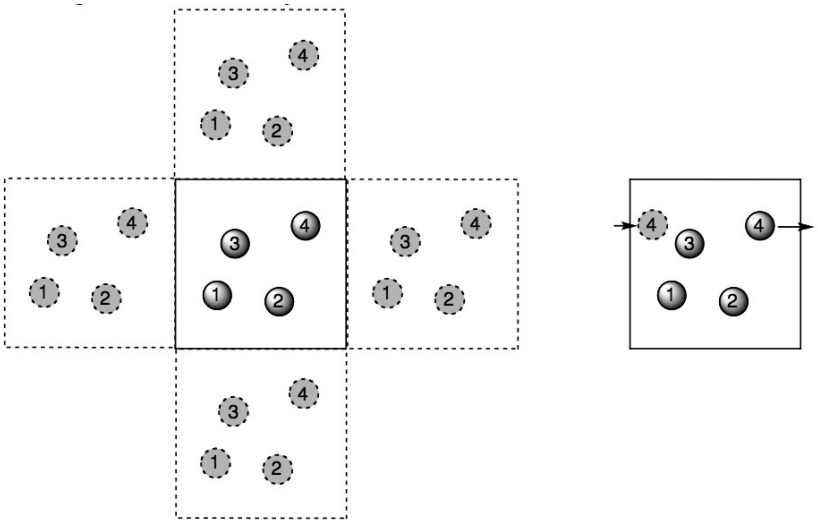

Figure 3.2: Periodic Boundaries and cells - When a particle leaves a cell on one edge it re-enters on a corresponding opposite or radial boundary, after Jensen [2010]

3.4 Contact Models

Following the process of contact detection, it is necessary to calculate forces where contacts have been detected. The contact forces are then calculated from the contact model, which represents the material behaviour. DEM contact models normally consist of a selection of springs, sliders and dash-pots to represent the stress at the contact point and both the normal and tangential force are normally calculated separately. Contact models tend to be relatively simplistic in the way they describe the material behaviour in an attempt to keep the computational costs down. Along with contact

detection, the calculation of contact forces is one of the most expensive parts of a DEM simulation. The accuracy and realism of the contact model can be improved by changing the force-displacement relationships for the spring, such as including non-linearity or by changing the set-up of springs and dash-pots in the model. The inclusion of adhesion forces is another important step in improving the realism of DEM contact models.

DEM contact models are normally broken down into two types; those for the normal and tangential direction. The tangential contact model has been less studied although several contact models are available and presented in Figure 3.3. Savkoor and Briggs [1977]; Thornton [1991] have extended the contact model to account for adhesion based on JKR contact. Most tangential models are elastic models and an improved elasto-plastic tangential force-displacement model was proposed by Vu-Quoc *et al.* [2004].

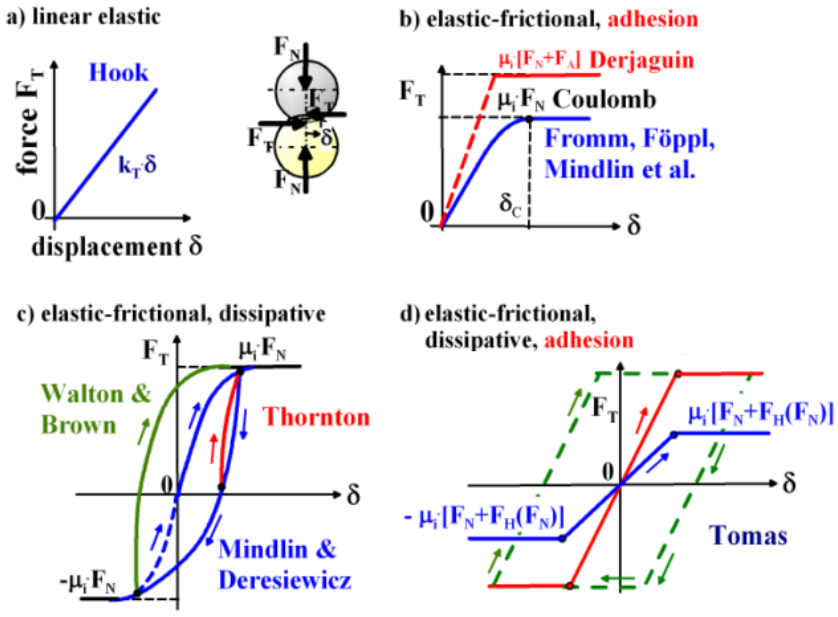

Figure 3.3: Tangential force models - Visual representation of various tangential contact models [Tomas, 2007*a*]

Most studies have focused on the normal direction and the normal attractive force that exists between particles and the most common DEM contact models are introduced in the following section. Some of the more common ones are illustrated in Figure 3.4. This is not an exhaustive review of all contact models and the finer details of each model will not be discussed. A more detailed listing of some of the available contact models (both normal and tangential) was compiled by Tomas [2007*a*]. The full details of the contacts models mentioned (and others) can be found in the PFC or EDEM

user manuals [DEM Solutions Ltd., 2010*b*, 2011*c*,*d*; Itasca, 2003] or text books on the topic of contact mechanics and DEM [Fischer-Cripps, 2007; Johnson, 1987; O' Sullivan, 2011].

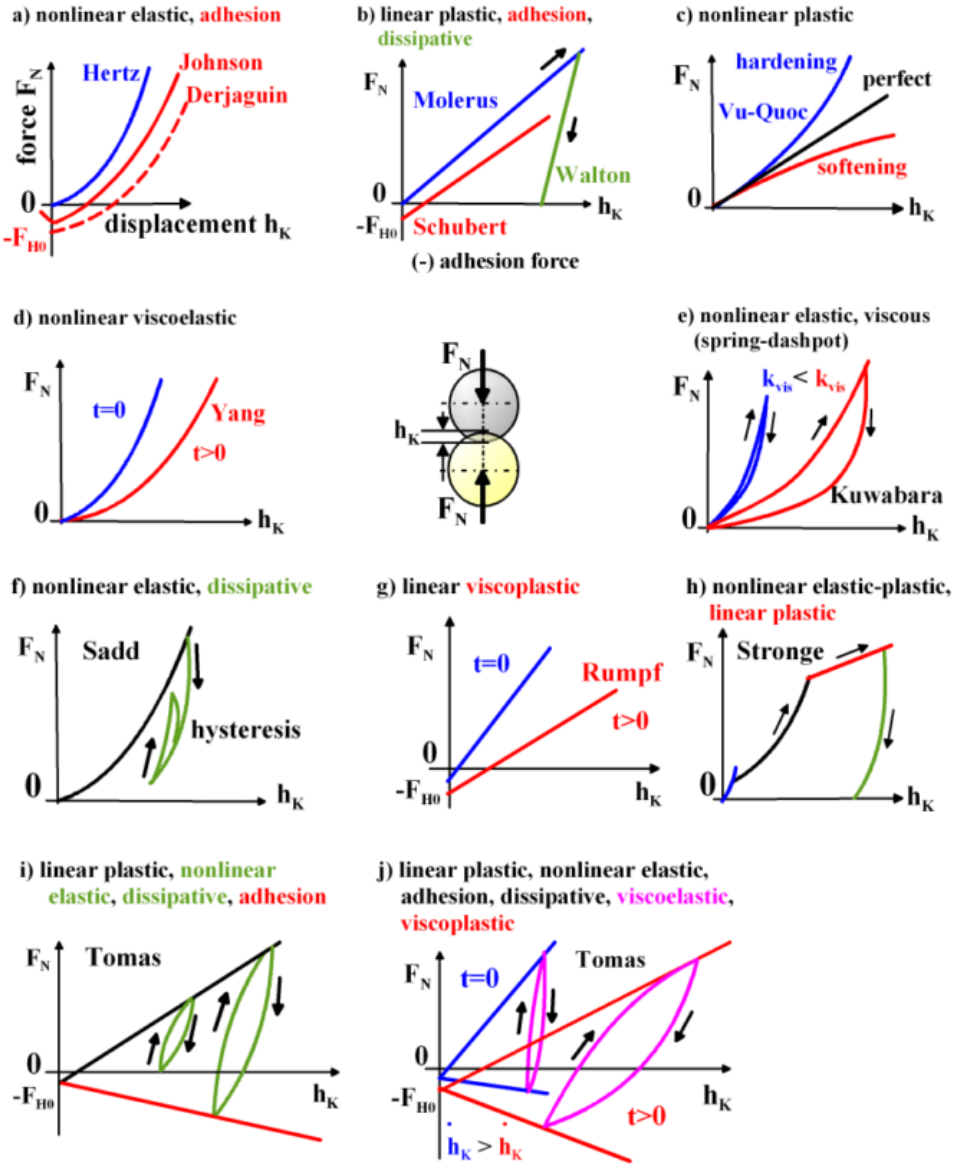

Figure 3.4: Normal force models - Visual representation of various contact models [Tomas, 2007*a*]

3.4.1 Cohesion-less Normal Contact Models

Cohesionless contact models are the dominant type of contact models that have traditionally been used in DEM simulations. There are several contact force-displacement models that are used in DEM and these are mostly derived from contact mechanics.

3.4.1.1 Hertz-Mindlin

In the late 19^{th} century Hertz [1882] developed a solution for the contact of two elastic sphere in being brought into contact. This normal force-displacement relationship provides a non-linear relation between the two. Mindlin and Deresiewicz [1953] developed and incremental tangential force-displacement model for elastic spheres under a frictional contact. The combination of these to force displacement relationships lead to the Hertz-Mindlin contact model. The Hertz-Mindlin (no slip) model [Tsuji *et al.*, 1992] is one of the most commonly used contact models in DEM.

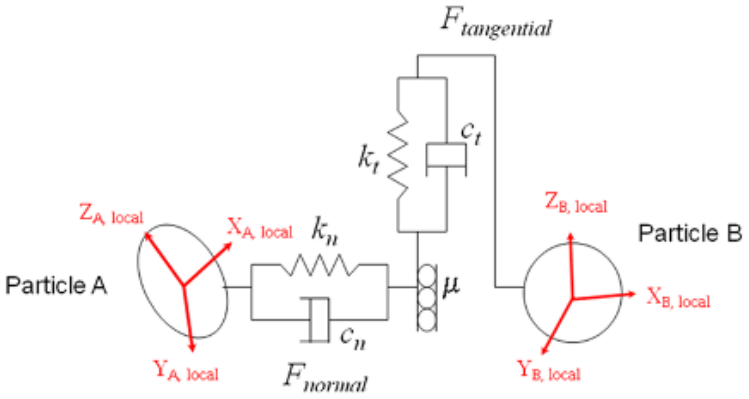

Figure 3.5: Hertz-Mindlin contact model - Simplified schematic of Hertz-Mindlin (no slip) contact model [DEM Solutions, 2012]

3.4.1.2 Linear Spring

The linear spring model [Cundall and Strack, 1979] is one of the simplest contact models that can be used be utilised for a DEM simulation. This is an elastic contact model based on Hooke's law and includes a slider and a dash-pot to account for energy dissipation in the contact. Due to the simplicity of the linear spring contact model, it is possibly the most widely used DEM contact model.

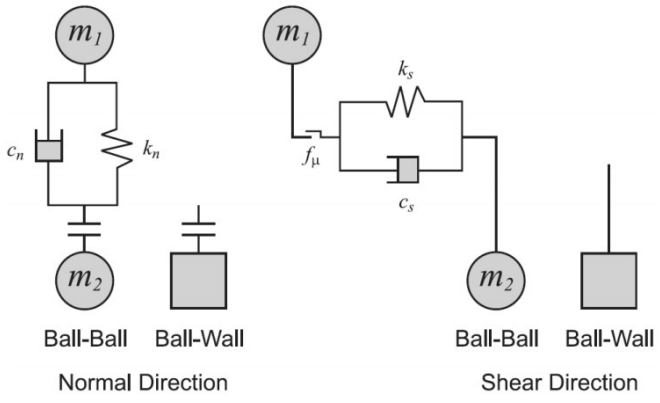

Figure 3.6: Linear spring-dash-pot model - Linear spring contact model from PFC^{3D} [Itasca, 2003]

3.4.1.3 Hysteretic Spring Models

In an elastic contact model energy is conserved, that is, the energy released during unloading is equal to the strain energy accumulated during the loading phase. Walton and Braun [1986] proposed a bi-linear hysteretic spring model that dissipates energy. They argued that kinetic energy should be dissipated during collisions. The tangential force model used was a simplification of that proposed by Mindlin and Deresiewicz [1953]. Vu-Quoc and Zhang [1999*a*] made further improvements to this model by revising the tangential force-displacement model based on finite element analysis (FEA). Thornton [1997] produced a normal force-displacement model that accounts for both elastic and plastic deformation. It also attempted to capture the decreasing coefficient of restitution with increasing collision velocity. However, Vu-Quoc and Zhang [1999*b*] showed that the normal force-displacement response of this model is too soft when compared to FEA results of normal contact of a sphere (Figure 3.7) and proposed that new model that provides a closer match to the FEA results. While both the models proposed by Walton and Braun and Vu-Quoc and Zhang include plastic deformation in the normal force-displacement relationship, this is not true for the tangential force-displacement relationship. To overcome this inconsistency, Vu-Quoc *et al.* [2001] proposed a new contact model that included a tangential force-displacement relationship that included plastic deformation, again based on the detailed finite element analysis of a sphere in contact.

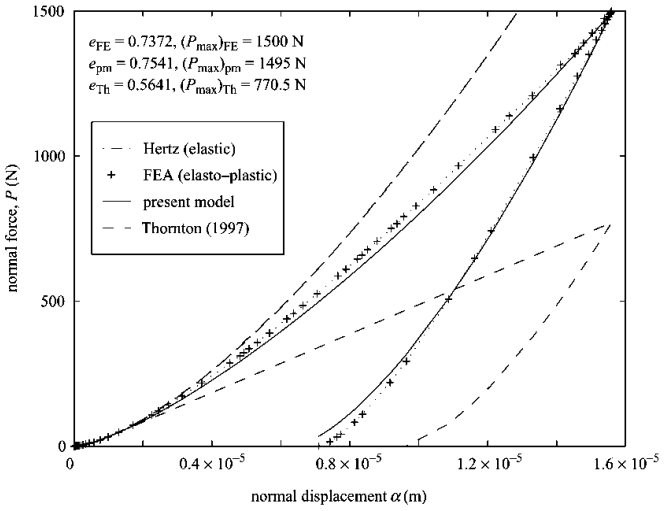

Figure 3.7: FEA-DEM comparison for single sphere normal contact - Comparison between Thornton model and Vu-Quoc & Zhang model [Vu-Quoc and Zhang, 1999*b*]

However, while both the model of Thornton [1997] and the model of Vu-Quoc *et al.* [2001] provide a more realistic response in capturing the plastic deformation of contact, it is difficult to establish the model parameters for various materials from laboratory experiments. This has led to the simpler Hertzian model proposed by Tsuji *et al.*

[1992] being much more widely adopted as the model parameters are more easily found from simple laboratory testing. A hysteretic spring model similar to that proposed by Walton and Braun [1986] has been available in the EDEM software package since version 2.4 in 2011 [DEM Solutions Ltd., 2011*c*,*d*].

3.4.2 Bonded Models

At this point it is necessary to make a distinction between bonded particle contact models and adhesive contact models. A bond is contact between two particles that has a finite strength value (this can be a tensile, compressive or bending strength) and once this value is exceeded the bond will fail and the particles will no longer be bonded together. Contact can exist between the particles but this will be governed by the cohesion-less contact model such as Hertz-Mindlin or Linear spring. All bonds are formed at an initial timestep but once a bond has broken it cannot reform. Adhesive contact models on the other hand can reform adhesive contacts following breakage. Bonded models can come in several types - commercial code PFC offers both a contact bond model and a parallel bond model [Itasca, 2003] while EDEM offers a similar model [DEM Solutions Ltd., 2011*d*; Potyondy and Cundall, 2004]. Other types such as beam and lattice models may also be implemented. Bonded models are typically used for simulation of rock or cementitious materials which are brittle materials. A bonded beam model based on Timoshenko theory has recently been implemented in EDEM by Brown [2013] and a more details review of bonded models in DEM is also presented there.

3.4.3 Elastic Adhesive Normal Contact Models

Adhesive contact models are typically used for the simulation of fine powders, which due to their fine particle size (often less than a few hundred microns) are significantly affected by surface forces such as van der Waals'forces. The adhesive contacts formed can be broken and reformed and is the main difference from bonded models. The adhesive force at play can come from several sources and this has led to the development of many different forms of adhesive contact models. Some of the most commonly used models will be introduce here.

3.4.3.1 JKR Model

The JKR [Johnson *et al.*, 1971] model was first proposed in 1971 in an attempt to include the effect of adhesion between a sphere and a flat surface. It had been noted [Johnson *et al.*, 1971; Kendall, 1969; Roberts, 1968] that at low loads the area of contact between the two spheres in intimate contact (no force applied to the contact) was much larger than that predicted by Hertz Theory. It also tended towards a finite

value as the loads applied were reduced to zero. They noted that strong adhesion forces were observed if the spheres were clean and dry but the observed behaviour closely matched Hertz theory at higher loads. These observations suggested that adhesive forces were at work during the contact, and while these were relatively insignificant at higher loads, they became increasing important as the loads tended towards zero. There has been a steady increase in the use of the JKR model in recent times [Thomson Reuters, 2013]. The majority of the research has been in the field of physics and has coincided with the development of Atomic Force Microscopy (AFM) in the late 1980's.

The JKR model has been mainly used to study breakage and agglomeration at micro- and nano-scale [Antony *et al.*, 2008; Baran *et al.*, 2009; Carrillo *et al.*, 2010; Hassanpour *et al.*, 2008; Mishra and Thornton, 2001; Modenese *et al.*, 2012; Moreno *et al.*, 2003; Moreno-Atanasio, 2012; Moreno-Atanasio *et al.*, 2005]. Although the JKR theory was originally developed for application on smooth spheres, its application on rough surface (which can lead to a reduction in adhesion) has also been considered [Greenwood and Williamson, 1966; Hodges *et al.*, 2004; Hui *et al.*, 2001; Morrow *et al.*, 2003; Waters *et al.*, 2009]. The adhesion force acting between two spherical surfaces, F_s, is not dependent on the elastic modulus of the materials of the spheres in contact. Even though the elastic modulus does affect the contact radius, a, because both the surface energy and elastic work vary as a^2, the adhesion force F_s can be shown to be independent of a, and hence E [Johnson *et al.*, 1971]. In order to separate the two bodies, mechanical work is required to overcome the adhesive forces. This work creates new surfaces and the energy required to create the surfaces (separate the particles) is defined as the free surface energy of the solid. The overlap caused by the additional surface force can be described by:

$$\delta_{JKR} = \frac{a^2}{R^*} - \sqrt{\frac{2\pi\Delta\gamma a}{E^*}} \tag{3.9}$$

where a is the contact radius, R* is the equivalent radius and E* is the equivalent Young's modulus, $\Delta\gamma$ is the surface energy of the contact which is generally it is defined by Equation (3.10). For two identical materials in contact $\Delta\gamma$ is equal to 2γ.

$$\Delta\gamma = \gamma_1 + \gamma_2 - \gamma_{12} \tag{3.10}$$

The hertz equation modified to include surface energy is given by:

$$F_{JKR} = \frac{4E^*a^3}{3R^*} - 4\sqrt{\pi\Delta\gamma E^* a^3} \tag{3.11}$$

While the contact radius is given by:

$$a_{JKR} = \sqrt[3]{\frac{3R^*}{4E^*}[P + 3\pi\Delta\gamma R^* + \sqrt{6\pi\Delta\gamma R^* P + (3\pi\Delta\gamma R^*)^2}]} \tag{3.12}$$

where P is the pull of force.

The critical pull-off force, which is the force required to separate the two contacting particles can be found from Equation (3.13).

$$P_{JKR} = -\frac{3}{2}\pi\Delta\gamma R^* \tag{3.13}$$

It should be noted that when the surface energy is zero, the JKR model will simply revert to the Hertz-Mindlin Theory. Under zero applied load the contact will remain due to the surface forces acting on it. The contact area under zero load is given by Equation (3.14).

$$a_0 = \left(\frac{6\pi\Delta\gamma {R^*}^2}{K}\right)^{\frac{1}{3}} \tag{3.14}$$

where K is defined in Equation (3.15):

$$K = \frac{4}{3E^*} \tag{3.15}$$

The JKR contact model has been implemented in the latest versions (2.4 or higher) of EDEM software [DEM Solutions Ltd., 2011*a*,*c*,*d*].

3.4.3.2 DMT Model

Unlike the JKR model which only considers surface forces within the contact area, the DMT also account for forces that act outside the contact area. Once separation has occurred it simplifies to the Bradley theory [Bradley, 1932]. Similar to the JKR model the normal overlap, contact radius, and critical pull-off force can be defined. The overlap caused by the additional surface force can be described by:

$$\delta_{DMT} = \frac{a^2}{R^*} \tag{3.16}$$

While the contact radius is given by:

$$a_{DMT} = \sqrt[3]{\frac{3R^*}{4E^*}[P + 2\pi\Delta\gamma R^*]} \tag{3.17}$$

The critical pull-off force required to separate the two particles can be found from:

$$P_{DMT} = -2\pi\gamma R^* \tag{3.18}$$

While initially the DMT model and JKR model were competing models, it has since been shown that that they are both limiting solutions to opposite ends of a general solution [Muller *et al.*, 1980; Tabor, 1977; Yao *et al.*, 2007]. The two models are united by what has become known as the Tabor parameter [Equation (3.19)] which has been used to derive adhesion maps (Fig. 3.8) of where certain contact models are appropriate. When $\mu << 1$ the DMT theory is more applicable while the JKR theory is suitable in the region of $\mu >> 1$.

$$\mu = \left(\frac{R^* \Delta\gamma^2}{E^{*2} Z^3}\right) \tag{3.19}$$

where Z is the effective range of surface forces.

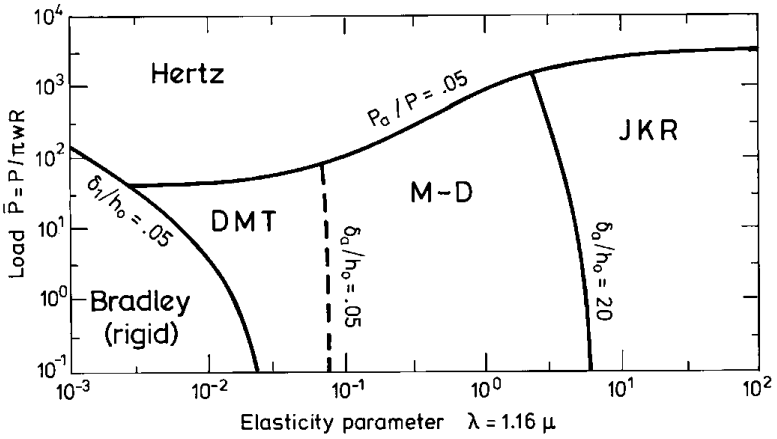

Figure 3.8: Adhesion map - Suggests which model to be used in relation to Tabor parameter [Johnson and Greenwood, 1997]

Much debate existed about the transition between the JKR and DMT contact theories and this led to Muller *et al.* [1980] proposing a new contact model to encompass the entire range using the Lennard-Jones potential. Following this, Maugis [1992] proposed a model based on the Dugdale potential which was found to be the general case with the JKR and DMT models describing the outer limits.

3.4.3.3 Linear Cohesion Model

The linear cohesion model [DEM Solutions Ltd., 2010*b*, 2011*c*,*d*] is a contact model implemented with EDEM to simulate cohesive particles. The contact model adds an

additional normal cohesive force to the Hertz-Mindlin contact model. There is no modification to the tangential force. The contact force is defined by Equation (3.20) where A is the contact area and k is the cohesion energy density (J/m^3).

$$F = kA \tag{3.20}$$

3.4.4 Adhesive Normal Contact Models Including Plasticity

This section will provide a brief review of the more commonly used adhesive contact models in the DEM. The full details of the models are available in the references.

3.4.4.1 Thornton & Ning Model

A contact model for elastic-perfectly plastic spheres with adhesion was proposed by Thornton and Ning [1998]. This model proposes that above a certain velocity (the yield point) that a contact becomes plastic and the force-displacement relationship becomes linear (the plastic force-displacement loading cove is tangential to the Hertz curve at the yield point). As a result of this plastic deformation energy dissipation takes places leading to a different unloading path. The unloading curves is calculated from Hertz theory, but the contact radius has been modified to account for the flattening of the contact patch (plastic deformation). The adhesive force in the model is calculated based on the popular JKR theory [Johnson *et al.*, 1971] with the inclusion of contact flattening.

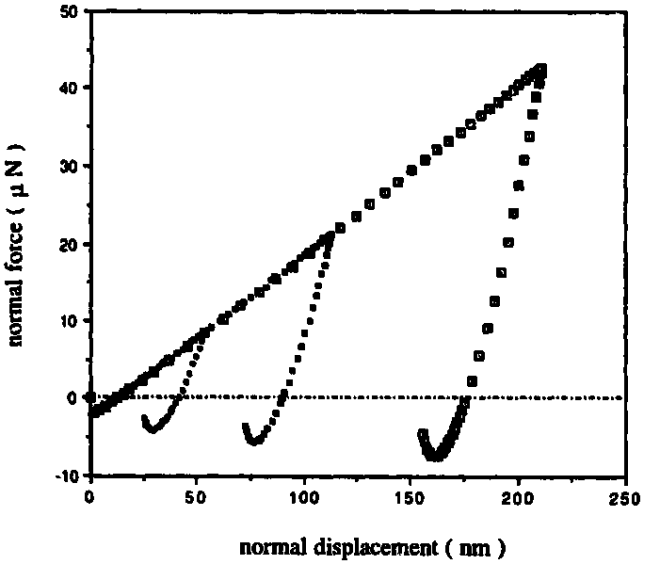

Figure 3.9: Thornton & Ning adhesion model - Elasto-plastic adhesion contact model proposed by Thornton and Ning [1998]

3.4.4.2 Tomas Model

An elaborate and detailed contact model (Figure 3.10) to include nonlinear-elastic and linear-plastic loading, plasticity with energy dissipation and adhesion was proposed by Tomas [2003*a*,*b*, 2004, 2007*a*,*b*].

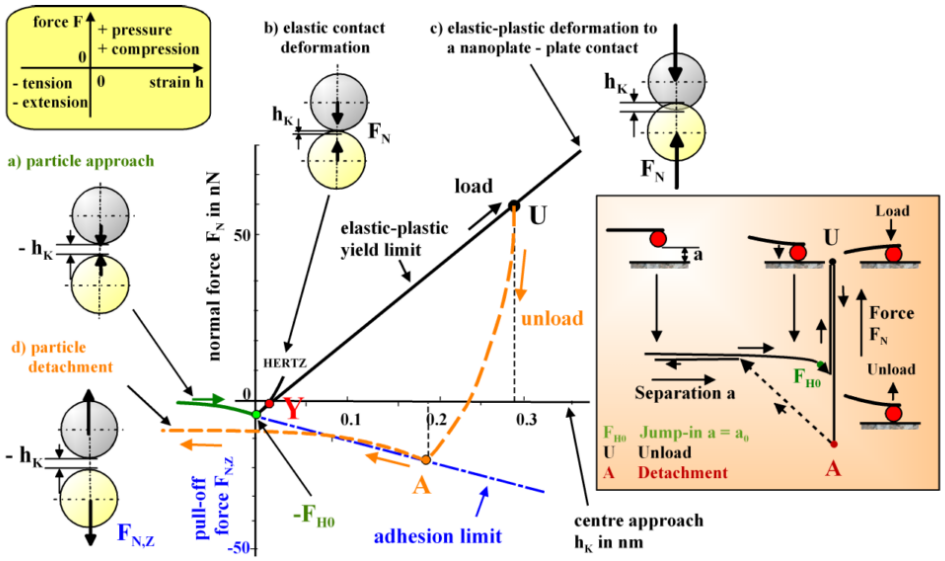

Figure 3.10: Elasto-plastic adhesion model - Force-displacement relationship for cohesive limestone particles [Tomas, 2004]

The model contains six independent mechanical material parameters and both linear and non-linear behaviour. The contact is initially non-linear elastic up to a yield limit, at which point it becomes linear. Unloading and reloading is non-linear and parabolic with increasing unload stiffness with increasing contact flattening. However this is a complex and computationally intensive contact model and a simpler model can achieve very similar results at a reduced computational cost [Tykhoniuk *et al.*, 2007].

3.4.4.3 Luding Model

A piecewise linear generalization of the hysteretic model first proposed by Walton & Braun which includes plastic deformation and history dependent adhesion has been developed by Luding [2005*a*,*b*, 2006, 2007, 2008*a*]. The contact model contains five parameters: the loading stiffness k_1, the reloading stiffness/plastic deformation parameter k_2, the adhesive stiffness k_c, the plastic overlap range of the model Φ_f and the viscous dissipation parameter γ_0. $\hat{K}_2$ is a variable in the model and interpolates linearly between k_1 and the maximum stiffness k_2. The model can revert to a simple linear spring model if $k_2 = k_1$.

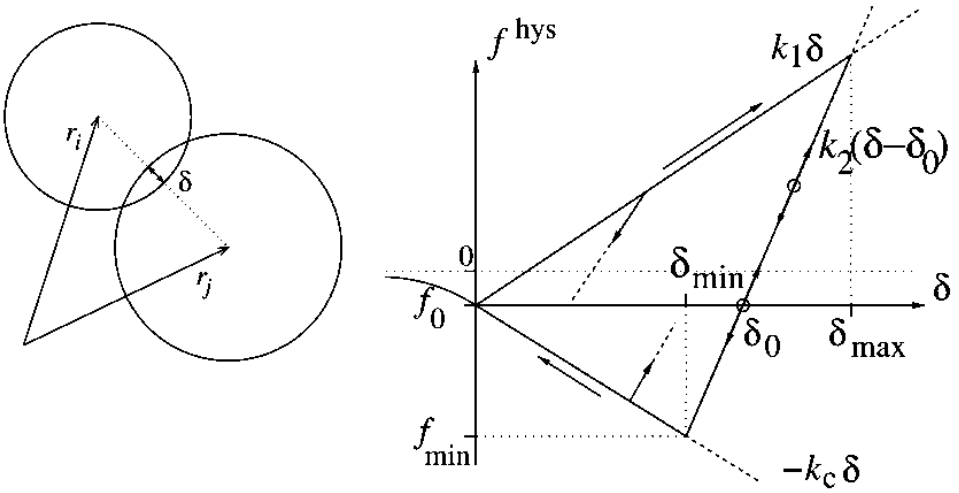

Figure 3.11: Luding adhesion contact model - Elasto-plastic Adhesion contact model proposed by Luding [2008*a*]

3.4.4.4 Walton & Johnson Model

The adhesive contact models proposed by Thornton & Ning, Tomas and Luding, while capturing the plasticity that is important for stress history dependent behaviour of adhesive granular solids, failed to account for the torsion or bending strength that may exist between adhesive particles. It has been suggested that the failure of these models to capture the very loose initial packing structures formed by fines powders is due to the lack of a twisting or bending moment in the contact [Walton, 2004]. As the particles experience plastic deformation, there is a flattening of the contact area and there is an increase in the force required to separate the particles, and while Thornton and Ning's model captures this, the additional resistance to rolling is not captured which means the particles continue rolling until more than one contact has been formed restraining the particle. As such Walton has proposed a contact model consisting of 4 inter-related modes of motion - normal, tangential, twisting and bending. More recently Walton and Johnson [2009] have proposed a linearised version (Figure 3.12) similar to that proposed by Luding [2005*a*, 2008*a*]. The key difference in this model is that the rate of increase of the pull-off force is separated from the slope of the adhesive strength branch. This requires the model to have an extra model parameter for stiffness compared to the Luding model. The contact model uses two history dependent parameters in the calculation of the normal forces at various points - the point when the normal force becomes zero (δ_0) and the reference/reloading cohesion C_R.

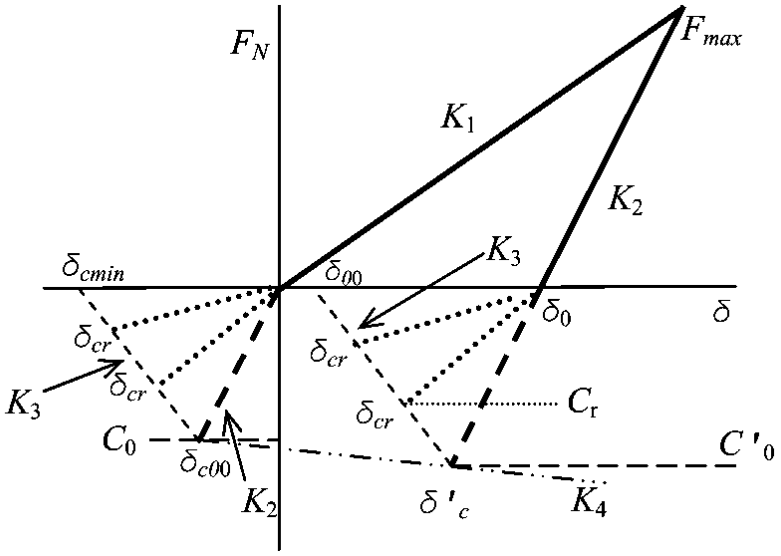

Figure 3.12: Walton & Johnson adhesion model - Schematic for Walton & Johnson linear adhesive model [Walton and Johnson, 2009])

3.4.5 Capillary Force Models

Capillary force or liquid bridge models are similar in principal to adhesive contact models in that liquid bridge can reform due to a new contact following a rupture. The force of the liquid bridge can be calculated using two methods - the boundary method and the gorge method. In each case the capillary force model is coupled with one of the typical cohesionless models such as the Hertz-Mindlin or linear spring models. Two of the most commonly used are introduced here.

3.4.5.1 Lian et al. Model

The following model was proposed by Lian *et al.* [1993] for use in DEM simulations and utilises the gorge method [Fisher, 1926] (toroidal approximation) is used in this contact model. The total force acting between two spherical bodies is given by Equation (3.21) which includes a contribution from the LaPlace (capillary) pressure Δp and surface tension γ.

$$F_{LB} = 2\pi R_2 \gamma + \pi {R_2}^2 \Delta p \tag{3.21}$$

Given that the Laplace pressure can be defined as:

$$\Delta p = \gamma \left(\frac{1}{R_1} - \frac{1}{R_2} \right) \tag{3.22}$$

The liquid bridge force can be re-written as:

$$F_{LB} = \pi\gamma R_2 \left(\frac{R_2}{R_1} + 1\right) \tag{3.23}$$

Where R_1 and R_2 are the principal radii of the liquid meniscus.

The critical separation distance at which the bridge will rupture

$$a_c = \left(1 + \frac{1}{2}\delta\right) {V_{LB}}^{\frac{1}{3}} \tag{3.24}$$

The volume of the liquid bridge can be solved analytically from an iterative equation as a toroidal geometry is assumed. The liquid bridge volume V_{LB} is a function of the separation distance a, the half filling angle β, the wetting angle δ, R_1 and R_2.

3.4.5.2 Mikami et al. Model

A model based on the regression expressions received from the numerical solutions of the LaPlace-Young equation was proposed by Mikami *et al.* [1998]. The capillary force between two spheres is given by equations 3.25 - 3.30. A different set of equations was derived for sphere-wall contact [Mikami *et al.*, 1998].

$$\hat{F}_{LB} = \exp(A\hat{h} + B) + C \tag{3.25}$$

Where F_{LB} is the normalised force

$$\hat{F}_{LB} = \frac{F_{LB}}{2\pi R\gamma} \tag{3.26}$$

The constants A,B and C are given by equations 3.27 - 3.29.

$$A = -1.1\hat{V}^{-0.53} \tag{3.27}$$

$$B = (-0.34 \ln \hat{V} - 0.96)\theta^2 - 0.0019 \ln \hat{V} + 0.48 \tag{3.28}$$

$$C = 0.0042 \ln \hat{V} + 0.0078 \tag{3.29}$$

The separation distance at which a bridges ruptures [Lian *et al.*, 1993; Mikami *et al.*, 1998] is given by Equation (3.30).

$$\hat{V}_c = (0.62\theta + 0.99)\hat{V}^{-0.34} \tag{3.30}$$

3.5 Particle Pre/Post-processor (P4) Toolbox

In most cases where DEM is used it is necessary to carry out some averaging of the data to a more representative scale of what is required. As such it is quite common for spatial averaging, temporal averaging or both to be applied to the DEM data. To aid the process, a toolbox for process DEM data both temporally and spatially has been implemented in the University of Edinburgh. The toolbox has been developed to support many codes such as EDEM, PFC, DEMPack and LAMMPS and provides a simple interface for the averaging process for the large datasets that DEM simulations produce. The toolbox provides both a coarse graining method for projecting the results on to a continuum field and a binning method. A study of the effect of both temporal averaging using this toolbox is presented in Labra *et al.* [2013] and some of the results are shown in Figure 3.13. Full details of the methods implemented in the toolbox are available in several papers [Goldenberg and Goldhirsch, 2004; Goldhirsch, 2010; Goldhirsch and Goldenberg, 2002; Weinhart *et al.*, 2012].

The coarse-grained density ρ is provided by Equation (3.31).

$$\rho(\mathbf{r}, t) = \sum_i m_i \phi(\mathbf{r} - \mathbf{r}_i(t)) \tag{3.31}$$

where $\mathbf{r}$ is a point in space where the values are to be evaluated, $\mathbf{r}_i(t)$ is the vector of the centres of mass of the particles at a given timestep t, and φ is the coarse graining function which is subject to the condition of its integral over space being unity.

The coarse-grained velocity $\mathbf{V}$ is provided from Equation (3.32)

$$\mathbf{V}(\mathbf{r}, t) \equiv \mathbf{p}(\mathbf{r}, t)/\rho(\mathbf{r}, t) \tag{3.32}$$

where $\mathbf{p}$ is the coarse-grained momentum density.

The stress tensor is given by Equation (3.33).

$$\sigma_{\alpha\beta} = \frac{1}{2}\sum_{i,j} f_{ij\alpha} r_{ij\beta} \int_0^1 ds\phi(\mathbf{r} - \mathbf{r}_i + s\mathbf{r}_{ij}) - \sum_i m_i v'_{i\alpha} v'_{i\beta} \phi(\mathbf{r} - \mathbf{r}_i) \tag{3.33}$$

where $f_{ij\alpha}$ is the interaction force between two particles, $r_{ij\beta}$ is the branch vector, s is the integral of the branch vector and v' is the fluctuating velocity of the particle.

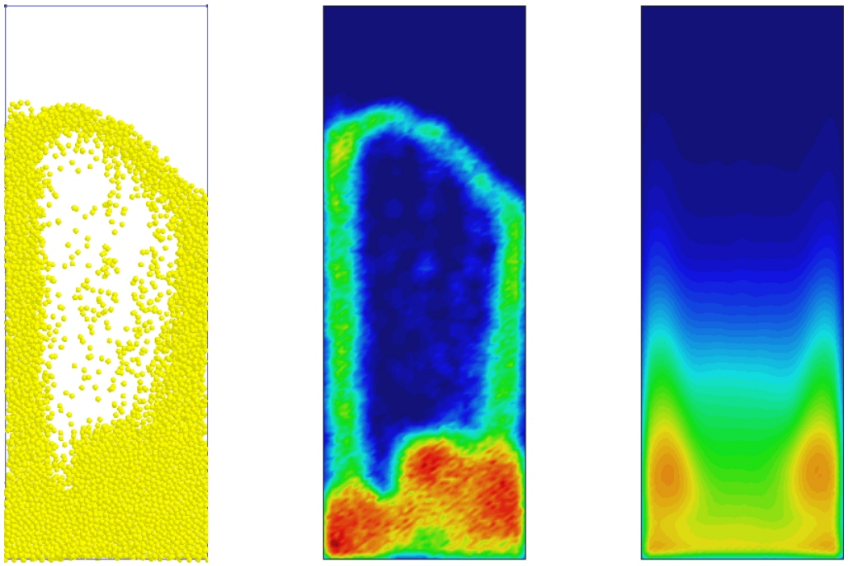

Figure 3.13: Example of P4 toolbox in use - Post-processing on a fluidised bed [Labra *et al.*, 2013]

3.6 DEM Simulations with JKR Contact Model

The JKR model is a commonly used contact model to implement cohesive forces for fine cohesive powders. An extensive DEM study has taken place to determine the suitability of the JKR model for the problem being examined. The JKR model is currently available by default with the commercial code EDEM, however only the contact force part of the model is implemented and the typical van der Waals force that acts over small distances is not included in the model. The force-displacement relationship for a two particle contact of 1 mm particles loaded with a force of 0.15 N for varying levels of adhesion for this contact model is presented in Figure 3.14. Upon contact there is a jump in the force to the maximum JKR adhesion strength and the contact is elastic for both loading and unloading. At contact level there is no stress history dependency in the model and a particle loaded to 10 N will have the same pull-off force as a particle loaded to 0.1 N, ignoring any deformation that may occur at the contact point and any subsequent this larger contact area may provide.

An evaluation of the JKR model's suitability for cohesive granular solids was carried out through numerous DEM simulations of a uniaxial compression test (both confined and unconfined) as demonstrated by 3.15. In each simulation the sample is subjected to an

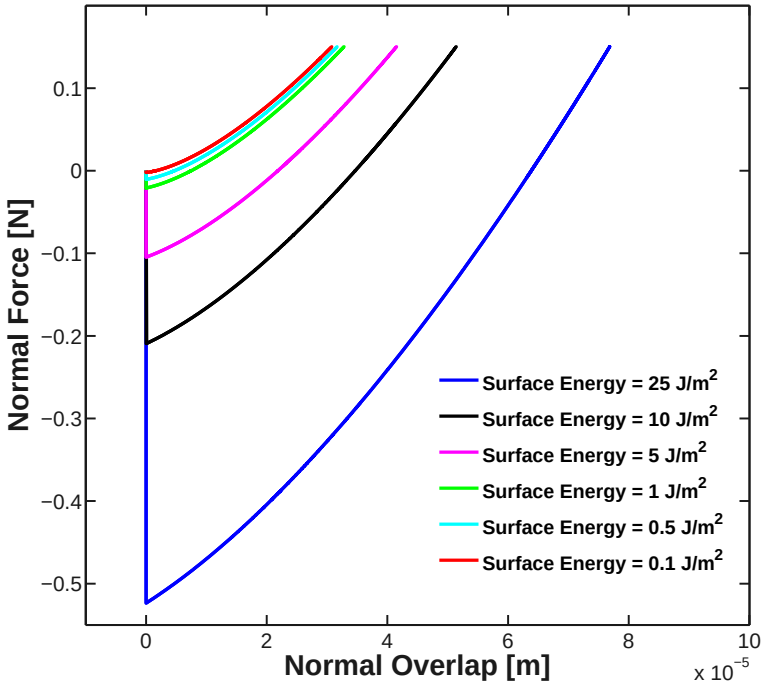

Figure 3.14: JKR force-overlap relationship - Different surface energy level for JKR contact model in EDEM

initial confined consolidation stress before being subjected to an unconfined compression test. To ensure that all simulations share the same packing structure and loading path (to the required stress levels), the first two stages of filling and consolidation occur in one simulation to the maximum consolidation stress to be considered. Models at each intermediate consolidation stress level were extracted from this simulation and unloaded at the specified consolidation stress, before being loaded to failure as a separate simulation. This simulation is based on the Edinburgh Powder Tester (EPT) which is a uniaxial tester used for measuring the level of cohesion in powders.

Figure 3.16 shows the results of a series of confined compression and unconfined compression to failure using the JKR model. In Figure 3.16a the effect of the elastic contact model is clearly visible where, following loading to three very different stress levels, the final unloaded stain of the sample is almost identical. The plastic strain in the sample is generated from particle re-arrangement that results from the initially loose fill generated by the adhesive forces. The strains in a system generated without adhesion during filling would be significantly less. The results of the unconfined yield strength are shown in Figure 3.16b where it can be seen that despite the significant difference in consolidation stress, the resulting unconfined strength are almost identical. Where both tests to 100 kPa and 200 kPa have the same final sample strain and hence porosity, the same unconfined strength of approximately 1.23 kPa is achieved. The sample to

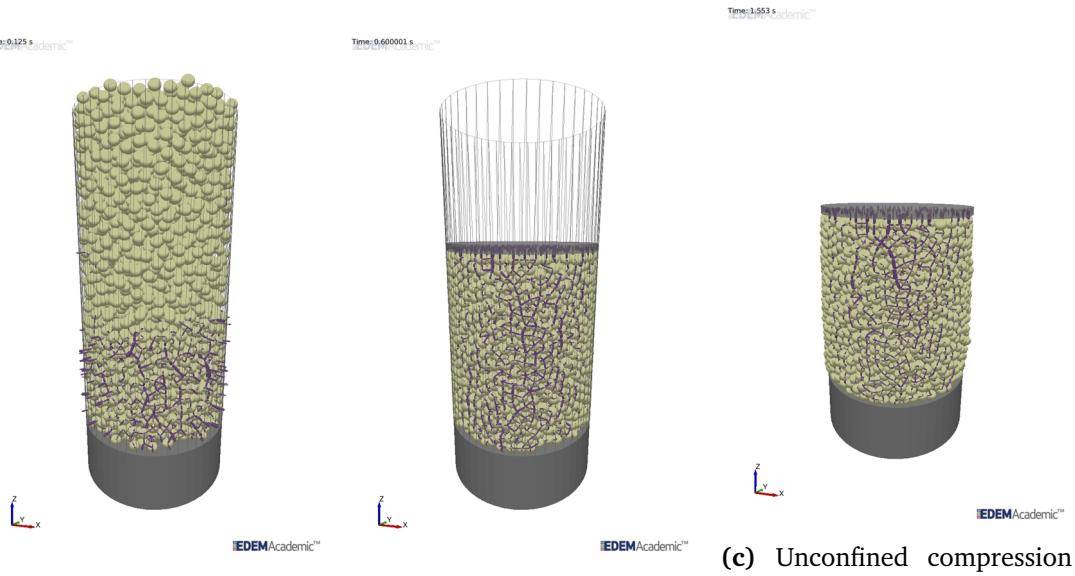

(a) Filling of cylinder **(b)** Confined consolidation **(c)** Unconfined compression to failure

Figure 3.15: JKR simulation process - Various stages of simulations

500 kPa contained slightly more rearrangement of particles during consolidation and as a result archived a slightly higher unconfined strength of approximately 1.33 kPa This small difference is what could be expected experimentally for a cohesive material tested several times as the same consolidation stress level.

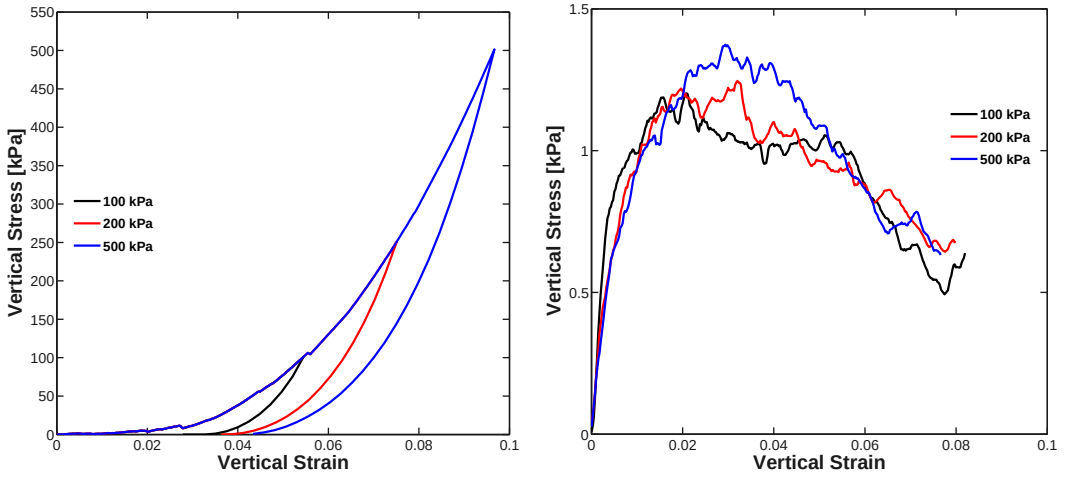

(a) Confined compression results **(b)** Unconfined compression results

Figure 3.16: JKR model evaluation - using JKR model in EDEM

3.7 Summary

This chapter has provided an overview of the discrete element method highlighting the key elements of a DEM code. The DEM code used in this study, EDEM®, and it's

capabilities for extension through the API have been introduced. A summary of some of the common contact models used for DEM simulations has also been presented.

The commonly used JKR contact model has been used for DEM simulations to determine whether it can replicate the stress history dependent behaviour that is commonly found in real cohesive materials. T he results from the DEM simulations show that while the JKR model can be used successfully for replicating situations such as powder packing, it fails to capture the stress history dependent behaviour that is so important for the of storage and handling systems for cohesive granular materials.

While many other contact models are available they each have their disadvantages. The Thornton model includes the effect of plasticity coupled with the JKR/van der Waals adhesion forces but there still exist problems calibrating surface energy parameters from AFM studies. Tomas proposed a complex model but later found that a simpler linear version with plasticity and stress history recording and adhesion could adequately capture the effects of adhesion on fines powders. Walton also proposed a complex model with plasticity but many of the parameters remain difficult to relate and measure for real particles. A similar problem exists for the simple linear adhesive model proposed by Luding, while it captures most of the correct behaviour, its definition of the adhesion strength through a tensile stiffness is difficult to relate to bulk material properties and the linear nature of the model may not adequately capture all material behaviours.

Capillary force models are suitable for materials where it is easy to relate levels of adhesion with liquid content but these models can be more computationally intensive, are elastic and likely to miss the stress history dependent behaviour, similar to the JKR model, and may struggle with the assumption of uniform moisture distribution in a system.

The effect of asperities and surface roughness is not explicitly considered in any of the commonly used contact models.

Chapter 4

Development of an Adhesive DEM Contact Model

This chapter will describe the development of an elasto-plastic adhesive contact model for studying the stress-history-dependent behaviour of a cohesive granular solid. The details of the model are presented and a verification of the implemented contact model is also presented, ensuring the desired material behaviour is reproduced by the contact model.

4.1 Introduction

The flow behaviour and handling characteristics of cohesive granular solids are strongly dependent on the prior consolidation stress experienced by the solid. As a result, the stress history in the material leading up to a handling scenario needs to be considered when evaluating its handling behaviour. Failure to account for this stress history dependence is ignoring one of the key sources of cohesion, and thus the handling problems experienced by cohesive granular solids and powders. For a DEM contact model to successfully capture this behaviour it must include contact plasticity.

Some of the prevalent contact models have been discussed in Chapter 3 and one of the key findings arising from the literature review is the prevalent use of the JKR contact model, a contact model specifically focussed on elastic, adhesive spheres. Many of the other existing contact models such as the DMT, EDEM linear cohesion model or capillary force models are also elastic models, and as such, may fail to capture the correct stress-history-dependent behaviour. Nevertheless, it has been shown that elastic adhesive models such as the JKR or van der Waals based models can recreate similar initial loose packings and, to a certain extent, capture the initial compression of the

material. The initial compression phase is mainly related to particle re-arrangement and occurs at very low stresses (<5 kPa). Much of the handling problems occur in materials in which the stress state has been much greater than several kPa and in these situations the elastic adhesive models will not be able to capture the stress-history-dependent behaviour.

While other adhesive models have been proposed and implemented in DEM as discussed in the previous chapter, each one has its limitations - Thornton and Ning [1998] suggested a non-linear adhesion model with plastic deformation, but it continued to use the elastic JKR theory for the adhesive force, Luding [2008*a*] proposed a simple hysteretic linear spring model but the linear adhesion branch is not representative of real solid behaviour and relating its tensile stiffness to bulk behaviour is not straight forward. Walton [2004]; Walton and Johnson [2009] also suggested a hysteretic linear spring model where the adhesion force was not defined by the tensile stiffness, but includes extra parameters making it more difficult to calibrate with experiments.

4.2 Proposed Model

Real life particle interactions are incredibly complex and consist of contacts that occur between particles of different sizes and shapes, with individual particles also varying at the contact interface, due to the surface roughness of materials. The varying size and shape of the particles and surface asperities coupled with various sources of adhesion and factors such as uneven moisture distributions in materials all add to the complexity of granular solids. As such, rather than trying to capture the complex micro-mechanical contact behaviour that can occur for the significant number of contacts, a new model is proposed that will consider the behaviour of bulk solids on a meso-scale rather than on a micro-scale. It has already been shown that, on a micro-scale, a more simplistic contact model that neglects some of the complexity of the contact can capture the salient behaviour of the real material being modelled Tykhoniuk *et al.* [2007].

The parameters for the proposed model are phenomenologically based with the target of capturing the key bulk characteristics exhibited by the solid. An elasto-plastic adhesive contact model, which will be referred to as the Edinburgh Elasto-Plastic Adhesive contact model (EEPA), is proposed. This methodology means that each DEM particle will represent the meso-structure of the bulk material. That is, each DEM particle will represent the associated local network, which will consist of a significant number of real particles or agglomerates that exist at a certain length-scale and the contacts and interactions between them. Interaction properties for this meso-scale interaction will

be calibrated from bulk scale experiments rather than measuring microscopic interaction properties, such as friction or adhesion surface energy, for individual microscopic particles.

The reasoning for this is threefold – firstly DEM simulations are computationally intensive. To model every individual particle at the real length-scale and include all types of adhesive forces would mean that only very small real life samples could be replicated and this limitation makes this approach un-feasible. Secondly, real particles rarely exist naturally as single particles and are usually found as agglomerates of multiple particles (Figure 4.1). It is the interaction between these agglomerates that contact model will aim to capture.

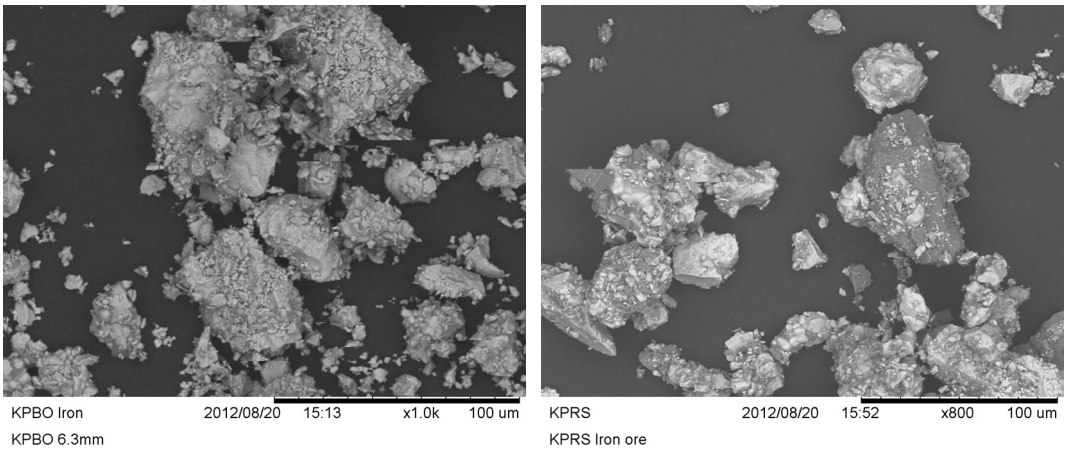

(a) KPBO - 1000x magnification **(b)** KPRS - 800x magnification

Figure 4.1: SEM images of iron ore fines - For both KPBO and KPRS fines

Finally, it should be easier to calibrate a model on a meso-scale rather than a micro-scale. Micro-scale calibration requires accurate and detailed information on properties such as contact stiffness, pull-off force or moisture distribution, which are difficult to obtain from experiments – for example, there is still some difficulty getting reliable data from AFM studies of particles and the standard deviation for repeated tests can be very large [Heim *et al.*, 2005].

However, AFM studies can be used to provide valuable information about general behaviour of particles in contact. The contact force-displacement relationship for microscopic particles has been observed by Jones [2003]. Observations were made on microscopic particles of titania, alumina, limestone, zeolite and fumed silica and displayed a nonlinear relationship as in Figure 4.2. The studies also reveal the sharp reduction in the adhesion strength of a contact as particles separate, with the possibility of almost 50% of the adhesive force being lost after a very small initial separation.

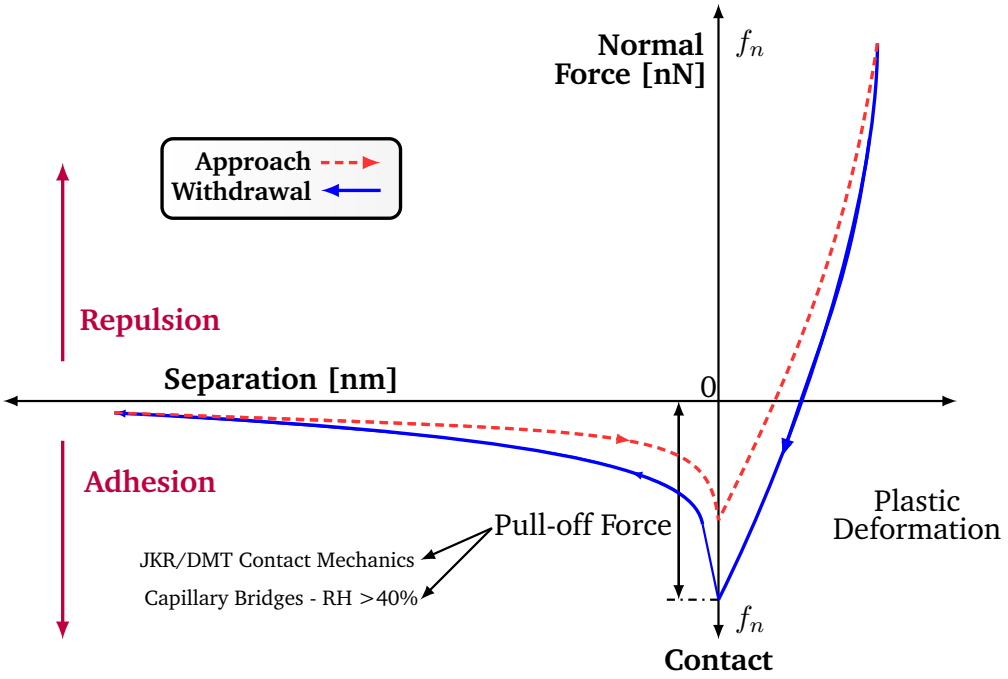

Figure 4.2: Force-separation curves from AFM - Schematic illustration of observed force-separation curves for adhesive particles, adapted from Jones [2003]

A DEM contact model that captures the above characteristics for agglomerates is presented, where the contact model parameters can easily be calibrated from bulk experiments. The details for that model are discussed in the following sections.

4.3 Model Implementation Details

The Edinburgh Elasto-Plastic Adhesive contact model has been implemented in the commercial DEM code EDEM (versions 2.3+) using the Application Programming Interface (API) feature that allows the addition of custom contact and external force models, custom properties, custom particle generation methods and couplings [DEM Solutions Ltd., 2010*a*, 2011*b*]. The API is written in the C++ language. The use of a verified commercial code allows focus to be given to the development of the contact model. Verification of the contact model is presented later in this chapter in Section 4.9.

The simulation sequence employed in the EDEM software is shown in Figure 4.3, with the location of the API contact model in the calculation process highlighted in yellow. The API contact model is called each time a contact is detected. The calculation process of the contact model is detailed in Figure 4.5 and will be discussed in detail in Section 4.9.

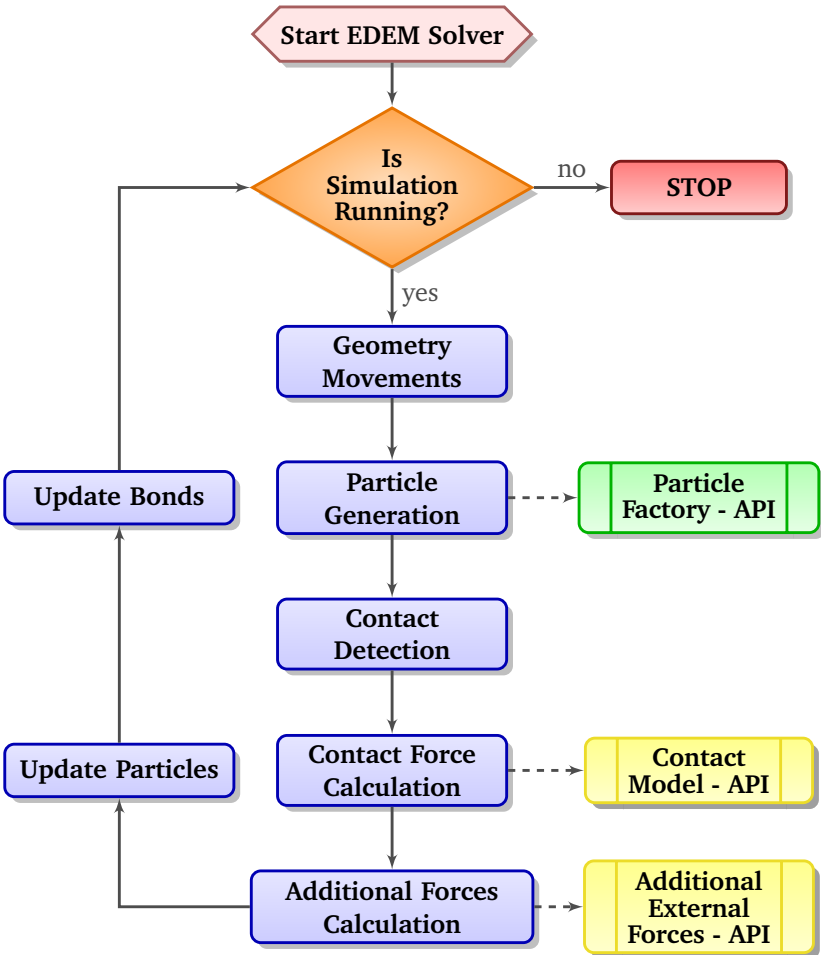

Figure 4.3: EDEM simulation sequence - Key stages of the DEM method as used by EDEM.

4.4 Model Overview

The force-overlap relationship for the EEPA contact model is presented in Figure 4.4 and the forces for each path are given by Equation (4.1). The model aims to replicate the behaviour of two particles or agglomerates in contact, where during contact they are pressed together and undergo elastic and plastic deformations. This causes an increase in the pull-off (adhesive) force as the plastic contact area increases with deformation. An overview of the calculation process for the contact model is presented in the flow diagram in Figure 4.5. The equations behind these calculations are presented in detail in the following sections.

$$f_{hys} = \begin{cases} f_0 + k_1\delta^n & f_1 \Rightarrow \text{ if } k_2\left(\delta^n - {\delta_p}^n\right) \geq k_1\delta^n \\ f_0 + k_2\left(\delta^n - {\delta_p}^n\right) & f_2 \Rightarrow \text{ if } k_1\delta^n > k_2\left(\delta^n - {\delta_p}^n\right) > -{k_{adh}}\delta^x \\ f_0 - {k_{adh}}^x & f_{adh} \Rightarrow \text{ if } -{k_{adh}}\delta^x > k_2\left(\delta^n - {\delta_p}^n\right) \end{cases} \tag{4.1}$$

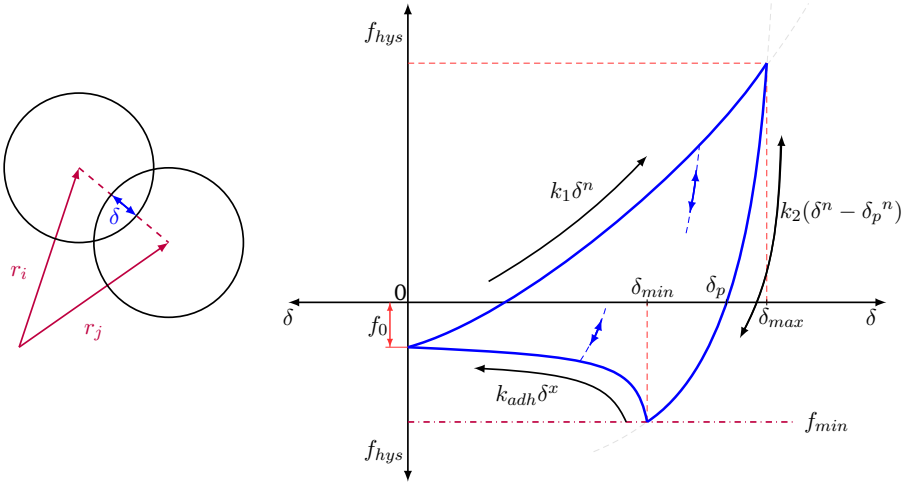

Figure 4.4: Edinburgh Elasto-Plastic Adhesion (EEPA) contact model - Schematic of normal force model

The model consists of a virgin loading branch, hereafter referred to as k_1, an unloading/reloading branch referred to as k_2 and an adhesive branch referred to as k_{adh}. This is based on the hysteretic linear spring originally proposed by Walton and Braun [1986]. To account for the non-linearity that exists during particle contacts (Figure 4.2) the model includes non-linear behaviour for both the k_1 and k_2 branches, which are controlled by the exponent *n*. The adhesive strength of the contact is governed by a limiting value, f_{min}, which is dependent on the contact patch area when two particles are in contact and is added to any additional non-contact forces accounted for by f_0. AFM studies have shown that as particles are removed from contact the force drops off sharply [Jones, 2003]. To account for this physical phenomena, the adhesive branch slope has been separated from the virgin loading and unloading/reloading branches and the softening behaviour is controlled by the exponent X. As the value of X increases from 1 (which represents a linear model [Luding, 2005*a*,*b*, 2008*a*]) the model will demonstrate a more sudden drop in adhesive strength, similar to what is seen in AFM measurements of particle interactions.

The contact model has an in-built versatility that allows it to be used in several modes – if the magnitude of the virgin loading stiffness k_1 and the unloading/reloading stiffness k_2 are equal the model reverts to being an elastic model. Furthermore, if the exponent *n=1* the model will be the well-known linear spring model and if $n = 1.5$ the model will replicate the Hertzian spring model. As the model is a hysteretic spring, the maximum plastic overlap that a contact has achieved δ_p, is recorded for each contact. This is updated during loading along the virgin loading branch k_1.

While the linear version of the proposed contact model is similar to the models of Luding [2005*a*,*b*, 2008*a*] and Walton [2004]; Walton and Braun [1986]; Walton and

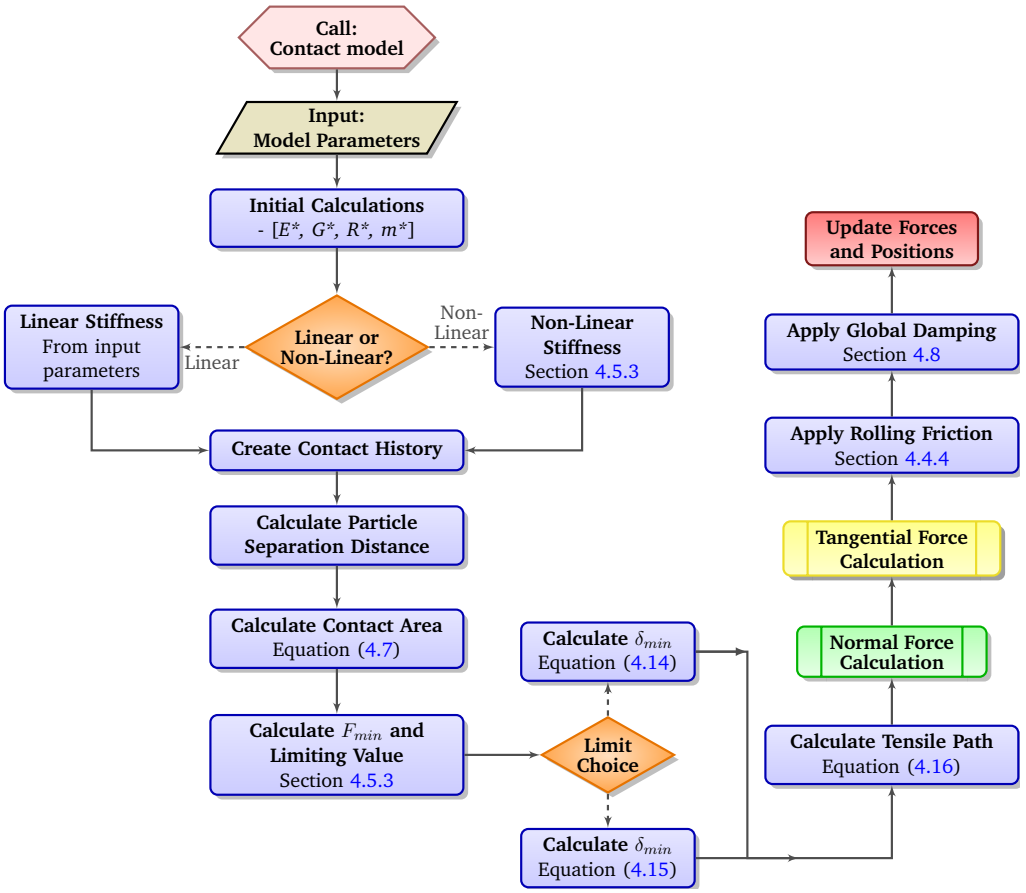

Figure 4.5: Contact model flow chart - Key stages of the calculation process

Johnson [2009], there are some key exceptions for the proposed model which can be summarised as follows:

- k_2 is a constant within the model and does not vary with applied load
- The coefficient of restitution in the contact model is a constant
- The history parameter being tracked is the plastic overlap δ_p value, rather than the δ_{max} value.
- The maximum adhesive force f_{min} is now determined from the product of the plastic contact overlap and the surface energy of the contact. Once the contact force reaches the limiting value f_{min}, separation of the contact can occur. The adhesion branch no longer controls the magnitude of adhesive force developed at the contact - in the contact model proposed by Luding [2005*a*,*b*, 2008*a*] the maximum amount of adhesion that can be generated at the contact is determined from the intersection of the *adhesion branch* stiffness and *unloading/reloading branch* stiffness.

4.4.1 Simulation Initialisation

At the initialisation of each simulation, the parameters of the model are loaded into the software from a preference file, which contains the following information for the contact model:

- $\mathbf{f_0}$ = Constant pull-off force: This can be used to incorporates ever presents forces that may occur, such as van der Waals type forces or electrostatic force. The magnitude of this force will not change for the simulation duration.
- **Adhesion energy value,** $\Delta\gamma$ = Contact adhesion energy (J/m^2): This is the level of adhesion that is used in the calculation of the load dependent adhesive force in the contact model, f_{min}.
- $\mathbf{k_1}$ = Virgin loading stiffness (N/m): The initial loading stiffness of the contact.
- $\mathbf{k_2} : \mathbf{k_1}$ ratio = Ratio of constant stiffness k_2 to k_1. This parameter defines the unloading/reloading stiffness magnitude as a ratio of the initial stiffness. This is the level of contact plasticity used in the model.
- $\mathbf{n}$ = power value for k_1 and k_2 F-D relationship: This is used to switch between linear [EEPA-L] and non-linear [EEPA-NL] force-overlap relationships for the contact model.
- $\mathbf{X}$ = Power value for adhesion branch: This defines the severity of the drop in adhesion force following the peak tensile force being reached. A value of unity give a linear more ductile separation curve, whereas a sharp drop in strength is found for values > X =2.
- $\boldsymbol{K_{tm}}$ = Tangential Stiffness multiplier: This allows the tangential stiffness used in the model to be varied.

These are then retained as constants for the duration of the simulation. Parameters can be changed any time the simulation is stopped and restarted, as this will reload the preference file.

4.4.2 Normal Force Calculation Method

The calculation procedure for the normal force-displacement relationship of the model (Figure 4.4) is presented in the flow chart in Figure 4.6. The EEPA contact model has the ability to be used as both a linear or non-linear model. The same normal force calculation procedure is employed for both linear and non-linear modes. The normal force F_n on each branch ($f_1, f_2\ and\ f_{adh}$) is initially calculated using Equation (4.1).

The correct loading path is the selected based on the criteria of Equation (4.1) through the use of a conditional loop. Once the loading path for the current timestep has been selected, the normal force is then known. The historical maximum plastic overlap, δ_p, is updated only while contacts take place on the virgin loading branch, k_1. Custom contact properties such as the historical maximum plastic overlap are stored using the additionally functionality provided by the EDEM API.

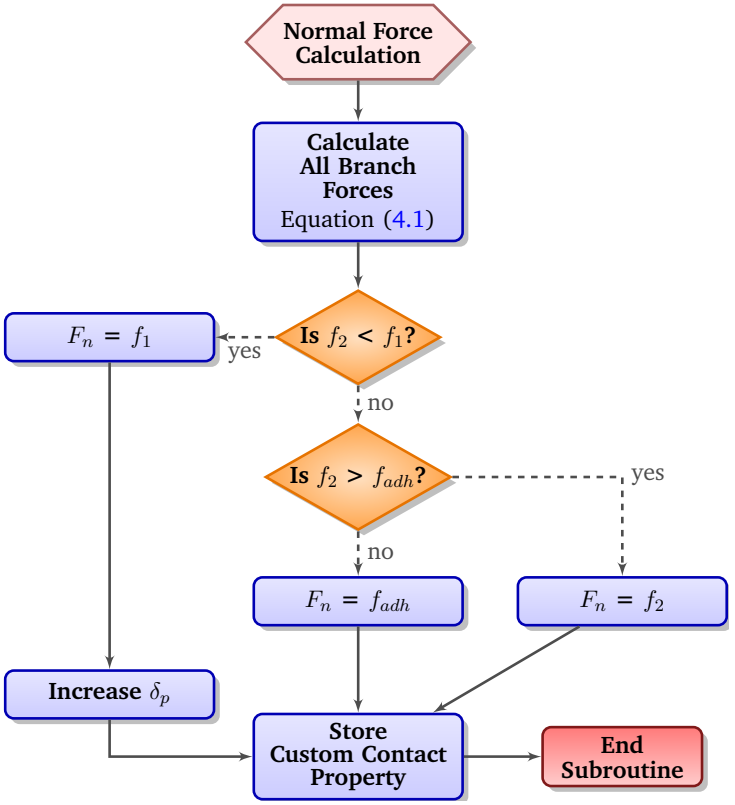

Figure 4.6: Normal force calculation method - Stages of normal force calculation procedure.

4.4.3 Contact Damping Method

As well as the non-viscous damping that is applied to the equations of motion over the whole simulation, viscous contact damping is also included in the contact model to help dissipate the excess kinetic energy arising from contact. A general overview of the calculation method is presented in Figure 4.7 for the normal direction and in Figure 4.8 for the tangential direction. The first step in the damping calculation process is to determine the damping coefficient β from the defined coefficient of restitution. If the coefficient or restitution is specified as zero, the damping coefficient will also be zero. The calculation method will also depend on whether the contact model is being used as linear or non-linear.

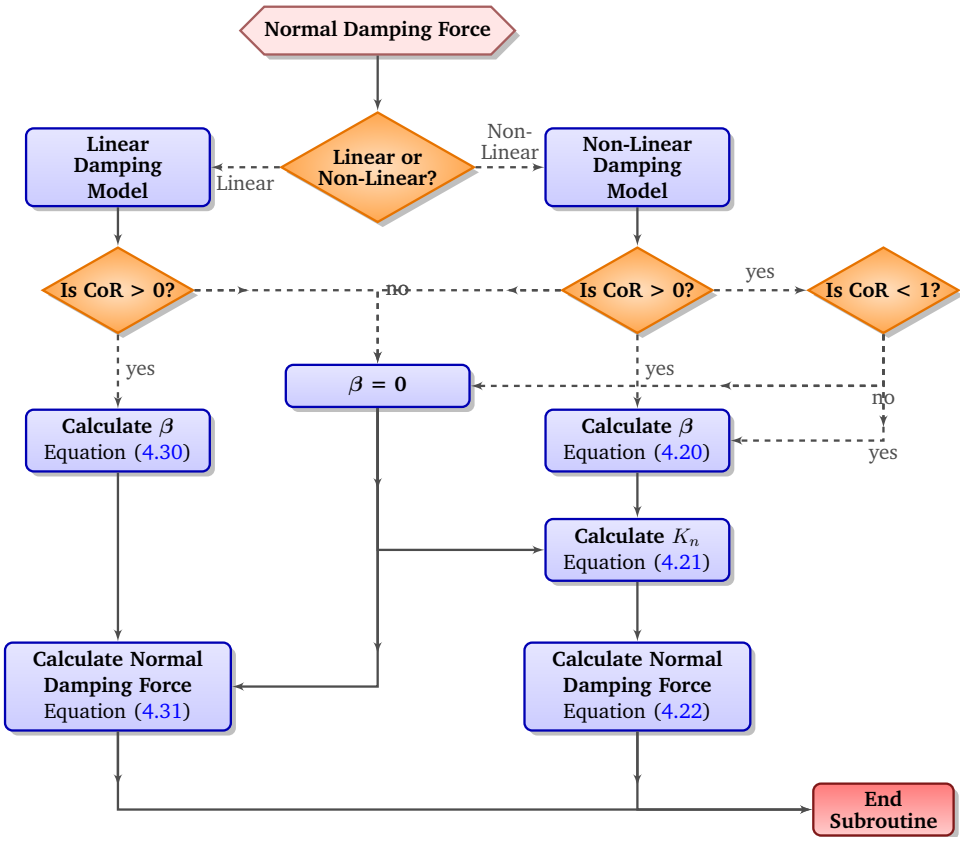

Figure 4.7: Normal damping force calculation method - Stages of normal damping calculation procedure.

For the damping in the tangential direction (Figure 4.8), a tangential stiffness and tangential force need to be defined and calculated in a similar fashion to the normal direction. A different calculation method is used for both the linear and non-linear portions of the models due the different tangential stiffness definition for each. The contact model parameters also provide an option to vary the tangential stiffness through a stiffness multiplier κ_{tm}.

4.4.4 Rolling Friction Model

Rolling friction can be applied to particle contacts to help resist the rolling that may occur with spherical particles in DEM simulations. The coefficient of rolling friction μ_R is a scalar value used to determine the amount of torque needed to be applied to an object at rest on a flat surface to set a particle in motion, for a given material. The direction of the applied torque is always opposite to the direction to the relative rotation. While there are many option for rolling friction models available the rolling friction model used by EDEM [DEM Solutions Ltd., 2010*b*], described as Model A by Ai

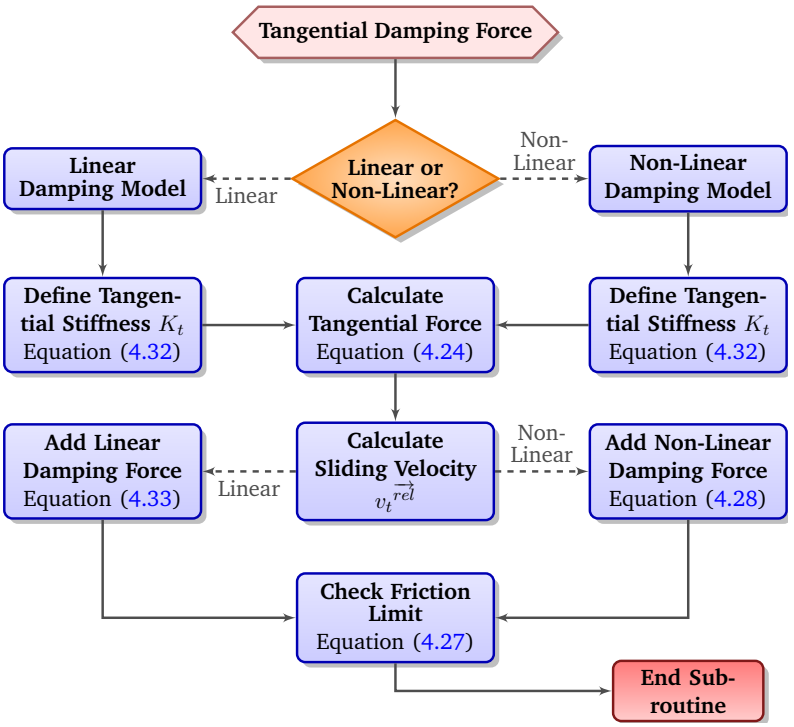

Figure 4.8: Tangential damping force calculation method - Stages of tangential damping calculation procedure.

et al. [2011], is implemented here. The total applied torque, τ_i, is given by:

$$\tau_i = -\mu_r \left| f_{hys} \right| R_i \boldsymbol{\omega_i} \tag{4.2}$$

where μ_r is the coefficient of rolling friction, R_i is the distance from the contact point to the particle centre of mass and $\boldsymbol{\omega_i}$ is the angular velocity at the contact point.

4.5 Initial Calculations

For each contact, the initial calculation step is to calculate the properties that are unique to each contact. These properties are re-calculated every time the contact model is called and are not stored. These calculations are performed regardless of the input parameters specified for the simulation. The relative velocity of the particles in contact is also calculated at this point.

4.5.1 Contact properties

The equivalent Radius, R^*, is calculated from Equation (4.3).

$$R^* = \frac{(r_i \times r_j)}{(r_i + r_j)} \tag{4.3}$$

where R_i and R_j are the radii of the two particles in contact.

The equivalent mass, m^*, is calculated from Equation (4.4):

$$m^* = \frac{(m_i \times m_j)}{(m_i + m_j)} \tag{4.4}$$

where m_i and m_j are the masses of the two particles in contact.

The equivalent Young's modulus, E^*, is calculated from Equation (4.5):

$$\frac{1}{E^*} = \frac{\left(1 - {\nu_i}^2\right)}{E_i} + \frac{\left(1 - {\nu_j}^2\right)}{E_j} \tag{4.5}$$

where E_i and E_j are the radii of the two particles in contact and ν_i and ν_j are the Poisson's ratios of the two particles.

The equivalent shear modulus, G^*, is calculated from Equation (4.6),

$$\frac{1}{G^*} = \frac{(2 - \nu_i)}{G_i} + \frac{(2 - \nu_j)}{G_j} \tag{4.6}$$

where G_i and G_j are the radii of the two particles in contact.

In the EDEM code, only the shear modulus and Poisson's ratio are set as input parameters with Young's Modulus calculated from these as required.

4.5.2 Particle Separation Distance, Contact Area and f_{min}

In the contact model, it is assumed that the adhesive strength is related to the surface area of the contact. During real particle contacts, the surface of a particle will flatten at the point of contact, and the amount of flattening that occurs will depend on the load applied. The plastic contact patch radius a at δ_p is calculated for each contact to allow the contact area, due to the plastic deformation of the contact, to be calculated from Equation (4.7) [Weisstein, 2013], where d is the distance between particle centres and R_i and R_j are the particle radii and is given by Equation (4.8).

$$a = \frac{1}{2d}\sqrt{4d^2{R_i}^2 - \left(d^2 - {R_j}^2 + {R_i}^2\right)^2} \tag{4.7}$$

$$d = \begin{cases} d_1, & \text{for } d_1 < d_2 \\ d_2, & \text{for } d_2 \geq d_1 \end{cases} \tag{4.8}$$

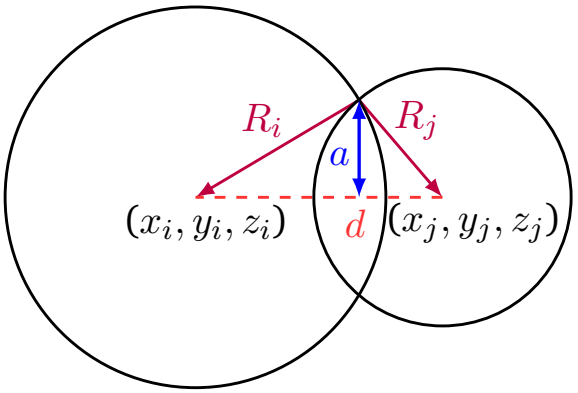

Figure 4.9: Overlapping spheres - Geometrical relationships for two spheres

The contact patch radius can vary between the maximum contact area that occurs during loading along k_1, or the residual plastically deformed contact area that remains while on k_2 and k_{adh}. The separation distance d_1 while along k_1 and the separation distance for other branches, d_2, is defined by Equations (4.9) and (4.10).

$$d_1 = (R_i + R_j) - \delta_{ij} \tag{4.9}$$

$$d_2 = (R_i + R_j) - \delta_p \tag{4.10}$$

Following the calculation of the plastic contact radius, the minimum adhesive force for the contact is defined by Equation (4.11).

$$f_{min} = \pi \Delta\gamma \psi a \tag{4.11}$$

where $\Delta\gamma$ is the surface energy (J/m^2) of the material and ψ is an adhesion constant similar in form to that found in JKR or DMT Theory.

For this study, adopting a value of $3/2$, the minimum adhesive force for the contact is defined by Equation (4.12). This results in a pull-off force (N), similar to JKR Theory, that if exceeded, the particles in contact will begin to separate.

$$f_{min} = \frac{3}{2}\pi \Delta\gamma a \tag{4.12}$$

4.5.3 f_{min} Limit

In the case of the non-linear version of the contact model a limit is required for f_{min} during initial loading. The maximum amount of adhesion any contact can develop is

limited by the unloading stiffness k_2. This is more important for the non-linear mode as the k_2 branch intersects with the y-axis at a much lower force than the linear mode due to the curvature. If no limit was placed on f_{min}, in certain situations the unloading along k_2 may not intersect with f_{min}, making the adhesive branch to separation unsolvable disappear due the location of δ_{min} being unsolvable. If no limit was placed on f_{min} and this was to occur it would mean that as a particle tried to separate, and as there was no available solution for the adhesion branch the particles would simply disappear from the simulation. The limiting value of f_{min} is given by Equation (4.13).

$$f_{2Lim} = -\left(k_2 {\delta_p}^n\right)\gamma \tag{4.13}$$

Where λ is a multiplier that cannot exceed unity. It is currently set at 0.5, meaning particle will begin to separate at 50% of the limiting force. In the case where f_{min} has been limited, a corresponding empirical limit is placed on δ_{min} also. This is detailed in Equation (4.14) in a later section. It should be noted that this limit is only applied in a small number of contacts such as at very small overlaps, when two particles come in to contact while falling, or when the surface energy value used for calculating the maximum adhesive strength of the contact is excessively high.

4.5.3.1 Location of Peak Adhesive Strength - δ_{min}

Further unloading along k_2 continues until the maximum adhesive force, -f_{min}, is reached at δ_{min}, where δ_{min} is defined by the following Equation (4.14):

$$\delta_{min} = \left(\frac{-f_{min} + k_2 {\delta_p}^n}{k_2}\right)^{\frac{1}{n}} \tag{4.14}$$

If the calculated f_{min} is lower than the $f_{2Limit,}$ the point at which the peak adhesive force is located is calculated from Equation (4.15).

$$\delta_{min} = 0.5\ \delta_{normal} \tag{4.15}$$

4.5.3.2 Adhesion Branch Stiffness

Once f_{min} and δ_{min} have been defined the stiffness value for the adhesive branch k_{adh} can be calculated from Equation (4.16).

$$k_{adh} = \left(\frac{f_{min}}{{\delta_{min}}^x}\right) \tag{4.16}$$

4.6 Non-Linear Mode

While other models [Luding, 2005*b*, 2008*a*; Walton and Johnson, 2009] use a linear relationship and Thornton [1997] proposed a model that was initially non-linear before switching to a linear relationship at a yield point, these linear models maybe too soft at higher stresses, as suggested by Vu-Quoc and Zhang [1999*b*]. For simplification purposes, the EEPA model omits the yield point and proposes a force-displacement relationship that is non-linear throughout. The model uses the same power *n* for the virgin loading branch and unloading/reloading branch. However the adhesion branch has a separate parameter that controls the adhesive unloading stiffness, to account for the sharper drop-off once peak adhesion force has been reached that is commonly seen in AFM force-displacement results for particle-particle contacts. The normal force relationship in Figure 4.4 is expressed mathematically in Equation (4.17).

$$f_{hys} = \begin{cases} f_0 + k_1\delta^n & \text{if } k_2\left(\delta^n - {\delta_p}^n\right) \geq k_1\delta^n \\ f_0 + k_2\left(\delta^n - {\delta_p}^n\right) & \text{if } k_1\delta^n > k_2\left(\delta^n - {\delta_p}^n\right) > -k_{adh}\delta^x \\ f_0 - {k_{adh}}^x & \text{if } -k_{adh}\delta^x > k_2\left(\delta^n - {\delta_p}^n\right) \end{cases} \tag{4.17}$$

The contact forces force each branch are calculated and checked against the selection criteria to determine which branch of the model is correct for that timestep.

The non-linear virgin loading stiffness k_1 is defined by Equation (4.18) which is based on Hertz contact Theory, instead of the value specified in the simulation properties.

$$k_1 = \frac{4}{3}\sqrt{R^*}E^* \tag{4.18}$$

Unloading occurs along k_2, reaching zero force at a specific overlap. This overlap is defined as the plastic overlap, δ_p , in Equation (4.19) and the the maximum historical normal overlap is recorded as the history parameter for the contact model in a custom contact property and is updated as necessary.

$$\delta_p = \left(1 - \frac{k_1}{k_2}\right)^{\frac{1}{n}}\delta \tag{4.19}$$

4.6.1 Normal Damping Model

In the non-linear portion of the contact model, the normal damping calculation is carried out as in the Hertz-Mindlin (No-Slip) model currently used in EDEM [DEM Solutions Ltd., 2010*b*, 2011*d*]. The damping coefficient β is given by Equation (4.20), where *e* is the coefficient of restitution used in the simulation.

$$\beta = \frac{\ln e}{\sqrt{\ln^2 e + \pi^2}} \tag{4.20}$$

The Hertzian normal stiffness (K_n) is calculated from Equation (4.21) and depends on the equivalent radius and Young's modulus, as well as the normal overlap δ_n.

$$K_n = 2E^* \sqrt{R^* \delta_n} \tag{4.21}$$

Finally the normal damping force is calculated from Equation (4.22):

$${f_n}^d = -2\sqrt{\frac{5}{6}}\beta\sqrt{K_n m^*}{v_n}^{\overrightarrow{rel}} \tag{4.22}$$

where ${v_n}^{\overrightarrow{rel}}$ is the normal component of the relative velocity.

The total contact normal force, F_n, is given by Equation (4.23) and is the sum of f_{hys}, the hysteretic spring force from Equation (4.17) and ${f_n}^d$, the normal damping force from Equation (4.22).

$$F_n = \left(f_{hys} + {f_n}^d\right)\hat{\boldsymbol{n}} \tag{4.23}$$

where $\hat{\boldsymbol{n}}$ is the unit normal vector pointing from the contact point to the particle centre.

4.6.2 Tangential Force & Damping Model

As both linear and non-linear relationships between load and friction have been found in the literature [Berman *et al.*, 1998; Briscoe and Kremnitzer, 1979; Ecke and Butt, 2001; Jones *et al.*, 2004; Ruths *et al.*, 2003; Schwarz *et al.*, 1997; Skinner and Gane, 1972], the non-linear normal calculation will be coupled with a non-linear tangential calculation. In this case the tangential calculation used in the Hertzian contact model is implemented. The un-damped tangential force is calculated from Equation (4.24).

$$f_t = -K_t \delta_t \tag{4.24}$$

The tangential stiffness is defined in Equation (4.25) where κ_{tm} is the tangential stiffness multiplier input parameter, which is defined as a decimal > 0.

$$K_t = 8G^* \sqrt{R^* \delta_n} \kappa_{tm} \tag{4.25}$$

The tangential force is coupled to the normal force through Coulomb's law, such that

$$F_t = \begin{cases} -K_t \delta_t + {f_t}^d & \text{for } f_t \leq \mu_s f_{hys} \\ f_{ct} & \text{for } f_t > \mu_s f_{hys} \end{cases} \tag{4.26}$$

where μ_s is the coefficient of sliding friction. The force is incremental below the Coulombic Limit f_{ct} that is given by Equation (4.27), which includes the adhesive contribution [Skinner and Gane, 1972], and is equal to the limiting friction above the Coulomb Limit.

$$f_{ct} \leq \mu \left| (f_{hys} + k_{adh} \delta^n - f_0) \right| \tag{4.27}$$

where f_{ct} is the limiting tangential force, f_{hys} is contact normal spring force from Equation (4.17) and μ is the friction coefficient.

The tangential damping force is calculated from Equation (4.28) and is added to the undamped tangential force [Equation (4.24)] to get the total damped tangential force F_{td}.

$${f_t}^d = -2\sqrt{\frac{5}{6}} \beta \sqrt{K_t m^*} {v_t}^{\overrightarrow{rel}} \tag{4.28}$$

Where $v_t^{\overrightarrow{rel}}$ is the normal component of the relative velocity and β is the damping coefficient value calculated from Equation (4.20).

4.7 Linear Mode

If the exponent *n* is set to unity in the EEPA contact model, the model becomes a linear contact model (Figure 4.10), similar to that of Luding [2005*a*, 2008*a*]; Luding *et al.* [2005] and Walton and Johnson [2009]. The equations of the model for the linear version can be simplified to those presented in Equation (4.29).

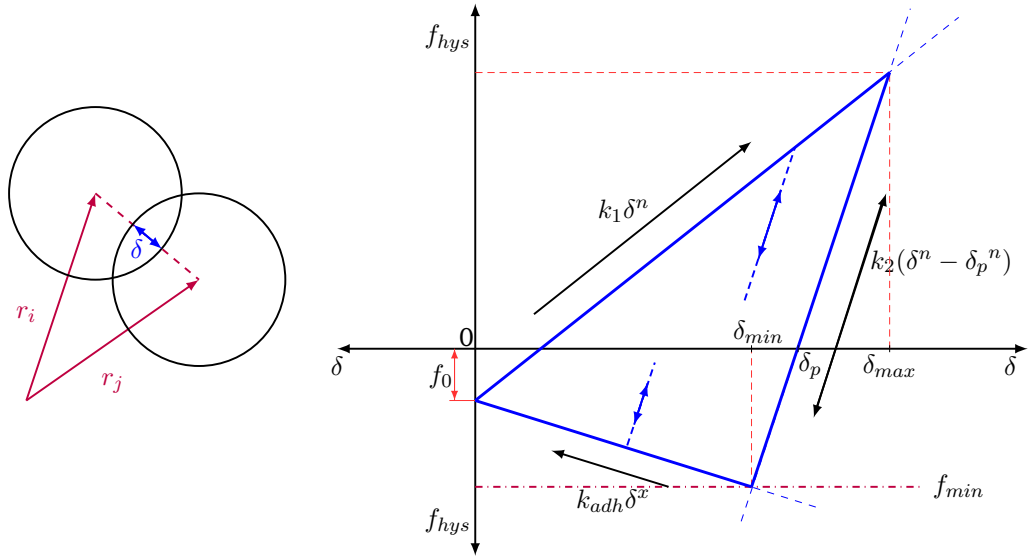

Figure 4.10: Edinburgh Elasto-Plastic Adhesion (EEPA-L) contact model - Linear version of model

$$f_{hys} = \begin{cases} f_0 + k_1\delta & \text{if } k_2\left(\delta - \delta_p\right) \geq k_1\delta \\ f_0 + k_2\left(\delta - \delta_p\right) & \text{if } k_1\delta > k_2\left(\delta - \delta_p\right) > -k_{adh}\delta^x \\ f_0 - {k_{adh}}^x & \text{if } -k_{adh}\delta^x > k_2\left(\delta - \delta_p\right) \end{cases} \tag{4.29}$$

4.7.1 Normal Damping

The dash-pot coefficient β is calculated based on the normal stiffness and the coefficient of restitution [DEM Solutions Ltd., 2010*b*, 2011*d*],

$$\beta = \sqrt{\frac{4m^* k_1}{1 + \left(\frac{\pi}{\ln e}\right)^2}} \tag{4.30}$$

where *e* is the coefficient of restitution ($0 > e \leq 1$). If *e=1*, then $\beta = 0$. The normal damping force is calculated from Equation (4.31), where $v_n^{\overrightarrow{rel}}$ is the normal component of the relative velocity.

$$f_n^d = -\beta v_n^{\overrightarrow{rel}} \tag{4.31}$$

The total normal contact force F_n is calculated in the same manner as in Equation (4.23).

4.7.2 Tangential Force & Damping Model

The tangential stiffness is calculated from Equation (4.32) and is normally set as a ratio of the normal stiffness [Cundall and Strack, 1979].

$$K_t = \kappa_{tm} k_1 \tag{4.32}$$

In the EDEM linear spring model the tangential stiffness K_t is equal to the normal stiffness [DEM Solutions Ltd., 2010*b*, 2011*d*] while a ratio of K_t/K_n of 0.2 is implemented in Luding's model [Luding, 2008*a*]. LAMMPS and PFC both use a ratio of 2/7. According to Walton [1994*b*] both the normal and tangential stiffness are harmonic oscillators and if the model system is to be designed such that the normal spring will be in its equilibrium position at the same time as the tangential spring then a set ratio of K_t/K_n must be used. For a 2D disc this is given as $K_t = 1/3\ K_n$ and $K_t = 2/7\ K_n$ for spheres. However, the ratio of tangential to normal stiffness for real elastic materials lies in the range of 2/3 to 1, and depends on Poisson's ratio of the material [Mindlin, 1949]. For most "real" contacts the frequency of normal and tangential springs will be different. Based on the variations for existing models and the dependency on material properties it has been decided to set the relationship between normal and tangential stiffness as a variable that can be adjusted within the model.

The un-damped tangential force is calculated from Equation (4.24) based on the tangential stiffness K_t and tangential overlap δ_t. The tangential damping force is calculated from Equation (4.33). Both the normal and tangential directions use the same method of contact damping in the linear model.

$$f_t^d = -\beta v_t^{\overrightarrow{rel}} \tag{4.33}$$

Where $v_t^{\overrightarrow{rel}}$ is the normal component of the relative velocity and β is the value calculated from Equation (4.30). Similar to the non-linear method, the tangential force is coupled to the normal force through Coulomb's law, where it is incremental below the Coulomb Limit and is equal to the limiting friction above the Coulomb Limit [Equation (4.26)].

4.8 Global Non-Viscous Damping

The global damping model relies heavily on the API features of EDEM and is implemented through the use of custom particle properties in the contact model and an

additional particle body force model to apply the damping force to all of the particles. Only the accelerations of particles are damped in this method.

The total force acting on each particle is calculated from Equation (4.34).

$$f_i = \sum_{i=1}^{N_c} \left(f_i^N + f_i^T \right) \tag{4.34}$$

The damping is applied such that the total force acting on particle *i* is then given as:

$$F_i^D = f_i - \gamma f_i \tag{4.35}$$

where γ is the global damping coefficient.

4.9 Model Verification

While the EDEM software has previously been verified my many users worldwide since its release, it is necessary to repeat some of the verification procedures when implementing a new contact model via the API. The contact model needs to be checked to ensure that it is reproducing the expected behaviour, that is to say that the mathematics behind the contact model have been implemented correctly. Failure to verify a contact model for simple problems would mean that the level of confidence in any further simulations results would be low.

The first series of tests will be basic visual tests to check whether the hysteretic spring model behaves as expected, that is that the corrected loading paths are being obtained as well as the correct linear or non-linear behaviour. Further detailed analysis will compare the theoretical solution for the contact model with the DEM results.

4.9.1 Linearity, Non-linearity, Unloading and Reloading

The initial verification process is a visual inspection to confirm that the normal-force relationship, as defined in Figure 4.4, has been achieved. A two particle simulation was carried out were the particle was subjected to loading and reloading several times (Figure 4.11), without breaking the contact. The test will also demonstrate whether the stress history of the contact is also being accounted for. The simulation properties used are given in Table 4.1.

The loading history for the contact is given by Figure 4.12 and the same loaded contact is presented in terms of the force-overlap relationship for the contact in Figure 4.13.

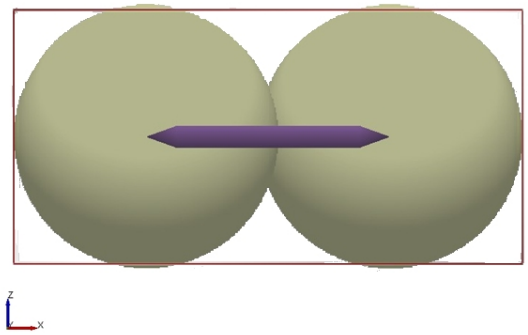

Figure 4.11: Two particle contact simulation - Particles are generated close to each other, but not in contact

Table 4.1: Simulation properties for two particle verification

Particle Density, ρ (kg/m^3)	4350
Loading Spring Stiffness, k_1 (N/m)	1×10^3
Unloading Spring Stiffness, k_2 (N/m)	$1k_1$,$2.5k_1$,$5k_1$,$10k_1$, $20k_1$, $40k_1$
Adhesive Force, f_0, (N)	0
Adhesive Surface Energy (J/m^2)	35
Adhesion branch exponent	10 (varied 1-40)
Coefficient of Restitution	0.05 (varied 0-1)
Particle Static Friction, μ_s	0.5
Particle Rolling Friction, μ_r	0.005
Simulation Time-step (s)	1×10^{-7}

The particle is initially loaded to 0.15 N and then unloaded to zero for a short period before continued unloading to approximately 0.13 N when separation starts to occur. Further loading to 0.25 N and 0.4 N increases the pull-off force from approximately 0.13 N to 0.15 N and finally to approximately 0.18 N confirming that the stress history of the contact is being captured.

Several characteristics of the model are highlighted and evaluated in Figure 4.12 and Figure 4.13. At point *A* the initial contact between the particles has occurred and the impulse causes the particles to try and separate, and while the force becomes tensile it is not enough to separate the particles. Loading continues along k_1 to point *B* before unloading along k_2 occurs. At point *C* separation occurs once the pull-off force f_{min} has been exceeded the contact force drops towards zero, before reloading occurs along k_2 again. At point *D* as the forces reaches the previous maximum, the contact model switches from reloading along k_2 to loading along k_1. Again at point *E* the force is removed and the particles remain in contact at an overlap equal to δ_p. Point *F* is another point where the contact switches from unloading to reloading along k_2 and further loading along k_1. At point *G* the viscous damping of the contact causes an oscillation

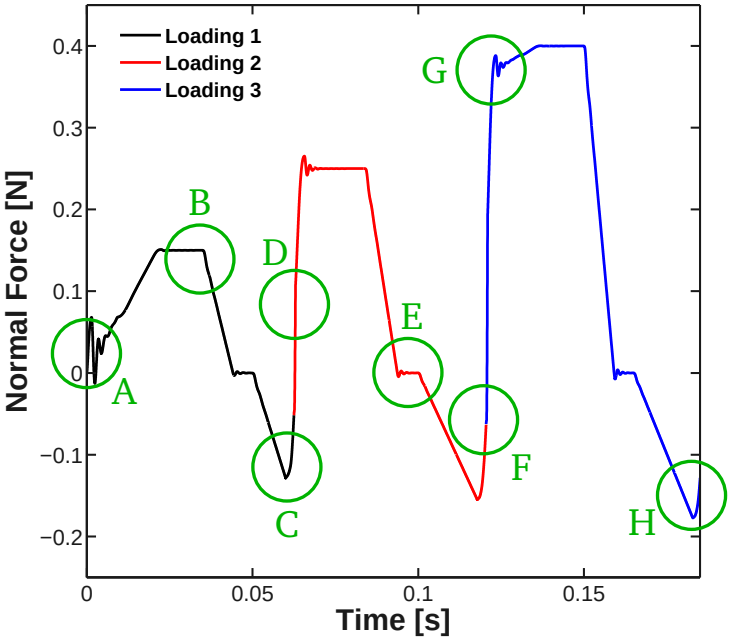

Figure 4.12: Force-history for multiple loadings - Two particle contact test

which forces the contact briefly back on to k_2. Finally at point *H* unloading to separation begins and the particles separate when the overlap reaches zero. The ability to have different rates of softening in the adhesion branch is demonstrated in Figure 4.14.

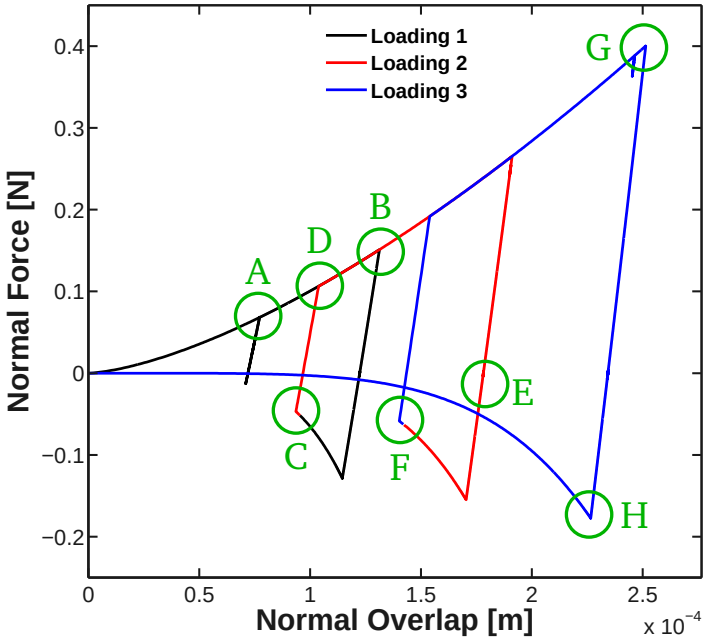

Figure 4.13: Force-overlap for multiple loadings - Two particle contact test

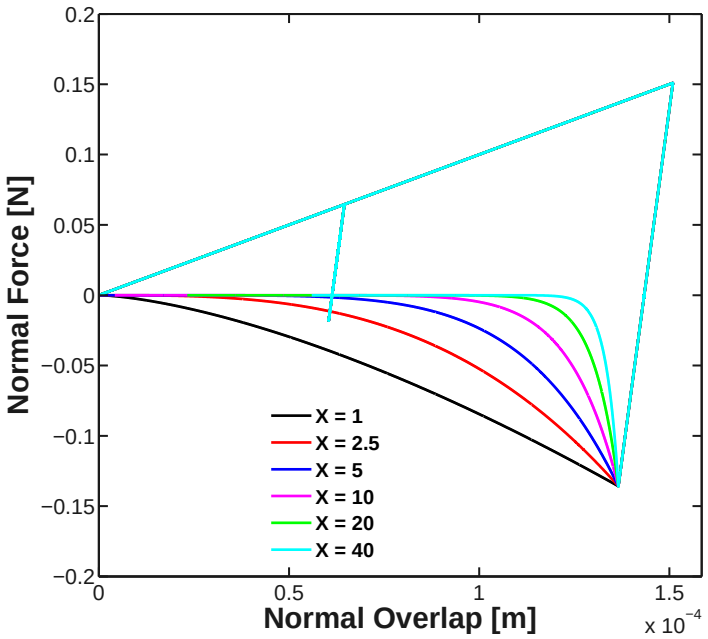

Figure 4.14: Adhesion branch slope test - Force-overlap relationship for different adhesion branch shapes

4.9.2 Contact Plasticity

For any numerical model it is important to verify that the mathematics of the contact model and ensure the correct results are being calculated by the programmed code of the contact model. The results for a two particle contact under a constant applied force can be compared to the expected mathematical solution as previously proposed for different levels of contact plasticity (Figures 4.15 and 4.16).

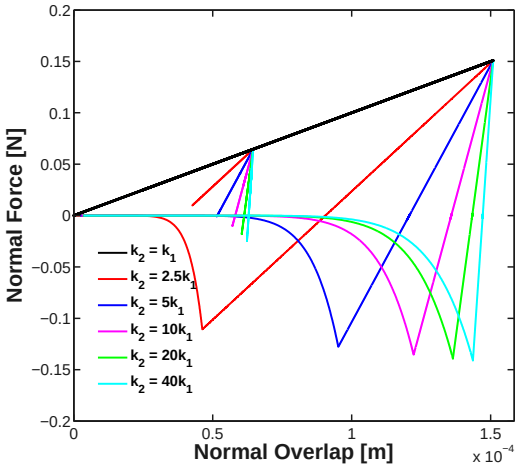

Figure 4.15: Linear force-overlap relationship for varying contact plasticity - For two particle contact test

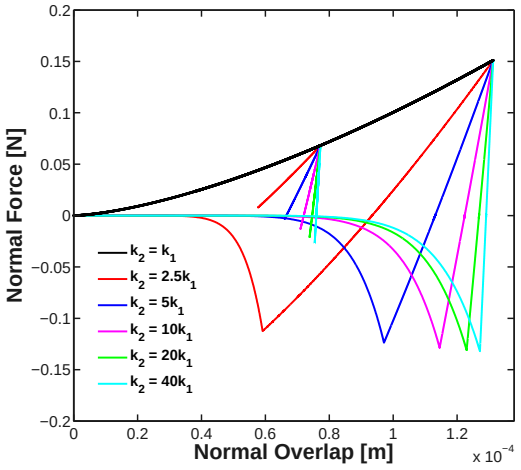

Figure 4.16: Non-linear force-overlap relationship for varying contact plasticity - For two particle contact test

For each level of contact plasticity the particles start at the same normal overlap before unloading until the particles separate. The plastic overlap δ_p, the maximum pull-off force f_{min} and the overlap at which it occurs δ_{min} can all be calculated from equations 4.11, 4.14 and 4.19. The results of this verification are presented in Table 4.2 and Table 4.3 for both the linear and non-linear modes of the contact model.

The results verify that the contact model implemented within EDEM is mathematically replicating the proposed force-displacement relationship. The errors between theoretical solutions and DEM results are very small and are numerical rounding errors over time and system precision.

Table 4.2: Comparison of theoretical prediction and DEM result for linear model

k_2:k_1 Ratio	1	2.5	5	10	20	40
Appl. δ	1.5093E-04	1.5093E-04	1.5093E-04	1.5093E-04	1.5093E-04	1.5093E-04
δ_p	0.00E+00	9.0600E-05	1.2070E-04	1.3580E-04	1.4340E-04	1.4720E-04
$\delta_{p,Sim}$	0.00E+00	9.0600E-05	1.2100E-04	1.3583E-04	1.4338E-04	1.4715E-04
% Diff.	0.0000%	-0.0001%	-0.0005%	-0.0002%	-0.0005%	-0.0006%
f_{min}	0.00E+00	-1.1073E-01	-1.2776E-01	-1.3546E-01	-1.3915E-01	-1.4095E-01
$f_{min,Sim}$	0.00E+00	-1.1100E-01	-1.2800E-01	-1.3543E-01	-1.3915E-01	-1.4094E-01
% Diff.	0.0000%	-0.0159%	-0.0382%	-0.0269%	-0.0022%	-0.0076%
δ_{min}	0.00E+00	4.6300E-05	9.5200E-05	1.2230E-04	1.3650E-04	1.4360E-04
$\delta_{min,Sim}$	0.00E+00	4.6300E-05	9.5200E-05	1.2228E-04	1.3642E-04	1.4363E-04
% Diff.	0.0000%	-0.0804%	-0.0437%	-0.0364%	-0.0205%	-0.0129%

Table 4.3: Comparison of theoretical prediction and DEM result for non-linear model

k_2:k_1 Ratio	1	2.5	5	10	20	40
Appl. δ	1.3128E-04	1.3128E-04	1.3128E-04	1.3128E-04	1.3128E-04	1.3128E-04
δ_p	0.0E+00	9.3400E-05	1.1310E-04	1.2240E-04	1.2690E-04	1.2910E-04
$\delta_{p,Sim}$	0.0E+00	9.3400E-05	1.1300E-04	1.2238E-04	1.2687E-04	1.2908E-04
% Diff.	0.0000%	0.0001%	0.0004%	-0.0001%	0.0003%	0.0002%
f_{min}	0.00E+00	-1.1244E-01	-1.2370E-01	-1.2862E-01	-1.3094E-01	-1.3208E-01
$f_{min,Sim}$	0.00E+00	-1.1200E-01	-1.2400E-01	-1.2860E-01	-1.3094E-01	-1.3207E-01
% Diff.	0.0000%	-0.0215%	-0.0010%	-0.0159%	-0.0059%	-0.0038%
δ_{min}	0.00E+00	5.9100E-05	9.7100E-05	1.1450E-04	1.2300E-04	1.2710E-04
$\delta_{min,Sim}$	0.00E+00	5.9100E-05	9.7100E-05	1.1453E-04	1.2298E-04	1.2715E-04
% Diff.	0.0000%	-0.0020%	0.0005%	-0.0010%	0.0002%	0.0003%

4.9.3 Damping Verification

The damping model can be verified through a simple particle collision where the coefficient of restitution is varied for several different collisions. The coefficient of restitution is ratio of the velocity before impact to the velocity after impact. The results for normal force, normal overlap and particle velocity for the collisions are presented in figures 4.17 to 4.19. The results for both the linear and non-linear damping are presented in terms of the coefficient of restitution in Figure 4.20 and verify that the damping component of the contact models performs as expected, with the DEM simulation results matching the theoretical values for the various levels of restitution.

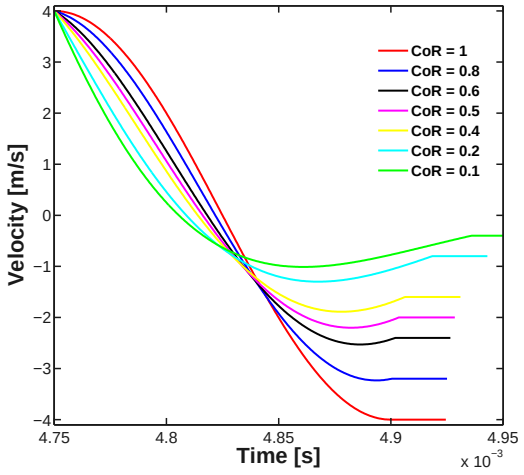

Figure 4.17: Velocity vs. time for collisions - using EEPA model in EDEM

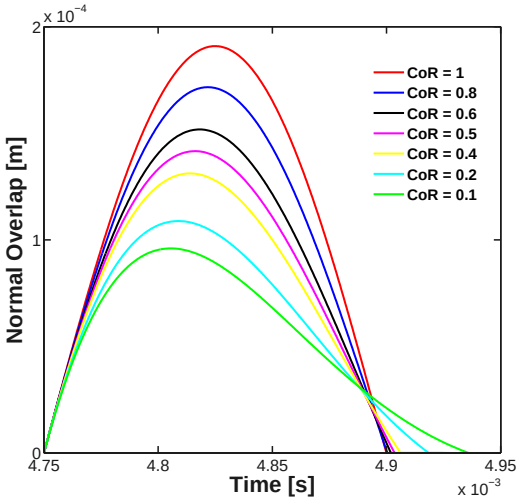

Figure 4.18: Normal overlap vs. time for collisions - using EEPA model in EDEM

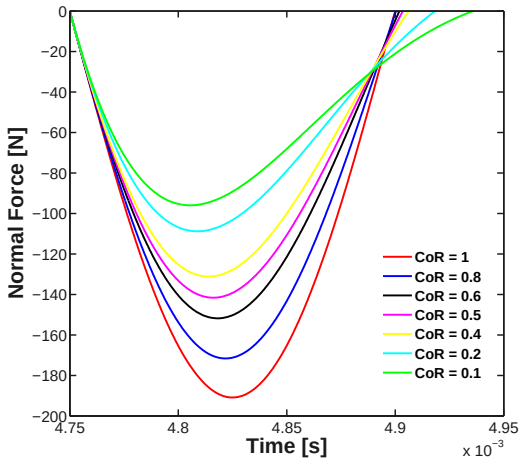

Figure 4.19: Normal force vs. time for collisions - using EEPA model in EDEM

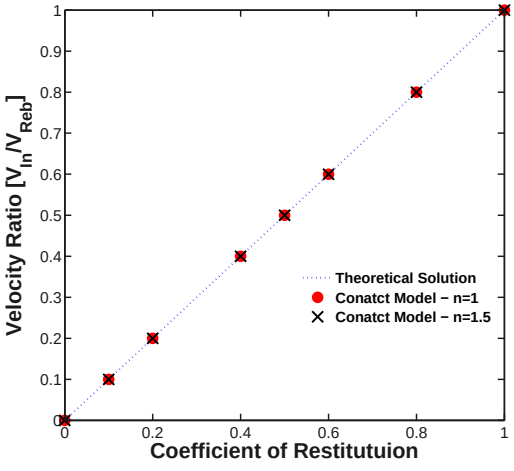

Figure 4.20: Restitution comparison for simulations - using EEPA model in EDEM

4.9.4 Force Verification

In the case where no damping is applied at the contact it is possible to verify whether the DEM calculation matches the theoretical solution for a purely elastic impact. The kinetic energy of a moving body is given by Equation (4.36) where m is the mass of the body and v is its velocity.

$$E_k = \frac{1}{2}mv^2 \tag{4.36}$$

If the impact is purely elastic and conservation of energy applies, the kinetic energy of the particle must be equal to the potential energy of a compressed spring, where all the spring compression has been caused by the impact. The potential energy in a spring is given by equation 4.37 where k is the spring stiffness and x is the amount of spring compression (which will be equal to the normal overlap of the impacting particle).

$$E_{p,s} = \frac{1}{2}kx^2 \tag{4.37}$$

In an elastic collision between a particle and another stationary, immovable object the overlap for the particle can be calculated from Equation (4.38), and once the overlap has been determined, the collisions force can be found from Equation (4.39).

$$\delta = \sqrt{\frac{mv^2}{k}} \tag{4.38}$$

$$F = k\delta \tag{4.39}$$

The simulation setup is shown in Figure 4.21, while the properties used are given in Table 4.4. The elastic linear spring is used as the contact law for the simulation.

The comparison between the DEM simulation and the theoretical solutions is presented in Table 4.5. The results show that the DEM simulation matches the theoretical prediction for the impact, verifying that the force calculation implemented in the contact model is correct. Again small differences exist due to the numerical artefacts of rounding of numbers and precision in the DEM calculations.

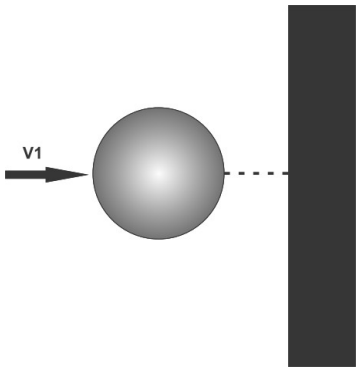

Figure 4.21: Force verification simulation setup - Sphere impacting with solid object

Table 4.4: Simulation properties for linear spring verification

Parameter	Value
Spring stiffness, k (N/m)	1.00E+006
Restitution Coefficient, e	1
Radius (m)	0.005
Density (kg/m^3)	4350
Particle Velocity, v (m/s)	0.1
Particle Volume (m^3)	5.24E-007
Particle Mass, m (kg)	2.28E-003

Table 4.5: Simulation results for linear model verification

	Theoretical Solution	DEM Simulation	% Difference
Kinetic Energy E_k [J]	0.0182	0.0182	-0.12%
Normal Overlap [m]	0.0001909	0.000191	0.00%
Normal Force [N]	190.899	190.899	0.00%

4.10 Summary

The reasoning behind a new contact model, the EEPA contact model, and the calculation method of the contact model has been presented in this chapter. The contact model has been implemented in the DEM code EDEM through the use of the API feature available in the software and a series of verification tests have been carried out to verify the model calculations have been implemented correctly. The elasto-plastic adhesive contact model has been found to be providing the expected results for several simple problems at a particle scale. An exploration of the effects of the model parameters on the bulk properties of an assembly is presented in Chapter 5 and calibration of the model from experimental data is presented in Chapter 7.

Chapter 5

Bulk Experiments for Material Characterisation

The flowability of bulk solids, particularly fine grained ones, is greatly affected by the adhesion that acts between the particles. This adhesion can be attributed to van der Waals, electrostatic, capillary or magnetic forces to name just a few possible sources and all are dependent on the separation distance of the particles. In moist bulk solids, the capillary forces tend to become the dominant adhesive force, while van der Waals forces become less influential as particle size increases past several microns.

The flowability of bulk solids is usually measured using the flow function, which is the functional relationship between the unconfined yield strength (σ_c) and the consolidation stress (σ_1). One of the most commonly used methods for this is the Jenike shear test [ASTM International, 2006] but this is a time consuming method and the results can be very operator dependent. These factors make the Jenike shear test difficult to implement in industry for the purpose of quality control. Uniaxial testers offer a different approach in which the unconfined yield strength can be easily tested both quickly and repeatedly, independent of the test operator. The confined compression test is used mainly for determining material characteristics such as bulk stiffness and the lateral pressure, K_0, which is an important parameter used in the design of silos and storage bunkers.

These experiments are used in this chapter to investigate the influence of moisture, and the resulting cohesion, on the behaviour of two types of iron ore fines from LKAB - KPBO and KPRS fines. Information garnered from these will be used for providing a knowledge base for the calibration of a DEM model.

5.1 Test Methods

The uniaxial compression test, confined compression test and Jenike shear tests are outlined in the following section, along with some of the underlying theory for each.

5.1.1 Uniaxial Compression Test

A common method for characterising the flowability of powders and fine granular materials is the uniaxial test [Bell *et al.*, 2007; Enstad and Ose, 2003; Freeman and Fu, 2011; Maltby and Enstad, 1993; Parrella *et al.*, 2008; Röck *et al.*, 2006] where the unconfined yield strength (σ_u) can be measured directly from the force required to fail a sample. A typical uniaxial test is shown in Figure 5.1 where the three main phases of the uniaxial test process are presented. The uniaxial tester usually consists of a hollow cylinder of cross-sectional area A and is manufactured from a material that is assumed to be "friction-less ". The effect of wall friction during confined compression can be significant and affect the unconfined yield strength [Schwedes, 2003]. Various attempts have been made to negate the effect of wall friction through either compacting in small layers [Williams *et al.*, 1971] or through the use of a membrane [Maltby and Enstad, 1993]. The height of the cylinder can vary between testers and is typically in the range given by an aspect ratio of 1-2.

Once the cylinder has been filled by the bulk material, the consolidation stress (σ_1) is applied and thus compresses the sample. The looser the initial packing of the sample, the more compressible the sample is and the larger the increase in bulk density during the test. Easy flowing materials consisting of larger, denser, cohesionless particles show very little change in bulk density from their initial state due to the initial low porosity packing that they generally tend to form.

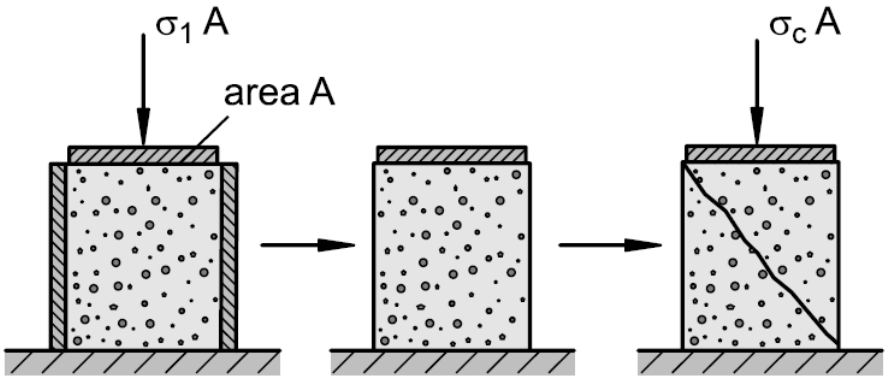

Figure 5.1: Uniaxial compression test - Schematic illustration, after Schulze [2008*a*]

The consolidation phase for uniaxial tests may be carried out for several minutes or several hours depending on the material being tested and its susceptibility to the effect of time consolidation. Following the consolidation, the confinement provided by the cylinder is removed to leave a free-standing sample, which when loaded again by another vertical compressive stress, fails at a certain stress level. This stress is defined as the unconfined yield strength of the material σ_u. The yield limit of bulk solids is also dependent on the stress history of a material, and as such the larger the applied consolidation stress (σ_1), the larger the unconfined yield strength σ_u.

5.1.2 Jenike Shear Test

The Jenike shear test is one of the most commonly used tests for bulk solids since its development by Jenike in the early 60's [Schwedes, 2003]. The translational shear tester is commonly used for measuring properties of particulate solids for use in the design of silos, hoppers and bins. Jenike introduced a test procedure, which together with the shear cell has become an international standard for testing [ASTM International, 2006; European Federation of Chemical Engineers, 1989]. The test procedure can be broken down into several distinct stages:

- Filling of the shear cell & levelling
- Pre-consolidation
- Removal of filling ring & levelling
- Application of normal stress
- Shearing of sample at constant rate

The shear cell (Figure 5.2) consists of several components: a bottom ring which is fixed to the base, a top ring that moves relative to the bottom ring, a serrated base and a serrated lid with loading bracket to apply the translational shear force. The base and the lid are roughened with 1 mm grooves as per recommendations. Standard dimensions for Jenike shear cells are listed in Table 5.1.

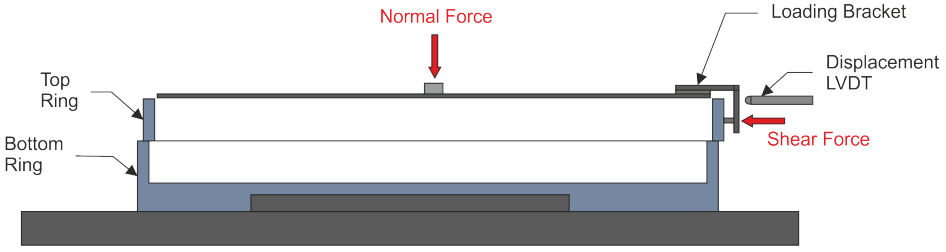

Figure 5.2: Jenike shear cell - Schematic of Jenike shear cell used in tests

Table 5.1: Jenike shear cell dimensions

Jenike Cell	**Standard**	**Small**	**Metric**
Diameter [mm]	95.25	63.5	95
Base Height [mm]	12.7	9.525	13
Top Ring Height [mm]	15.875	11.113	16
Cell Material	Stainless-Steel / Aluminium	Aluminium	Stainless-Steel / Aluminium

One of three behaviours can be observed during a test; the material may be under-consolidated, over-consolidated or critically consolidated. Ideally the sample should be critically consolidated for each test, as an under-consolidated sample may not reach the critical shear stress while an over-consolidated sample will initially exceed it but may not return to this value before the test ends.

The total travel of the relative displacement of the shear cell is approximately 6 mm so a steady state must be reached in the first 3-5 mm of travel during the test. To achieve this criterion the sample must be in a critically consolidated state at the onset of the shearing. This is normally achieved in the pre-consolidation stage by a trial and error process through a sequence of loading and twisting a pre-consolidation lid rather than the normal shearing lid. When consolidation is complete, the normal load is removed and the load for shearing is applied to the sample and a shear force reapplied until a failure plane has developed. Since the maximum shear displacement for the standard Jenike cell is about 6 mm, it is suitable for testing materials up to approximately 5% of the cell diameter [European Federation of Chemical Engineers, 1989].

The test cell is used in a slightly different form to determine wall-friction properties, where the bottom ring is replaced by the wall material to be tested. The effect of time consolidation can be investigated by leaving the material under load for a required period of time before performing the shear test. A number of quantities which are expressions of different aspects of the resistance of the solid to flow may be determined from this failure curve; for example, unconfined yield strength, angle of internal friction and apparent cohesion. Due the lengthy procedure and detailed test method a trained and competent operator is required to carry out the tests. However, the procedure to achieve a critically consolidated sample is operator sensitive; it is not guaranteed that results between different operators will be exactly comparable. This operator sensitivity and the length of time required to derive a flow function for a material are some of the biggest drawbacks of the Jenike method.

For all tests carried out with Jenike Tester the top ring was translated at a nominal rate of 0.5 mm/min (actual displacement rate between 0.4-0.6 mm/min). The displacement of the top ring was measured by a Linear Variable Differential Transformer (LVDT). The shear force applied was measured using a load cell with an accuracy of 0.14N. Dilation and position of the lid were not recorded. All data were recorded at 4Hz.

5.1.3 Confined Compression (K_0) Test

The confined compression test, which may also be referred to as a K_0 test or Lambda-test, was designed to investigate the mechanical response of granular material under a vertical load and the load transferred to the confining walls. The K_0 tester used in the research (Figure 5.3) is similar to that proposed by Masroor *et al.* [1987] and a newer construction to that used previously (Figure 5.4) by other researchers [Chung, 2006; Johnstone, 2010; Reinke, 2011]. It is also similar in design to the test apparatus that is defined in the European standard EN 1991-4 for measuring the lateral pressure ratio in silo design [British Standards Institution, 2006].

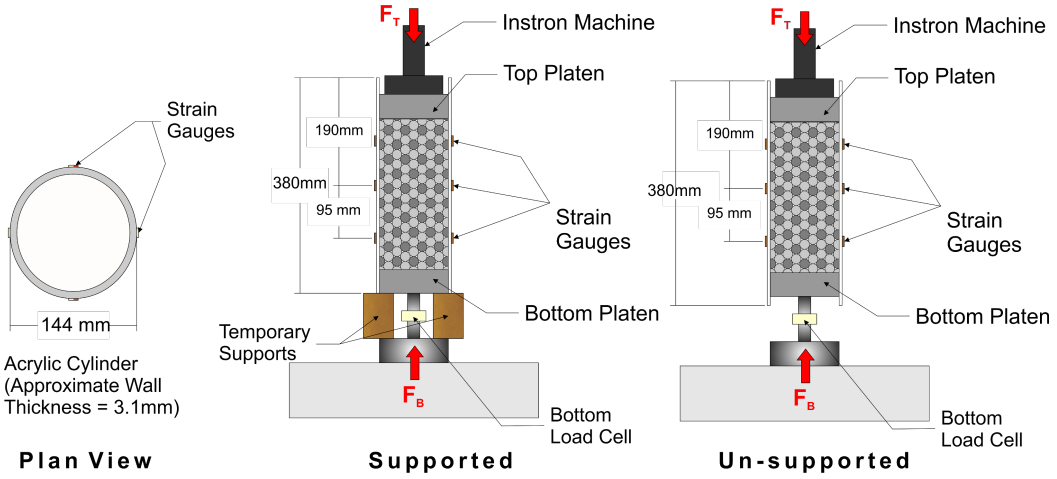

Figure 5.3: Confined compression test set-up - Schematic of experimental set-up in both supported and unsupported conditions

A load is applied to the granular material from the top by the INSTRON machine at a constant displacement rate of between 0.5-1.5mm/min. The applied vertical load is measured by the INSTRON machine at the top and the load cell at the bottom. The forces transmitted to the cylinder walls are measured by 12 pairs of strain gauges, spaced equally around the circumference of the cylinder at three different levels. The lateral pressure ratio, K, can be evaluated from Equation (5.1) [Chung, 2006; Chung and Ooi, 2007; Masroor *et al.*, 1987],

$$K = \frac{\sigma_H}{\sigma_V} \tag{5.1}$$

where (σ_H) is the mean horizontal stress in the cylinder measured by the gauges and (σ_V) is the average vertical stress in the bulk solid.

The average vertical stress can be calculated from Equation (5.2) [Chung, 2006; Chung and Ooi, 2007; Masroor *et al.*, 1987]:

$$\sigma_V = \frac{2(F_T + F_B)}{(\pi D^2(1+\varepsilon_\theta)^2)} \tag{5.2}$$

where F_T and F_B are the forces acting on the top and bottom platens, D is the cylinder diameter, and ε_θ is the hoop strain recorded at the gauges.

The horizontal stress is calculated from the strain reading as follows (Equation (5.3)) [Chung, 2006; Chung and Ooi, 2007; Masroor *et al.*, 1987]:

$$\sigma_H = \frac{2tE_w(\varepsilon_\theta + \nu_w\varepsilon_a)}{D(1-{\nu_w}^2)} \tag{5.3}$$

where t is the cylinder wall thickness, E_w is the Young's modulus for the cylinder, ν is the Poisson's ratio and ε_θ & ε_a are the hoop and axial strains recorded at the gauges.

The average shear stress $\bar{\tau}$ when the cylinder is restrained from movement at the bottom, resulting in different forces being measured in the top and bottom platens, can be calculated from Equation (5.4) [Masroor *et al.*, 1987].

$$\bar{\tau} = \frac{F_T - F_B}{\pi D h(1-\varepsilon_a)} \tag{5.4}$$

The tester can be set up with the cylinder wall locked in position relative to the bottom platen, through the provision of supports beneath the cylinder, or with the cylinder unrestrained, in which the friction between the material and cylinder prevents it slipping off. In the latter situation the top and bottom force is nearly always equal with minor variations noted due to measurement error.

The bulk wall friction coefficient can also be determined from Equation (5.5).

$$\mu_{Bulk} = \frac{\bar{\tau}}{\sigma_H} \tag{5.5}$$

The previous K_0 tester (and set-up) used by Chung [2006]; Chung and Ooi [2007] is shown in Figure 5.4b, in which only a squat sample centred about one set of gauges

was used while the cylinder was restrained from moving by supports, providing a set-up similar to that of a lambdameter tester where one way compression is applied to the sample. The set-up used by Johnstone [2010] is given by Figure 5.4c in which the cylinder was un-restrained allowing for two way compression to occur. The set-up used by Reinke [2011] combines both previous set-ups (Figures 5.4b and 5.4c) - only one layer of gauges at the bottom of the cylinder was used to maintain a sample D/h ratio similar to that of a lambdameter and the cylinder could be used both supported and unsupported. While the geometry of the tester has remained much the same, there are several key differences in the set-up.

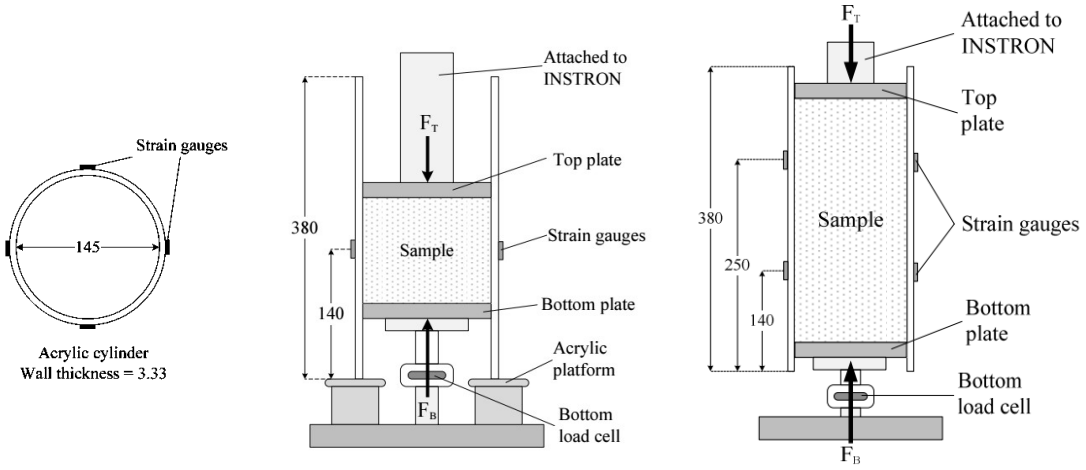

(a) Cylinder cross-section **(b)** Supported - Chung [2006] **(c)** Unsupported - Johnstone [2010]; Reinke [2011]

Figure 5.4: Previous experimental set-ups - Dimensions and support conditions for previous studies

5.1.4 Flowability

The flowability of a bulk material is characterised mostly by its unconfined yield strength (σ_1) as a function of the consolidation stress (σ_1), storage and consolidation time or both [Masuda *et al.*, 2010; McGlinchey, 2008, 2009; Rotter, 2001; Schulze, 2008*a*]. This is termed the material flow function (FF). The flow function for most materials is either linear of non-linear behaviour (seen in material A and B in Figure 5.5). Very rarely is a material behaviour similar to material C found.

The flowability of a material is often classified by its flow factor number ff_c [Jenike, 1964], which is the ratio of the unconfined yield strength (σ_u) to the consolidation stress (σ_1) as given by Equation (5.6).

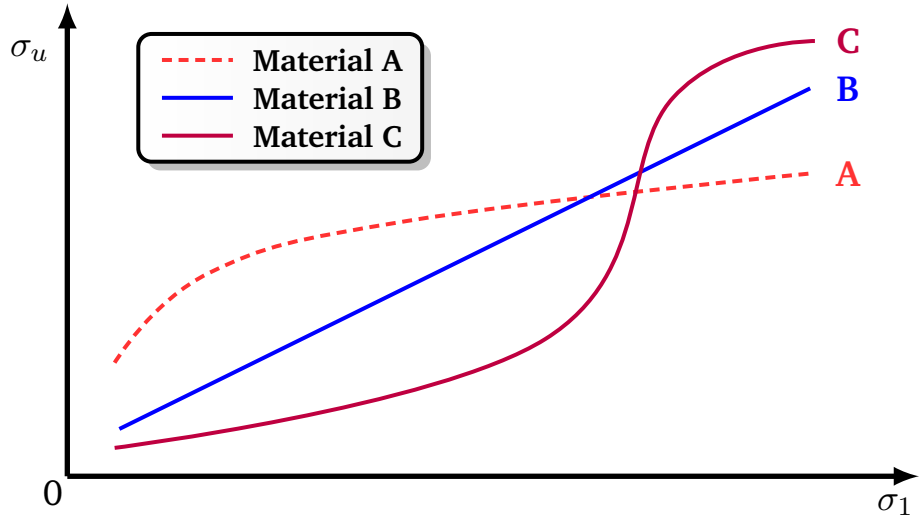

Figure 5.5: Material flow functions - Possible types of flow functions, adapted from [Schulze, 2008*a*]

$$ff_c = \frac{\sigma_1}{\sigma_u} \tag{5.6}$$

This means that the larger the ff_c, the more easily the material will flow. Jenike [1964] proposed a classification to describe the flow behaviour of a material (Table 5.2) and this can be seen applied in Figure 5.6.

Table 5.2: Flow factor classification

Flow-factor	Behaviour
$ff_c < 1$	not flowing
$1 < ff_c > 2$	very cohesive
$2 < ff_c < 4$	cohesive
$4 < ff_c < 10$	easy-flowing
$10 < ff_c$	free-flowing

Some care needs to be taken when comparing two materials by their flow factor, as the consolidation stress used to classify the material should be similar as a material can cross different classifications, as can be seen with material A in Figure 5.6. It is also worth pointing out that two materials with the same flow factor but significantly different densities will flow differently as gravity will have a larger effect on the larger bulk density. This is particularly important in systems based on gravity flow.

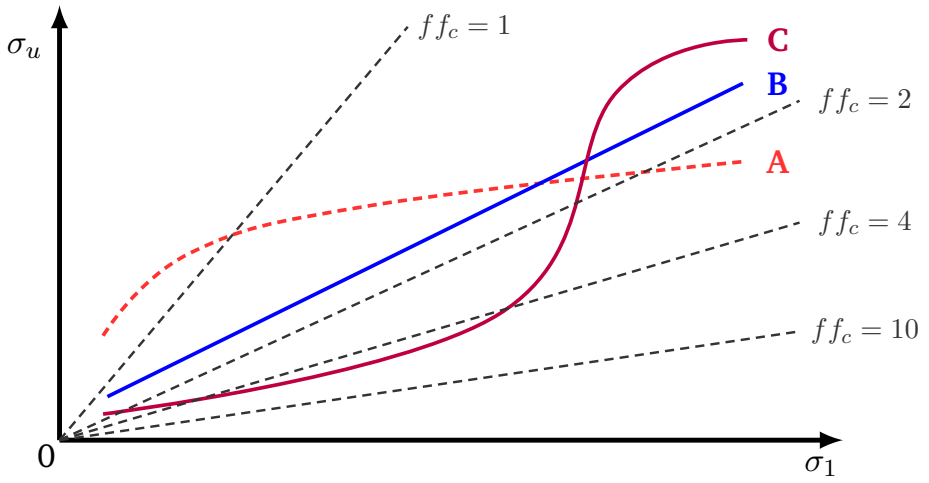

Figure 5.6: Flow factor classification - Using classification proposed by Jenike [1964]

5.1.5 Effective Angle of Internal Friction

The effective angle of internal friction is an important parameter for silo design as the friction angle controls the failure of the granular solid, allowing flow in silos. The failure of a granular mass can be described by the Mohr-Coulomb failure criterion which is given by Equation (5.7)

$$\tau_f = c + \sigma_n \tan \phi_{im} \tag{5.7}$$

where τ_f and σ_n are the limiting shear and normal stresses on the failure plane, c is the cohesion constant for the material (which is zero for cohesionless materials) and ϕ_{im} is the angle of internal friction for the bulk solid.

The Mohr condition is based on the assumption that the failure of the material depends only on the maximum principal stress, σ_1, and the minimum principal stress, σ_3. The shape of the failure envelope can be linear or non-linear; Coulomb's criterion is based on a linear failure envelope to determine the critical combination of τ and σ. From this relationship the effective angle of internal friction can be determined from a linear regression analysis of the normal shear force relationship or a relevant stress range. For a cohesionless material ($c = 0$) this is normally found from shear cell test using the following relationship.

$$\tan^{-1}\left(\frac{\tau_f}{\sigma_n}\right) = \phi_{im} \tag{5.8}$$

The effective angle of internal friction of materials is discussed further in the following sources [Masuda *et al.*, 2010; McGlinchey, 2008, 2009; Rotter, 2001; Schulze, 2008*a*].

5.1.6 Lateral Pressure Ratio, K

The lateral pressure ratio, *K*, describes the resulting horizontal stress that occurs in granular materials under the application of a vertical load. This relationship is an important factor for silo design as it strongly influences the pressure regime, particularly if the geometry is squat [Rotter, 2001]. For silo design the lateral pressure ratio is normally considered as the ratio of the horizontal stress at the wall to the mean vertical stress across the silo cross-section at the same height. While it can be influenced by the wall roughness and flexibility, it is normally taken as a material constant. The lateral pressure ratio can be determined from the angle of internal friction ϕ_{im} for the material, where Equation (5.9) which is the Jaky equation [Jaky, 1944, 1948] multiplied by a factor of safety, but direct measurement according to the method described in Eurocode 1 part 4 is preferred [British Standards Institution, 2006].

$$K = 1.1\,(1 - \sin\phi_{im}) \tag{5.9}$$

For computer simulations of silo pressures it is recommended that Poisson's ratio υ, be selected as the value from Equation (5.10) [Rotter, 2001].

$$\upsilon = \frac{K}{1 + K} \tag{5.10}$$

In soil mechanics there are three types of lateral pressure ratio; the active earth pressure K_a, the passive earth pressure K_p and the at-rest pressure K_0. Both the active and passive earth pressures are limiting plastic states while the at-rest pressure K_0 is an elastic state (Figure 5.7). The Rankine earth pressure is a lower bound plasticity solution which considers the stress state in the soil when shear failure is on the point of occurring. If the case of a smooth, vertical wall restraining a semi-infinite mass of soil with a horizontal surface is considered, the active and passive cases can be defined. If the wall moves away from the soil mass the horizontal stress in the soil drops, and when the displacement is large enough the soil reaches plastic failure and the stress decreases to a critical value. Rankine [1857] defined this as the active pressure which is given by Equation (5.11). When the horizontal stress in the soil mass becomes equal to the active pressure it is said to be in the Rankine active state.

$$K_a = \frac{(1 - \sin\phi_{im})}{(1 + \sin\phi_{im})} \tag{5.11}$$

In the case where the wall moves toward the mass of soil there is a lateral compression and the horizontal stress will increase until a plastic equilibrium is reached. This state can be defined as the Rankine passive state and is given by Equation (5.12).

$$K_p = \frac{(1 + \sin \phi_{im})}{(1 - \sin \phi_{im})} \tag{5.12}$$

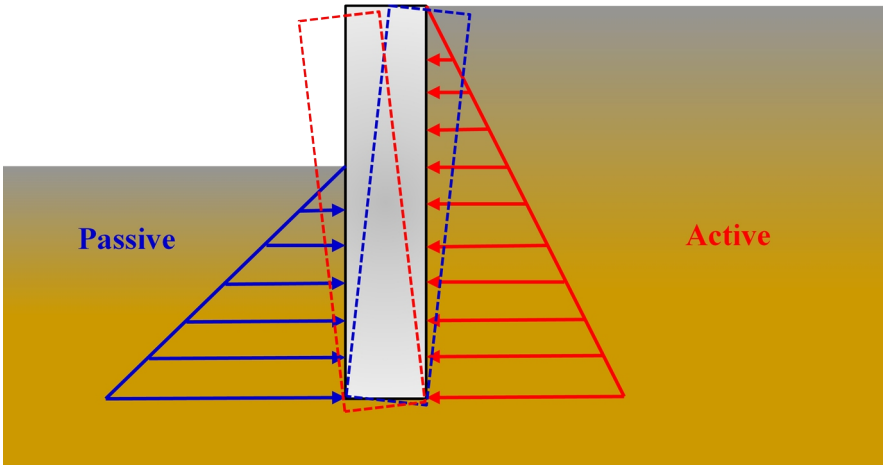

Figure 5.7: Active and passive earth pressure states - Typical scenarios leading to development of various states

The amount of strain required to mobilize the passive pressure is significantly larger than that to mobilize the active pressure state, and as such it is more likely to find soil in the active state (Figure 5.8).

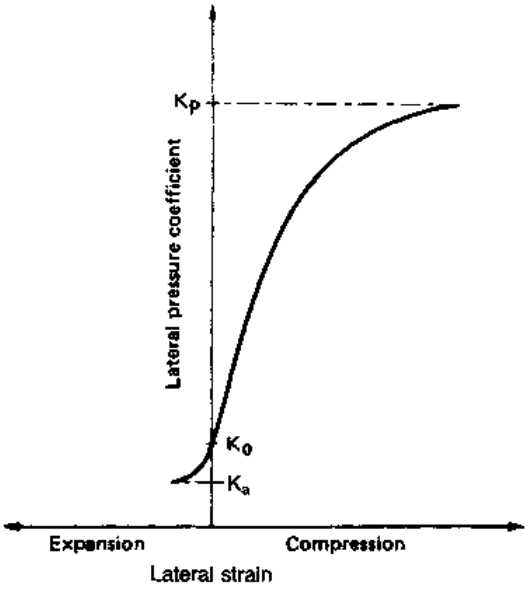

Figure 5.8: Active and Passive earth pressures - Relationship between lateral strain and lateral pressure coefficient, after Craig [2004]

In both the active and passive states the soil is under some strain. In the case of zero lateral strain the soil is said to be at rest and this is defined as the lateral earth pressure at-rest K_0. Normally in the design of silos and other storage structures K_0 is used, as the granular solids within the structure are considered to undergo zero lateral strain due to the restraint of the structure. Although this is not always the case when flexible silos are used [Ooi and Rotter, 1990].

In soil mechanics K_0 can often be used as 0.4 regardless of the soil type. However, it actually varies greatly depending on the type and stress history of the soil. For example, heavily over-consolidated soils can have $K_0 > 1$ due to a proportion of the at rest pressure being retained when the vertical stress is reduced. Some typical values for K_0 for soils [Craig, 2004] are given in Table 5.3 and for some other materials [Johnstone, 2010] in Table 5.4.

Table 5.3: Some typical K_0 values for common soils, after Craig [2004]

Soil Type	***K_0 Value***
Dense sand	0.35
Loose sand	0.6
Normally consolidated clays	0.5-0.6
Heavily over-consolidated London clay (OCR=3.5)	1

Table 5.4: Some typical K_0 values for other materials, after Johnstone [2010]

Material	***K_0 Value***
Glass Beads, Single	0.65
Glass Beads, Pairs	0.7
PET Pellets	0.4
Black Eyed Beans	0.55
Black Eyed Kidney Beans	0.5

Coulomb [1776] also proposed solution for the lateral earth pressure but this is an upper bound solution which means the failure load is always greater than the true failure load. This is considered an unsafe solution as it is always possible that the soil could find a more efficient path to failure. For a smooth, vertical wall retaining a mass of soil with a horizontal surface both methods will give the same solution. Coulombs'theory has been further expanded [Das, 2010] by others such as Poncelet [1840], Mayniel [1808] and Müller-Breslau [1906] to account for wall friction and non-horizontal surfaces. Neither method explicitly accounts for cohesion in the soil.

5.2 Test Materials

While the main focus of this project is on the behaviour of iron ore fines, and the two types of fines KPBO and KPRS, a range of different materials have been used throughout this project and for different tests. Gypsum is used as a control sample for initial testing of the Edinburgh Powder Tester (EPT).

5.2.1 Gypsum Calibration Mix

The gypsum calibration mix (Figure 5.9) is a specially blended mixture that was produced for calibration of the EPT. The mixture is a largely invariable cohesive solid that allows for highly repeatable tests to be carried out. The mixture is very stable within the temperature range of 10-20°C and a humidity range of 50% -75% and long term storage does not affect the stability of the mixture.

Figure 5.9: Gypsum calibration mix - A stable material used for testing of the EPT

5.2.2 Iron Ore Fines

Iron ore fines are the finer fractions (< 6.3 mm) that are broken off the main iron ore pellets during handling or storage. Pellet plants can produce two different types of pellets: blast furnace (BF) and direct reduction (DR) pellets. Blast furnace pellets are used in the coke-based blast furnace process, which is the most common method of producing molten iron for steel-making. Blast furnace pellets are delivered mainly to steel mills. DR pellets are used in the direct reduction processes to produce sponge iron, which is an alternative process route, as an initial stage from iron to steel. The DR process is primarily based on the use of natural gas and has become increasingly common in countries with access to inexpensive natural gas. The iron ore fines used in this study are from LKAB, and both KPRS (DR) and KPBO (BF) pellet fines have been studied. KPRS pellets are dolomite fluxed and coated for optimal behaviour in the DR-shaft. They have a low amount of silica and alumina (<0.9%) and the low acidity

means higher reducibility in the furnace and lower costs in steel-making. KPBO fines include an olivine additive, which gives them excellent high-temperature characteristics.

The fines have a quoted bulk density of 2300 kg/m^3 and solid density of 3700 kg/m^3 and form an angle of repose of 28°. The expected delivery moisture content is approximately 1.5% for KPRS fines and for KPBO fines is 1.2%. The particle size distribution is given for the iron fines in Figure 5.10. Both types of fines have the same quoted size distribution and very similar grading curves have been measured for both using sieve analysis.

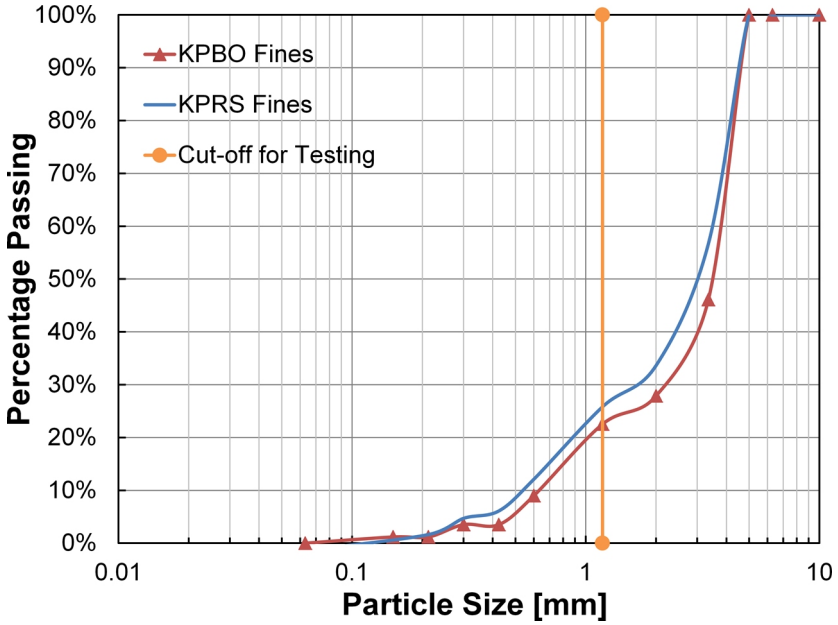

Figure 5.10: Particle size distribution for iron ore fines - For both KPBO and KPRS fines

The iron ore fines have been tested at different grading levels - the finer portion was used with the EPT, which was everything passing a 1.18 mm sieve (Figure 5.11) and particles up to 6.3 mm (Figure 5.12) were used with both the confined compression test (K_0) and Jenike Shear test.

The finer portion of the fines will generally demonstrate the highest cohesion, as the Cohesive Granular Bond number will increase as the particle size decreases at a constant level of adhesion, and as such are more appropriate for testing with the EPT. This has been confirmed from a cut-sieve analysis carried out on both fines at different moisture contents, shown in Figure 5.13. When the Cohesive Granular Bond Number is high due to the large particle the unconfined yield strength is low or zero. As the larger particles are removed, at the same moisture content, the unconfined strength increases with decreasing particle size.

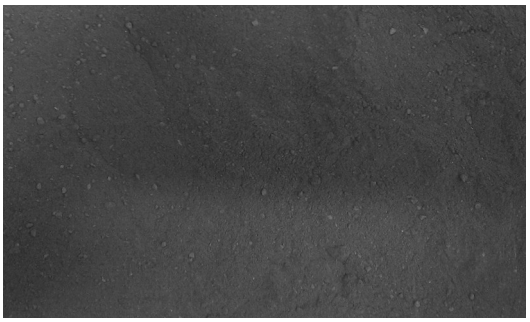

Figure 5.11: Iron ore fines < 1.18 mm - Reduced size fraction used for testing

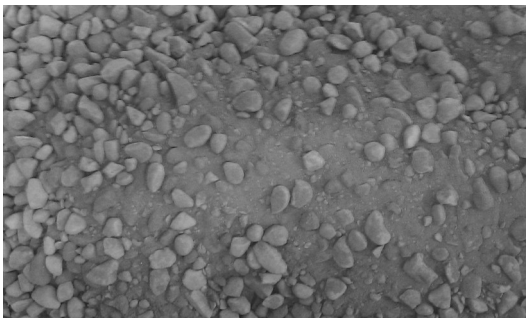

Figure 5.12: Iron ore fines < 6.3 mm - Screened-off fines - as received

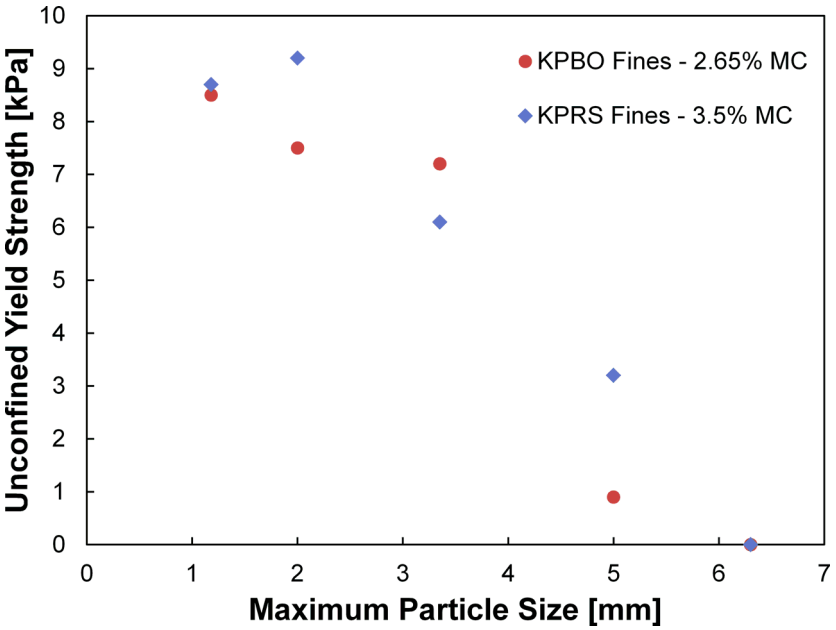

Figure 5.13: Cut-sieve analysis for iron ore fines - For both KPBO and KPRS fines

From soil mechanics [Craig, 2004] we can define the coefficient of uniformity C_u, for a material by Equation (5.13) where D_{10} is the effective grain size and D_{60} is the particle size such that 60% (by mass) is less than that size. Both values are obtained through sieve analysis of the sample.

$$C_u = \frac{D_{60}}{D_{10}} \tag{5.13}$$

The coefficient of curvature C_z for a material, which defines the slope and shape of the distribution curve, can be calculated from Equation (5.14).

$$C_z = \frac{{D_{30}}^2}{D_{10}D_{60}} \tag{5.14}$$

The results of the sieve analysis in Figure 5.10 are tabulated in Table 5.5 and suggest that the iron ore fines can be classed as a well graded sample.

Table 5.5: Size properties of iron ore fines

Particle Size [mm]		**Coefficient [-]**	
$\mathbf{D_{10}}$	0.59	$\mathbf{C_u}$	6.34
$\mathbf{D_{30}}$	1.97	$\mathbf{C_z}$	1.71
$\mathbf{D_{60}}$	3.71		

5.2.2.1 Chemical Constitution

The chemical data [Niiniskorpi, 2001] is given in Table 5.6 and trace elements for both fines are given in Figure 5.14 and Table 5.7. While the make-up of both materials is similar, KPBO fines contain higher proportions of cobalt, chromium, manganese, nickel and zinc. KPRS pellets contain a dolomite additive while KPBO fines contain an olivine (Mg_2SiO_4) additive.

Table 5.6: Chemical makeup of iron ore fines, after [Niiniskorpi, 2001]

	Fe_2O_3	FeO	MnO	CaO	MgO	Al_2SO_3	SiO_2	TiO_2	V_2O_5	P_2O_5	Na_2O	K_2O
KPBO [%]	94.6	0.4	0.08	0.5	1.55	0.22	2.05	0.24	0.2	0.06	0.04	0.04
KPRS [%]	96.3	0.3	0.08	1.05	0.75	0.19	0.85	0.14	0.21	0.06	0.04	0.03

Table 5.7: Trace elements for iron ore fines [ppm]

Trace	**Material**		**Trace**	**Material**	
Element	**KPBO**	**KPRS**	**Element**	**KPBO**	**KPRS**
Ag	0.1	0.1	**Mo**	0.291	0.298
As	1	1	**Ni**	245	184
Bi	0.06	0.06	**Pb**	1.67	1
Cd	0.06	0.06	**Sb**	0.108	0.124
Co	91.8	87.6	**Se**	0.06	0.06
Cr	51.9	10.4	**Sn**	1.71	1.98
Cu	6.71	4.89	**Te**	0.1	0.197
Hg	0.1	0.1	**Ti**	0.1	0.1
Mn	575	458	**Zn**	25	17.8

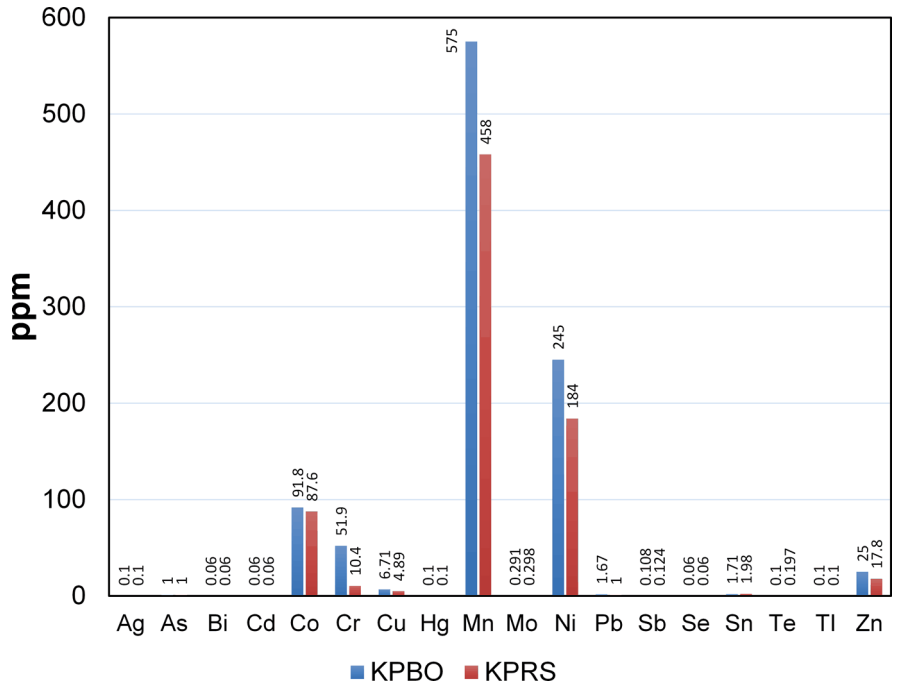

Figure 5.14: Iron ore trace elements - Elements found in both KPBO and KPRS fines

5.2.2.2 Scanning Electron Microscopy (SEM) Images

Scanning Electron Microscopy (SEM) produces images of a sample by scanning it with a beam of focused electron. The signal response of the electrons with those electrons in the sample allows a topographical image of the surface of the sample to be produced. Generally SEM images can achieve up to resolutions of 1nm. SEM images of both KPBO and KPRS fines are presented in Figures 5.15 and 5.16. The images show the roughness and angularity of the iron ore particles and also how the fines behave as agglomerates, even in the dry state.

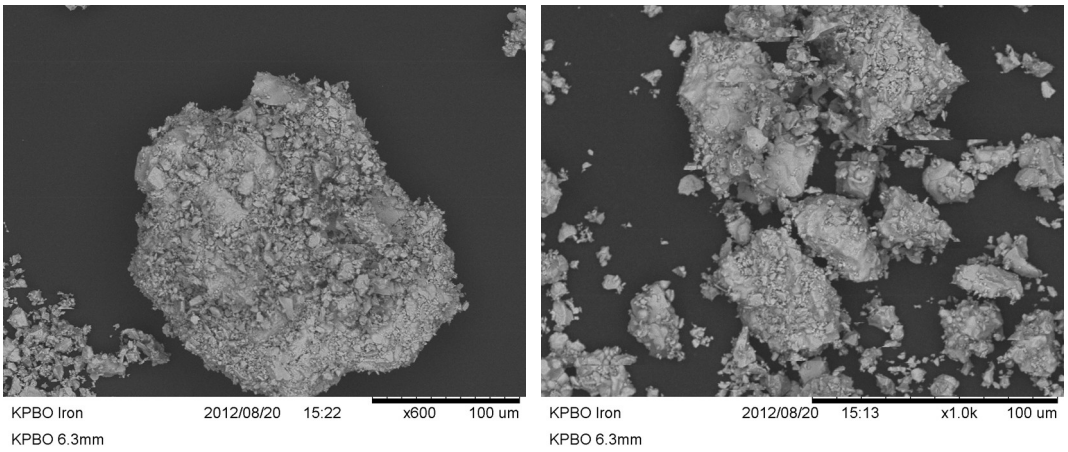

(a) 600x magnification **(b)** 1000x magnification

Figure 5.15: SEM images of KPBO fines - Two different levels of magnification

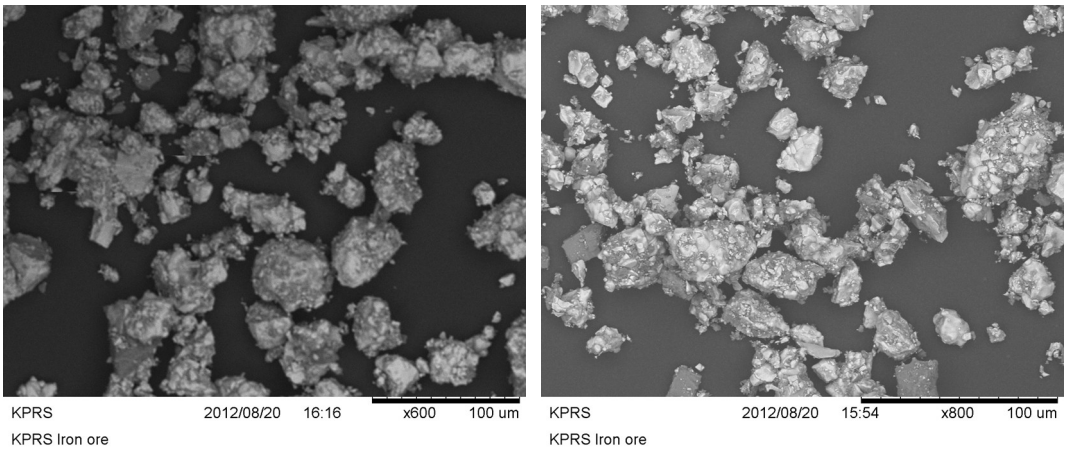

(a) 600x magnification **(b)** 1000x magnification

Figure 5.16: SEM images of KPRS fines - Two different levels of magnification

5.2.2.3 Testing Regimes

The behaviour of the iron ore fines is expected to be affected by both the moisture content and the temperature of the sample. Only the effect of moisture content was investigated. The fines were evaluated at eight different moisture content levels for the confined compression tests: ranging from dry (< 0.2%) to 10% and at 5 different levels for the unconfined uniaxial test: 1%, 2%, 3%, 4% and 6%. The moisture content (MC) was measured by drying a sample in an oven at 105°C for 24 hours. Different particle size gradings were used depending on the test method - less than 1.18mm for the EPT and less than 6.3mm for both the Jenike shear test and confined compression test.

5.3 The Edinburgh Powder Tester (EPT)

The Edinburgh Powder Tester (EPT) is a semi-automated uniaxial tester (Figure 5.17), in which the cohesive strength of a bulk solid is evaluated from an unconfined compression test, following a period of consolidation to a pre-defined stress level (σ_1). After the removal of the consolidation stress, the confining tube is slid off carefully and a vertical force is applied to the sample through the top platen until failure of the sample. Both the confined and unconfined responses of the material can be assessed by the EPT. The EPT also allows for the evaluation of the bulk compressibility of a material by measuring the height of the sample at incremental consolidation loads during a confined compression test. As the load is applied, the sample height is allowed time to stabilise and is recorded as the consolidated height. Not only can the confined vertical stress-strain response be measured, but also the variation in bulk density during loading, provided the sample mass is known. If particle properties are known the porosity relationship for the material can be also evaluated.

(a) Edinburgh Powder Tester (EPT)

(b) Confined consolidation

(c) Unconfined compression

(d) Failed Sample

Figure 5.17: Edinburgh Powder Tester (EPT) - Different stages of testing with the EPT

During the loading process, the force acting on the top platen, as well as the displacement, are recorded, from which the unconfined stress-strain curve can be obtained. The unconfined yield strength σ_u is the maximum vertical stress recorded during a test for a particular consolidation stress. By repeating the experiment for a range of consolidation stresses the flow function of a bulk solid can be obtained quickly. In order to define the flow function, at least three data points are recorded for each stress level. If any value is more than 10% lower than the mean value, it is discarded. A minimum of two remaining points, after discarding the lowest value outside the 10% range, are

then used for the calculation of the average unconfined strength for a particular consolidation stress. The previously described low values are discarded from the calculations as they can be caused by anomalies relating to the experimental procedure, such as, for example, non-uniform sample formation, poor alignment of the sample or excessive disturbance of the sample while removing the confinement during a test. All high values must be included in the reporting of the unconfined strength.

5.3.1 Modification of the EPT

For use in scientific research several minor modifications have been made to the EPT to introduce additional capabilities and provide additional data. An additional consolidation load has been fitted for measuring the effect of friction during the application of consolidation load while a new data-logger has also been fitted.

5.3.1.1 EPT Data Logger

The commercial EPT machine only maintains a record of the peak strength achieved during the test which is output as the unconfined yield strength of the sample (σ_u). An additional data logger capable of recording up to 16 channels at a frequency of 10 kHz has been fitted to the EPT to ensure that the unconfined loading response to failure is recorded in detail. This is particularly important for brittle materials that may fail in a very short period of time. It will also provide experimental data on a similar time scale to what is produced in DEM simulations, allowing a more comparable set of data.

5.3.1.2 Consolidation Load Cell

In the EPT the consolidation stress is applied through the application of a known weight that provides a constant load (Figure 5.17b) without the need for servo-controlled loading rams - the consolidation is stress controlled rather than displacement controlled. However, due to the nature of mechanical systems, friction cannot be eliminated so a small amount of the applied load is lost through friction. To account for this, an additional load cell (Figure 5.18) has been added to the EPT. This ensures that the actual applied consolidation stress, which is the applied weight minus the frictional loss through the mechanical system, rather than the assumed load of the applied weight is recorded. The consolidation load cell has a maximum capacity of 150 N ($\approx$125 kPa) and an accuracy of 0.1 N. Data can be acquired from the load cell up to a maximum frequency of 25 Hz.

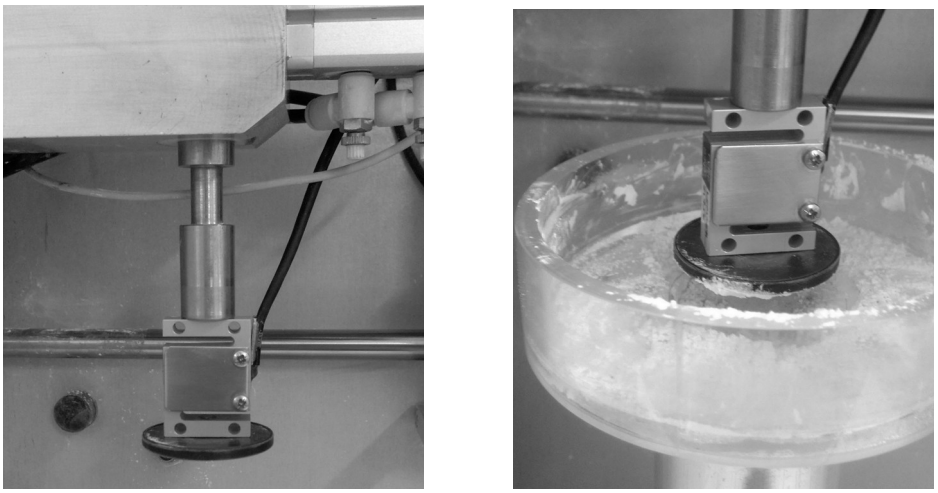

(a) Before test **(b)** During consolidation

Figure 5.18: New EPT consolidation load cell - After installation

5.4 Assessment of EPT

The gypsum calibration mix was used as a control sample for assessing the performance of the EPT due to its consistent behaviour in the laboratory environment.

5.4.1 Repeatability

One of the key strengths of the EPT is the speed at which tests can be carried out without a loss in the repeatability of results. The repeatability for the EPT has been assessed on two separate occasions with the gypsum calibration mix. On both occasions the coefficient of variation averaged across all consolidation stress ranges was found to be less than 5%. The results of this study are summarised in Figure 5.19. All tests are generally carried out utilising two-way compression of the sample which will allow the sample to consolidated from both ends. This will provide a more evenly consolidated sample and reduce the effect of wall friction on the unconfined strength.

The effect of one-way and two-way compression is also presented in Figure 5.19 where a direct comparison is made between the two methods at consolidation stresses of 20 kPa and 100 kPa. Two-way compression is provided from the unsupported mould which has the ability to move during consolidation. During initial filling of the EPT mould with sample a restraining pin is used to hold the mould in place and prevent collapse of the sample, as very few solids have the cohesive strength necessary to be free-standing under zero consolidation stress. A small load of 1 kPa is applied to measure the initial height of the sample. Following this, the load is incremented to 5-10 kPa depending on the material and the restraining pin is then removed at this stage to allow two-way

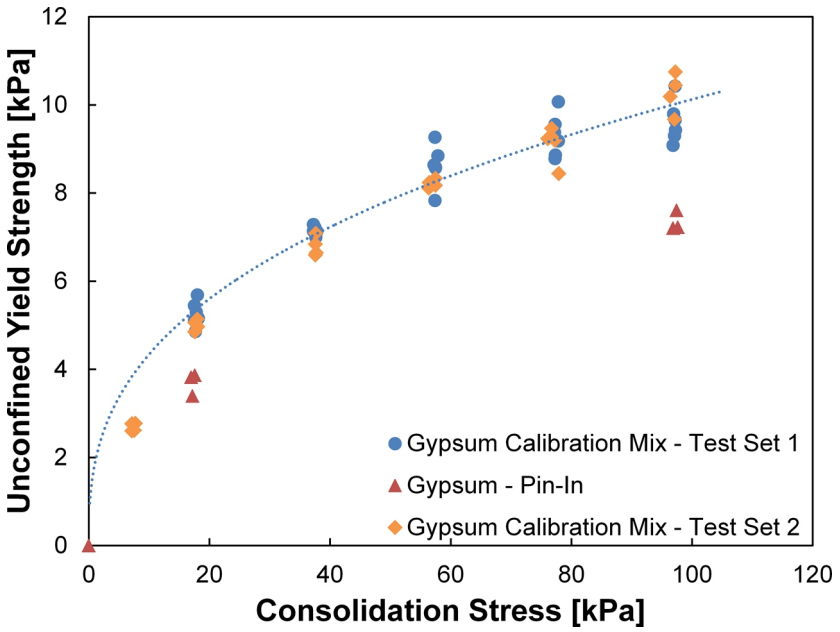

Figure 5.19: Repeatability assessment for EPT - Results for test using gypsum calibration mix

compression for the remainder of the additional consolidation load. Failure to remove the restraining pin will mean that the sample will not be evenly compressed due to the effect of wall friction.

5.4.2 Sample Aspect Ratio

The aspect ratio of the tester is simply the relationship between the height and diameter of the sample (H/D). Work carried out by Williams *et al.* [1971] found that if the aspect ratio of a sample is greater than two (>2) the effect of aspect ratio is negligible and small when above approximately 1.5. Bishop and Green [1965] found that there is a relationship between the amount of end friction generated at the platens and the unconfined strength of the sample with higher levels of end friction leading to higher unconfined yield strengths. The effect of this slenderness can clearly be seen in the results from the EPT (Figure 5.20) in which there is a generally decreasing trend between the peak force and the increasing aspect ratio, similar to that observed by Williams *et al.* [1971], with the value tending towards a constant above an aspect ratio of 1.5. There also appears to be a correlation between the magnitude of the consolidation stress and the amount of the decrease in strength. It is likely this is related to the amount of wall friction acting on the taller samples during consolidation.

The EPT has been designed to test consolidated samples with an aspect ratio of between 1.0 - 1.5, although a simple modification has been implemented to allow exploration of sample aspect ratios greater than that. The EPT has been designed to account for

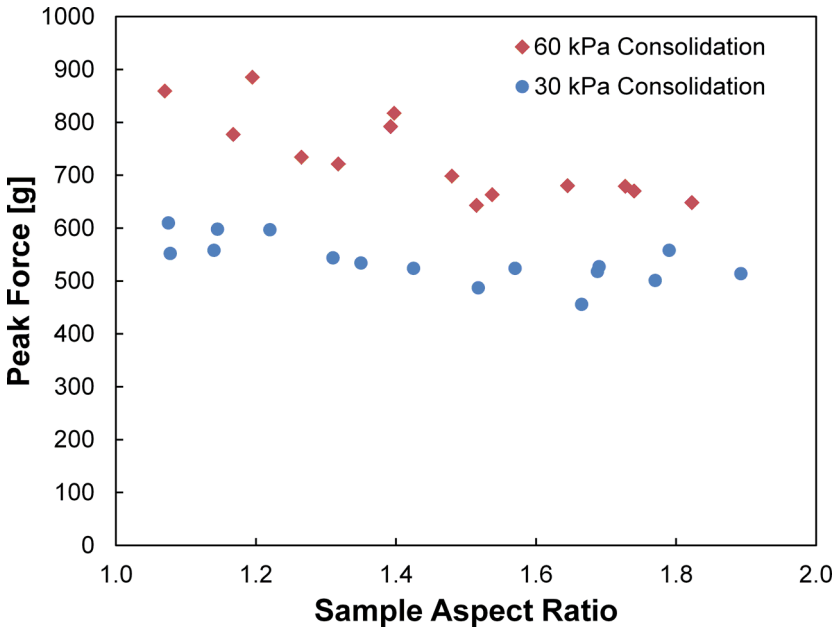

Figure 5.20: Relationship between aspect ratio and measured peak force

the effects observed in Figure 5.20 and will correct the unconfined strength for the associated slenderness effects such that samples are comparable for different aspect ratios tested. To account for the observed decrease, the EPT modifies the unconfined strength based on the consolidated aspect ratio of the sample.

The corrected unconfined strengths for a range of aspect ratios obtained by the EPT for the data in Figure 5.20 is shown in Figure 5.21. The results show that the EPT produces similar unconfined strengths regardless of the aspect ratio in the designed operating range of aspect ratios of 1.1 - 1.5. The EPT has been modified to accommodate taller samples but Figure 5.21 suggests that the EPT correction for sample aspect ratio is over-compensating for the slenderness effect at aspect ratios greater than 1.5, as the corrected unconfined strength is seen to be increasing above this aspect ratio. However, in the normal operating range of sample heights for the EPT, with an aspect of 1.1 - 1.5, there is little variation in the corrected unconfined strength. As all samples tested in this study lie within the range of 1.25 - 1.45, the effect of aspect ratio on the results can be neglected here.

5.4.3 Crushing Strain Rate

The EPT is capable of testing at different crushing speeds (0.4mm/s – 1.5mm/s *or* $0.006s^{-1}$ – $0.025s^{-1}$) during unconfined compression to failure. Different crushing speeds within this range have been tested with the gypsum calibration mix and no significant variation in unconfined strength was found.

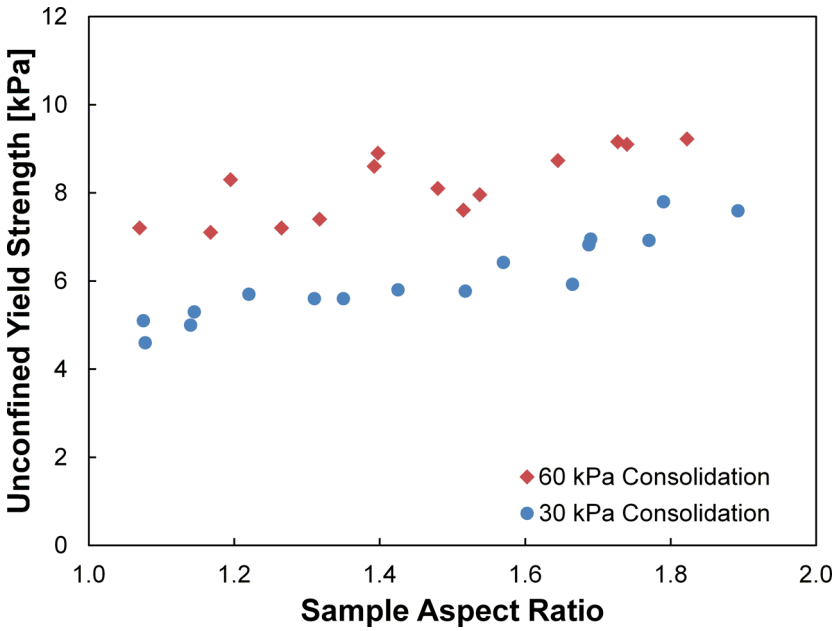

Figure 5.21: Relationship between aspect ratio and corrected unconfined strength - Height corrected results from EPT

5.5 Construction & Calibration of New K_0 Tester

The existing confined compression tester had been in use at the research institute for more than ten years. While the Perspex® used for the previous tester had a 10 year lifetime guarantee it was decided that the combination of existing gauges and cylinder was in need of replacement to give confidence in the confined compression test results. The task of constructing a new confined compression tester and a method of calibrating the cylinder was assigned as part of an undergraduate final year project. A new extruded acrylic cylindrical tube of the same height (380 mm) and slightly smaller diameter (144 mm) than the previous K_0 tester cylinder was sourced and fitted with 12 pairs of horizontal and vertical strain gauges, fitted at three different heights as shown in Figure 5.3. The strain gauges are 90° 2-element Cross, plane type gauges from TML Ltd (Figure 5.22) and the main properties are given by Table 5.8.

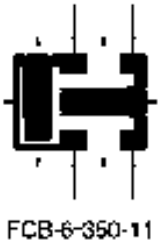

Figure 5.22: Strain Gauge Rosette - 90° 2-element Cross, Plane type

Table 5.8: Strain gauge properties

Parameter	Value
Supplier	TML Ltd.
Type	TCB-6-350-11
Gauge length	6 mm
Gauges resistance	350 Ω
Gauge factor	x = 2.11, y = 2.11
Temperature compensation	11 x 10-6 /°C

A zero degree meridian was arbitrarily chosen and the related 90, 180 and 270 degree meridians marked from this before placement of the gauges. The gauges are named based on their measured strain (V or H), the meridian the gauge is located on (0,90,180 or 270) and it vertical location (T,M or B). For example, V90-T is the vertical strain gauge on the 90 degrees meridian, located at the top layer of gauges. The constructed cylinder is shown in Figure 5.23. From thin-walled membrane theory it is possible to calculate the radial stress that is related to the internal pressure applied to the cylinder with the hoop stress in the cylinder wall inferred from the measured strains at the gauges. In the case of a granular solid, this radial stress is the horizontal stress in the solid, used in the determination of the K_0 value, and is given by Equation (5.3).

5.5.1 Calibration of Cylinder

The cylinder was placed in the calibration rig with all strain gauges attached to a data-logger and recording for the duration of the test. An inflatable bladder was placed inside the cylinder and air was pumped into the cylinder. The bladder was inflated to different known pressures while the data-logger records the related strains on the cylinder. The calibration set-up is depicted in Figure 5.24. An initial small pressure of approximately 1-2 kPa was required to inflate the bladder until contact was made with the cylinder walls. This initial pressure is then subtracted from the internal pressure of the bladder to get the applied pressure on the cylinder.

5.5.1.1 Calculations

The Poisson's ratio, υ, for the acrylic cylinder is determined from the ratio of the vertical (ε_a) to horizontal strain (ε_θ) given by Equation (5.15).

$$\upsilon = \frac{\varepsilon_a}{\varepsilon_\theta} \tag{5.15}$$

Young's modulus for the acrylic cylinder can be obtained from Equation (5.16) which is derived from Equation (5.3).

$$E = \frac{\sigma D\left(\left(1-{\nu_w}^2\right)\right.}{2t\left(\varepsilon_\theta + \nu\varepsilon_a\right)} \tag{5.16}$$

5.5.2 Load Cell Calibration

A simple procedure was implemented for the calibration of the bottom load cell. The applied force is calculated from Equation (5.17), where the force is the measure voltage times a calibration factor for the load cell. A known weight is added to the load cell

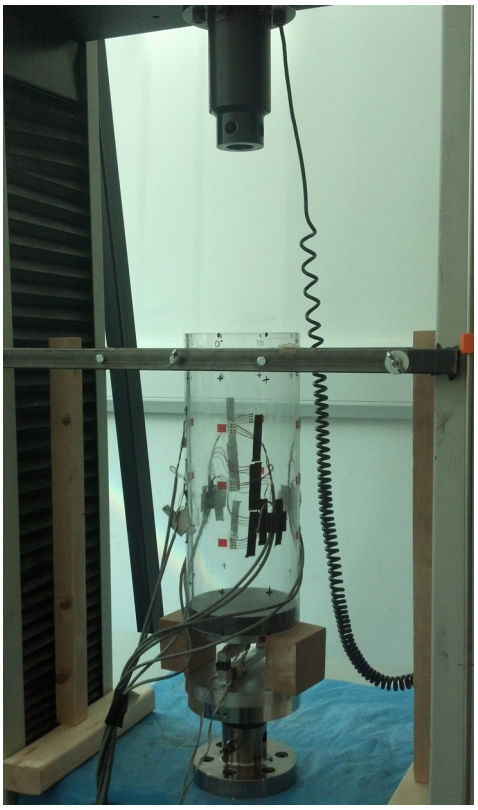

Figure 5.23: Constructed K_0 tester - Set-up for testing with INSTRON

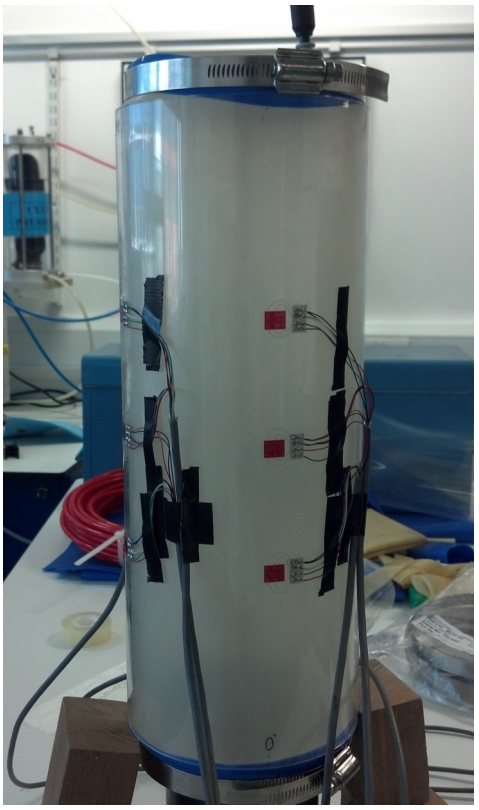

Figure 5.24: K_0 tester during calibration - Showing 3 levels of gauges along the 0° meridian with bladder inflated

allowing the calibration factor to be determined.

$$C_F = \frac{mg}{D_v} \tag{5.17}$$

where C_F is the calibration factor and the D_v is the measured voltage from the load cell, m is the mass of the applied load and g is gravity.

5.5.3 Calibration Results For K_0 Cylinder

The results of the calibration procedure and the calibrated properties found for the cylinder are detailed in Appendix B. An initial assessment to determine the effect of the strain gauge location is carried out in Appendix B.1 with the observed responses in Appendix B.1.1. The initial assessment of the strain gauge responses under applied pressure found that there was a relationship between the meridional location of the gauges and the amount of measured strain. This was found to be related to the large variation in wall thicknesses and probable local curvature of the cylinder. As such, the K_0 cylinder properties have been determined based on the meridional location from a set of four separate calibration tests (Appendix B.2) and are given in Table 5.9.

Table 5.9: Calibrated cylinder properties for K_0 tester

Cylinder Properties	Gauge Location			
	0°	90°	180°	270°
Thickness, t [mm]	2.438	2.871	3.024	3.252
Young's modulus, E [MPa]	3768	3768	3768	3768
Poisson's Ratio, ν	0.263	0.292	0.307	0.309

A simple verification was carried out with the selected calibration properties (Appendix B.3) and a close match was observed at pressures greater than 10 kPa. Below 10 kPa the results were inconsistent as the air bladder was inflated and did not apply even pressure on the cylinder walls.

5.6 Test Results for Iron Ore Fines

Both the confined and unconfined behaviour of KPBO fines and KPRS fines have been evaluated using the EPT. The confined compression tests were carried out separately to the tests used for the unconfined results. For each test a small sample of iron ore fines that contained enough sample for 5-6 tests (approximately 800g) was weighed and placed in an airtight container for the duration of the testing procedure. For a sample of this size it was possible to carefully control the moisture content during testing. The sample was initially tested in the dry state, although despite being air-dried for several days, a small amount of moisture (approximately 0.1%) remained. Moisture was added to the dry sample incrementally using a pipette or spray bottle (depending on amount of sample) in steps of approximately 1% moisture content as the sample mass was known. At each increment the moisture was added to the sample in two stages to try to more evenly distribute the moisture content of the sample, adding approximately half the required amount each time. This was then mixed vigorously with the sample in a sealed, air-tight container for several minutes. Samples were taken at the start and end of each group of tests to monitor the variation of the moisture content and to ensure that the sample was not drying between tests. The average value was taken as being the tested moisture content. The moisture contents used for confined compression tests in the EPT are given in Tables 5.10 and 5.11 and for the unconfined compression tests in Tables 5.12 and 5.13. Dotted lines separate different test samples of the same material. The average moisture content variation across all groups of tests was 0.2%. The results of the confined compression and unconfined compression tests are presented in Sections 5.6.1 and 5.6.2.

Table 5.10: Moisture content of KPRS fines for confined compression tests

Added	Initial measured	Final measured	Average MC%
0%	-	0.11%	0.05%
1.09%	1.20%	1.47%	1.33%
1.17%	2.64%	2.51%	2.57%
0.99%	3.50%	3.47%	3.48%
1.04%	4.51%	4.53%	4.52%
1.02%	5.55%	5.62%	5.59%
1.13%	6.75%	7.19%	6.97%
7.79%	7.79%	8.31%	8.05%
2.00%	10.31%	10.04%	10.18%

Table 5.11: Moisture content of KPBO fines for confined compression tests

Added	Initial measured	Final measured	Average MC%
0%	-	0.09%	0.05%
0.94%	1.03%	0.51%	0.77%
1.16%	1.67%	1.46%	1.57%
1.04%	2.50%	2.72%	2.61%
1.30%	4.01%	3.75%	3.88%
4.75%	4.75%	5.16%	4.95%
1.07%	6.23%	6.16%	6.19%
2.13%	8.29%	8.21%	8.25%
2.09%	10.30%	10.33%	10.31%

Table 5.12: Moisture content of KPRS fines for unconfined compression tests

Avg. MC%	1.06%	2.01%	2.98%	4.09%	6.22%
ST DEV	0.000663	0.002099	0.002995	0.00265	0.003176
CoV	6.24%	10.43%	10.04%	6.49%	5.11%

Table 5.13: Moisture content of KPBO fines for unconfined compression tests

Avg. MC%	1.04%	2.11%	3.10%	4.17%	6.36%
ST DEV	0.000693	0.001139	0.001172	0.00176	0.000767
CoV	6.64%	5.40%	3.78%	4.22%	1.21%

5.6.1 EPT Confined Compression

The loading response during confined compression is evaluated to help calibrate the loading stiffness and amount of plasticity required in the contact model for DEM simulations. At moisture contents above 8% for the KPRS fines and 10% for the KPBO fines the materials behave as large clumps, greater than 10 mm, and became difficult to handle and were not suitable for testing in the EPT which has a mould diameter of 40 mm. The key results are presented in this section and the full test data sets can be found in Appendix C.

Figure 5.25 shows the confined stress-strain curves for the KPRS iron ore fines at various moisture content levels. It is noted that the iron ore fines have a high stiffness compared to many other granular materials. For dry fines the axial strain required to reach 10 kPa is approximately 1% and as most particle and packing re-arrangement occurs at low stresses it is clear that the dry iron ore fines initially form a very dense packing with little re-arrangement occurring. Following the confined compression of the sample to approximately 120 kPa the unloading response is also measured. For the iron ore fines the bulk plasticity is clearly evident in Figure 5.25, where the unloading curves are almost vertical for all moisture contents. The amount of vertical strain increases with additional moisture content to a maximum value of approximately 37% at 3% moisture content. Further addition of moisture does not exceed this limit. It should be noted that while the axial strain in the sample is increasing, it does not mean that the sample is compressing to a shorter height with increasing moisture content. The addition of moisture to the sample leads to the development of a looser packing of the sample, with a taller initial filled height. This apparent increase in volume with the addition of moisture is termed the bulking effect.

The corresponding bulk density variation is shown in Figure 5.26 and the results for the KPRS fines clearly show the bulking effect from addition of moisture. The initial dry bulk density of the sample is close to 2500 kg/m^3 but this drops significantly on the addition of moisture to a minimum density of 2050 kg/m^3 at 3-4% moisture content, where the bulk density of the sample begins to increase, most likely due to the lubricating effect of the additional moisture in the sample. This bulking effect is primarily visible at low consolidation, where the sample remains more loosely packed than its initial dry density. At consolidation stresses of less than 30 kPa the sample remains in a looser state than its initial dry state up to the maximum moisture content at which it was possible to test the sample. At higher consolidation stresses, such as when the consolidation pressure is greater than 100 kPa, there is little or no bulking seen in the sample and the density remains constant until the lubricating effect of the additional moisture allows for the sample to densify significantly above a moisture content of 4%.

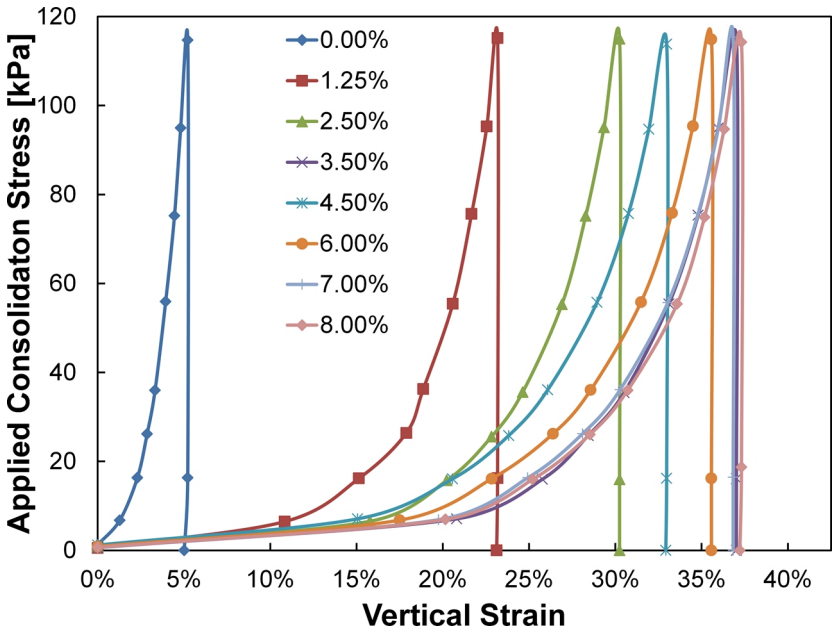

Figure 5.25: Stress-strain response during consolidation for KPRS fines - For various moisture contents

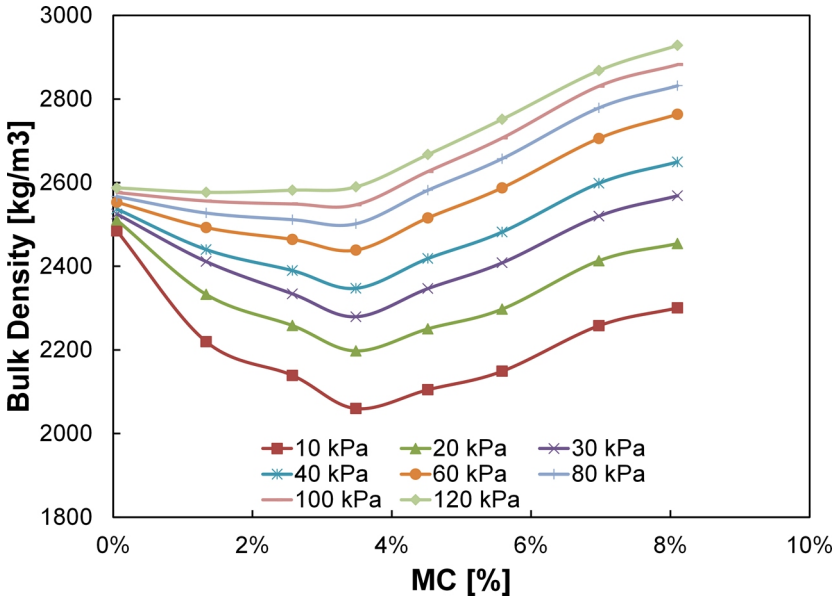

Figure 5.26: Bulk density variation during consolidation for KPRS fines - For various moisture contents

Figure 5.27 and Figure 5.28 show the stress-strain responses and bulk density variation for KPBO fines during confined consolidation. These also exhibit the same trends seen in the KPRS fines of a very stiff material during compression that also is affected by the addition of moisture. Although the general trends remain the same, there is a significant difference in the reaction of the KPBO fines to the addition of moisture.

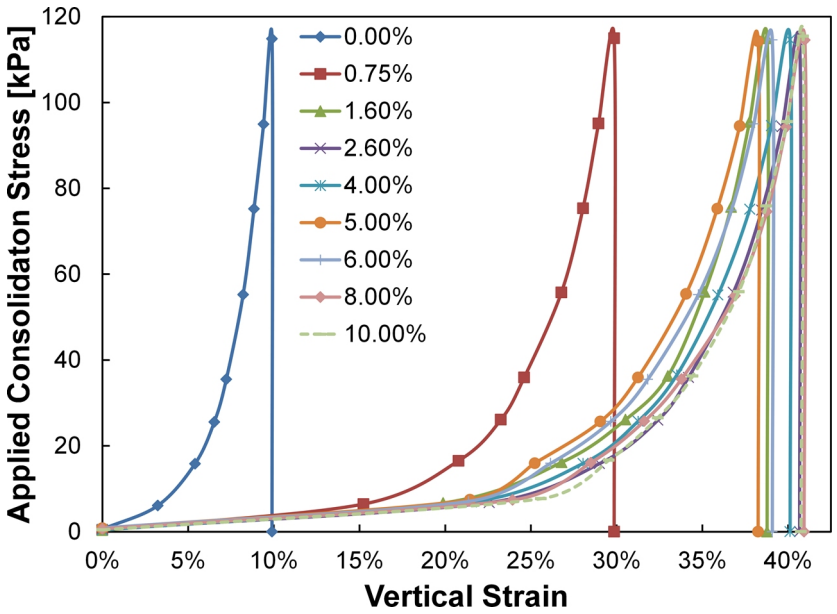

Figure 5.27: Stress-strain response during consolidation for KPBO fines - For various moisture contents

While the KPBO fines initially demonstrate a much higher initial dry density of approximately 2700 kg/m^3, this density drops very sharply to almost 1900 kg/m^3 with the addition of just under 2% additional moisture. This is a significantly more rapid decrease in density in comparison to the KPRS fines, which required almost twice as much additional moisture to reach a slightly denser state. The KPBO fines are also able to sustain this looser packing as the density plateaus until they finally start to increase again above 6% moisture content. Even with a consolidation stress of close to 120 kPa at the maximum moisture content it was possible to test with, the KPBO fines remain in a looser state than the equivalent dry density. These results suggest that the KPBO fines are significantly more susceptible to the effect of additional moisture than the KPRS fines. It is likely that this response to additional moisture would have a significant effect on the handleability of the fines.

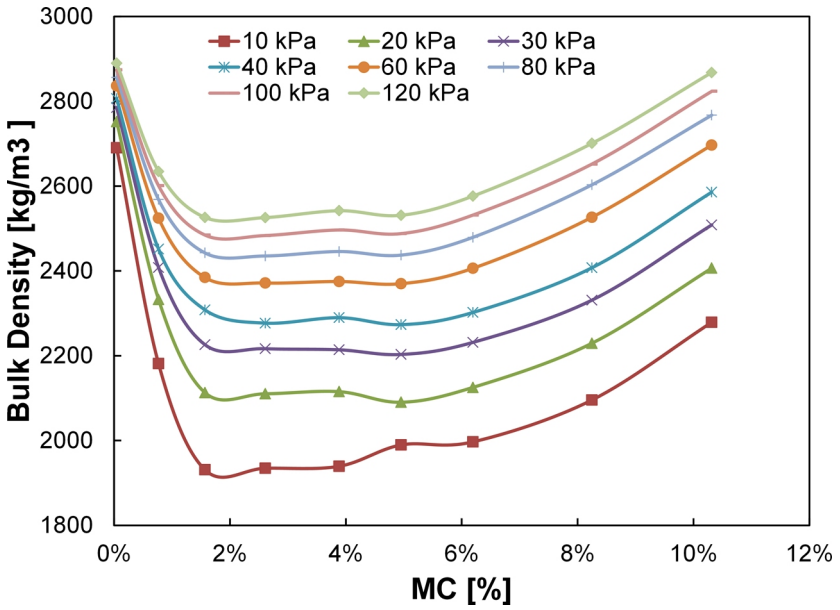

Figure 5.28: Bulk density variation during consolidation for KPBO fines - For various moisture contents

5.6.2 EPT Unconfined Compression

The unconfined yield strength of iron ore fines is evaluated from the EPT for a range of moisture contents between 0 - 6%. Samples with much larger moisture contents, such as in Figure 5.29c, were not tested as the large agglomerates and voids caused problems with achieving consistent results. Dry iron ore fines, which demonstrated no cohesion and collapsed as the confinement was removed, have been omitted.

(a) Sample at 1% MC **(b)** Failed sample at 1% MC **(c)** Sample at 11% MC

Figure 5.29: Unconfined tests using EPT - Iron ore fines at various stages and moisture contents

While the EPT records the key failure criteria of peak unconfined yield strength and sample height values, the response during loading to failure is also captured by the EPT. Figure 5.30 plots the unconfined stress-strain responses for 20, 40, 60, 80 and 100 kPa consolidation stresses at a single moisture content (MC = 4%) for two tests on KPRS fines and Figure 5.32 plots the unconfined stress-strain responses at a single moisture content (MC = 6%) for two tests on KPBO fines.

The unconfined stress-strain responses for all samples tested are available in Appendix D. The observed stress-strain curve is more typical of a brittle material, where the collapse load and ultimate load are the same. All samples demonstrate over-consolidated behaviour with a clearly defined peak value at the maximum unconfined yield strength. Initially, due to the elastic rebound in the sample following removal of the confining walls and the lack of horizontal confinement, all samples display a much softer response for the start of loading. Once the sample has compacted slightly and removed the free space, the measured stress increases significantly with increasing strain, mostly in a linear fashion until the peak collapse load is reached. In some samples intermediate local failure is observed during unconfined compression where a temporary reduction in strength occurs during strain hardening such as in Figure 5.30b or more obviously in Figure 5.32a. More obvious intermediate peaks are observed for the KPBO fines and at lower moisture contents (see in Appendix D) where the sample is more brittle and localised failure occurs. Following the peak yield strength, the measured stress reduces significantly as the sample continues to shear under the continuous displacement of the EPT until a complete collapse of the sample occurs. The unconfined strength increases with the consolidation stress demonstrating the stress history dependent behaviour.

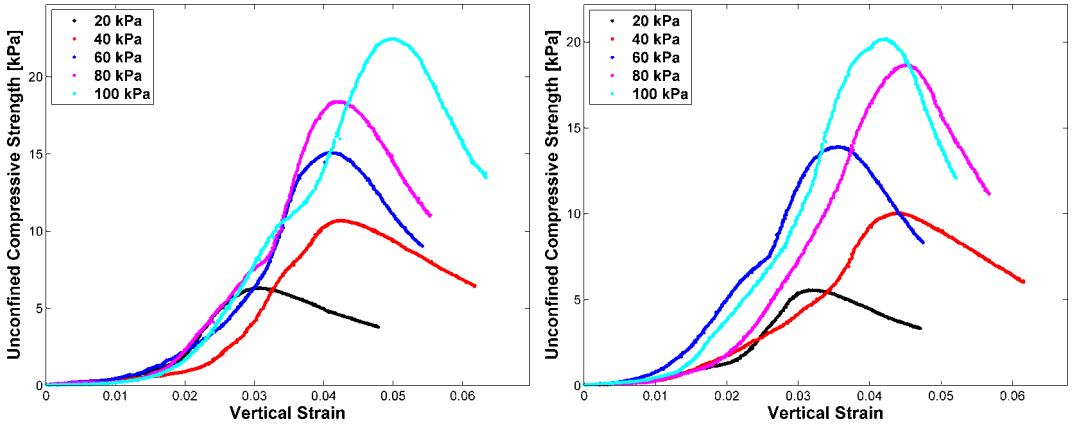

(a) Test Group 1 **(b)** Test Group 2

Figure 5.30: Stress-strain response for KPRS fines at 4% M.C. - For selection of different tests

Following the unconfined tests, the mean and standard deviations for each consolidation stress level and moisture content were calculated and the flow function plotted as the best fit line through the test data. An example of the results for 1% MC is presented in Table 5.14 while the full data sets for all tests on iron ore fines are presented in Appendix E. The flow functions for the KPRS iron ore fines at various moisture contents are plotted in Figure 5.31.

Table 5.14: Unconfined test results for KPRS fines at 1% MC

	Mean					St. DEV				
Con. Stress [kPa]	17.72	37.4	57.47	77.46	98.15	0.49	0.32	0.33	0.17	0.28
Max force [g]	357	547	894	1186	1400	74	46	57	185	173
Peak Stress [kPa]	3.58	5.96	9.68	13.15	15.52	0.46	0.48	0.46	2.09	1.11
Peak Strain	0.03	0.04	0.06	0.04	0.04	0.01	0.01	0.02	0	0.01
Initial AR	1.54	1.63	1.84	1.93	1.93	0.09	0.22	0.03	0.04	0.06
Con. AR	1.3	1.4	1.39	1.42	1.43	0.1	0.03	0.04	0.01	0.08

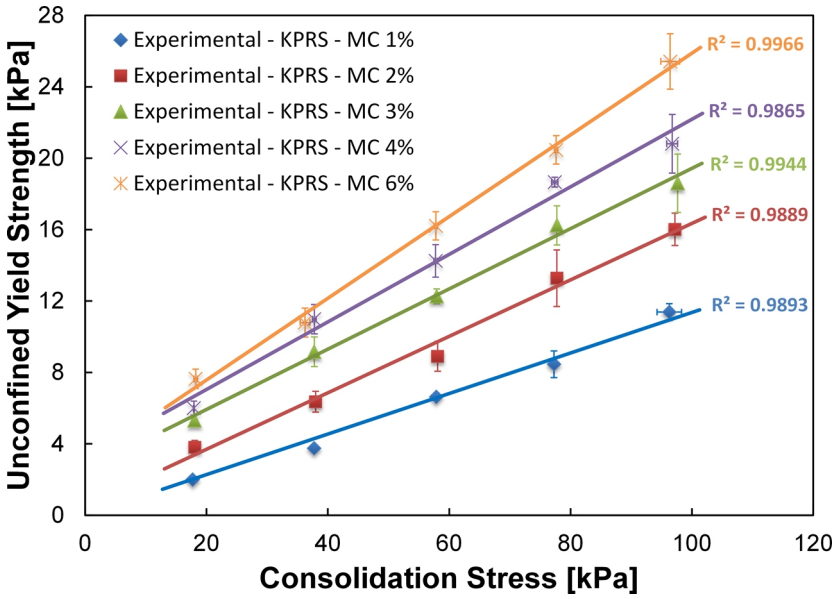

Figure 5.31: Flow function for KPRS fines - For moisture contents of 1% - 6%

The flow function for KPRS fines demonstrates a linear behaviour with increasing consolidation stress up to the maximum tested stress of 100 kPa. The strength dependence on moisture content is clearly visible as there is a significant increase in strength with each increase in moisture content. Error bars are plotted showing the standard deviations for each group of tests. The standard deviation for the unconfined yield strength increases with moisture content. This is likely linked to the behaviour of the fines that prevented testing at moisture contents greater than 10%. The coefficient of variation for tests at the different moisture contents lies with the 5-10%.

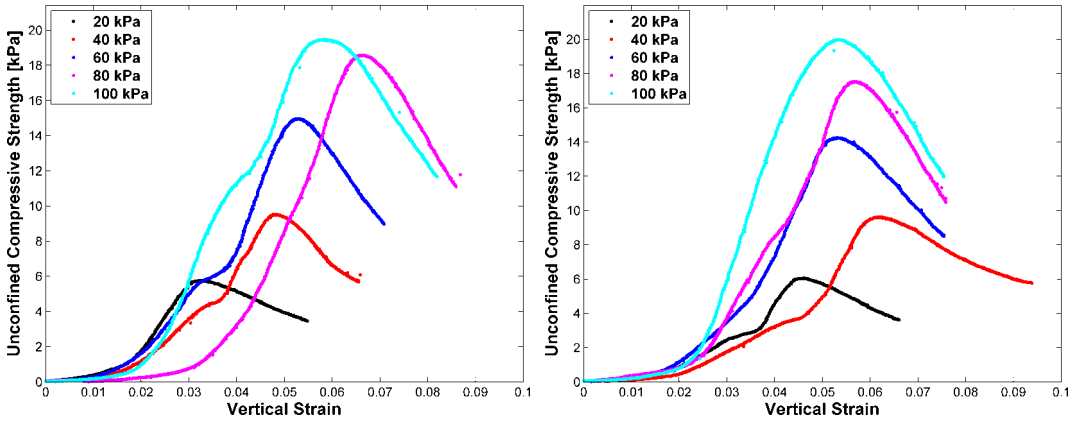

(a) Test Group 1 **(b)** Test Group 2

Figure 5.32: Stress-strain response for KPBO fines at 6% M.C. - For selection of different tests

The flow function for KPBO fines at various moisture contents is presented in Figure 5.33. While the KPBO fines demonstrate the same stress history dependence, the effect from additional moisture content is different. After initially demonstrating the same linear flow function at 1% moisture content, the flow function is best described by a non-linear function for higher moisture contents. At low consolidation stresses the unconfined strength does not appear to vary significantly with moisture contents above 2%. This can be explained by the results of the confined compression test in which the bulk density of the KPBO fines changes significantly up to approximately 2% moisture where the packing density reaches a plateau. As the consolidation stress increases above 40 kPa there is a slight divergence for the flow functions of 2-4% moisture contents. At moisture contents of above 4% the KPBO bulk density starts to increase in the confined compression and the unconfined yield strength also starts to increase more quickly in conjunction with the denser packing and tends towards a linear relationship again.

Figure 5.34 shows the unconfined stress-strain responses for 4 tests at the same consolidation stress and MC% for KPBO fines. It is worth noting that the peak stress does not occur at the same strain value for each test, and that the presence of some intermediate peaks, resulting from a local failure in the sample during the unconfined compression, leads to a lower unconfined strength than in samples where there is no local failure. These features highlight the variability that exists in any granular material and may be related to a different packing structure formed by each sample or by an uneven distribution of moisture throughout the whole sample.

A comparison between the flow function of the KPRS and KPBO fines is made in Figure 5.35 where only the upper and lower moisture content test limits are plotted. The

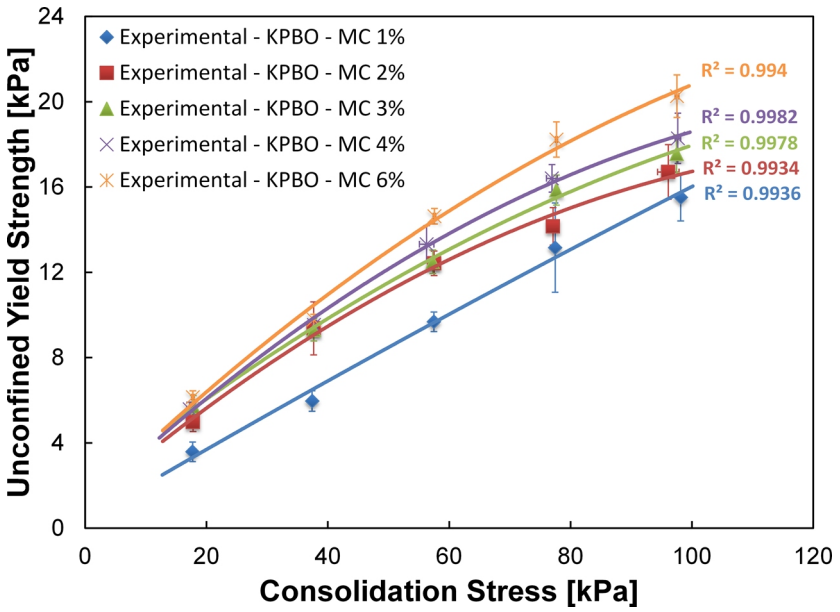

Figure 5.33: Flow function for KPBO fines - For moisture contents of 1% - 6%

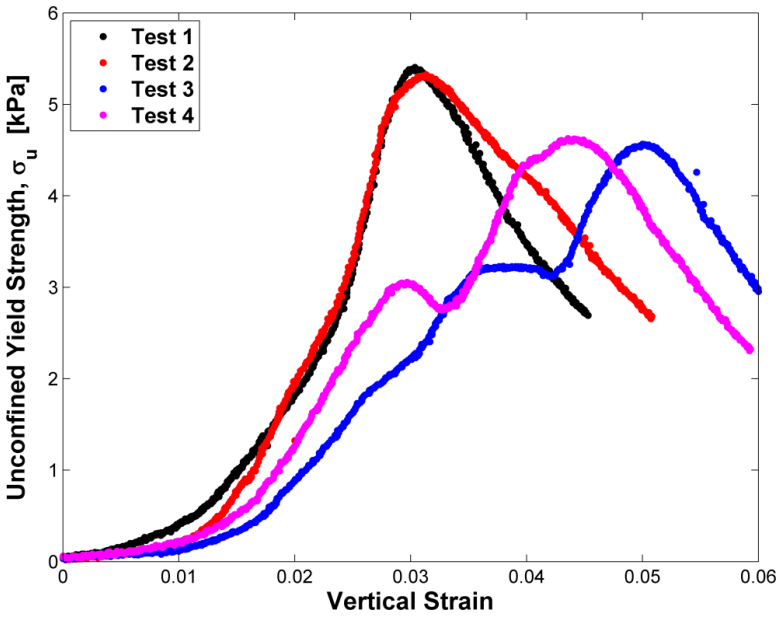

Figure 5.34: KPBO fines 40 kPa consolidation stress - For moisture contents of 2%

results show that at a low moisture content the KPBO fines demonstrate higher cohesion, and as the moisture content in the samples increases above approximately 2% the KPRS fines become more cohesive than the KPBO fines. The results suggest that if the handling conditions allow the moisture content to remain below 2% the KPBO would be the more difficult to handle, while the KPRS fines would most likely be more difficult to handle at moisture contents above 3%.

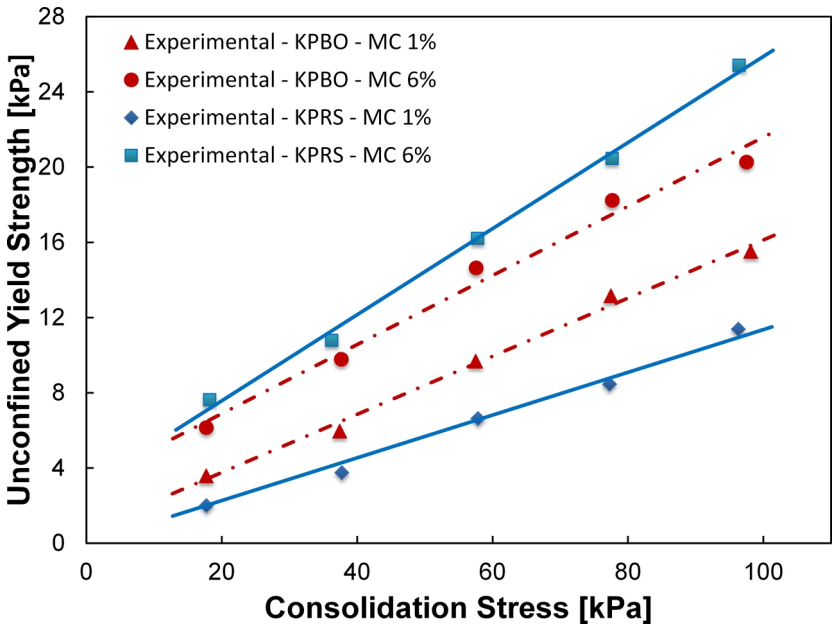

Figure 5.35: Flow function comparison for fines - Upper and lower limits for both types of fines

5.6.2.1 Unconfined Strength - Moisture Content Relationship

The relationship between unconfined strength and moisture content is presented for KPRS fines in Figure 5.36 and KPBO fines in Figure 5.37. Both samples demonstrate a strong dependence on the amount of moisture added, with unconfined strength increasing dramatically from dry fines, which are cohesionless and collapse on the removal of confinement, to significant values of unconfined strength.

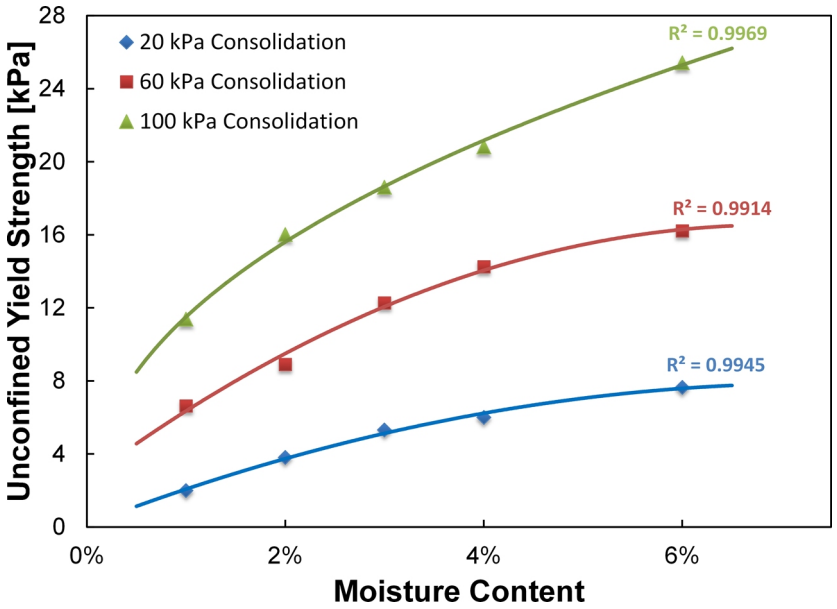

Figure 5.36: Unconfined strength - moisture content relationship for KPRS fines - For three different consolidation stresses

The effect of additional moisture content reduces above a sample moisture content of approximately 4%, with a plateau in the unconfined strength beginning to develop at low consolidation stresses for the KPRS fines. However at higher consolidation stresses the KPRS fines unconfined strength appears to be still increasing significantly at 6% moisture content for higher consolidation stresses. The plateau is more clearly evident for the KPBO fines (Figure 5.37) at all consolidation stress levels, where after an initial significant gain in strength, the rate of increasing strength tends towards a constant at approximately 6% moisture content.

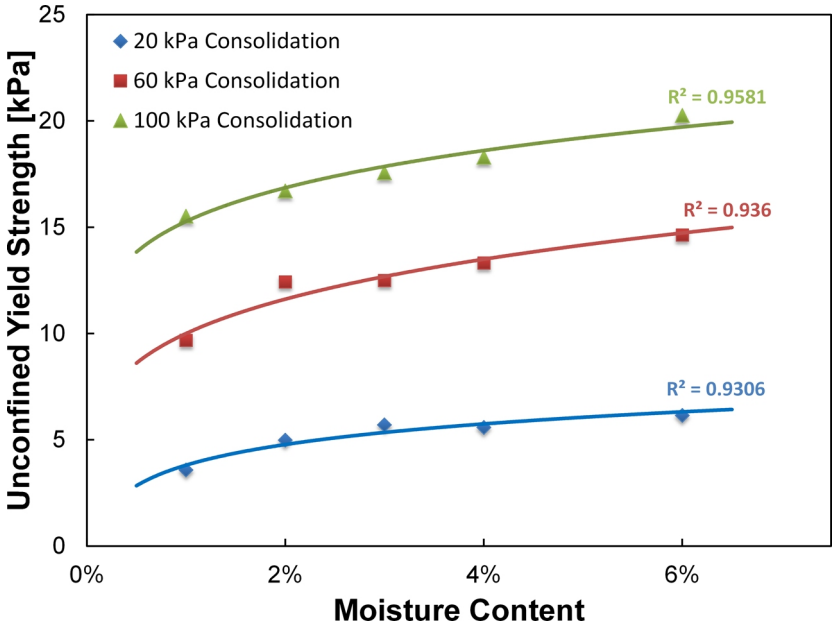

Figure 5.37: Unconfined strength - moisture content relationship for KPBO fines - For three different consolidation stresses

A direct comparison is made between the two samples in Figure 5.38 at both the highest and lowest consolidation stresses at which the materials were tested. It is clear from the results that at moisture contents lower than 3% the KPBO fines generate a much higher unconfined strength before reaching a plateau. The KPRS fines strength continues to increase rapidly with increasing moisture content and is almost a third higher at 6% moisture content.

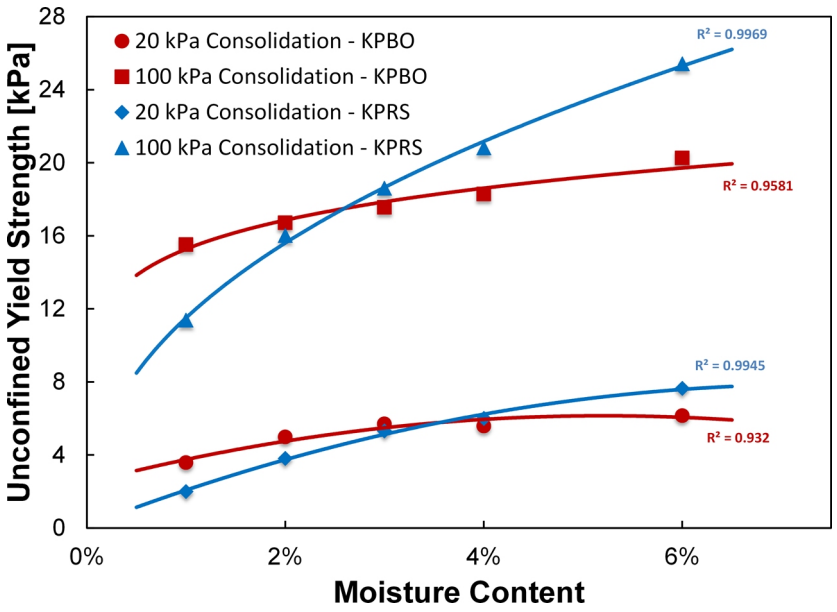

Figure 5.38: Unconfined strength - moisture content relationship for both fines - Upper and lower limits for both types of fines

5.6.2.2 Caking behaviour

An interesting point worth noting is the behaviour of the fines (less than 1.18mm) as they dry from a high moisture content. When the wet fines are mixed with moisture, agglomerates start to form and the higher the moisture content, the larger the size of the agglomerates tends to be. Figure 5.39 shows typical examples of both types of fines after air drying. The KPRS fines tend to sustain the agglomerates that form when the sample is wet while the KPBO fines return to almost the original condition of no agglomerates in the dry state. While a few agglomerates remain in the KPBO fines, these tend to be small in size and likely crumble as they are picked up. The remaining agglomerates for the KPRS fines are much stronger and require significantly more pressure to break the agglomerates.

For oven dried fines (less then 6.3mm), the same trends can be observed in the probability of the fines to cake (Figure 5.40). Despite the larger particle size, agglomerates are still formed for the KPRS fines and strong bonds are formed for the elevated temperatures experienced in the oven. For the KPBO fines at this size, little or no agglomeration is observed between the particles. Both of the results suggest that the KPRS are significantly more susceptible to caking, regardless of size grading or temperature.

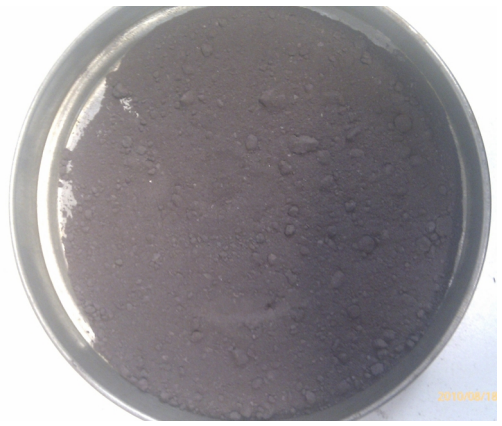

(a) KPBO Fines - Few agglomerates remain

(b) KPRS Fines - Large, hard agglomerates

Figure 5.39: Air dried iron ore fines (< 1.18mm) - After 48 hours of air drying

(a) KPBO Fines - Little/no agglomerates

(b) KPRS Fines - Significant agglomeration

(c) KPBO Fines - Little/no agglomerates

(d) KPRS Fines - Significant agglomeration

Figure 5.40: Oven dried iron ore fines (< 6.3mm) - After 24 hours at 105°C

5.6.3 Jenike Shear Test

While the iron ore fines do contain particles up to 6 mm in diameter, more than 70% by mass of the particles are less than 3 mm in diameter (Figure 5.10). To measure the properties of iron ore fines a 95 mm Jenike standard cell was selected. A nominal shearing rate of 1 mm/min was used for all tests under normal loads of 5, 10, 15 and 20 kg respectively. The shearing response for dry KPRS fines is shown in Figure 5.41. Results for all tests on KPRS and KPBO fines are presented in Appendix F.

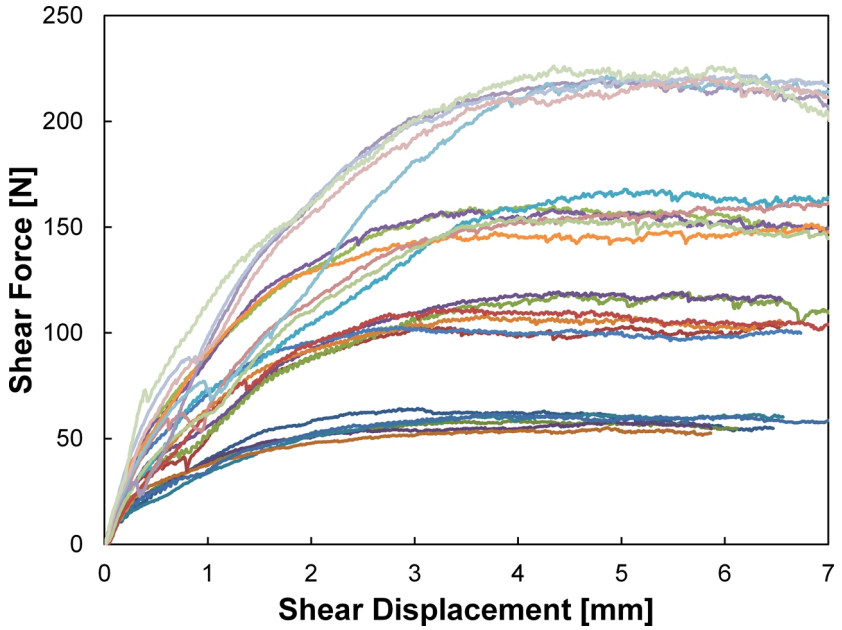

Figure 5.41: Shearing Response for dry KPRS Fines - Results from four different applied normal stresses

The angle of internal friction was calculated from the relationship between the normal stress and the shear stress which is shown in Figure 5.42. Using Equations (5.7) and (5.8) and applying a linear regression to the results the angle of internal friction can be calculated. Dry iron ore fines are cohesionless and hence $c = 0$ can be applied during the linear regression analysis. In the case of wet iron ore fines cohesion is possible and no limit on this value is enforced. Negative cohesion is physically impossible in all cases and care needs to be taken to ensure that this does not occur. The results from all tests are summarised in Table 5.15. The angle of internal friction is rounded to the nearest whole degree. The variation in the consolidated bulk density is within the variation of the measured volume of the shear cell of approximately 3.5%.

In both wet and dry states the results from the respective fines are quite comparable. For dry fines the friction angle for both KPRS and KPBO can be found to be 44 and 45 degrees respectively. The iron ore fires are a highly angular and rough material so a high friction angle is expected. The addition of moisture content leads to the

Table 5.15: Jenike shear cell results

	Moisture Content	Bulk Density [kg/m^3]	Bulk Density [CoV]	Slope	Cohesion, c [kPa]	φim °
KPRS	0.1%	2760	3.1%	0.976	0	44
KPBO	0.1%	2800	3.3%	0.998	0	45
KPBO	7.5%	2720	1.5%	0.909	2.18	42
KPRS	8.5%	2770	2.0%	0.868	1.36	41

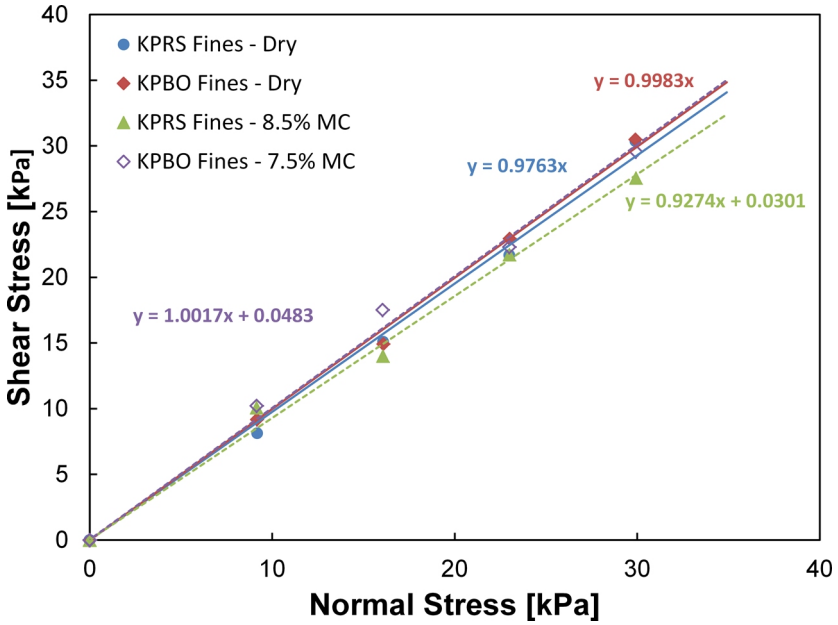

Figure 5.42: Jenike shear test results - Results from both KPRS and KPBO fines at various moisture contents

development of cohesion in the sample and a reduction in the friction angle due to the lubricating effect of moisture content. The friction angle is found to be 3 degrees less for both types of fines after the addition of approximately 8% moisture content.

5.6.4 K_0 Test

Confined compression tests were carried out to evaluate the at rest lateral pressure K_0 for iron ore fines in a dry state and the effect of the addition of moisture. For all tests the iron ore fines were loaded with a vertical force of 1000 N, which is approximately 63 kPa. In the case of dry fines, which form a very dense initial packing with little room for rearrangement of particles, a loading rate of 0.5mm/min was used to ensure that an adequate number of data points are recorded. For wet fines, which form a much looser packing and compress significantly more, a loading rate of 1mm/min was selected.

All tests were carried out using the unsupported cylinder set-up which allowed for two-way compression of the sample in the cylinder. Due to the highly abrasive nature of the stiff iron ore particles a protective layer of $50\mu m$ thick Mylar® sheet was used to prevent damage to the acrylic cylinder. The iron ore fines were tested at three different moisture content levels - dry, $\approx$ 6% moisture content and $\approx$ 8% moisture content. Multiple tests were carried out to assess the consistency and variability of the iron ore fines with respect to the lateral pressure ratio.

5.6.4.1 Correction Factors

Initially, all gauges data are set to zero by subtracting the initial strain gauge reading so that the data is in term of relative strain variation. The initial timestep is selected based on the following criteria: the INSTRON cross-head is moving and the force on the top platen is non-zero. This allows the initial timestep and its corresponding strain readings to be identified from the test data and used to zero the initial strain for the test. The final timestep is selected as the first timestep after which the cross-head stops moving following unloading while the force on both the top and bottom platens is not changing. To account for any variation in the measured strains arising from the local environmental conditions as the test is taking place, a correction is applied to the measured strain gauge data to ensure that the final strain also returns to zero. The thermal drift per timestep is calculated from Equation (5.18) for each gauge, where N_t is the the total number of recorded timesteps in the duration of the test, and then the correction is applied to each individual gauge at each timestep.

$$ThermalDrift = \frac{GaugeData_{t_{init}} - GaugeData_{t_{fin}}}{N_T} \qquad \textbf{(5.18)}$$

Figure 5.43 shows the responses of all stain gauges after the results have been zeroed at the initial timestep. The figure also shows a gauge that appears to be returning an erroneous reading for the vertical strain. At this point any such gauges can be removed from the calculation leaving the remaining gauges to calculate the lateral pressure ratio for the granular material. The number of gauges located on the cylinder allows for individual gauges to be discarded from the calculation procedure without affecting the reliability of the result.

Despite the erroneous readings, the gauges are still functional and can continue to be used for further testing without problems. These errors were normally caused by one of two errors - failure to zero the voltage in the data logger for that gauge following a previous test, or in some cases, material getting caught between the protective sheeting

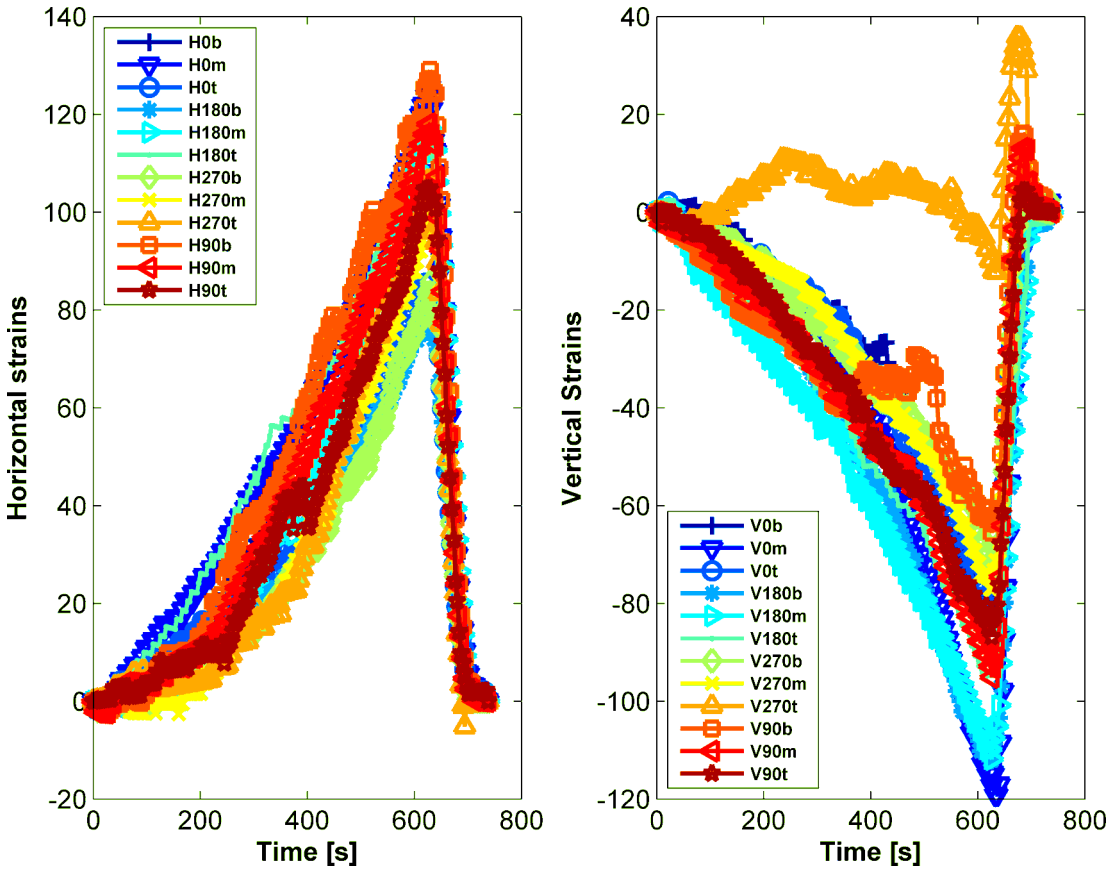

Figure 5.43: Gauge response for test on iron ore fines - Horizontal strain on left, vertical strain on right

and cylinder wall in the vicinity of the gauge which prevented the recording of the full data.

5.6.4.2 Stress-Strain Response

The mean vertical stress applied to the sample from the platens is calculated using Equation (5.2). This method includes a correction in the area term to account for the deformation of the cylinder under an applied load. While a correction for the change in cross-sectional area has been applied, actual change in area is not significant due to the small strains that actually occur under confined compression. The platen forces measured are shown in Figure 5.44, while the resultant stresses are shown in Figure 5.45. Although the forces recorded in the top and bottom platens are not equal, the difference between measured force at the bottom and applied force at the top is very small and mainly due to measurement error.

Due to the effect of wall friction some of the applied force from the top platen is transmitted in to the cylinder walls. In cases where there is significant wall friction in action, the vertical stress in the bulk solid may be significantly different from the assumed mean

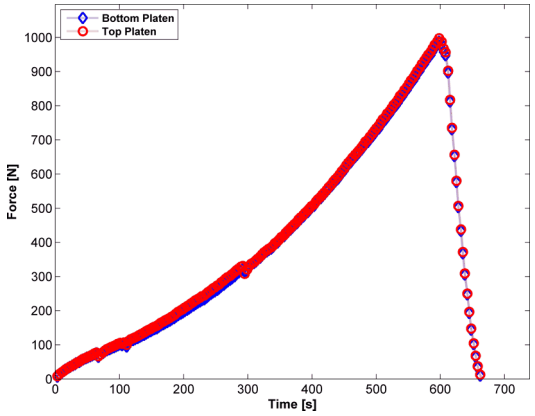

Figure 5.44: Measured platen forces - For top and bottom platens

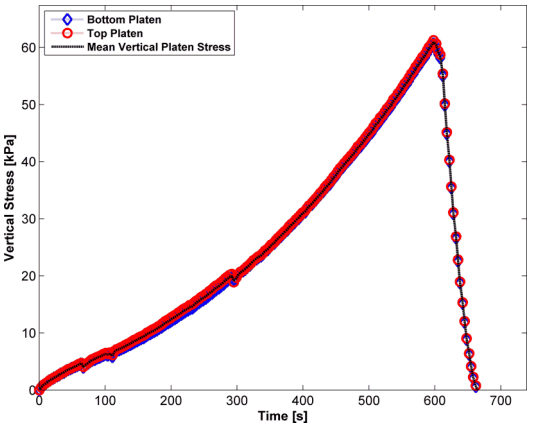

Figure 5.45: Calculated platen stresses - For top and bottom platens

applied stress. To account for this the stress in the bulk solid can be calculated from Equation (5.19), which includes the vertical force being transmitted in the cylinder wall (Equation (5.20)).

$$\sigma_{V_{Bulk}} = \frac{2\left(F_T + F_B\right) + \pi D t E_w \sigma_a}{\pi\left(D\left[1 + \varepsilon_\theta\right]\right)^2} \tag{5.19}$$

$$\sigma_a = \frac{E_w\left(\varepsilon_a + \upsilon_w \varepsilon_\theta\right)}{\left(1 - {\upsilon_w}^2\right)} \tag{5.20}$$

The vertical stress in the solid, calculated from Equation (5.19), is shown in Figure 5.46a. There are no significant differences seen between the vertical stresses calculated at different heights in the cylinder. The horizontal stress in the solid is calculated from Equation (5.3). For the horizontal stresses in the solid (Figure 5.46b) there is no significant difference between the three different levels of gauges.

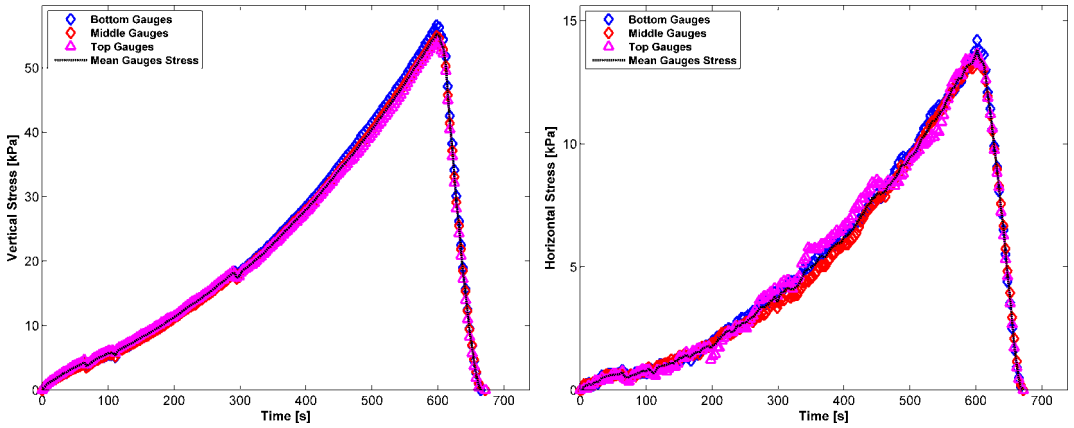

(a) Vertical Stress **(b)** Horizontal Stress

Figure 5.46: Stresses in the solid - At all gauge levels including average

Due to the nature of granular materials, the strains experienced may vary across the sample. To negate this, the average axial strain in the sample will be used in this study which is determined from the differential height of the loading platens when contact exists with the granular material. The resulting average stress-strain curves are presented in Figure 5.47 and shows that the mean vertical stress calculated from the platen forces is approximately equal to the applied 63 kPa.

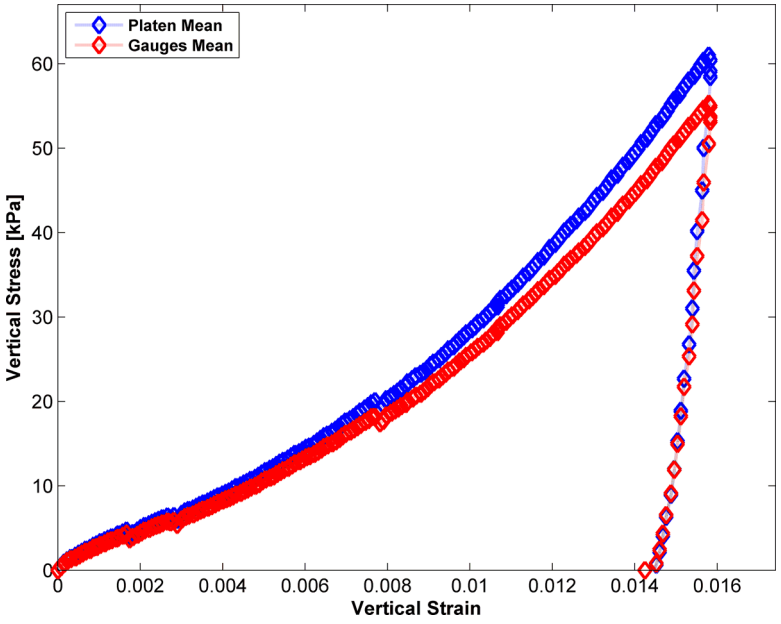

Figure 5.47: Average Stress vs. strain - Average values for the platens and gauges

When the forces being transferred onto the cylinder wall from local friction or other devices such as poor geometrical alignment are accounted for, the mean vertical stress experienced by the contained solid is reduced to approximately 58 kPa. Although the

small reduction in the measured vertical stress will lead to a slightly higher K_0 being evaluated, it is a more robust method of evaluating the stress in the solid as opposed to an assumed average.

5.6.4.3 Lateral Pressure Ratio

The relationship between mean applied vertical stress and the mean radial pressure is presented in Figure 5.48. The gradient of this slope gives the ratio of horizontal to vertical pressure, which is otherwise known as the lateral pressure ratio, as defined by Equation (5.1).

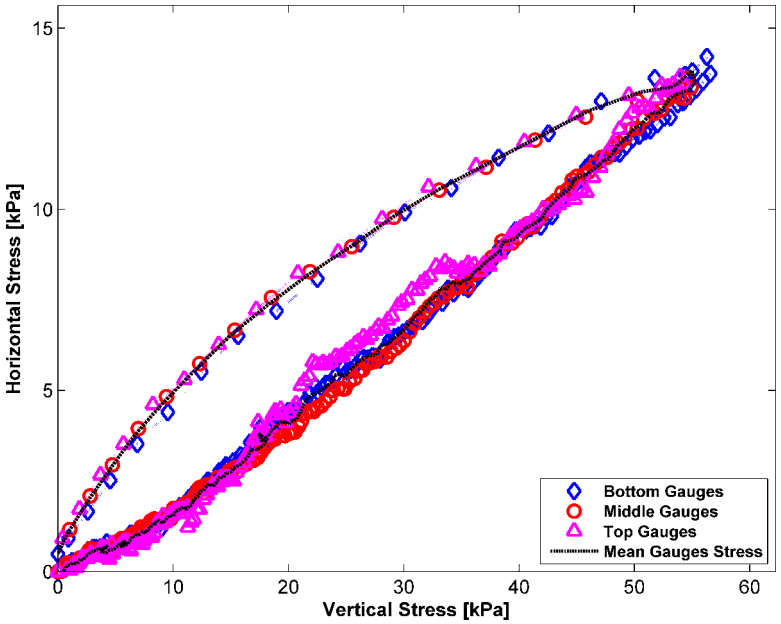

Figure 5.48: Mean vertical stress vs. mean radial stress - At all gauge levels including average

The lateral pressure is calculated from the ratio between the horizontal and vertical stresses calculated at the gauges from Equation (5.21). The vertical stress in this case is calculated from Equation (5.19) and is the applied vertical stress minus the stress carried in the cylinder.

$$K_0 = \frac{\sigma_{H_{Mean}}}{\sigma_{V_{Bulk}}} \tag{5.21}$$

The lateral pressure ratio is found from the average value calculated at each gauge. The results at different cylinder heights are shown in Figure 5.49a while the average value calculated from all gauges is shown in Figure 5.49b. There is little variation throughout the cylinder and as such the average value is chosen as the lateral pressure ratio of the material.

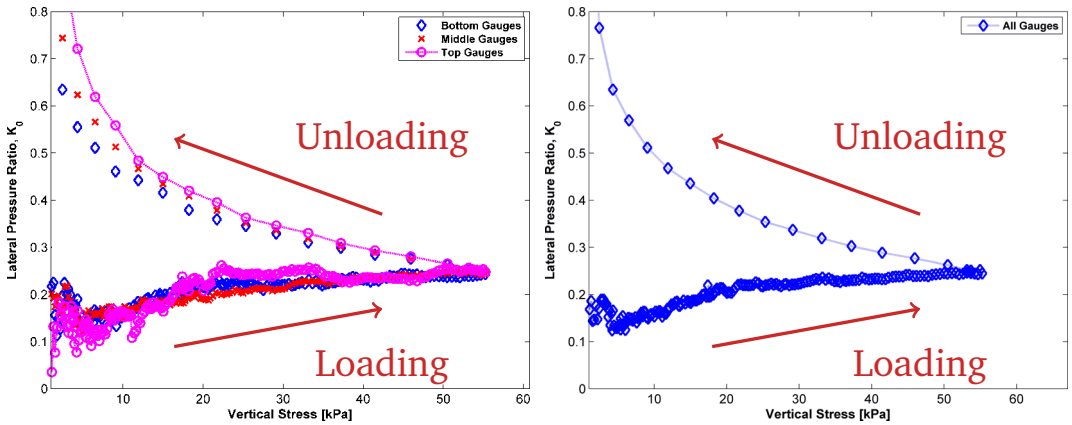

(a) At gauge levels **(b)** Average value

Figure 5.49: Lateral pressure ratio K - At all gauge levels including average

5.6.4.4 Results for iron ore fines

The above calculations have been performed on all test data for the iron ore fines and the lateral pressure ratio for all samples was evaluated as the near constant value found as the peak consolidation stress is applied. The results for both fines are presented in Table 5.16 and Table 5.17 and displayed in Figure 5.50.

Table 5.16: K_0 results for KPBO fines

	Dry Fines			Wet Fines					
	Mean	**STD**	**CoV**	**Mean**	**STD**	**CoV**	**Mean**	**STD**	**CoV**
MC %	0.002	-	-	0.0566	0.001	1.80%	0.0791	0.001	1.30%
Peak Strain	0.0161	0.0011	6.80%	0.0962	0.0035	3.60%	0.0782	0.0122	15.60%
K_0	0.235	0.017	7.20%	0.246	0.007	2.80%	0.293	0.026	8.90%
Stress [kPa]	53.4	1.4	2.60%	51.6	2.1	4.10%	50.4	1.8	3.60%

Table 5.17: K_0 results for KPRS fines

	Dry Fines			Wet Fines					
KPRS	**Mean**	**STD**	**CoV**	**Mean**	**STD**	**CoV**	**Mean**	**STD**	**CoV**
MC %	0.002	-	-	0.0568	0.003	5.30%	0.0863	0.0014	1.60%
Peak Strain	0.0184	0.0022	12.00%	0.1059	0.0022	2.10%	0.0765	0.0059	7.70%
K_0	0.241	0.016	6.60%	0.254	0.018	7.10%	0.302	0.019	6.30%
Stress [kPa]	53.2	1.2	2.30%	51.6	1.9	3.70%	49.8	1.2	2.40%

There is some slight variability in the results which can be related to the unique packing structure that exists for each individual test. As the moisture content rises, and the level of lubrication between the particles increases, the lateral pressure ratio begins to gradually rise. This is particularly clear where the moisture content is greater than 6%

and the lateral pressure ratio increases significantly between 6% and 9% moisture content. Below 6% moisture content there is little change in the lateral pressure ratio from the dry state as the results fall within the scatter of the dry test. The lateral pressure is expected to decrease as the level of adhesion increases, but the effect of lubrication from the moisture appears to cancel out this effect below 5% moisture content.

The results for the lateral pressure ratio calculated based on the friction angle found in the previous Jenike results and using the Jaky part of Equation (5.9) are included as a comparison on Figure 5.50. As the moisture content in the sample increases, the angle of internal friction between the particles decreases and this leads to a larger horizontal thrust as there is less resistance to the applied vertical load. Eurocode 1-4 [British Standards Institution, 2006] suggests that the value found from the Jaky equation be multiplied by a factor of 1.1, further increasing the difference between the results from a confined compression test and those calculated indirectly from the friction angle.

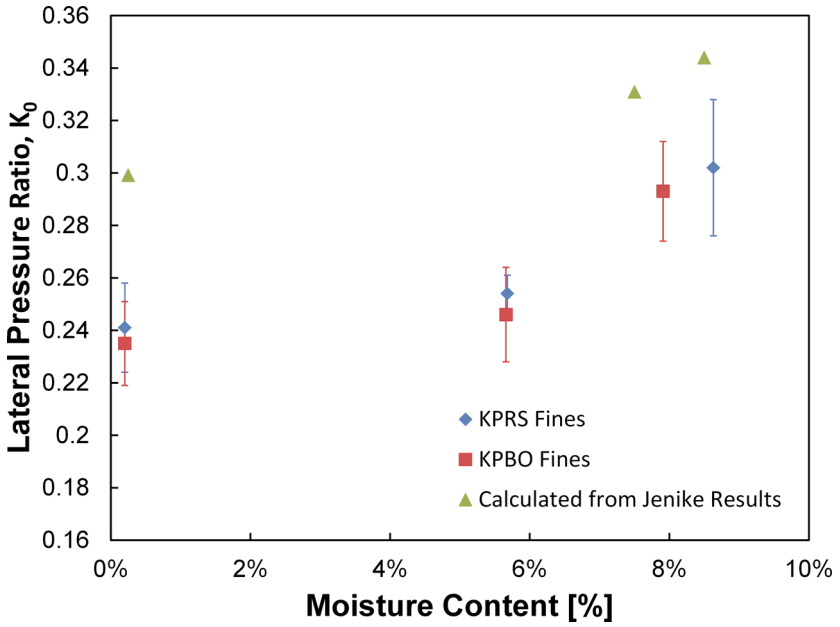

Figure 5.50: K_0 results - For both KPRS and KPBO fines at various moisture contents

However, there is a discrepancy in the results compared to those predicted from the measured friction angle and is likely due to the presence of the protective Mylar® sheet within the K_0 cylinder. As the iron ore fines are quite abrasive, the effect of the Mylar® sheet has been assessed using other materials such as barley and fine sand. The Mylar® sheeting was found to reduce the predicted K_0 value in these tests by approximately 0.05. Applying this correction to the results garnered from the K_0 test with Mylar®, a corrected value for K_0 can be appraised. The adjusted results are shown in Figure 5.51. In the corrected results there is a much closer agreement between the actual measured

K_0 value from the compression test and the value predicted from the Jaky equation using the angle of internal friction found in Jenike shear tests.

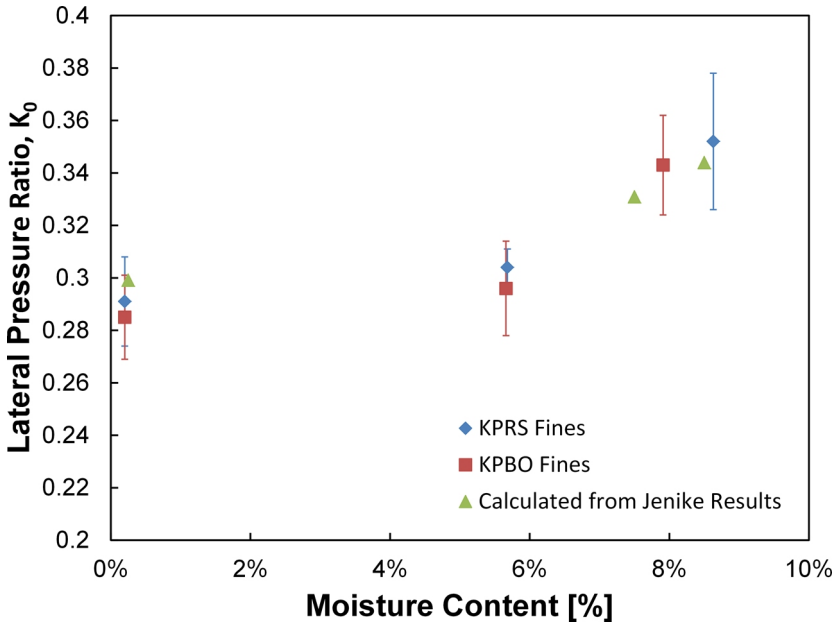

Figure 5.51: Mylar corrected K_0 results - Adjusted to account for effect of Mylar sheet for both KPRS and KPBO fines at various moisture contents

5.7 Summary

The LKAB iron ore fines have been evaluated through a series of characterisation experiments. The Jenike shear cell has shown that iron ore fines are a highly frictional material with an angle of internal friction of 44 degrees for KPRS fines and 45 degrees for KPBO fines.

The effect of moisture on the friction angle of both materials is similar and both have a reduction in friction angle of 3 degrees. The effect of moisture content on the behaviour of the iron ore fines has been evaluated and both types of fines have shown a significant dependence on the moisture content for the development of cohesion to occur. The Edinburgh powder Tester (EPT) has been used to derive the flow function for both types of fines under various moisture contents. The packing and compression behaviour has also been assessed using the EPT.

KPRS fines have a much higher unconfined strength and flow function at higher moisture contents, and also show a greater increase in cohesion with the addition of moisture. This suggests more difficult handling for KPRS fines in wetter conditions, while at moisture contents of less than 2% the KPBO fines demonstrate higher unconfined yield strength and are also more susceptible to the bulking behaviour related to the addition of moisture content.

The lateral pressure ratio and bulk loading and unloading stiffness of the iron ore fines have been evaluated from a confined compression test. Both types of fines share a similar behaviour and return a K_0 value of approximately 0.29 in the region of 0-5% moisture content before the lateral pressure then increases with the further addition of moisture and the level of inter-particle lubrication increases.

An observation on the caking behaviour of the two kinds of fines during different types of drying suggests that the KPRS fines are more susceptible to caking behaviour which would lead to additional handling problems when dealing with the KPRS fines. Large caked, agglomerates were observed for the KPRS fines at different size gradings and for both air dried and oven dried samples.

Chapter 6

Parametric Study for Cohesive Model Parameters

In Chapter 3 the DEM has been introduced and in Chapter 4 a new contact model for dealing with adhesive contacts involving plasticity has been presented. This chapter aims to investigate how the various parameters of the Edinburgh Elasto-Plastic Adhesion (non-linear) [EEPA-NL] contact model affect the resulting bulk behaviour predicted by the model. The DEM parameters will be assessed through the simulation of uniaxial confined and unconfined compression tests, which can be related to the results from experiments using both the Edinburgh Powder Tester (EPT) and K_0 Tester.

6.1 Simulation Setup

A DEM Model of equal dimensions to the EPT has been created within the EDEM package to replicate the experimental setup. While the dimensions of the test setup are maintained, a favourable number of particles with respect to computational cost were selected as the mesoscopic representation of the agglomerated real particles, where each DEM particle represents a cohesive agglomerate. The three main stages of the experiments are shown from the simulation in Figure 6.1 and include the filling of sample, the confined compression and the unloading and unconfined compression to failure of a sample.

For this study both spherical and non-spherical particles have been used. While non-spherical particle shapes are more representative of the real particle shapes and are used to capture the realistic geometric interlocking, spherical particles have also been used to explore the parameters as the interpretation of some results may be easier for spherical particles. For example, it is easier to quantify the effect of rolling friction

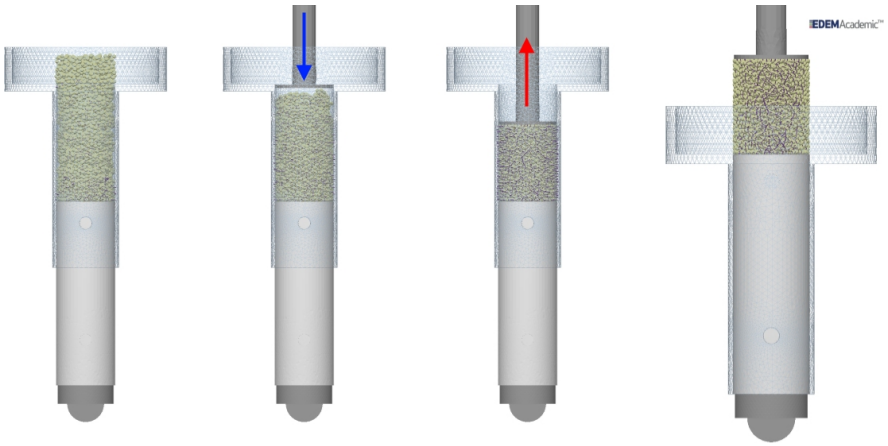

Figure 6.1: DEM model of uniaxial test - From L to R: a) filling, b) loading, c) unloading, and d) unconfined compression

for spherical particles than for non-spherical. Non-spherical particles each consisting of two overlapping spheres of 1.25 mm diameter giving a particle aspect ratio of 1.5 (see Figure 6.2) were used, while spherical particles of 1.25 mm diameter (aspect ratio = 1) were also employed. Mono-sized particles were employed for all simulations to ensure that the scaling effects related to particles of different radii were not affecting interpretation of the results.

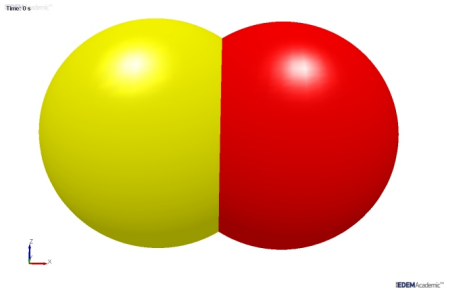

Figure 6.2: Paired particle consisting of two spheres - Aspect ratio of 1.5

Sitharam and Nimbkar [2000] found that samples with exactly parallel gradations will have the same fabric and will behave the same under identical boundary conditions and increases in particle size do not significantly change the shear strength or volumetric behaviour. However, for samples with the same minimum particle size and different gradations the behaviour will be because of the different initial arrangement or fabric. Particle density was selected such that the filled assembly would have approximately the same mass as that observed in the experiments from Chapter 5. This equates to a particle density of 4350 kg/m^3 for particles with a radius of 1.25 mm. In order to keep simulation results between spherical and non-spherical particles comparable, each simulation has approximately the same total mass. For a simulation consisting of 5000 spherical particles, this equates to 3000 non-spherical particles with the same particle

density and an aspect ratio of 1.5. Particle contact interactions were kept the same for spherical and non-spherical particles by maintaining the same particle radius and thus there was no requirement to scale the particle stiffness with different particle radii.

The EEPA contact model was only applied to particle-particle interactions while particle-geometry interactions were modelled using the Hertz-Mindlin (no-slip) contact model, therefore no particle-geometry adhesion was considered. In an attempt to replicate the two way compression that occurs in both the EPT and K_0 tester, friction between cylinder and particles was set to zero during confined compression. This means for each test the force acting on the top and bottom platens is approximately equal with the bottom platen carrying the load of particles also. The friction coefficient between platens and particles was set to 0.5 and its main purpose is to provide lateral stability and prevent slippage of sample during unconfined compression.

This study covers a variety of different parameters, such as particle-particle friction, rolling friction, restitution coefficient, the virgin loading stiffness k_1, the unloading stiffness k_2 and the level of adhesion, used in the simulations. The loading stiffness k_1 was so chosen to cover a range that is sufficiently stiff to avoid excessive particle overlap, but not too stiff so as to incur significant computational cost, while maintaining a range relevant to the real materials to be modelled. Increasing contact stiffness leads to decreasing simulation time-steps (see Section 3.3.3.1) due to the smaller contact duration that occurs. In order to maintain stability in the simulation and not miss important data the time-step may need to be reduced significantly. The ratio of k_2/k_1 was varied from 1 to 50 by maintaining a constant k_1 while increasing k_2. All simulations were conducted with the non-linear version of the model. The amount of adhesion has also been investigated by varying the applied surface energy, and hence f_{min} limit. The constant pull-off force f_0 has not been studied here as it was seen to be of little significance for materials consisting of particles larger than a few hundred microns. While a more detailed study on the effect of contact plasticity and the varying sources of adhesion has been carried out by Thakur *et al.* [2013] using linear loading and unloading stiffness, this study will focus on the non-linear portion of the model. Based on the findings in the literature [Cleary, 2000; O' Sullivan and Bray, 2004], the simulation time-step was chosen to be less than or equal to $0.17\sqrt{m/k}$. The main parameters used in the study are presented in Table 6.1.

Similar to the experiments, the initial filling height varied with DEM input parameters. However, the consolidated aspect ratio of the sample for the DEM simulations was kept in a narrow range of approximately 1.20 to 1.45 which was used in the experiments. Each simulation consists of three stages - filling the cylindrical mould to form the initial

Table 6.1: Simulation properties

Number of Particles	3000 paired/5000 spheres
Particle Density, ρ (kg/m^3)	4350
Loading Spring Stiffness, k_1 (N/m)	1×10^3
Unloading Spring Stiffness, k_2 (N/m)	$10k_1$, $25k_1$, $40k_1$, $50k_1$
Adhesive Force, f_0, (N)	0
Adhesive Surface Energy (J/m^2)	0 - 50
Adhesion branch exponent	20 (1-40)
Particle Static Friction, μ_s	0.5 (0.2 - 0.8)
Particle Rolling Friction, μ_r	0.005 (0 - 0.5)
Wall Friction, μ_w	0
Top and Bottom Platen Friction, μ_P	0.5
Simulation Time-step (s)	$8 \times 10^{-7} \sim 2 \times 10^{-6}$

packing used for all stress levels; confined consolidation to the required stress level and subsequent unloading; and finally unconfined compression of the sample to failure after the removal of the mould. The process is visualised in Figure 6.1.

The effect of the generation scheme is presented in Figure 6.3 for spherical particles. In the stationary static method (Figure 6.3a) all particles are generated in a single timestep in a volume larger than the cylinder to be used. The particles are then allowed to settle under gravity. With the stationary dynamic factory (Figure 6.3b) the generation volume is only slightly larger than the cylinder geometry and the particles are generated over a longer period of time at a set generation rate (e.g. 5000 particle per sec), which allows for the generation of contacts during filling aiding the formation of a loose packing typically seen in fine cohesive materials. The moving dynamic factory (Figure 6.3c) involves a small generation volume that is moved upwards in conjunction with a high particle generation rate to allow the assembly to be generated quickly. All random packings were used during the study and these were generated from a random rainfall method which employed the moving factory to reduce the time required to generate the packings. As there are two contact vectors per contact, the contact orientation plot is symmetrical for both azimuth and elevation angle. The static factory is shown to generate an isotropic initial packing with an equal distribution of the vertical contacts in the assembly. The horizontal contacts are equally distributed also, with some peaks noted at 60°, 135°, 225° and 300°, which are likely to be related to the random dense spherical packing formed in a static factory. Both dynamic factories generate a more anisotropic packing. The stationary dynamic factory has an even horizontal distribution but a preferential vertical contact orientation of approximately 60° is seen. The moving dynamic factory leads to a clear preferential direction in the elevation angles with the majority of the contact being between 30° and 90°. The more anisotropic packings

formed by the dynamic factories may be more representative of the packing formed for a real granular material as filled in the experiment. A moving dynamic factory has been adopted as the method of filling the samples due to its speed benefits.

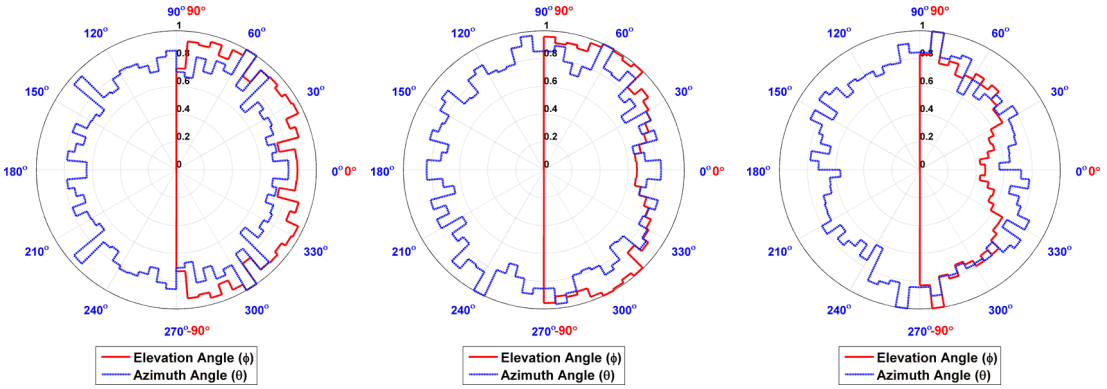

(a) Fixed & Static Factory **(b)** Fixed & Dynamic Factory **(c)** Moving & Dynamic Factory

Figure 6.3: Contact orientations - For 5 degree bins for various methods

Following particle generation, a rest period was provided for all simulations to allow particles to settle and ensure that the systems were in a quasi-static state before the commencement of loading. Loading only commenced when the kinetic energy in the system reached a constant value that was less than 10^{-5}J. This ensured that particle velocities were in the order of 10^{-8} m/s with a constant coordination number.

The confined consolidation process was conducted by translating the top platen vertically downwards at a constant rate of 25 mm/s (strain rate ≈ 0.3 s^{-1}) to apply a vertical compression. The process is similar to the procedure in the experiments. After consolidating the sample to the desired stress level, the assembly was unloaded by translating the top platen upwards at the same constant speed. The lateral confining walls were removed when the unloading was complete and the unconfined sample was allowed to relax for a short period of time to again leave the kinetic energy generated from the removal of the confining wall and upward movement of the top platen to dissipate and drop to an acceptable stable value. The sample was then crushed to failure by moving the top platen downwards again at a constant rate of 5 mm/s (strain rate ≈ 0.05 s^{-1}). A higher compression rate was used for the confined compression as the inertial effect of the higher loading rate is not as significant as in the unconfined compression test, where a high platen velocity can lead to impact damage of the sample at the point of initial loading in the unconfined test. However, in both cases the inertia number [GDR Midi, 2004; Langston *et al.*, 2013; Sun and Sundaresan, 2011] is less than 10^{-3}, confirming that the simulations are in the quasi-static regime. In all simulations the bottom platen, which represents the stationary base in the experiments, remained stationary in

all stages. The results for these simulations are presented in the following sections and the effect on the filled, confined and unconfined stages of the simulation are assessed.

6.2 Spring Stiffness

The spring stiffness of the particle contact is one of the most important model parameters as it controls the amount of force and overlap that develops during a contact. The virgin loading stiffness k_1 is active during all loading above the previous historical maximum and generally controls the bulk stiffness response of the assembly during loading. The level of plasticity that the assembly achieves is controlled by the unloading/reloading stiffness k_2. The combination of k_1 and k_2 has a major effect on the cohesive strength developed in an assembly. A soft loading stiffness will allow large overlaps and as the adhesion force is dependent on the plastic overlap k_2 will then control the amount of the overlap generated from loading that is used for calculating the adhesive forces in the model.

6.2.1 Virgin Loading Stiffness

The effect of changing the virgin loading stiffness k_1 is explored for some typical situations such as filling, consolidation and unconfined compression of the assembly. The loading stiffness will dictate what size overlaps occur for a particular force, with a lower stiffness leading to larger overlaps. A low contact stiffness will also lead to a low bulk stiffness with large strains developing during compression. Where the EEPA-NL variation is employed, the virgin loading stiffness is calculated from Equation (4.18), where the contact stiffness is dependent on the particle shear modulus in a manner similar to that used in the Hertz-Mindlin contact model.

6.2.1.1 Initial Filling

At a given set of parameters for friction and adhesion there is little variation in the filled height and porosity as k_1 is varied with the range that is suitable for representing an adhesive agglomerate (Table 6.2). The effect of the loading stiffness becomes more important during stress consolidation as the applied forces become larger than those generated during filling (See Table 6.2).

The forces generated, and hence overlaps, during filling were small enough such that across a stiffness range such as used here, there was little difference in the filled height. However, if the contact stiffness was to be increased by several orders of magnitude, a more significant difference in the filled porosity would be noted, particularly for a cohesive assembly, where the adhesion forces are dependent on the level of overlap achieved.

Table 6.2: Effect of virgin loading stiffness for consolidation to 100 kPa

Shear Modulus, G (Pa)	2.5×10^6	5×10^6	7.5×10^6
Initial Porosity	0.670	0.672	0.671
Consolidated Porosity	0.491	0.514	0.527
Initial Aspect Ratio	2.13	2.14	2.13
Consolidated Aspect Ratio	1.39	1.45	1.50

6.2.1.2 Confined Compression

The results of the confined compression tests are given in Figure 6.4. The effect of the loading stiffness is clearly visible, as is the non-linear response of the bulk material. As each filling had almost the same filled height and number of initial contacts, there is little difference in the stress-strain response (Figure 6.4a) below 10% strain. However above that value the effect of the loading stiffness of the contact model becomes increasingly distinct. The initial gentle loading response is most likely due to the initial re-arrangement of the packing that is occurring, and then once a stable, denser packing has been achieved at approximately 10 kPa the stiffness at the particle contact comes into play and from this point any further strain is more dependent on the overlaps being generated between particles.

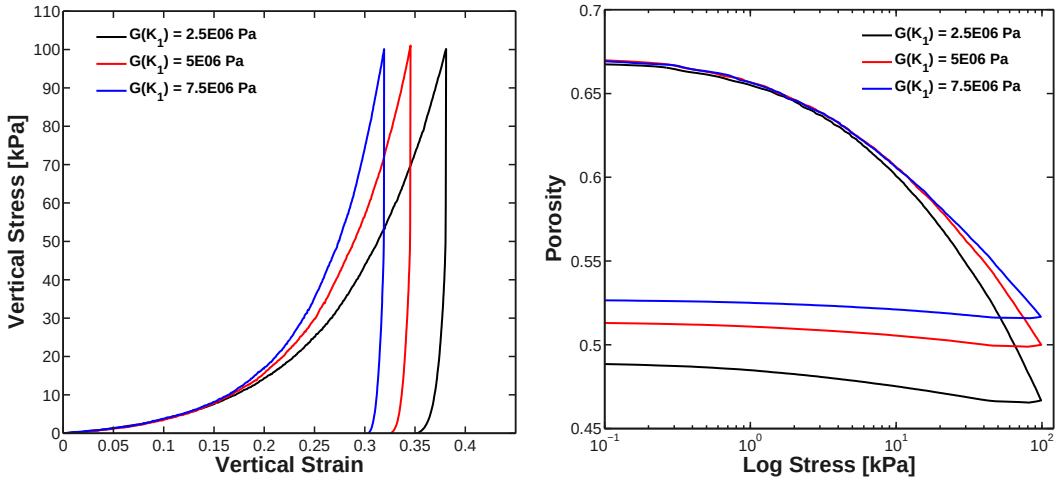

(a) Stress-strain response **(b)** Stress-porosity relationship

Figure 6.4: Confined compression results for varying loading stiffness k_1

The softer loading stiffness leads to the development of larger overlaps in the contact, which would lead to the development of larger adhesive forces at higher consolidation stress, if k_2 is a constant across all assemblies. Another effect of a lower spring stiffness, demonstrated in Figure 6.4b, is that for the same consolidation stress a much larger change in porosity, and hence density, will occur. This provides some indication on how

one might model materials that are highly cohesive but have a small change in porosity during consolidation.

6.2.1.3 Unconfined Compression

The initial stiffness during loading has a significant effect on the unconfined strength achieved by an assembly of particles. Although during the unconfined compression particle contacts will be reloading and therefore should be on the k_2 reloading/unloading path, the unconfined strength generated arises from the plastic overlap achieved by particles during the confined compression stage, and therefore if a larger overlap is achieved higher adhesion forces are generated and the assembly will have a higher strength. This is shown in Figure 6.5, where the assembly in which a higher contact stiffness was used achieved the lowest unconfined strength due to the fact that smaller overlaps were generated between the particles.

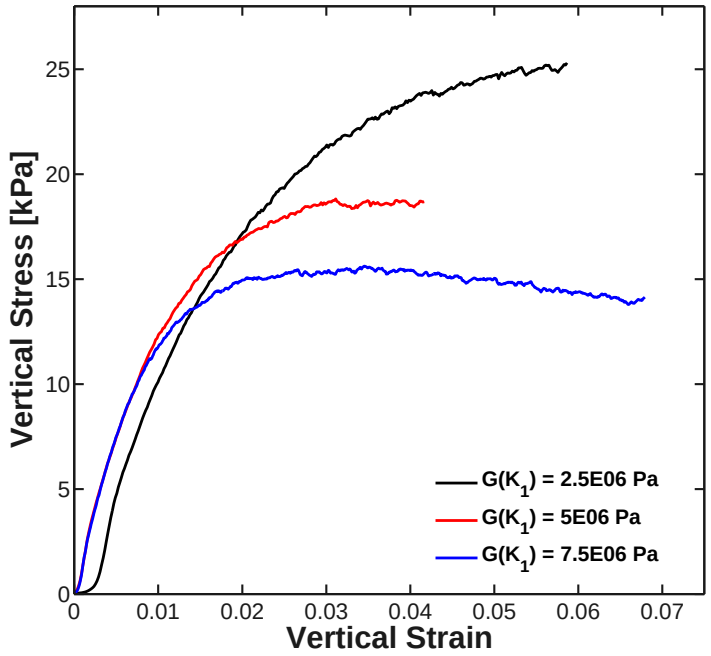

Figure 6.5: Effect of virgin loading stiffness on unconfined yield strength - For particles with an aspect ratio of 1.5

By adopting a meso-scale approach to modelling cohesive granular materials it is the stiffness of the agglomerate that needs to be considered, rather than the stiffness of the individual particle in a micro-scale approach where the DEM particles are assumed to be real particles. The stiffness of an agglomerate can change, typically becoming softer, with factors such as increasing adhesion forces leading to initially looser packings with larger bulk strains. This has the effect of reducing the observed bulk stiffness during loading.

6.2.1.4 Lateral Pressure Ratio

The effect of the varying loading stiffness on the lateral pressure ratio during confined compression is shown in Figure 6.6. As the load is applied to the assembly of particles there is an increase in the amount of load transmitted laterally into the confining cylinder walls, leading to an increase in the lateral pressure ratio. Above approximately 40 kPa the lateral pressure ratio tends towards a constant value. As the sample is unloaded the lateral pressure ratio increases significantly as the vertical stress reduces. The horizontal stresses remain "locked-in" due to the plastic deformation of the sample exacting a horizontal stress on the cylinder walls. The influence of loading stiffness on the lateral pressure appears to be minimal as all three asymptotic values are between 0.34 - 0.35. The variation in the K_0 value does not follow any particular trend in relation to the variation in loading stiffness and suggests that the difference in results may be related to the variation in particle packing that occurs because of the different stiffness during loading. This agrees with findings by Chung [2006] on quasi-static assemblies of cohesionless particles where several orders of magnitude difference in stiffness were found to only have small effects on the value of K_0.

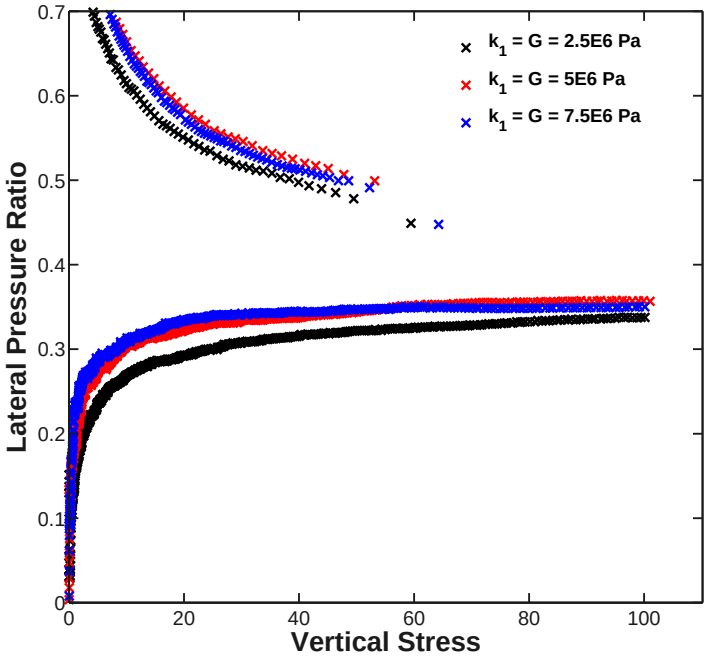

Figure 6.6: Effect of varying k_1 on lateral pressure ratio - For particles with an aspect ratio of 1.5

6.2.2 Unloading/Reloading Stiffness

The unloading/reloading stiffness ratio can have a significant effect on the behaviour of the bulk assembly created and is dependent largely on the level of contact plasticity. The contact plasticity C_p [Thakur *et al.*, 2011] in the model is given by Equation (6.1);

where δ is the maximum contact overlap and δ_p is the residual plastic overlap; and is a measure of the total plastic overlap remaining after a contact is unloaded. A low ratio for k_2:k_1 will tend toward elastic behaviour while higher ratios of contact plasticity will mean more permanent plastic deformation in the bulk assembly and this behaviour has a significant effect on the strength of an assembly.

$$C_p = \frac{\delta_p}{\delta} = 1 - \frac{k_1}{k_2} \tag{6.1}$$

This topic has been discussed in more detail elsewhere [Thakur *et al.*, 2011] and only a cursory look at the effects is included here for completeness. Unloading/reloading stiffness that provide a similar level of plasticity as that observed in the experiment (Chapter 5) have been selected for this study.

6.2.2.1 Unconfined Compression from Different Consolidated States

The effect of k_2 on the unconfined strength of an assembly is generated during the confined compression where it affects the magnitude of the plastic contact overlap and thus the adhesive strength generated at each contact. This effect is portrayed in Figure 6.7 where different values of k_2 have been used during the confined consolidation stage, where increasing k_2 leads to higher unconfined strengths.

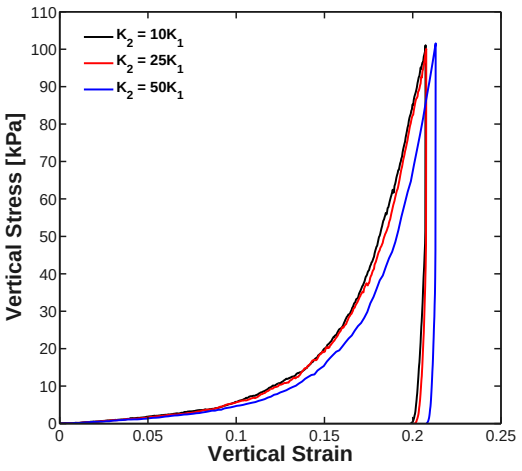

Figure 6.7: Confined stress-strain response for varying stiffness k_2 - From same initial filling

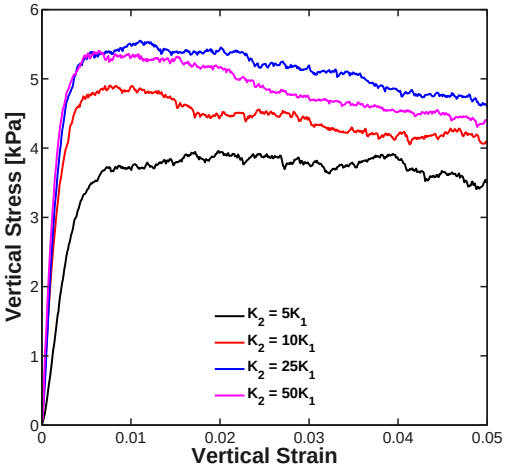

Figure 6.8: Unconfined stress-strain response for varying loading stiffness k_2 - From different consolidated packings

It should also be noted that while k_2 is the unloading/reloading stiffness at a contact level, the bulk stiffness is still dependent on porosity of the sample - the lower the consolidated porosity the stiffer the unconfined response to failure will be.

6.2.2.2 Unconfined Compression from Same Consolidated States

The effect of porosity on bulk stiffness is again highlighted in Figure 6.9 where all unconfined tests were carried out from the same consolidated assembly which had been consolidated with the highest k_2:k_1 ratio of 50. As all tests started from almost identical porosities all sample had effectively the same bulk stiffness for the unconfined test until close to the peak strength. Figure 6.10 explains why samples with a higher k_2 value achieved a lower strength. By changing the ratio to a more elastic value ($k_2 = 5k_1$) at the end of consolidation and before the unconfined compression begins, the sample is allowed to swell slightly which generates additional contacts at this stage. As the adhesion force is determined by the level of contact plasticity (k_2), reducing the stiffness at this point will not affect the historical value for the contact strength, however, the additional contacts formed from the sample swelling mean that there is a small increase in the final unconfined strength. This agrees with previous findings relating unconfined strength to the number of contacts [Pietsch *et al.*, 1969; Rumpf, 1962; Thakur *et al.*, 2013].

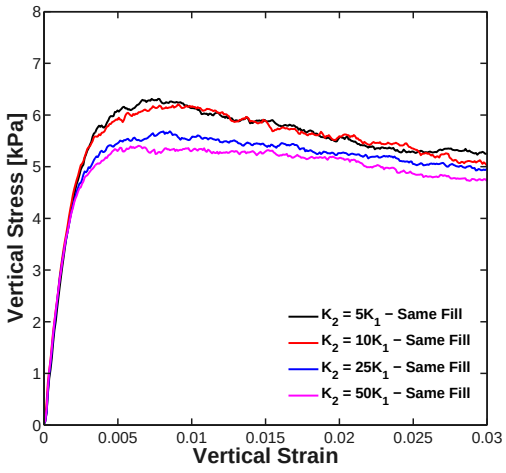

Figure 6.9: Confined stress-strain response for varying stiffness k_2 - From same consolidated packing

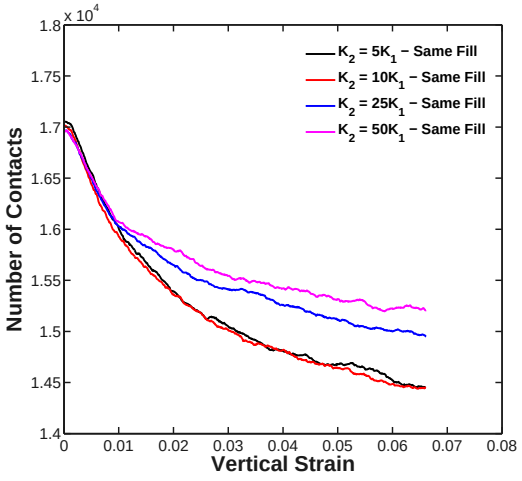

Figure 6.10: Unconfined contact evolution for varying loading stiffness k_2 - From same consolidated assembly

6.2.2.3 Lateral Pressure Ratio

The effect of the unloading/reloading stiffness k_2 on the lateral pressure ratio is shown in Figure 6.11a. In an attempt to remove the effect of different packing structures, all simulations were carried out from the same consolidated packing. In this case the common input deck used was for a contact plasticity of $C_p = 0.98$. This was selected as the previous maximum historical overlap, which would affect the adhesive forces generated, remained the same for each assembly. If the assembly with the lowest k_2 was selected the adhesive forces would change immediately with the change in k_2,

meaning the effect of adhesion rather than the unloading/reloading stiffness was being investigated. The lateral pressure ratio is seen to be relatively insensitive to the unloading/reloading stiffness provided a reasonable level of contact plasticity is used. All simulations irrespective of the contact plasticity employed tend towards the same value.

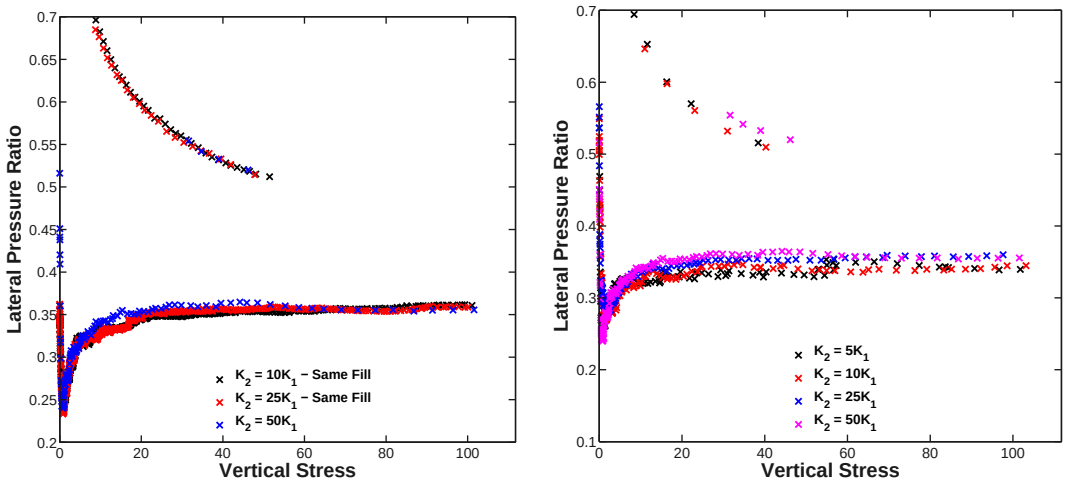

(a) For same consolidated porosity **(b)** For respective filled porosities

Figure 6.11: Effect of varying k_2 on lateral pressure ratio - Using paired particles

As noted by Chung and Ooi [2007], the DEM result can be sensitive to the initial packing structure of an assembly of particles, and Figure 6.11b highlights this, where the different initial packings were used. A greater spread in the final K_0 value was observed for different packing than for significantly different stiffness with the same packing (Figure 6.11a).

6.2.3 Tangential Stiffness

The effect of tangential stiffness on a system is investigated through the variation of the tangential stiffness multiplier in the contact model parameters. It has previously been suggested [Mindlin, 1949; Walton, 1994*b*] that the tangential stiffness is related to the material properties, and in such a case the tangential stiffness should not be a fixed constant hard-coded in to the model, but a variable that can be calibrated based on the material being used.

However, in many DEM studies in the literature, tangential stiffness did not receive much attention and indeed in several commonly used codes, the tangential stiffness is often related to the normal stiffness by a constant or a simple expression [DEM Solutions Ltd., 2010*b*, 2012; Itasca, 2003]. The effect of tangential stiffness on a particulate system is investigated here through the variation of the tangential stiffness multiplier

in the contact model parameters. A tangential stiffness multiplier of unity gives the tangential stiffness as that proposed in the non-linear Hertz-Mindlin (no-slip) model and a range of tangential stiffness between zero and unity is investigated here.

6.2.3.1 Initial Filling

The effect of the tangential stiffness on the filled porosity is presented in Table 6.3. The variation in the tangential stiffness has little effect on the initial filled height and porosity of the sample with a total difference of just over 1% porosity across all filled samples. While there appears to be a trend in the initial filled height, the magnitude of the difference is not large enough to be of significance.

Table 6.3: Effect of tangential stiffness on filled height

Tangential Stiffness Multiplier (K_{tm})	**0.05**	**0.1**	**0.25**	**0.5**	**0.75**	**1**
Initial Porosity	0.565	0.568	0.571	0.572	0.573	0.573
Consolidated Porosity	0.389	0.396	0.398	0.398	0.398	0.398
Initial Aspect Ratio	1.87	1.88	1.89	1.90	1.90	1.90
Consolidated Aspect Ratio	1.34	1.35	1.36	1.37	1.37	1.37

6.2.3.2 Confined Compression

While the tangential stiffness had little effect on the initial filled height of the sample its affect is more clearly visible during consolidation of the sample where the frictional contacts are more mobilised. The effect of reducing the tangential stiffness became increasingly more significant when the original stiffness was reduced to 25% or less (Figure 6.12), giving rise to a significant increase in the compression strain. The tangential stiffness has little effect on the final consolidated strain, but does increase the elasticity during unloading of the samples.

The reduction in the shear strength of the assembly, from the reduction in the contact shear stiffness, allows particles more freedom to rearrange during loading, leading to the greater strain. The reduction in shear strength also prevents the particles from maintaining the dense packing and further re-arrangement can occur during unloading. In the case of the spherical packings, all final porosities tend towards that of a random close packing for poured spheres [Dullien, 1991].

Figure 6.12 shows the different response between spherical and paired particles for varying tangential stiffness. For the spherical particles, reducing the tangential stiffness below 50% leads to a gradually increasing strain with reducing stiffness, whereas the trend for paired particles shows only a small variation initially to 10% of the stiffness,

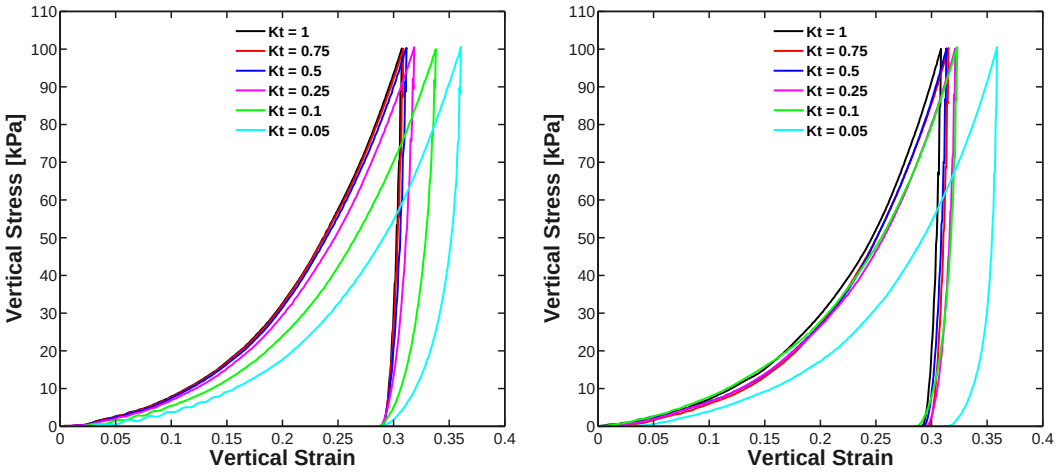

(a) Spherical particles **(b)** Paired particles

Figure 6.12: Confined stress-strain with varying tangential stiffness - Comparison for different particle aspect ratios

before significantly reducing strain after that. The change in porosity for each is shown in Figure 6.13. For both paired and spherical packings similar initial porosities were achieved during filling but there is a slight variation in the total change in porosities with the paired packings reaching lower porosities at the lowest tangential stiffness. However this small variation is more likely to be relating to the initial packing structure created between different particle shapes.

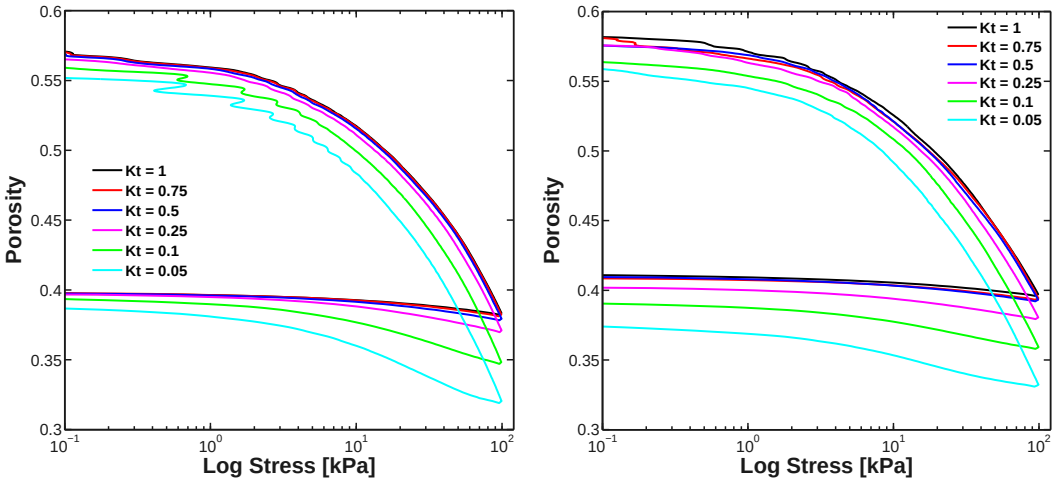

(a) Spherical particles **(b)** Paired particles

Figure 6.13: Confined stress-porosity with varying tangential stiffness - Comparison for different particle aspect ratios

The above results suggest that the tangential stiffness would play an important role in the loading regimes when frictional shear is being mobilised more. For the meso-scale approach adopted in this thesis, the tangential stiffness should be chosen to reflect

the real internal friction mobilisation of the material. In addition, using commonly adopted tangential stiffness as proposed in the literature, which are largely derived from purely elastic contact between perfect spheres, would most likely be far too stiff for the complex, multi-asperity contacts between non-spherical particles. This effect on the bulk behaviour is further studied next.

6.2.3.3 Unconfined Compression

The tangential stiffness plays a significant role in the response of the assembly during unconfined compression where the key mode of failure is through shear in the sample. While the unloading/reloading stiffness k_2 was initially expected to be the governing parameter as an assembly was reloaded to failure following consolidation, the tangential stiffness has been found to have a much larger role in the unconfined stress-strain behaviour of an assembly. The unconfined stress-strain responses for assemblies of paired and spherical parties are presented in Figure 6.14.

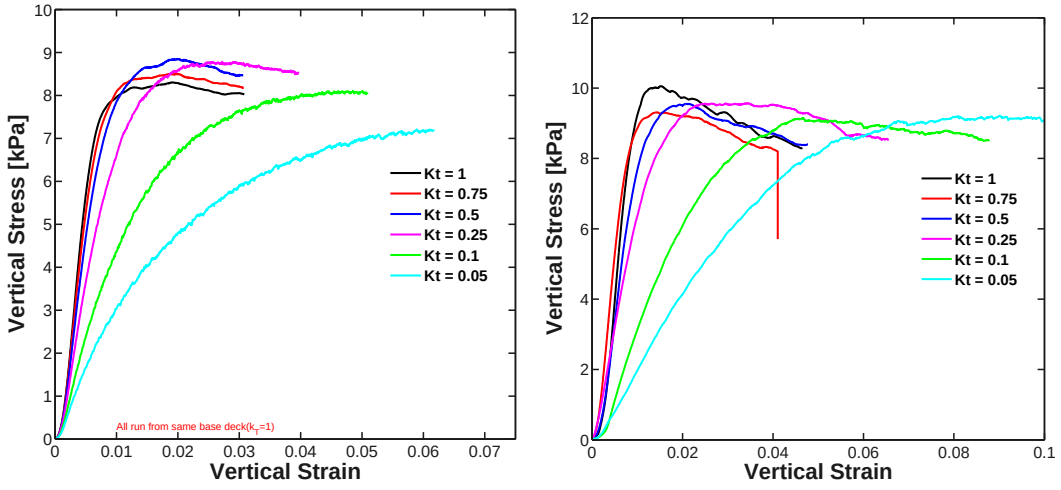

(a) Spherical particles **(b)** Paired particles

Figure 6.14: Unconfined stress-strain with varying tangential stiffness - Comparison for different particle aspect ratios

Both assemblies demonstrate the effect of varying tangential stiffness where a high tangential stiffness leads to a very stiff unconfined loading response, with peak strains being achieved at values of approximately 1%. As the tangential stiffness is reduced the unconfined response becomes increasingly softer with the location of the peak strain also increasing. And while the reducing tangential stiffness increases the peak strain to be more representative of the response seen experimentally, with a softer loading response and peak strain in the 3-6% region, the over-consolidated behaviour clearly evident at higher tangential stiffness is lost.

6.2.3.4 Lateral Pressure Ratio

The lateral pressure ratio for various levels of tangential stiffness is presented in Figure 6.15. The results show that the tangential stiffness has a significant influence on the confined compression behaviour of an assembly of particles. However, the effect becomes less pronounced as the tangential stiffness multipliers close on unity and further increases are not expected to change significantly. As tangential stiffness decreases, the mobilised shear of the assembly is significantly reduced, which has a similar effect on the obtained K_0 value to a reduced effective friction angle for the assembly. As the shear strength of an assembly is reduced, the ability of contacts to restrict particle rearrangement is reduced and vertically applied forces are more likely to result in particle re-arrangement with greater forces being transferred horizontally. Where an assembly has a high shear strength it is able to transfer the vertical forces without significant particle movement, which leads to lower horizontal force transfer and hence a reduction in the lateral pressure ratio is observed.

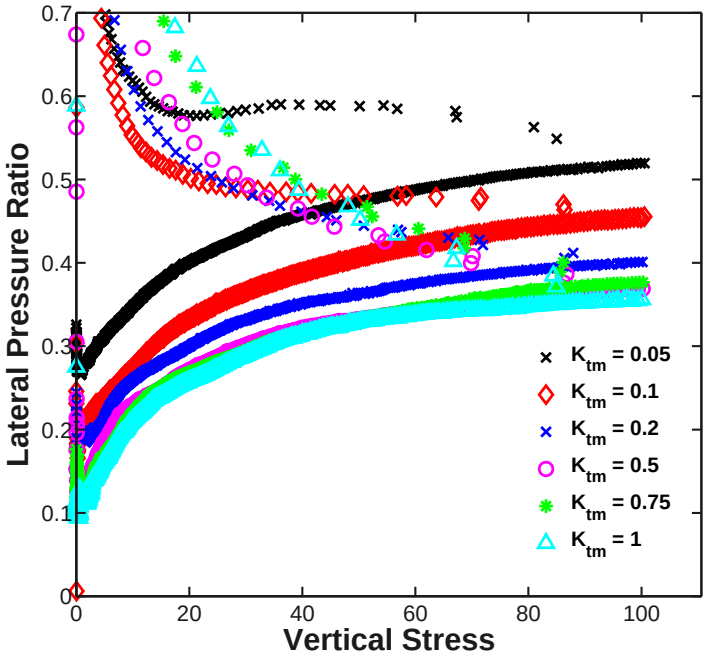

Figure 6.15: Effect of varying $\mathbf{k_{tm}}$ on lateral pressure ratio - Using paired particles

6.3 Adhesion Parameters

The unconfined strength of a sample is dependent on the surface energy of the contact; the higher the surface energy the higher the adhesion force generated in each contact. The rate at which the particle separates is controlled by the adhesion exponent, x, in the contact model. At an exponent value of $x = 1$ the unloading branch is linear until separation, whereas an exponent value of $x = 20$ represents a non-linear separation with

a sharp drop off in force during separation, which should lead to a more brittle failure mode in unconfined compression tests without significantly affecting the ultimate strength.

6.3.1 Constant Pull-off Force

The constant pull-off force has not been utilised in this study but the effect of the constant pull-off force has been studied elsewhere by Thakur *et al.* [2011, 2013].

6.3.2 Adhesion Energy

The effect of adhesion energy on both the confined compression behaviour and the unconfined strength of an assembly have been studied through a series of simulations. Samples were filled with different levels of adhesion energy, $\Delta\gamma$, and the effect of adhesion on the filled porosity and packing density was evaluated. The effect on the consolidation and unconfined response has also been evaluated.

6.3.2.1 Initial Filling

The initial filled height and porosity for an assembly is significantly affected by the increasing adhesion energy during the filling process for the ranges of selected adhesion energies (Table 6.4). As the adhesion energy is increased, the adhesive forces between particles will become larger allowing particles to more easily stick together following contact during filling. The adhesive forces generated are then larger than the particle weight and inhibit the compaction of the particle assembly under its own weight, forming a much looser initial packing structure. This increase in porosity with adhesion energy is similar to the bulking effect seen experimentally for iron ore fines when moisture is added (Section 5.6) and also correlates with the results previously reported [Dong *et al.*, 2006; Gröger *et al.*, 2003; Xu *et al.*, 2004; Yang *et al.*, 2007, 2000, 2003*a*,*b*, 2008, 2006]. The effect of surface energy on the filled porosity will eventually saturate at a certain ratio of adhesion force to particle mass, at which point any further increases in adhesion will not lead to a noticeable increase in the porosity of the sample.

Table 6.4: Effect of adhesion energy on the filled height of the sample

Adhesion Energy (J/m^2)	**5**	**15**	**25**
Initial Porosity	0.532	0.554	0.564
Consolidated Porosity	0.389	0.400	0.408
Initial Aspect Ratio	1.76	1.85	1.89
Consolidated Aspect Ratio	1.36	1.39	1.40

While the change in porosity from an adhesion energy of 5 J/m^2 to 25 J/m^2 is quite small at only 3%, the effect would be much more noticeable with the inclusion of a random close packing normally found for cohesionless assemblies, which would typically have a porosity of approximately 0.4.

6.3.2.2 Confined Compression

The stress-strain response and stress-porosity relationship for different values of adhesion energy are presented in Figure 6.16. Each sample started from the same input deck at the same initial aspect ratio and porosity (Figure 6.16b). From this it is clear to see that the assembly with the higher adhesion energy demonstrates a stiffer bulk response achieving a lower final strain at 100 kPa. The additional adhesive force acts to provide additional resistance to collapse and rearrangement at low stresses and provides a stiffer sample during confined compression. The lower force in the stress strain curve and the different porosity at an adhesion energy of 5 J/m^2 suggests that at lower levels of adhesion, particle rearrangement is less restricted and the assembly can be compressed to a denser state more easily.

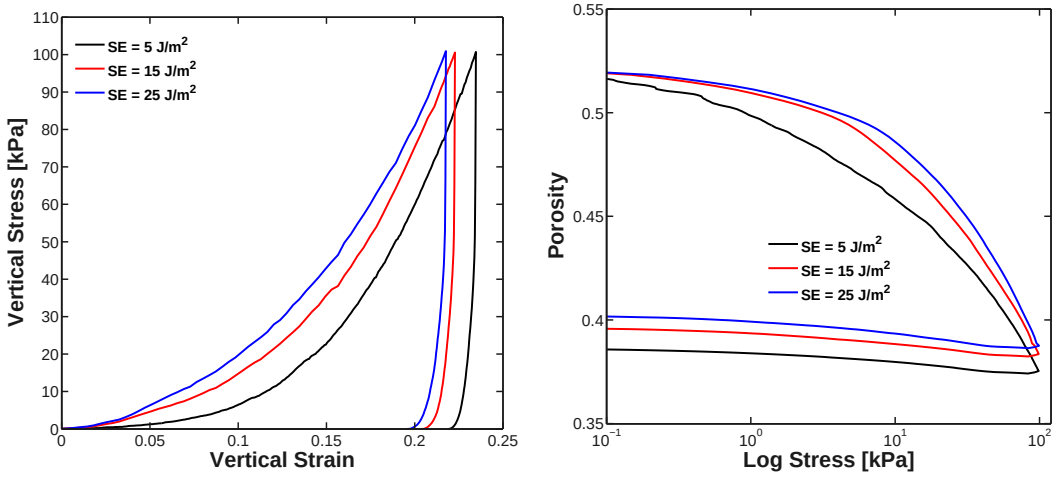

(a) Stress-strain response **(b)** Stress-porosity relationship

Figure 6.16: Confined compression results for varying levels of adhesion - Using paired particles

The additional adhesive force acts to provide additional resistance to collapse and rearrangement at low stresses and provides a stiffer sample during confined compression. The lower force in the stress strain curve and the different porosity at an adhesion energy of 5 J/m^2 suggests that at lower levels of adhesion, particle rearrangement is less restricted and the assembly can be compressed to a denser state more easily.

6.3.2.3 Unconfined Compression

The effect of increasing levels of adhesion is most evident from the unconfined strength computed for an assembly. Assemblies with high levels of adhesion energy have a significantly higher unconfined yield strength. In Figure 6.17a the unconfined strength is measured for the assemblies for the consolidation of the assembly with the respective adhesion energy. This leads to the assemblies having different consolidated porosities as shown in Figure 6.16b. The densest packings have more contacts and thus a higher coordination number than the more adhesive, looser packing. Nevertheless this has not significantly affected the trend for the unconfined yield strength where the largest adhesion energy leads to the highest strength. In Figure 6.17b the unconfined strength is shown for three identical assemblies with a final consolidated porosity of 0.387, but with varying levels of adhesion for the unconfined compression to failure of the assembly.

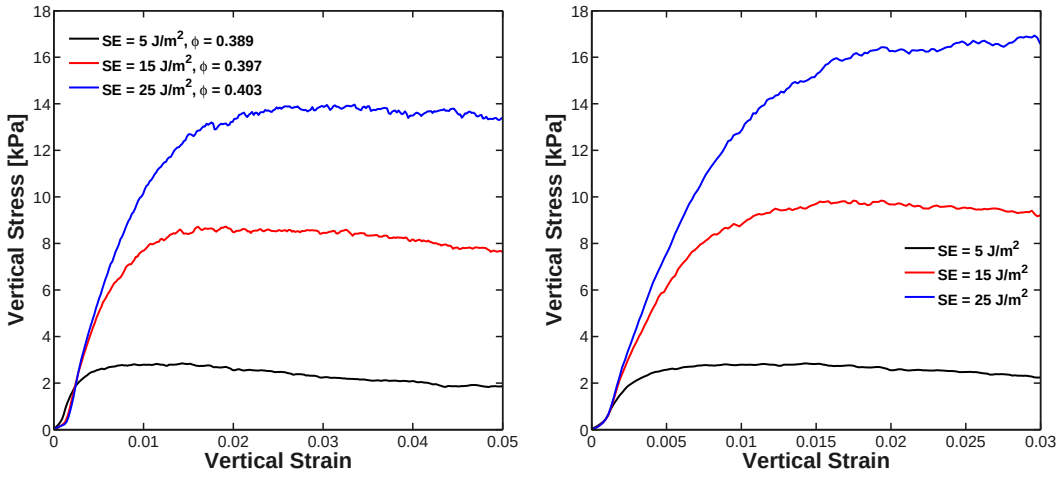

(a) For same filled sample **(b)** for same consolidated sample

Figure 6.17: Unconfined compression results for varying levels of adhesion - Using paired particles

The results show the same trends as in Figure 6.17a where increasing adhesion energy leads to a higher unconfined strength. However, by removing the effect of the additional resistance during consolidation of the assembly, a significantly higher unconfined strength is computed. This highlights that while increasing adhesion energy leads to increasing unconfined strength, there is also a compromise to be made; as large adhesion energies lead to higher consolidated porosities, which in turn lead to a saturation of the unconfined strength of an assembly.

6.3.2.4 Lateral Pressure Ratio

The effect of varying adhesion energy on the lateral pressure ratio is shown in Figure 6.18 and the variation in number of contacts is shown in Figure 6.19. All assemblies start from the same initial configuration and are consolidated to 100 kPa. Although the increasing adhesion energy leads to a stiffer bulk response and consolidates to a lower porosity, there is little or no clear effect on the lateral pressure ratio at larger stress levels as all three assemblies provide approximately the same final value.

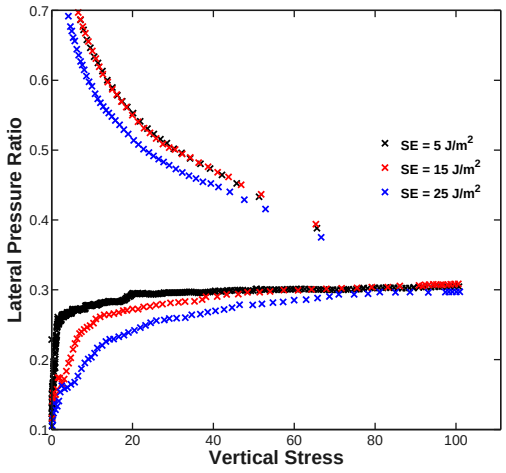

Figure 6.18: Effect of adhesion energy on lateral pressure ratio - Using paired particles

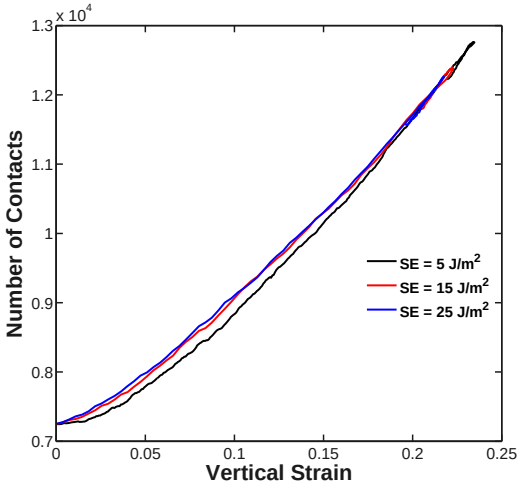

Figure 6.19: Variation in contacts during consolidation - From same initial assembly

6.3.3 Adhesion Branch Slope

The adhesion branch exponent controls the rate of drop off in adhesive strength of a contact following the peak tensile force (Figure 4.4). An exponent value of unity represents a linear unloading path and a more ductile contact. As the exponent is increased, the rate at which the tensile strength will reduce increases significantly, such that at a value of $x = 25$ the tensile strength will have dropped close to zero almost immediately after the peak contact strength is reached. A high exponent value with a sharp drop in tensile force should lead to more brittle behaviour in the assembly as a whole.

6.3.3.1 Initial Filling

The effect of the adhesion branch exponent during the filling process is small but still visible. A slightly decreasing sample height and porosity is found with an increasing branch exponent during filling (Table 6.5). The linear unloading curve which maintains a higher strength contact for longer allows for a looser packing to develop under gravity filling. During the filling process, as the exponent increases the filled packing becomes

denser, as a sharp drop-off in the contact force means particles will be more likely to separate after collisions during the filling process.

Table 6.5: Effect of adhesion branch slope on the filled height of the sample

Shape Exponent, *x*	**1**	**5**	**10**	**20**
Initial Porosity	0.488	0.484	0.483	0.478
Consolidated Porosity	0.453	0.452	0.450	0.450
Initial Aspect Ratio	1.59	1.58	1.57	1.56
Consolidated Aspect Ratio	1.53	1.52	1.52	1.52

6.3.3.2 Confined Compression

The effects of the adhesion branch exponent can be expected to be small during confined consolidation of the sample. During confined compression of the sample more than approximately 98% of all the contacts lie along either the k_1 or k_2 loading path which means that the adhesion branch can have little or no impact when particles are under compression. The results are shown in terms of the stress-strain relationship in Figure 6.20a and porosity in Figure 6.20b.

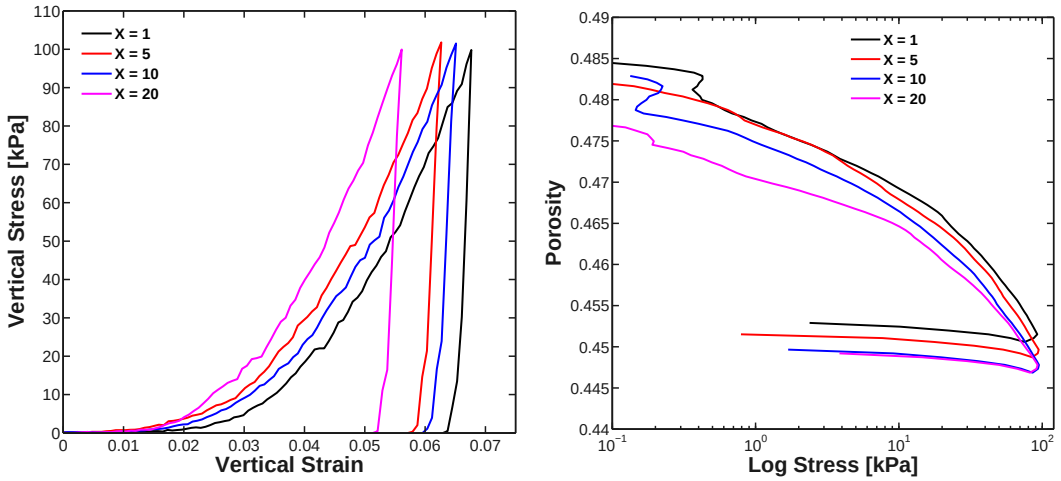

(a) Stress-strain response **(b)** Stress-porosity relationship

Figure 6.20: Confined compression results for varying adhesion branch slope - Using spherical particles

The variation in the stress strain curves and peak consolidated strain shown in the above figures have arisen from the different initial porosities achieved from the filling process. While the looser packing formed from the linear adhesion branch would initially have fractionally more contacts and provide greater resistance to the compaction,

the difference in the number of contacts is not significant enough to affect the confined compression behaviour. This is supported by the total change in porosity between initial and consolidated porosity, which is approximately equal for all assemblies.

6.3.3.3 Unconfined Compression

The effect of the adhesion branch exponent is more visible during the unconfined compression to failure. In Figure 6.21a the unconfined strength is shown for the assemblies which were consolidated with their respective exponent values and had different consolidated porosities seen in Figure 6.20. The results in the peak strength achieved reflect the final consolidated porosity, with the densest sample achieving the highest unconfined strength. However, despite this, the effect of the adhesion branch exponent is still visible. With an exponent value of $x = 1$, the computed stress-strain response was a very smooth curve as particles gradually separate in the failure zones. As the exponent increased, the response became more fluctuating as particles were forced to separate much quicker.

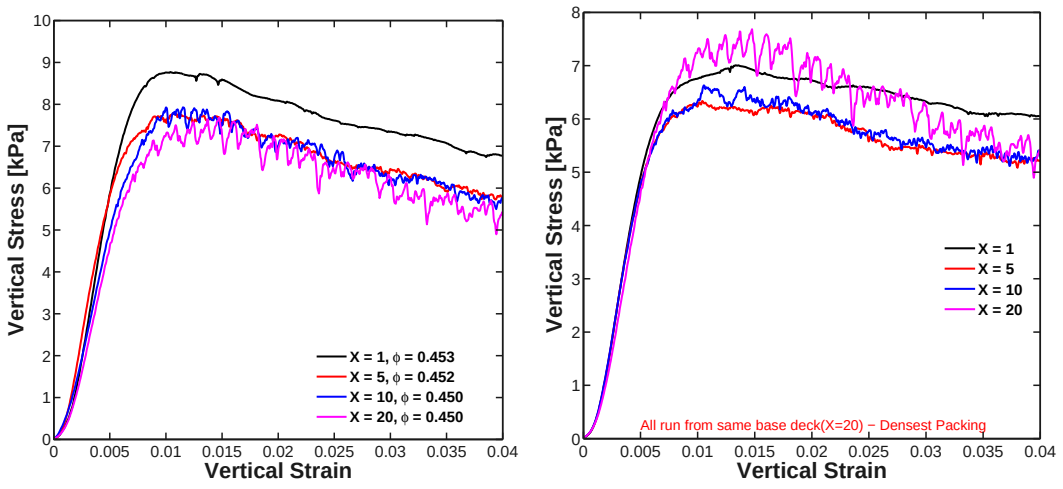

(a) different consolidated porosities **(b)** same consolidated porosities

Figure 6.21: Unconfined stress-strain relationship for varying adhesion branch exponents - Using spherical particles

In Figure 6.21b the unconfined compression was carried out with all assemblies starting from the same consolidated porosity. In this case there is a variation in the unconfined strength achieved by the various assemblies without any consistent trend, as a result of the variability introduced from more contacts separating. A further observation is that at higher exponent values the over-consolidation behaviour becomes more evident with a sharper drop-off in strength following the peak values. Despite the increased over-consolidation behaviour and the increasingly erratic fluctuations in the measured stress, this does not lead to a full collapse of the assembly as there are many other contacts

which will carry the force, offering plenty of redundancies in the system. There is also the possibility that particles can separate and then form further new contacts that are weaker. This is the likely reason that the unconfined strength will decrease but in which the assembly fails to collapse - new contacts are continually formed and "consolidated" with an ever decreasing pressure, meaning that the unconfined strength generated will continually be decreasing.

6.4 Sliding & Rolling Friction

In a cohesionless system friction is one of the crucial parameters for transferring forces between particles and is particularly important in the case of shearing force between particles. Increasing friction leads to stronger assemblies of particles with greater resistance to shearing. It is also a significant energy dissipation mechanism in the system.

Sliding friction is applied through the use of a frictional slider in the tangential direction of the contact model where the tangential forces represent the surface friction between particles in contact (see Figures 3.5 and 3.6 for typical arrangement). The tangential force is limited by the Coulomb-type friction law in which the tangential force is set equal to the friction limit if the tangential force exceeds the maximum shear force allowed by the frictional slider. Full details of the tangential model implemented are given in Sections 4.6.2 and 4.7.2.

A rolling friction model that incorporates torques in the rotational direction to account for rolling resistance is included in the contact model. The rolling friction model implemented is of the type termed *Model A* by Ai *et al.* [2011]. Details of the implemented model have been presented in Section 4.4.4.

6.4.1 Sliding Friction

The effect of sliding friction on a cohesive assembly of particles is investigated at three distinct levels of friction and its effect on the filling, consolidation and unconfined strength is considered. In this study the coefficients of static and dynamic sliding friction are assumed to be the same. A comparison between different particle shapes is also made at a sliding friction coefficient of $\mu_s = 0.5$.

6.4.1.1 Initial Filling

The effect of the sliding friction coefficient on the filled height of assemblies of both spherical particles and paired particles with an aspect ratio of 1.5 is shown in Table 6.6. As the friction coefficient increases from 0.2 to 0.5 for spherical particles the initial porosity and fill height increase, however above a friction coefficient of 0.5 no further

effect is noticed and, in fact, a denser packing than the $\mu_s = 0.5$ case was found. For paired particles there was a consistent trend of increasing fill height and porosity with increasing sliding friction up to 0.8. This correlates well with previous findings for sliding friction for spherical particles [Härtl and Ooi, 2011], which tend to saturate at values greater than $\mu_s \approx 0.5$.

Table 6.6: Effect of sliding friction on the filled height of the sample

	Spherical			**Paired**		
Sliding Friction Coefficient, μ_s	0.2	0.5	0.8	0.2	0.5	0.8
Initial Porosity	0.495	0.505	0.498	0.504	0.518	0.523
Consolidated Porosity	0.310	0.352	0.370	0.327	0.377	0.401
Initial Aspect Ratio	1.61	1.64	1.62	1.66	1.71	1.73
Consolidated Aspect Ratio	1.19	1.28	1.3	1.24	1.34	1.39

Table 6.7 presents a comparison in the filled height of an assembly of particles of different aspect ratios ranging from 1-2 at a constant coefficient of sliding friction of 0.5. An aspect ratio of 2 when formed of two primary particles was found to provide the highest filled porosity. When an aspect ratio of 2 was formed from 3 primary particles, a much denser packing structure was observed. Due to the additional particle there is no longer a large area of void between the two primary constituent spheres giving the 3 particle multi-sphere a greater volume and mass than a 2 particle multi-sphere. The additional mass also makes the particle heavier than the adhesive forces can carry and due to the larger volume there will also be less free space between the packed particles. The sample also provided the greatest resistance to compaction, due to the larger coordination number which provides extra frictional contacts per particle and the reduced free space which restricts particle rearrangement, leading to a stiffer bulk response.

Table 6.7: Effect of particle shape with a friction coefficient of $\mu_s = 0.5$

Particle Aspect Ratio	**1**	**1.5**	**1.75**	**2 (2P)**	**2 (3P)**
Initial Porosity	0.505	0.518	0.591	0.631	0.500
Consolidated Porosity	0.352	0.377	0.401	0.448	0.431
Initial Aspect Ratio	1.64	1.71	1.92	1.85	1.66
Consolidated Aspect Ratio	1.28	1.34	1.42	1.21	1.36

6.4.1.2 Confined Compression

The stress-strain relationship for both spherical and paired particles at various friction coefficients are presented in Figure 6.22. Both show the same trend in increased bulk stiffness and reduced total strain with increasing contact friction. This arises

through the additional restriction on particle movements provided by the increasing shear strength from contact friction.

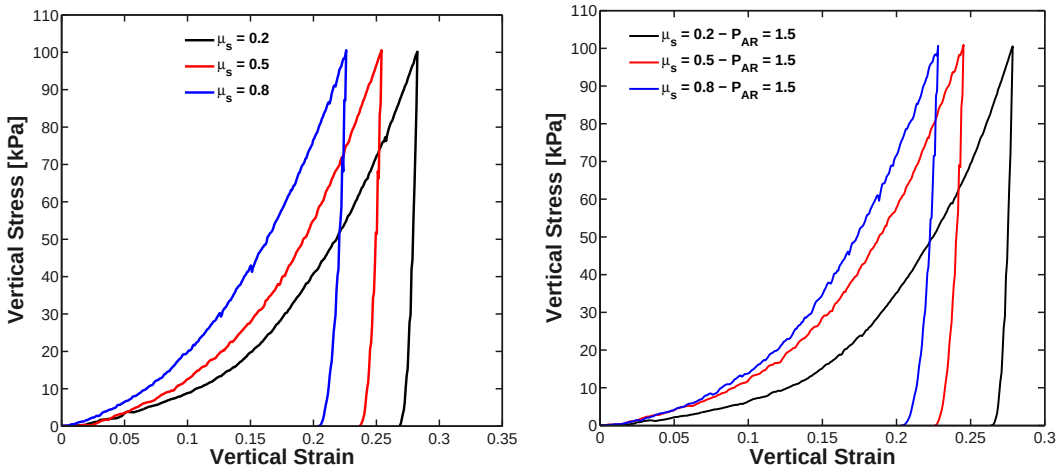

(a) Spherical particles **(b)** Paired particles, AR = 1.5

Figure 6.22: Confined stress-strain response for varying levels of sliding friction - For different particle aspect ratios

To account for any variations that may have occurred due to different initial porosities, a comparison was made with spherical particles from the same filled assembly of particles with varying sliding friction coefficients. The results are shown in Figure 6.23. The trends reported for the paired and spherical particles from different fillings remain though, with the higher friction coefficient leading to a stiffer bulk response and lower strain, while a significantly higher unloaded porosity is observed for the higher friction coefficient.

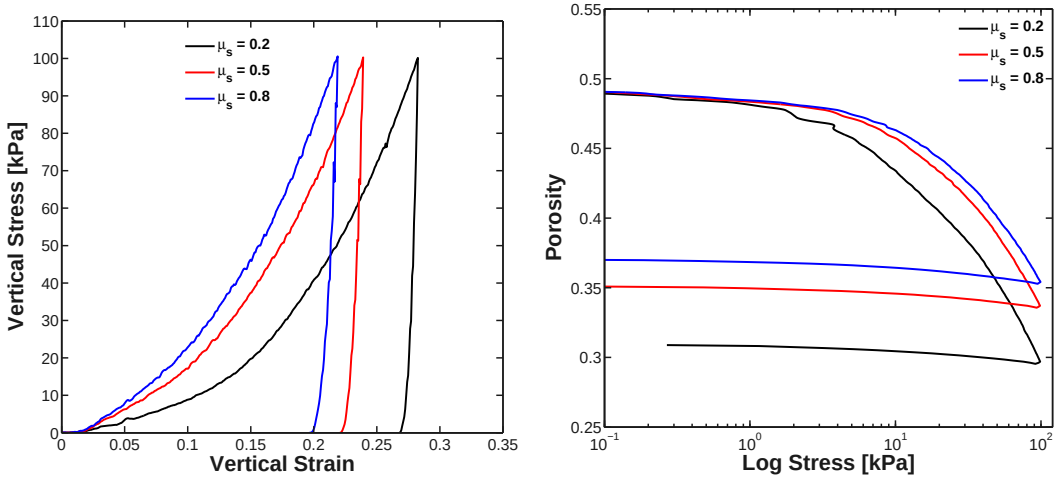

(a) Stress-strain response **(b)** Stress-porosity relationship

Figure 6.23: Confined compression results for varying levels of sliding friction - Using spherical particles with same initial packing

While the higher coefficient of friction will increase the shearing resistance of the assembly, by reducing the amount of consolidation in the assembly there will be smaller overlaps generated as well as a smaller number of particle contacts, both of which will affect the strength of a sample generated from adhesion forces. This may lead to a situation where the increasing sliding friction does not increase the unconfined yield strength of a cohesive assembly. This effect has also been noted by Härtl and Ooi [2011] where the effect of inter-particle friction on the bulk friction of a cohesionless assembly was investigated using DEM simulations of a shear test. They observed that after a certain level of particle-particle friction, further increase in sliding friction had no effect on the measured bulk friction of the sheared assembly.

6.4.1.3 Unconfined Compression

The unconfined yield strengths measured for the assemblies of spherical and paired particles, which were filled and consolidated with the respective friction values, are presented in Figure 6.24. Both show an increase in strength from a friction coefficient of 0.2 to 0.5, whereas there is little difference in the strength measured for an increase above 0.5. This is partly due to the effect of the friction during consolidation where the higher friction coefficient leads to a looser packing with a higher porosity and lower number of contacts in the assembly. As the strength of a cohesive assembly of particles is dependent on the coordination number (number of contacts) [Rumpf, 1962; Thakur *et al.*, 2013], there is a reduction in the cohesive strength generated.

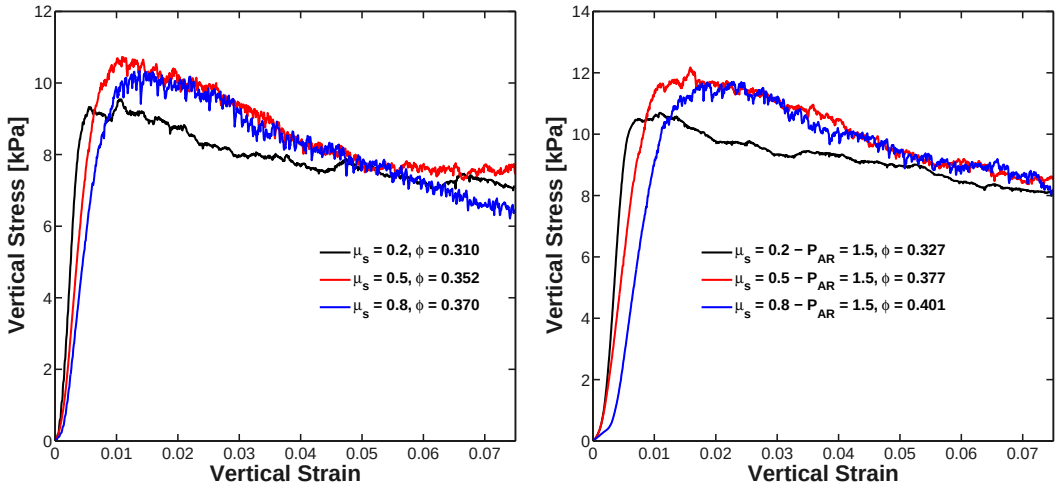

(a) Spherical particles **(b)** Paired particles, AR = 1.5

Figure 6.24: Unconfined stress-strain response for varying levels of sliding friction - For different particle aspect ratios

To properly assess the effect of friction only, the unconfined compression tests were all carried out for the same assembly of spherical particles where the levels of friction were

varied at two different stages in the process - after the assembly had been filled initially (Figure 6.25a) and on the consolidated assembly before confined compression begins (Figure 6.25b). The assembly of spherical particles shows a modest increase in unconfined strength when the sliding friction coefficient is increased before consolidation, increasing approximately 20% when μ increased from 0.2 to 0.8. While increasing the friction coefficient will help generate a higher unconfined yield strength, the additional friction during the consolidation is restricting the development of a dense packing with a higher number of contacts, which leads to a higher unconfined strength. A much more significant increase in strength is seen for the paired particles when the friction is increased from 0.2 to 0.8 after consolidation, where the unconfined strength of the assembly is approximately doubled.

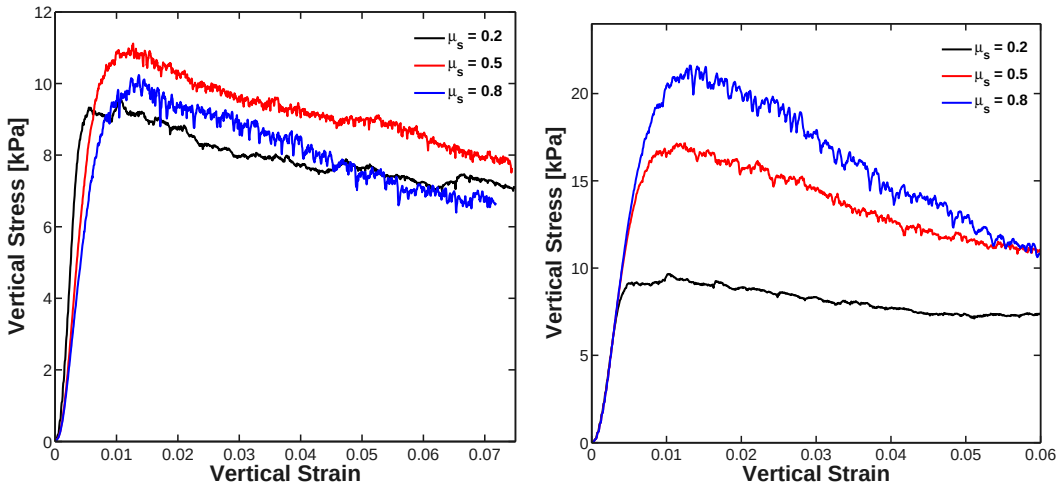

(a) From same initial packing **(b)** From same consolidated packing

Figure 6.25: Unconfined stress-strain response for varying levels of sliding friction and packing - For spherical particles

6.4.1.4 Particle Aspect Ratio

A comparison on the effect of particle shape on the confined and unconfined behaviour of an assembly of particles has also been made. In Figure 6.26 the stress strain behaviour is presented for various particle aspect ratios. The amount of consolidation achieved in an assembly decreases with increasing particle aspect ratio. The additional interlocking provided by the particle shape increased the resistance to the rearrangement of particles and reduced the amount of consolidation.

The effect of the particle shape on the unconfined strength is presented in Figure 6.27. Again the additional interlocking, and additional contacts resulting from increasing particle aspect ratio lead to higher unconfined strengths. The spherical particles have

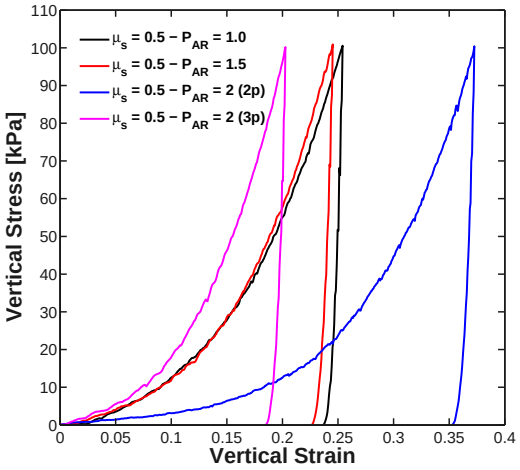

Figure 6.26: Confined stress-strain with varying sliding friction - For various particle shapes

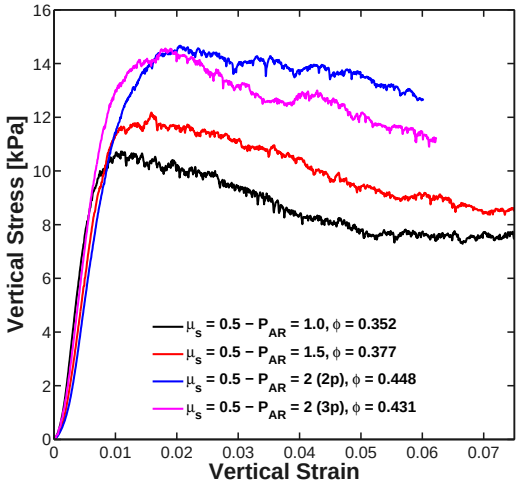

Figure 6.27: Unconfined stress-strain with varying sliding friction - For various particle shapes

the lowest porosity which leads to the largest number of contacts generated per assembly (Figure 6.28). However, despite the lower number of contacts for the larger aspect particles, due to their larger size (fewer particles fit in the same assembly) a larger coordination number is found Figure 6.29. This leads to an enhanced shear resistance which jointly contributes with the additional interlocking and rolling resistance to produce the higher unconfined strength observed in Figure 6.27.

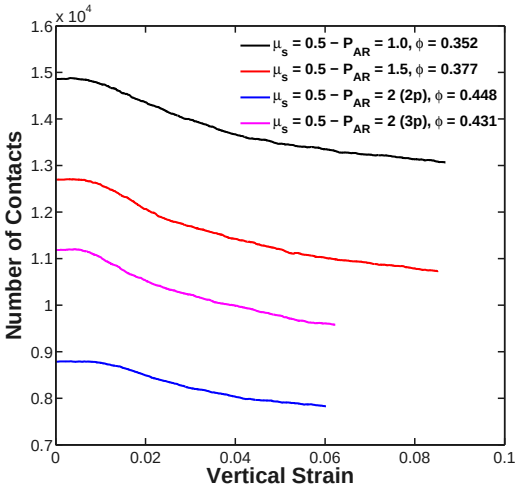

Figure 6.28: Evolution of number of contacts - During unconfined compression

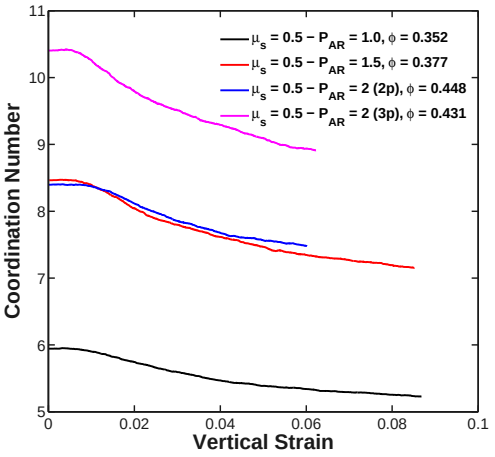

Figure 6.29: Evolution of coordination number - During unconfined compression

6.4.1.5 Lateral Pressure Ratio

The effect of varying coefficient of sliding friction on the lateral pressure ratio is presented for both spherical and paired particles in Figure 6.30. The results show that with

an increasing sliding friction there is a significant decrease in the DEM predicted lateral pressure ratio for both spherical and non-spherical particles. The increased friction coefficient enhances the shearing resistance of the assembly of particles and by doing so it will restrict the movement and re-arrangement of the particles, forcing more of the load to be carried vertically rather than horizontally. In the case of the non-spherical particles where the shapes create additional interlocking, the lateral pressure ratio reduces further still. These results are consistent with theory; increasing the bulk friction, either through increasing contact friction or through increased interlocking between particles, leads to a lower K_0 value.

To investigate the effect of packing structure further, Figure 6.30a also includes simulation results for values of static friction of 0.5 and 0.8 that were run from the same assembly of particles as that with a friction coefficient of 0.2. These results show that although the lateral pressure ratio varies at low stresses for these values, as the stress increases, the different assemblies tend towards the same value, reinforcing that the response is related to the changing sliding friction coefficient rather than the packing structure.

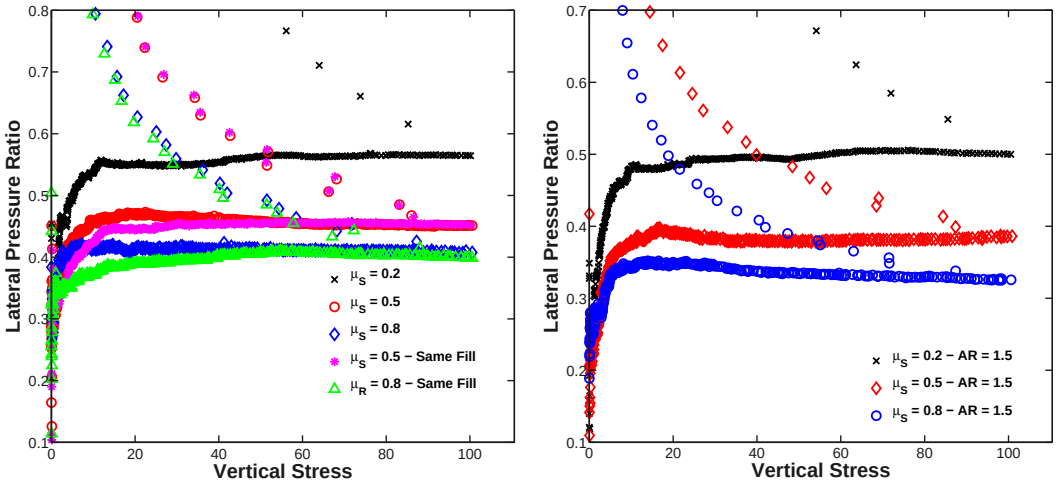

(a) For spherical particles **(b)** For paired particles

Figure 6.30: Lateral pressure ratio with varying sliding friction - For various particle shapes

The effect of particle shape is further investigated in Figure 6.31 where aspect ratios of 1.75 and 2 are compared. For multi-sphere particles consisting of two primary particles, there is little variation in the K_0 values, with an aspect ratio of 1.75 proving the lowest K_0 value. However, the assembly consisting of oblong particles with an aspect ratio of 2 and made from 3 primary spheres provides a significantly lower K_0 value. It is likely that the additional interlocking created by the oblong shape and the tendency of a three

particle multi-sphere to lie horizontal has led to the reduced K_0 value for this shape. The results shown here are in agreement with those found for a cohesionless system by Wiącek *et al.* [2012*a*].

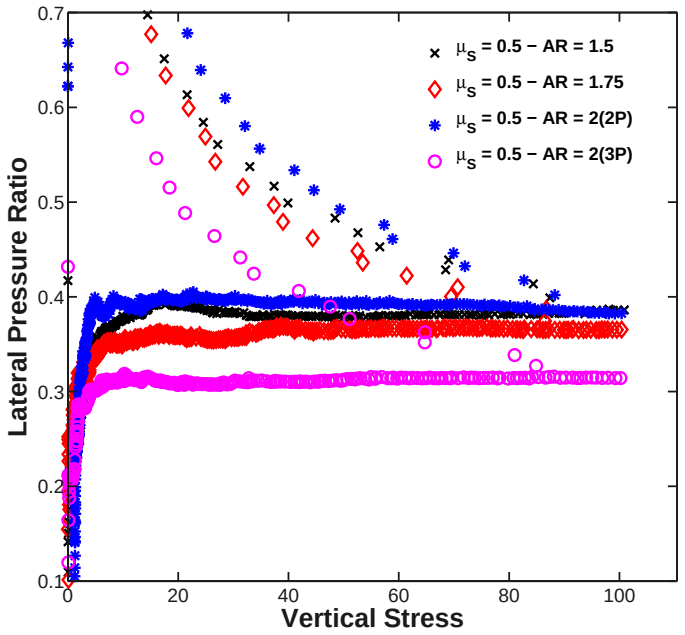

Figure 6.31: Lateral pressure ratio with varying sliding friction - For paired particles

6.4.2 Rolling Friction

As the main function of rolling friction is to attempt to account for shape with spherical particles, it is expected that particles with a shape term will not be affected significantly by additional rolling friction. The effect of rolling friction on both spherical and paired particles is presented in this section. A set of parameters is chosen and only the rolling friction value is varied during the simulations.

6.4.2.1 Initial Filling

The effect of increasing rolling friction on spherical particles is presented in Table 6.8. It can be seen that as the rolling friction is increased and the rotation of the particles is restrained a much looser initial packing is formed at high rolling friction values.

Table 6.8: Effect of rolling friction on initial filling for spherical particles

Friction Coefficient, μ_r	**0.001**	**0.005**	**0.01**	**0.025**	**0.05**	**0.1**	**0.3**	**0.5**
Initial Porosity	0.499	0.508	0.510	0.513	0.512	0.519	0.548	0.565
Consolidated Porosity	0.244	0.247	0.253	0.259	0.267	0.281	0.288	0.293
Initial Filled Aspect Ratio	1.62	1.65	1.66	1.67	1.67	1.69	1.8	1.87
Consolidated Porosity	1.1	1.11	1.12	1.11	1.12	1.14	1.17	1.16

While for the spherical particles the filled porosity increases as rolling friction increases, the same trend is less clear for the paired particles in Table 6.9. In the case of the paired particles, the additional rolling friction has little effect to the initial packing under values of 0.1, while a rolling friction value of 0.5 gives a significantly looser packing.

Table 6.9: Effect of rolling friction on initial filling for paired particles

Friction Coefficient, μ_r	**0**	**0.025**	**0.1**	**0.5**
Initial Porosity	0.536	0.522	0.545	0.574
Consolidated Porosity	0.289	0.296	0.313	0.306
Initial Filled Aspect Ratio	1.78	1.72	1.81	1.93
Consolidated Porosity	1.18	1.19	1.21	1.2

6.4.2.2 Confined Compression

Figure 6.32 presents the results of the confined compression for both paired and spherical particles while the porosity relationship is shown in Figure 6.33. The results for the unloaded strain show that below a rolling friction value of 0.1, despite the initial bulking effect that can be seen in the initial filled heights, all tests tend towards a value of 0.35, while at higher rolling friction values there is significantly higher strain relating to the increasingly loose initial packing that is formed.

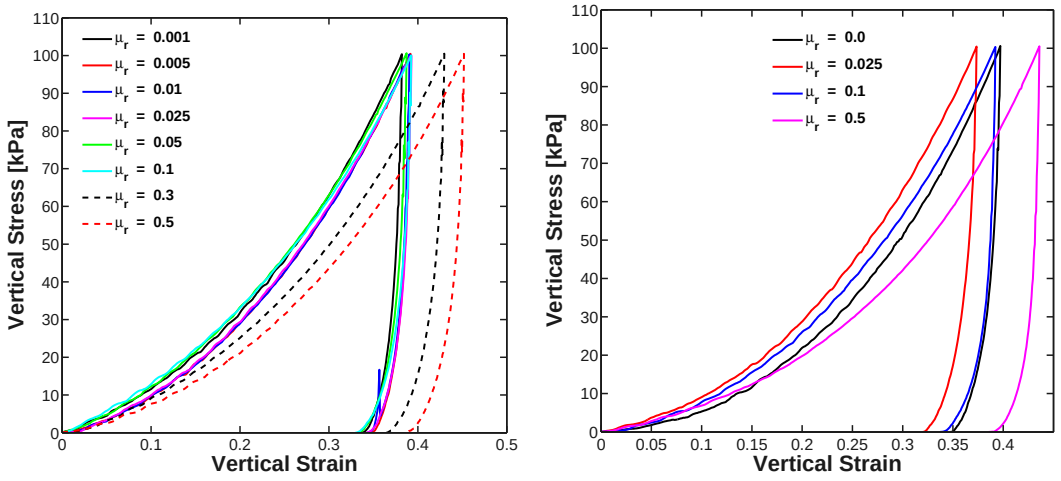

(a) For spherical particles **(b)** For paired particles, AR = 1.5

Figure 6.32: Confined stress-strain response with varying rolling friction - For different particle shapes

Looking at the porosity stress relationship it can be seen that as the rolling friction value increases the consolidated porosity also increases with the lowest rolling friction producing the densest packing. Also, despite the unloaded strain being similar for most of the packings, there is a large spread in the final porosity achieved at this point.

The consolidated porosity produced by all of the spherical packings is less than that produced by the paired particles.

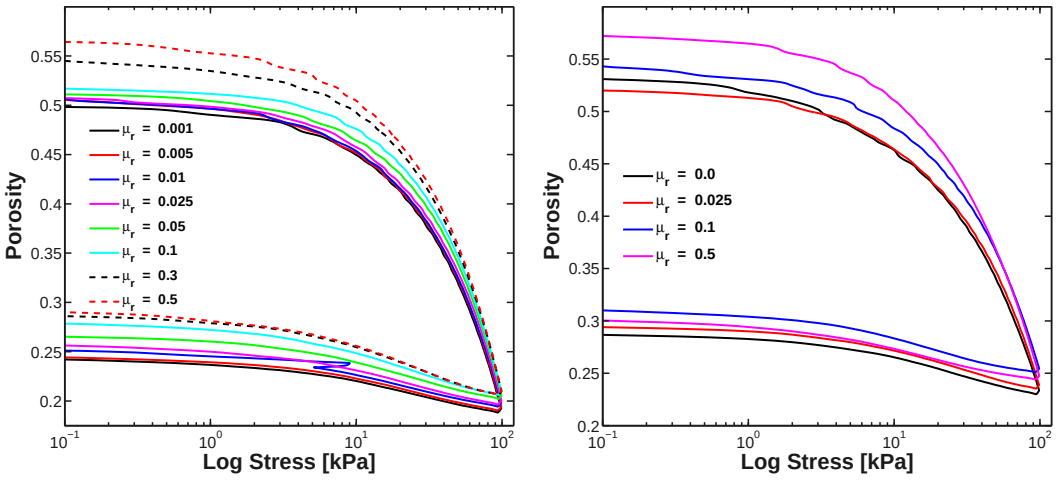

(a) For spherical particles **(b)** For paired particles, AR = 1.5

Figure 6.33: Confined stress-porosity relationship with varying rolling friction - For different particle shapes

6.4.2.3 Unconfined Compression

The effect the consolidated packing has on the unconfined strength of sample is nicely demonstrated by the unconfined strength of the samples if all are tested from their respective packings. Initially, for the spherical particles (Figure 6.34a), the increase in rolling friction seems to have little effect at very low values and as the rolling friction increased there is a change in the stress strain response, with higher rolling friction values proving a softer loading response to achieve a slightly higher peak at a larger sample strain. However for the paired particles (Figure 6.34b) the rolling friction appears to reduce the unconfined strength. While this may appear to be the case, the unconfined strength generated is dependent on the final consolidated porosity and the number of contacts as previously found by Thakur *et al.* [2013].

If the effect of the particle packing is removed (Figure 6.35) the effect of the rolling friction can then be quantified fully. By carrying out the test from the same starting point; in this case the densest packing from a rolling friction of 0.001; and then varying the coefficient of rolling friction, the dependence of the unconfined strength on the rolling friction is more visible. For the spherical particles in Figure 6.35a there is a significant increase in strength noted as the rolling friction increases. Figure 6.35b shows the same results for the paired particles and while there is a small increase in the unconfined strength, it is small compared to what is found in the spherical particles.

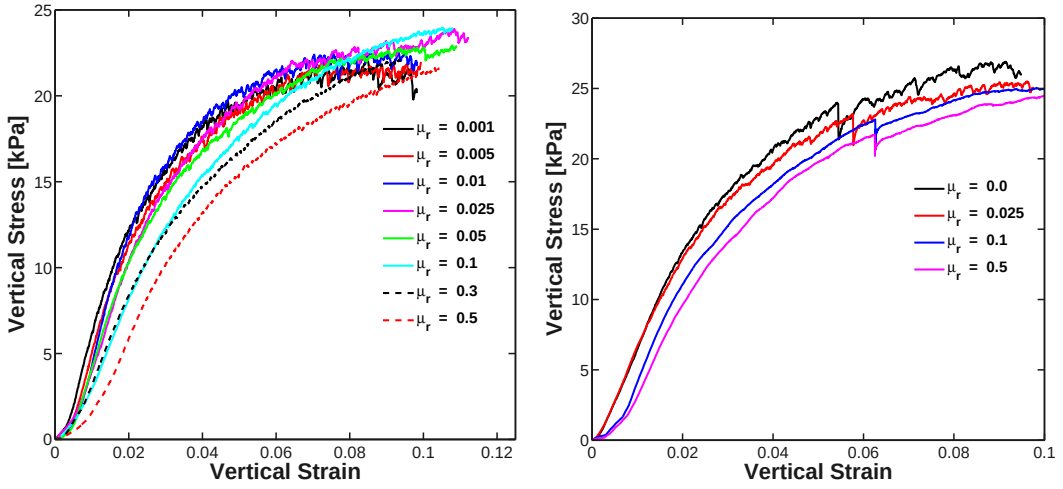

(a) For spherical particles **(b)** For paired particles, AR = 1.5

Figure 6.34: Unconfined stress-strain response with varying rolling friction - For different particle shapes and different consolidated packings

In the paired particles the rolling friction has a stabilising effect on the packing, with much of the fluctuations during loading being reduced.

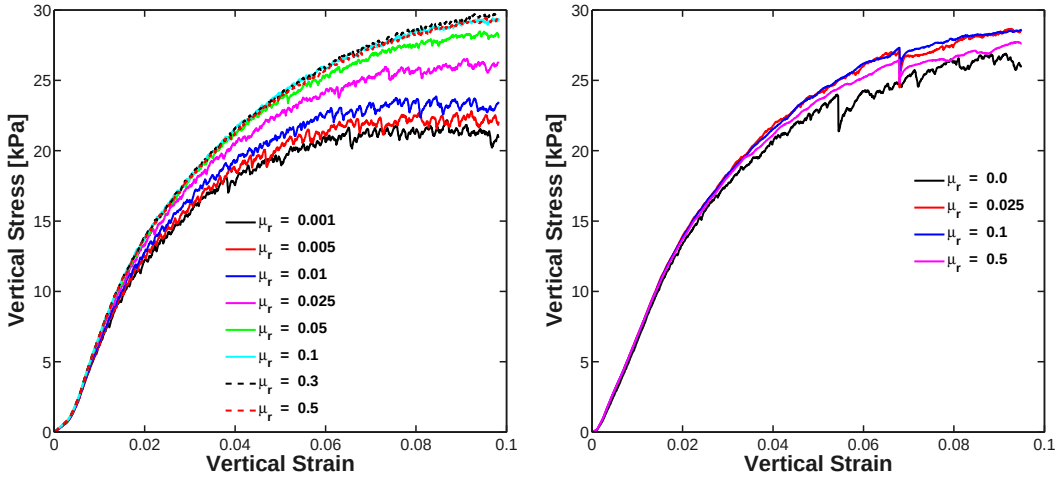

(a) For spherical particles **(b)** For paired particles, AR = 1.5

Figure 6.35: Unconfined stress-strain response with varying rolling friction and same consolidated packing - For different particle shapes

6.4.2.4 Lateral Pressure Ratio

The lateral pressure ratio variation with changing rolling friction parameters are presented in Figure 6.36 for spherical and paired particles. The increase in rolling friction for spherical particles imitates the inclusion of shape and interlocking in an assembly and for spherical particles there is a clearly visible trend of a decreasing K_0 value with increasing rolling friction. The lateral pressure ratio decreases significantly at low

stress, with the difference tending towards a constant at higher stress. The effect of the rolling friction saturates at a coefficient of $\mu_r = 0.1$, where increasing the rolling friction significantly above this value has little effect on the lateral pressure ratio across the entire stress range.

The results are less clear for paired particles. At low stresses, (approximately 0-10 kPa) the increasing rolling friction coefficient leads to a significant reduction in the observed K_0 value. However, at higher stresses the trend of decreasing K_0 with increasing rolling friction is only valid up to a rolling friction coefficient of $\mu_r = 0.1$. Above this value the K_0 value increases with increasing rolling friction. For both spherical and paired particles, high rolling friction coefficients lead to significantly reducing K_0 values during unloading, as the resistance to re-arrangement prevents significant horizontal relaxation as the vertical force is removed.

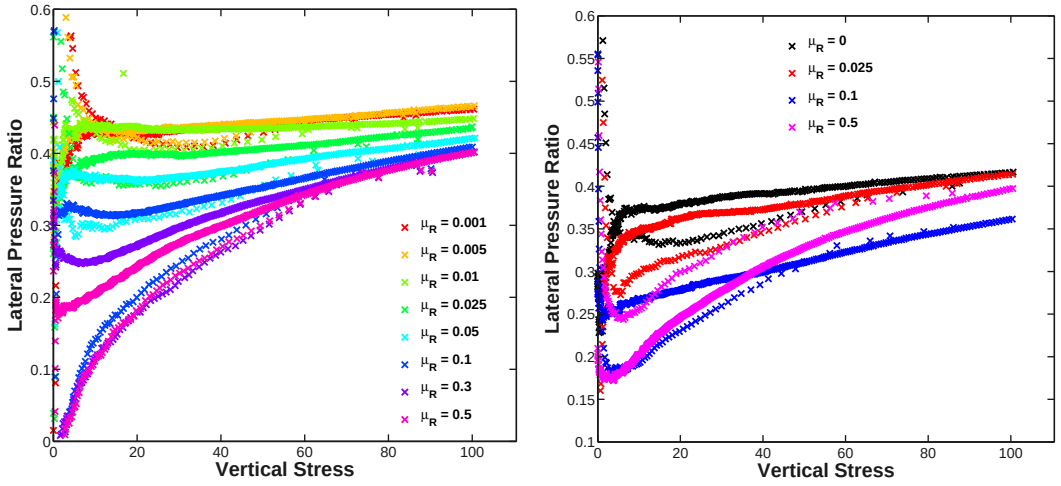

(a) For spherical particles **(b)** For paired particles, AR = 1.5

Figure 6.36: Lateral pressure ratio with varying rolling friction - For different particle shapes

The reduction in the lateral pressure ratio with increasing rolling friction coefficient is logical as the rolling friction has the effect of increasing the bulk friction for the material through the additional interlocking effect it provides through restricting re-arrangement. The restriction of movement leads to more force being transferred vertically through the assembly rather than laterally if particles are more free to move. The reduction in transfer of force from the strong vertical force network to the weak horizontal network results in the decreasing K_0 value.

6.5 Damping

Damping is applied in almost every DEM simulation carried out as a means to dissipate the kinetic energy in a system more quickly. It is generally applied through either contact level damping or global system damping, or a combination of both. Improper use of the damping coefficient can lead to erratic and erroneous results and care needs to be taken to ensure that it is not affecting the major underlying phenomena being investigated.

6.5.1 Global Damping

To evaluate the effect of the global damping application, a series of simulations have been carried out both with and without the damping model with varying levels of damping applied during the simulations. The level of damping has been varied between zero and 0.75. The PFC^{3D} code uses a default value of 0.7 for the global damping coefficient.

6.5.1.1 Initial Filling

The initial filled height for various simulations is presented below in Table 6.10. The results include two simulations without any damping - one in which a damping coefficient of zero has been used and the other without any global damping model applied. In both cases there should be no effect of damping, and any small scatter in the results is that related to the random variations that can occur between two simulations where the same parameters have been used. At low damping coefficients the effect on the initial packing is minimal and very similar to those generated without global damping. However at much higher values the global damping coefficient has a much stronger effect on the packing generated. The high damping value allows for the generation of significantly looser structures of particles as it reduces the chance of two particles that collide during the filling to separate, which helps create the loose packing. This effect is likely to be more closely representative of a real system where there are other dissipative mechanisms acting that are not considered in DEM. These additional mechanisms allow for a faster dissipation of energy in a real system, and as such, the use of a high damping may reflect what happens in the real systems.

Table 6.10 presents the results for porosity and aspect ratio at various coefficients of damping and would suggest that there is very little change in the confined compression behaviour. Figure 6.37a also appears to suggest this, as each simulation reaches a similar final strain. The effect of the damping coefficient on the porosity is presented in Figure 6.37b which highlights the high porosity generated by a high damping coefficient. The variation in the initial porosity for the two simulations with the same

Table 6.10: Effect of global damping coefficient on the filled height of the sample

Global Damping Coefficient	No Damping	0	0.2	0.75
Initial Porosity	0.516	0.508	0.521	0.554
Consolidated Porosity	0.367	0.367	0.384	0.416
Initial Aspect Ratio	1.68	1.65	1.69	1.82
Consolidated Aspect Ratio	1.30	1.30	1.34	1.42

parameters show almost a 1% difference initially, before converging to the same packing porosity after several kPa of consolidation.

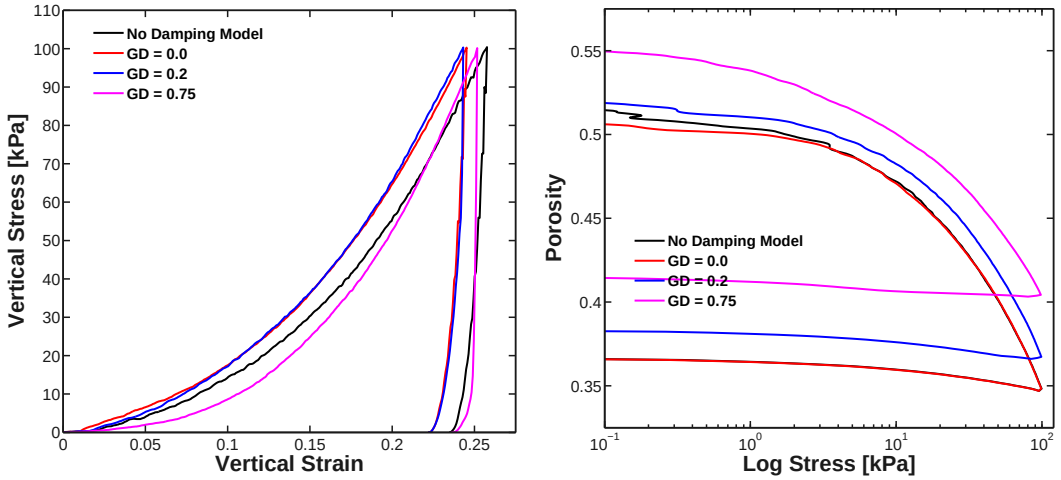

(a) Stress-strain response **(b)** Stress-porosity relationship

Figure 6.37: Confined compression results for various damping coefficients - Different initial packings created from different damping values

6.5.1.2 Confined Compression

The effect of the global damping coefficient has been evaluated by carrying out the consolidation phase for different values from the same initial filling (Figure 6.38a). The damping coefficient clearly has an effect on the confined compression behaviour, with simulations with a higher value compressing significantly less (Figures 6.38a and 6.38b).

Due to the explicit nature of DEM it is possible that when using a contact model that has a separate unloading/reloading path to account for plasticity that the force may oscillate along the unloading/reloading path as the damping is applied. This oscillation is not physical and if the oscillation is sufficiently large, it can lead to premature separation of the particle contacts. The application of global damping reduces the chance of particles separating prematurely. Reducing the number of premature contact separations will generally produce an assembly which has fewer contacts (Figure 6.39), but

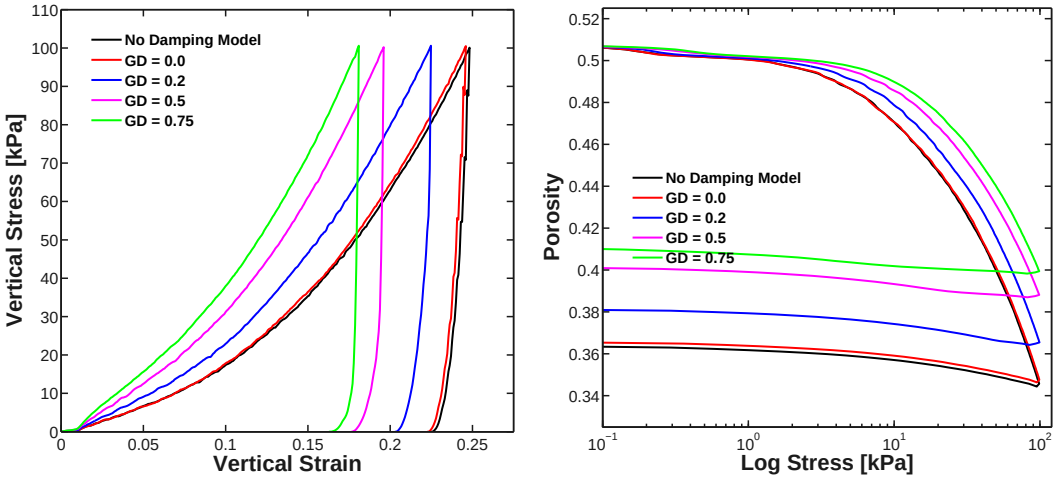

(a) Stress-strain response **(b)** Stress-porosity relationship

Figure 6.38: Confined compression results for various damping coefficients and same consolidated packing - For various damping values

ones that are slightly stronger (Figure 6.40), and thus the assembly will be able to resist the rearrangement of the packing more in the initial stages of compression, leading to lower strain at the same applied stress. A global damping coefficient of 0.75 reduces the change in porosity by approximately 5% porosity.

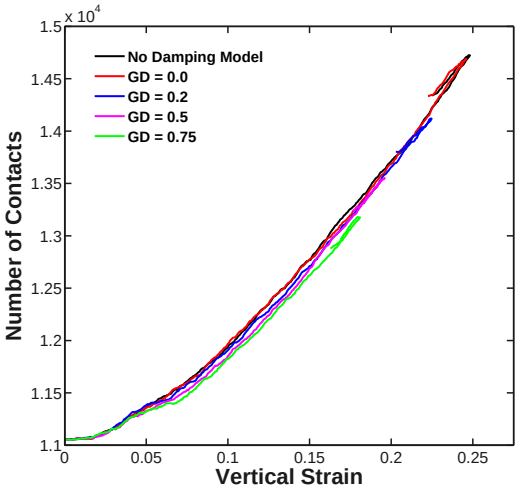

Figure 6.39: Number of contacts generated for same initial packing during compression - For all damping coefficients

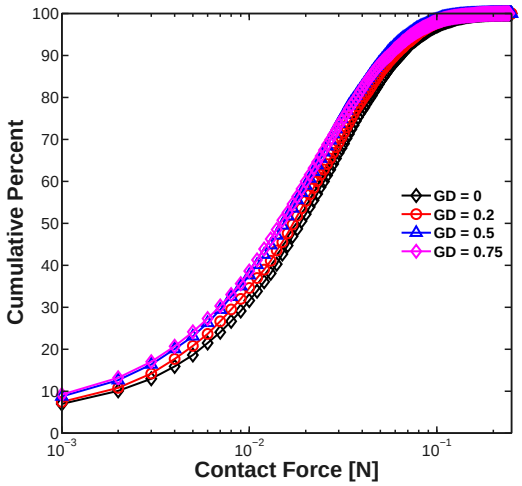

Figure 6.40: Average contact force distribution at the end of consolidation for same initial packing - For all damping coefficients

6.5.1.3 Unconfined Compression

The effect of the global damping coefficient on the unconfined strength of an assembly of particles has been assessed under three different conditions. The first is where all assemblies are generated with unique damping coefficients during filling and these

parameters are maintained through all three stages of the uniaxial test to determine the unconfined strength (Figure 6.41a). The second condition sees the damping coefficient varied through the confined consolidation stage only as all simulations are consolidated from the same initial filled assembly after the global damping coefficient has been changed (Figure 6.41b). The final condition sees the damping coefficient varied only for the unconfined compression of the sample, the same global damping coefficient was used for the filling and consolidation of the sample (Figure 6.42). By employing this method the effect of the global damping on each aspect of the uniaxial test can be evaluated.

In both situations where different values of damping were applied during the confined compression, this resulted in the highest unconfined strength being related to the highest damping coefficient. This is particularly the case when all simulations were carried out from the same initial filling where the unconfined strength increases with increasing damping coefficient (Figure 6.41b). The effect is less clear where different fills have been used, although the largest damping coefficient still results in the highest unconfined strength.

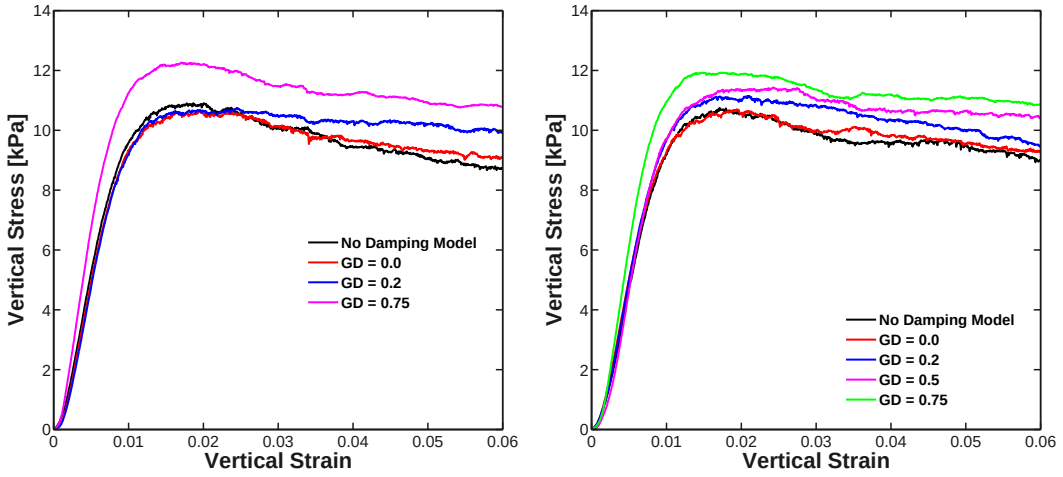

(a) For different assemblies during consolidation

(b) For same assembly during consolidation

Figure 6.41: Unconfined stress-strain response with varying global damping coefficient - For variation of packing

Global damping has little effect when only applied to the unconfined stage, as can be seen in Figure 6.42, where the contacts have already been formed and there is little or no re-arrangement of particles and formation of new contacts.

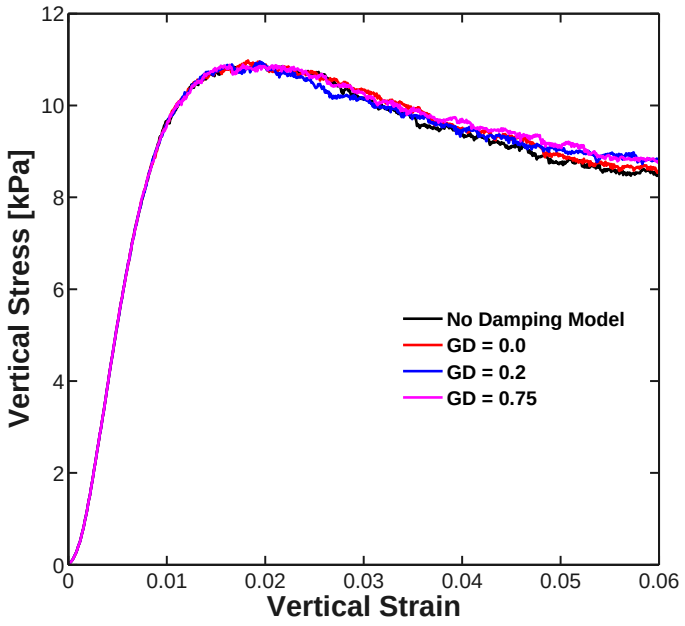

Figure 6.42: Effect of varying of global damping coefficient - For same consolidated fill

6.5.2 Restitution Coefficient

The restitution coefficient is the contact damping parameter specified to dissipate the kinetic energy during particle contact, as described in Chapter 4.

6.5.2.1 Initial Filling

The effect of contact level restitution has a similar effect on the initial filled height and porosity of an assembly, when compared to the global damping, with a higher restitution coefficient leading to a denser packing (Table 6.11). A higher coefficient of restitution means less damping is applied - a coefficient of restitution of unity will mean that a particle will have the same initial and rebound velocity. A contact will also have a higher normal contact force with a higher coefficient of restitution.

Table 6.11: Effect of coefficient of restitution on the filled height of the sample

Coefficient of Restitution	0.2	0.5	0.8
Initial Porosity	0.532	0.524	0.516
Consolidated Porosity	0.385	0.385	0.386
Initial Aspect Ratio	1.74	1.71	1.68
Consolidated Aspect Ratio	1.34	1.34	1.35

During the filling process, the higher coefficient of restitution means that more particles separate after collision as the damped normal force is greater than the adhesive force of the contact. As the coefficient of restitution reduces the damped normal force will

also reduce, leading to a greater probability of particles adhering following a collision. This leads to the development of a looser initial packing when a lower coefficient of restitution is employed.

6.5.2.2 Confined Compression

Despite the difference found in the initial filled height of the assemblies all samples reach approximately the same porosity at stress levels greater than 50 kPa and each assembly retains the same final consolidated porosity (Figure 6.43b). The variation in filled height and initial porosity leads to a variation in total strain for the assembly with the most highly damped assembly forming the densest packing initially and thus a lower strain (Figure 6.43a).

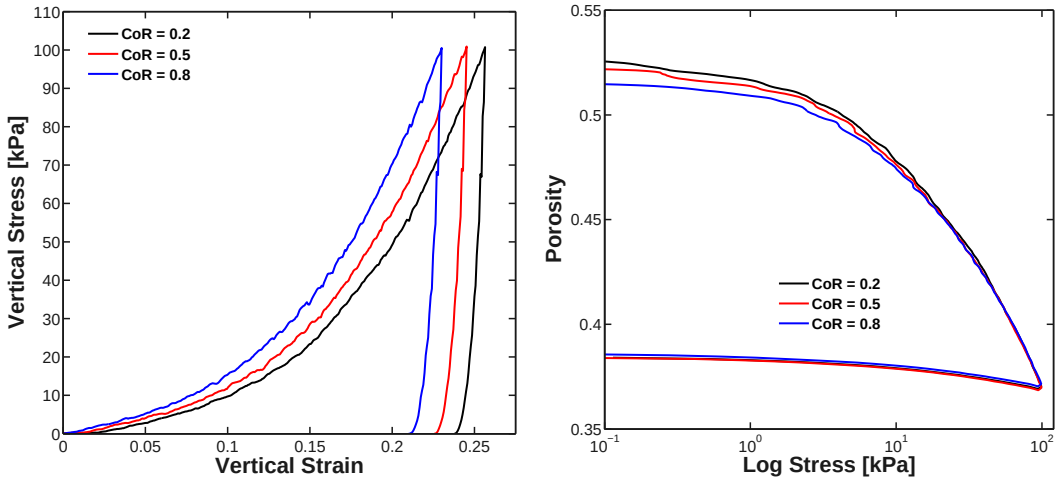

(a) Stress-strain response **(b)** Stress-porosity relationship

Figure 6.43: Confined compression results for various restitution coefficients - For paired particles

6.5.2.3 Unconfined Compression

The effect of restitution on the unconfined strength has been assessed in two situations - one where different fillings with different restitution coefficients were used (Figure 6.44a) and one where the same consolidated packing was used with different coefficients of restitution (Figure 6.44b). For different fillings there is a slight variation in the different restitution but the effect is unclear, despite the same final porosity being achieved by all three packings. In the case where the unconfined test is carried out from the same consolidated packing (Figure 6.44b) the result is more obvious, a higher coefficient of restitution leads to a higher unconfined yield strength as it maintains more contacts during the unconfined compression.

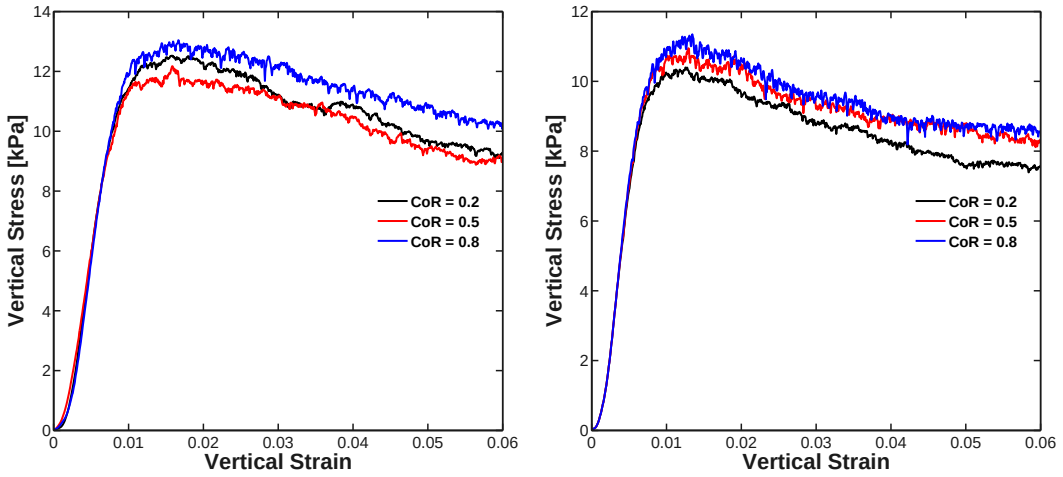

(a) For different consolidated packings **(b)** For same consolidated packing

Figure 6.44: Unconfined stress-strain response with varying restitution coefficient - For paired particles

6.6 Summary

The adhesion energy of the contact is an important parameter for controlling the amount of adhesion in the system. In addition, the adhesion between particles is also affected by many other parameters such as the loading and unloading stiffness which determine the magnitude of the plastic overlap that can occur at a contact. A lower k_1 value allows for the development of larger contact overlap, which in turn can lead to the development of greater adhesion forces. A higher k_2 stiffness allows the generation of large adhesion values and is an important parameter for controlling the strength of the flow function. The effect of varying k_2 was found to be minimal when observing unconfined bulk stiffness to loading with both the packing porosity and the tangential stiffness proving important here. The tangential stiffness was found to be important for controlling the unconfined bulk stiffness to the yield point while the assembly of particles is undergoing shear.

While increasing the adhesion branch slope allows for particles to separate from contact more quickly once the contact limit has been reached, this did not lead to a more brittle assembly such as that seen in the experiments, as when a contact breaks, a new contact can be immediately reformed. While this leads to a reduction in the unconfined strength of the assembly, as the history of the contact is lost, the new contact can develop a significant strength if the assembly has a high unconfined yield strength, which prevents a brittle failure occurring.

Inter-particle friction and shape were found to have a strong influence on the unconfined strength of a sample. Typically a higher coefficient of inter-particle friction led

to a macroscopically stronger assembly, which often led to a more pronounced peak strength followed by a distinct drop in the strength. However, with the inclusion of higher sliding friction and rolling friction during the filling and consolidation process the effect of both have been found to saturate at close to 0.5 due to the additional frictional resistance reducing the consolidation in the sample and hence the development of further adhesive strength.

The lateral pressure ratio was found to be relatively insensitive to the changing loading and unloading stiffness and adhesion energy values during confined compression, but the effects of these parameters on the initial packing that is formed has an effect on the observed lateral pressure. Static friction and rolling friction were found to have a significant effect on the lateral pressure ratio, with a significant decrease in the lateral pressure ratio occurring for increasing static and rolling friction, which added extra frictional and shearing resistance to the assembly. The variation of the tangential stiffness also had a significant effect on the lateral pressure ratio observed with increasing tangential stiffness and shearing resistance leading to a significantly lower K_0 value. Particle shape was also found to be an important factor that can affect the lateral pressure ratio.

Particle interlocking for non-spherical particles allowed for a larger tangential force to be carried by the contact thus increasing the strength of the assembly. Greater interlocking from non-spherical particles also has the effect of larger dilation of the sample in the shear bands, due to the additional resistance to rolling.

The coefficient of restitution was found to have little effect on the compression process or the resulting unconfined strength generated by an assembly whereas the effect of global non-viscous damping was found to be more significant. The global damping prevents the breakage of contacts during the initial filling of the assembly and initial stage of compression where particle re-arrangement occurs. By preventing the breakage of weak contact, more strong contacts remained and allowed for the assembly to reach a higher unconfined strength.

No significant effects of global damping have been observed when applied during the unconfined compression to failure of a sample and suggests that global damping can be used in a quasi-static system to achieve a faster dissipation to reach the steady-state condition. However, care needs to be taken when used in a dynamic situation, such as during filling, where it can affect the very dynamic process that take place.

Chapter 7

Calibration and Comparison of DEM Simulations with Experiments

In this chapter the DEM parameters for the Edinburgh Elasto-Plastic Adhesion (EEPA) model are calibrated with those measured for the iron ore fines in Chapter 5. The model should be calibrated such that a single set of stiffness and friction parameters can predict the entire flow function for a single level of adhesion, without the need to change any parameters for different consolidation stresses. The increasing yield strength with increasing moisture will be calibrated for the adhesion parameters only.

A comparison is made between the predicted DEM flow functions and those measured for the iron ore fines. Investigations into the failure mode in the DEM simulations are made to determine whether the simulations predict the same failure mode as observed in the uniaxial experiments.

7.1 DEM Simulation Setup

The KPRS iron ore fines with 1% moisture content were selected as the test material for calibration of the model. A uniaxial compression simulation for the test material was conducted using the above contact model. Closely following the EPT physical test procedure, the simulation consisted of three stages - filling the cylindrical mould to form the initial packing, confined consolidation to the required stress level, followed by unloading, and finally unconfined compression of the sample to failure after the removal of the confining mould. A cylinder of 40 mm diameter and 80 mm in height, the same size EPT mould, was filled with 10,000 mono-sized multi-sphere particles with an aspect ratio of 1.5. The DEM simulation setup is presented in Figure 7.1, where the 4 stages are visually described.

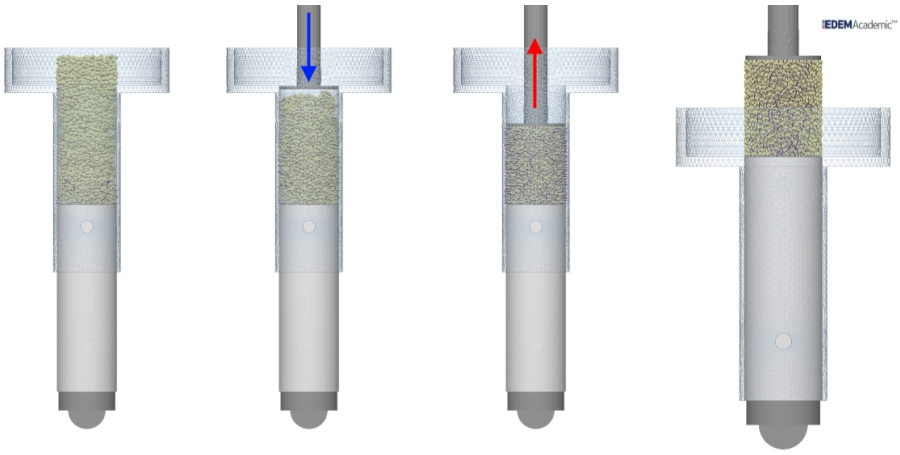

Figure 7.1: DEM model of uniaxial test - From L to R: a) filling, b) loading, c) unloading, and d) unconfined compression

Adhesion between particles was accounted for in the filling process to allow for the development of a filled packing similar to the experimental data. The random rainfall method was adopted to provide a similar filling method to that used in the experiment where the material was filled in several spoonfuls. The simulations are carried out using the proposed EEPA-NL contact model with a shape exponent $n = 1.5$ used for all particle-particle interactions. The adhesive interactions between particles and walls were not considered in this study, and, as such, the built in Hertz-Mindlin (no slip) model was used to help reduce computation times.

7.2 Selection of Model Parameters

In order to calibrate the DEM model a direct comparison with some experimental results is required. Two experimental results were used to calibrate the flow function at a particular moisture content level, 1% moisture content is used in this case. To calibrate the model for increasing moisture content, one further value from each flow function was required.

The experimental results that were used for the calibration of the model are shown in Figure 7.2. Two experimental data points were used for calibrating the flow function for 1% moisture content - one at 40 kPa consolidation stress and a second at 100 kPa. To calibrate for the increasing strength for increasing moisture content 3 further experimental data points, each at a consolidation stress of 100 kPa, were required for the remaining moisture contents of 2%, 4% and 6%. It should be noted that each experimental point shown in Figure 7.2 is the mean of a minimum of three experimental uniaxial tests.

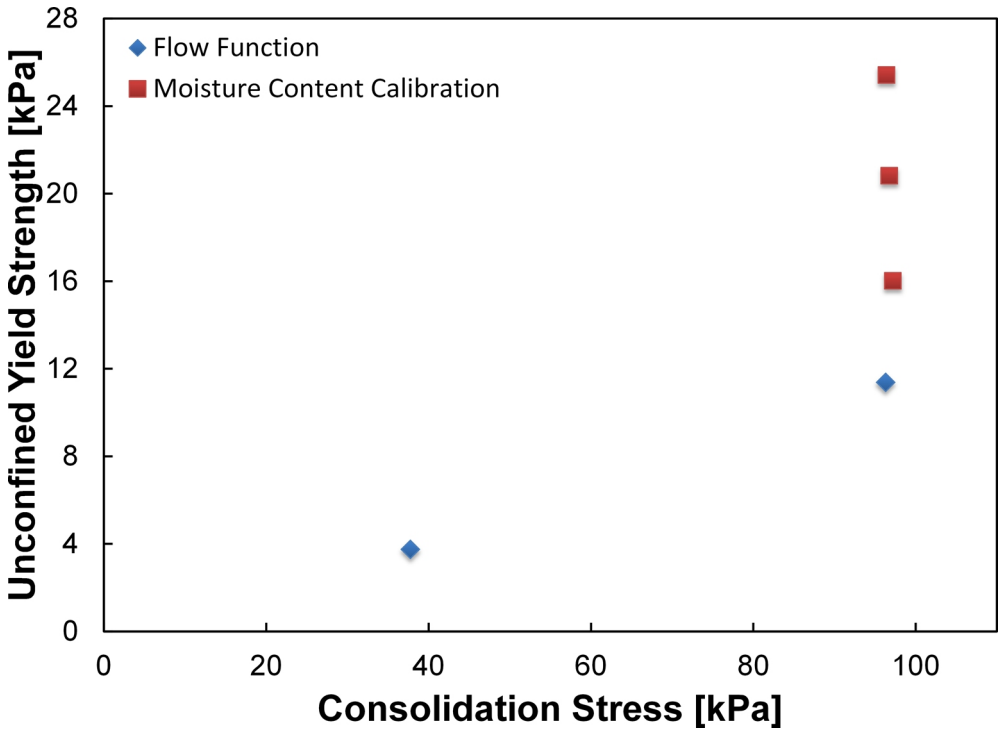

Figure 7.2: Experimental results used for calibration of DEM model - Separated for flow function and varying moisture content

7.2.1 Particle Shape and Inter-particle Friction Values

The iron ore fines particles are inherently very angular and non-spherical in nature and a typical particle shape is shown in Figure 7.3. While the shape for the iron ore particles is not consistent, it is not practical to characterise many individual particle shapes, nor simulate many different particle shapes. It is also not the goal to model each individual particle and, as such, multi-sphere paired particles with an aspect ratio of 1.5, shown in Figure 7.4, were selected to represent the iron ore fines agglomerates. An aspect ratio of 1.5 provides the shape necessary to achieve such a large bulk friction angle. A two sphere particle is preferential to a three-or-more sphere clump due to the additional computational costs associated with those.

Figure 7.3: Iron ore fines particle - Typical shape

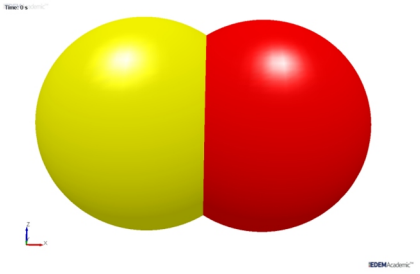

Figure 7.4: DEM multi-sphere paired particle - With aspect ratio AR = 1.5

From Jenike Shear Tests on iron ore fines (Chapter 5) the angle of internal friction was found to be 45°, reducing slightly with additional moisture content. Härtl and Ooi [2011] conducted DEM simulations of a Jenike shear cell and mapped the relationship found between the measured bulk friction coefficient and the particle contact friction for cohesionless particles of different particle aspect ratios between 1-2. Using the relationship found between contact friction and bulk friction angle for different particle shapes (Figure 7.5) the coefficient of sliding friction for the selected particle aspect ratio of 1.5 for cohesionless particles is approximately 0.44. An approximate value of $\mu_s = 0.5$ is therefore selected to represent the cohesive nature of the iron ore fines and allow for any variation that may relate to the best-fit line.

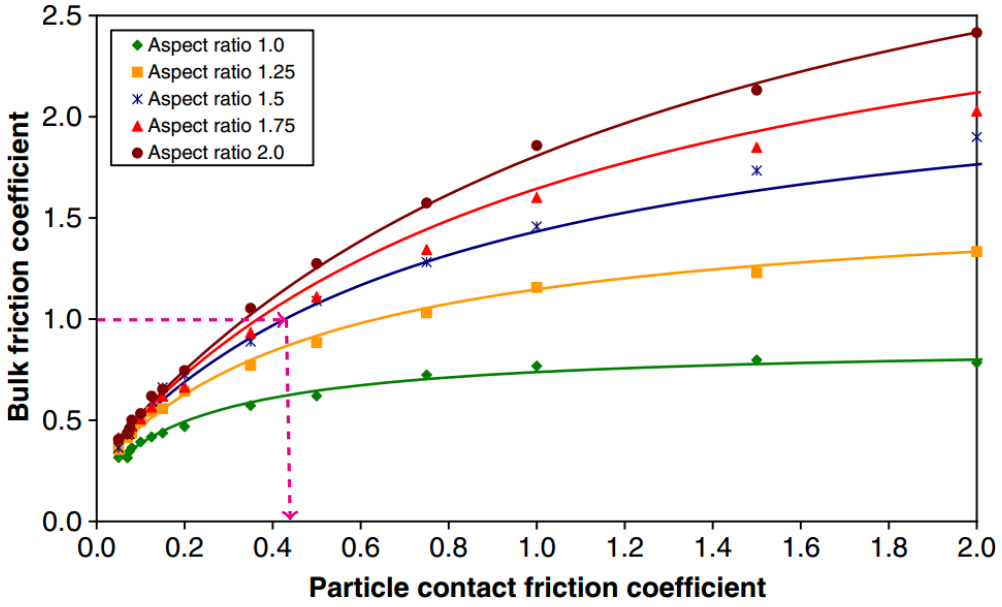

Figure 7.5: Influence of inter-particle friction on bulk friction - For particles of different aspect ratio, after Härtl and Ooi [2011]

Although the use of multi-sphere particles should include the contribution of interlocking of the non-spherical iron ore particles, the DEM representation of the shape has the rounded surface of the constitutive spheres which may not account for the flatter angular nature of the iron ore particles. As such, and to account for the significant angularity of the iron ore particles that may contribute additional strength through further interlocking and flatter surfaces, a small amount of rolling friction, set to $\mu_r = 0.005$ is also included. A value of $\nu = 0.225$ has been used for the Poisson's ratio for the particles. Particle damping is included with a coefficient of restitution $e = 0.5$ and a global damping coefficient of 0.5 used during consolidation and unconfined compression. The parametric study in Chapter 6 showed that the effect of the restitution coefficient during quasi-static compression (both confined and unconfined) was minimal while the effect of the global damping coefficient was found to have a greater effect during the

initial filling of the assembly. While the observed effect of the global damping is greater than that of the contact damping, it provides an effective means of dissipating the kinetic energy in the system and reduces that amount of oscillation at contact between loading and unloading. A smaller value than the default amount used in PFC^{3D} has been selected.

7.2.2 Particle-wall Friction Interaction Properties

The EPT uses the principle of two-way compression, where the mould is free to move during compression, to reduce the effect of wall friction on the consolidation of the sample. In order to replicate this, the wall friction coefficient between particles and the cylinder wall geometry was set to zero. Failure to include any wall friction between the particles and platens would result in excessive slippage and movement of the assembly of particles from underneath the loading platens in the unconfined compression stage of the experiments. In extreme cases where no wall friction has been applied, the assembly of particles has been observed to move almost completely out of contact with the end platens as the particle do not produce a level surface and are squeezed out without sufficient end restraint. Zhou [2010] found that end friction has a significant effect on the bulk response and type of shear band formed in DEM simulations. Frictionless ends lead to a single dominant shear band in a sample, whereas when end friction was employed conjugate shear bands, which are commonly observed experimentally, were found in the simulation. In order to replicate the EPT experiment, where frictional stainless steel end platens lead to the development of conjugate shear bands, the sliding friction coefficient for particle interaction between the top and bottom platens has been set to $\mu_s = 0.5$. Table E.1 of Eurocode 1-4 [British Standards Institution, 2006] provides a list of particulate solid properties for use in design if experimental data is unavailable. For a wall type D2 (smooth steel surface) the mean wall friction coefficient for iron ore pellets is given as 0.54 (approximately 28°). However, as the relationship between the macroscopic bulk wall friction and the microscopic particle wall friction coefficient is not well defined, the wall friction coefficient for the end platens is sufficiently high. It was also noted by Zhou [2010] that increasing end platen friction from 0.1 to 0.3 produced no noticeable difference in the bulk response as this is governed by the particle-particle interactions.

7.2.3 Loading & Unloading Stiffness

An attempt is made to calibrate the DEM bulk stiffness to cover the entire range of moisture contents simulated with a single set of stiffness and friction parameters. The initially dry iron ore fines have a high bulk stiffness, but the addition of moisture to the

sample results in a reduction in the bulk stiffness of the assembly. Increasing moisture content leads to the effect of bulking of the sample and formation of agglomerates, which have a lower stiffness than the individual iron ore particles. In order to calibrate the bulk stiffness a direct comparison was made with a range of DEM simulations in which the particle shear modulus was varied by a single order of magnitude from 2.5×10^6 Pa to 5×10^7 Pa. A comparison between the DEM simulations and the experiment is presented in Figure 7.6 and shows that the increase in contact stiffness in the DEM simulation leads to a much closer result in comparison to the experimental bulk stiffness. From this, it can be seen that a particle shear modulus greater than 5×10^7 Pa would provide a very close match to the experimental bulk stiffness. The increasing contact stiffness also leads to a smaller difference between the initial densities for the DEM simulation and experiment and further increasing the stiffness would provide a very close match for both the bulk stiffness and bulk density when compared to the experimental results.

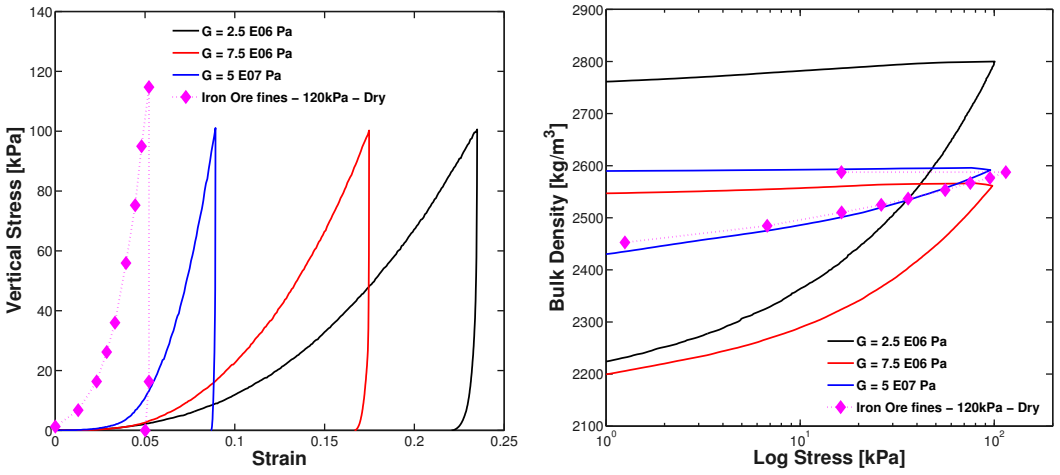

(a) Stress-strain response **(b)** Stress-density relationship

Figure 7.6: Confined compression results comparison for dry iron ore fines - At 100 kPa consolidation stress

There is also a very close match in the unloading stiffness for the experiment and stiffer DEM simulation. While both simulations used the same ratio of k_2:k_1 (25×), the simulation with the higher k_1, and hence k_2, showed the best correlation between the experimental results. This shows that the ultimate magnitude of k_2 is more important than the ratio of k_2:k_1 when matching the experimental results. The effect of the unloading stiffness on the flow function has been previously discussed in Chapter 6 and it has been shown that the higher the ratio of k_2:k_1, the more cohesive the resulting flow function will be. However, as the level of bulk plasticity demonstrated by the iron

ore fines at various moisture contents is consistently high, there is little opportunity for variation of this parameter if a match is to be made to the experimental results.

The results in Figure 7.6 would suggest that a shear modulus of the order of approximately 10^8 Pa would be required to represent the bulk confined behaviour of the iron ore fines. However, consideration also needs to be made for the resulting unconfined yield strength and flow function. A greater contact stiffness will mean that smaller overlaps exist for the same equivalent force applied at the contact. This is demonstrated in Figure 7.7 where all parameters except the virgin loading stiffness k_1 are kept constant. As the virgin loading stiffness k_1 was reduced, the resulting unconfined strength increased, resulting in a significantly more cohesive flow function for a lower k_1. The highest stiffness used here at 1×10^7 Pa was of an order of magnitude lower than that suggested to be a close representation of the bulk stiffness of dry iron ore fines in Figure 7.6a and produces the most free flowing flow-function. However, even at this stiffness, if the flow function was to be predicted, the predicted unconfined strength for a consolidation stress of 20 kPa would be almost double that of the experimental value, based on a calibrated match of unconfined strength at 100 kPa of consolidation stress.

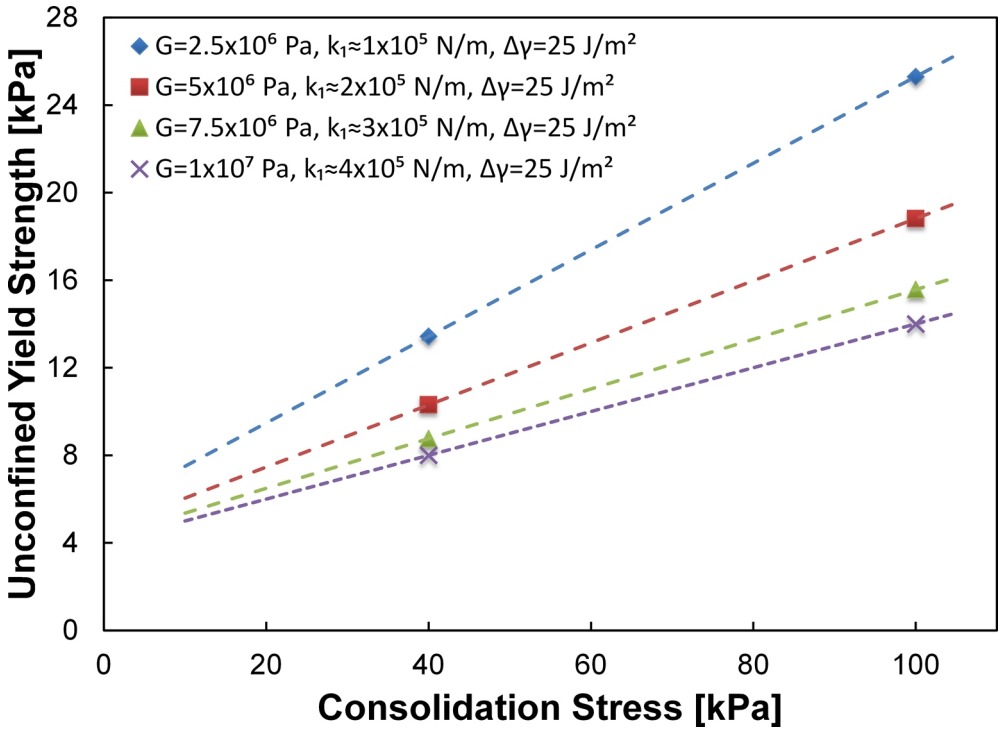

Figure 7.7: Flow function variation with virgin loading stiffness - For varying loading stiffness k_1

It can also be seen from Figure 7.7 that in order for a higher contact stiffness to be able to produce a higher unconfined yield strength, a higher adhesion energy, $\Delta\gamma$, is required. And while the computed unconfined strength can be increased by increasing

the adhesion energy $\Delta\gamma$, this will not provide the same flow function as a lower stiffness assembly. In this case the unloading stiffness k_2 is already set to a very large value (a k_2:k_1 ratio of 40 equates to a contact plasticity of $C_p = 0.98$) to match the bulk plasticity of the iron ore fines, increasing it further beyond this point will have little effect on the flow function. Matching the unconfined strength at higher consolidation stresses with a stiffer assembly will mean over prediction of unconfined strength at lower consolidation stresses and vice-versa.

A series of flow functions with an intermediate shear modulus of 7.5×10^6 Pa was carried out in an attempt to replicate the flow function for the iron ore fines at various moisture contents. The results of this study are shown in Figure 7.8 for varying levels of adhesion energy. The results show that, although a close match for the unconfined strength from a consolidation of 100 kPa is made with the experimental results, when the flow function is determined from simulations carried out at lower consolidation stresses, the DEM simulations significantly over predict the unconfined strength and fail to match the experimental flow function for the iron ore fines.

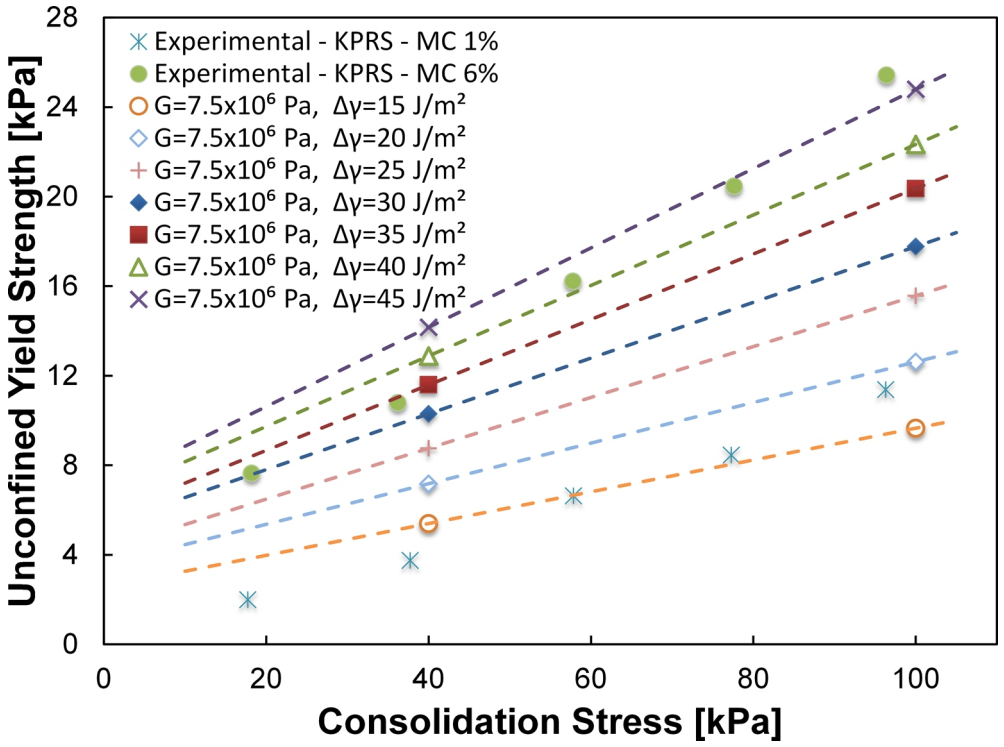

Figure 7.8: Flow function comparison for intermediate particle stiffness - Comparison for different levels of adhesion

A comparison of the flow function resulting from two different virgin loading stiffness is made in Figure 7.9. At comparable unconfined yield strengths resulting from 100 kPa of consolidation stress the higher stiffness assembly consistently overestimates the unconfined yield strength for lower consolidation stresses. A comparison is also included

for two experimental points. The lower stiffness assembly was found to provide a flow function that is the closest match to the experiment.

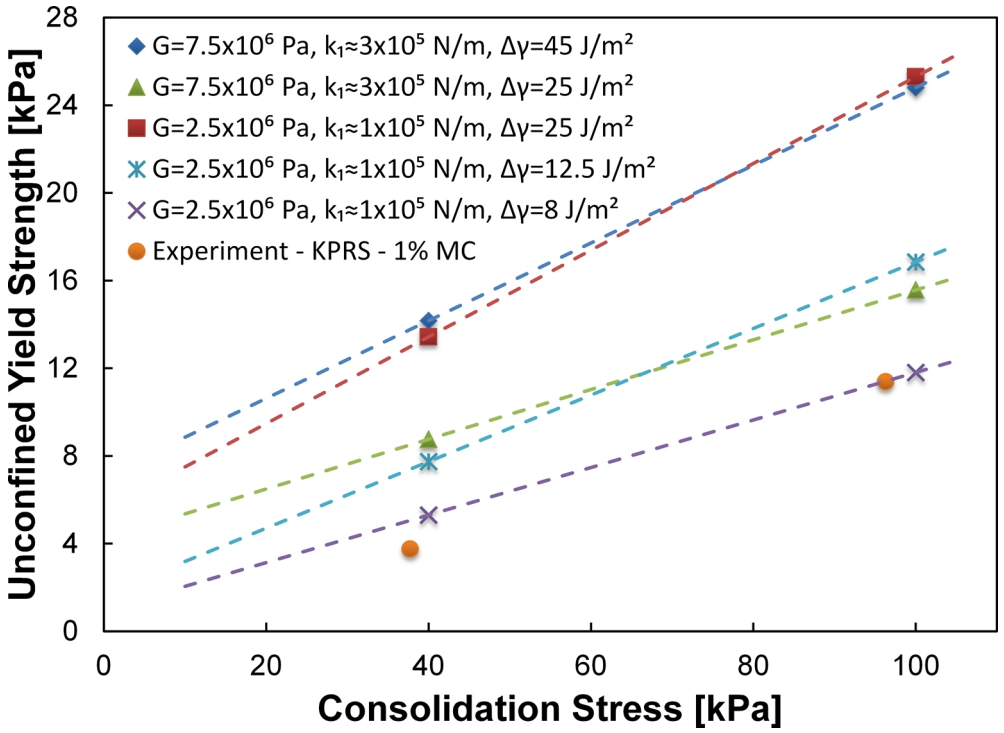

Figure 7.9: Flow function comparison for varying $\Delta\gamma$ - Comparison for different stiffness

The DEM simulations have shown that an excellent match for the bulk stiffness and bulk density of dry iron ore fines can be achieved (Figures 7.6a and 7.6b) but a compromise is required between exactly predicting the material bulk stiffness during confined compression and predicting the unconfined flow function. If too high a virgin loading stiffness is chosen it will prevent the flow function being matched due to a smaller overlap being generated from the stiffer, non-linear force relationship at the same consolidation stresses. This leads to a smaller range of contact overlaps between the smallest and largest consolidations stresses, leading to a less cohesive flow function. Based on this, a virgin loading stiffness k_1 based on a Shear Modulus(G) of 2.5×10^6 has been chosen as it offers the best opportunity to replicate the experimental flow function with the compromise of only predicting the experimental bulk stiffness for moisture contents greater than 1%. A k_2:k_1 ratio of 40 has been adopted for this study to account for the significant bulk plasticity seen in the iron ore fines and to maximize the cohesive flow function [Thakur *et al.*, 2011].

7.2.4 Adhesion Parameters

Calibration of the adhesion energy was carried out through a regression analysis. Several simulations were carried out at varying levels of adhesion and with a constant

consolidation stress used for each simulation. A consolidation stress of 100 kPa was chosen for calibrating for various moisture contents. The material behaviour should be more consistent at different adhesion levels for higher consolidation stresses as the effect of the initial packing will have less effect than at lower consolidation stresses where some particle re-arrangement may still be occurring. The regression analysis was carried out on the data in Table 7.1. The data from Table 7.1 is plotted in Figure 7.10 and a non-linear relationship for adhesion energy against unconfined yield strength passing through the origin was found - a sample in which no adhesion energy or no constant pull-off force are applied will not have any cohesive strength and would collapse under its self-weight. A non-linear relationship, with a R^2 value of 0.9985, describes the relationship between adhesion energy and unconfined yield strength very closely.

Table 7.1: Variation of unconfined strength with adhesion energy at 100 kPa

Adhesion Energy J/m^2	**Unconfined Strength** *kPa*
2	2.84
5	7.15
10	13.01
13.5	18.05
20	23.56
25	27.02

A simple check on the repeatability of the simulation results using the derived non-linear relationship was carried out. Adhesion energy values were selected to provide an unconfined strength that is similar to that of the experimental results for a consolidation stress of 100 kPa in Figure 7.2. The DEM simulations using the selected adhesion energy values provide an unconfined strength that closely matches the corresponding predicted values from the regression analysis (Table 7.2).

Table 7.2: Predicted unconfined strength from 100 kPa consolidation

Adhesion Energy J/m^2	**Predicted UC Strength** kPa	**DEM Result** kPa	**% Difference**
8.5	11.74	11.81	0.5%
12.5	16.37	16.85	3.0%
18.5	22.22	22.83	2.7%
23.5	26.11	26.88	2.9%

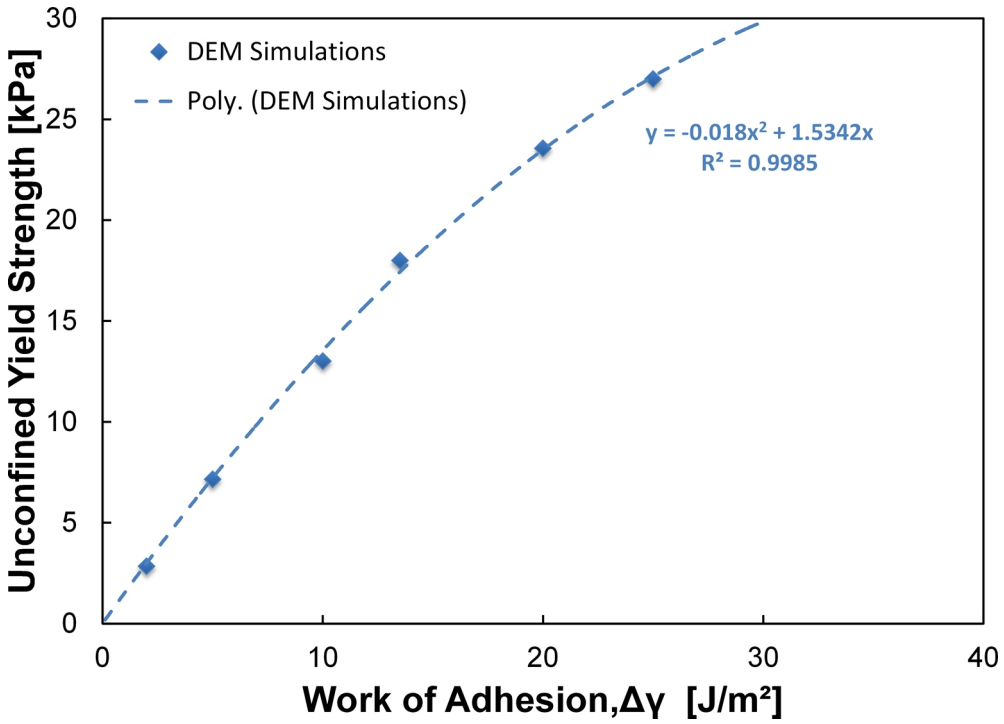

Figure 7.10: Variation of unconfined yield strength with adhesion energy - At 100 kPa consolidation stress

7.2.5 Selected DEM Parameters

The DEM parameters have been selected based on the calibration process detailed previously and the full values are listed in Table 7.3. A comparison between these simulation parameters and the experimental results they have been calibrated from is presented in Figure 7.11. A lower particle stiffness was used to ensure that the flow function measured from the DEM simulation is a close match to the experimental value.

Table 7.3: Simulation parameters

Particle Radius, R (m)	0.00085	**Poisson's Ratio,** ν	0.225
Particle Aspect Ratio, AR_p	1.5	**Adhesion Energy,** $\Delta\gamma$ **(J/m^2)**	8, 12.5, 18.5, 23.5
Particle Density, ρ **(kg/m^3)**	4150	**Particle Sliding Friction,** μ_s	0.5
Young's Modulus, E (Pa)	6.13×10^6	**Particle Rolling Friction,** μ_r	0.005
Shear Modulus, G (Pa)	2.5×10^6	**Wall Friction,** μ_w	0.0
Spring Stiffness, k_1 **(N/m)**	1×10^5	**Platen Friction,** μ_p	0.5
Spring Stiffness, k_2 **(N/m)**	4×10^6	**Simulation Timestep (s)**	2.5×10^{-6}

The DEM results are slightly higher than the experimental results they were calibrated from. This is due to the DEM simulations being consolidated to exact values, whereas the experiment had a nominal stress applied with the exact consolidation stress measured. In all cases the measured experimental consolidation stress is recorded as lower.

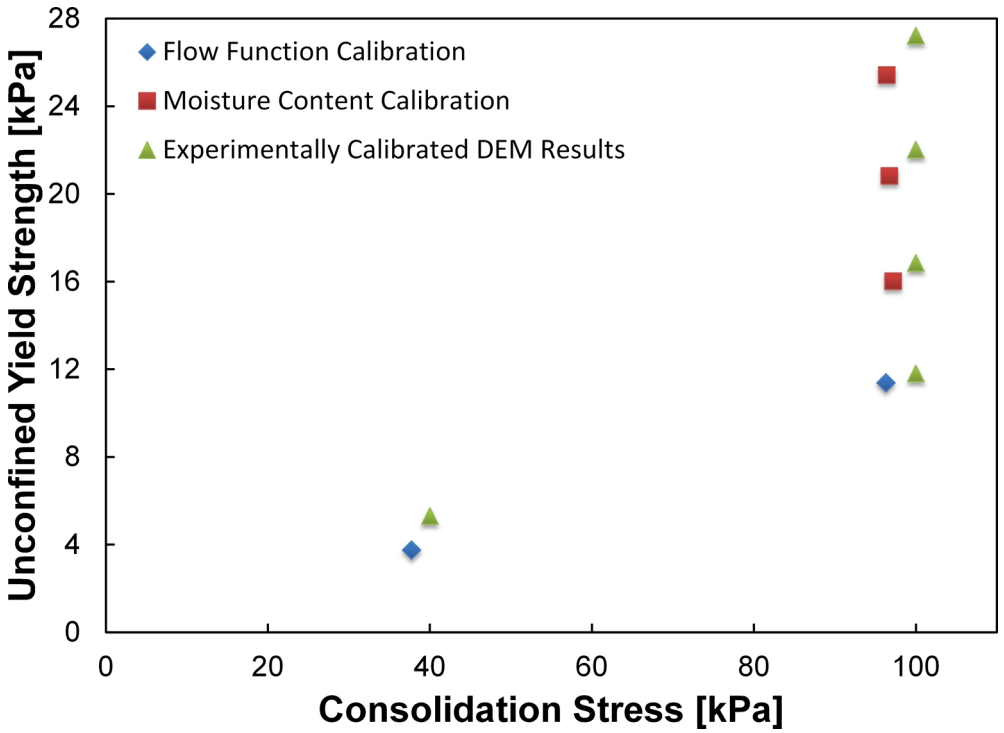

Figure 7.11: Comparison between Calibrated DEM simulations and experimental results - At 100 kPa consolidation stress

7.3 DEM Results & Experimental Comparison

The flowability of a material is significantly affected by the adhesion forces between particles and this has already been demonstrated by the flow functions of the experimental results. In the following section the simulation results are compared to the experimental results for the unconfined compression test. The results are considered in terms of the unconfined strength, the consolidated density and the lateral pressure ratio. In Figure 7.12 the DEM simulation results are highlighted to separate those used for calibration from the experiment with those used to predict the flow function.

The measured aspect ratios of the various DEM samples are given in Figure 7.13. The sample with the highest adhesion energy during the filling process leads to the highest initial filled height and lowest initial density of the sample, while the lowest adhesion energy leads to the densest initial packing. A similar trend is found in the experiments, with the initial density reducing with increasing moisture content. The consolidated aspect ratios for the DEM simulations are in line with those observed experimentally for consolidation stresses greater than 40 kPa, but the computed aspect ratios at 20 kPa and 40 kPa are slightly greater than what was found experimentally, suggesting that the DEM simulation is under-predicting the consolidation at these consolidation stress levels. While the sample with the highest adhesion energy consolidates the most, as

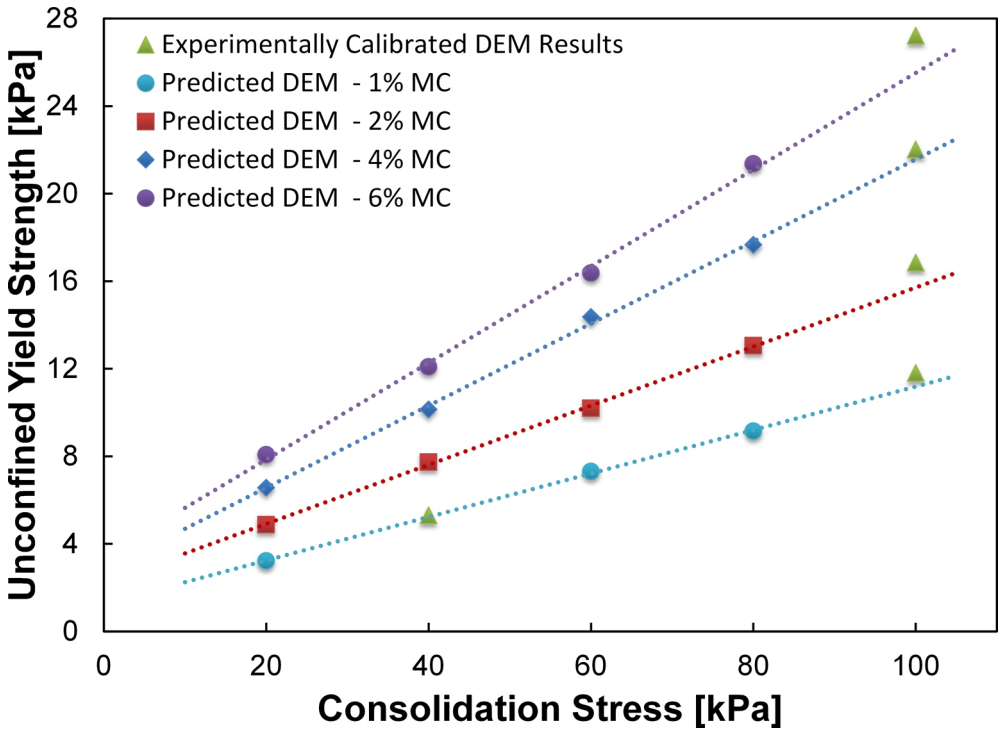

Figure 7.12: Calibrated and predicted DEM simulations - At 100 kPa consolidation stress

the sample consolidation stress increases, the aspect ratio for all samples tend towards a limiting value of the cohesionless fill.

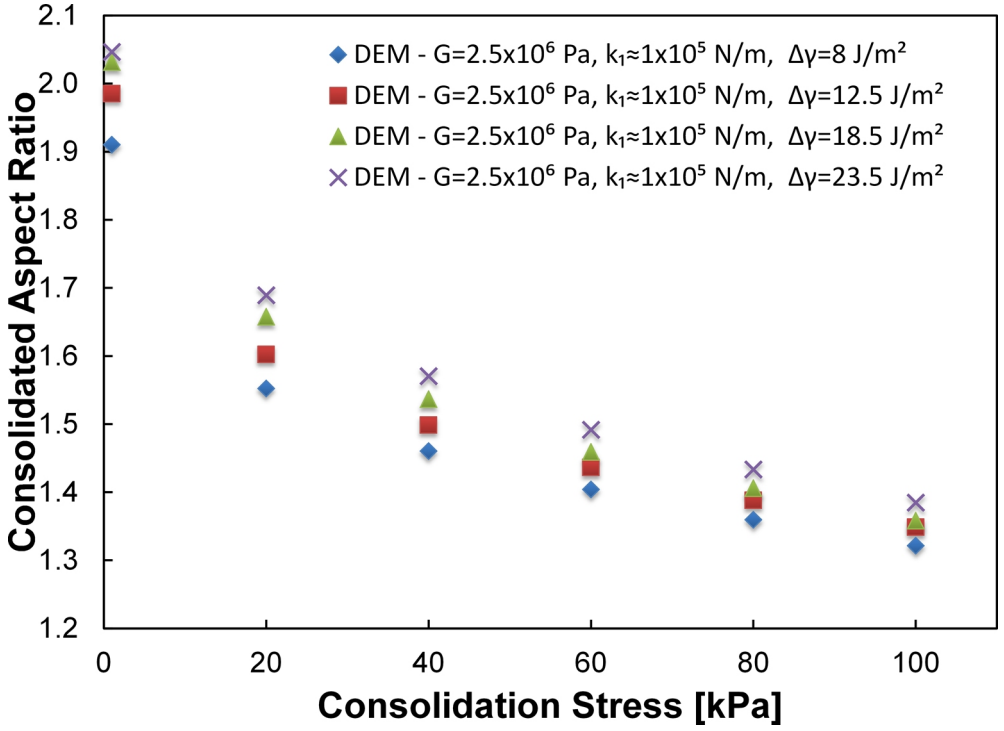

Figure 7.13: Aspect ratio of DEM samples - At varying consolidation stresses

7.3.1 Bulk Density & Bulk Stiffness

The predicted confined stress curves for loading and unloading for all consolidation stresses of the flow function are plotted for an adhesion energy value of 8 J/m^2 and for an adhesion energy value of 23.5 J/m^2 in Figure 7.14. Each sample shares the same initial loading path to the required consolidation before unloading of the assembly to zero stress. The high level of bulk plasticity seen in the experiment is replicated in the DEM simulations due to the large unloading stiffness k_2 used in the simulations.

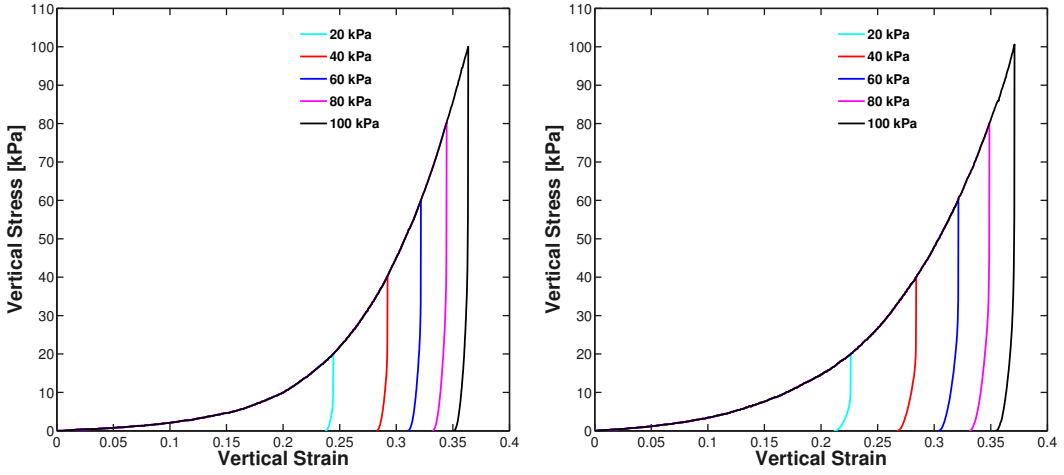

(a) Adhesion energy 8 J/m^2 **(b)** Adhesion energy 23.5 J/m^2

Figure 7.14: Confined stress-strain relationship for DEM simulations - For different adhesion energy values

The level of plastic deformation is consistent for all simulations, with the unloading portions of the stress-strain curves approximately parallel for each simulation. An increased elasticity is visible in the unloading path below approximately 5 kPa. It is possible that this difference at the end of unloading may be explained by the lack of wall friction in the DEM simulation, allowing a greater elastic rebound of the particles compared to the experimental setup where the friction present between the sample and walls prevented such a rebound occurring. While the inclusion of friction between particles and the confining cylinder could help to reduce this discrepancy, it would also have a significant effect on the whole consolidation procedure. The issue could also be remedied by increasing the unloading stiffness k_2, but an unloading stiffness of at least an order of magnitude larger would be required and this would reduce the required computational timestep and thus increase the total run time significantly.

The effect of increasing levels of adhesion in terms of the bulk density is shown in Figure 7.15. The assembly with the highest level of adhesion demonstrates the highest resistance to consolidation and in each case is a more porous assembly with a lower

density. The increased resistance to compression is also supported by Figure 7.16 where the stress strain relationship for increasing adhesion levels at a consolidation stress of 100 kPa is presented. Despite the increased adhesion and lower initial density, a similar peak strain and consolidated strain is found for a lower adhesion energy value and higher density. This is due to the additional resistance to particle movement and re-arrangement provided by the higher adhesive force in the assembly. And while there is a similar trend in the behaviour of both, there is a significant difference in the magnitude of the peak strain at the 1% moisture comparison level where for the experiment there is approximately 15% lower strain required to reach the same consolidation stress.

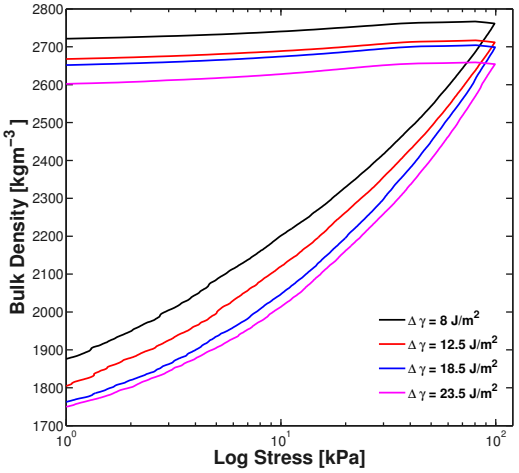

Figure 7.15: Confined Stress-Density relationship for DEM simulations - 100 kPa consolidation stress

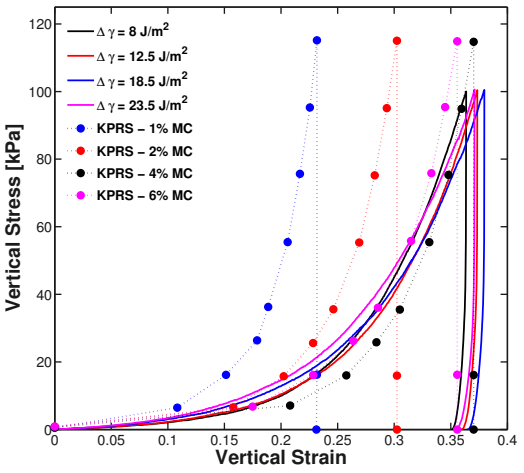

Figure 7.16: Confined stress-strain relationship for consolidation stress of 100 kPa - DEM/Experimental Comparison

A comparison between the DEM simulations and experiments is also made in Figure 7.16 for the consolidation strain. The DEM simulations and experiments both show the same trend in terms of the peak strain during consolidation, with the 4% moisture content sample and DEM equivalent both having the highest peak strain. This difference during consolidation is a result of the compromise made in the selection of the simulation parameters - a low loading stiffness is required to replicate the experimental flow function, but in doing so a softer response was found for the DEM simulations of the lower moisture content. The simulation results had a similar initial softer response to that of the experiment, which became stiffer as the deformation increased.

In Figure 7.17 the consolidated density computed from the DEM simulations is compared with the experimental results. And while much of the consolidation behaviour below approximately 10 kPa is related to the initial packing structure and the rearrangement of the constituent particles, there is good agreement between simulation and experiment. The DEM simulations seem to under-predict the amount of re-arrangement

at 20 kPa with the DEM simulation generally predicting a looser packing. However, in nearly all cases the predicted densities fall within the limits found in the experimental results.

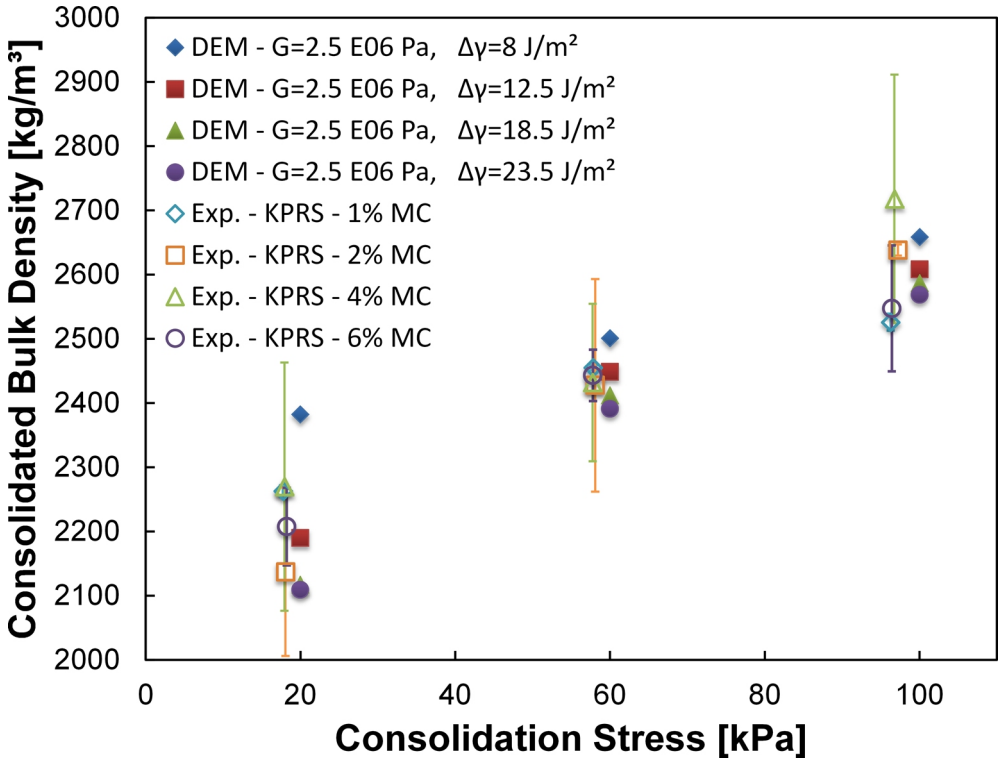

Figure 7.17: Confined stress-strain relationship for consolidation stress of 100 kPa - DEM/Experimental Comparison

7.3.2 Unconfined Yield Strength and Flow Function

The peak strength achieved in each of the simulations is plotted against the consolidation stress giving the flow function in Figure 7.18, with the test results from the EPT also included for comparison. A linear best fit line through the DEM simulation results was found for all adhesion energies.

The DEM results show a strong dependence on the prior consolidation stress applied and are in close agreement with those obtained experimentally from the EPT. Both display a similar linear trend with increasing adhesion. Increasing unconfined strength with increasing levels of adhesion is also found to be similar to the experiment where the increasing moisture content leads to an increased unconfined strength. A better match is found between experimental results for the higher moisture contents and the DEM simulations for higher adhesion energy values, with both producing similar values of unconfined strength. In many cases the DEM simulation result lies within the standard deviations found in the EPT tests. At lower moisture contents the DEM simulation

results are in close agreement with the experiment for higher consolidation stresses but over-predicts the unconfined strength below a consolidations stress of 60 kPa.

Only the adhesion energy value has been modified between the various DEM simulations and this has been shown to be an excellent approximation of the addition of moisture content to the iron ore fines and replicates the experimental flow function.

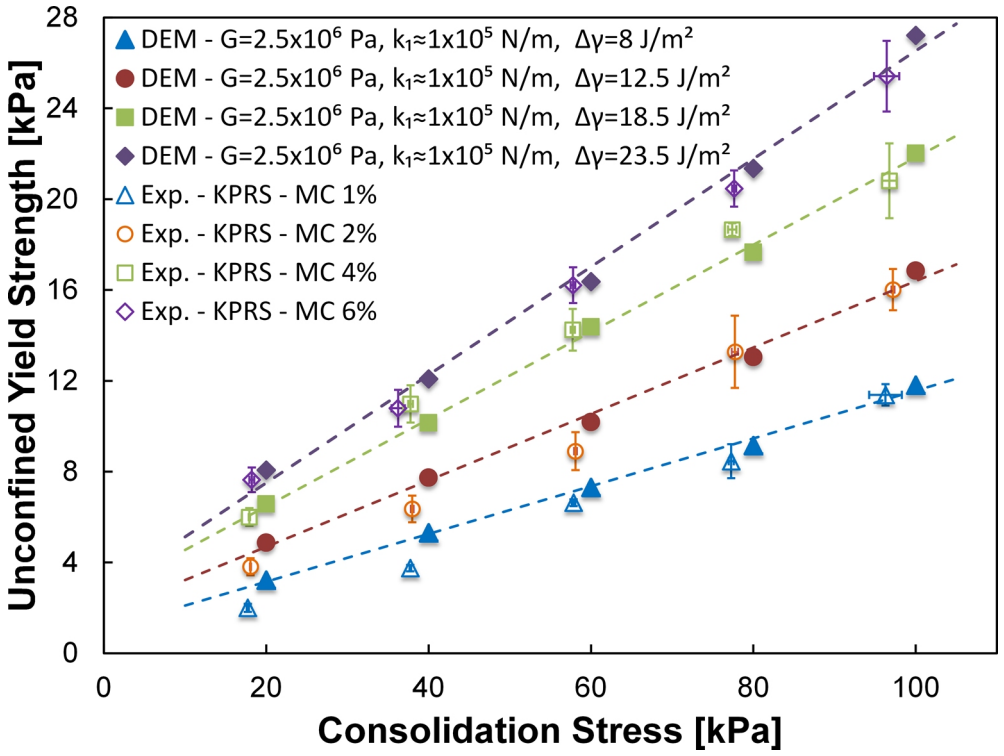

Figure 7.18: DEM flow function comparison with experimental results - Experimental results plotted as open symbols with reliability limits

The unconfined stress-strain behaviour for the DEM simulations is presented in Figure 7.19 for the various levels of adhesion energy used. At higher consolidation stresses the DEM results demonstrate a clear peak value, similar to the over-consolidated behaviour observed in the experiments. However, as the consolidation stress decreases, and the consolidated porosity rises above approximately 40%, the over-consolidated behaviour in the DEM results is lost, leaving only a plateau as the peak values. The observed peak is more visible at lower consolidated porosities (either higher consolidation stress or lower adhesion energy can lead to this) as the dilatency caused during shearing of the sample will be more prominent in a dense packing.

In Figures 7.20 and 7.21 a comparison is made between the DEM and experimental behaviour during the unconfined compression. The DEM simulations provide a much stiffer loading response to failure which gives a peak unconfined strain in the range of

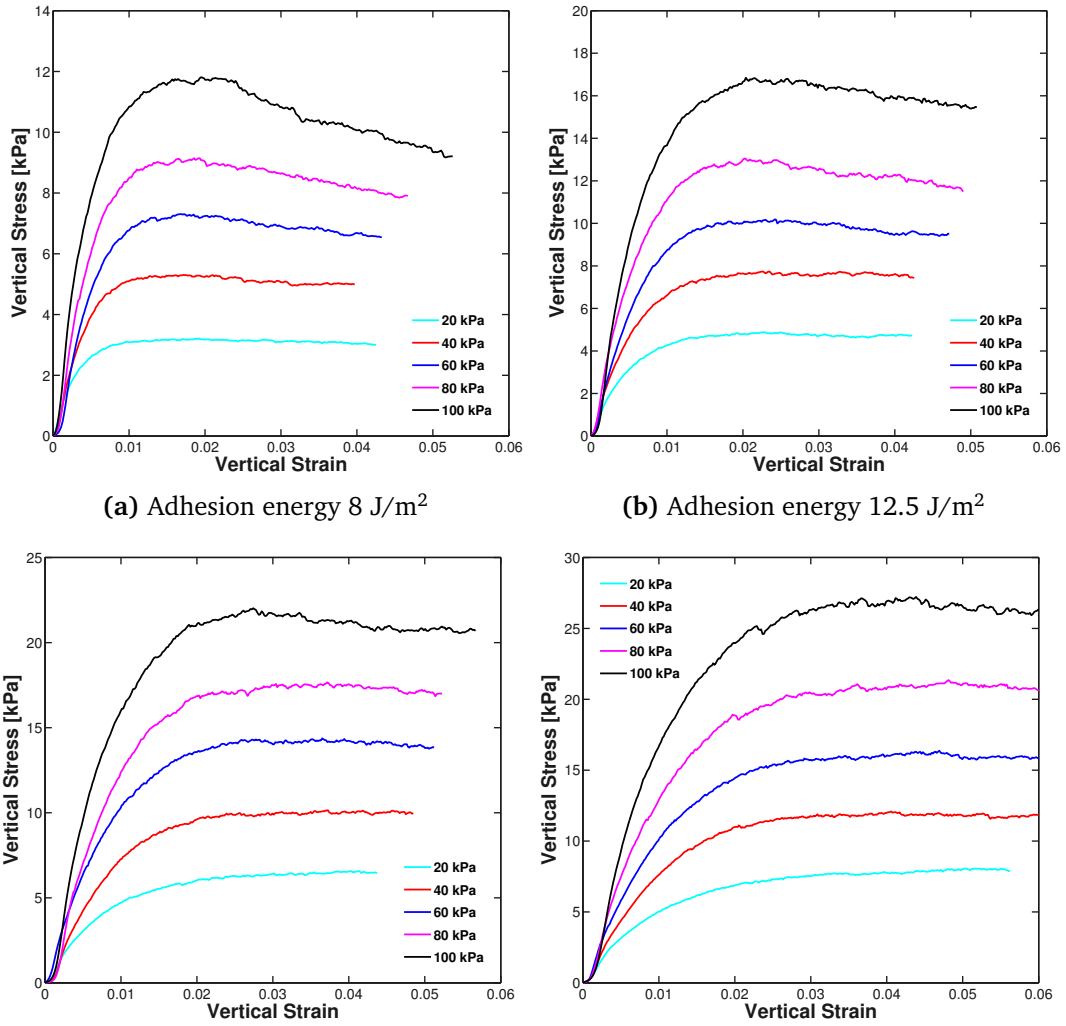

(a) Adhesion energy 8 J/m^2

(b) Adhesion energy 12.5 J/m^2

(c) Adhesion energy 18.5 J/m^2

(d) Adhesion energy 23.5 J/m^2

Figure 7.19: Unconfined stress-strain curves for varying consolidation stress - For all consolidation stresses

1.5 - 3% for the DEM simulations. While the range of peak strains measured experientially varies between approximately 1 - 7%, it is typically in the region of 3 - 6%, as shown in Figure 7.21.

As the sample is in a state of shearing during the unconfined compression, the tangential stiffness and contact model have a significant impact on the result. The tangential stiffness if often not considered when selecting DEM model parameters or is hard-coded into the DEM contact model and not available for modification. In the case of the simulations above, a further reduced tangential stiffness would provide a peak strain more in-line with the experimental values. Another point worth noting is that the peak strain increases with each increase in consolidation stress in the DEM simulations, as each simulation was extracted from the same assembly of particles. It is more likely that the

location of the peak would vary if different assemblies of particles were used, which is the case experimentally where each test is a unique packing.

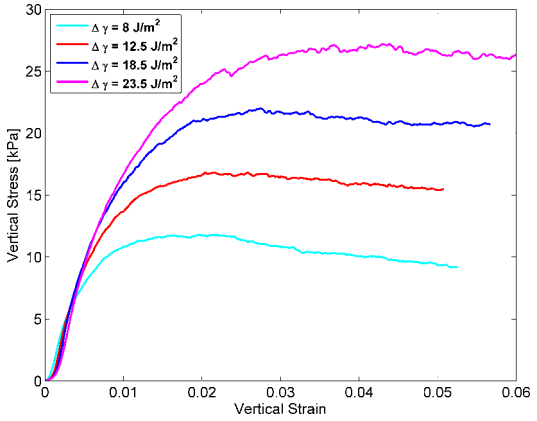

Figure 7.20: Unconfined stress-strain curves for varying $\Delta\gamma$ - DEM Simulation at 100 kPa consolidation stress

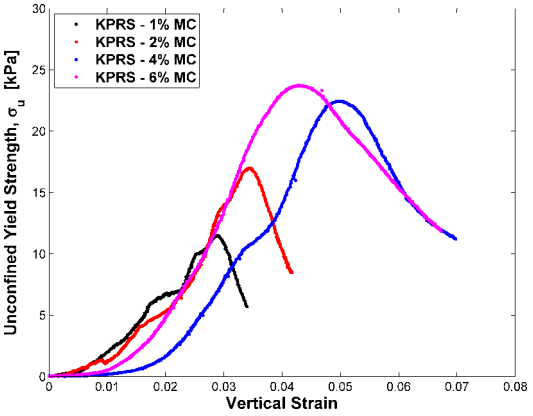

Figure 7.21: Unconfined stress-strain curves for varying moisture content - Experiment at 100 kPa consolidation stress

It is clearly evident that the DEM simulation is not producing the same over-consolidated behaviour as the iron ore fines, which unlike the experiment, reduces with increasing adhesion. It is possible that the mono-sized particles and single shape adopted in the DEM study contributes to this by creating a more homogeneous structure than is observed experimentally. Further study into the effect of particle packing on the post peak behaviour is required.

7.3.3 Lateral Pressure Ratio Comparison

The lateral pressure ratio has been evaluated from the DEM simulations of the experimental flow function and is shown in Figure 7.22. The predicted DEM response is similar to that found experimentally in Chapter 5 where the K_0 value increased during compression until a plateau is reached at high consolidation stresses. Following compression, as the sample is unloaded the lateral pressure ratio begins to rise as the vertical force drops more quickly than the horizontal force, a portion of which remains due to the permanent plastic deformation of the assembly.

The results show a clear trend that is affected by the increasing levels of adhesion where the predicted DEM K_0 values decrease from 0.34 to 0.32 with increasing adhesion. The trend suggests that as the level of adhesion within the assembly increases it is developing greater resistance to particle re-arrangement and preventing the applied load from being transferred horizontally through the particle contacts. This leads to a small decrease in the measured K_0 value.

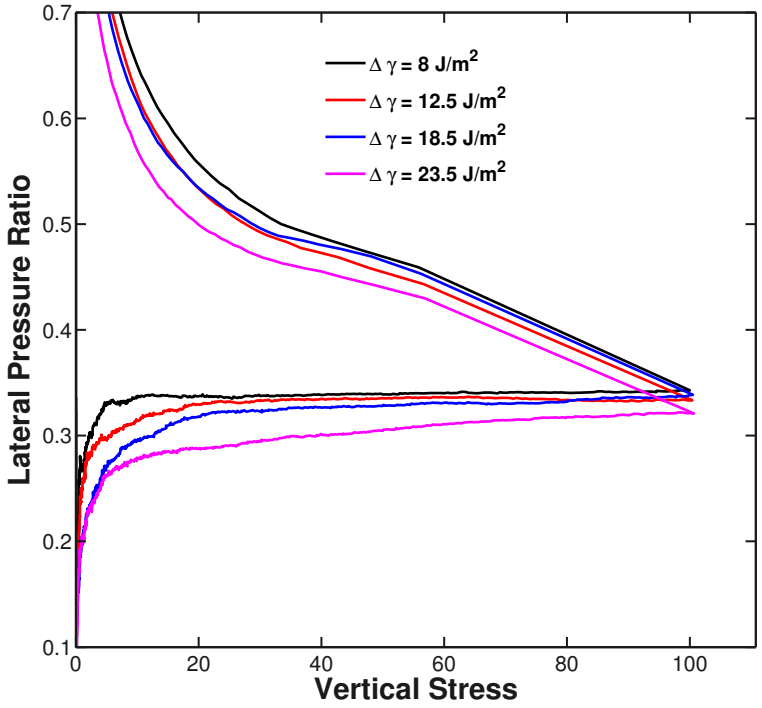

Figure 7.22: Lateral pressure ratio from flow function - DEM Comparison

The DEM simulation predictions are in excellent agreement with the theoretical values using the friction angle measured from the Jenike shear test (Table 7.4). The K_0 value predicted from the DEM simulations fall well within the predicted range based on Eurocode 1 [British Standards Institution, 2006] which is the value normally used for the design of silos and storage structures.

Table 7.4: K_0 values calculated from friction angle

	Moisture Content		
	0.25%	**7.50%**	**8.50%**
Measured Friction Angle	44.5°	42°	41°
K_0 - Jaky Equation	0.299	0.331	0.344
K_0 - Eurocode 1 (Eq. 5.9)	0.329	0.364	0.378

The experimentally measured values remain almost constant between a moisture content of 0-6% at a value of approximately 0.24 before increasing significantly with further addition of moisture content, which acts as a lubricant at such high moisture contents. The experimental values are significantly lower than those predicted by the DEM simulation and theoretical predictions, and were likely affected by the protective sheet. When a correction is applied to account for the protective sheet the experimentally observed values rise to 0.29, which although still slightly lower, is a close match to the DEM predictions.

DEM simulation results are known to be sensitive to the initial packing of the assembly [Chung and Ooi, 2006, 2007] and it is possible that a variation in the predicted K_0 related to the different packings generated at the different levels of adhesion also exists. The porosity of each packing is shown in Figure 7.23 for the entire confined compression of the samples to 100 kPa. The final porosity achieved by each sample mirrors the trends in the final lateral pressure ratio achieved where the lowest adhesion energy produces the lowest porosity which in turn leads to the highest K_0 value. The highest adhesion energy leads to the highest porosity and lowest K_0 value.

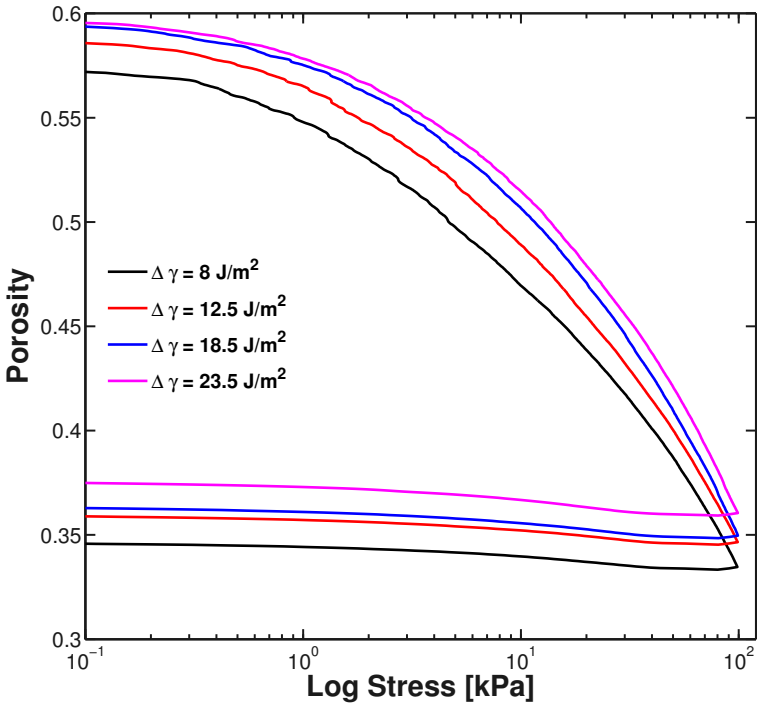

Figure 7.23: Porosity for confined consolidation - DEM Comparison

In the assembly with the highest adhesion energy, the adhesion forces provide greater resistance to the consolidation procedure and a higher final porosity is achieved. While the sample is still being consolidated much of the applied force is being transmitted vertically, whereas at low porosity more force will be transmitted laterally as the particles try to re-arrange.

7.4 Strain Localisation

In soil mechanics when a material fails along a well-defined shear plane, a zone of highly localised shear strain exists, normally across a width of several grain diameters. This is often defined as strain localisation. The formation of shear bands along which a sample fails is an important failure mechanism in granular materials. Studying the

phenomena of shear bands is difficult at an experimental level but DEM simulations are more suited. However more recently the use of x-ray imaging has become a viable option for investigating the internal structure of granular assemblies. Zhou [2010] conducted a detailed study on strain localisation in a bi-axial test with a single layer DEM model. Key micro-mechanical quantities such as void ratio, particle orientation, contact orientation as well as stress and strain were observed and used as markers for investigating the development and location of a shear band in a sheared granular assembly. The approximate shear strains have been calculated based on the relative displacement of the nodes of the coarse-grained mesh and is analogous to the method proposed by Bagi [1996]; Durán *et al.* [2010]. However, as the strain is based on the averaged particle displacement in coarse-grained nodes, the magnitude of the strain computed will be less than that of the actual strain based on individual particles. Due to this, the shear strain is only included to support the predictions of the other interpretation methods.

7.4.1 Experiment

The sample tested in the EPT is compressed between two end platens made of stainless steel. As the sample is compressed between the platens, frictional forces are generated at the ends. If the end friction is large enough this will provide restraint against sliding and lateral expansion. The inclusion of the additional restraint against sliding and lateral expansion causes the sample to develop a secondary shear band with an opposite inclination to the first, resulting in the typical conjugate shear bands seen in many bi-axial and tri-axial tests. The typical failure mode found in the EPT is that of conjugate shear bands (Figures 7.24b and 7.25) due to the end restraint provided by the frictional stainless steel platens.

It should be noted that the failure plane is not always visible in the failed sample, such as shown in Figure 7.24a, where the material bulges, but not much else can be seen. If the outer layers are carefully removed in a manner something similar to Figure 7.25, the conjugate failure planes become easily visible.

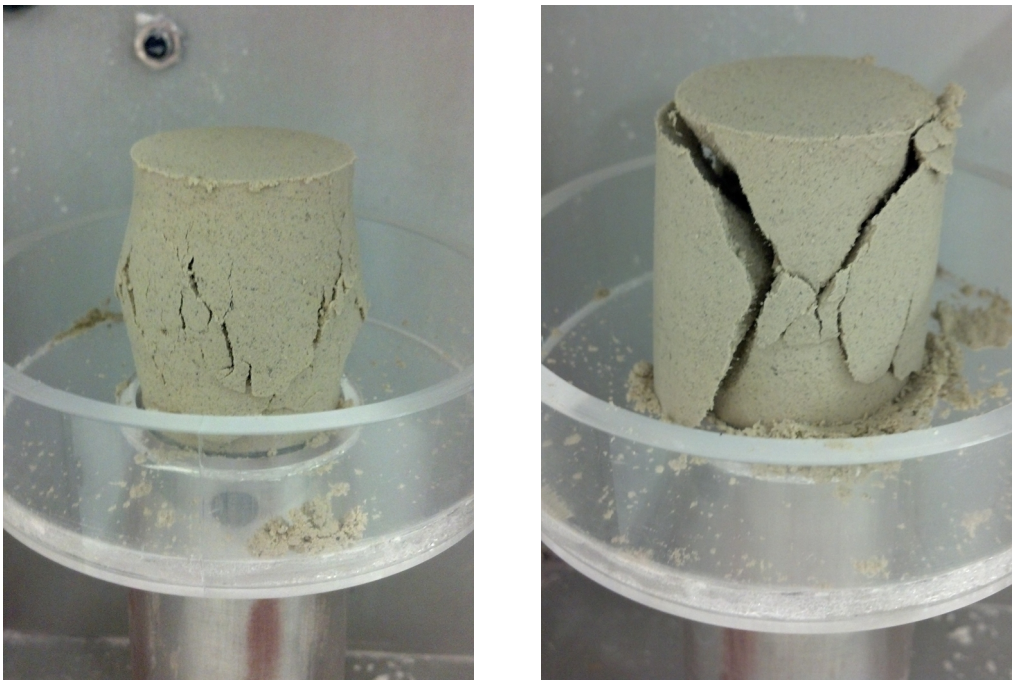

(a) No visible shear planes **(b)** Clear conjugate shear bands

Figure 7.24: Failed sample of Gypsum calibration mix - No visible shear planes

Figure 7.25: Distinctive hourglass failure in granular material - Gypsum calibration mix after outer layer has been peeled back

7.4.2 DEM Simulation

In order to determine whether the shear failure mode of the experiment is being replicated in the DEM simulations, several markers such as angular velocity, cumulative particle displacement and porosity have been used to search for the presence of the shear bands and identify the failure mode.

7.4.2.1 Quasi 2D Problem

Similar to the assembly used by Zhou [2010], a single layer granular assembly is used as an example problem for ease of interpretation and presentation. The 50 mm x 100 mm assembly consists of 6000 poly-disperse spherical particles, with particle size ranging from 0.95 to 1.05 mm and following a normal distribution with a mean diameter of 1 mm and a standard deviation of 0.05. Both the front and rear boundary geometries are frictionless and serve to prevent out-of-plane movement of the particles. A coefficient of friction $\mu_s = 0.5$ is assigned between the particles and the base and top platen. The full simulation parameters are listed in Tables 7.5 and 7.6.

Table 7.5: Planar simulation parameters

Poisson's Ratio, ν	0.3
Shear Modulus, G (Pa)	1×10^{10}
Young's Modulus, E (Pa)	2.6×10^{10}
Particle Radius, R (m)	0.0005
Particle Density, ρ (kg/m^3)	10000
Loading Spring Stiffness, k_1 (N/m)	1×10^3
Unloading Spring Stiffness, k_2 (N/m)	1×10^4
Adhesive Parameter Stiffness, k_{adh} (N/m)	4×10^2
Simulation Timestep (s)	1×10^{-6}

Table 7.6: Interaction properties

Interaction	μ_s	μ_r	**CoR**
Particle - Particle	0.5	0.001	0.4
Particle - Geometry	0.5	0.001	0.4

The single layer model simulation consists of three stages - the initial gravity filling stage to create a random packing structure, the confined consolidation stage where the sample was consolidated to a predefined stress level followed by unloading of the sample and the removal of the confinement, and finally the unconfined compression to failure of the sample at an axial strain rate of 0.05 s^{-1}. The numerical simulation shows a typical shear failure with a conjugate pair of shear bands, which is similar to the experiment and is clearly visible, as can be seen in Figure 7.26.

Particles located within the shear band experience significant rotation during shearing and as such the angular velocity can be used as an indicator of areas where large particle rotations are taking place. Hence, areas such as the shear band can be identified as in Figure 7.27 which shows the location of the conjugate shear bands from Figure 7.26 more clearly. The angular velocities were spatially averaged using a binning technique

where the average angular velocity for a bin of approximately 3 particle diameters was exported from the DEM simulation and contour maps produced. The results have also been temporally averaged over a time period of 0.2s. Zhou [2010] noted that initially particle rotations are randomly dispersed through the assembly but as shear continues the rotations become more prominent and localised in zones of shear develop just after the peak stress is reached. Continued straining of the sample eventually leads to very well structured shear patterns being observed.

Figure 7.26: DEM simulation with shear planes - Sample after peak UC strength

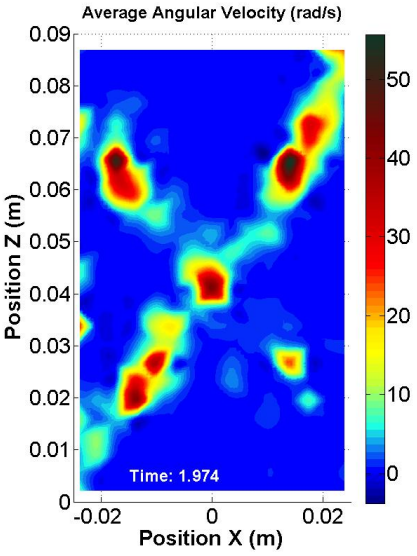

Figure 7.27: Average angular velocity at peak unconfined stress - Sample after peak UC strength

The development of the shear planes in demonstrated in Figures 7.28 and 7.29 through the visualisation of the cumulative displacement of the particles in the assembly. The magnitude of the vectors represents the magnitude of the displacement of the particle and is also colour coded using the same criteria, where red represents the largest displacements.

As the sample undergoes loading the particles at the bottom are restrained from movement by the bottom platen causing particles to move about this bottom wedge. This leads to the initialisation of a shear plane passing from opposing corners. As the sample reaches the peak unconfined strength in Figure 7.28c a shear plane is clearly visible as the top left corner of the sample attempts to move as one. Further loading past the peak strength leads to the development of the conjugate shear bands shown in Figure 7.26 and Figure 7.27.

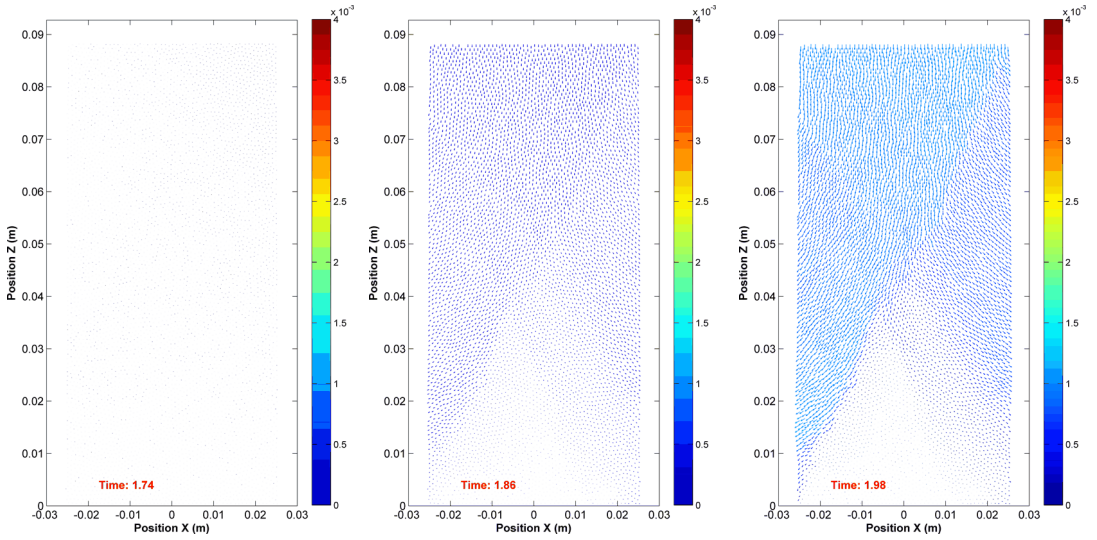

(a) Start of compression **(b)** Shear plane beginning to develop **(c)** Shear plane developed from bottom left to top right

Figure 7.28: Shearing of assembly during unconfined compression - Pre-peak unconfined strength

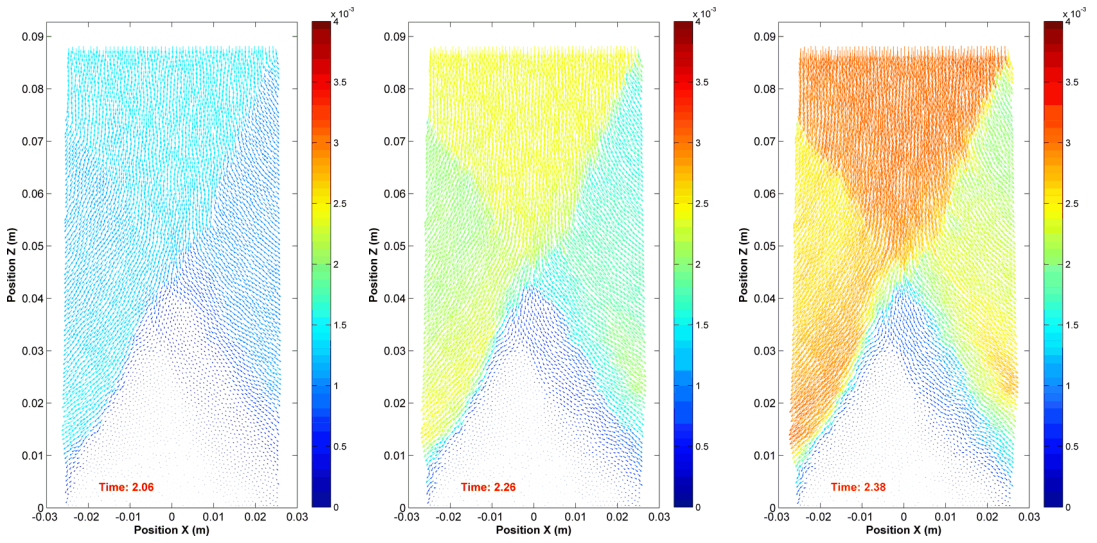

(a) Development of conjugate shear band **(b)** Continued shearing of sample **(c)** Final state as show in Figure 7.26

Figure 7.29: Shearing of assembly during unconfined compression - Post-peak unconfined strength

A single layer planar model makes the process of identification of the shear bands more straight-forward as it limits particle movement to just two directions with all particle interactions occurring on a single plane. In multi-layer models the view may be hindered by the presence of the additional particles and while particle displacements are still restricted in one direction, contacts are now happening in three dimensions making visualisation of the data more difficult.

7.4.2.2 Planar 3D Simulations

Even in an assembly of particles that is just a few particles thick the dilation that is occurring during shearing can be lost through interactions with particles in three dimensions instead of two. Figure 7.30a shows a planar simulation that is similar to the single layer model with the exception of the additional depth of the model. The simulation now contains approximately 50,000 particles with a depth of five particle diameters. Looking at the final assembly for the planar model (Figure 7.30b) it is no longer obvious whether or not the sample has failed in shear as the additional layers of particles obscure the areas where dilation of the sample has occurred. By using the coarse graining method of analysing data it is possible to determine the failure mode within the 3D assembly. A coarse graining radius of 3R has been employed with the *Heaviside* coarse graining function [Babic, 1997; Goldenberg and Goldhirsch, 2002; Goldhirsch, 2010].

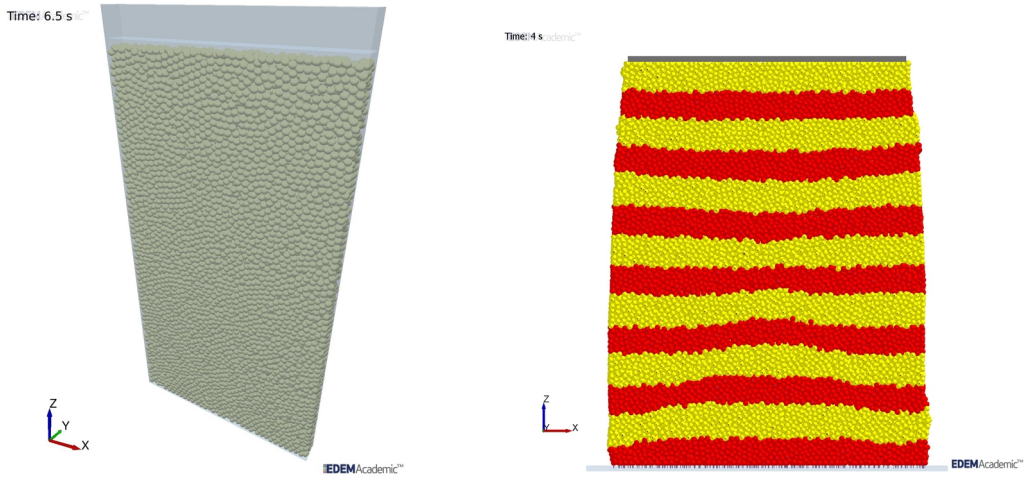

(a) Initial assembly **(b)** Sample after peak UC strength

Figure 7.30: DEM planar simulation 3-5 particles thick - With frictionless front and back walls

Again by looking at the angular velocity as in Section 7.4.2.1 for a single layer model, in this case using a time-averaged magnitude of 0.1s, and searching for areas of high particle rotation it is possible to find a zone of local shearing, such as in Figure 7.31 where the conjugate shear bands are visualised in 3D at two different timesteps post-peak in the simulation. The results show that in 3D simulations shear failure of the sample is still predicted and can be identified with the correct parameters over a suitable time scale, even where particle movements are not restricted.

It is possible to identify the location of the shear band from several different parameters, such as local void ratio, cumulative displacements stresses and strains, however not all of these will be applicable in every case. For example, cumulative displacements

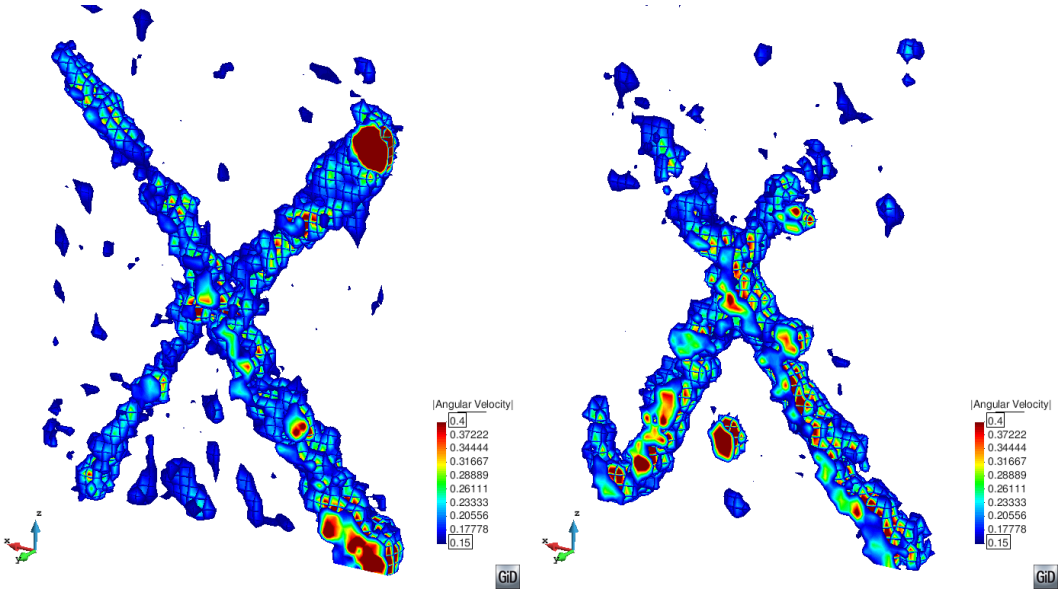

(a) t = 1.9sec - Post-peak **(b)** t = 2.2sec - Post-peak

Figure 7.31: Shear failure planes located from angular velocity in planar simulation - Progressing corner to corner

are well suited where the number of particles remains constant but will struggle in simulations where the particle numbers fluctuate, either due to particles leaving the system or through new ones being created. In relatively densely packed assemblies (approximately < 45% porosity) it is possible to use the local voidage developed in the shear zones from the dilation that occurs. Zhou [2010] noted that the void ratio found within the shear band was significantly higher than when compared to the rest of the assembly, approximately 7.5% greater in cases with low contact friction and up to 30% greater for non-spherical particles with high contact friction.

The solid fraction is presented Figure 7.32 and shows that there is a lower solid fraction (approximately 20 - 30% lower than the rest of the assembly) in a band that runs from the bottom left corner to the top right corner. The reduced particle density is a likely result of the dilation that is occurring in the shear band of the assembly. This is supported by Figure 7.33, at the same timestep, which is the angular velocity of the particles in the assembly. It is generally accepted that particles located in the shear band undergo larger rotations than particles elsewhere in the assembly. The band of high rotational velocity ties in with the area of lower solid fraction. The angular velocity also highlights the possible location of the secondary conjugate shear band forming from the bottom right corner towards the centre of the assembly.

The cumulative particle displacement from the start of the unconfined compression is presented in terms of the vertical displacements and horizontal displacements in

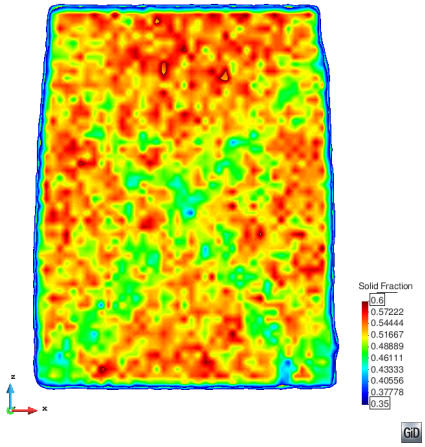

Figure 7.32: Solid fraction in planar simulation - Progressing corner to corner

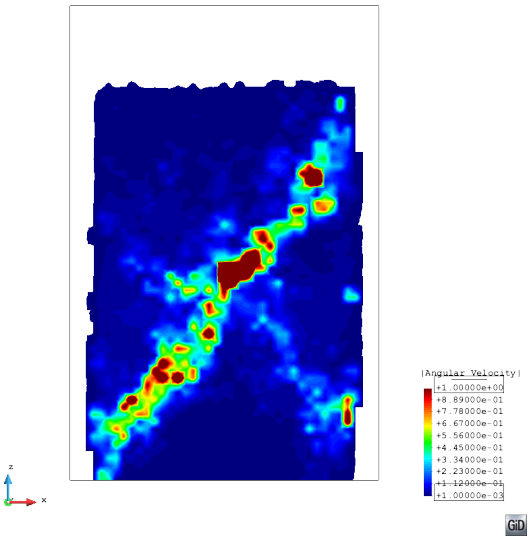

Figure 7.33: Angular velocity in planar simulation - Progressing corner to corner

Figure 7.34. The zones of relative movement of the particles are highlighted and an hourglass type pattern of movement is seen, which is similar to that of a single layer model shown in Figures 7.28 and 7.29.

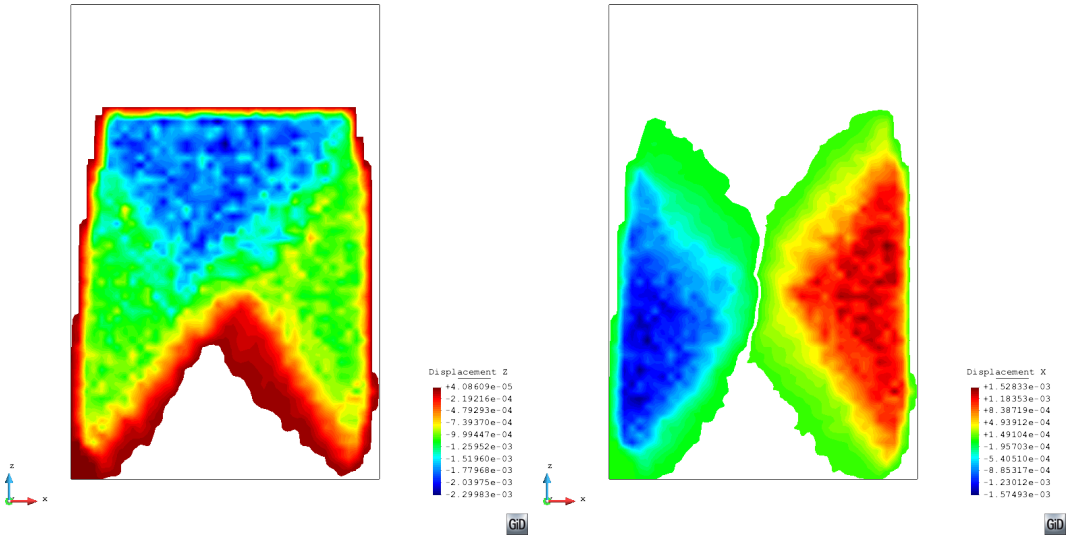

(a) Vertical particle displacement **(b)** Horizontal particle displacement

Figure 7.34: Cumulative displacement of particles in planar simulation -Development of conjugate shear bands

The vertical and horizontal components of particle velocity are shown in Figure 7.35 for the sheared assembly of particles. The vertical component of velocity shows a shear plane that has developed from the bottom left corner to the top right corner with the upper section moving as a single mass. While this section moves along a single shear

band a second conjugate band can been seen forming from the bottom right corner of the assembly. At the very bottom of the assembly a wedge of particles where movement is restricted by the geometry is formed. However, there is a clear conjugate shear band forming as the particles on the right side move away. This agrees well with the angular velocity (Figure 7.33) which displays a major shear plane from the bottom left to top right corner of the assembly, with a conjugate shear band beginning to appear from the bottom right corner.

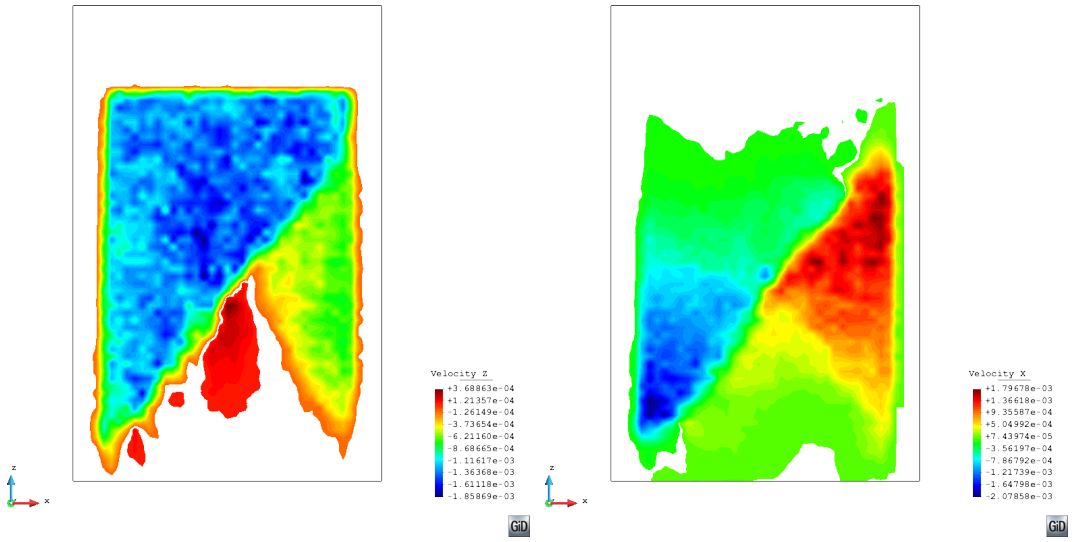

(a) Vertical velocity Z **(b)** Horizontal velocity X

Figure 7.35: Particle velocities in planar simulation - Development of conjugate shear bands

These simple planar simulations have shown that the EEPA contact model has the ability to reproduce the shearing behaviour that is the common failure mechanism seen in the uniaxial experiments. It has also been shown that for a simulation that is several particles thick it is possible to identify and locate the shear failure zones in the simulation.

7.4.2.3 3D Uniaxial Simulations

The simulations in the previous section all had frictionless walls, both front and back, which even in the case of the planar simulation that was several particles thick, partially restricted movement in the y-direction in the simulation, which guides the direction in which particles can move, helping to emphasise the shear zones.

In a full 3D simulation, such as the cylindrical assembly used to replicate the uniaxial tests, there is no solid boundary to restrict the particle movements. In such cases there is the possibility that no shear zone will exist, or that it may not be possible to detect it.

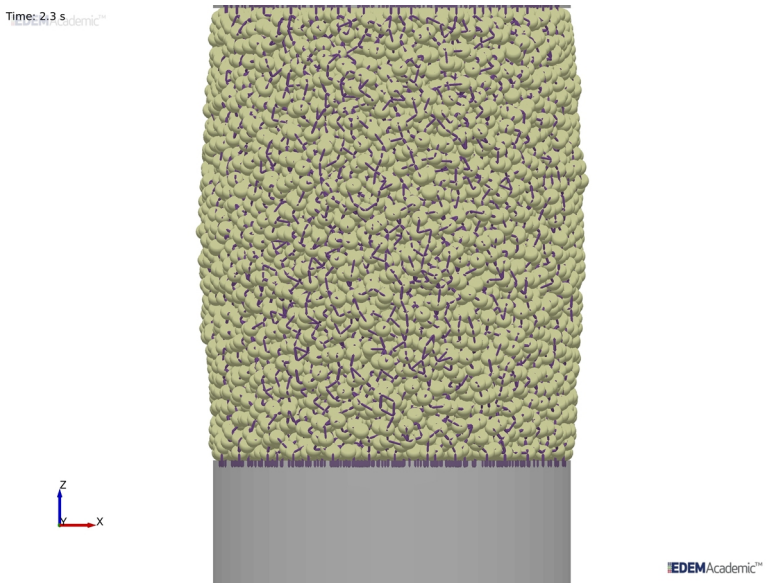

Figure 7.36: DEM simulation from iron ore fines flow function simulations - Consolidated at 100 kPa with an adhesion energy of 8 J/m^2

The uniaxial simulation, consolidated to 100 kPa with a $\Delta\gamma$ of 8 J/m^2, which was used to predict the flow function in Figure 7.18 is shown in Figure 7.36. The stress-strain relationship for the failed sample is in Figure 7.19a. On first viewing there is no obvious indication of the failure of the assembly of particles, other than a bulging of the assembly in the middle. However, by using the coarse graining method of analysing data it is possible to determine the failure mode within the 3D assembly. A coarse graining radius of 2.5R has been employed with the *Heaviside* coarse graining function [Babic, 1997; Goldenberg and Goldhirsch, 2002; Goldhirsch, 2010]. Two orthogonal cuts are made through the assembly of particles: one on the XZ plane and another on the YZ plane. All results have been temporally averaged over 0.1s. The results shown in Figures 7.37 to 7.40 are all from the same post-peak timstep for the simulation shown in Figure 7.36.

The horizontal displacements on both of these planes are shown in Figure 7.37. Similar to the planar simulation a clear distinction exists in the particle movements during unconfined compression, with an hour-glass pattern evident, suggesting the presence of developed shear bands.

The angular velocities in the assembly are shown in Figure 7.38. Areas of high rotations were found to exist along zones that run between the opposing outer edges of the assembly. This is a result of the dilation that occurs in the area of shearing, particularly when non-spherical particles are used. However, the result is not as clear as for the simple planar simulations where particle movement was restricted to just two planes.

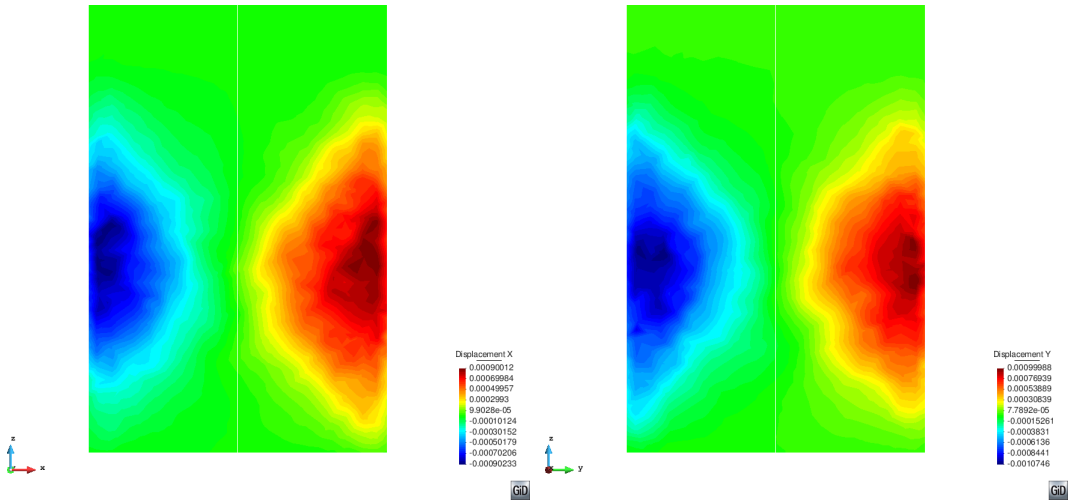

(a) On XZ plane **(b)** On YZ plane

Figure 7.37: Cumulative horizontal displacement for 3D cylindrical assembly - Post peak

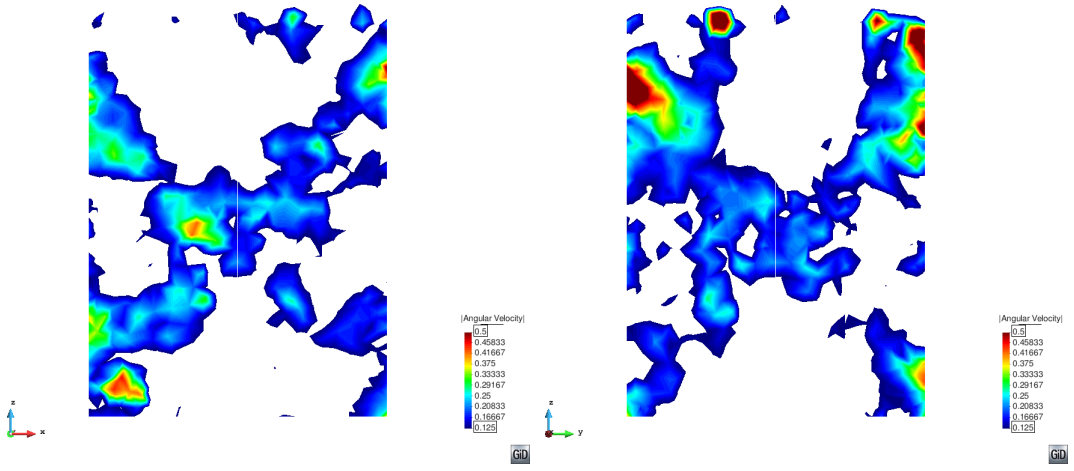

(a) On XZ plane **(b)** On YZ plane

Figure 7.38: Angular velocity for 3D cylindrical assembly - Post peak

Together with the shear stresses shown in Figure 7.39 and the approximate shear strains in Figure 7.40 a clear picture on the particle behaviour during unconfined compression can be obtained. Despite the computed strains being approximate, there is still clear indication of the conjugate shear bands appearing in the DEM simulation. Following the peak strength being reached in unconfined compression, the development of the shear bands in the assembly becomes more evident.

In a similar manner to the experiment where the shearing behaviour in the material is not always obvious until the sample is removed to reveal the typical "*hourglass*" failure mode, it is not always possible to visually see the shear bands in the DEM simulation

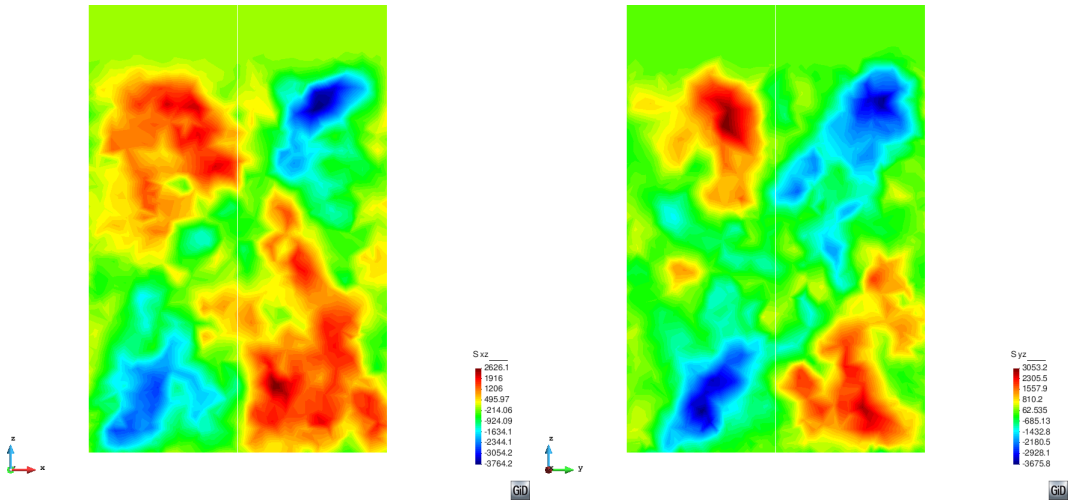

(a) On XZ plane **(b)** On YZ plane

Figure 7.39: Shear stress for 3D cylindrical assembly - Post peak

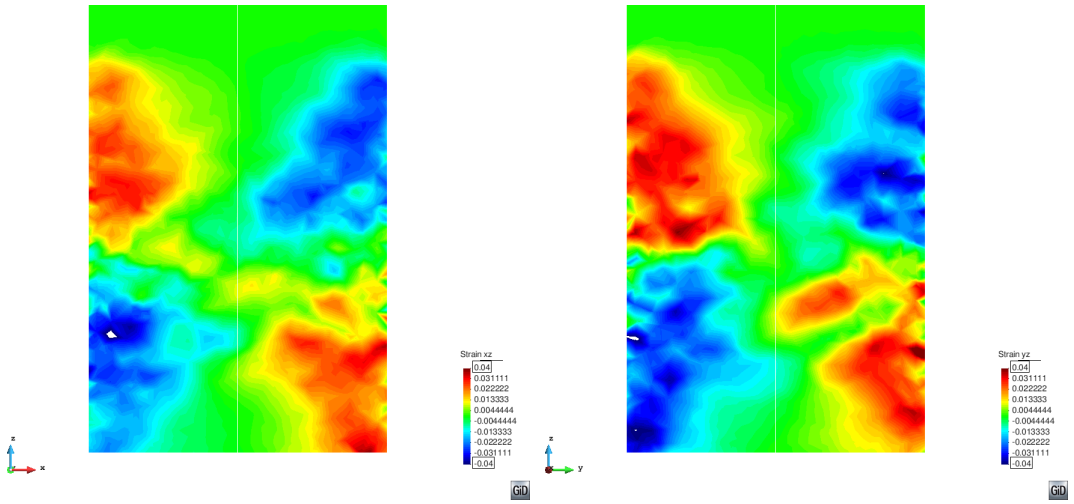

(a) On XZ plane **(b)** On YZ plane

Figure 7.40: Approximate shear strain for 3D cylindrical assembly - Post peak

without stripping away the outer layers of the assembly of particles. By looking at slices through the particle assembly it is possible to isolate the shear band through a number of markers and confirm the existence of shear bands in the DEM simulation.

7.5 Summary

The EEPA contact model has been used to predict an experimental flow function of KPRS iron ore fines. The contact model has demonstrated the ability to capture the stress history dependent behaviour that exists in cohesive granular solids.

The DEM simulations have been calibrated from a selection of uniaxial experiment results and the remainder have been used for comparison with the DEM simulation predictions. The friction parameters have been selected based on the measured bulk friction angle from the Jenike shear angle and the reported relationship between particle shape, contact friction and bulk friction. An attempt has been made to match the loading and unloading stiffness values that have been measured experimentally from confined compression tests. The iron ore particles require a high virgin loading stiffness for a close match between the DEM simulation and measured values. However such a loading stiffness has been shown to be unable to provide a matching flow function and a lower stiffness has been selected to allow a closer match to the experimental flow function.

With a sufficiently low loading stiffness used, the DEM simulations provide a very close match to the experimental flow functions, with the predicted unconfined strengths found to be within the standard deviations of the experimental results. The DEM simulations also predicted densities similar to those found experimentally, although the unconfined loading stiffness and resulting stress strain relationships have not been matched in a compromise to predict the material flow function. Experimental results display a clear over consolidated behaviour across all consolidation stress and levels of cohesion tested, however the DEM simulations only predict the over-consolidation in cases where the porosity of the sample is below a porosity of approximately 45%. The failure of the DEM simulations to predict the over consolidation behaviour may be related to the homogeneity of the DEM assemblies where a uniform particle size and shape has been used. The introduction of different particle size and shape would lead to a greater variety and distribution in the calculated contact forces and may lead to a more brittle failure mode as seen in the experiment as the anisotropy of the packing would increase.

Investigations into the failure mode predicted by the DEM simulations shown that the samples are failing from the development of shear planes similar to those observed experimentally. The shear failure has been detected in simple single layer planar simulations and larger full 3D simulations of a cylindrical sample through the use of such indicators as cumulative particle displacements, particle velocity and angular velocities which are an indicator of particle rotations.

Chapter 8

Application of Edinburgh Elasto-Plastic Adhesive Contact Model for DEM Simulations

In this chapter the Edinburgh Elasto-Plastic Adhesion [EEPA-NL] contact model is used to carry out DEM simulations of a flat bottomed silo during discharge, across a spectrum of adhesion energy values. The level of adhesion in the system in increased incrementally from cohesionless until flow is completely retarded by the levels of adhesion in the system.

Rather than a validation study in comparison to a full scale model, this study serves as an exploration of the effect of adhesive forces on the discharge process and an assessment of the capability of the contact model to qualitatively predict the phenomena that are present in the discharge of a silo. A flat bottomed silo has been chosen due to its simplicity and ease of comparison to theories such as Janssen's wall pressure theory and Beverloo's discharge theory.

8.1 DEM Implementation of Model

While it is not possible or feasible to conduct a DEM study of a full scale silo, it is important that any simplifications and scaling applied to the model do not affect the results. The objective of this study is not to replicate any particular material, and as such, a set of particle parameters has been chosen arbitrarily.

A particle aspect ratio of 1.5 has been chosen to better represent a real granular solid as opposed to using spherical particles with large rolling friction values, which may

still undergo large rotations which are unrealistic. A particle radius of 2mm has been selected to provide multi-sphere particles that are approximately 4mm x 6mm in size. Reduced particle stiffness has been utilised to reduce the computational timestep required for the simulations. Particle-particle friction has been set to a value of 0.5 as low friction values of less than approximately 0.2 lead to the situation where discharge rates becomes dependent of the fill height of the assembly [Anand *et al.*, 2008; Ketterhagen *et al.*, 2009]. Particle-Wall friction has been set to a value of 0.5, as parameters measured from the Jenike shear test may be significantly lower than those actually developed in the actual silo [Härtl, 2008]. The coefficient of restitution has been found to have negligible effect on silo discharge and a value of 0.5 has been selected. A small amount of rolling friction of 0.005 has also been included.

In order to represent a real silo, periodic boundaries have been applied to allow free movement of the particles in all directions during discharge. The periodic boundaries should be more representative of the behaviour of a real silo than a model with rigid walls. In order to avoid the effect of particles interacting with themselves or having an unwanted effect on itself, a sufficiently large distance is required to prevent this. The periodic boundaries have been spaced such that the thickness of the simulation is between 4-6 particle diameters. In order to avoid any mechanical arching around the outlet, an opening width of approximately 12-15 particle diameters has been utilised. The ratio of the opening width to the total silo width has been set at 0.2. The final model silo dimensions are 0.85m tall by 0.3m wide. The model silo has a depth of 0.025m between periodic boundaries with an opening width of 0.06m which is located centrally for the whole depth of the slice. The number of particles used to fill the model silo is slightly under 61,000 particles after the top surface has been levelled by removal of some particles.

The filling of the sample took place using a centrally located dynamic factory that filled the assembly under normal gravity over a period of 1.5s, before settling for a further second. The sample was initially filled in the absence of cohesion. The same assembly of particles was then used with varying levels of adhesion energy to avoid any effects that may develop from different assemblies. The filling process is illustrated in Figure 8.1 and is similar to a central filling that may occur in a full scale industrial silo. The resulting filled assembly is shown in Figure 8.2. By implementing a gravity fill method a more realistic packing structure will be formed than that of an *en-masse* generation scheme, which places all particles at once. Typically, an *en-masse* method will hinder the arching and development of friction that is necessary to successfully predict the real life situation.

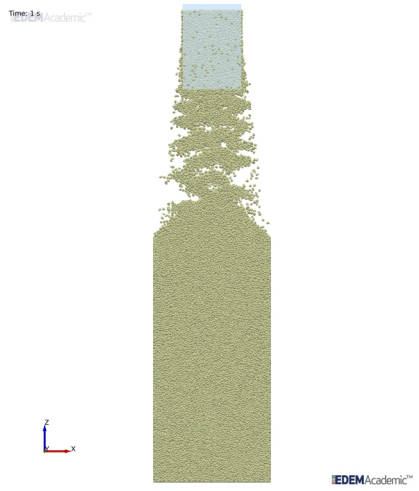

Figure 8.1: Initial filling of silo assembly - Concentric Filling

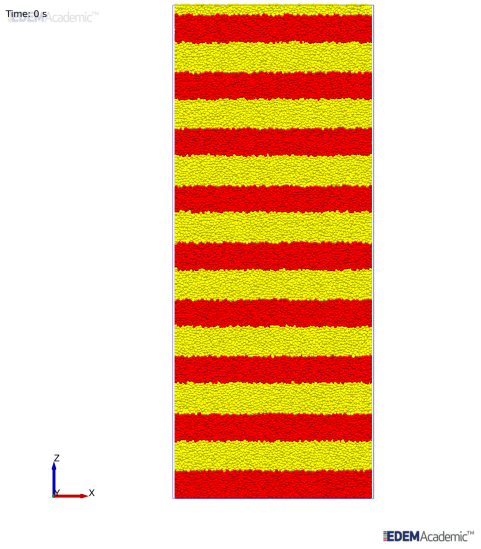

Figure 8.2: Initial assembly of particles before discharge - Adhesion energy 0 J/m^2

The full set of parameters used for the simulations are given in Table 8.1. A simulation timestep of 5×10^{-6}s, which is approximately $0.075\sqrt{m/k}$ has been selected for all simulations. Data is recorded for each simulation at a frequency of 100Hz. The post-processing of the simulations has been carried out using the P4 post-processing toolbox. A coarse graining radius of 2.5R has been employed with the Heaviside coarse graining function [Babic, 1997; Goldenberg and Goldhirsch, 2002; Goldhirsch, 2010].

Table 8.1: Simulation parameters

Parameter	Value	Parameter	Value
Particle Radius, R (m)	0.002	Poisson's Ratio, ν	0.25
Particle Aspect Ratio, AR_p	1.5	Adhesion Energy, $\Delta\gamma$ (J/m^2)	0,5,10,12.5,15
Particle Density, ρ (kg/m^3)	5400	Particle Sliding Friction, μ_s	0.5
Young's Modulus, E (Pa)	1.25×10^8	Particle Rolling Friction, μ_r	0.005
Shear Modulus, G (Pa)	5×10^7	Wall Friction, μ_{wf}	0.5
Spring Stiffness, k_1 (N/m)	3×10^6	Base Friction,μ_{bf}	0.5
Spring Stiffness, k_2 (N/m)	7.5×10^7	Simulation Timestep (s)	5×10^{-6}

The contact orientations that results from the generation scheme and periodic slice set-up is presented in Figure 8.3 in terms of the horizontal (Azimuth) and vertical (Elevation) orientation of the contacts. The initial assembly consists of approximately 61,000 particles which generate approximately 205,000 particle-particle contacts. This gives the assembly a co-ordination number of 6.7. A bin size of 5° has been used in the contact orientation plot. As there are two contact vectors per contact, the contact

orientation plot is symmetrical for both azimuth and elevation angle. Figure 8.3 shows that the contacts are not uniformly distributed horizontally and have a preferential orientation in the y-direction, which in the direction of the periodic slice boundaries. As the silo is filled concentrically under gravity, there is a preference towards vertical contacts with a reduction in the number of vertical contacts less than 30°.

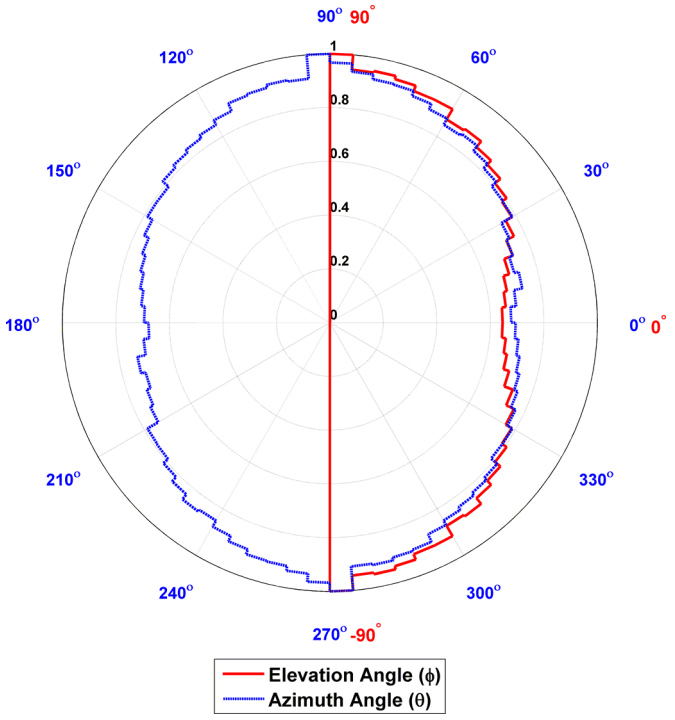

Figure 8.3: Contact orientations for periodic slice assembly - Before discharge, $t_d = 0s$

8.2 Flow Patterns

Typically during discharge one of the three key types of flow modes will develop - mass flow, mixed flow or funnel flow. In the case of DEM simulations the flow mode can often simply be determined from a visual inspection of the particle movements. To better visualise the flow patterns in the silo during discharge, particles have been coloured in alternating layers to highlight any flow patterns more easily.

8.2.1 Cohesionless System

The initial particle assembly before discharge begins is shown in Figure 8.4a and flow commences. As the flow progresses a mixed mode of flow can be seen developing in Figure 8.4 at various times from the beginning of discharge, t_d. In the upper section of the silo the flow mode is mainly mass flow, whereas due to the flat bottom a flow channel develops from the opening at approximately 45° towards the silo walls.

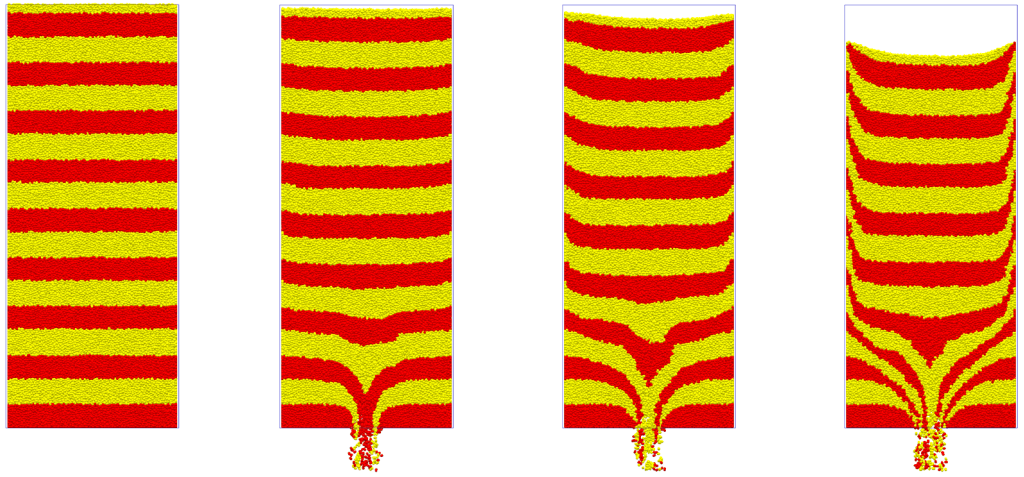

(a) $t_d = 0$s **(b)** $t_d = 0.5$s **(c)** $t_d = 1$s **(d)** $t_d = 2.5$s

Figure 8.4: Initial stages of discharge for cohesionless particles

Studies carried out by Munch-Andersen [1986] using grains found that a boundary layer of particles is observed near the silo wall while the material is discharging from the silo. The thickness of the layer observed was found to vary with the roughness of the wall, with rougher, more frictional surfaces leading to a thicker layer. A detailed experimental study on the discharge of sand from a silo Munch-Andersen *et al.* [1992] also documented the same effect (Figure 8.5).

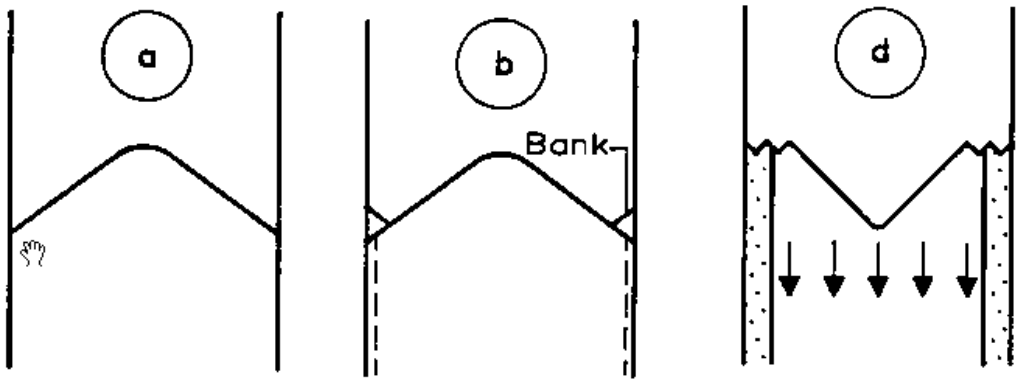

(a) Initial Shaped Surface **(b)** Development of "Bank" **(c)** Final Stages

Figure 8.5: Experimental observation of the development of a boundary layer - After Munch-Andersen *et al.* [1992]

The boundary effect of wall friction is also seen in the DEM simulation results, in which a layer of slow moving particles approximately 5-10 particles thick exists. Due to the larger particle size of the DEM particles, the effect is more obvious but nonetheless displays the same trends as seen in the experiment, with the formation of a bank starting to develop in Figure 8.4d and more prominent in Figure 8.6a.

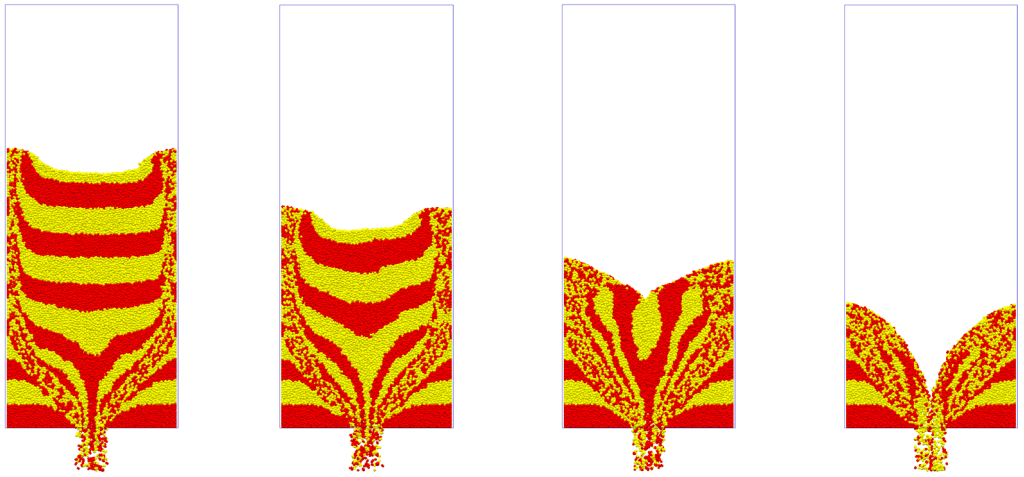

(a) t_d = 7.5s **(b)** t_d = 10s **(c)** t_d = 12.5s **(d)** t_d = 15s

Figure 8.6: Continued discharge for cohesionless particles

The surface profile remains relatively unchanged initially, but as the simulation progresses; the effect of the faster flow in the centre leaves a more pronounced dip in the centre of the surface profile, similar to what was reported by Munch-Andersen *et al.* [1992], in Figure 8.5c. Throughout discharge there is a stagnant zone on each side of the outlet which remains once discharge has ceased. Dead zones such as these are commonly found in flat bottomed hoppers and can cause problems for materials that expire with time. The features found in the DEM simulations are also well described by the kinematic model for solid flow in flat bottomed hoppers by Zhang and Ooi [1998].

8.2.2 Effect of Cohesion in a System

There are some important differences in the flow patterns as the level of adhesion increases in a system. In a system where very high levels of cohesion were applied, both blockage of the silo and a ´´*no-flow*`` case were found to occur. At the highest adhesion energy studied, a complete blockage with no discharge was found to be the case (Figure 8.7) as the amount of adhesion lead to a permanent cohesive arch forming over the outlet of the silo, allowing only a few particles exit the outlet. Due to this, no further comparisons for discharge can be made for the highest level of applied adhesion energy in this study.

A comparison is made between the remaining four adhesion energy levels, from cohesionless to highly cohesive, in Figure 8.8. While there appears to be very little visible differences between cohesionless and an adhesion energy $\Delta\gamma$ of 5 J/m^2, as the level of adhesion increase further some differences become visible. The additional adhesion energy acts as a retardant to the initialisation of flow. In the cohesionless case, particles

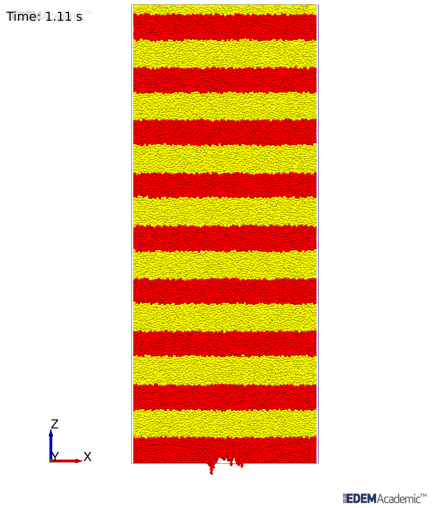

Figure 8.7: End of Discharge for an adhesion energy = 15 J/m^2 - at $t_d = 1.11s$

in the 7th layer are already beginning to move while at an adhesion energy of 10 J/m^2 the flow has already been limited to just the third layer. At an adhesion energy of 12.5 J/m^2 a temporary cohesive arch has formed preventing discharge for a short period.

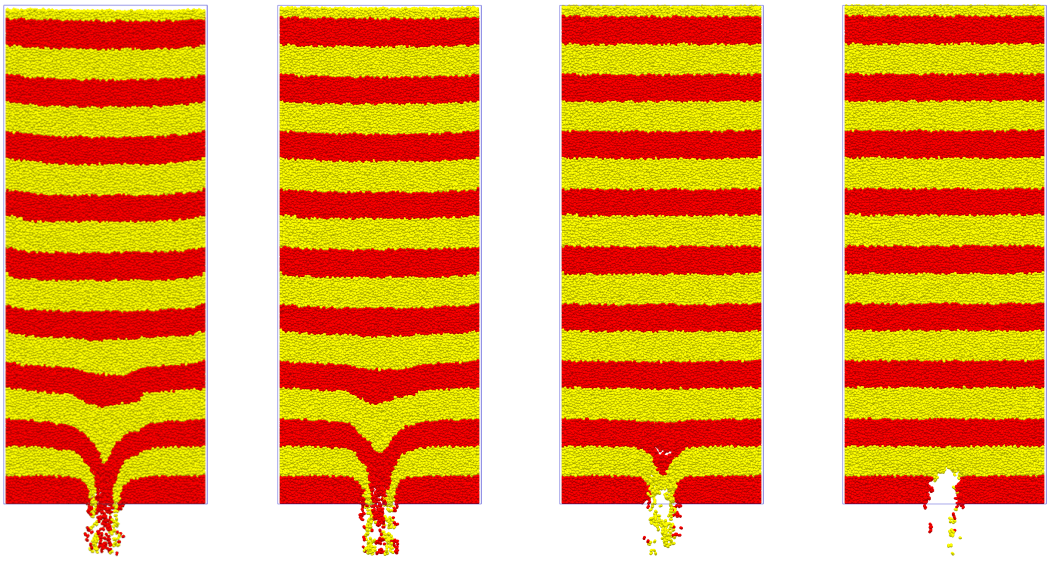

(a) $\Delta\gamma = 0J/m^2$ **(b)** $\Delta\gamma = 5J/m^2$ **(c)** $\Delta\gamma = 10J/m^2$ **(d)** $\Delta\gamma = 12.5J/m^2$

Figure 8.8: Discharge at $\mathbf{t_d = 0.5s}$ - for varying levels of adhesion energy

Following the initial phase of developing flow at the start of discharge, the flow patterns for different adhesion levels remain quite similar until discharge is complete, with similar dead zones existing for all adhesion levels after completion of discharge (Figure 8.9). Due to the lower discharge rate observed at higher levels of adhesion, there are still some particles left to exit the silo at $t_d = 22.5$s for an adhesion energy of 12.5 J/m^2.

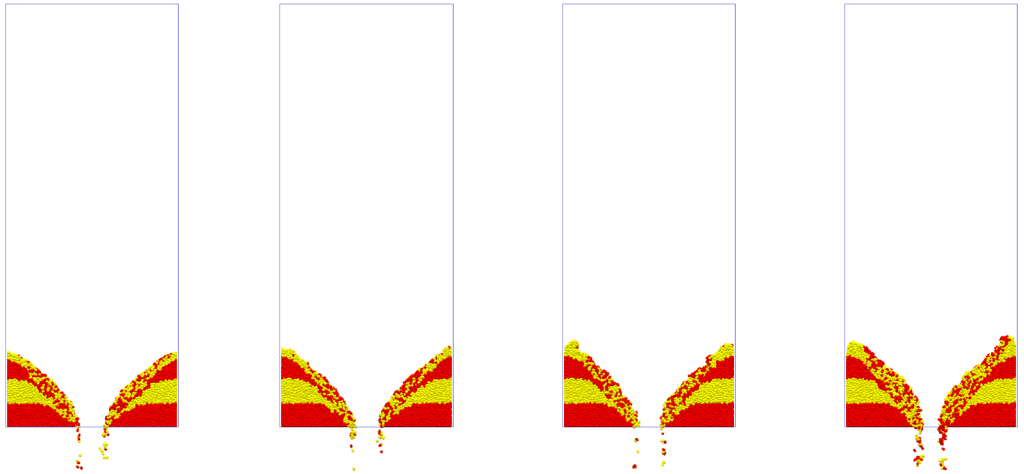

(a) $\Delta\gamma = 0J/m^2$ **(b)** $\Delta\gamma = 5J/m^2$ **(c)** $\Delta\gamma = 10J/m^2$ **(d)** $\Delta\gamma = 12.5J/m^2$

Figure 8.9: Discharge at $\mathbf{t_d = 22.5s}$ - for varying levels of adhesion energy

8.3 Discharge Rates

The discharge rate was investigated for the varying levels of adhesion during the discharge process for the flat bottomed hopper. In the case of the cohesionless assembly; the discharge from the silo is mixed/funnel flow; the widely used Beverloo theory [Beverloo *et al.*, 1961] can be applied to compare the theoretical discharge rate with that predicted from the DEM simulation. As the Beverloo solution was derived for circular silo, the modified Beverloo equation for rectangular silo with a rectangular slot proposed by Myers and Sellers [1971] and given by Equation (2.19) will be used. As non-spherical particles with an aspect ratio of 1.5 have been used, the Beverloo coefficient *k*, which is normally considered to be 1.5 for spherical particle and increases with non-sphericity [Mankoc *et al.*, 2007; Nedderman, 1992], has been set as 1.65 for the paired particles used in this study with the initial bulk density for the silo found to be 3310 kg/m^3. The predicted DEM mass flow rate along with the theoretical prediction are presented in Figure 8.10. The first observation is the large scatter that is to be found in the instantaneous values from the DEM simulation which fluctuates between 0.5 - 1.5 kg/s during discharge. The temporally averaged value over a time period of 0.25s is superimposed on this data to present a more a more representative discharge rate for the DEM simulation. The temporally averaged discharge rate is found to be quite stable with only small fluctuations during discharge rate until the silo is almost empty at $t_d =$ 15s, at which point the discharge rate begins to drop. The DEM prediction was found to be in excellent agreement with the theoretical prediction for the silo geometry used.

The discharge rates for additional levels of adhesion energy, $\Delta\gamma$, are presented in Figure 8.11 and Figure 8.12 for different ranges of temporal averaging. While there are

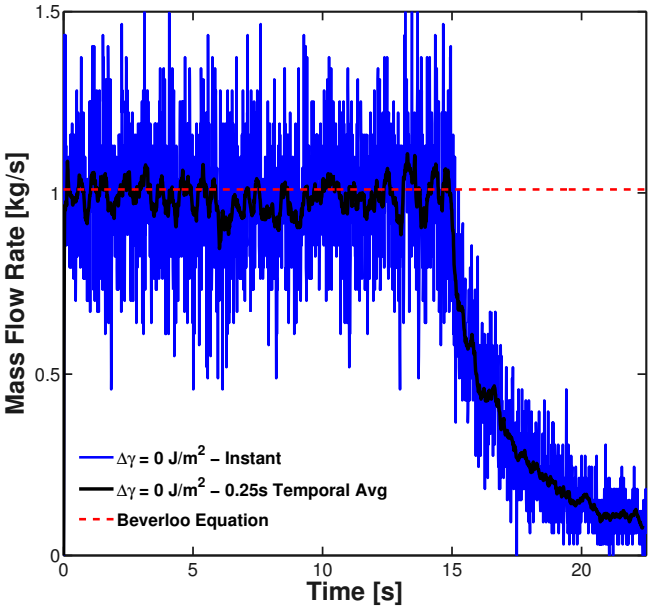

Figure 8.10: Comparison of cohesionless discharge with Beverloo prediction - for DEM Simulations

fluctuations to be found in the discharge rate a general trend of reducing discharges rates with increasing adhesion can be found from the DEM simulations. The reduction in discharge rate also leads to a longer discharge time for the simulations. While the lower discharge rates contribute to the longer discharge times, a significant portion of the extra time comes from intermittent arching at the initial stages of flow. This is particularly evident for adhesion energies of 10 J/m^2 and 12.5 J/m^2, where the stable discharge rate is not reached until approximately two seconds into discharge compared to approximately 0.2s for the cohesionless case. This reduction in discharge rate is similar to that found by Anand *et al.* [2009] for wet, cohesive particles using a capillary force model.

In the case of an adhesion energy of 12.5 J/m^2 a significant arch develops after approximately 0.25s which reduces discharge to zero for close to half a second. The effects of smaller intermittent arches are seen for an adhesion energy of 10 J/m^2 but these are not significant enough to stop discharge completely. The cumulative discharge is presented in Figure 8.13 and again highlights the longer discharge time for the higher adhesion energies. The lower discharge rates shown in the temporally averaged data in Figure 8.11 and Figure 8.12 are confirmed by the slopes of the cumulative discharge which decrease with increasing adhesion.

The slope of cumulative discharge vs time (Figure 8.13) can be defined as the mass flow rate of the discharging silo and will give the mean value of the discharge rate plotted in Figures 8.11 and 8.12. As the bulk density of the system is known in the initial filled

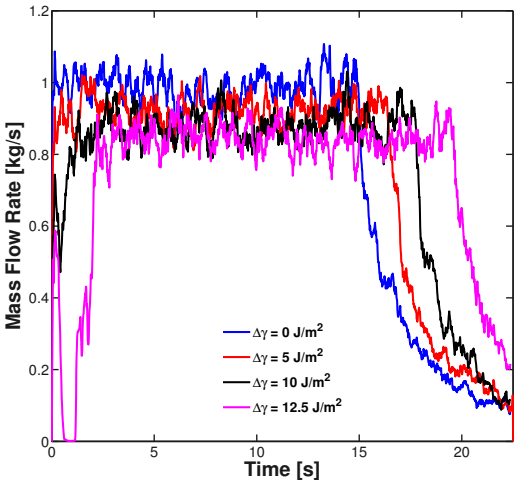

Figure 8.11: Discharge rates averaged temporally over 0.25s - For all adhesion levels

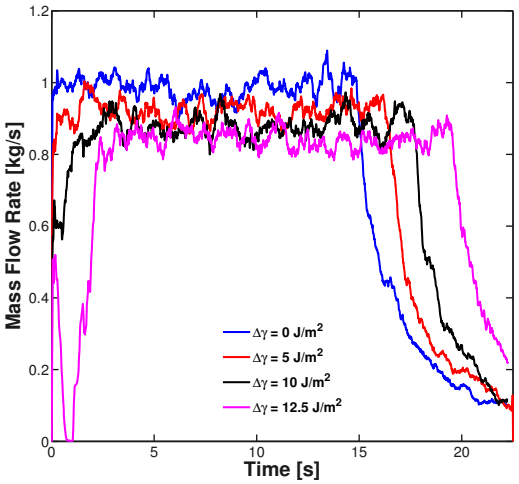

Figure 8.12: Discharge rates averaged temporally over 0.5s - For all adhesion levels

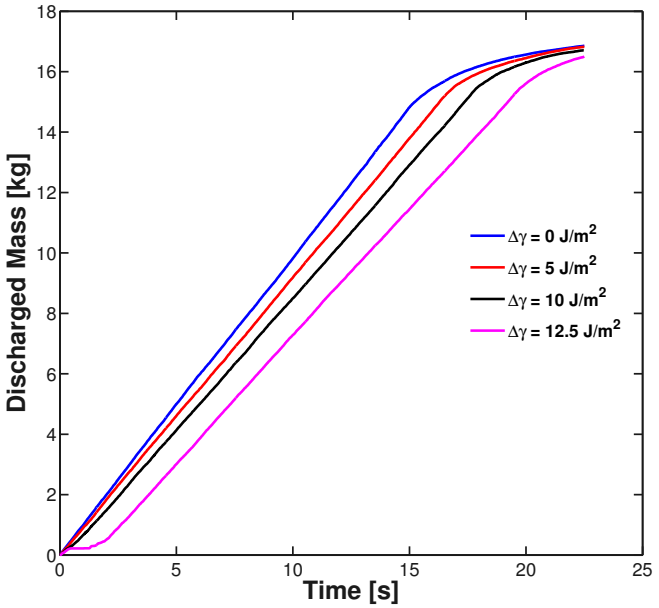

Figure 8.13: Cumulative discharge from model silo - For various levels of adhesion in DEM Simulations

state, and the areas of mass flow do not significantly alter this density during discharge, the mass flow velocity V_{MF} can be determined from the volumetric flow rate given in Equation (8.1)

$$Q = VA \tag{8.1}$$

where Q is the volumetric flow rate $[m^3/s]$, V is the flow velocity [m/s] and A is the cross-sectional area $[m^2]$. The mass flow rates for discharge and the mass flow

velocities V_{MF} for different adhesion energy values are given in Table 8.2.

Table 8.2: Evaluated discharge properties

Adhesion Energy $[J/m^2]$	**Mass Flow Rate** $[kg/s]$	**Mass Flow Velocity,** $\mathbf{V_{MF}}$ $[m/s]$
0	0.98	0.039
5	0.92	0.037
10	0.88	0.035
12.5	0.84	0.034

8.4 Discharge Velocity Profiles

The velocity profiles at selected vertical locations in the silo are presented for an adhesion energy of $\Delta\gamma = 0$ J/m^2 and $\Delta\gamma = 12.5$ J/m^2 for various timesteps during discharge in Figures 8.14 to 8.19. Velocity profiles were extracted from the P4 analysis which was temporally averaged to 10 Hz but comparisons with binned average results directly from the DEM simulation, also temporally averaged at 10 Hz, are also presented for the cohesionless cases in sub-figure (a). The results from both methods are found to be in excellent agreement with each other. In all cases presented where a peak velocity was noted, the highest velocities were noted at central locations in the model silo.

A constant discharge rate was found in the cohesionless case from approximately t_d = 0.5s onwards and the developing flow can be seen in Figure 8.14a, with mass flow developing higher in the silo and funnel flow at lower heights. In the case of an adhesion energy of 12.5 J/m^2, a cohesive arch forms at approximately $t_d = 0.25$s, restricting discharge for a period slightly greater than 0.6s. In the highly cohesive system at $t_d = 0.5$s, shown in Figure 8.14b, the development of a temporary cohesive arch has reduced flow to almost a complete standstill, with velocities significantly lower than the cohesionless case. Velocities at mid-height in the silo are measured at zero, but particles in the upper portion still have momentum and very small velocities were measured.

In the cohesionless system (Figure 8.15a), a stable discharge rate has developed by 1s and this is reflected in the velocity profiles from t_d = 1s - 10s (Figures 8.15a to 8.19a respectively) which are almost identical. In the upper section of the model silo mass flow is found with a velocity of approximately 0.04m/s measured across the silo, with the exception of the boundary layer of 5-10 particles on each side where velocities are significantly reduced. This matches closely the mass flow velocity V_{MF} presented in Table 8.2. A transition from mass flow to funnel flow occurs at a height of approximately

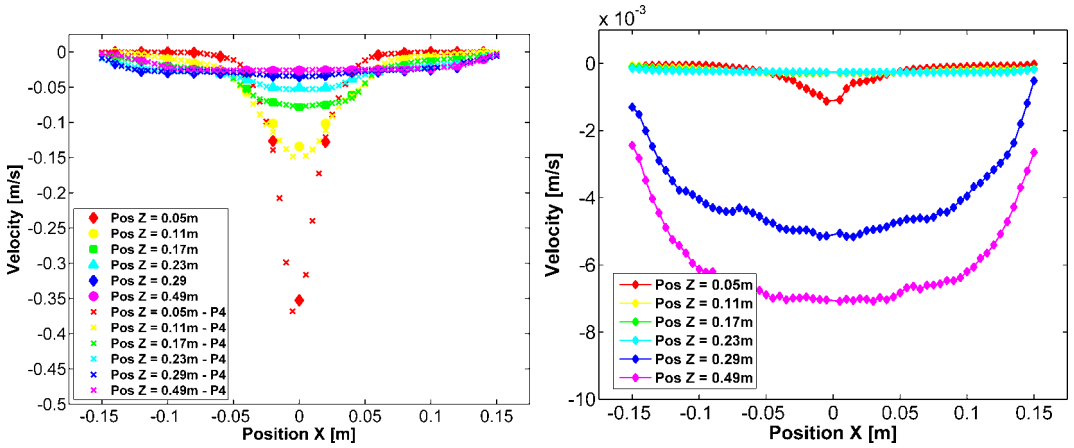

(a) $\Delta\gamma = 0J/m^2$ - Stable discharge **(b)** $\Delta\gamma = 12.5J/m^2$ - During arch formation

Figure 8.14: Velocity profiles for t_d = 0.5s - Cohesionless ($\Delta\gamma = 0J/m^2$) includes DEM and P4 comparison

0.2m, with a flow channel developing below this height. The velocity at the edges of the silo reduces due to the presence of the stagnant zones and the velocity at the centre of the silo increases in a central zone above the outlet. The maximum velocity at a height of 0.05m above the outlet remains consistent at a magnitude of approximately 0.35m/s.

At t_d = 1s, as stable discharge continues for the cohesionless assembly, the temporary cohesive arch begins to collapse at close to 1s, and velocity begins to increase centrally, directly over the outlet (Figure 8.15b). At this point in time velocities are still significantly lower than the cohesionless assembly.

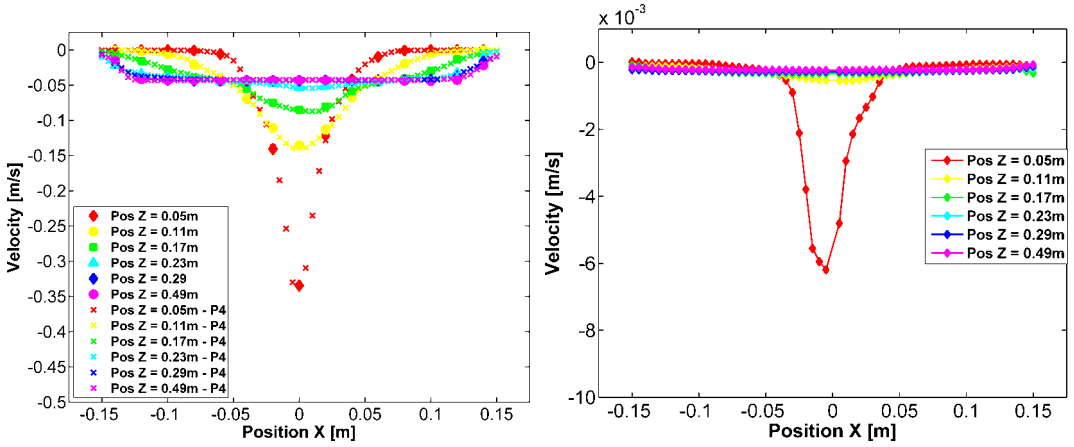

(a) $\Delta\gamma = 0J/m^2$ - Stable discharge **(b)** $\Delta\gamma = 12.5J/m^2$ - Breakage of arch

Figure 8.15: Velocity profiles for t_d = 1s - Cohesionless ($\Delta\gamma = 0J/m^2$) includes DEM and P4 comparison

In the system with the highest adhesion energy of 12.5 J/m^2 a stable discharge rate does not develop until after 2s (Figure 8.16b) and is not fully developed until approximately t_d = 5s (Figure 8.17b).

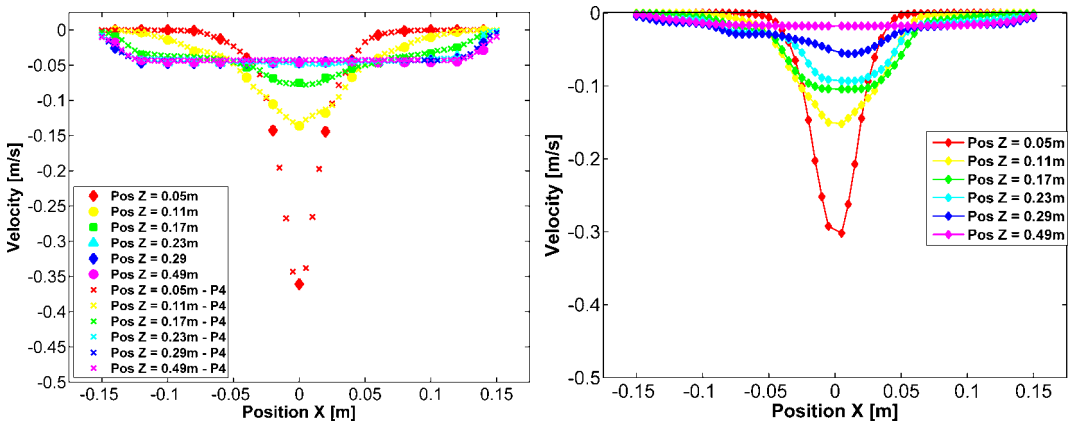

(a) $\Delta\gamma = 0J/m^2$ - Stable discharge **(b)** $\Delta\gamma = 12.5J/m^2$ - Stable discharge

Figure 8.16: Velocity profiles for t_d = 2.5s - Cohesionless ($\Delta\gamma = 0J/m^2$) includes DEM and P4 comparison

During stable discharge, for both cohesive and cohesionless assemblies, the velocity profiles in Figures 8.17 and 8.18 are quite similar with the same flow pattern developing, but lower velocities measured in the case with cohesion. For the cohesive assembly mass flow has been observed above a height of 0.2m and a flow channel to the outlet developed below this height. The maximum velocity measured at a height of 0.05m is close to 20% lower than the cohesionless assembly at slightly under 0.3 m/s.

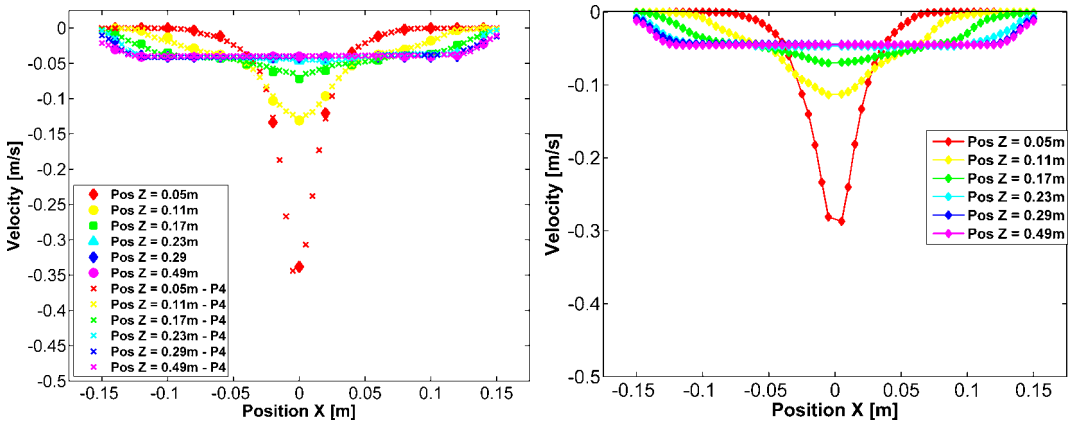

(a) $\Delta\gamma = 0J/m^2$ - Stable discharge **(b)** $\Delta\gamma = 12.5J/m^2$ - Stable discharge

Figure 8.17: Velocity profiles for t_d = 5s - Cohesionless ($\Delta\gamma = 0J/m^2$) includes DEM and P4 comparison

As the cohesionless silo begins to empty in Figure 8.19a, when the height of the top surface is close to the transition height, there is an increase in the velocity near the

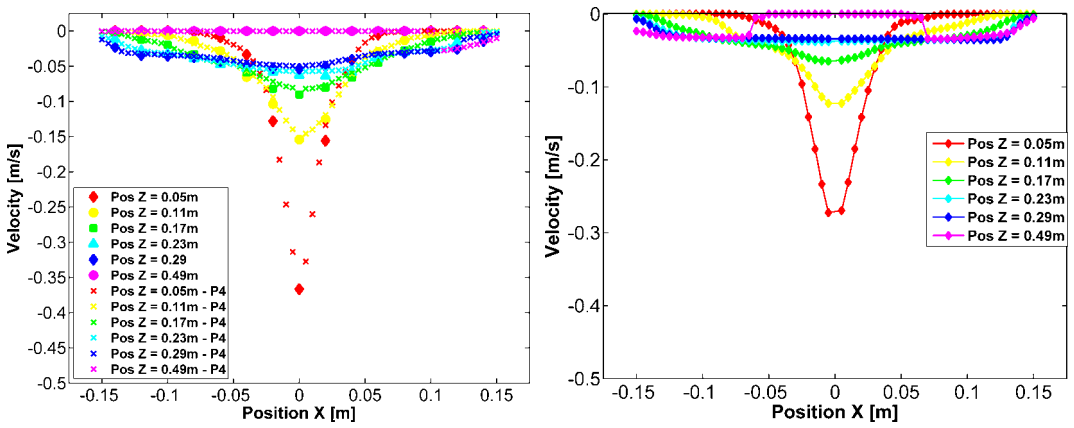

(a) $\Delta\gamma = 0J/m^2$ - Stable discharge **(b)** $\Delta\gamma = 12.5J/m^2$ - Stable discharge

Figure 8.18: Velocity profiles for t_d = 10s - Cohesionless ($\Delta\gamma = 0J/m^2$) includes DEM and P4 comparison

outlet, with no flow being measured centrally above a height of 0.15m. At t_d = 15s, the cohesive assembly (Figure 8.19b) free surface is just reaching the effective transition height, after which point it will transition to the flow behaviour seen for the cohesionless assembly in Figure 8.19a.

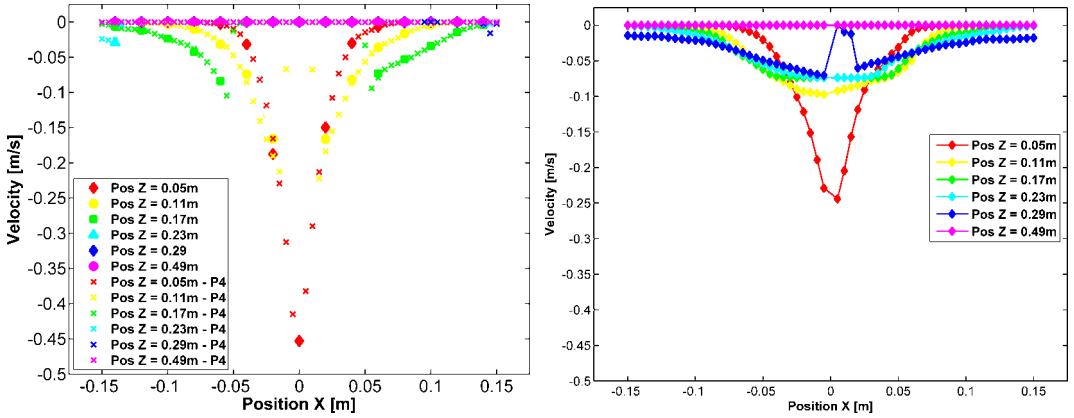

(a) $\Delta\gamma = 0J/m^2$ - Stable discharge **(b)** $\Delta\gamma = 12.5J/m^2$ - Stable discharge

Figure 8.19: Velocity profiles for t_d = 15s - Cohesionless ($\Delta\gamma = 0J/m^2$) includes DEM and P4 comparison

8.4.1 Flow Channels

Where mass flow exists, the variation in velocities are small and the flow channel can be easily defined, but where funnel flows exists it can be difficult to determine the limits of the flow channel. The measured velocity profiles suggest that mass flow occurs in the silo above a height of 0.25m - the effective transition. The areas of particle flow can be determined from the velocity contours of the simulation and are plotted for the upper and lower limits of the adhesion energy values that resulted in flow in Figures 8.20

and 8.21. In both cases a velocity magnitude of approximately 15% of the mass flow velocity, V_{MF}, from Table 8.2 was selected as the lower limit for flowing particles. The selected velocity, which equates to a velocity of 0.005m/s represents a low enough velocity such that any velocities below that limit are negligible and can be considered stagnant.

Using these limits a area of flow can easily be determined for the discharging silos and suggests that flow channel extends upwards from the edges of the outlet at approximately 55 - 60°, with the stagnant zones at each side of the outlet creating an effective transition height of approximately 0.22 - 0.26m above the silo base. Above this height the flow has been determined to be mass flow from the velocity profiles with a consistent velocity of 0.04m/s. An asymmetry is seen in the flow channel of both cases and with the effective transition slightly lower on the left hand side in both cases. This flow boundary will also partially include the shear zone at the edge of the stagnant zone as seen in Figures 8.4 and 8.6.

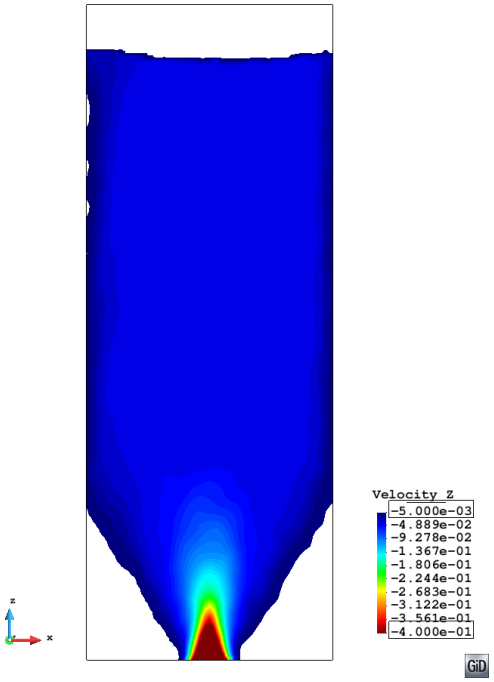

Figure 8.20: Discharge velocity for $\Delta\gamma = 0\mathbf{J/m^2}$ - At t_d= 1s

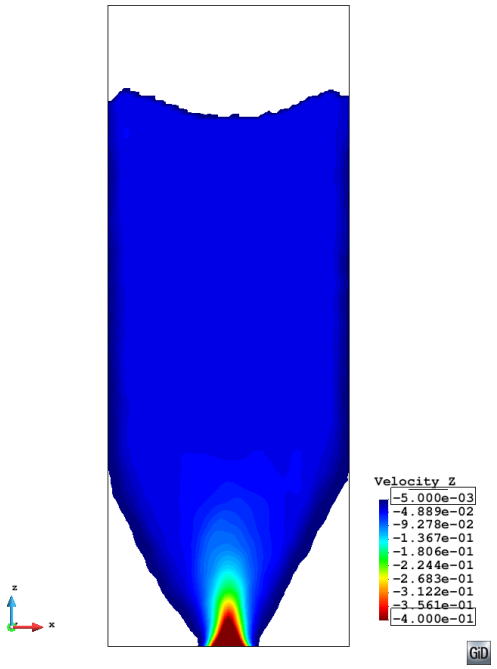

Figure 8.21: Discharge velocity for $\Delta\gamma = 0\mathbf{J/m^2}$ - At t_d= 5s

Applying a limiting value of $1.25\ V_{MF}$, the core flow channel can be better visualised for the limiting adhesion values in Figures 8.22 and 8.23 by removing the areas of flow determined to be mass flow. The resulting limits highlight a flow channel resembling an elongated bulb that exist centrally above the outlet to the effective transition height. The flow channel is slightly unsymmetrical and varies with time, with the likely effect of this being unsymmetrical wall pressures on the lower third of the silo. The flow

boundaries identified are in good agreement with the simplified flow zones proposed by Zhang and Ooi [1998].

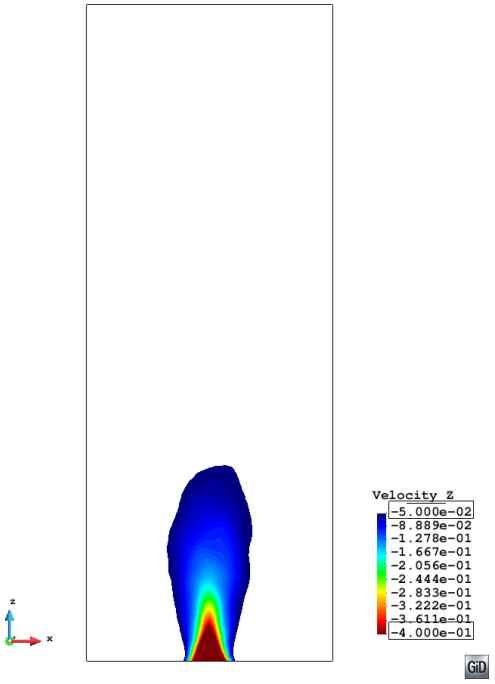

Figure 8.22: Discharge velocity for $\Delta\gamma = 0\mathrm{J/m^2}$ - At t_d= 1s

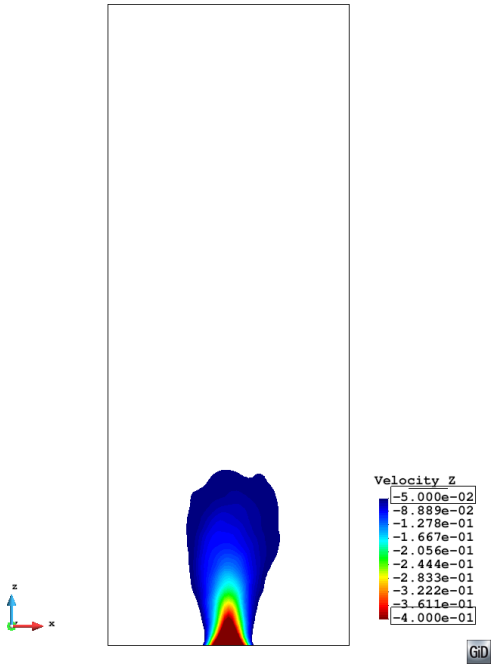

Figure 8.23: Discharge velocity for $\Delta\gamma = 0\mathrm{J/m^2}$ - At t_d= 5s

As discharge continues and the free surface reaches the effective transition height, the mass flow zone has diminished and the high velocity central flow channel eventually extends upwards into it, as far as the free surface (Figures 8.24 and 8.25). As this occurs the velocity increases significantly above the outlet, resulting in a more 'flame' like flow channel instead of the elongated bulb seen during stable discharge.

While the addition of adhesion to the system reduces the magnitude of the velocities observed, the flow behaviour and trends remain largely similar across the different adhesion levels with the exception of the temporal location. The effect of increasing adhesion was found to have little affect of the flow patterns, which appear to be dominated by the silo geometry and type.

The results presented on flow have used the more consistent temporally averaged values as opposed to the instantaneous velocities which can fluctuate significantly between timesteps. Some of the instantaneous results that formed the temporally averaged value in Figure 8.22 are presented in Figure 8.26. This shows that the temporal average, while not significantly changing the underlying results, filters out the fluctuations that exists in the data for discharge. It also highlights that the asymmetry shown in the

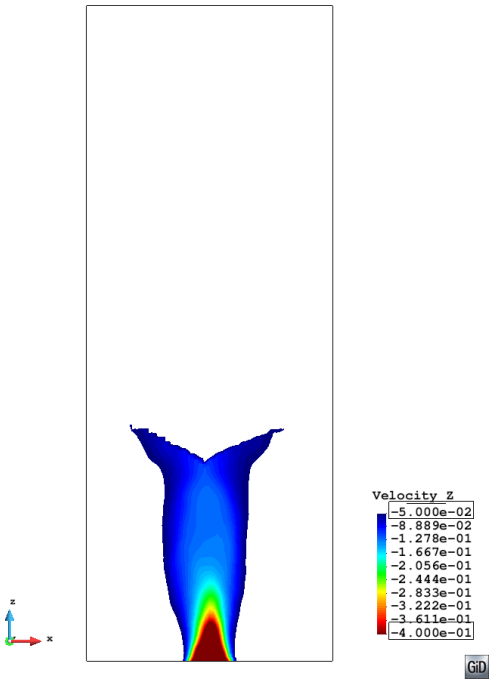

Figure 8.24: Discharge velocity for $\Delta\gamma = 0\mathrm{J/m^2}$ - At t_d= 12.5s

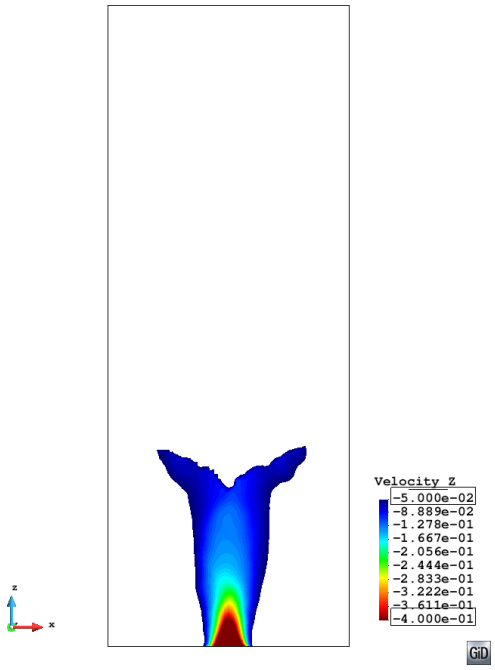

Figure 8.25: Discharge velocity for $\Delta\gamma = 0\mathrm{J/m^2}$ - At t_d= 17.5s

temporally averaged values can vary with each timestep in the fast flowing core zone and flicker from side to side.

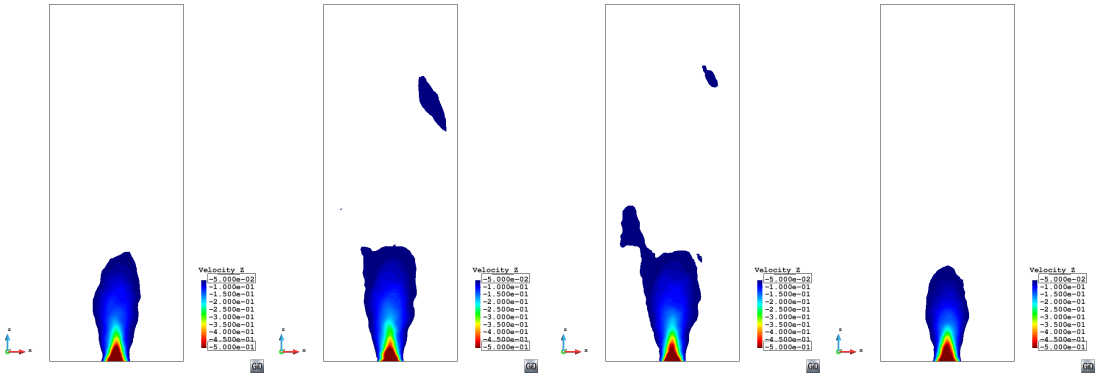

(a) $t_d = 0.96s$ **(b)** $t_d = 0.98s$ **(c)** $t_d = 1.0s$ **(d)** $t_d = 1.05s$

Figure 8.26: Variation between individual timesteps for temporal average - For cohesionless assembly

8.5 Wall Pressures

The flow pattern in a silo during discharge is known to have an effect on the wall pressure developed [Chen *et al.*, 2007], particularly in the case of eccentric flow. Normal wall pressures can increase significantly where there is mass flow with the possibility of

higher forces in mixed flow. High pressures are to be expected in the region of the effective transition [Rotter, 2001]. It is also possible that the small asymmetry developing in the flow channel can lead to significantly unsymmetrical resulting wall pressures.

8.5.1 Spatial & Temporal Averaging

The wall pressures from the DEM simulation are calculated using a spatial averaging method of the particle-wall normal forces along the length of the wall, as shown by Figure 8.27. The total number of normal wall contacts is counted for each averaging area and the normal forces are summed and divided by the segment area to provide the average pressure at the centre of the averaging area. The segment is then moved by a chosen distance and the averaging process repeated for that location. The length of the averaging area is chosen based on the particle diameter, D, such that the area is specified as 5D or 10D. The distance between averaging areas can be selected such that the segments overlap, providing additional data points for a smother wall pressure distribution. Care needs to be made in the selection of the averaging area size, too small a size and there is significant scatter in the data and too large an area will smooth out results. The effect of varying segment length is demonstrated by Figure 8.28.

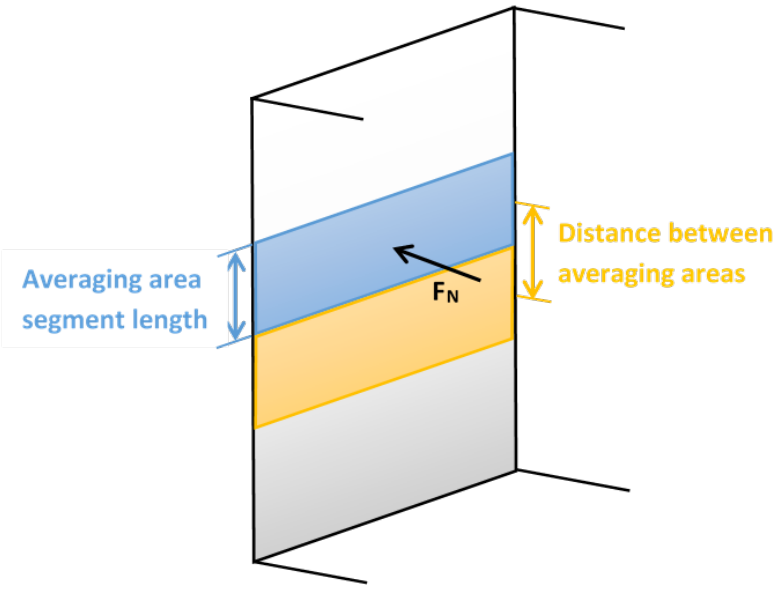

Figure 8.27: Averaging method for calculation of wall pressures - For DEM Simulations

It is also important to consider temporal effects when averaging data. A DEM simulation presents data on a timescale dependant on the data save interval specified and is often in the region of thousandths of a second. Such a small time scale is often not representative of the forces that are of importance for the integrity of the structure and

a more appropriate timescale length should be used. Temporal averaging will remove the fluctuations that occur between individual time-steps to better represent what is happening in the system. The effect of temporal averaging (denoted as δt) is also included along with the spatially averaged data (denoted as $\bigtriangledown s$) in Figure 8.29 as the solid line through the instantaneous spatially averaged data for the same timestep. A data save interval of 100Hz was used for the simulation, while a temporal averaging of ten timesteps, equal to 0.1s, is applied.

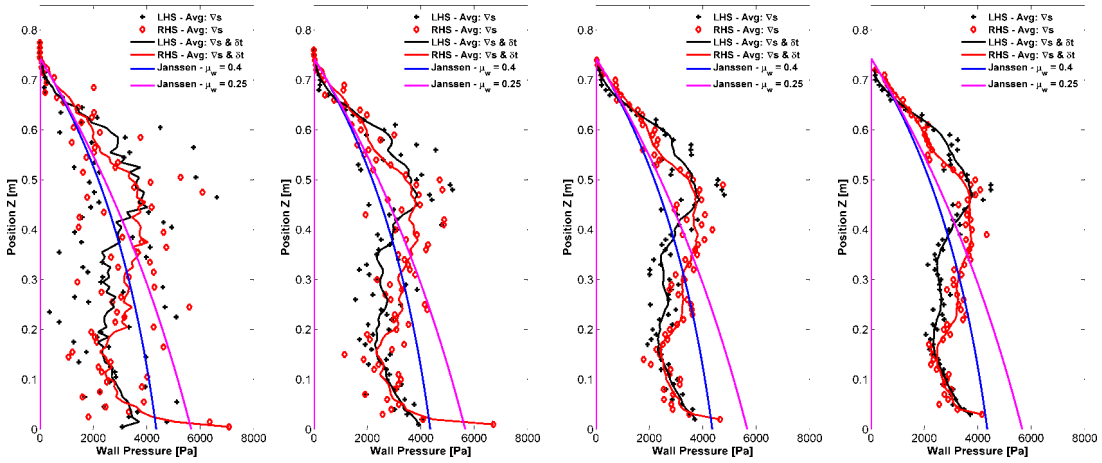

(a) Segment length = 2.5D **(b)** Segment length = 5D **(c)** Segment length = 10D **(d)** Segment length = 15D

Figure 8.28: Variation of averaging area size at same spacing distance - For $t_d = 0.5s$

As the averaging area length increases there is a distinct reduction in the amount of scatter measured for the instantaneous wall pressure data. Despite the varying averaging area size, the temporally averaged data is relatively consistent for all, with the magnitude of the wall pressures consistent and the prediction of pressure fluctuations. As the averaging area length increases the instantaneous data tends towards the profile of the temporally averaged data. In relation to the size of the averaging area, Härtl [2008] found that an averaging area of at least $50D^2$ was required for a representative pressure distribution; which when applied to this set of periodic slice simulations that are approximately 5D thick, a minimum segment length of 10D should be used. This agrees well with the results in Figure 8.28 where segment lengths greater than 10D show less scatter. A segment length of 10D was also used by Holst *et al.* [1999].

The effect of the spacing between overlapping averaging areas is presented in Figure 8.29 where the spacing length has been varied between 1D and 10D The main effect of increasing the spacing distance between is the reduction in the number of data points, with the 5D spacing distance having 4 times as many data points. The results for a spacing of 5D to 10D are relatively similar and tend towards a straighter wall

pressure profile with much of the local variation being lost. A segment spacing of 2.5D allows for more of the local variation to be captured in the wall pressure distribution. A segment spacing of 1D was used by Holst *et al.* [1999].

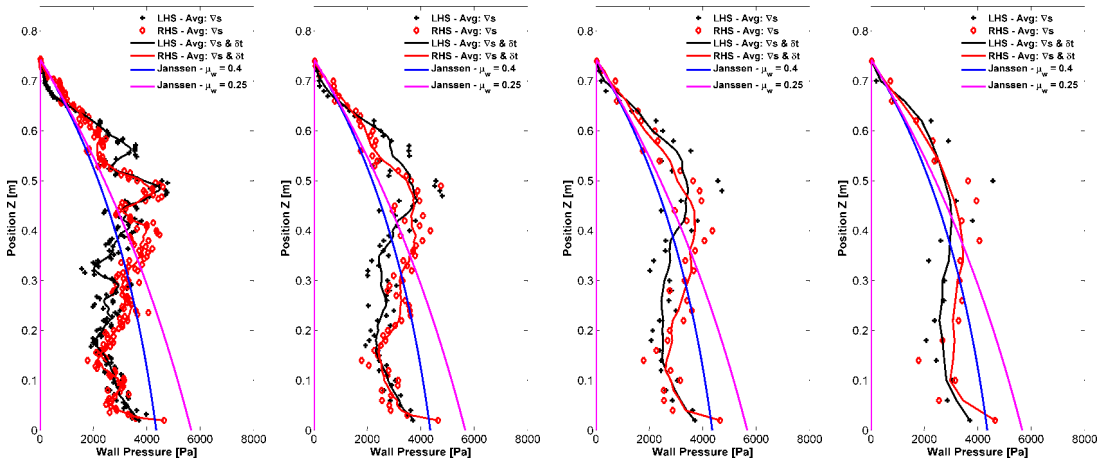

(a) Segment distance = 1D **(b)** Segment distance = 2.5D **(c)** Segment distance = 5D **(d)** Segment distance = 10D

Figure 8.29: Variation of averaging area spacing for segment length of 10D - For $t_d = 0.5s$

The effect of temporal averaging is investigated in Figure 8.30 where the wall pressure distribution at $t_d = 0.5s$ is compared for different levels of temporal averaging ranging from 1Hz to the DEM sampling frequency of 100 Hz. At 100Hz, this is the instantaneous value recorded in the DEM simulation and relates to the average of just one timestep in this case, whereas a temporal average for 1Hz relates to the average of 100 timesteps centred on $t_d = 0.5s$. At 100Hz there is significant fluctuation in the data, but increasing the sampling rate allows a smoother well pressure distribution to be obtained with less fluctuation between the individual timestep. At the opposite end of the scale a temporal average relating to 1Hz, which includes 100 data points, provides a smooth wall pressure similar to the theoretical Janssen solution and has averaged out all the local fluctuations in the data. Typically the events occurring that are of interest in silo discharge are not in the order of hundreds or thousands of Hertz, but are much likely to be in the range of 1-10 Hz.

In an attempt to capture the events that occur during discharge in as much details as possible, a temporal average for 10 Hz is selected for temporally averaging the data, unless otherwise stated.

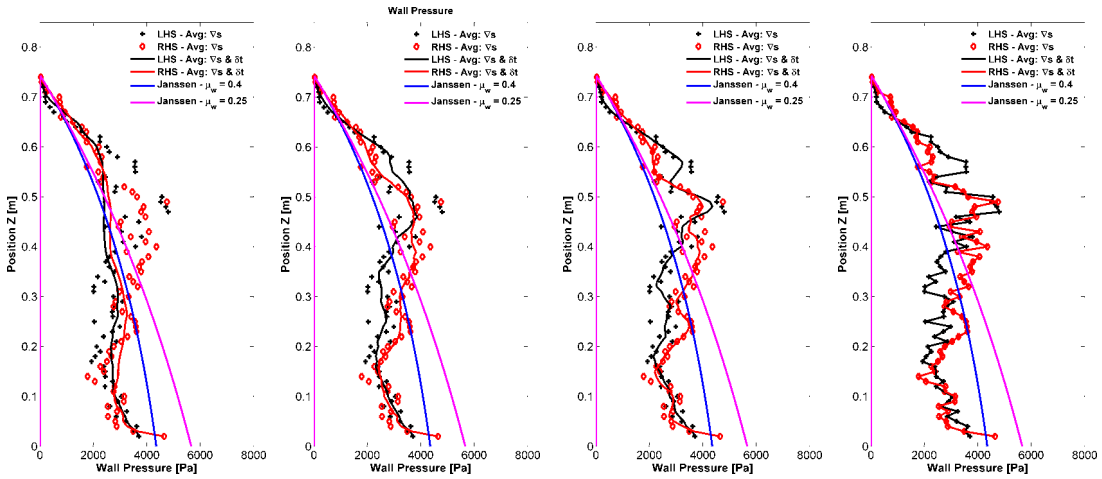

(a) 1 Hz Temporal Avg. **(b)** 10 Hz Temporal Avg. **(c)** 20 Hz Temporal Avg. **(d)** 100 Hz Temporal Avg.

Figure 8.30: Variation of temporal averaging rate - For $t_d = 0.5s$

8.5.2 Mobilized Friction

For the DEM simulation a limiting friction of $\mu_s = 0.5$ has been specified for particle-wall interactions, and while this is the limiting value only a small portion of the wall contact will actually reach this value, with the majority having a mobilized friction value significantly lower than the limiting value. The mobilized friction has been calculated for the DEM simulations and histograms from varying levels of adhesion for selected timesteps are plotted in Figures 8.31 and 8.32.

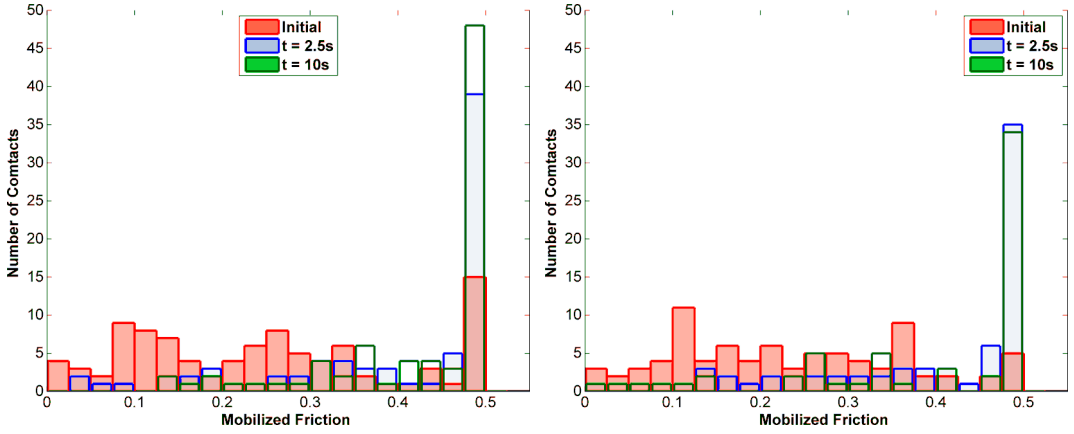

(a) For LHS **(b)** For RHS

Figure 8.31: Mobilized wall friction for adhesion energy = 0 $\mathbf{J/m^2}$ - For Both LHS and RHS

While a portion of contacts have fully mobilized wall friction, initially for a cohesionless system, this is less than half of all contacts and there is a large variation in the wall friction values. As discharge continues the proportion of contacts that become fully

mobilized increases. Similar trends are found on both the left and right hand sides of the models silo. Similar trends are noted for high adhesion where the proportion of contacts with fully mobilized wall friction also increases during discharge, although the number of wall contacts are found to be slightly reduced with increasing adhesion.

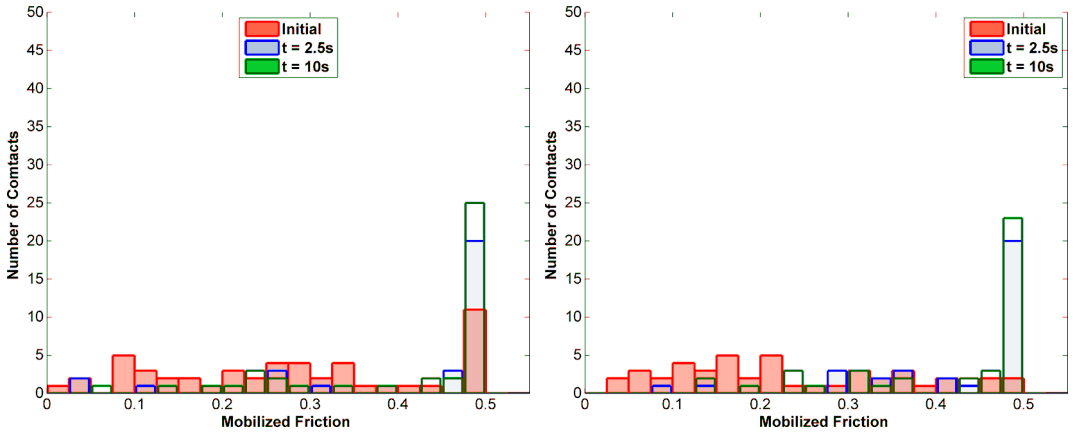

(a) For LHS **(b)** For RHS

Figure 8.32: Mobilized wall friction for adhesion energy = 0 $\mathbf{J/m^2}$ - For Both LHS and RHS

The average of the mobilized friction values calculated for all timesteps for each adhesion energy level are summarised in Table 8.3. The calculated values of mobilized wall friction will be used for the wall friction coefficient using Janssen's wall pressure theory.

Table 8.3: Mobilized friction values for discharge simulations

Adhesion Energy	**Avg. Mobilized Friction**
Initial Static Value	0.25
$\Delta\gamma = 0J/m^2$	0.40
$\Delta\gamma = 5J/m^2$	0.39
$\Delta\gamma = 10J/m^2$	0.39
$\Delta\gamma = 12.5J/m^2$	0.40

8.5.3 Wall Pressures

The silo flow patterns are presented in conjunction with the wall pressure distribution averaged both spatially and temporally for all levels of adhesion energy where flow existed. The Janssen theory for rectangular geometries has been used with the mobilized wall friction measured from the DEM simulations (Table 8.3). A K_0 value of 0.35 has

been used for the paired particles used in the simulations. Both spatially and temporally averaged pressures are presented based on a averaging segment length of 15D with a segment spacing of 2D. The spatially averaged results are instantaneous values, while temporally averaged values at 10Hz are also included. At the onset of discharge, the wall-friction is not yet fully mobilised, as shown in Figures 8.31 and 8.32, a lower wall friction value of 0.25 is measured at the initial static timestep, before increasing as discharge progresses.

The wall pressure distribution of both sides of the model silo at the start of discharge is presented in Figure 8.33 and the wall pressure distributions for the four different levels of adhesion, along with the accompanying discharge patterns, are presented in Figures 8.35 to 8.51 for a further selection of timesteps as the silo is discharged. In the initial static case, which is common for all assemblies, the wall pressure distribution is decreasing linearly near the free surface of the filled material in the manner of hydrostatic pressure. As the pressure developed in a silo of granular material are dominated by frictional criteria, the normal wall pressure tends towards an asymptotic value at large depths and is largely independent of height. As the wall friction plays a significant role, lower wall friction coefficients lead to higher wall pressures.

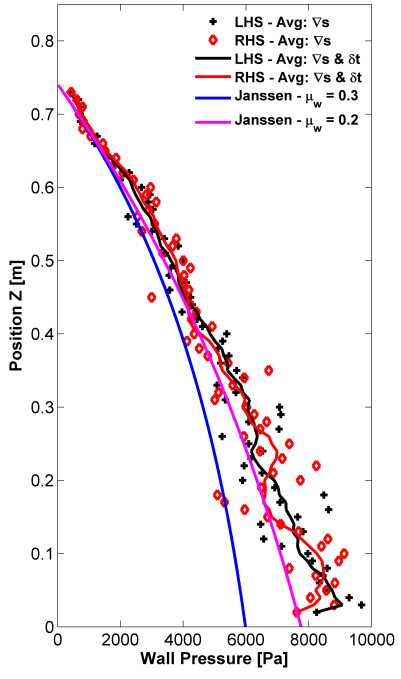

Figure 8.33: Initial DEM static wall pressure distribution - With upper and lower friction limits after concentric filling

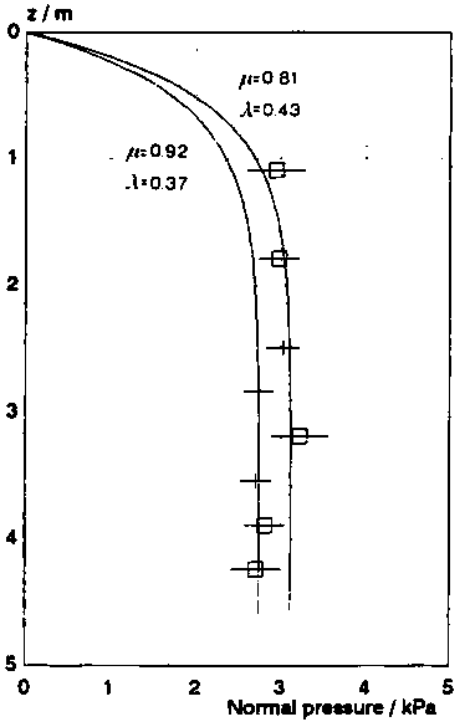

Figure 8.34: Experimental wall pressure measurement - Upper and lower wall friction limits, after Munch-Andersen *et al.* [1992]

The DEM results are in good agreement with the Janssen solution when a lower wall friction coefficient is used for the first timestep. As the discharge continues a higher mobilized friction value is found in the DEM simulations and the values listed in Table 8.3 are employed for the remainder of the simulations. Figure 8.34 shows and experimental wall pressure distribution for experiments on discharge of sand where two different wall friction coefficients have been used to match the data, creating an upper and lower limit for the wall pressures that develop during discharge.

The images of discharge and the respective wall pressures 0.25s after discharge has commenced are shown in Figures 8.35 and 8.36. For the cohesionless assembly, where flow occurred almost immediately once the outlet was opened, a sharp drop in wall pressures is noted between approximately 0.05 - 0.2m. This area is in the region of the high velocity core flow channel above the outlet that extends to approximately 0.25m. The effective transition where the flow channels intersect the silo wall and at which mass flow occurs was estimated to be approximately 0.25 - 0.3m. Rotter [2001] stated that higher wall pressures in the region above the effective transition can be expected in the case of mixed flow with mass flow occurring, along with asymmetrical pressures in relation to the development of an asymmetric flow channel. Both of these features are seen in the case of cohesionless discharge.

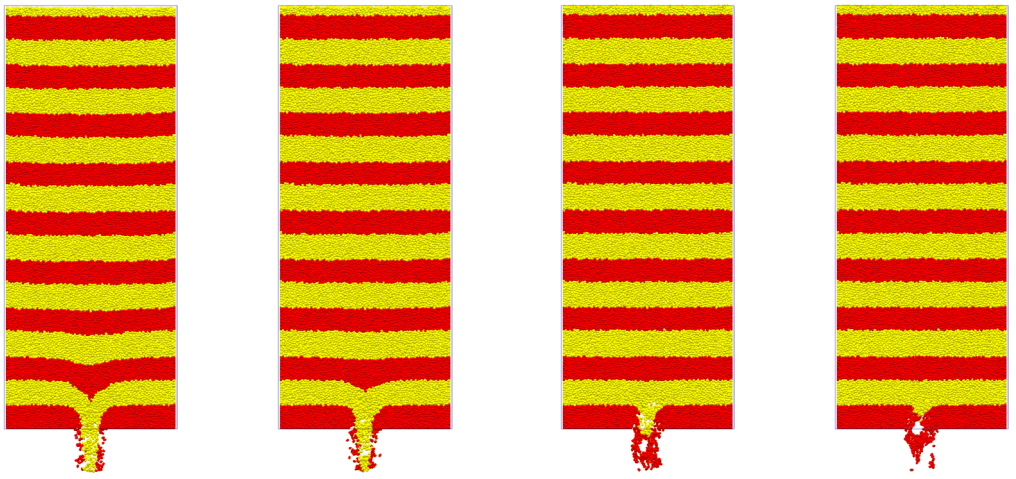

(a) $\Delta\gamma = 0J/m^2$ **(b)** $\Delta\gamma = 5J/m^2$ **(c)** $\Delta\gamma = 10J/m^2$ **(d)** $\Delta\gamma = 12.5J/m^2$

Figure 8.35: Discharge snapshots at $\mathbf{t_d = 0.25s}$

The effect of the additional adhesion leads to the slower development of flow following the opening of the outlet. In the case of the higher adhesion energies of 10 J/m^2 and 12.5 J/m^2 there has been little flow other than the particles directly above the outlet and the wall pressure distribution has shown little change, although pressures are starting to reduce in the area of the expected flow channel. At 5 J/m^2 there appears to be a transition from the static pressure distribution still seen in the higher adhesion

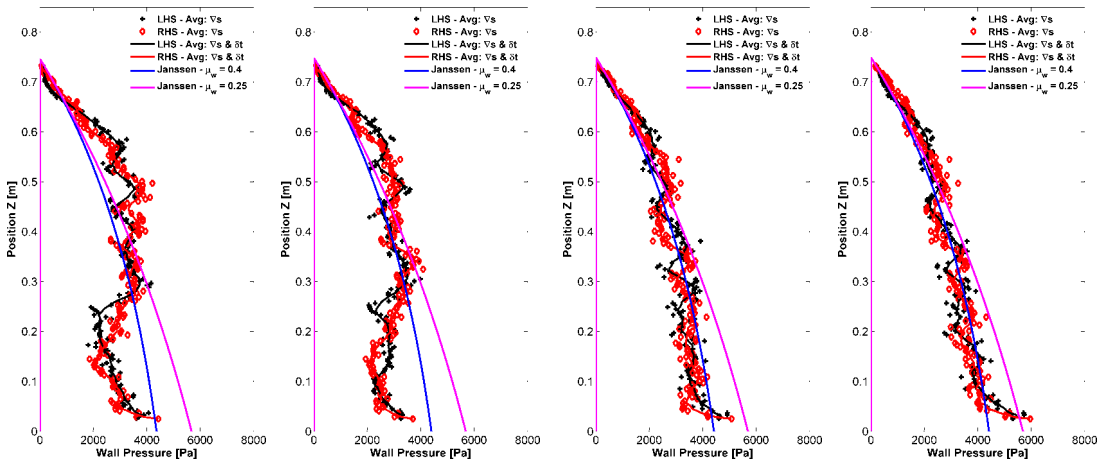

(a) $\Delta\gamma = 0J/m^2$ **(b)** $\Delta\gamma = 5J/m^2$ **(c)** $\Delta\gamma = 10J/m^2$ **(d)** $\Delta\gamma = 12.5J/m^2$

Figure 8.36: Wall Pressures at $t_d = 0.25s$

energies to the developed flow pressure distribution seen in the cohesionless case with higher pressures above the effective transition.

As discharge continues at $t_d = 0.5s$, in Figures 8.37 and 8.38, the cohesionless case maintains a profile with higher wall pressures being developed in the region above the effective transition. The asymmetry in wall pressures has become more obvious at this time step. The wall pressure profile developed at 5 J/m^2 resembles that of the cohesionless discharge at an earlier time of 0.25s and the adhesion energy of 10 J/m^2 also resembles the flow pattern of the 5 J/m^2 case at 0.25s, highlighting that the additional adhesion acts as a deterrent to the initiation of flow at the onset of discharge.

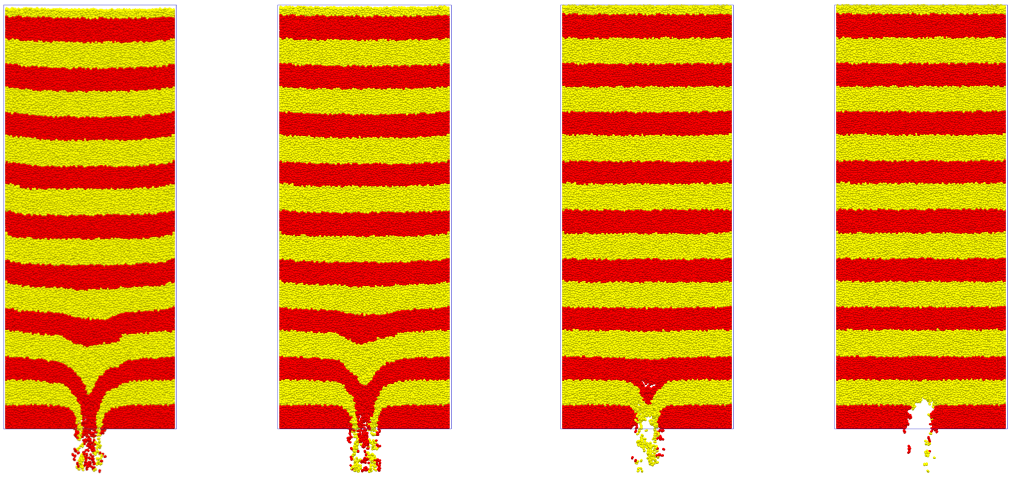

(a) $\Delta\gamma = 0J/m^2$ **(b)** $\Delta\gamma = 5J/m^2$ **(c)** $\Delta\gamma = 10J/m^2$ **(d)** $\Delta\gamma = 12.5J/m^2$

Figure 8.37: Discharge snapshots at $t_d = 0.5s$

At 0.5s a cohesive arch has formed in the case of high adhesion with discharge halted and the wall pressure distribution remains very similar to the initial static wall pressure profile.

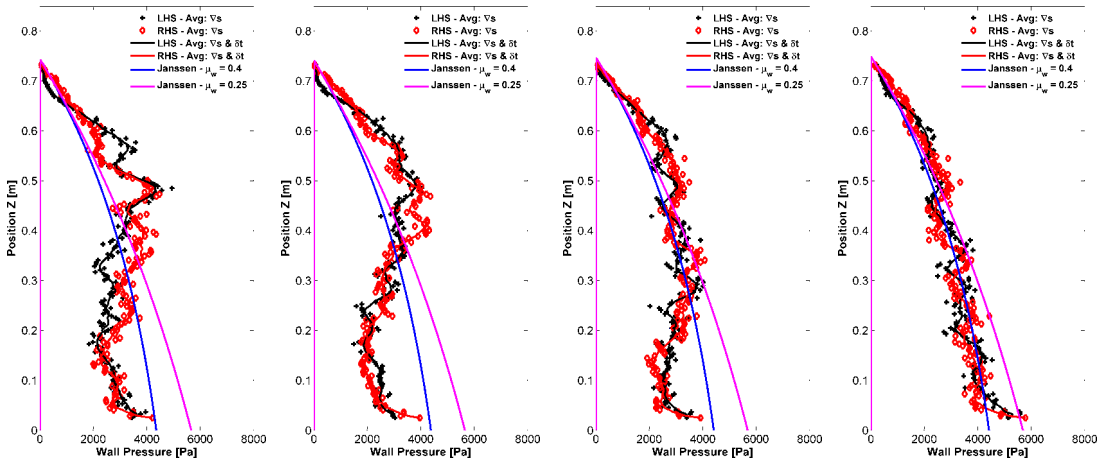

(a) $\Delta\gamma = 0J/m^2$ **(b)** $\Delta\gamma = 5J/m^2$ **(c)** $\Delta\gamma = 10J/m^2$ **(d)** $\Delta\gamma = 12.5J/m^2$

Figure 8.38: Wall pressures at $t_d = 0.5s$

At $t_d = 1s$ (Figures 8.39 and 8.40), the cohesive arch for $\Delta\gamma = 12.5J/m^2$ has remained intact and there is no change in the wall pressure distribution. At 10 J/m^2 the flow channel and effective transition have started to develop and a drop in the wall pressure in the region of the flow channel with a higher wall pressure noted further up the walls, above the effective transition height. This is similar to the profile seen in the cohesionless case at $t_d = 0.25s$ and for 5 J/m^2 at $t_d = 0.5s$. A significant dip in the wall pressure is noted for both 5 J/m^2 and cohesionless discharge between 0.4 and 0.5m in the region of mass flow above the effective transition.

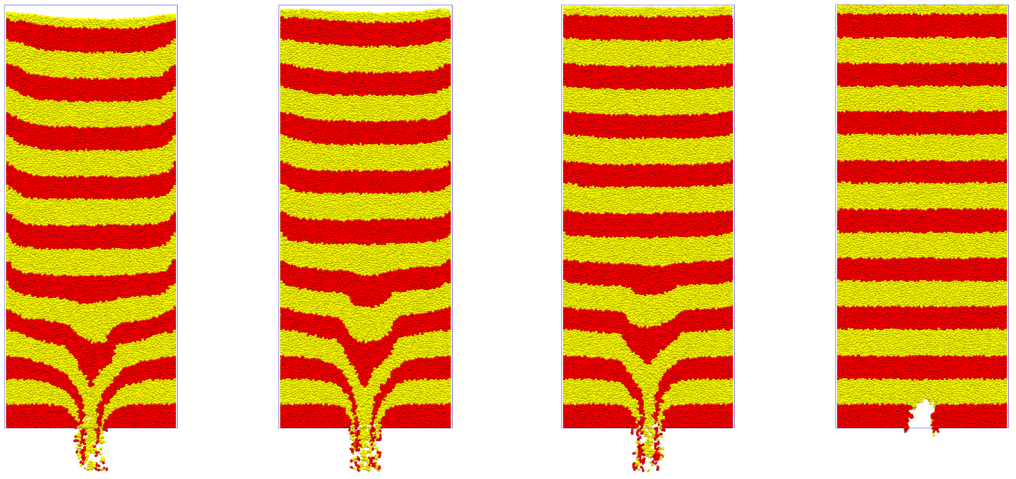

(a) $\Delta\gamma = 0J/m^2$ **(b)** $\Delta\gamma = 5J/m^2$ **(c)** $\Delta\gamma = 10J/m^2$ **(d)** $\Delta\gamma = 12.5J/m^2$

Figure 8.39: Discharge snapshots at $t_d = 1s$

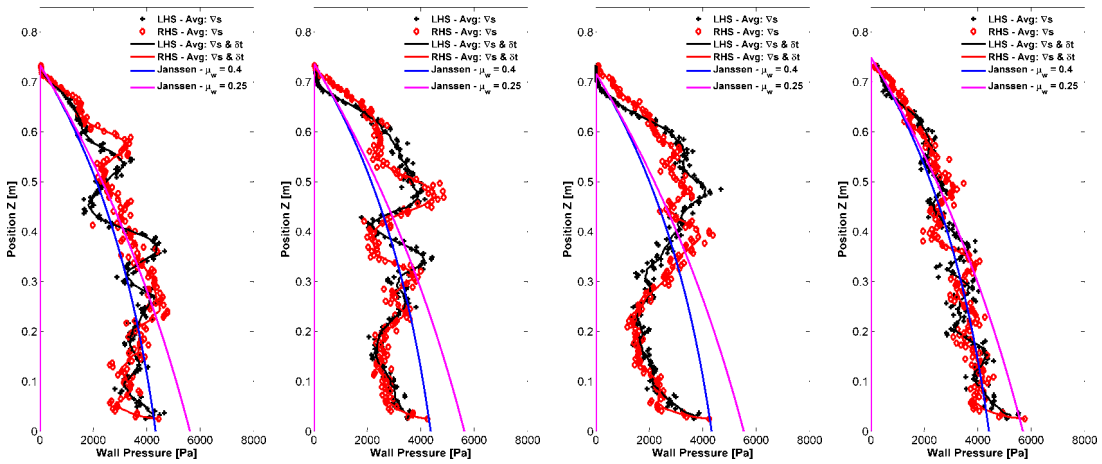

(a) $\Delta\gamma = 0J/m^2$ **(b)** $\Delta\gamma = 5J/m^2$ **(c)** $\Delta\gamma = 10J/m^2$ **(d)** $\Delta\gamma = 12.5J/m^2$

Figure 8.40: Wall pressures a $t_d = 1s$

As discharges continues, large variations in the wall pressure distribution exist between both the varying levels of adhesion and between both sides of the model silo. The flow patterns and silo wall pressures for $t_d = 2.5s$ are shown in Figures 8.41 and 8.42. After the collapse of the cohesive arch for an adhesion energy of 12.5 J/m^2 flow has developed since approximately $t_d = 1s$, with a significant drop in pressure around the area of the flow channel and an area of higher wall pressures much further up the silo. While there is variation in the magnitude and location of certain features, a trend can be seen of an area of low pressure in the region above the outlet with a further region of higher pressures related to the effective transition and mass flow above that. The wall pressure finally displays a hydrostatic type pressure as it gets close to the free surface of the particles.

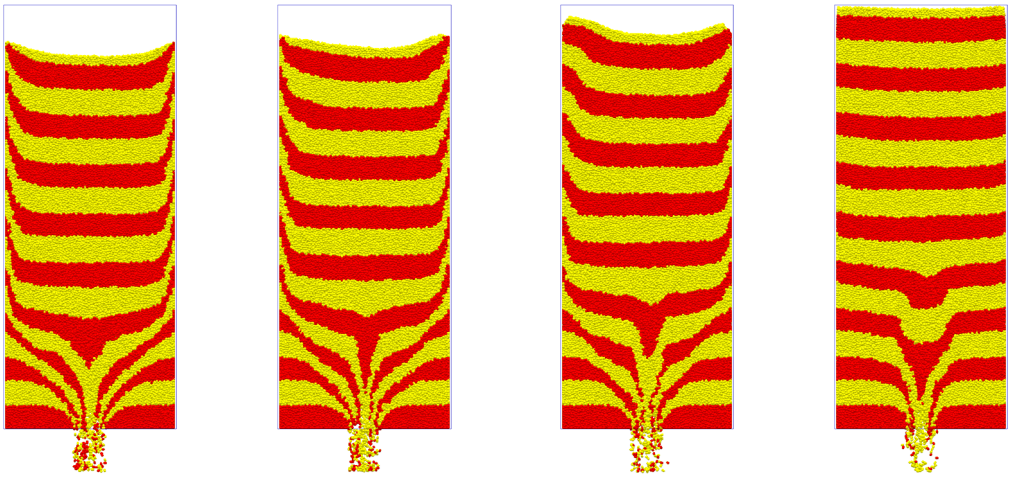

(a) $\Delta\gamma = 0J/m^2$ **(b)** $\Delta\gamma = 5J/m^2$ **(c)** $\Delta\gamma = 10J/m^2$ **(d)** $\Delta\gamma = 12.5J/m^2$

Figure 8.41: Discharge snapshots at $t_d = 2.5s$

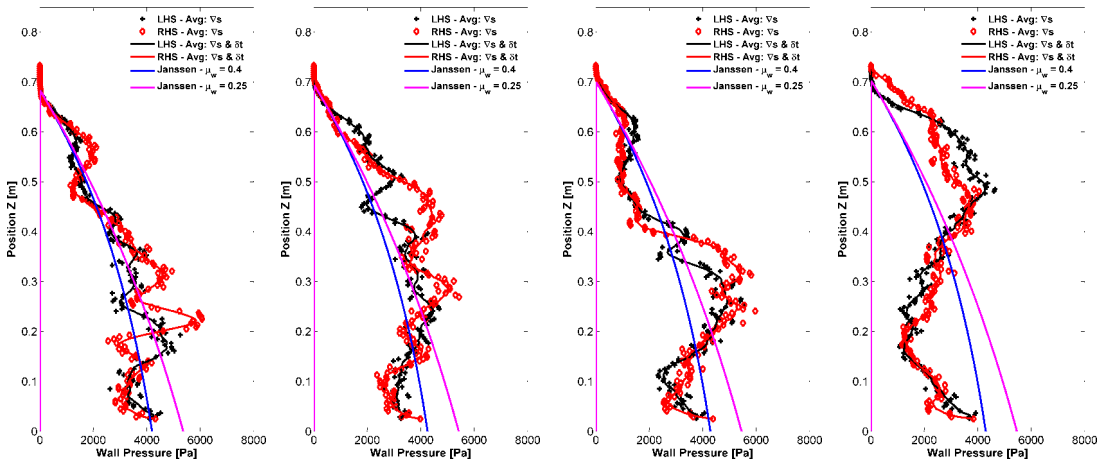

(a) $\Delta\gamma = 0J/m^2$ **(b)** $\Delta\gamma = 5J/m^2$ **(c)** $\Delta\gamma = 10J/m^2$ **(d)** $\Delta\gamma = 12.5J/m^2$

Figure 8.42: Wall pressures a $t_d = 2.5s$

For $t_d = 5s$ (Figures 8.43 and 8.44) the change in wall pressures does not vary significantly from that at 2.5 sec with the exception of an adhesion energy of 12.5 J/m^2, which after the formation and collapse of the cohesive arch, a stable discharge rate has developed since approximately $t_d = 4s$ (Figure 8.12) and the wall pressure profile is more in keeping with that found from other adhesion levels at previous timesteps.

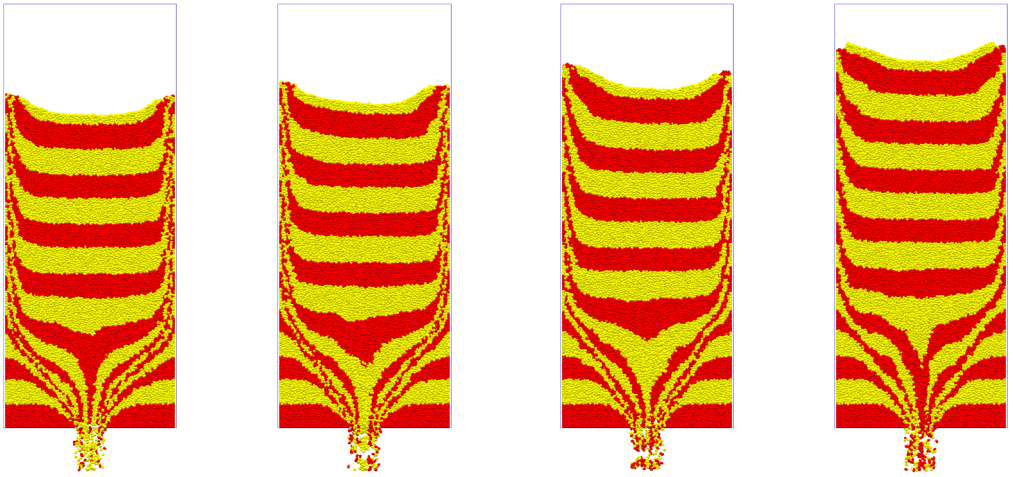

(a) $\Delta\gamma = 0J/m^2$ **(b)** $\Delta\gamma = 5J/m^2$ **(c)** $\Delta\gamma = 10J/m^2$ **(d)** $\Delta\gamma = 12.5J/m^2$

Figure 8.43: Discharge snapshots at $t_d = 5s$

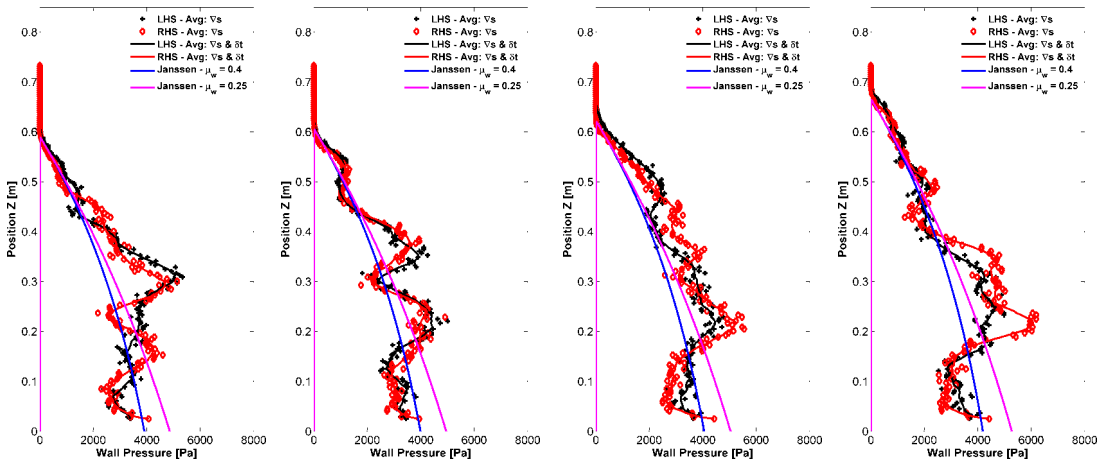

(a) $\Delta\gamma = 0J/m^2$ **(b)** $\Delta\gamma = 5J/m^2$ **(c)** $\Delta\gamma = 10J/m^2$ **(d)** $\Delta\gamma = 12.5J/m^2$

Figure 8.44: Wall pressures a $\mathbf{t_d = 5s}$

From $t_d = 7.5s$ (Figures 8.45 and 8.46) to $t_d = 10s$ (Figures 8.47 and 8.48) the discharge wall pressures for all adhesion levels seem to be in close agreement with the theoretical Janssen solution, although the normal pressure is being over-predicted near the free surface. This is mainly due to the boundary effects seen at the edges of the silo, leading to the free surface of the particles becoming concave due to the higher velocity of the particles outside of the boundary layer.

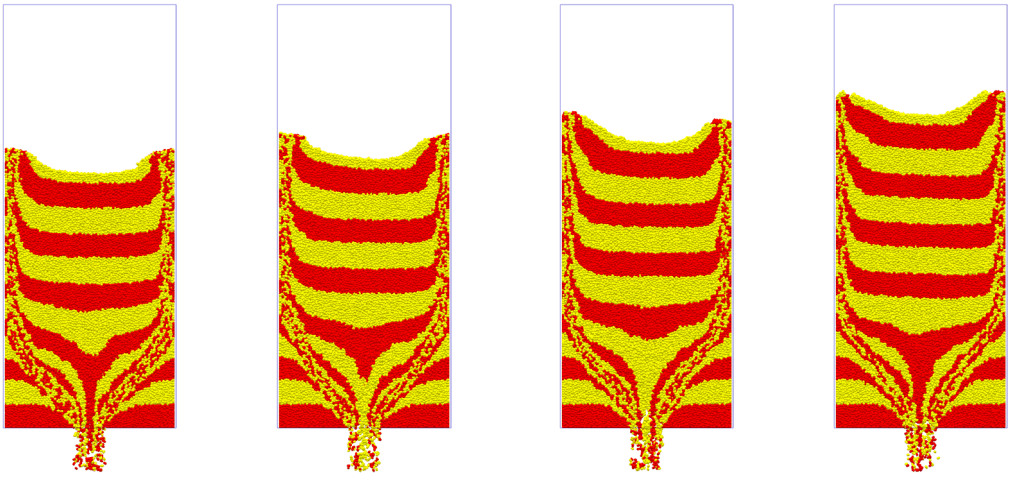

(a) $\Delta\gamma = 0J/m^2$ **(b)** $\Delta\gamma = 5J/m^2$ **(c)** $\Delta\gamma = 10J/m^2$ **(d)** $\Delta\gamma = 12.5J/m^2$

Figure 8.45: Discharge snapshots at $\mathbf{t_d = 7.5s}$

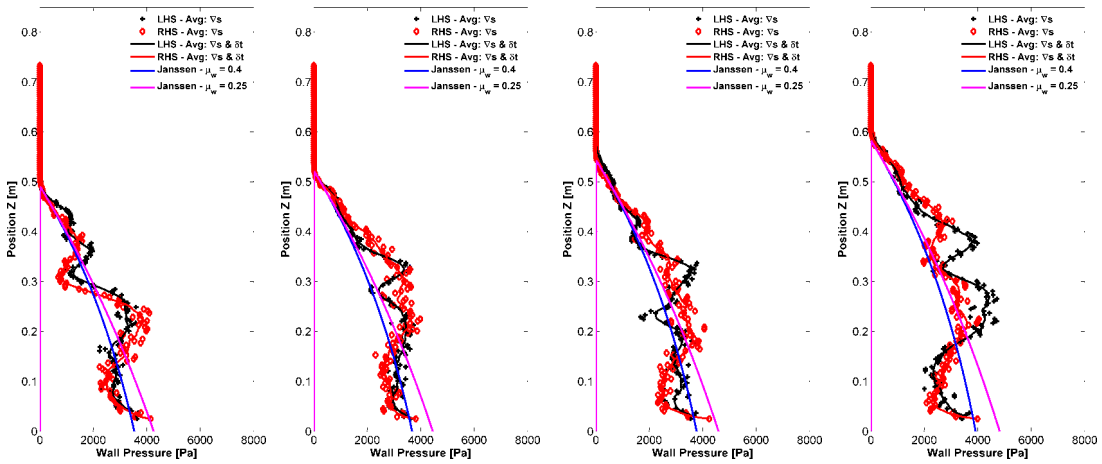

(a) $\Delta\gamma = 0J/m^2$ **(b)** $\Delta\gamma = 5J/m^2$ **(c)** $\Delta\gamma = 10J/m^2$ **(d)** $\Delta\gamma = 12.5J/m^2$

Figure 8.46: Wall pressures a $t_d = 7.5s$

At $t_d = 10s$ the concave profile has become significant leading to a larger mismatch for adhesion levels of 0, 5 and 10 J/m^2 in the upper portion of the silo.

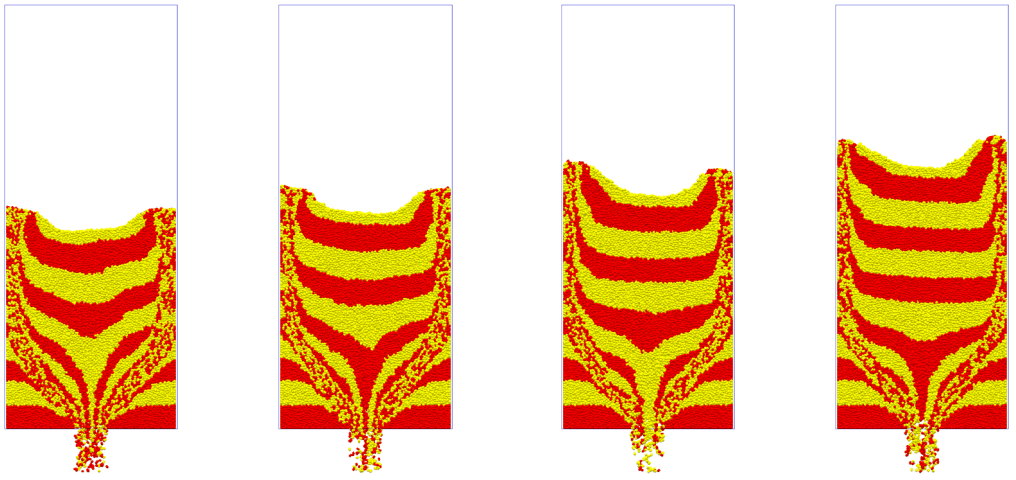

(a) $\Delta\gamma = 0J/m^2$ **(b)** $\Delta\gamma = 5J/m^2$ **(c)** $\Delta\gamma = 10J/m^2$ **(d)** $\Delta\gamma = 12.5J/m^2$

Figure 8.47: Discharge snapshots at $t_d = 10s$

By $t_d = 12.5s$ (Figures 8.49 and 8.50)the silos have significantly emptied to the point below the effective transition and flow at this point is mainly funnel flow only with increased velocities in the flow channel, with the exception of an adhesion energy of 12.5 J/m^2 which is taking longer to empty. As the flow mode changes to funnel flow only with reducing height the normal wall pressures become a linearly decreasing wall pressure, similar to hydrostatic pressure, with the maximum wall pressure predicted near the base still similar to the Janssen predicted magnitude.

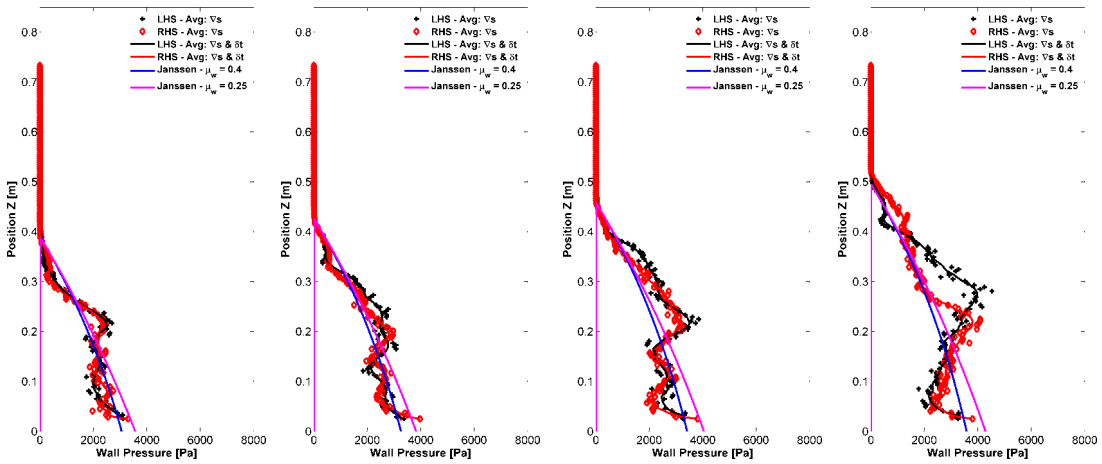

(a) $\Delta\gamma = 0J/m^2$ **(b)** $\Delta\gamma = 5J/m^2$ **(c)** $\Delta\gamma = 10J/m^2$ **(d)** $\Delta\gamma = 12.5J/m^2$

Figure 8.48: Wall pressures a $t_d = 10s$

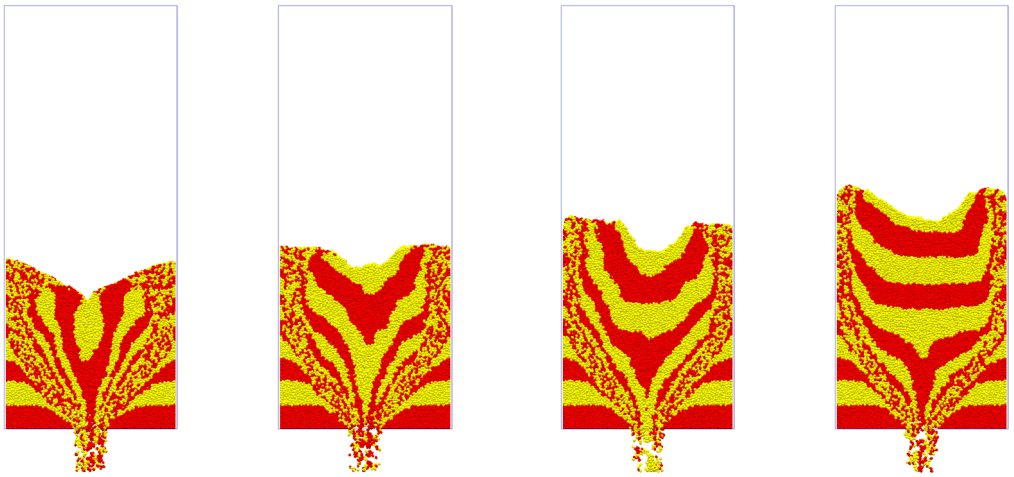

(a) $\Delta\gamma = 0J/m^2$ **(b)** $\Delta\gamma = 5J/m^2$ **(c)** $\Delta\gamma = 10J/m^2$ **(d)** $\Delta\gamma = 12.5J/m^2$

Figure 8.49: Discharge snapshots at $t_d = 12.5s$

At $t_d = 15s$, the discharge is almost complete for the lower adhesion energies with very small wall pressures relating to the materials left in the stagnant zones found. The highest adhesion energy of 12.5 J/m^2 has become funnel flow only and displays the same linearly decreasing wall pressure seen previously for the lower adhesion levels.

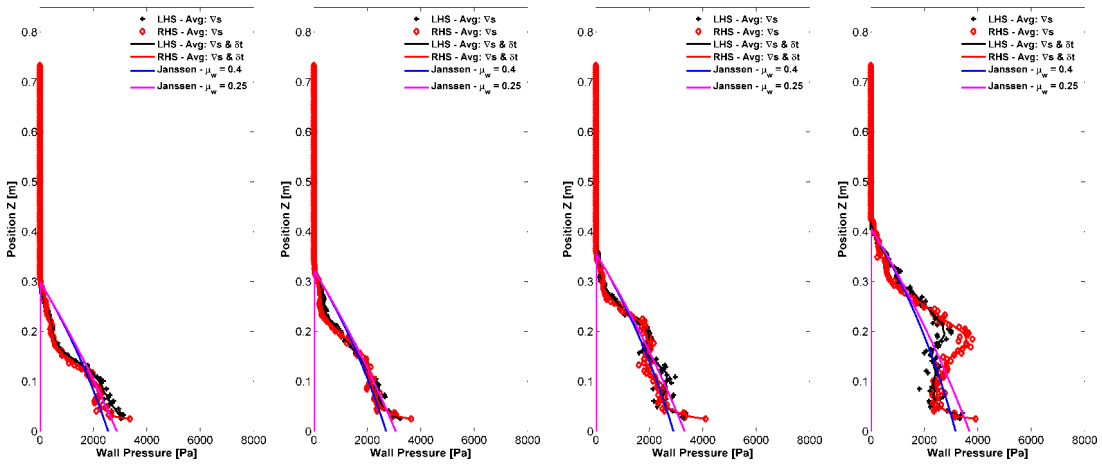

(a) $\Delta\gamma = 0J/m^2$ **(b)** $\Delta\gamma = 5J/m^2$ **(c)** $\Delta\gamma = 10J/m^2$ **(d)** $\Delta\gamma = 12.5J/m^2$

Figure 8.50: Wall pressures a $t_d = 12.5s$

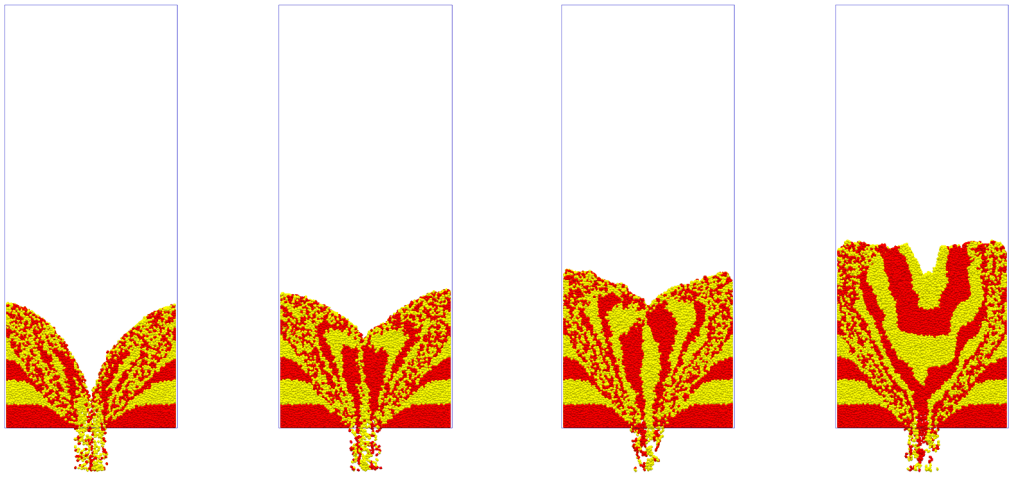

(a) $\Delta\gamma = 0J/m^2$ **(b)** $\Delta\gamma = 5J/m^2$ **(c)** $\Delta\gamma = 10J/m^2$ **(d)** $\Delta\gamma = 12.5J/m^2$

Figure 8.51: Discharge snapshots at $t_d = 15s$

8.6 Relationship to Internal Stress

The results presented in the previous sections have shown that there is a strong correlation between the flow patterns and channels that develop during discharge and the resulting wall pressured measured at the silo walls. In the areas of mass flow, above the effective transition, high wall pressures were recorded, while at lower heights a dip is often noticed below the effect transition.

8.6.1 Cohesionless Discharge

At $t_d = 0.5s$, after stable discharge has developed in the cohesionless assembly, the observed wall pressures in Figure 8.38a show an area of high pressure above the effective

transition with lower pressures observed below 0.25m. The wall pressures observed are also unsymmetrical with pressure on the left-hand side lower than the right. While not much information can be gleaned from the solid fraction in Figure 8.52a other than a slightly lower solid fraction in the vicinity of the high velocity core flow channel, a clear link between the internal horizontal and vertical stresses in the solid and the wall pressures can be made. In Figure 8.52b the horizontal stresses are clearly much higher in the zone of mass flow above the effective transition, with what appears to be a greater concentration of areas of high stress along the right hand side as compared to the left. The zone also appears to extend lower on the right hand side. Figures 8.52b and 8.52c show that in the high velocity core flow zone above the outlet there are significantly reduced stress in the stored solid as arching behaviour in the mass flow zone transmits the force into the silo walls and also into the solid in the stagnant zones which experiences high vertical stress, much like a column transmitting load in a structure.

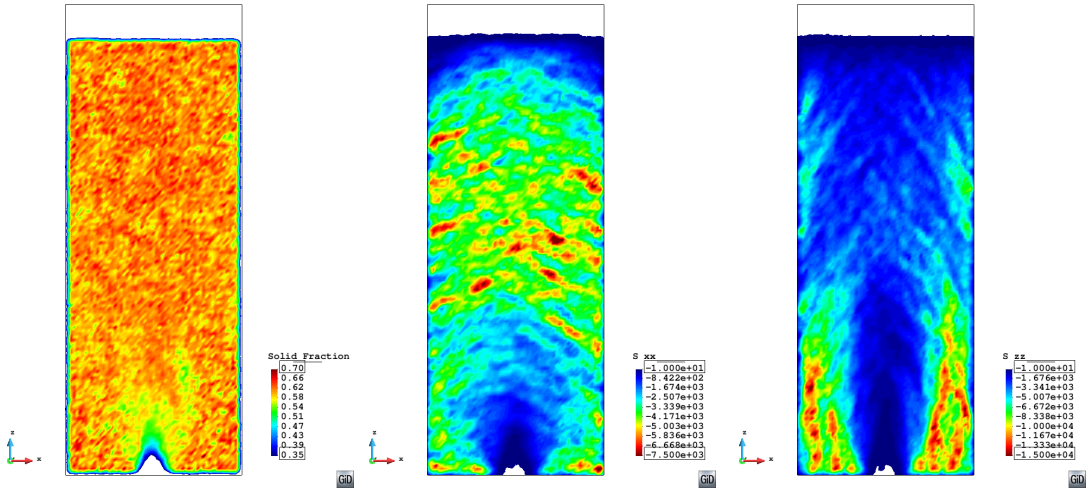

(a) Solid Fraction **(b)** Horizontal Stress **(c)** Vertical Stress

Figure 8.52: Cohesionless contour fields at t_d = 0.5s - For $\Delta\gamma = 0 J/m^2$

In Figure 8.53, at t_d = 1s, the relationship with the unsymmetrical wall pressures is more obvious. In the wall pressure distribution in Figure 8.40a, there is a higher pressure observed at both the right and left side at a heigh of 0.25m (the effective transition height). Above this, the pressure on the right side gradually decreases, while on the left side it is maintained initially before there is a significant and sudden dip in the pressure at about 0.45m which increase again towards the hydrostatic limit as it nears the free surface. This pattern is clearly reflected in the horizontal stress in Figure 8.53b, where significant horizontal stresses are seen arching across the central flow channel. This stress drops gradually on the right hand side, but is maintained on the left before a dip is noted, displaying the same patterning as the reported wall pressures. The vertical stress shown in Figure 8.53c also shows a more noticeable area

of vertical stress at the base of the mass flow zone where there appears to be significant arching.

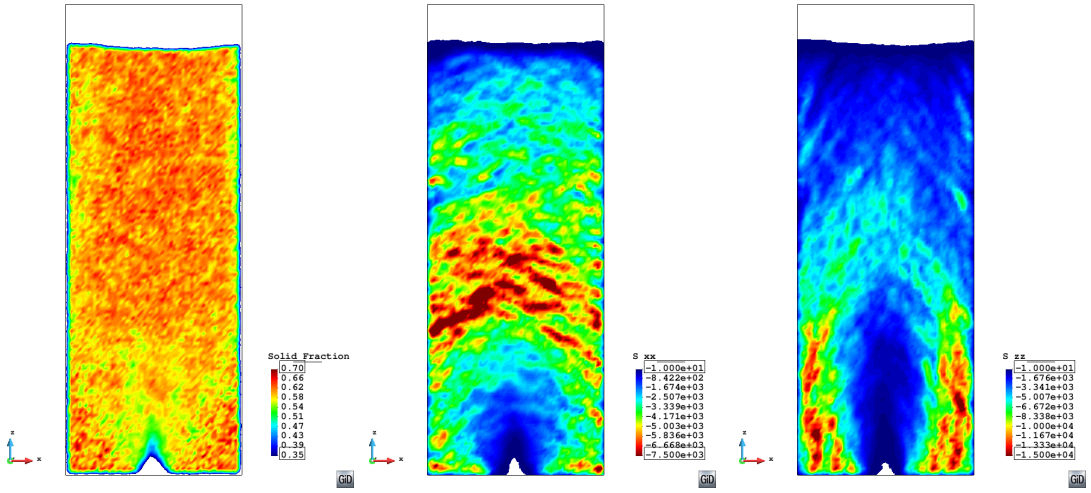

(a) Solid Fraction **(b)** Horizontal Stress **(c)** Vertical Stress

Figure 8.53: Cohesionless contour fields at t_d = 1s - For $\Delta\gamma = 0J/m^2$

At t_d = 2.5s, a strong correlation between the wall pressures observed in Figure 8.42a and the horizontal stress in Figure 8.54b exists,with higher wall pressures and horizontal stresses found in the right side with the location of the high stress also found to be higher on the right hand side. A similar pattern to previous timesteps is noted for the vertical stress in Figure 8.54c, where high vertical stress are found in the stagnant zones either side of the core flow channel.

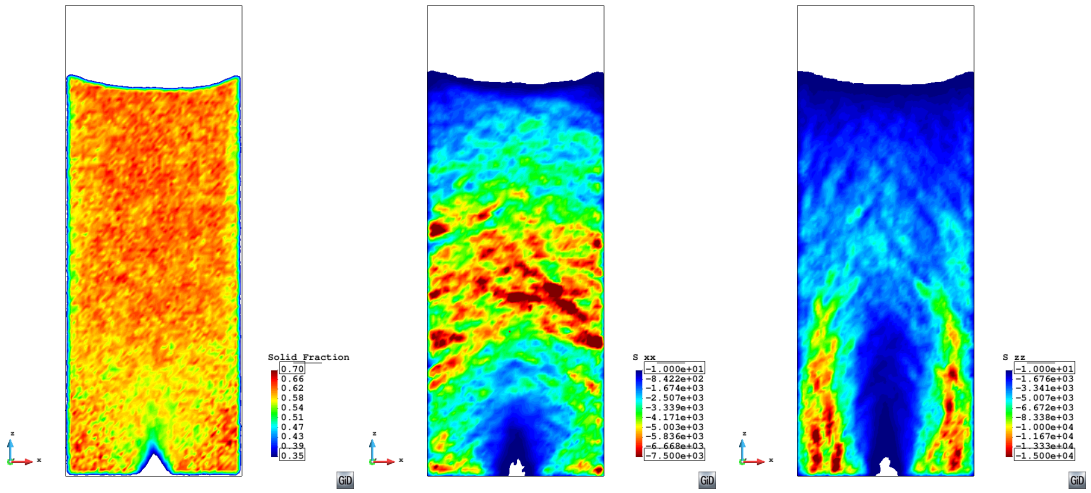

(a) Solid Fraction **(b)** Horizontal Stress **(c)** Vertical Stress

Figure 8.54: Cohesionless contour fields at t_d = 2.5s - For $\Delta\gamma = 0J/m^2$

8.6.2 Cohesive Discharge

The solid volume fraction at various timesteps for cohesive flow is presented in sub-figure (a) of Figures 8.55 to 8.57. It can be seen that following the collapse of the temporary arch in Figure 8.55a there is a area of significantly lower solid fraction in the vicinity of the high velocity central flow channel identified previously in Section 8.4.1. While this may be expected immediately following the collapse of the temporary arch, Figure 8.55 is more than 1.5s after the collapse of the arch (Figure 8.12) and the initiation of flow. A loosely packed flow channel is further supported by the horizontal and vertical stresses in Figures 8.55b and 8.55c where significantly lower stresses are found in the flow channel.

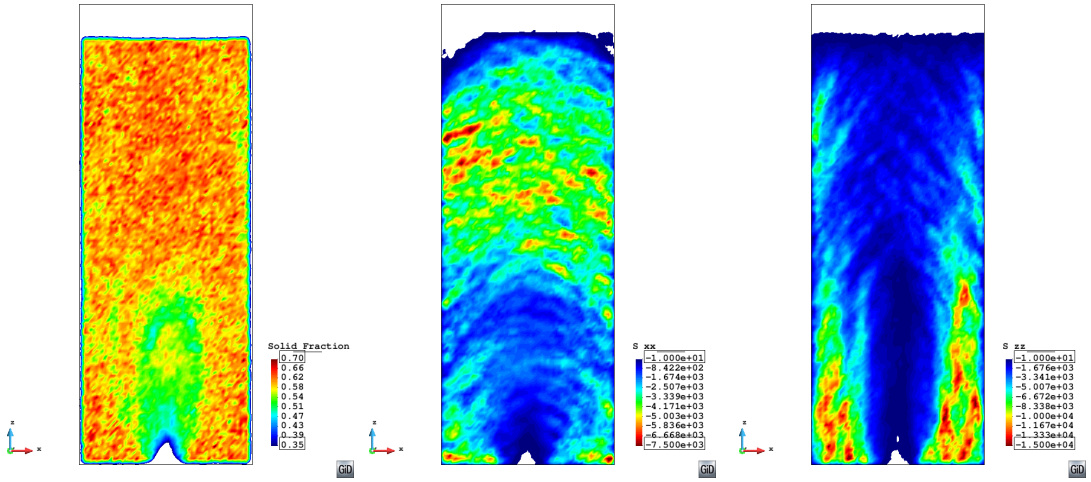

(a) Solid Fraction **(b)** Horizontal Stress **(c)** Vertical Stress

Figure 8.55: Cohesive contour fields at t_d = 2.5s - For $\Delta\gamma = 12.5 J/m^2$

The results in Figures 8.55 and 8.56 suggest that further arching higher in the silo allows the core flow zone above the outlet to empty first, before further material from the edges of the funnel flow zone enters, which finally leads to the collapse of the arch formed around the effective transition height. The lower solid fraction is maintained at following timesteps once stable flow has developed, as shown in Figures 8.56 and 8.57. The observed behaviour of the highly cohesive assembly is different from that of the cohesionless assembly in which all particles start to flow immediately, whereas with large amount of cohesion a much looser packing is found in the funnel flow zone as adhesion prevents all particles flowing immediately.

A porosity of 0.42 was measured for t_d = 5s and a porosity of 0.43 was measured at t_d = 7.5s for an adhesion energy of 12.5 J/m^2. This compares similarly to the porosity of the cohesionless assembly at the same timesteps, which was measured as 0.43 at both times. With both assemblies having a similar global porosity at the two timestpes a

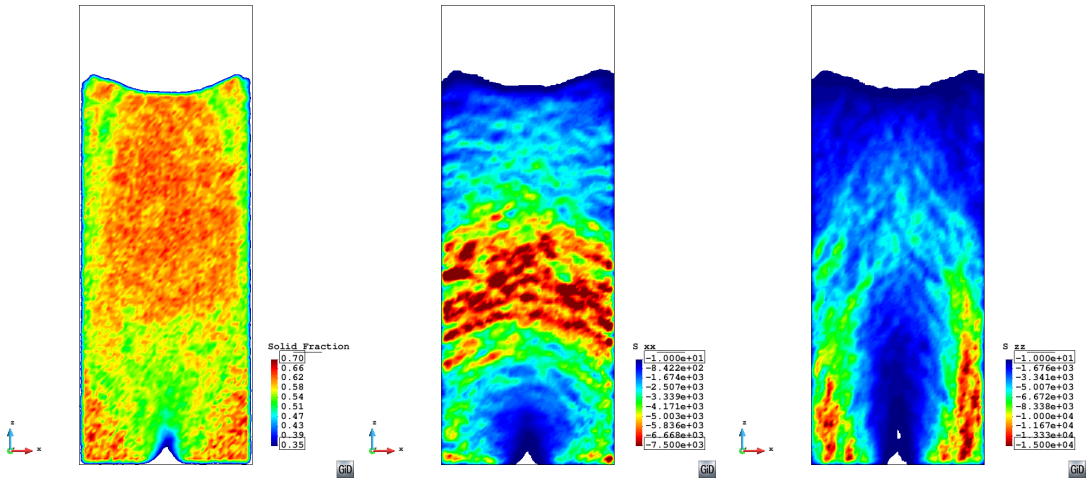

(a) Solid Fraction **(b)** Horizontal Stress **(c)** Vertical Stress

Figure 8.56: Cohesive contour fields at t_d = 5s - For $\Delta\gamma = 12.5 J/m^2$

comparison can be made to the solid fraction found in the cohesionless discharge for a similar period. Figures 8.52a to 8.54a show the solid fraction for a similar time period during stable discharge.

In all levels of adhesion significant horizontal stresses are noted in the region of the effective transition and significant vertical stresses in the stagnant zones either side of the high velocity core flow zone.

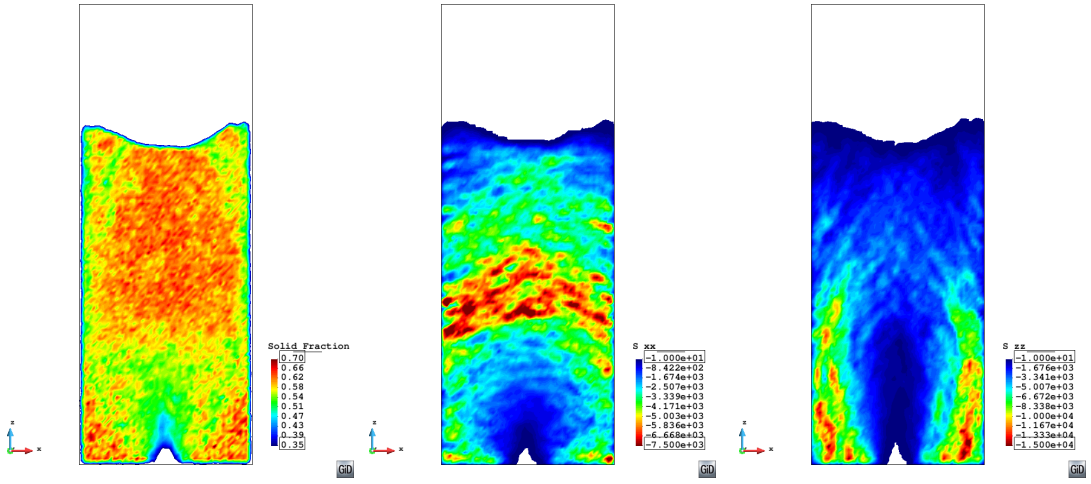

(a) Solid Fraction **(b)** Horizontal Stress **(c)** Vertical Stress

Figure 8.57: Cohesive contour fields at t_d = 7.5s - For $\Delta\gamma = 12.5 J/m^2$

8.7 Cohesive Arching

In the most cohesive of the silo flow simulations at an adhesion energy of $\Delta\gamma$ = 12.5 J/m^2, flow was interrupted by the development of a temporary arch after a quarter of

a second which lasted for approximately 0.6s before the arch collapsed and discharge resumed. The horizontal and vertical stresses in the solid are presented at the mid-timestep of the arch at t_d = 0.5s in Figure 8.58. In cohesionless discharge the vertical stress in the solid begins to decrease almost immediately when the outlet is opened and particles begin to flow. Where adhesion is included in the system, additional restraint to the acceleration of the particle towards the outlet is provided by the increased adhesion. The leads to higher stresses, related to resisting the mass of solid above the arch, being observed.

The arch formed in this case is a weak arch which eventually fails under the weight of the material above it and begins to flow as seen in Figures 8.55 to 8.57.

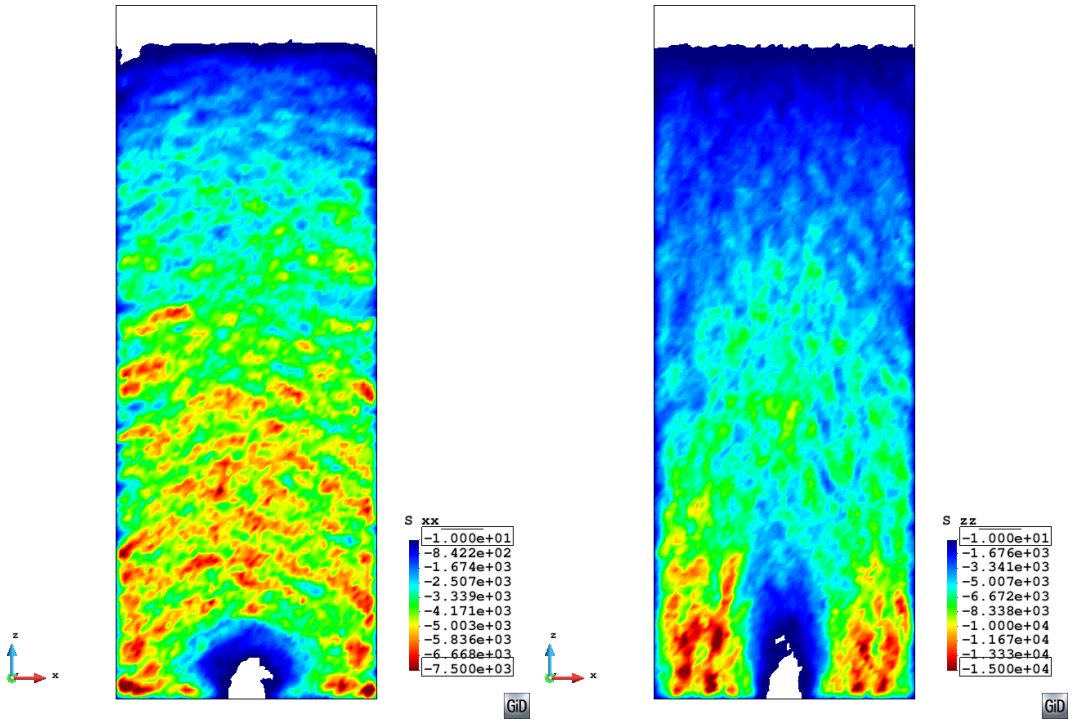

(a) Horizontal Stress **(b)** Vertical Stress

Figure 8.58: Temporary cohesive arch stress contours at t_d = 0.5s - For $\Delta\gamma = 12.5 J/m^2$

At the highest adhesion energy tested of $\Delta\gamma$ = 15 J/m^2 in the discharge study a permanent cohesive arch developed at the onset of discharge, preventing any flow from the silo. In Figure 8.59 the horizontal and vertical stresses are plotted where a permanent arch has formed and prevented discharge form the silo from occurring. The resulting stresses measured are much than in the case of the temporary arch

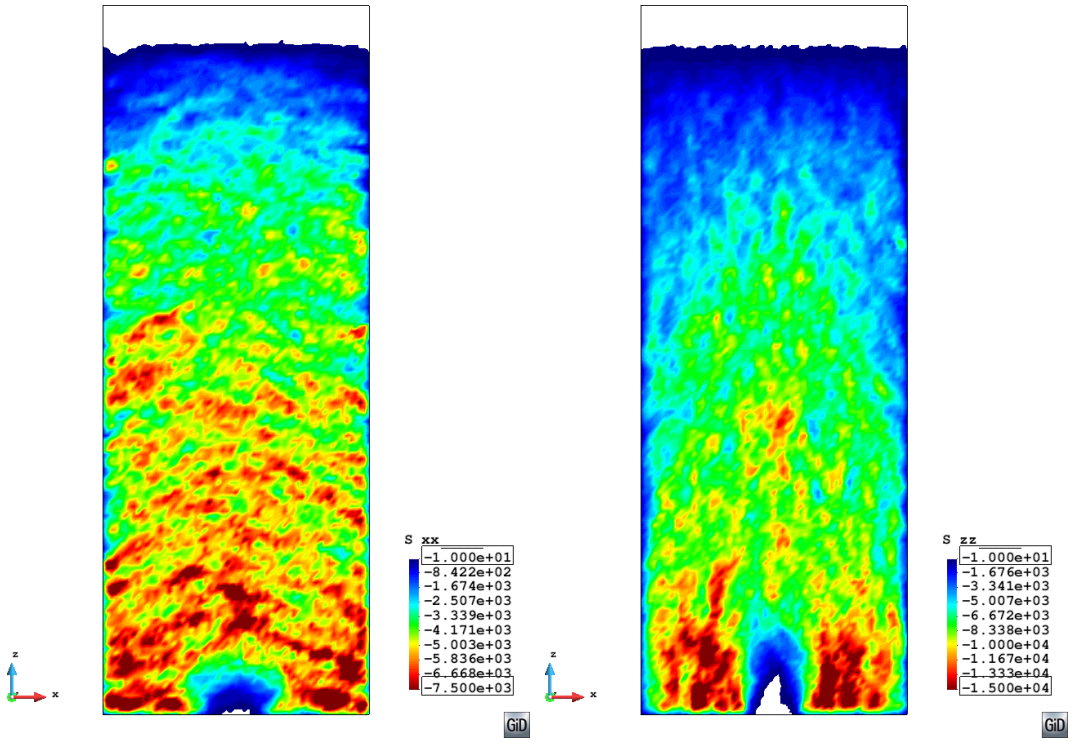

(a) Horizontal Stress **(b)** Vertical Stress

Figure 8.59: Permanent cohesive arch stress contours at t_d = 0.5s - For $\Delta\gamma = 15J/m^2$

8.8 Summary

The effect of increasing levels of adhesion has been explored for a flat bottomed silo where the level of adhesion has been varied. The DEM simulations were found to capture the major phenomena occurring in silo flow including the various flow zones associated with a flat bottomed hopper and the effective transition and mass and funnel flow associated with a mixed flow pattern observed in the silo.

The location of the effective transition height was identified at a height of approximately 0.25m from a combination of the velocity profiles and the velocity contours for the silo. Above this mass flow was observed, with the velocity determined from the discharge rate and the velocity profiled found to be in excellent agreement. A high velocity core flow zone was observed above the outlet where velocities were greater than $1.25\ V_{MF}$. The location of the high velocity core flow zone agrees well with that proposed in the literature.

The wall pressures measured in the model silo were found to be in good agreement with theoretical predictions and experimental observation with higher wall pressure measured above the effective transition where mass flow occurred. The wall pressures were found to be sensitive to flow patterns during discharge, where minor variations

in the flow channel lead to asymmetry in the measured wall pressures. The additional adhesion did not lead to significantly different wall pressures, although the reduced discharge rate lead to certain features appeared at different times.

The increase in the level of adhesion in the silo was not found to significantly alter the flow patterns observed. However,as the level of adhesion in the silo increased, a reduced flow rate was found until the eventual blockage of the silo at a high level of adhesion was found. As the level of adhesion increased the probability of arching also increased, and the formation of intermittent arching behaviour was noted in the cases with higher levels of adhesion in the system. A significant temporary arch preventing discharge for over 0.5s was observed at an adhesion energy of $\Delta\gamma = 12.5J/m^2$. The arch eventually collapsed due to insufficient strength to carry the weight of the material about it.

Chapter 9

Conclusions & Recommendations

The research in this thesis has been carried out to study the behaviour of cohesive granular solids from experimental methods and used this information to calibrate DEM simulations and improve the ability of DEM to capture the stress-history dependent nature of cohesive granular fines. The effect of cohesion on the behaviour of iron ore fines supplied by LKAB has been investigated, while DEM simulations have been carried out to reproduce the experimental flow function measured from uniaxial experiments. Finally, an exploratory study into the effect of cohesion on the discharge from a flat bottomed silo has been carried out with the presented contact model.

This chapter summarises the conclusions drawn over the course of the thesis and suggests relevant research topics for future investigations

9.1 General Conclusions

The conclusions drawn from this work can be broken down in to two main areas: Experimental studies and DEM studies. The conclusions from each are presented in the following sections.

9.1.1 Experimental Work

A comprehensive study on the effect of cohesion arising from the addition of moisture on the behaviour of two types of LKAB iron ore fines (KPBO and KPRS) has been carried out. The addition of moisture to the sample has been found to have a significant effect on both kinds of fines.

A uniaxial tester in the form of the Edinburgh Powder Tester (EPT) has been used to derive the flow function for both types of fines under various moisture contents. The

packing and compression behaviour for both materials up to a consolidation stress of 120 kPa has also been assessed using the EPT. The measuring capabilities of the EPT have been improved by the addition of an extra load cell and a higher speed digital data logger. The repeatability of the EPT has been found to be excellent with a coefficient of variation of less than 5% observed for a stable gypsum calibration mix and slightly greater than 5% for the tests carried out on iron ore fines.

The unconfined strength and resulting flow functions have been experimentally determined for both types of LKAB fines at varying moisture content levels between 1-6%. Significant differences in the two types of fines were observed for different moisture content levels. KPRS fines have a much higher unconfined strength and flow function at higher moisture contents, and also show a greater increase in cohesion with the addition of moisture. This suggests more difficulty in handling of KPRS fines in wetter conditions, while at moisture contents of less than 2% the KPBO fines demonstrate higher unconfined yield strength and are also more susceptible to the bulking behaviour related to the addition of moisture content. The KPBO fines achieve a significantly looser initial packing at much lower moisture content when compared to the KPRS fines. Both materials were found to behave similarly under confined compression.

Observations made on the behaviour of both types of fines during drying, suggest that across all size ranges the KPRS fines are more susceptible to caking with large agglomerates noted. Little or no agglomeration was observed for dried KPBO fines. The susceptibility of the KPRS fines to caking may also lead to significantly more handling problems.

The effect of moisture content on the angle of internal friction for both types of fines has been evaluated from Jenike shear cell tests. The results have shown that the very rough and angular iron ore fines are a highly frictional material with an angle of internal friction of 44 degrees measured for KPRS fines and 45 degrees for KPBO fines. The addition of large amount of moisture to the sample was found to reduce the angle of internal friction only slightly and the addition of 8% moisture content led to a reduction in the friction angle of about 3 degrees.

The lateral pressure ratio and bulk loading and unloading stiffness of the iron ore fines have been evaluated from a confined compression test. The lateral pressure ratio has been determined for each type of iron ore fines for three different moisture contents. The coefficient of variation for the determined K_0 value over 10 tests at each moisture content was less than 10%. Both types of iron ore fines were found to share a similar behaviour and return a K_0 value of approximately 0.24 in the region of 0-5% moisture content before the lateral pressure then increases with the further addition of moisture

as the level if inter-particle lubrication increases. After a further increase in moisture content to 8%, the lateral pressure increased significantly to over 0.3. If the measured lateral pressure ratio is corrected to account for the protective sheeting that was in place during the test, the values rise by approximately 0.05 to 0.29 for the 0-5% range before increasing to 0.36 at 8% moisture level. The corrected values are in close agreement with the lateral pressure ratios found when calculated based on the measured angle of internal friction using Jaky theory.

9.1.2 DEM Simulations

In this study a mesoscopic adhesive contact model that accounts for contact plasticity and stress history dependency in the bulk solid, the Edinburgh Elasto-Plastic Adhesion (EEPA) mode, has been presented. The contact model has been carefully verified mathematically to ensure that the contact model has been correctly implemented in the DEM code EDEM. The elasto-plastic adhesive contact model has been found to be providing the expected results for several simple problems at a particle scale.

A parametric study of the DEM contact model parameters was conducted to gain a deeper understating of the effect of input parameters on the simulated cohesive bulk behaviour. The key conclusions are summarised as follows:

- The adhesion energy of the contact is an important parameter for controlling the amount of adhesion in the system. In addition, the adhesion between particles is also affected by many other parameters such as the loading and unloading stiffness which determine the plastic overlap at a contact.
- The tangential stiffness was found to be important for controlling the unconfined bulk stiffness to the yield point while the assembly of particles is undergoing shear. The predicted lateral pressure ratio is also significantly affected by the tangential stiffness.
- While increasing the adhesion branch slope allows for particles to separate from contact more quickly once the contact limit has been reached, this does not lead to a more brittle assembly such as that seen in the experiments.
- Inter-particle friction and shape were found to have a strong influence on the unconfined strength of a sample. Typically, a higher coefficient of inter-particle friction lead to macroscopically stronger assembly, which often lead to a more pronounced peak strength followed by a distinct drop in the strength.
- The lateral pressure ratio was found to be relatively insensitive to the loading and unloading stiffness and adhesion energy values during confined compression, but

the effects of these parameters on the initial packing that is formed has an effect on the observed lateral pressure.

- Static friction and rolling friction were found to have a significant effect on the lateral pressure ratio, with a significant decrease in the lateral pressure ratio for increasing static and rolling friction which added extra frictional and shearing resistance to the assembly. Particle shape was also found to be an important factor that can affect the lateral pressure ratio.

- Particle interlocking for non-spherical particles allowed larger tangential forces to be transmitted through the contacts thus increased the strength of the assembly. Greater interlocking in non-spherical particles also has the effect of larger dilation of the sample in the shear bands, due to the additional resistance to rolling.

- The use of global damping is a powerful method of dissipating energy in the systems being simulated, but care needs to be taken when applied to dynamic systems where it can affect the dynamic processes that are being considered.

The EEPA contact model has been used to predict an experimental flow function of KPRS iron ore fines. The contact model has demonstrated the ability to capture the stress history dependent behaviour that exists in cohesive granular solids. The DEM simulations have been calibrated from a selection of uniaxial experiment results and the remainder have been used to compare to the DEM simulation predictions. The friction parameters have been selected based on the measured bulk friction angle from the Jenike shear angle and the reported relationship between particle shape, contact friction and bulk friction. An attempt has been made to match the loading and unloading stiffness values that have been measured experimentally from confined compression tests. The iron ore particles require a high virgin loading stiffness for a close match between the DEM simulation and measured values. However such a loading stiffness has been shown to be unable to provide a matching flow function and a lower stiffness has been selected as a compromise to allow a closer match to the experimental flow function.

Strong correlations between the DEM simulations and experimental results were observed for the confined compression, with the development of the lateral pressure ratio found to be similar to that of the confined compression tests. The K_0 value from the DEM simulations was found to be between 0.32 - 0.34 which is in excellent agreement with values found from the Eurocode 1 calculation method from internal angles of friction for the material.

The DEM simulations provide a very close match to the experimental flow functions, with the predicted unconfined strengths found to be within the standard deviations of the experimental results. The DEM simulations also predicted densities similar to those found experimentally, although the unconfined loading stiffness and resulting stress strain relationships have not been matched in a compromise to predict the material flow function. While the DEM simulations are in excellent agreement with the unconfined strength, the experimental results display a clear over-consolidated behaviour across all consolidation stresses and levels of cohesion tested, which the DEM simulation cannot predict. Over-consolidation behaviour in the DEM simulations is observed in cases where the porosity of the samples is below approximately 45%.

Investigations into the failure mode predicted by the DEM simulations have shown that the samples are failing from the development of shear planes similar to those observed experimentally. The shear failure has been detected in simple single layer planar simulations and larger full 3D simulations of a cylindrical sample through the use of such indicators as cumulative particle displacements, particle velocity, angular velocities which are an indicator of particle rotations and internal stresses in the samples.

The effect of increasing levels of adhesion has been explored for a flat bottomed silo where the level of adhesion has been varied. The DEM simulations were found to capture the major phenomena occurring in silo discharge including the various flow zones associated with a flat bottomed silo. Funnel flow, the effective transition and mass flow which are associated with a mixed flow pattern were observed in the model silo. The location of the effective transition height was identified: above this was mass flow. The velocity determined from the discharge rate was found to be in excellent agreement with the velocity profiles found in the zones of mass flow. A high velocity core flow zone was observed above the outlet where velocities were greater than 1.25 times the mass flow velocity, V_{MF}. The location of the high velocity core flow zone agrees well with that proposed in the literature. The increase in the level of adhesion in the silo was not found to significantly alter the flow patterns observed. However, as the level of adhesion in the silo increased, a reduced flow rate was found until the eventual blockage of the silo at a high level of adhesion was found.

The wall pressures measured in the model silo were found to be in good agreement with those predicted from Janssen Theory and also experimental observation where higher wall pressure measured are noted above the effective transition where mass flow occurs. The wall pressures were also found to be sensitive to flow patterns during discharge, where minor variations in the flow channel lead to asymmetry in the measured wall pressures. The additional adhesion did not directly lead to significantly different

wall pressures, although the reduced discharge rate lead to certain features appearing at different times. As the level of adhesion increased the probability of arching also increased, and the formation of intermittent arching behaviour was noted in the cases with higher levels of adhesion in the system. The development of both temporary and permanent cohesive arches over the silo outlet were also observed with stopped flow from the silo.

9.2 Recommendations for Future Research

The thesis has presented an elasto-plastic adhesive contact model for use in the simulation of cohesive granular solids. The model has been calibrated from bulk experiments to replicate the flow function of KPRS iron ore fines and an exploratory study on the effect of cohesion on silo discharge has been performed. Several areas where further investigation would be beneficial are listed below.

9.2.1 Experimental Work

The effect of moisture content on the development of cohesion in iron ore fines has been evaluated. Observations made during the characterisation of the iron ore fines showed that wet samples of the fines that were left to dry following testing displayed slightly different behaviour. KPRS fines were found to dry to agglomerates that were quite strong and required significantly more pressure to break than the KPBO fines. It is likely, that due to the addition of moisture and the slightly different chemical makeup for the two types of fines, a different long-term caking behaviour exists between the two materials. Further testing is required to investigate this phenomenon and determine the factors that lead to the different behaviour. All experimental studies presented on the iron ore fines were carried out at room temperature. During transport and initial storage the iron ore pellets and fines are subjected to elevated temperatures between 30-70°C as the pellets cool. The elevated temperatures may affect the chemical make-ups of the KPRS and KPBO fines in the presence of moisture differently. Observations made during drying of samples suggest that KPRS fines are more susceptible to caking at high temperature. Further research could investigate the effect of temperature on the different types of fines. While DEM simulations have been carried out for cohesive silo discharge no experimental studies were carried out. A validation study for cohesive discharge using a small scale silo could be carried out to confirm the observations

9.2.2 DEM Simulations

The failure of the DEM simulations to predict the over consolidation behaviour may be related to the homogeneity of the DEM assemblies, where a uniform particle size and

shape has been used. The introduction of different particle size and shape may lead to a greater variety and distribution in the calculated contact forces and may lead to a more brittle failure mode as seen in the experiment, as the anisotropy of the packing would increase. A detailed study of poly-dispersity and mixed shapes should be conducted. Time dependent processes such as caking are currently not considered in the model. For many materials, time consolidation can have a significant impact on the measured unconfined strength. A method of accounting for this time dependency could be added to the model to investigate this issue. The tangential stiffness has not been studied in detail for cohesive, non-spherical particles in the literature but was found to have significant effects on the observed lateral pressure ratios and bulk unconfined stiffness to failure in the simulations. Further research is required to fully quantify the effects of the tangential stiffness on DEM bulk behaviour.

Appendix A

SEM Images For Iron Ore Fines

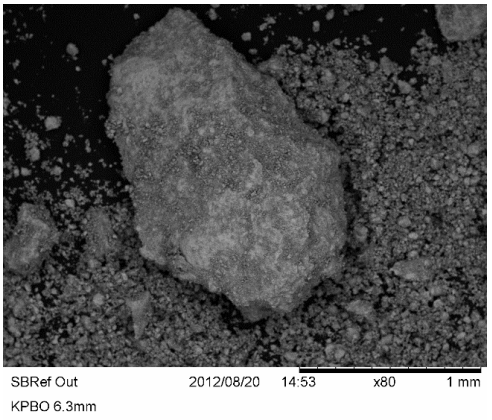

Figure A.1: KPBO Fines - Magnification - 80x

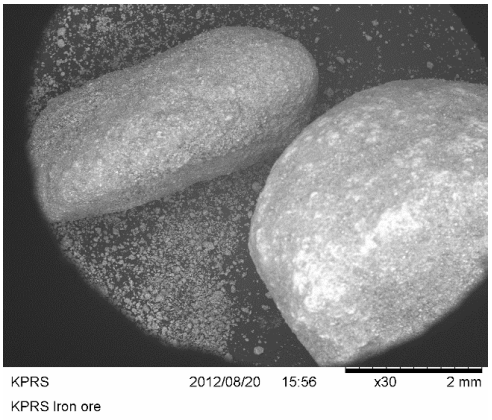

Figure A.2: KPRS Fines - Magnification - 30x

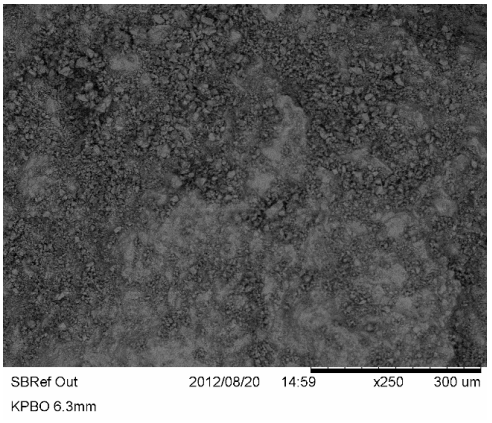

Figure A.3: KPBO Fines - Magnification - 250x

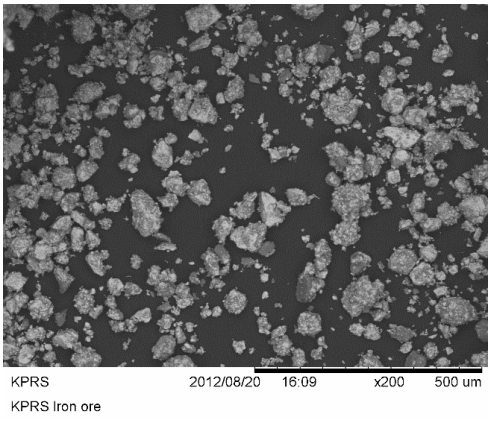

Figure A.4: KPRS Fines - Magnification - 200x

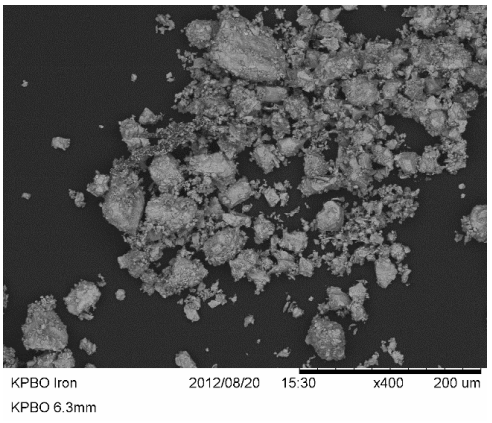

Figure A.5: KPBO Fines - Magnification - 400x

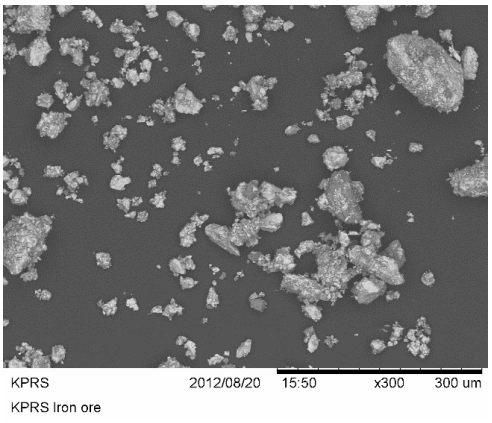

Figure A.6: KPRS Fines - Magnification - 300x

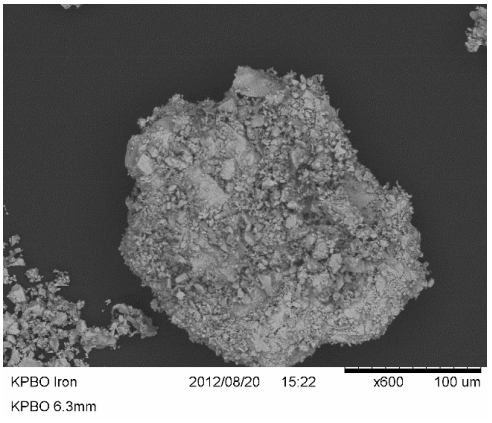

Figure A.7: KPBO Fines - Magnification - 600x

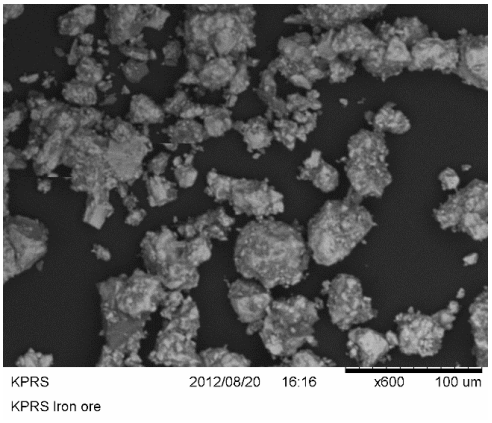

Figure A.8: KPRS Fines - Magnification - 600x

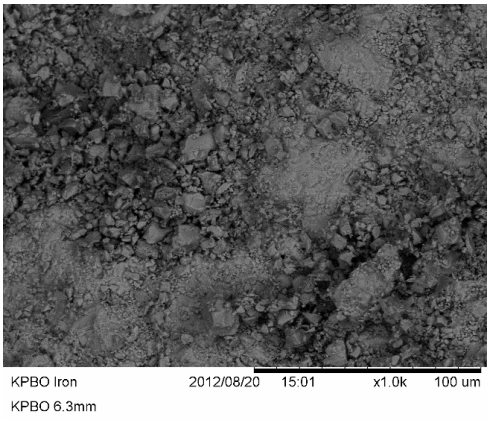

Figure A.9: KPBO Fines - Magnification - 1000x

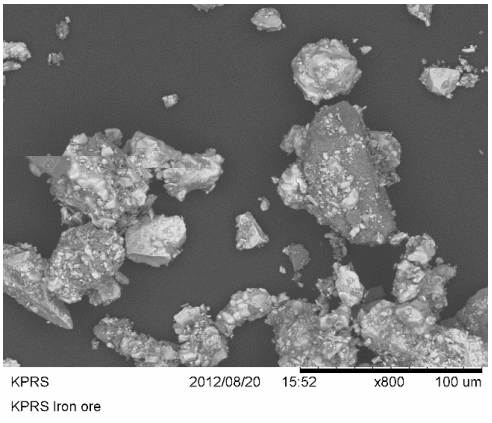

Figure A.10: KPRS Fines - Magnification - 800x

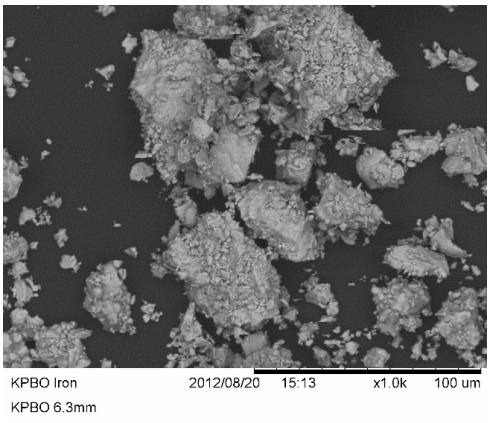

Figure A.11: KPBO Fines - Magnification - 1000x

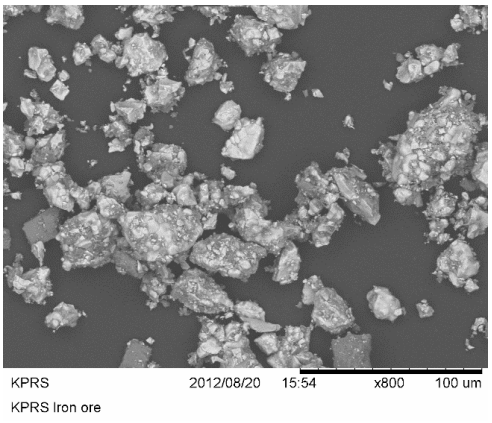

Figure A.12: KPRS Fines - Magnification - 800x

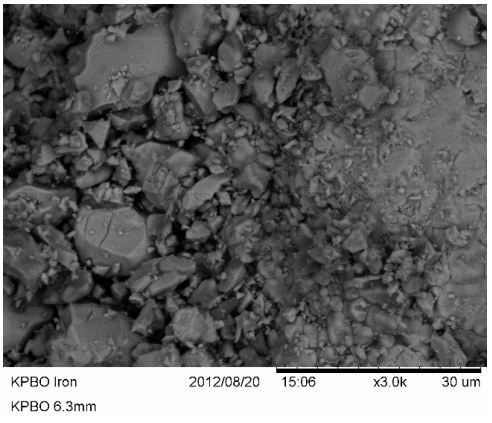

Figure A.13: KPBO Fines - Magnification - 3000x

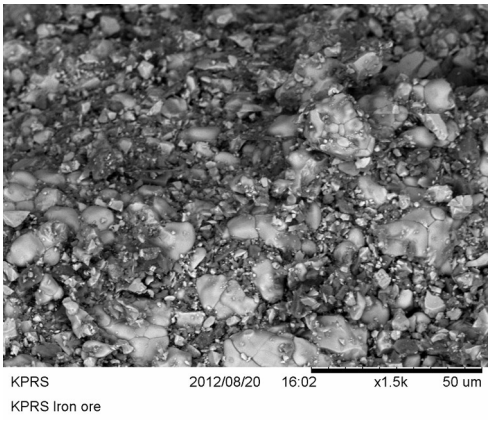

Figure A.14: KPRS Fines - Magnification - 1500x

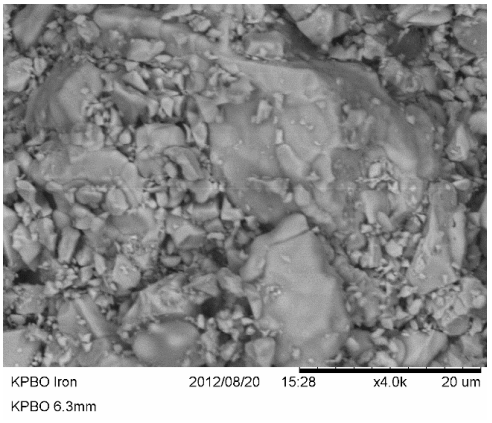

Figure A.15: KPBO Fines - Magnification - 4000x

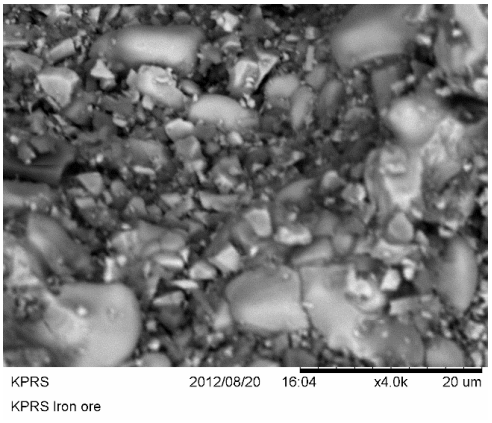

Figure A.16: KPRS Fines - Magnification - 4000x

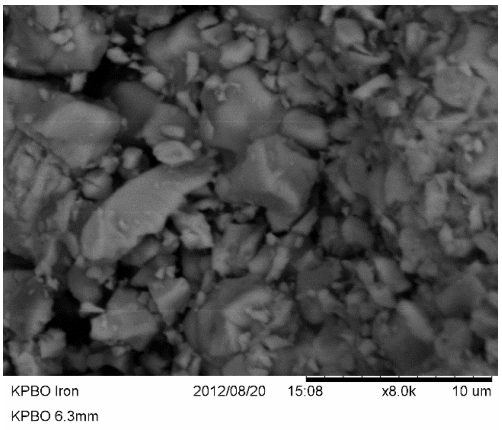

Figure A.17: KPBO Fines - Magnification - 8000x

Appendix B

K_0 Calibration Data

A total of four tests where air pressure was used to apply a uniform internal pressure to cylinder were carried out. The air bladder (as seen in Figure 5.24) was inflated in approximately equal steps of 10 kPa up to, and including, approximately 50 kPa, which is slightly higher than the normal testing limits when set-up in the Instron test machine.

B.1 Initial Strain Gauge Assessment

An initial assessment of the K_0 was carried out to consider the placement of the gauges and the strain response in relation to each other. The gauges were considered in terms of being grouped together by vertical location on the cylinder (Bottom, Middle and Top) or by the meridional location on the cylinder (0°, 90°, 180° and 270°).

B.1.1 Strain Response by location

The measured strain response for all gauges during a test are presented in Appendix B.1.1 for each test. It can clearly be seen in Figures B.1 to B.8 that the strain response tends to fall into three distinct groups, the zero degree meridian, the 90° meridian and the remaining gauges.

B.1.1.1 Test 1

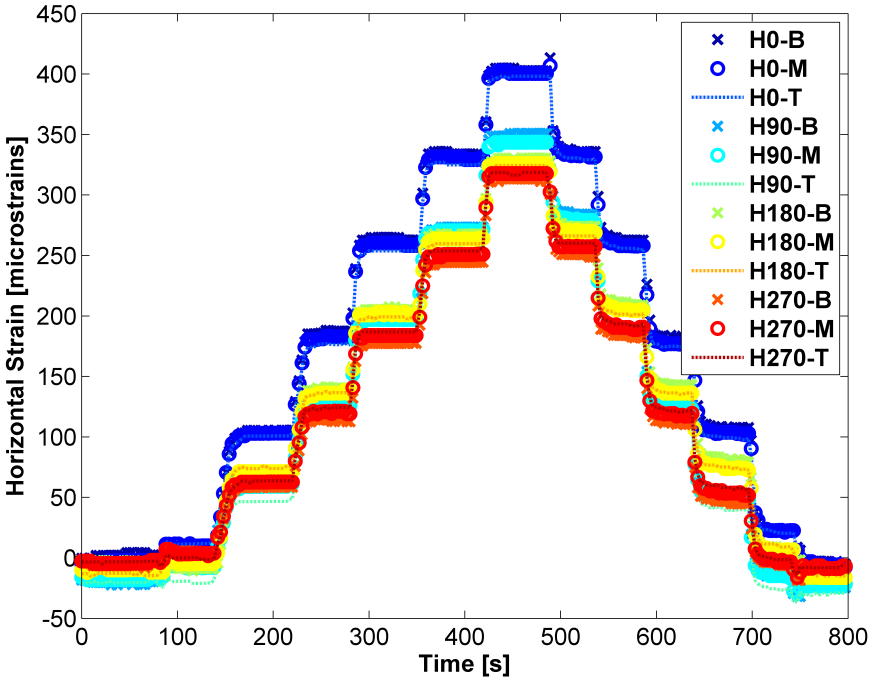

Figure B.1: Horizontal strain response vs time - Results for calibration test 1.

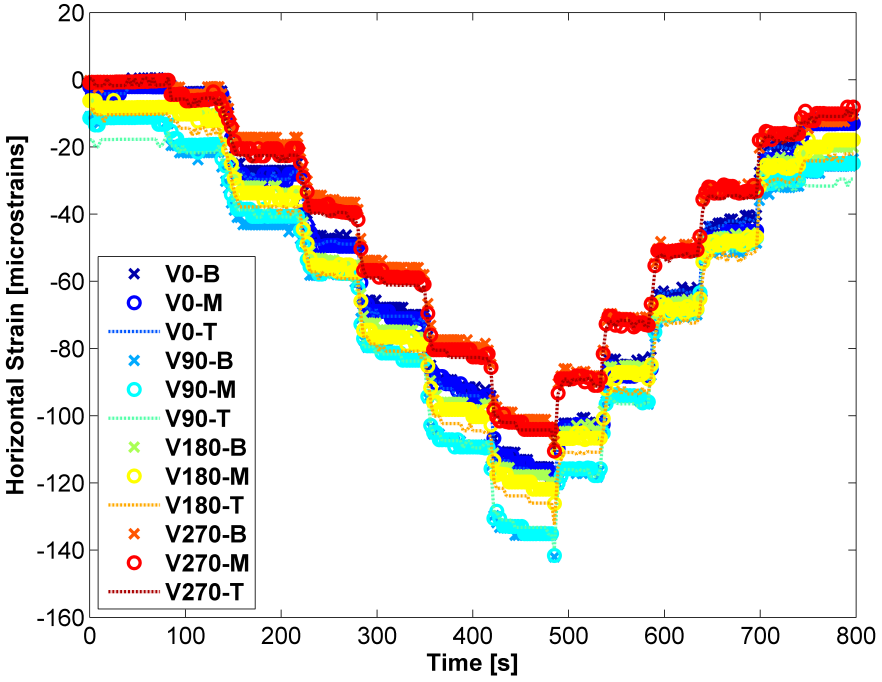

Figure B.2: Vertical strain response vs time - Results for calibration test 1.

B.1.1.2 Test 2

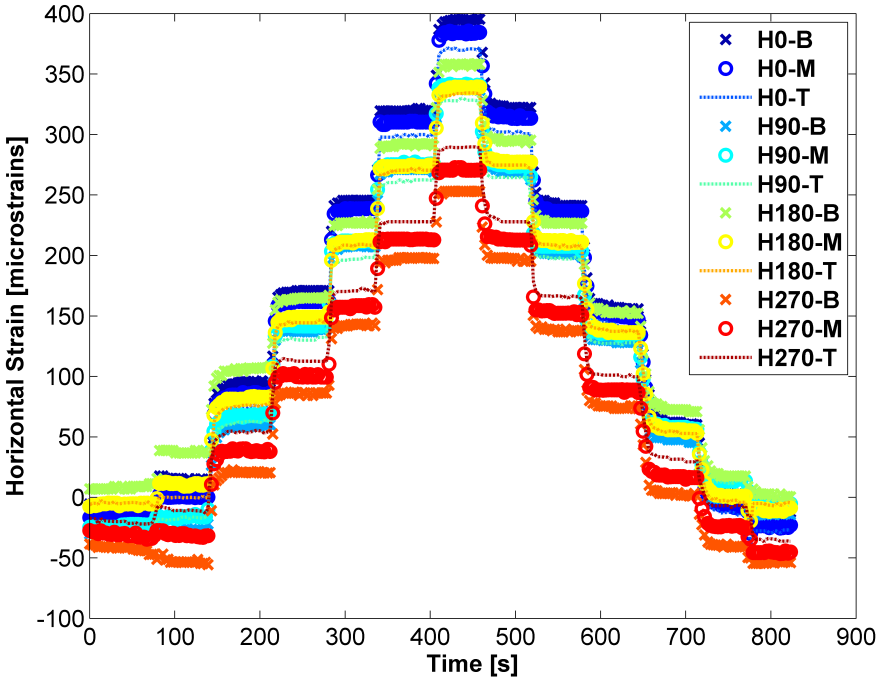

Figure B.3: Horizontal strain response vs time - Results for calibration test 1.

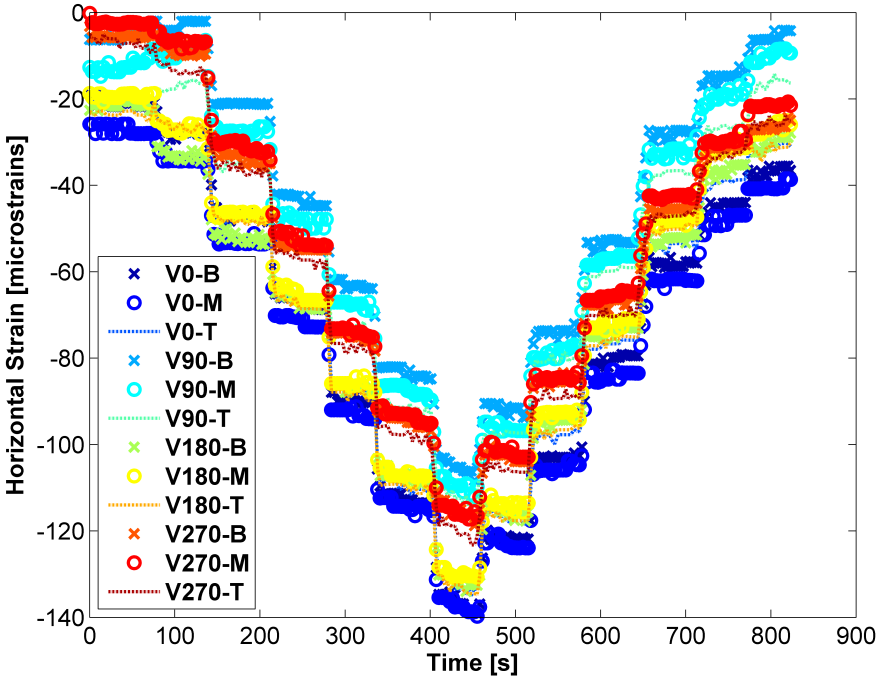

Figure B.4: Vertical strain response vs time - Results for calibration test 1.

B.1.1.3 Test 3

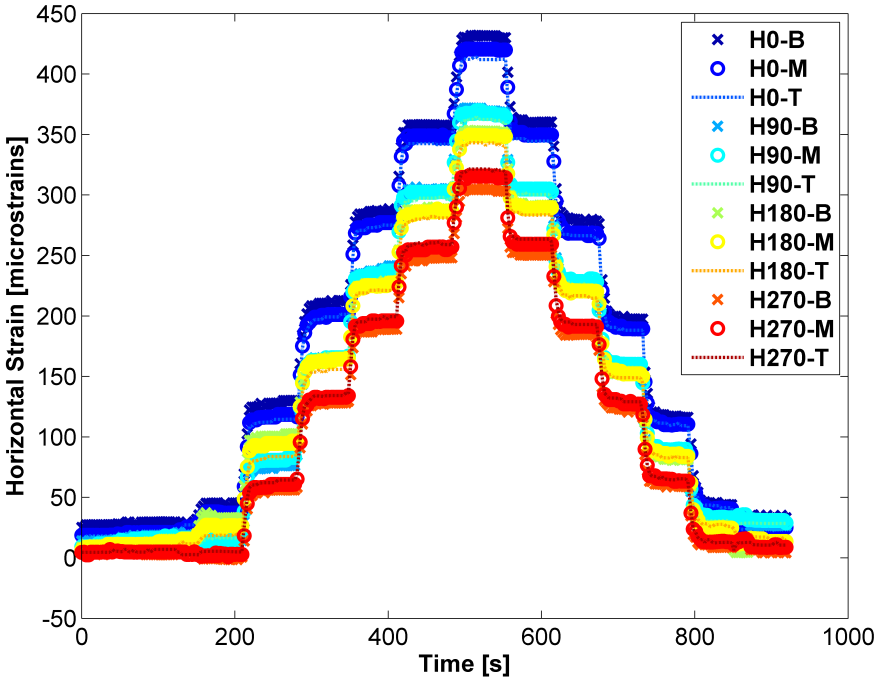

Figure B.5: Horizontal strain response vs time - Results for calibration test 1.

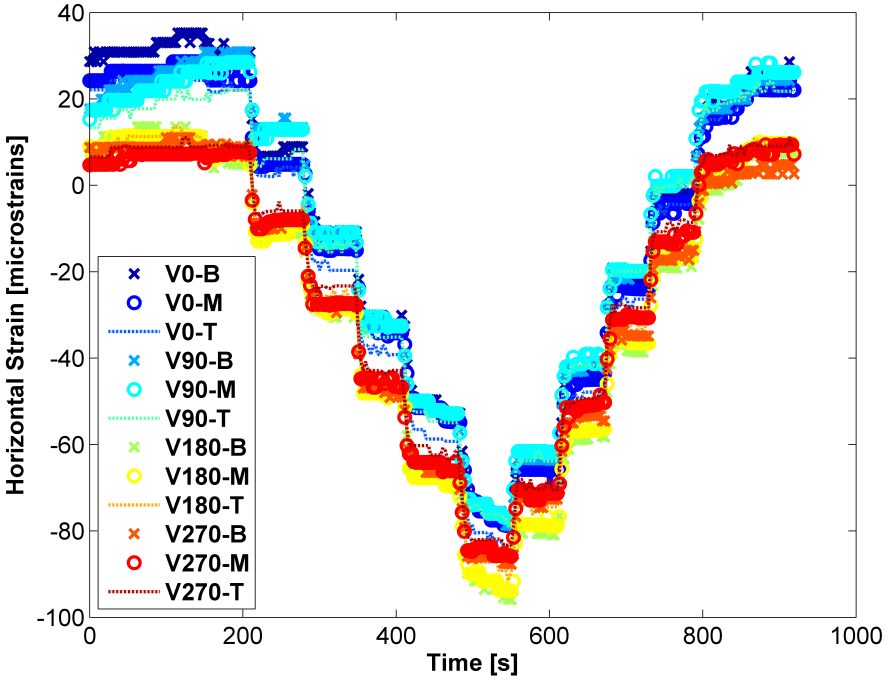

Figure B.6: Vertical strain response vs time - Results for calibration test 1.

B.1.1.4 Test 4

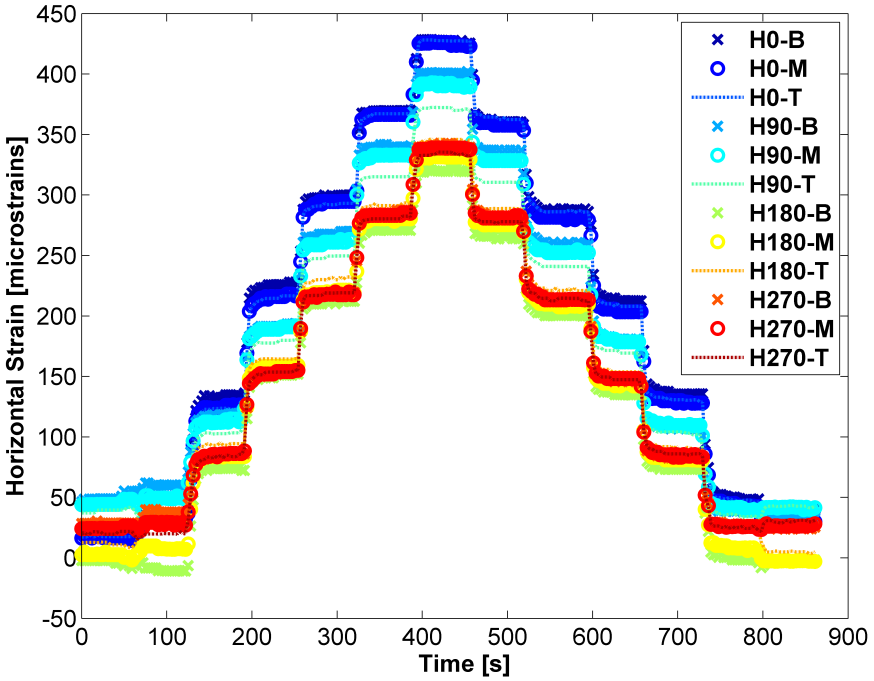

Figure B.7: Horizontal strain response vs time - Results for calibration test 4.

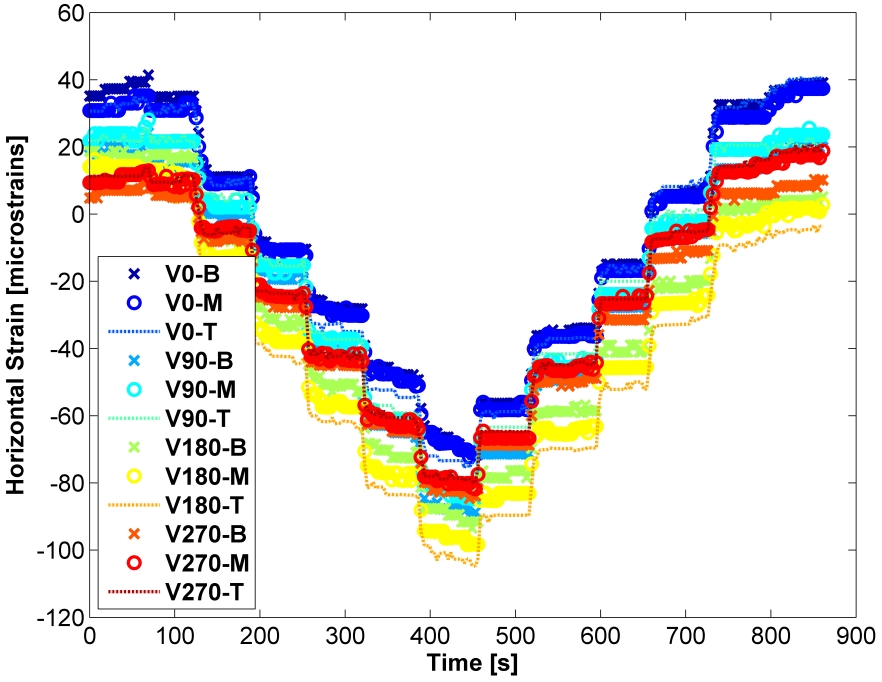

Figure B.8: Vertical strain response vs time - Results for calibration test 4.

B.1.2 Variation by Location

Following the previous visual assessment of the response of the strain gauges a more exact interrogation of the variation is presented in this section. The variation in the strain response has been analysed in terms of the gauges grouped by meridian and vertical location. The results for one test case of the four conducted are presented in Tables B.1 and B.2 for both scenarios. All gauge data was zeroed from their initial measured strain before comparisons were made. All four calibration tests returned similar findings. An initial pressure of 1-2 kPa was used to inflate the bladder in the cylinder to the point where it was just in contact with the cylinder walls. This small pressure was then subtracted from the total pressure to determine the pressure applied to the cylinder. The small inflation pressure also lead to a large variation in the strain gauge readings being observed in the data at this low pressure as the bladder may not have been in contact with all of the cylinder at this time.

The results clearly show that as the pressure is applied to the cylinder, the gauges along the four selected meridians of the cylinder show the same response, with the CoV for the three gauges at the different vertical locations on each meridian consistently within 5% of each other. When the gauges are grouped according to the layer (4 meridian gauges at a certain height) the spread in the response from the strain gauges is significantly larger. This suggests the properties of the cylinder such as wall thickness and/or Young's Modulus are related to their meridian location on the cylinder. While there may be a slight variation in the thickness of the cylinder at different meridians, it is also possible that the cylinder is not perfectly circular and that some local curvature variations exist around the cylinder circumference which can lead to significant bending effects.

Table B.1: CoV for average measured strain when grouped by cylinder meridian

	Gauge Location							
kPa	**H_0**	**H_{180}**	**H_{270}**	**H_{90}**	**V_0**	**V_{180}**	**V_{270}**	**V_{90}**
1	2.7%	36.4%	-62.2%	-185.6%	-153.7%	-68.1%	127.2%	33.1%
12	2.9%	8.9%	4.7%	8.5%	-5.5%	-12.0%	-5.6%	-11.2%
21	0.8%	2.6%	1.5%	0.3%	-4.1%	-4.8%	-4.2%	-2.7%
31	0.6%	1.1%	1.8%	1.2%	-3.5%	-2.8%	-2.3%	-1.4%
42	1.0%	1.2%	1.9%	1.0%	-3.1%	-2.7%	-1.4%	-1.1%
52	1.2%	1.4%	2.1%	1.0%	-2.3%	-2.4%	-0.8%	-1.8%
42	0.9%	1.5%	1.8%	0.8%	-1.9%	-2.8%	-0.6%	-2.2%
32	0.7%	1.5%	1.3%	0.6%	-2.2%	-2.7%	-1.0%	-2.6%
21	0.2%	1.9%	1.2%	0.5%	-3.0%	-4.6%	-3.6%	-4.8%
11	1.9%	2.5%	1.2%	0.1%	-4.8%	-7.0%	-7.5%	-5.8%
1	26.5%	13.1%	29.5%	28.4%	-7.8%	-18.1%	-24.2%	-33.1%

Table B.2: CoV for average measured strain when grouped by layer

	Gauge Location					
kPa	**H_B**	**H_M**	**H_T**	**V_B**	**V_M**	**V_T**
1	215.4%	161.9%	118.4%	2418.8%	489.8%	2605.3%
12	31.4%	25.2%	21.0%	-30.7%	-29.6%	-60.5%
21	15.8%	14.4%	14.4%	-8.4%	-7.0%	-57.7%
31	13.6%	12.4%	12.1%	-4.4%	-4.1%	-56.5%
42	12.3%	11.4%	10.5%	-4.3%	-3.4%	-56.3%
52	11.9%	10.8%	9.8%	-5.3%	-4.4%	-56.3%
42	12.0%	11.0%	10.4%	-6.7%	-5.4%	-56.4%
32	13.5%	12.4%	12.4%	-7.5%	-6.5%	-56.7%
21	14.6%	14.1%	14.4%	-9.2%	-8.6%	-57.6%
11	19.0%	19.5%	20.8%	-16.1%	-13.3%	-59.2%
1	44.1%	64.1%	85.9%	-35.8%	-37.1%	-75.5%

Wall thicknesses have been measured at the top and bottom edges of the cylinder and the variation is shown in Table B.3. It was not possible to gather thicknesses that were accurate to more than 0.1mm for all of the gauge locations due to the difficulty caused by the height of the cylinder. As it is difficult to attribute the differences to different factors, it is assumed that they can all be attributed to Young's modulus at different locations. For ease of interpretation cylinder properties will be calibrated for each side based on the measured variation of thickness, neglecting any bending effect arising from any such variation.

Table B.3: Measured cylinder wall thickness [mm]

	Gauge Location				Statistics		
	0°	**90°**	**180°**	**270°**	**Mean**	**STDEV**	**CoV**
Top [mm]	3.01	2.93	3.04	3.19	3.0425	0.1087	3.57%
Bottom [mm]	3.06	2.99	3.09	3.22	3.09	0.0962	3.12%

B.2 Selected Calibration Properties

The nominal cylinder properties provided by the manufacturer *Ensinger UK Ltd.* are 3300 MPa for Young's modulus with a nominal wall thickness of 3 mm. To account for the wall thickness variation seen in Table B.3, varying curvature of the cylinder and the additional stiffness provided by the adhesive that attaches the gauges the properties of the cylinder are calibrated from the results of the four tests.

The material parameters (E and ν) are estimated from Equations (5.15) and (5.16) for the four calibration tests presented in Appendix B.1.1. The Young's modulus parameter is dependent on the wall thickness and a constraint that Young's modulus is equal for all meridians is put in place., which will allow a corresponding wall thickness to be determined at each gauge location. An optimised solution using the built-in solver in EXCEL is used to find the optimised thickness that yields the constrained solution. The wall thicknesses are limited to range of 2.6 - 3.4 mm, which is the possible range of thicknesses for the cylinder wall which is nominally 3 mm. Using this method the mean properties for each 90° meridian location can be found from several calibration tests. The calibration results in Tables B.4 and B.5 suggests that 3 of the four meridians have the same properties, while one was found to have a significantly lower Poisson's ratio (0° meridian), possibly due to some local curvature in the cylinder that cannot be easily measured.

Table B.4: Young's Modulus [GPa] Calibration Properties

Test	**Gauge Location**			
No.	**0°**	**90°**	**180°**	**270°**
1	3.611	3.611	3.611	3.611
2	3.724	3.724	3.724	3.725
3	3.904	3.905	3.905	3.905
4	3.833	3.833	3.833	3.833
Mean	3.768	3.768	3.768	3.768
St. Dev.	0.128	0.128	0.128	0.128
CoV	3.40%	3.40%	3.40%	3.40%

Table B.5: Poisson's Ratio Calibration Properties

Test	**Gauge Location**			
No.	**0°**	**90°**	**180°**	**270°**
1	0.2651	0.3084	0.3131	0.3026
2	0.2602	0.2738	0.3013	0.3351
3	0.262	0.2856	0.2964	0.3009
4	0.2628	0.3005	0.3161	0.2992
Mean	0.263	0.292	0.307	0.309
St. Dev.	0.002	0.015	0.009	0.017
CoV	0.80%	5.30%	3.10%	5.50%

The results of the wall thickness evaluation are given in Table B.6 and the mean values of the tests match closely to the measured values for 90° 180° and 270°. The calibrated values found for the 0° meridian are significantly thinner than the measured value by approximately 0.5 mm. While it is possible that this section of the cylinder is significantly thinner than the rest, it is also possible that there is some local curvature of the cylinder at this location which is causing a different Young's modulus/thickness to be measured.

Table B.6: Wall Thickness [mm] Calibration Properties

Test	**Gauge Location**			
No.	**0°**	**90°**	**180°**	**270°**
1	2.492	2.923	3.024	3.32
2	2.493	2.862	2.911	3.289
3	2.414	2.85	2.87	3.21
4	2.35	2.85	2.891	3.185
Mean	2.438	2.871	2.924	3.252
St. Dev.	0.069	0.035	0.068	0.064
CoV	2.80%	1.20%	2.30%	2.00%

If the evaluated thickness for the 0° meridian is constrained much closer to the nominal value is used for the 0° meridian then the values in Table B.7 are found for Young's Modulus. The values for 90° 180° and 270° would remain the same, while the value E for 0° would drop to 3.14 GPa.

Table B.7: Young's Modulus [GPa] Calibration Properties

Test	**Gauge Location**			
No.	**0°**	**90°**	**180°**	**270°**
1	3.078	3.611	3.611	3.611
2	3.176	3.724	3.724	3.725
3	3.224	3.905	3.905	3.905
4	3.081	3.833	3.833	3.833
Mean	3.14	3.768	3.768	3.768
St. Dev.	0.073	0.128	0.128	0.128
CoV	2.30%	3.40%	3.40%	3.40%

Evaluating the effect of both sets of calibrated properties with PPE yields minimal difference in the results. In this case, the properties based on the measured thickness for all meridians will be used.

Table B.8: Effect of Different Calibrations

	Peak Strain	Peak K0 Value	Peak Stress [kPa]
Equating t	0.017255	0.2676	53.195
Equating E	0.017255	0.2682	53.168

B.3 Applied Pressure Verification

The horizontal (radial) stress can be calculated for each individual gauge and as the inflatable bladder will apply a uniform pressure to the cylinder walls, the horizontal stresses calculated at each gauge location should be a close match to the known internal pressure applied from the inflatable bladder. The calculated pressures can then be grouped together based on their location and the results from these calculations are given in Table B.9 to Table B.12 for both grouped by meridional location and grouped by vertical location.

The results show that there is an excellent agreement between the applied and calculated air pressure in the cylinder at a stress greater than approximately 10-15 kPa. In each case the pressure calculated by using the average of four strain gauges at the same height yields a result within 1kPa of the applied internal pressure of the inflated bladder.

Table B.9: Predicted Vs. Applied pressure for calibration test 1

	Average By Meridian [kPa]					Average By Layer [kPa]			
kPa	**0°**	**90°**	**180°**	**270°**	**Avg**	**Bottom**	**Middle**	**Top**	**Avg**
1	1.8	1.5	0.9	1.2	1.36	1.3	1.4	1.3	1.36
12	13.2	11.2	12.3	11	11.93	12	11.9	11.9	11.93
21	22.9	20.5	22	20.5	21.48	21.5	21.5	21.5	21.48
31	32.3	30.7	31.6	30.9	31.39	31.4	31.5	31.2	31.39
42	41	41.1	40.7	41.8	41.15	41.3	41.3	40.9	41.15
52	49.5	51.7	50.1	52.7	50.98	51.2	51.1	50.7	50.98
42	41.1	42.5	41.7	42.8	42	42.2	42.1	41.7	42
32	32	32	32.1	31.7	31.95	32	32	31.8	31.95
21	22.2	20.7	22.3	20	21.29	21.4	21.3	21.2	21.29
11	13.2	9.9	13.2	9.5	11.44	11.4	11.5	11.5	11.44
1	3.4	0.6	3.3	0.5	1.93	1.8	2	2	1.93

Table B.10: Predicted Vs. Applied pressure for calibration test 2

	Average By Meridian [kPa]					Average By Layer [kPa]			
kPa	**0°**	**90°**	**180°**	**270°**	**Avg**	**Bottom**	**Middle**	**Top**	**Avg**
1	2.2	1.1	2.5	-0.1	1.4	1.3	1.4	1.5	1.41
12	13.1	13.3	13.4	11.9	12.9	12.9	13	12.8	12.94
22	23.1	23.9	23.3	22.6	23.2	23.3	23.4	23	23.22
32	32.8	33.7	32.7	32.4	32.9	33	33.1	32.6	32.91
41	42.1	42.9	42.1	41.8	42.2	42.4	42.4	41.9	42.22
51	51.5	52.3	51.7	51.8	51.8	52	51.9	51.5	51.83
41	39.8	39.2	39.8	39.1	39.5	39.6	39.6	39.2	39.46
31	34.8	33.6	34.7	34	34.3	34.4	34.4	34	34.29
20	21.8	21.2	21.8	21.4	21.5	21.5	21.6	21.5	21.53
8	9.7	9.5	9.5	9.8	9.6	9.5	9.7	9.7	9.64
1	2.1	2.9	1.4	3.3	2.4	2.2	2.5	2.6	2.42

Table B.11: Predicted Vs. Applied pressure for calibration test 3

	Average By Meridian [kPa]					Average By Layer [kPa]			
kPa	**0°**	**90°**	**180°**	**270°**	**Avg**	**Bottom**	**Middle**	**Top**	**Avg**
1	2.1	-0.1	2.3	-0.5	0.9	0.9	0.9	1	0.94
11	12	9.5	12.2	8.9	10.7	10.6	10.7	10.6	10.65
22	22.4	21.5	22.4	20.9	21.8	21.8	21.9	21.7	21.79
31	31.6	31.7	31.7	31.1	31.5	31.5	31.6	31.4	31.51
41	40.4	41.2	40.5	41	40.8	40.8	40.9	40.6	40.76
51.5	49	50.4	49.4	50.6	49.9	49.9	50	49.7	49.86
41	40.1	40.7	40.3	41.1	40.5	40.6	40.7	40.4	40.55
30.5	30.1	29.2	30.1	29.7	29.8	29.8	29.8	29.7	29.77
20	20.4	19.1	20.1	19.5	19.8	19.7	19.9	19.7	19.77
10	10.4	8.6	10	8.9	9.5	9.3	9.6	9.6	9.5
1	1.8	0.5	1.3	0.5	1	0.9	1.1	1.2	1.04

Table B.12: Predicted Vs. Applied pressure for calibration test 4

	Average By Meridian [kPa]					Average By Layer [kPa]			
kPa	**0°**	**90°**	**180°**	**270°**	**Avg**	**Bottom**	**Middle**	**Top**	**Avg**
1	1.9	0.7	0.5	0.7	0.9	0.9	1	0.9	0.95
12	12.8	10.1	11.9	9.9	11.2	11.2	11.3	11.2	11.21
23	23.8	21.3	22.9	21.1	22.3	22.3	22.4	22.1	22.28
33	32.9	31.9	32.4	31.8	32.2	32.4	32.3	32.1	32.24
42.5	41.5	42	41.3	42.4	41.8	42	41.9	41.4	41.8
52	48.3	50.5	48.8	51.2	49.7	49.9	49.8	49.3	49.68
42	40	41.2	40.5	41.5	40.8	41	40.9	40.5	40.82
31.5	30.8	30.5	30.7	30.5	30.6	30.8	30.6	30.6	30.64
21	21.4	19.6	21	19.6	20.4	20.5	20.4	20.3	20.4
11	12.1	9.5	11.9	9.2	10.7	10.6	10.7	10.7	10.67
1	1.7	-0.4	1.3	-0.3	0.6	0.5	0.6	0.7	0.59

Appendix C

EPT Confined Compression Test Data

C.1 KPBO Fines

Table C.1: Confined Compression Data for Dry KPBO fines

Consolidation Load [N]	0.7	7.6	19.9	32.1	44.6	69.4	94.5	119.3	144.3	0
Consolidated Height [mm]	47.5	46	44.9	44.4	44.1	43.6	43.3	43	42.8	42.8
Consolidation Load [kPa]	0.6	6.1	15.8	25.5	35.5	55.2	75.2	94.9	114.8	0
Bulk Density [kg/m^3]	2604	2691	2752	2785	2807	2837	2856	2874	2890	2890
Consolidated Aspect Ratio	1.19	1.15	1.12	1.11	1.10	1.09	1.08	1.08	1.07	1.07
Change in Height [mm]	0	1.5	1	0.5	0.3	0.5	0.3	0.3	0.2	0
Consolidation Strain [%]	0.21	3.35	5.48	6.57	7.26	8.21	8.83	9.38	9.86	9.86
STDEV										
Consolidation Load [kPa]	0.26	0.59	0.32	0.52	0.1	0.28	0.56	0.65	0.32	0
Bulk Density [kg/m^3]	29.34	19.48	21.02	23.42	19.95	22.5	22.14	18.46	21.51	21.51
Coefficient of Variation										
Consolidation Load [%]	43.83	9.66	2.01	2.04	0.28	0.50	0.74	0.69	0.28	0
Bulk Density [%]	1.13	0.72	0.76	0.84	0.71	0.79	0.78	0.64	0.74	0.74

Table C.2: Confined Compression Data for Wet KPBO fines - 1.25% MC

Consolidation Load [N]	0.5	8.1	20.8	32.8	45.2	70.1	94.7	119.5	144.5	0
Consolidated Height [mm]	66.1	56	52.4	50.7	49.8	48.4	47.6	47	46.4	46.4
Consolidation Load [kPa]	0.4	6.5	16.5	26.1	35.9	55.7	75.4	95.1	115.0	0
Bulk Density [kg/m^3]	1850	2182	2333	2409	2452	2524	2568	2601	2635	2635
Consolidated Aspect Ratio	1.65	1.40	1.31	1.27	1.25	1.21	1.19	1.17	1.16	1.6
Change in Height [mm]	0	10.1	3.7	1.6	0.9	1.4	0.8	0.6	0.6	0
Consolidation Strain [%]	0.0	14.4	19.7	22.1	23.3	25.4	26.6	27.5	28.3	28.3
STDEV										
Consolidation Load [kPa]	0.08	0.48	0.51	0.52	0.28	0.51	0.6	0.92	0.36	0
Bulk Density [kg/m^3]	80.58	55.36	25.36	31.4	28.49	30.69	24.93	20.73	16.32	16.32
Coefficient of Variation										
Consolidation Load [%]	20.00	7.51	3.10	2.00	0.78	0.91	0.80	0.97	0.31	0
Bulk Density [%]	4.35	2.54	1.09	1.30	1.16	1.22	0.97	0.80	0.62	0.62

Table C.3: Confined Compression Data for Wet KPBO fines - 2.5% MC

Consolidation Load [N]	8.4	20.3	32.8	45.6	70.2	95.1	119.9	144.4	0
Consolidated Height [mm]	57.2	52.3	49.6	47.9	46.3	45.2	44.5	43.7	43.7
Consolidation Load [kPa]	6.7	16.2	26.1	36.3	55.9	75.7	95.4	115.0	0
Bulk Density [kg/m^3]	1931	2113	2226	2308	2385	2443	2485	2526	2526
Consolidated Aspect Ratio	1.43	1.34	1.24	1.20	1.16	1.13	1.11	1.09	1.09
Change in Height [mm]	14.2	4.9	2.7	1.8	1.5	1.1	0.8	0.7	0
Consolidation Strain [%]	20.40	27.49	31.32	33.86	36.06	37.64	38.75	39.80	39.80
STDEV									
Consolidation Load [kPa]	0.08	0.42	0.29	0.71	0.24	0.32	0.36	0.40	
Bulk Density [kg/m^3]	37.79	30.97	13.65	24.21	2.93	4.03	2.23	4.06	4.06
Coefficient of Variation									
Consolidation Load [%]	1.19	2.61	1.10	1.97	0.43	0.43	0.38	0.35	0
Bulk Density [%]	1.96	1.47	0.61	1.05	0.12	0.17	0.09	0.16	0.16

Table C.4: Confined Compression Data for Wet KPBO fines - 3.5% MC

Consolidation Load [N]	0.6	8.5	19.9	32.6	45.2	70.1	94.1	118.6	143.3	0
Consolidated Height [mm]	72.5	56.2	51.5	49	47.7	45.8	44.6	43.8	43	43
Consolidation Load [kPa]	0.5	6.8	15.9	26.0	35.9	55.8	74.9	94.4	114.0	0
Bulk Density [kg/m^3]	1499	1935	2110	2217	2277	2372	2435	2484	2526	2526
Consolidated Aspect Ratio	1.81	1.40	1.29	1.23	1.19	1.15	1.12	1.09	1.08	1.08
Change in Height [mm]	0	16.4	4.7	2.5	1.3	1.9	1.2	0.9	0.7	0
Consolidation Strain [%]	0.00	24.14	31.02	34.66	36.58	39.38	41.15	42.43	43.51	43.51
STDEV										
Consolidation Load [kPa]	0.26	0.18	0.41	0.12	0.45	0.21	0.24	0.41	0.28	0
Bulk Density [kg/m^3]	27.06	20.63	6.7	5.65	3.07	11.7	12.06	8.4	8.13	8.13
Coefficient of Variation										
Consolidation Load [%]	50.76	2.71	2.57	0.47	1.26	0.38	0.32	0.43	0.24	0
Bulk Density [%]	1.80	1.07	0.32	0.25	0.13	0.49	0.50	0.34	0.32	0.32

Table C.5: Confined Compression Data for Wet KPBO fines - 4.5% MC

Consolidation Load [N]	8.7	20	32.3	45.9	69.3	94.4	118.9	144.1	0
Consolidated Height [mm]	57.8	53	50.7	49	47.2	45.9	44.9	44.1	44.1
Consolidation Load [kPa]	6.9	15.9	25.7	36.5	55.2	75.1	94.6	114.6	0
Bulk Density [kg/m^3]	1939	2115	2214	2290	2375	2446	2497	2542	2542
Consolidated Aspect Ratio	1.45	1.33	1.27	1.23	1.18	1.15	1.12	1.10	1.10
Change in Height [mm]	15.9	4.8	2.4	1.7	1.8	1.4	0.9	0.8	0
Consolidation Strain [%]	22.32	29.07	32.40	34.74	37.22	39.15	40.46	41.58	41.58
STDEV									
Consolidation Load [kPa]	0.26	0.6	0.54	2.28	0.84	0.73	1.2	1.37	0
Bulk Density [kg/m^3]	41.71	15.1	7.19	35.89	9.07	5.96	4.44	4.07	4.07
Coefficient of Variation									
Consolidation Load [%]	3.71	3.77	2.11	6.23	1.52	0.97	1.27	1.20	0
Bulk Density [%]	2.15	0.71	0.32	1.57	0.38	0.24	0.18	0.16	0.16

Table C.6: Confined Compression Data for Wet KPBO fines - 5.5% MC

Consolidation Load [N]	1	9.4	20.1	32.3	45.2	69.6	94.6	118.8	143.6	0
Consolidated Height [mm]	71.4	56.1	53.4	50.6	49.1	47.1	45.8	44.8	44.1	44.1
Consolidation Load [kPa]	0.8	7.5	16.0	25.7	35.9	55.4	75.3	94.5	114.3	0
Bulk Density [kg/m^3]	1564	1990	2090	2203	2273	2370	2437	2488	2531	2531
Consolidated Aspect Ratio	1.78	1.40	1.33	1.27	1.23	1.18	1.14	1.12	1.10	1.10
Change in Height [mm]	0	15.3	2.7	2.7	1.6	2	1.3	0.9	0.8	0
Consolidation Strain [%]	0.00	20.79	24.46	28.17	30.30	33.02	34.78	36.05	37.09	37.09
STDEV										
Consolidation Load [kPa]	0.3	0.41	0.54	0.24	0.24	0.2	0.29	0.83	1	0
Bulk Density [kg/m^3]	47.16	21.42	11.35	3.99	4.63	3.75	3.21	2.47	1.68	1.68
Coefficient of Variation										
Consolidation Load [%]	36.64	5.48	3.39	0.95	0.68	0.36	0.38	0.87	0.88	0
Bulk Density [%]	3.02	1.08	0.54	0.18	0.20	0.16	0.13	0.10	0.07	0.07

Table C.7: Confined Compression Data for Wet KPBO fines - 7% MC

Consolidation Load [N]	1.1	8.9	20	32.3	44.6	69.4	94.1	119.4	144	0
Consolidated Height [mm]	71.1	55.9	52.5	50	48.5	46.4	45	44.1	43.3	43.3
Consolidation Load [kPa]	0.9	7.1	15.9	25.7	35.4	55.3	74.9	95.0	114.6	0
Bulk Density [kg/m^3]	1570	1997	2125	2232	2302	2406	2479	2532	2577	2577
Consolidated Aspect Ratio	1.78	1.40	1.31	1.25	1.21	1.16	1.13	1.10	1.08	1.08
Change in Height [mm]	0	15.2	3.4	2.5	1.5	2.1	1.4	0.9	0.8	0
Consolidation Strain [%]	0.00	21.38	26.16	29.68	31.83	34.79	36.71	38.02	39.10	39.10
STDEV										
Consolidation Load [kPa]	0.16	0.24	0.23	0.64	0.48	0.8	0.87	0.94	0.9	0
Bulk Density [kg/m^3]	14.48	47.11	17.54	10.19	12.3	12.87	7.9	11.36	8.29	8.29
Coefficient of Variation										
Consolidation Load [%]	18.18	3.37	1.44	2.49	1.36	1.45	1.17	0.99	0.78	0
Bulk Density [%]	0.92	2.36	0.83	0.46	0.53	0.53	0.32	0.45	0.32	0.32

Table C.8: Confined Compression Data for Wet KPBO fines - 8% MC

Consolidation Load [N]	0.8	9.3	20.2	32.4	44.7	69.1	93.7	118.4	143.9	0
Consolidated Height [mm]	73.7	56.1	52.7	50.4	48.8	46.5	45.1	44.3	43.5	43.5
Consolidation Load [kPa]	0.7	7.4	16.1	25.8	35.6	55.0	74.6	94.3	114.5	0
Bulk Density [kg/m^3]	1595	2096	2229	2331	2407	2527	2603	2652	2701	2699
Consolidated Aspect Ratio	1.84	1.40	1.32	1.26	1.22	1.16	1.13	1.11	1.09	1.09
Change in Height [mm]	0	17.6	3.4	2.3	1.6	2.3	1.4	0.8	0.8	0
Consolidation Strain [%]	0.00	25.15	29.96	33.24	35.52	38.80	40.75	41.94	43.08	43.03
STDEV										
Consolidation Load [kPa]	0.3	0.08	0.32	0.36	0.42	0.36	1.07	1.21	1.01	0
Bulk Density [kg/m^3]	27.84	17.22	7.64	17.36	15.96	22.63	25.08	20.24	19.4	17.6
Coefficient of Variation										
Consolidation Load [%]	45.43	1.08	2.00	1.39	1.18	0.65	1.43	1.28	0.88	0
Bulk Density [%]	1.75	0.82	0.34	0.74	0.66	0.90	0.96	0.76	0.72	0.65

Table C.9: Confined Compression Data for Wet KPBO fines - 10% MC

Consolidation Load [N]	0.5	9.7	20.9	33.4	45.6	70.3	95.4	120.1	145	0
Consolidated Height [mm]	79.1	58.9	55.7	53.5	51.9	49.7	48.5	47.5	46.8	46.9
Consolidation Load [kPa]	0.4	7.7	16.7	26.6	36.3	55.9	75.9	95.6	115.4	0
Bulk Density [kg/m^3]	1695	2279	2407	2509	2586	2697	2767	2824	2868	2862
Consolidated Aspect Ratio	1.98	1.47	1.39	1.34	1.30	1.24	1.21	1.19	1.17	1.17
Change in Height [mm]	0	20.2	3.1	2.3	1.6	2.1	1.3	1	0.7	-0.1
Consolidation Strain [%]	0.00	25.58	29.54	32.41	34.43	37.13	38.73	39.95	40.88	40.75
STDEV										
Consolidation Load [kPa]	0.09	0.05	0.24	0.17	0.3	0.45	0.17	0.74	0.6	0
Bulk Density [kg/m^3]	13.08	20.71	5.36	8.3	6.34	5.26	10.79	11.31	14.83	14.76
Coefficient of Variation										
Consolidation Load [%]	21.65	0.60	1.46	0.62	0.83	0.81	0.22	0.77	0.52	0
Bulk Density [%]	0.77	0.91	0.22	0.33	0.25	0.19	0.39	0.40	0.52	0.52

C.2 KPRS Fines

Table C.10: Confined Compression Data for Dry KPRS fines

Consolidation Load [N]	1.6	8.5	20.5	32.9	45.2	70.3	94.5	119.3	144.1	20.5	0
Consolidated Height [mm]	65.2	64.3	63.7	63.3	63	62.6	62.3	62	61.8	61.8	61.9
Consolidation Load [kPa]	1.3	6.8	16.3	26.2	36.0	55.9	75.2	95.0	114.7	16.3	0
Bulk Density [kg/m^3]	2453	2485	2510	2525	2537	2553	2567	2576	2588	2588	2582
Consolidated Aspect Ratio	1.63	1.61	1.59	1.58	1.58	1.57	1.56	1.55	1.54	1.54	1.55
Change in Height [mm]	0	0.8	0.7	0.4	0.3	0.4	0.3	0.2	0.3	0	-0.1
Consolidation Strain [%]	0.0	1.28	2.30	2.86	3.32	3.94	4.45	4.81	5.22	5.22	5.01
STDEV											
Consolidation Load [kPa]	0.09	0.21	0.09	0.35	0.3	0.32	0.88	1.23	1.44	0.32	0
Bulk Density [kg/m^3]	16.23	17.74	24.07	24.92	24.6	24.18	26.18	24.87	25.68	25.68	23.44
Coefficient of Variation											
Consolidation Load [%]	7.37	3.11	0.56	1.32	0.84	0.58	1.17	1.30	1.26	1.95	0
Bulk Density [%]	0.66	0.71	0.96	0.99	0.97	0.95	1.02	0.97	0.99	0.99	0.91

Table C.11: Confined Compression Data for Wet KPRS fines - 0.75% MC

Consolidation Load [N]	0.7	8.1	20.3	33.2	45.6	69.7	95.1	119.7	144.7	20.4	0
Consolidated Height [mm]	64.3	57.3	54.6	52.8	52.2	51.1	50.4	49.8	49.4	49.4	49.4
Consolidation Load [kPa]	0.5	6.5	16.2	26.4	36.3	55.4	75.7	95.3	115.2	16.3	0
Bulk Density [kg/m^3]	1980	2220	2333	2411	2440	2493	2527	2556	2577	2577	2575
Consolidated Aspect Ratio	1.61	1.43	1.36	1.32	1.30	1.28	1.26	1.25	1.24	1.24	1.24
Change in Height [mm]	0	7	2.8	1.8	0.6	1.1	0.7	0.6	0.4	0	0
Consolidation Strain [%]	0.00	10.83	15.14	17.88	18.87	20.58	21.67	22.55	23.17	23.17	23.12
STDEV											
Consolidation Load [kPa]	0.26	0.32	0.2	0.71	0.09	0.45	0.12	0.3	0.29	0.21	0
Bulk Density [kg/m^3]	8.38	15.07	12.04	22.83	8.51	9.11	8.22	9.13	10.19	10.19	12.87
Coefficient of Variation											
Consolidation Load [%]	48.22	4.97	1.24	2.70	0.25	0.82	0.16	0.32	0.25	1.30	0
Bulk Density [%]	0.42	0.68	0.52	0.95	0.35	0.37	0.33	0.36	0.40	0.40	0.50

Table C.12: Confined Compression Data for Wet KPRS fines - 1.5% MC

Consolidation Load [N]	1.1	8.2	19.8	32.1	44.7	69.5	94.5	119.5	144.5	20	0
Consolidated Height [mm]	62.9	53	50.2	48.6	47.4	46	45.1	44.5	43.9	43.9	43.9
Consolidation Load [kPa]	0.9	6.6	15.7	25.6	35.6	55.3	75.2	95.1	115.0	15.9	0
Bulk Density [kg/m^3]	1801	2139	2258	2334	2390	2464	2512	2549	2582	2582	2582
Consolidated Aspect Ratio	1.57	1.33	1.26	1.21	1.19	1.15	1.13	1.11	1.10	1.10	1.10
Change in Height [mm]	0	9.9	2.8	1.6	1.1	1.4	0.9	0.7	0.6	0	0
Consolidation Strain [%]	0.00	15.78	20.23	22.83	24.63	26.91	28.28	29.34	30.24	30.24	30.24
STDEV											
Consolidation Load [kPa]	0.2	0.12	0.29	0.12	0.29	0.53	0.83	0.87	0.86	0.2	0
Bulk Density [kg/m^3]	17	37.48	31.41	26.44	22.14	18.38	16.39	12.82	15.26	15.26	15.26
Coefficient of Variation											
Consolidation Load [%]	23.59	1.86	1.82	0.48	0.81	0.96	1.10	0.92	0.75	1.26	0
Bulk Density [%]	0.94	1.75	1.39	1.13	0.93	0.75	0.65	0.50	0.59	0.59	0.59

Table C.13: Confined Compression Data for Wet KPRS fines - 2.5% MC

Consolidation Load [N]	0.8	8.9	20.1	32.4	44.6	69.6	94.7	119.3	144.1	20.3	0
Consolidated Height [mm]	69.1	54.7	51.3	49.4	48	46.2	45	44.2	43.5	43.5	43.5
Consolidation Load [kPa]	0.6	7.1	16.0	25.8	35.5	55.4	75.3	94.9	114.7	16.1	0
Bulk Density [kg/m^3]	1631	2060	2198	2279	2347	2439	2502	2547	2590	2590	2590
Consolidated Aspect Ratio	1.73	1.37	1.28	1.24	1.20	1.16	1.13	1.11	1.09	1.09	1.09
Change in Height [mm]	0	14.4	3.4	1.8	1.4	1.8	1.2	0.8	0.7	0	0
Consolidation Strain [%]	0.00	20.80	25.77	28.43	30.50	33.11	34.80	35.96	37.02	37.02	37.02
STDEV											
Consolidation Load [kPa]	0.09	0	0.5	0.44	0.56	0.41	0.36	0.38	0.28	0.48	0
Bulk Density [kg/m^3]	13.44	19.66	12.35	17.33	13.29	9.48	7.54	8.91	8.49	8.49	8.49
Coefficient of Variation											
Consolidation Load [%]	15.06	0.00	3.11	1.70	1.58	0.74	0.48	0.40	0.24	2.97	0
Bulk Density [%]	0.82	0.95	0.56	0.76	0.57	0.39	0.30	0.35	0.33	0.33	0.33

Table C.14: Confined Compression Data for Wet KPRS fines - 4% MC

Consolidation Load [N]	1.5	8.9	20.2	32.4	45.4	70.1	95.2	119	143	20.3	0
Consolidated Height [mm]	67.7	57.5	53.8	51.6	50.1	48.1	46.9	46.1	45.4	45.4	45.4
Consolidation Load [kPa]	1.2	7.1	16.1	25.8	36.1	55.8	75.7	94.7	113.8	16.2	0
Bulk Density [kg/m^3]	1790	2105	2251	2347	2419	2516	2582	2627	2667	2667	2665
Consolidated Aspect Ratio	1.69	1.44	1.35	1.29	1.25	1.20	1.17	1.15	1.14	1.14	1.14
Change in Height [mm]	0	10.2	3.7	2.2	1.5	1.9	1.2	0.8	0.7	0	0
Consolidation Strain [%]	0.00	15.06	20.56	23.82	26.08	28.94	30.76	31.94	32.97	32.97	32.92
STDEV											
Consolidation Load [kPa]	0.28	0.36	0.29	0.64	0.32	0.37	0.62	1.59	1.57	0.41	0
Bulk Density [kg/m^3]	75.7	23.23	21.35	19.4	26.67	22.25	22.74	17.75	20.89	20.89	19.97
Coefficient of Variation											
Consolidation Load [%]	23.09	5.15	1.78	2.49	0.89	0.66	0.82	1.68	1.38	2.52	0
Bulk Density [%]	4.23	1.10	0.95	0.83	1.10	0.88	0.88	0.68	0.78	0.78	0.75

Table C.15: Confined Compression Data for Wet KPRS fines - 5% MC

Consolidation Load [N]	1.1	8.5	20.3	32.9	45.3	70.1	95.3	119.9	144.4	20.4	0
Consolidated Height [mm]	68.6	56.6	52.9	50.5	49	47	45.8	44.9	44.2	44.2	44.2
Consolidation Load [kPa]	0.9	6.8	16.1	26.2	36.1	55.8	75.8	95.4	114.9	16.2	0
Bulk Density [kg/m^3]	1774	2149	2298	2408	2482	2588	2657	2707	2752	2752	2752
Consolidated Aspect Ratio	1.72	1.42	1.32	1.26	1.23	1.18	1.14	1.12	1.11	1.11	1.1
Change in Height [mm]	0	12	3.7	2.4	1.5	2	1.2	0.8	0.7	0	0
Consolidation Strain [%]	0.00	17.49	22.84	26.38	28.57	31.49	33.28	34.50	35.57	35.57	35.57
STDEV											
Consolidation Load [kPa]	0.36	0.3	0.09	0.17	0	0.32	0.32	0.3	0.26	0.12	0
Bulk Density [kg/m^3]	37.55	11.37	13.63	17.69	18.58	16.92	15.73	11.72	17.21	17.21	17.21
Coefficient of Variation											
Consolidation Load [%]	41.66	4.44	0.57	0.63	0.00	0.58	0.42	0.32	0.22	0.75	0
Bulk Density [%]	2.12	0.53	0.59	0.73	0.75	0.65	0.59	0.43	0.63	0.63	0.63

Table C.16: Confined Compression Data for Wet KPRS fines - 6% MC

Consolidation Load [N]	0.8	8.7	20.5	33	45.4	70	95.1	119.9	145	20.7	0
Consolidated Height [mm]	72.2	58	54.2	51.9	50.4	48.4	47.1	46.2	45.6	45.6	45.6
Consolidation Load [kPa]	0.6	6.9	16.3	26.2	36.1	55.7	75.7	95.4	115.4	16.5	0
Bulk Density [kg/m^3]	1812	2258	2413	2520	2598	2706	2779	2831	2868	2868	2868
Consolidated Aspect Ratio	1.81	1.45	1.36	1.30	1.26	1.21	1.18	1.16	1.14	1.14	1.14
Change in Height [mm]	0	14.3	3.7	2.3	1.6	2	1.3	0.9	0.6	0	0
Consolidation Strain [%]	0.00	19.75	24.92	28.10	30.27	33.04	34.79	35.99	36.83	36.83	36.83
STDEV											
Consolidation Load [kPa]	0	0.12	0.08	0.2	0.3	0.24	0.44	0.59	0.73	0.23	0
Bulk Density [kg/m^3]	4.15	10.77	9.33	18.49	15.37	16.22	12.15	14.73	13.59	13.59	13.59
Coefficient of Variation											
Consolidation Load [%]	0.00	1.76	0.49	0.76	0.83	0.43	0.58	0.61	0.63	1.40	0
Bulk Density [%]	0.23	0.48	0.39	0.73	0.59	0.60	0.44	0.52	0.47	0.47	0.47

Table C.17: Confined Compression Data for Wet KPRS fines - 8% MC

Consolidation Load [N]	0.8	8.7	20.1	32.7	45.2	69.6	94.1	119	143.6	23.5	0
Consolidated Height [mm]	73.3	58.5	54.8	52.4	50.8	48.7	47.5	46.7	45.9	45.9	46.0
Consolidation Load [kPa]	0.7	7.0	16.0	26.1	36.0	55.4	74.9	94.7	114.3	18.7	0
Bulk Density [kg/m^3]	1836	2301	2454	2569	2650	2764	2832	2882	2928	2928	2924
Consolidated Aspect Ratio	1.83	1.46	1.37	1.31	1.27	1.22	1.19	1.17	1.15	1.15	1.15
Change in Height [mm]	0	14.8	3.7	2.4	1.6	2.1	1.2	0.8	0.7	0	-0.1
Consolidation Strain [%]	0.00	20.15	25.20	28.53	30.71	33.58	35.17	36.31	37.31	37.31	37.22
STDEV											
Consolidation Load [kPa]	0.05	0.24	0.18	0.28	0.08	0.08	0.38	0.59	0.92	1.21	0
Bulk Density [kg/m^3]	15.24	37.33	9.14	13.92	16.88	7	12.68	12.65	12.41	12.41	11.59
Coefficient of Variation											
Consolidation Load [%]	6.93	3.50	1.15	1.07	0.22	0.14	0.50	0.62	0.80	6.44	0
Bulk Density [%]	0.83	1.62	0.37	0.54	0.64	0.25	0.45	0.44	0.42	0.42	0.40

Appendix D

Unconfined Stress-Strain Data From EPT

D.1 KPBO Fines

D.1.1 Results - 1% MC

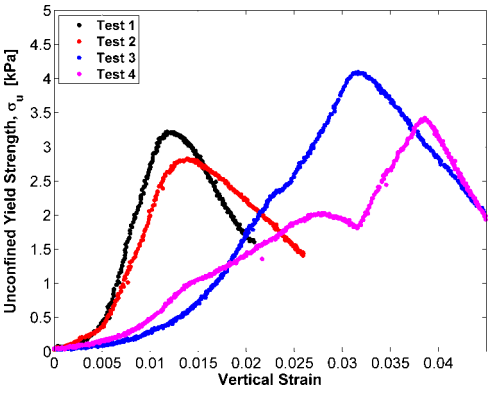

Figure D.1: KPBO Fines - 20 kPa Consolidation Stress

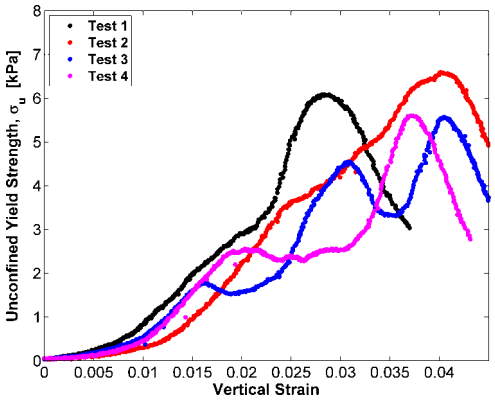

Figure D.2: KPBO Fines - 40 kPa Consolidation Stress

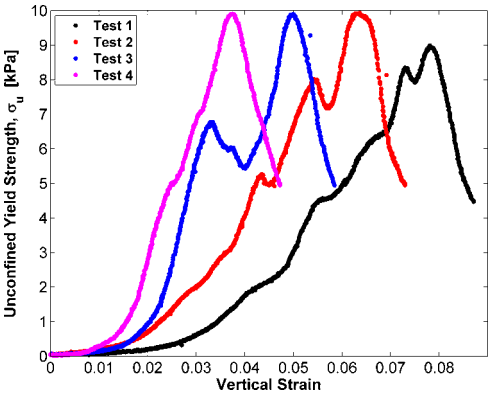

Figure D.3: KPBO Fines - 60 kPa Consolidation Stress

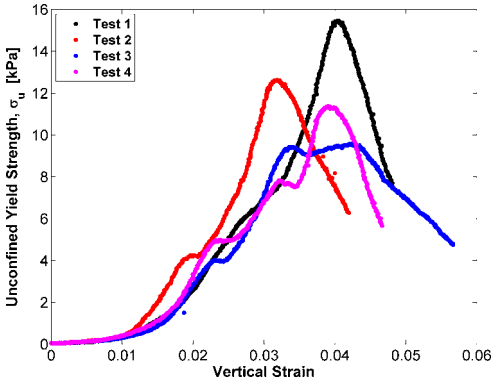

Figure D.4: KPBO Fines - 80 kPa Consolidation Stress

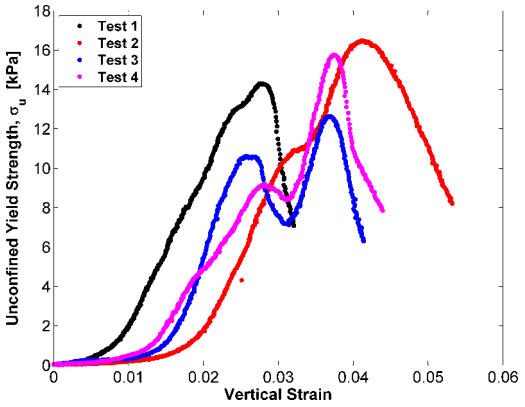

Figure D.5: KPBO Fines - 100 kPa Consolidation Stress

D.1.2 Results - 2% MC

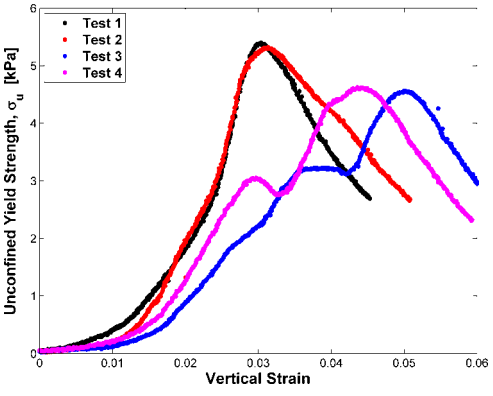

Figure D.6: KPBO Fines - 20 kPa Consolidation Stress

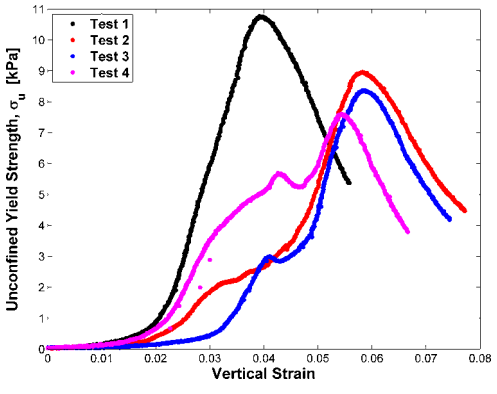

Figure D.7: KPBO Fines - 40 kPa Consolidation Stress

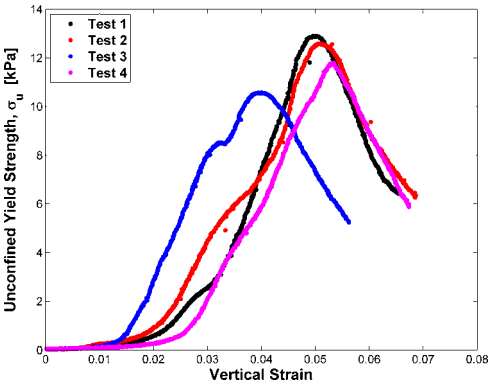

Figure D.8: KPBO Fines - 60 kPa Consolidation Stress

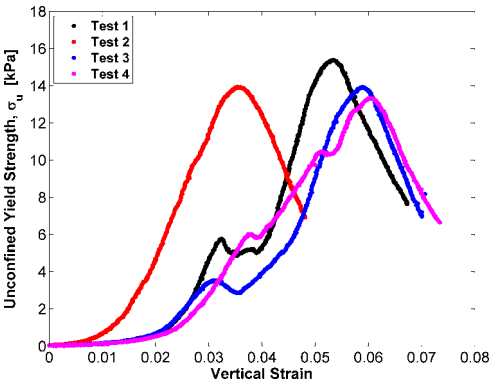

Figure D.9: KPBO Fines - 80 kPa Consolidation Stress

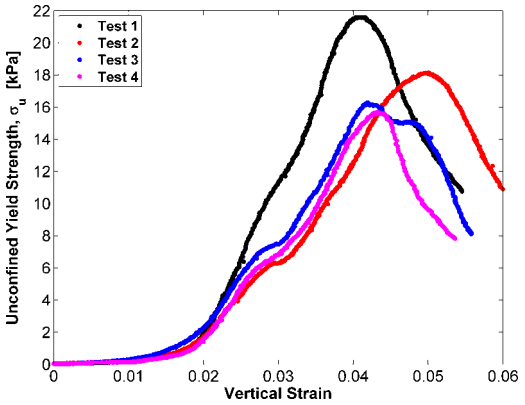

Figure D.10: KPBO Fines - 100 kPa Consolidation Stress

D.1.3 Results - 3% MC

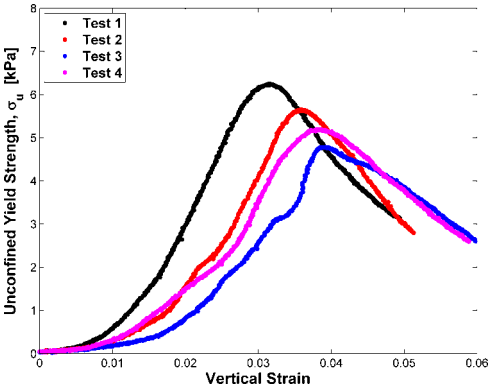

Figure D.11: KPBO Fines - 20 kPa Consolidation Stress

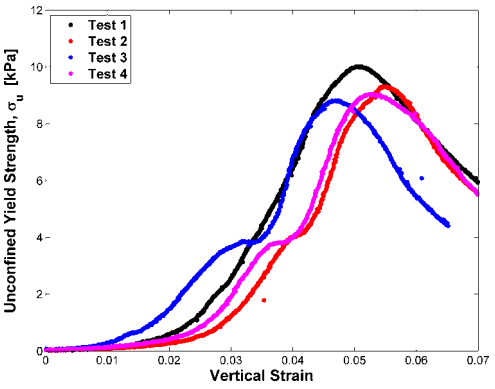

Figure D.12: KPBO Fines - 40 kPa Consolidation Stress

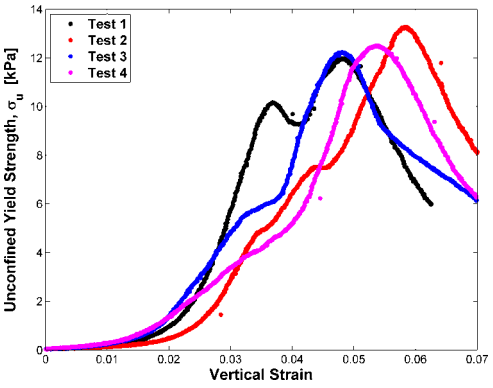

Figure D.13: KPBO Fines - 60 kPa Consolidation Stress

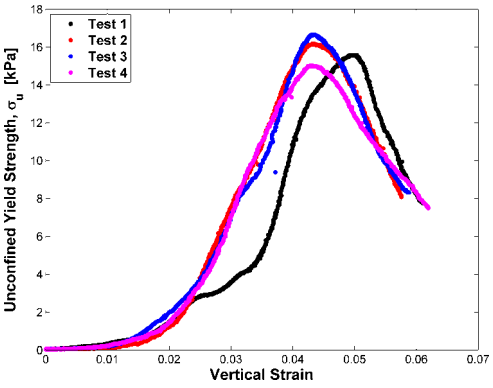

Figure D.14: KPBO Fines - 80 kPa Consolidation Stress

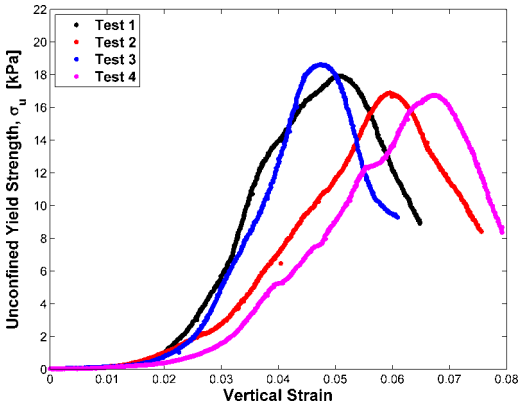

Figure D.15: KPBO Fines - 100 kPa Consolidation Stress

D.1.4 Results - 4% MC

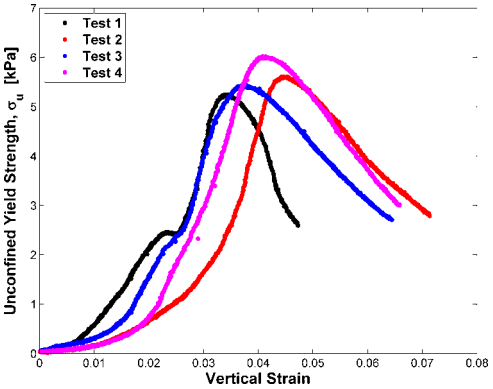

Figure D.16: KPBO Fines - 20 kPa Consolidation Stress

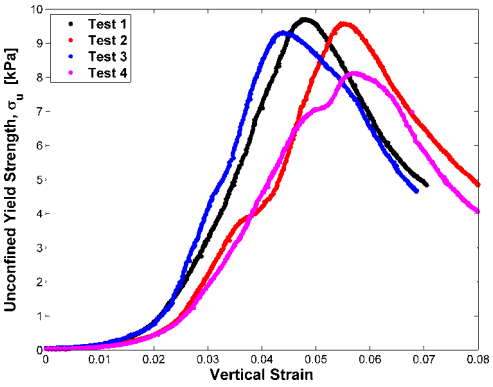

Figure D.17: KPBO Fines - 40 kPa Consolidation Stress

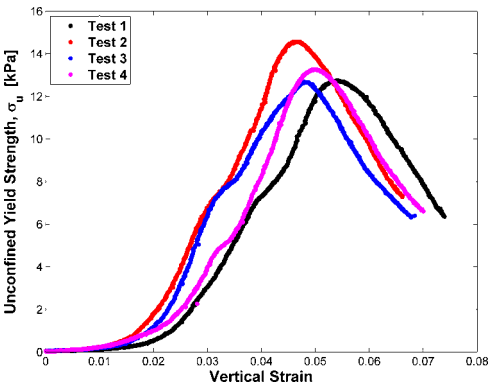

Figure D.18: KPBO Fines - 60 kPa Consolidation Stress

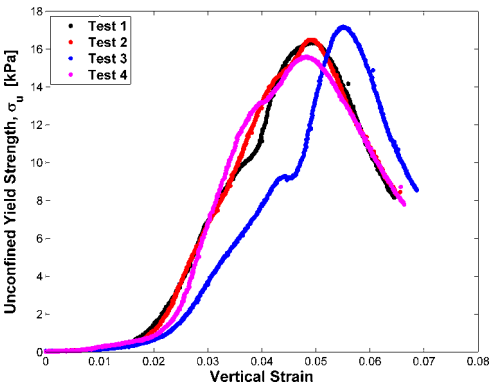

Figure D.19: KPBO Fines - 80 kPa Consolidation Stress

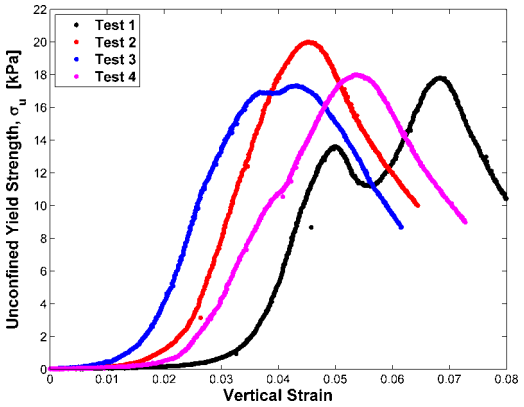

Figure D.20: KPBO Fines - 100 kPa Consolidation Stress

D.1.5 Results - 6% MC

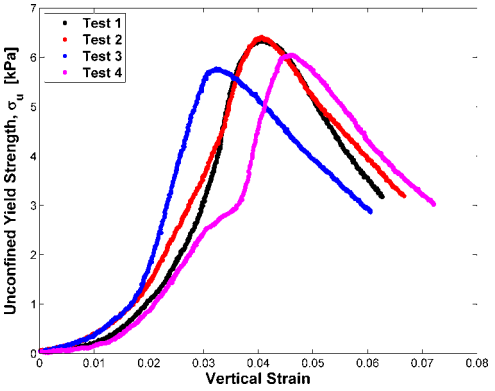

Figure D.21: KPBO Fines - 20 kPa Consolidation Stress

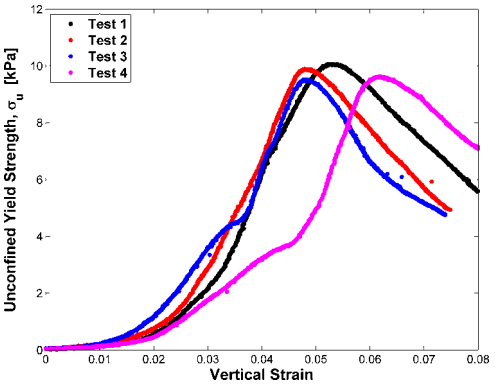

Figure D.22: KPBO Fines - 40 kPa Consolidation Stress

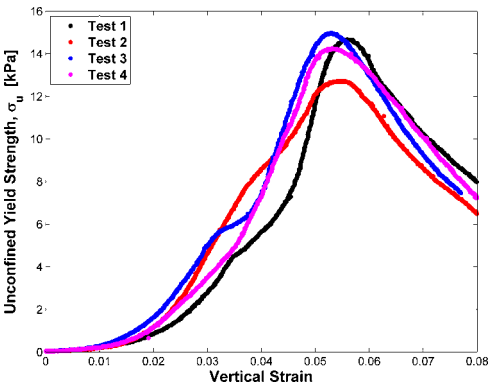

Figure D.23: KPBO Fines - 60 kPa Consolidation Stress

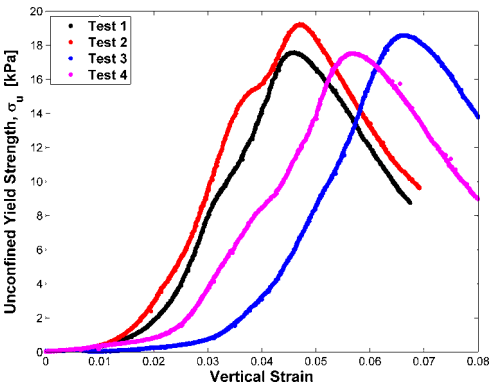

Figure D.24: KPBO Fines - 80 kPa Consolidation Stress

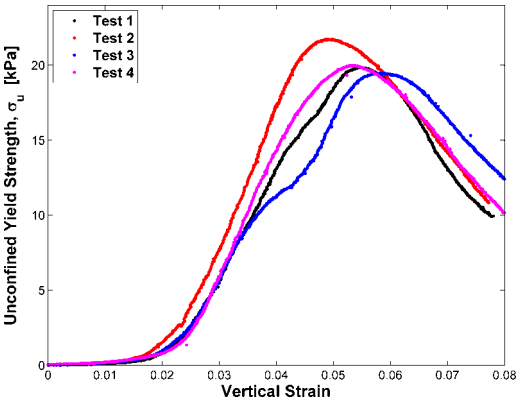

Figure D.25: KPBO Fines - 100 kPa Consolidation Stress

D.2 KPRS Fines

D.2.1 Results - 1% MC

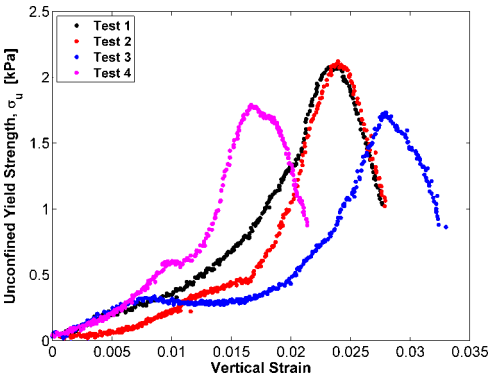

Figure D.26: KPRS Fines - 20 kPa Consolidation Stress

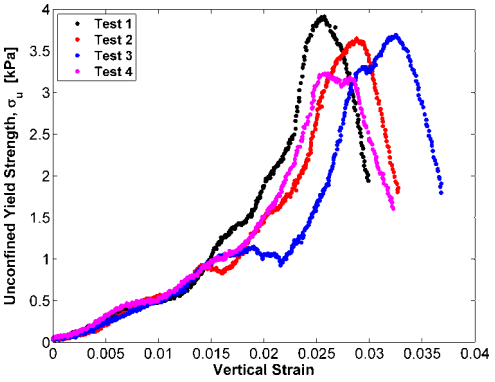

Figure D.27: KPRS Fines - 40 kPa Consolidation Stress

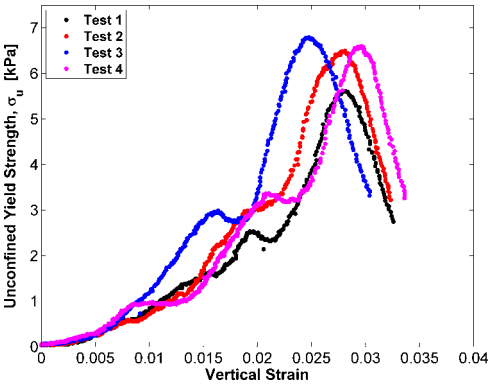

Figure D.28: KPRS Fines - 60 kPa Consolidation Stress

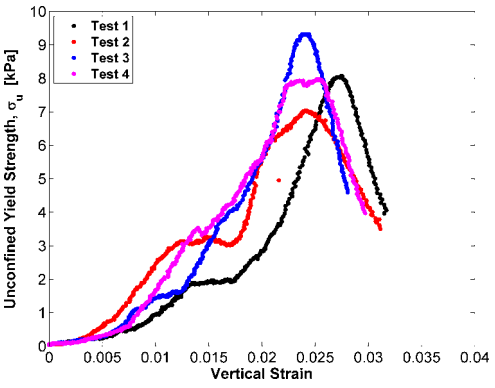

Figure D.29: KPRS Fines - 80 kPa Consolidation Stress

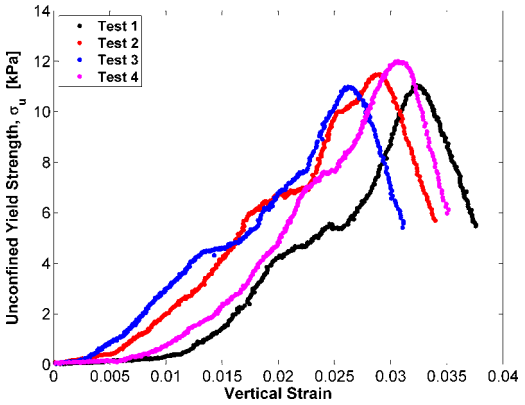

Figure D.30: KPRS Fines - 100 kPa Consolidation Stress

D.2.2 Results - 2% MC

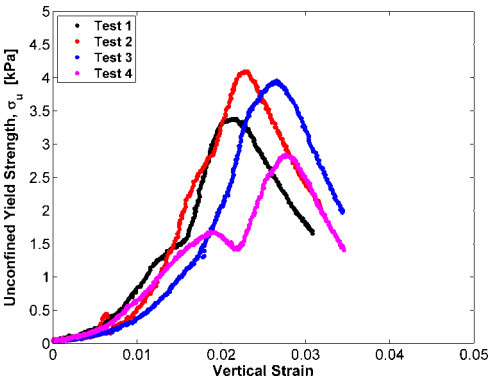

Figure D.31: KPRS Fines - 20 kPa Consolidation Stress

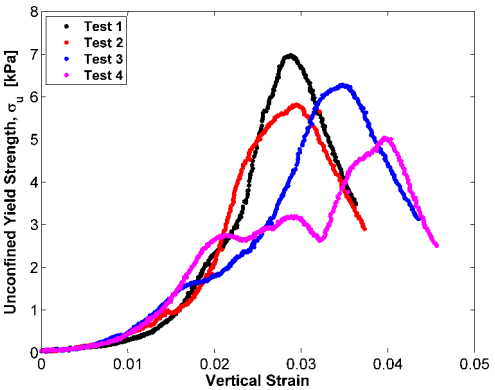

Figure D.32: KPRS Fines - 40 kPa Consolidation Stress

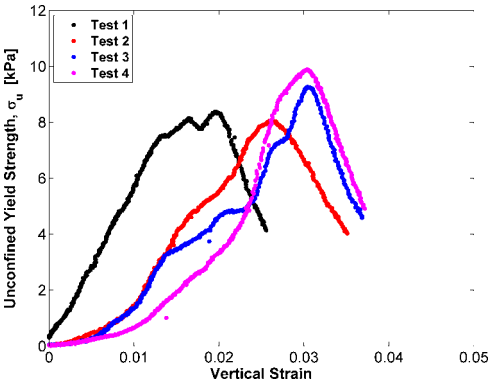

Figure D.33: KPRS Fines - 60 kPa Consolidation Stress

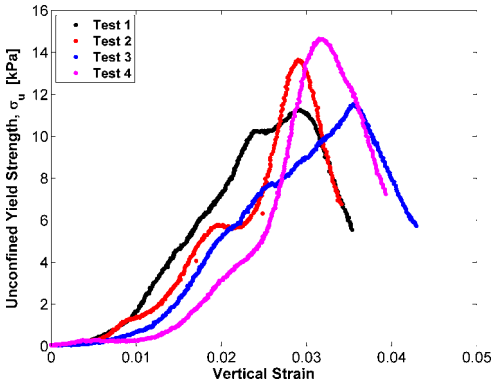

Figure D.34: KPRS Fines - 80 kPa Consolidation Stress

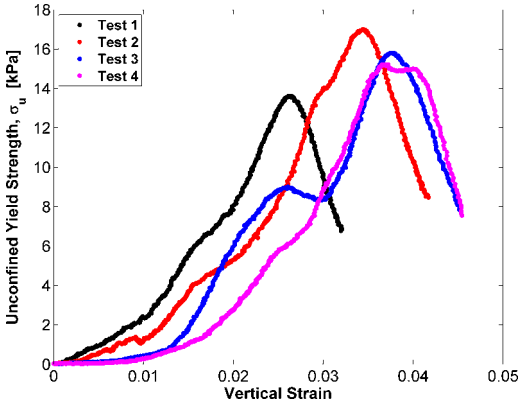

Figure D.35: KPRS Fines - 100 kPa Consolidation Stress

D.2.3 Results - 3% MC

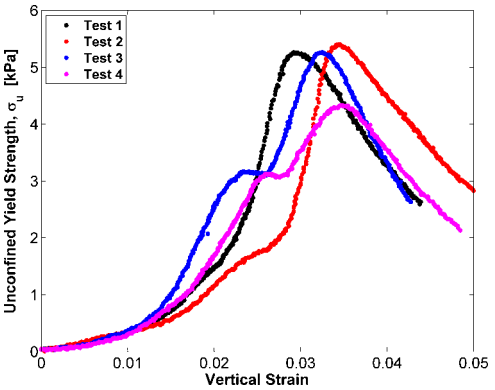

Figure D.36: KPRS Fines - 20 kPa Consolidation Stress

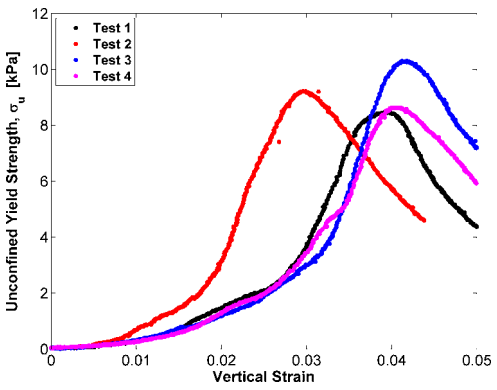

Figure D.37: KPRS Fines - 40 kPa Consolidation Stress

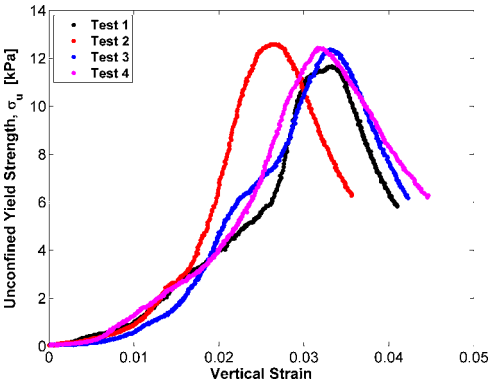

Figure D.38: KPRS Fines - 60 kPa Consolidation Stress

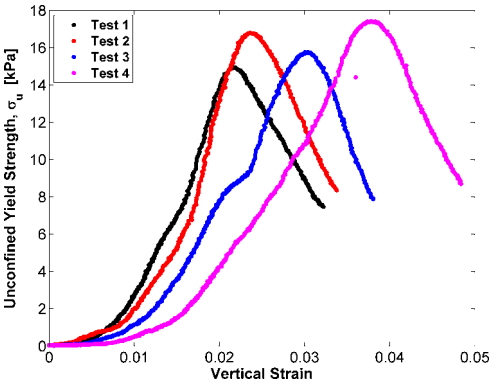

Figure D.39: KPRS Fines - 80 kPa Consolidation Stress

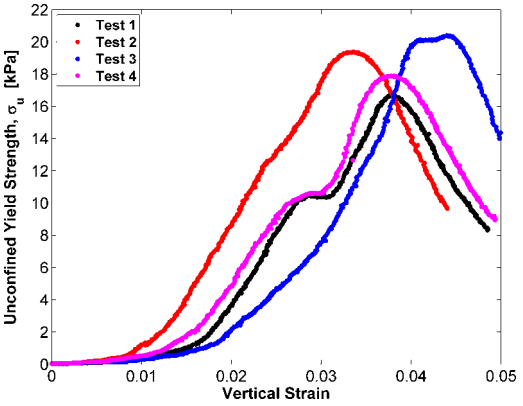

Figure D.40: KPRS Fines - 100 kPa Consolidation Stress

D.2.4 Results - 4% MC

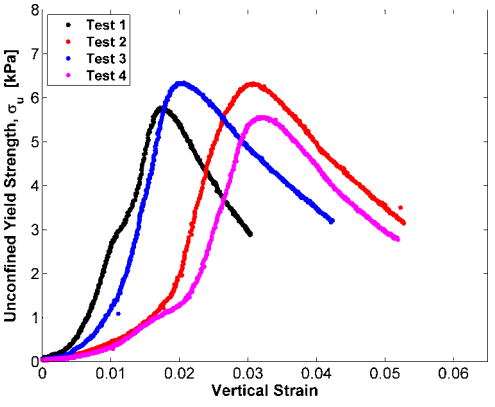

Figure D.41: KPRS Fines - 20 kPa Consolidation Stress

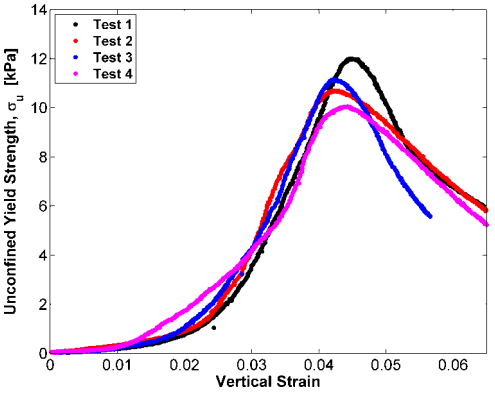

Figure D.42: KPRS Fines - 40 kPa Consolidation Stress

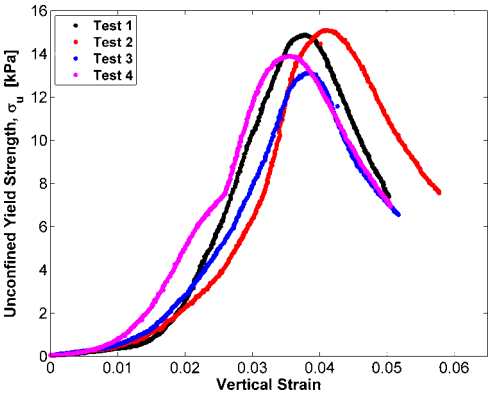

Figure D.43: KPRS Fines - 60 kPa Consolidation Stress

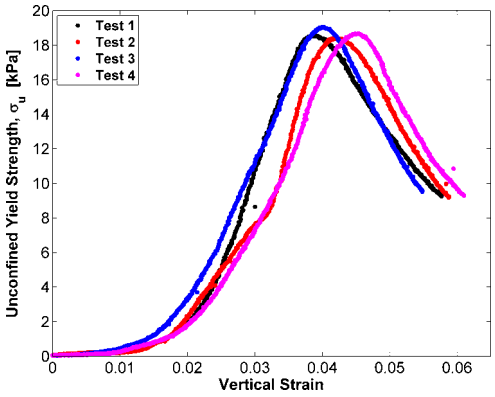

Figure D.44: KPRS Fines - 80 kPa Consolidation Stress

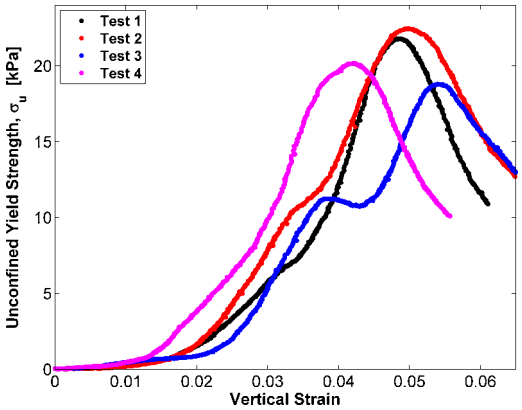

Figure D.45: KPRS Fines - 100 kPa Consolidation Stress

D.2.5 Results - 6% MC

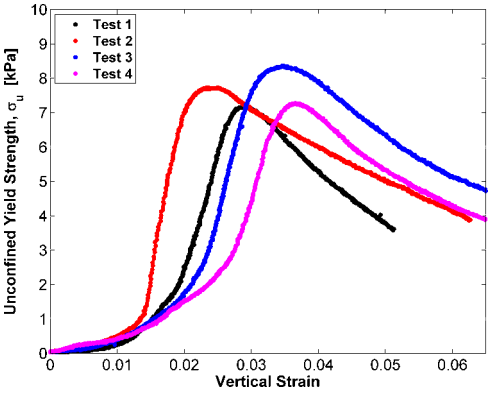

Figure D.46: KPRS Fines - 20 kPa Consolidation Stress

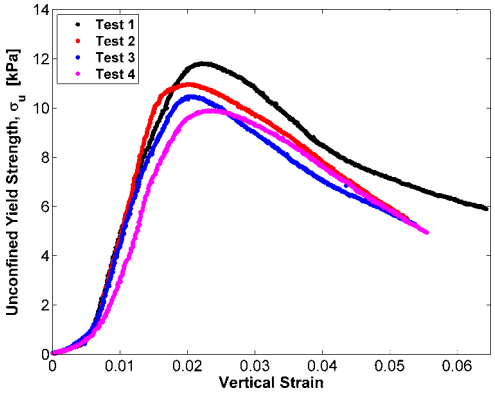

Figure D.47: KPRS Fines - 40 kPa Consolidation Stress

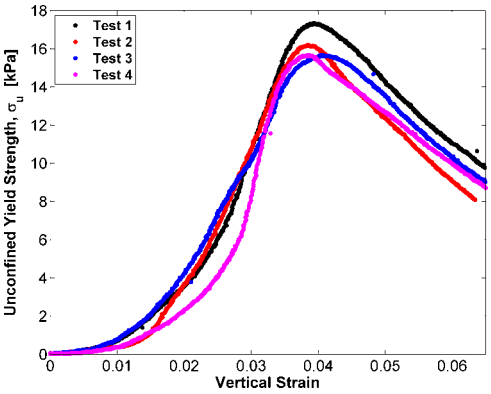

Figure D.48: KPRS Fines - 60 kPa Consolidation Stress

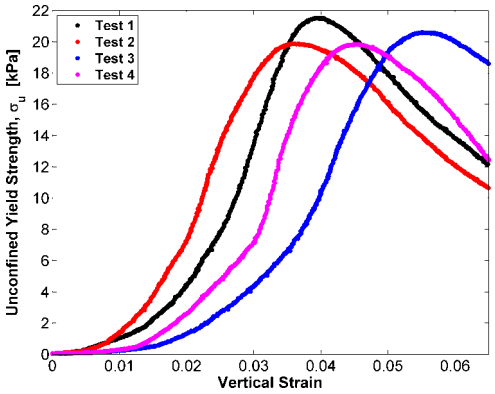

Figure D.49: KPRS Fines - 80 kPa Consolidation Stress

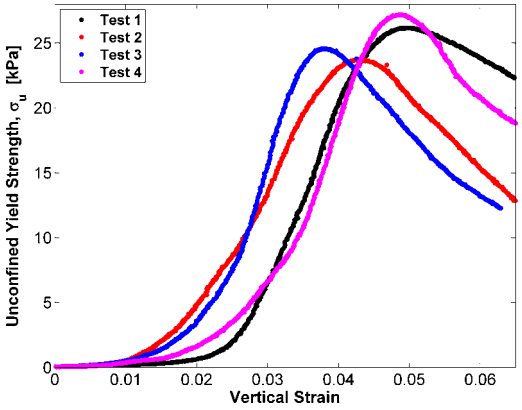

Figure D.50: KPRS Fines - 100 kPa Consolidation Stress

Appendix E

EPT Unconfined Compression Test Data

E.1 KPBO Fines

Table E.1: Unconfined Compression Data for Wet KPBO Fines - 1% MC

	Mean					Standard Deviation					Coefficient of Variation				
	20	**40**	**60**	**80**	**100**	**20**	**40**	**60**	**80**	**100**	**20**	**40**	**60**	**80**	**100**
Consolidation Stress [kPa]	17.72	37.40	57.47	77.46	98.15	0.49	0.32	0.33	0.17	0.28	2.7%	0.9%	0.6%	0.2%	0.3%
Max force [gf]	357	547	894	1186	1400	74	46	57	185	173	20.7%	8.4%	6.4%	15.6%	12.4%
Unconfined Strength [kPa]	3.58	5.96	9.68	13.15	15.52	0.46	0.48	0.46	2.09	1.11	12.8%	8.1%	4.8%	15.9%	7.1%
Peak Strain	0.03	0.04	0.06	0.04	0.04	0.01	0.01	0.02	0.00	0.01	50.9%	15.4%	30.6%	12.3%	20.1%
Initial Height [mm]	61.7	65.2	73.4	77.2	77.2	3.5	8.8	1.2	1.4	2.4	5.7%	13.4%	1.6%	1.8%	3.1%
Confined Consolidated Height [mm]	50.0	53.2	52.1	54.8	55.5	4.3	1.2	1.2	0.1	3.6	8.5%	2.3%	2.3%	0.2%	6.5%
Consolidated Height [mm]	51.9	55.8	55.6	56.8	57.1	3.9	1.0	1.7	0.3	3.2	7.6%	1.8%	3.1%	0.5%	5.7%
Failed Height [mm]	50.5	53.8	52.4	54.7	55.1	3.9	1.3	1.0	0.0	3.5	7.8%	2.4%	1.9%	0.1%	6.4%
Initial Aspect Ratio	1.54	1.63	1.84	1.93	1.93	0.09	0.22	0.03	0.04	0.06	5.7%	13.4%	1.6%	1.8%	3.1%
Consolidated Aspect Ratio	1.30	1.40	1.39	1.42	1.43	0.10	0.03	0.04	0.01	0.08	7.6%	1.8%	3.1%	0.5%	5.7%
Sample compression [mm]	6.0	7.0	8.2	7.3	7.2	1.3	0.4	1.1	0.3	0.4	21.2%	5.3%	13.0%	3.5%	5.4%
Sample Rebound [mm]	1.9	2.6	3.5	2.1	1.6	1.2	0.3	1.1	0.2	0.4	65.1%	12.8%	32.3%	11.3%	23.3%
Mass of Sample [g]	145	163	161	174	179	12	3	3	2	14	8.6%	2.1%	1.6%	0.9%	7.6%
Initial Bulk Density [kg/m^3]	1865	2018	1744	1796	1847	59	279	8	33	83	3.2%	13.8%	0.5%	1.8%	4.5%
Consol. Bulk Density [kg/m^3]	2216	2323	2306	2441	2499	31	15	42	30	73	1.4%	0.7%	1.8%	1.2%	2.9%

Table E.2: Unconfined Compression Data for Wet KPBO Fines - 2% MC

	Mean					Standard Deviation					Coefficient of Variation				
	20	**40**	**60**	**80**	**100**	**20**	**40**	**60**	**80**	**100**	**20**	**40**	**60**	**80**	**100**
Consolidation Stress [kPa]	17.79	37.67	57.51	77.11	97.27	0.19	0.23	0.17	0.45	0.58	1.1%	0.6%	0.3%	0.6%	0.6%
Max force [gf]	459	922	1189	1333	1734	43	95	76	52	201	9.4%	10.3%	6.4%	3.9%	11.6%
Unconfined Strength [kPa]	4.98	9.37	12.42	14.15	18.68	0.45	1.25	0.58	0.88	2.69	9.0%	13.3%	4.6%	6.2%	14.4%
Peak Strain	0.04	0.05	0.05	0.05	0.04	0.01	0.01	0.00	0.01	0.01	24.7%	21.5%	3.7%	22.0%	11.6%
Initial Height [mm]	70.3	68.6	74.9	77.9	70.7	2.9	2.1	2.3	3.5	13.6	4.1%	3.1%	3.0%	4.5%	19.3%
Confined Consolidated Height [mm]	52.8	49.8	50.6	51.3	53.0	2.9	2.3	1.3	2.4	1.6	5.5%	4.6%	2.6%	4.6%	3.1%
Consolidated Height [mm]	55.7	52.0	53.6	54.4	55.1	2.7	1.7	1.5	2.1	1.5	4.9%	3.3%	2.8%	3.9%	2.7%
Failed Height [mm]	53.5	49.3	50.8	51.5	52.6	2.8	2.2	1.4	2.2	1.6	5.3%	4.5%	2.7%	4.3%	3.0%
Initial Aspect Ratio	1.76	1.72	1.87	1.95	1.77	0.07	0.05	0.06	0.09	0.34	4.1%	3.1%	3.0%	4.5%	19.3%
Consolidated Aspect Ratio	1.39	1.30	1.34	1.36	1.38	0.07	0.04	0.04	0.05	0.04	4.9%	3.3%	2.8%	3.9%	2.7%
Sample compression [mm]	7.1	7.6	7.7	8.0	7.7	0.5	0.5	0.4	0.6	0.1	7.1%	6.9%	5.1%	7.8%	1.7%
Sample Rebound [mm]	2.9	2.2	2.9	3.1	2.0	0.5	1.4	0.2	0.9	0.2	16.8%	63.5%	6.9%	29.7%	8.9%
Mass of Sample [g]	144	141	151	159	166	7	6	4	6	5	5.1%	4.4%	2.8%	4.1%	3.0%
Initial Bulk Density [kg/m^3]	1615	1882	1717	1785	2087	81	13	85	89	620	5.0%	0.7%	5.0%	5.0%	29.7%
Consol. Bulk Density [kg/m^3]	2037	2485	2399	2556	2575	58	22	112	112	150	2.9%	0.9%	4.7%	4.4%	5.8%

Table E.3: Unconfined Compression Data for Wet KPBO Fines - 3% MC

	Mean					Standard Deviation					Coefficient of Variation				
	20	**40**	**60**	**80**	**100**	**20**	**40**	**60**	**80**	**100**	**20**	**40**	**60**	**80**	**100**
Consolidation Stress [kPa]	17.83	37.70	57.30	77.65	97.46	0.24	0.20	0.42	0.04	0.20	1.3%	0.5%	0.7%	0.1%	0.2%
Max force [gf]	540	941	1184	1511	1717	53	52	57	97	84	9.8%	5.5%	4.8%	6.4%	4.9%
Unconfined Strength [kPa]	5.70	9.30	12.49	15.85	17.56	0.53	0.52	0.55	0.71	0.88	9.2%	5.6%	4.4%	4.5%	5.0%
Peak Strain	0.04	0.05	0.05	0.04	0.06	0.00	0.00	0.00	0.00	0.01	9.5%	6.8%	9.5%	7.0%	16.2%
Initial Height [mm]	68.9	70.1	76.7	78.4	71.9	0.7	2.0	0.6	2.4	13.8	1.1%	2.8%	0.8%	3.1%	19.2%
Confined Consolidated Height [mm]	51.5	47.4	51.2	51.7	50.0	0.4	0.6	0.9	1.6	1.7	0.8%	1.3%	1.8%	3.2%	3.4%
Consolidated Height [mm]	54.2	50.7	54.0	53.8	52.4	0.5	0.5	1.0	1.9	1.7	0.9%	1.1%	1.8%	3.5%	3.2%
Failed Height [mm]	52.2	48.1	51.2	51.4	49.5	0.4	0.4	0.9	1.6	1.6	0.7%	0.8%	1.8%	3.2%	3.3%
Initial Aspect Ratio	1.72	1.75	1.92	1.96	1.80	0.02	0.05	0.02	0.06	0.34	1.1%	2.8%	0.8%	3.1%	19.2%
Consolidated Aspect Ratio	1.35	1.27	1.35	1.35	1.31	0.01	0.01	0.02	0.05	0.04	0.9%	1.1%	1.8%	3.5%	3.2%
Sample compression [mm]	6.9	7.4	7.9	7.5	8.0	0.3	0.3	0.3	0.2	0.4	4.1%	3.8%	4.1%	3.2%	5.4%
Sample Rebound [mm]	2.7	3.2	2.8	2.1	2.5	0.3	0.2	0.4	0.3	0.4	9.6%	6.4%	12.5%	12.5%	17.3%
Mass of Sample [g]	138	136	153	157	155	2	1	2	6	5	1.6%	0.8%	1.6%	3.7%	3.0%
Initial Bulk Density [kg/m^3]	1695	1850	1670	1772	2039	107	18	21	62	468	6.3%	1.0%	1.2%	3.5%	22.9%
Consol. Bulk Density [kg/m^3]	2158	2559	2370	2582	2706	145	48	44	106	146	6.7%	1.9%	1.9%	4.1%	5.4%

Table E.4: Unconfined Compression Data for Wet KPBO Fines - 4% MC

	Mean					Standard Deviation					Coefficient of Variation				
	20	**40**	**60**	**80**	**100**	**20**	**40**	**60**	**80**	**100**	**20**	**40**	**60**	**80**	**100**
Consolidation Stress [kPa]	17.23	37.69	56.28	76.93	97.68	0.51	0.26	1.19	0.90	0.46	3.0%	0.7%	2.1%	1.2%	0.5%
Max force [gf]	525	957	1270	1569	1806	34	21	80	53	136	6.5%	2.2%	6.3%	3.4%	7.5%
Unconfined Strength [kPa]	5.58	9.54	13.32	16.40	18.29	0.33	0.20	0.88	0.65	1.18	5.9%	2.1%	6.6%	4.0%	6.5%
Peak Strain	0.04	0.05	0.05	0.05	0.05	0.00	0.01	0.00	0.00	0.01	11.7%	10.9%	7.0%	6.2%	21.7%
Initial Height [mm]	72.2	69.3	77.5	74.4	74.4	3.2	0.6	3.4	10.6	7.3	4.4%	0.9%	4.4%	14.3%	9.8%
Confined Consolidated Height [mm]	51.7	48.1	51.5	51.3	49.8	1.1	1.2	0.7	1.0	0.8	2.1%	2.5%	1.3%	1.9%	1.6%
Consolidated Height [mm]	54.5	51.1	53.7	53.6	51.9	0.9	0.9	1.0	1.0	1.0	1.7%	1.8%	1.8%	2.0%	1.9%
Failed Height [mm]	52.3	48.6	51.1	50.9	49.2	1.1	1.1	1.1	0.9	0.8	2.1%	2.2%	2.1%	1.9%	1.6%
Initial Aspect Ratio	1.81	1.73	1.94	1.86	1.86	0.08	0.02	0.08	0.27	0.18	4.4%	0.9%	4.4%	14.3%	9.8%
Consolidated Aspect Ratio	1.36	1.28	1.34	1.34	1.30	0.02	0.02	0.02	0.03	0.02	1.7%	1.8%	1.8%	2.0%	1.9%
Sample compression [mm]	7.0	7.2	7.6	7.7	7.7	0.3	0.2	0.2	0.2	0.6	3.9%	2.4%	2.1%	2.2%	8.2%
Sample Rebound [mm]	2.8	3.0	2.3	2.3	2.1	0.3	0.6	0.7	0.2	0.6	9.9%	19.2%	31.8%	9.0%	29.2%
Mass of Sample [g]	138	138	153	157	154	3	4	5	3	3	2.1%	2.7%	3.1%	2.1%	1.7%
Initial Bulk Density [kg/m^3]	1572	1865	1654	1897	1921	94	42	54	300	233	5.9%	2.2%	3.3%	15.8%	12.1%
Consol. Bulk Density [kg/m^3]	2083	2530	2383	2591	2732	132	25	50	42	140	6.3%	1.0%	2.1%	1.6%	5.1%

Table E.5: Unconfined Compression Data for Wet KPBO Fines - 6% MC

	Mean					Standard Deviation					Coefficient of Variation				
	20	**40**	**60**	**80**	**100**	**20**	**40**	**60**	**80**	**100**	**20**	**40**	**60**	**80**	**100**
Consolidation Stress [kPa]	17.77	37.66	57.56	77.67	97.52	0.20	0.18	0.20	0.17	0.31	1.1%	0.5%	0.3%	0.2%	0.3%
Max force [gf]	560	956	1366	1701	2007	16	31	11	64	74	2.9%	3.2%	0.8%	3.8%	3.7%
Unconfined Strength [kPa]	6.15	9.78	14.63	18.23	20.26	0.30	0.25	0.36	0.83	1.00	4.8%	2.5%	2.5%	4.5%	4.9%
Peak Strain	0.04	0.05	0.05	0.05	0.05	0.01	0.01	0.00	0.01	0.00	14.2%	12.4%	3.1%	17.9%	6.5%
Initial Height [mm]	66.1	73.2	76.1	81.0	71.3	7.2	1.0	2.5	2.2	13.8	10.8%	1.3%	3.3%	2.7%	19.4%
Confined Consolidated Height [mm]	53.4	49.2	51.9	52.4	49.7	2.1	2.3	1.0	1.3	1.6	3.8%	4.7%	1.9%	2.4%	3.2%
Consolidated Height [mm]	56.3	52.4	54.9	54.9	51.7	2.1	2.2	1.1	0.9	1.5	3.7%	4.1%	2.1%	1.6%	2.9%
Failed Height [mm]	54.0	49.7	51.9	51.9	48.9	2.0	2.3	1.0	1.3	1.6	3.7%	4.7%	2.0%	2.4%	3.2%
Initial Aspect Ratio	1.65	1.83	1.90	2.03	1.78	0.18	0.02	0.06	0.05	0.35	10.8%	1.3%	3.3%	2.7%	19.4%
Consolidated Aspect Ratio	1.41	1.31	1.37	1.37	1.29	0.05	0.05	0.03	0.02	0.04	3.7%	4.1%	2.1%	1.6%	2.9%
Sample compression [mm]	7.1	7.5	8.0	7.9	7.6	0.4	0.2	0.1	0.5	0.2	5.1%	3.3%	1.4%	6.3%	3.2%
Sample Rebound [mm]	2.9	3.2	3.0	2.5	2.0	0.3	0.5	0.2	0.4	0.3	10.0%	13.9%	5.3%	17.6%	17.1%
Mass of Sample [g]	147	145	161	164	157	7	13	5	5	6	4.6%	9.0%	2.9%	2.8%	3.6%
Initial Bulk Density [kg/m^3]	1739	1772	1671	1714	2059	295	34	57	57	498	17.0%	1.9%	3.4%	3.3%	24.2%
Consol. Bulk Density [kg/m^3]	2019	2477	2316	2529	2747	171	132	44	49	232	8.5%	5.3%	1.9%	2.0%	8.5%

E.2 KPRS Fines

Table E.6: Unconfined Compression Data for Wet KPRS Fines - 1% MC

	Mean					Standard Deviation					Coefficient of Variation				
	20	**40**	**60**	**80**	**100**	**20**	**40**	**60**	**80**	**100**	**20**	**40**	**60**	**80**	**100**
Consolidation Stress [kPa]	17.75	37.75	57.85	77.27	96.27	0.14	0.09	0.21	0.32	2.02	0.8%	0.2%	0.4%	0.4%	2.1%
Max force [gf]	186	334	597	739	1000	20	3	14	49	37	10.9%	1.0%	2.4%	6.6%	3.7%
Unconfined Strength [kPa]	2.00	3.75	6.63	8.46	11.38	0.18	0.14	0.15	0.75	0.47	9.0%	3.8%	2.2%	8.9%	4.1%
Peak Strain	0.02	0.03	0.03	0.03	0.03	0.00	0.00	0.00	0.00	0.00	19.7%	11.7%	9.0%	7.2%	8.8%
Initial Height [mm]	60.4	65.7	65.2	68.5	69.9	2.2	3.5	1.2	2.6	3.0	3.6%	5.3%	1.9%	3.8%	4.2%
Confined Consolidated Height [mm]	53.2	55.3	55.2	57.3	57.1	1.8	2.7	0.3	1.5	2.6	3.4%	4.8%	0.5%	2.6%	4.6%
Consolidated Height [mm]	55.2	57.6	57.0	58.6	58.3	1.8	2.6	0.4	1.5	2.5	3.2%	4.6%	0.7%	2.5%	4.3%
Failed Height [mm]	54.0	56.0	55.4	57.1	56.6	1.8	2.7	0.3	1.6	2.5	3.4%	4.9%	0.6%	2.7%	4.5%
Initial Aspect Ratio	1.51	1.64	1.63	1.71	1.75	0.05	0.09	0.03	0.07	0.07	3.6%	5.3%	1.9%	3.8%	4.2%
Consolidated Aspect Ratio	1.38	1.44	1.42	1.46	1.46	0.04	0.07	0.01	0.04	0.06	3.2%	4.6%	0.7%	2.5%	4.3%
Sample compression [mm]	6.0	6.6	6.6	6.7	6.9	0.1	0.2	0.1	0.1	0.2	2.4%	3.0%	1.8%	2.0%	2.3%
Sample Rebound [mm]	2.0	2.3	1.7	1.3	1.3	0.2	0.4	0.1	0.0	0.1	9.2%	15.0%	5.9%	3.1%	10.6%
Mass of Sample [g]	157	169	176	185	185	5	8	1	5	9	3.4%	4.6%	0.6%	2.6%	4.6%
Initial Bulk Density [kg/m^3]	2068	2044	2146	2148	2109	51	49	34	39	19	2.5%	2.4%	1.6%	1.8%	0.9%
Consol. Bulk Density [kg/m^3]	2263	2330	2455	2508	2526	9	9	4	3	13	0.4%	0.4%	0.2%	0.1%	0.5%

Table E.7: Unconfined Compression Data for Wet KPRS Fines - 2% MC

	Mean					Standard Deviation					Coefficient of Variation				
	20	**40**	**60**	**80**	**100**	**20**	**40**	**60**	**80**	**100**	**20**	**40**	**60**	**80**	**100**
Consolidation Stress [kPa]	18.06	37.98	58.09	77.72	97.19	0.08	0.18	0.19	0.39	0.20	0.4%	0.5%	0.3%	0.5%	0.2%
Max force [gf]	340	602	802	1164	1436	25	23	92	142	87	7.5%	3.8%	11.4%	12.2%	6.1%
Unconfined Strength [kPa]	3.81	6.36	8.90	13.28	16.02	0.38	0.58	0.84	1.59	0.91	9.9%	9.2%	9.4%	11.9%	5.7%
Peak Strain	0.02	0.03	0.03	0.03	0.04	0.00	0.00	0.01	0.00	0.00	11.1%	10.6%	19.4%	10.4%	4.8%
Initial Height [mm]	67.7	64.4	68.8	71.5	72.3	1.8	4.6	2.9	0.9	0.7	2.7%	7.1%	4.3%	1.3%	1.0%
Confined Consolidated Height [mm]	55.2	51.8	55.3	57.0	55.4	1.4	4.1	2.5	0.8	0.6	2.5%	8.0%	4.6%	1.4%	1.1%
Consolidated Height [mm]	57.4	54.1	57.0	58.5	57.1	1.5	4.2	2.6	0.5	0.6	2.5%	7.9%	4.6%	0.8%	1.1%
Failed Height [mm]	56.0	52.4	55.5	56.6	55.1	1.4	4.2	2.8	0.6	0.6	2.4%	8.1%	5.1%	1.0%	1.1%
Initial Aspect Ratio	1.69	1.61	1.72	1.79	1.81	0.05	0.11	0.07	0.02	0.02	2.7%	7.1%	4.3%	1.3%	1.0%
Consolidated Aspect Ratio	1.43	1.35	1.42	1.46	1.43	0.04	0.11	0.07	0.01	0.02	2.5%	7.9%	4.6%	0.8%	1.1%
Sample compression [mm]	6.2	6.5	6.5	7.0	7.3	0.1	0.1	0.3	0.3	0.0	1.4%	2.1%	4.9%	3.7%	0.2%
Sample Rebound [mm]	2.1	2.3	1.7	1.5	1.7	0.1	0.2	0.1	0.3	0.1	5.2%	7.0%	7.3%	21.4%	3.4%
Mass of Sample [g]	159	157	177	184	182	3	14	10	3	2	1.8%	8.9%	5.5%	1.5%	1.0%
Initial Bulk Density [kg/m^3]	1812	2088	2010	2041	2086	115	51	126	59	5	6.4%	2.5%	6.3%	2.9%	0.3%
Consol. Bulk Density [kg/m^3]	2137	2487	2428	2496	2638	131	78	166	108	9	6.1%	3.1%	6.8%	4.3%	0.3%

Table E.8: Unconfined Compression Data for Wet KPRS Fines - 3% MC

	Mean					Standard Deviation					Coefficient of Variation				
	20	**40**	**60**	**80**	**100**	**20**	**40**	**60**	**80**	**100**	**20**	**40**	**60**	**80**	**100**
Consolidation Stress [kPa]	18.04	37.78	57.93	77.75	97.64	0.12	0.16	0.06	0.23	0.23	0.7%	0.4%	0.1%	0.3%	0.2%
Max force [gf]	485	871	1089	1465	1703	18	79	72	159	158	3.8%	9.1%	6.6%	10.8%	9.3%
Unconfined Strength [kPa]	5.31	9.16	12.26	16.24	18.60	0.08	0.83	0.41	1.10	1.64	1.5%	9.1%	3.3%	6.8%	8.8%
Peak Strain	0.03	0.04	0.03	0.03	0.04	0.00	0.01	0.00	0.01	0.00	8.3%	14.6%	10.8%	25.9%	11.1%
Initial Height [mm]	69.8	69.1	72.4	74.2	73.7	2.2	2.5	2.6	3.9	1.0	3.2%	3.6%	3.6%	5.2%	1.4%
Confined Consolidated Height [mm]	53.6	51.2	56.1	55.6	54.7	1.5	1.6	2.7	2.8	1.0	2.8%	3.2%	4.9%	5.0%	1.9%
Consolidated Height [mm]	56.2	53.9	57.8	57.0	56.0	1.4	1.4	2.8	2.4	0.7	2.5%	2.5%	4.8%	4.3%	1.3%
Failed Height [mm]	54.4	51.8	56.0	55.4	53.8	1.5	1.6	2.7	2.8	0.8	2.7%	3.1%	4.8%	5.0%	1.4%
Initial Aspect Ratio	1.74	1.73	1.81	1.86	1.84	0.06	0.06	0.06	0.10	0.03	3.2%	3.6%	3.6%	5.2%	1.4%
Consolidated Aspect Ratio	1.40	1.35	1.45	1.42	1.40	0.03	0.03	0.07	0.06	0.02	2.5%	2.5%	4.8%	4.3%	1.3%
Sample compression [mm]	6.7	6.9	6.8	6.7	7.2	0.1	0.3	0.3	0.2	0.1	1.5%	3.9%	3.9%	3.1%	1.7%
Sample Rebound [mm]	2.6	2.6	1.7	1.3	1.3	0.1	0.3	0.2	0.4	0.7	5.4%	13.0%	13.4%	26.6%	55.2%
Mass of Sample [g]	152	154	180	181	179	5	5	9	9	2	3.3%	3.2%	5.2%	5.2%	1.2%
Initial Bulk Density [kg/m^3]	1757	1959	1908	1963	2002	74	140	98	147	110	4.2%	7.2%	5.2%	7.5%	5.5%
Consol. Bulk Density [kg/m^3]	2180	2511	2393	2554	2634	33	144	158	154	150	1.5%	5.7%	6.6%	6.0%	5.7%

Table E.9: Unconfined Compression Data for Wet KPRS Fines - 4% MC

	Mean					Standard Deviation					Coefficient of Variation				
	20	**40**	**60**	**80**	**100**	**20**	**40**	**60**	**80**	**100**	**20**	**40**	**60**	**80**	**100**
Consolidation Stress [kPa]	17.23	37.69	56.28	76.93	97.68	0.51	0.26	1.19	0.90	0.46	3.0%	0.7%	2.1%	1.2%	0.5%
Max force [gf]	525	957	1270	1569	1806	34	21	80	53	136	6.5%	2.2%	6.3%	3.4%	7.5%
Unconfined Strength [kPa]	5.58	9.54	13.32	16.40	18.29	0.33	0.20	0.88	0.65	1.18	5.9%	2.1%	6.6%	4.0%	6.5%
Peak Strain	0.04	0.05	0.05	0.05	0.05	0.00	0.01	0.00	0.00	0.01	11.7%	10.9%	7.0%	6.2%	21.7%
Initial Height [mm]	72.2	69.3	77.5	74.4	74.4	3.2	0.6	3.4	10.6	7.3	4.4%	0.9%	4.4%	14.3%	9.8%
Confined Consolidated Height [mm]	51.7	48.1	51.5	51.3	49.8	1.1	1.2	0.7	1.0	0.8	2.1%	2.5%	1.3%	1.9%	1.6%
Consolidated Height [mm]	54.5	51.1	53.7	53.6	51.9	0.9	0.9	1.0	1.0	1.0	1.7%	1.8%	1.8%	2.0%	1.9%
Failed Height [mm]	52.3	48.6	51.1	50.9	49.2	1.1	1.1	1.1	0.9	0.8	2.1%	2.2%	2.1%	1.9%	1.6%
Initial Aspect Ratio	1.81	1.73	1.94	1.86	1.86	0.08	0.02	0.08	0.27	0.18	4.4%	0.9%	4.4%	14.3%	9.8%
Consolidated Aspect Ratio	1.36	1.28	1.34	1.34	1.30	0.02	0.02	0.02	0.03	0.02	1.7%	1.8%	1.8%	2.0%	1.9%
Sample compression [mm]	7.0	7.2	7.6	7.7	7.7	0.3	0.2	0.2	0.2	0.6	3.9%	2.4%	2.1%	2.2%	8.2%
Sample Rebound [mm]	2.8	3.0	2.3	2.3	2.1	0.3	0.6	0.7	0.2	0.6	9.9%	19.2%	31.8%	9.0%	29.2%
Mass of Sample [g]	138	138	153	157	154	3	4	5	3	3	2.1%	2.7%	3.1%	2.1%	1.7%
Initial Bulk Density [kg/m^3]	1572	1865	1654	1897	1921	94	42	54	300	233	5.9%	2.2%	3.3%	15.8%	12.1%
Consol. Bulk Density [kg/m^3]	2083	2530	2383	2591	2732	132	25	50	42	140	6.3%	1.0%	2.1%	1.6%	5.1%

Table E.10: Unconfined Compression Data for Wet KPRS Fines - 6% MC

	Mean					Standard Deviation					Coefficient of Variation				
	20	**40**	**60**	**80**	**100**	**20**	**40**	**60**	**80**	**100**	**20**	**40**	**60**	**80**	**100**
Consolidation Stress [kPa]	17.77	37.66	57.56	77.67	97.52	0.20	0.18	0.20	0.17	0.31	1.1%	0.5%	0.3%	0.2%	0.3%
Max force [gf]	560	956	1366	1701	2007	16	31	11	64	74	2.9%	3.2%	0.8%	3.8%	3.7%
Unconfined Strength [kPa]	6.15	9.78	14.63	18.23	20.26	0.30	0.25	0.36	0.83	1.00	4.8%	2.5%	2.5%	4.5%	4.9%
Peak Strain	0.04	0.05	0.05	0.05	0.05	0.01	0.01	0.00	0.01	0.00	14.2%	12.4%	3.1%	17.9%	6.5%
Initial Height [mm]	66.1	73.2	76.1	81.0	71.3	7.2	1.0	2.5	2.2	13.8	10.8%	1.3%	3.3%	2.7%	19.4%
Confined Consolidated Height [mm]	53.4	49.2	51.9	52.4	49.7	2.1	2.3	1.0	1.3	1.6	3.8%	4.7%	1.9%	2.4%	3.2%
Consolidated Height [mm]	56.3	52.4	54.9	54.9	51.7	2.1	2.2	1.1	0.9	1.5	3.7%	4.1%	2.1%	1.6%	2.9%
Failed Height [mm]	54.0	49.7	51.9	51.9	48.9	2.0	2.3	1.0	1.3	1.6	3.7%	4.7%	2.0%	2.4%	3.2%
Initial Aspect Ratio	1.65	1.83	1.90	2.03	1.78	0.18	0.02	0.06	0.05	0.35	10.8%	1.3%	3.3%	2.7%	19.4%
Consolidated Aspect Ratio	1.41	1.31	1.37	1.37	1.29	0.05	0.05	0.03	0.02	0.04	3.7%	4.1%	2.1%	1.6%	2.9%
Sample compression [mm]	7.1	7.5	8.0	7.9	7.6	0.4	0.2	0.1	0.5	0.2	5.1%	3.3%	1.4%	6.3%	3.2%
Sample Rebound [mm]	2.9	3.2	3.0	2.5	2.0	0.3	0.5	0.2	0.4	0.3	10.0%	13.9%	5.3%	17.6%	17.1%
Mass of Sample [g]	147	145	161	164	157	7	13	5	5	6	4.6%	9.0%	2.9%	2.8%	3.6%
Initial Bulk Density [kg/m^3]	1739	1772	1671	1714	2059	295	34	57	57	498	17.0%	1.9%	3.4%	3.3%	24.2%
Consol. Bulk Density [kg/m^3]	2019	2477	2316	2529	2747	171	132	44	49	232	8.5%	5.3%	1.9%	2.0%	8.5%

Appendix F

Jenike Shear Test Data

F.1 KPBO Fines

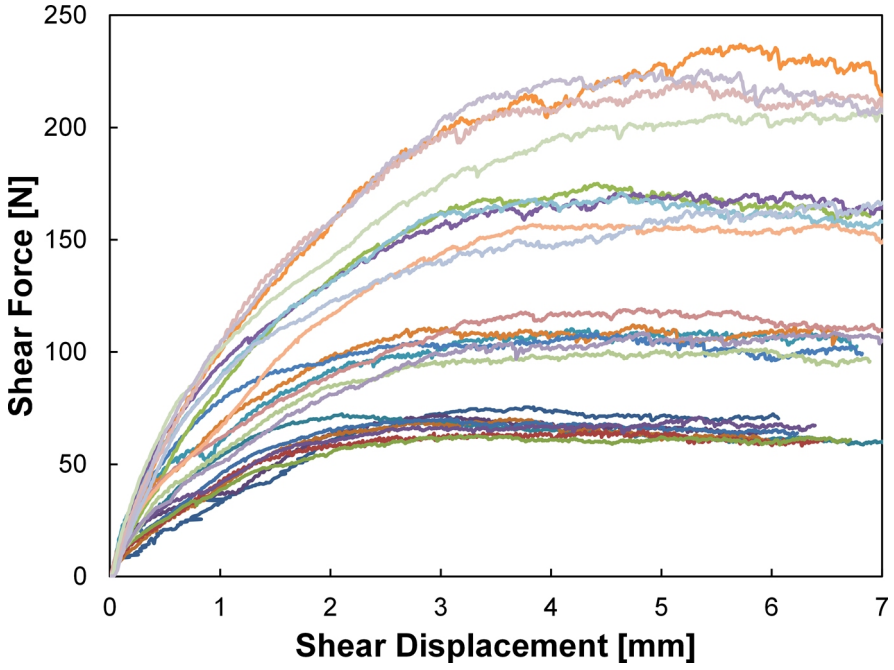

Figure F.1: KPBO Fines - Shearing response for dry fines

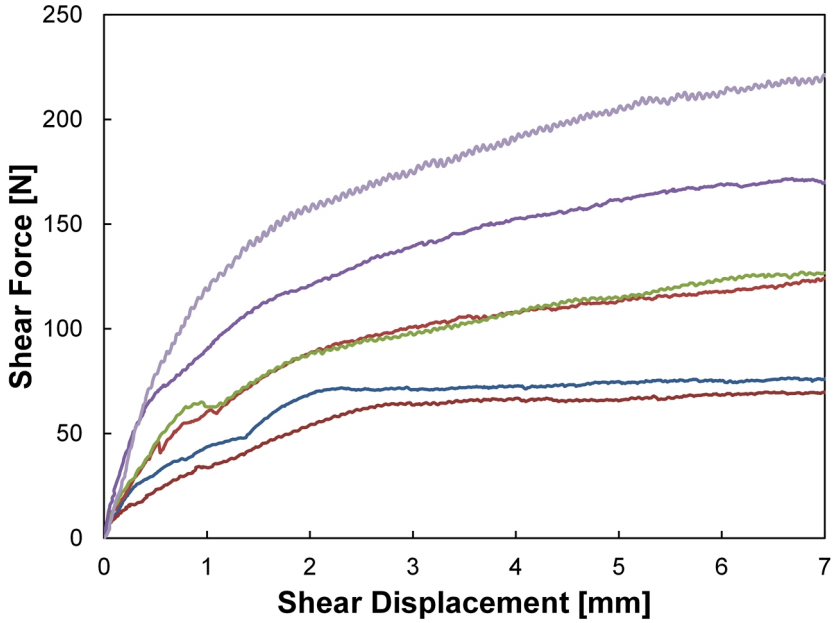

Figure F.2: KPBO Fines - Shearing response for wet fines

F.2 KPRS Fines

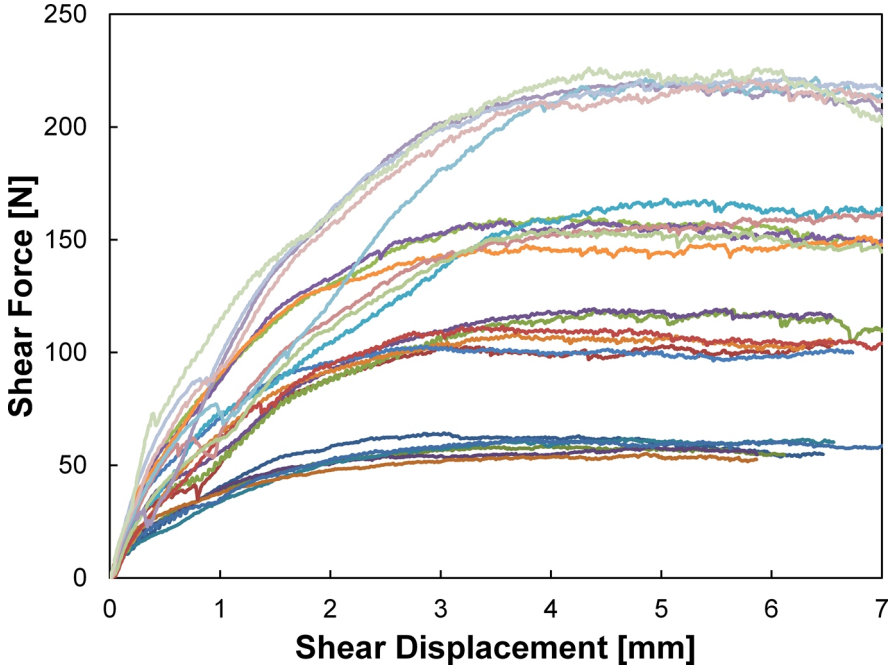

Figure F.3: KPRS Fines - Shearing response for dry fines

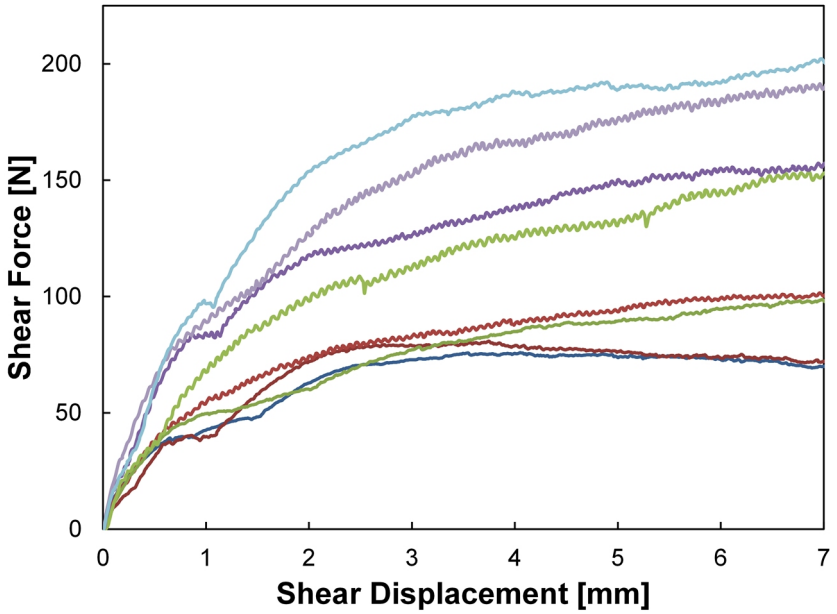

Figure F.4: KPRS Fines - Shearing response for wet fines

List of References

Abbaspour-Fard, M.H. (2004). Theoretical Validation of a Multi-sphere, Discrete Element Model Suitable for Biomaterials Handling Simulation. *Biosystems Engineering*, **88**(2): pp. 153–161, doi:10.1016/j.biosystemseng.2004.03.010. (p. 28)

Adams, M.J., Johnson, S.A., Seville, J.P.K., and Willett, C.D. (2002). Mapping the Influence of Gravity on Pendular Liquid Bridges between Rigid Spheres. *Langmuir*, **18**(16): pp. 6180–6184, doi:10.1021/la011823k. (p. 19)

Ai, J., Chen, J.F., Rotter, J.M., and Ooi, J.Y. (2011). Assessment of rolling resistance models in discrete element simulations. *Powder Technology*, **206**(3): pp. 269–282, doi:10.1016/j.powtec.2010.09.030. (p. 35, 43, 72, 163)

Anand, A., Curtis, J.S., Wassgren, C.R., Hancock, B.C., and Ketterhagen, W.R. (2008). Predicting discharge dynamics from a rectangular hopper using the discrete element method (DEM). *Chemical Engineering Science*, **63**(24): pp. 5821–5830, doi:10.1016/j.ces.2008.08.015. (p. 29, 30, 32, 33, 218)

Anand, A., Curtis, J.S., Wassgren, C.R., Hancock, B.C., and Ketterhagen, W.R. (2009). Predicting discharge dynamics of wet cohesive particles from a rectangular hopper using the discrete element method (DEM). *Chemical Engineering Science*, **64**(24): pp. 5268–5275, doi:10.1016/j.ces.2009.09.001. (p. 30, 33, 34, 225)

Anand, A., Curtis, J.S., Wassgren, C.R., Hancock, B.C., and Ketterhagen, W.R. (2010). Segregation of cohesive granular materials during discharge from a rectangular hopper. *Granular Matter*, **12**(2): pp. 193–200, doi:10.1007/s10035-010-0168-9. (p. 20, 34)

Antony, S.J., Moreno-Atanasio, R., Musadaidzwa, J., and Williams, R.A. (2008). Impact Fracture of Composite and Homogeneous Nanoagglomerates. *Journal of Nanomaterials*, **2008**: pp. 1–7, doi:10.1155/2008/125386. (p. 50)

Ashmawy, A.K., Sukumaran, B., and Hoang, V.V. (2003). Evaluating the influence of particle shape on liquefaction behavior using discrete element modeling. *Proceedings of The Thirteenth International Offshore and Polar Engineering Conference*: pp. 542–549. (p. 28)

ASTM International (2006). ASTM D6128 - 06: Standard Test Method for Shear Testing of Bulk Solids Using the Jenike Shear Cell. doi:10.1520/D6128-06. (p. 90, 92)

Babic, M. (1997). Average balance equations for granular materials. *International Journal of Engineering Science*, **35**(5): pp. 523–548, doi:10.1016/S0020-7225(96)00094-8. (p. 209, 213, 219)

Bagi, K. (1996). Stress and strain in granular assemblies. *Mechanics of Materials*, **22**: pp. 165–177. (p. 204)

Balevičius, R., Kačianauskas, R., Mróz, Z., and Sielamowicz, I. (2008). Discrete-particle investigation of friction effect in filling and unsteady/steady discharge in three-dimensional wedge-shaped hopper. *Powder Technology*, **187**(2): pp. 159–174, doi:10.1016/j.powtec.2008.02.006. (p. 32)

Balevičius, R., Kačianauskas, R., Mróz, Z., and Sielamowicz, I. (2011*a*). Analysis and DEM simulation of granular material flow patterns in hopper models of different shapes. *Advanced Powder Technology*, **22**(2): pp. 226–235, doi:10.1016/j.apt.2010.12.005. (p. 32)

Balevičius, R., Sielamowicz, I., Mróz, Z., and Kačianauskas, R. (2011*b*). Investigation of wall stress and outflow rate in a flat-bottomed bin: A comparison of the DEM model results with the experimental measurements. *Powder Technology*, **214**(3): pp. 322–336, doi:10.1016/j.powtec.2011.08.042. (p. 32)

Balevičius, R., Sielamowicz, I., Mróz, Z., and Kačianauskas, R. (2012). Effect of rolling friction on wall pressure, discharge velocity and outflow of granular material from a flat-bottomed bin. *Particuology*, **10**: pp. 672–682, doi:10.1016/j.partic.2012.07.002. (p. 33)

Baran, O., DeGennaro, A., RameÌĄ, E., Wilkinson, A., Nakagawa, M., and Luding, S. (2009). DEM Simulation of a Schulze Ring Shear Tester. In: *AIP Conference Proceedings*, AIP, pp. 409–412, doi:10.1063/1.3179948. (p. 50)

Bardet, J.P. (1994). Observations on the effects of particle rotations on the failure of idealized granular materials. *Mechanics of Materials*, **18**: pp. 159–182. (p. 43)

Baxter, J., Abou-Chakra, H., TüZün, U., and Mills Lamptey, B. (2000). A DEM Simulation and Experimental Strategy for Solving Fine Powder Flow Problems. *Chemical Engineering Research and Design*, **78**(7): pp. 1019–1025, doi:10.1205/026387600528139. (p. 30)

Bell, T.A., Catalano, E.J., Zhong, Z., Ooi, J.Y., and Rotter, J.M. (2007). Evaluation of the Edinburgh Powder Tester. In: *PARTEC 2007 - Congress on Particle Technology*, University of Edinburgh, Nürnberg, pp. 1–6. (p. 91)

Berman, A., Drummond, C., and Israelachvili, J.N. (1998). Amontons' law at the molecular level. *Tribology letters*, **4**: pp. 95–101. (p. 78)

Beverloo, W.A., Leniger, H.A., and Van de Velde, J. (1961). The flow of granular solids through orifices. *Chemical Engineering Science*, **15**: pp. 260–269. (p. 24, 224)

Bishop, A.W. and Green, G.E. (1965). The Influence of End Restraint on the Compression Strength of a Cohesionless Soil. *Geotechnique*, **15**(3): pp. 243–266, doi:10.1680/geot.1965.15.3.243. (p. 111)

Bradley, M.A. (1932). The cohesive force between solid surfaces and the surface energy of solids. *Philosophical Magazine Series 7*, **13**(86): pp. 853–862, doi:10.1080/14786449209461990. (p. 51)

Bradley, M.S.A., Pittman, A.N., Bingley, M., Farnish, R.J., and Pickering, J. (2000). Effects of wall material hardness on choice of wall materials for design of hoppers and silos for the discharge of hard bulk solids. *Tribology International*, **33**(12): pp. 845–853, doi:10.1016/S0301-679X(00)00130-4. (p. 23)

Briscoe, B.J. and Kremnitzer, S.L. (1979). A study of the friction and adhesion of polyethyleneterephthalate monofilaments. *Journal of Physics D: Applied Physics*, **12**(4): pp. 505–516, doi:10.1088/0022-3727/12/4/008. (p. 78)

British Standards Institution (2006). BS EN 1991-4:2006: Eurocode 1 - Actions on structures - Part 4: Silos and tanks. (p. 23, 29, 94, 99, 138, 187, 202)

Brown, C.J. and Nielsen, J. (2004). *Silos: Fundamentals of Theory, Behaviour and Design*. Taylor & Francis, illustrated edition, ISBN 0203223519, 856 pp. (p. 21, 23)

Brown, N. (2013). *Discrete Element Modelling of a Cementitious Material*. Ph.d. thesis, University of Edinburgh. (p. 49)

Brown, R.L. and Richards, J.C. (1960). Profile of flow of granules through apertures. *Transactions of the Institution of Chemical Engineers*, **38**: pp. 243–250. (p. 24, 25)

Brown, R.L. and Richards, J.C. (1965). Kinematics of the flow of dry powders and bulk solids. *Rheologica Acta*. (p. 25)

Buick, J.M., Chavez-Sagarnaga, J., Zhong, Z., Ooi, J.Y., Campbell, D.M., and Greated, C.A. (2005). Investigation of Silo Honking: Slip-Stick Excitation and Wall Vibration. *Journal of Engineering Mechanics*, **131**(3): pp. 299–307, doi:10.1061/(ASCE)0733-9399(2005)131:3(299). (p. 24)

Burnham, N.A. and Kulik, A.J. (1999). Surface forces and adhesion. In: *Handbook of Micro/-Nano Tribology*, (ed.) B. Bhushan, CRC Press, 2nd edition, pp. 1–31. (p. 17)

Butt, H.J. (2008). Capillary forces: influence of roughness and heterogeneity. *Langmuir : the ACS journal of surfaces and colloids*, **24**(9): pp. 4715–21, doi:10.1021/la703640f. (p. 18)

Butt, H.J., Graf, K., and Kappl, M. (2003). *Physics and Chemistry of Interfaces*. Wiley-VCH Verlag GmbH & Co. KGaA, Weinheim, FRG, ISBN 3527404139, doi:10.1002/3527602313. (p. 17)

Butt, H.J. and Kappl, M. (2009). Normal capillary forces. *Advances in colloid and interface science*, **146**(1-2): pp. 48–60, doi:10.1016/j.cis.2008.10.002. (p. 19, 20)

Carrillo, J.M.Y., Raphael, E., and Dobrynin, A.V. (2010). Adhesion of nanoparticles. *Langmuir : the ACS journal of surfaces and colloids*, **26**(15): pp. 12973–9, doi:10.1021/la101977c. (p. 50)

Castellanos, A. (2005). The relationship between attractive interparticle forces and bulk behaviour in dry and uncharged fine powders. *Advances in Physics*, **54**(4): pp. 263–376, doi:10.1080/17461390500402657. (p. 13, 18)

Chen, J.F., Ooi, J.Y., and Rotter, J.M. (1996). A rigorous statistical technique for inferring circular silo wall pressures from wall strain measurements. *Engineering Structures*, **0141**(4): pp. 321–331. (p. 24)

Chen, J.F., Rotter, J.M., and Ooi, J.Y. (1998). Statistical inference of unsymmetrical silo pressures from comprehensive wall strain measurements. *Thin-Walled Structures*, **31**(1-3): pp. 117–136, doi:10.1016/S0263-8231(98)00013-5. (p. 24)

Chen, J.F., Rotter, J.M., Ooi, J.Y., and Zhong, Z. (2007). Correlation between the flow pattern and wall pressures in a full scale experimental silo. *Engineering Structures*, **29**(9): pp. 2308–2320, doi:10.1016/j.engstruct.2006.11.011. (p. 24, 233)

Chou, S.H., Liao, C.C., and Hsiau, S.S. (2010). An experimental study on the effect of liquid content and viscosity on particle segregation in a rotating drum. *Powder Technology*, **201**(3): pp. 266–272, doi:10.1016/j.powtec.2010.04.009. (p. 20)

Chung, Y.C. (2006). *Discrete element modelling and experimental validation of a granular solid subject to different loading conditions*. Ph.d. thesis, The University of Edinburgh. (p. 28, 34, 35, 40, 94, 95, 96, 149)

Chung, Y.C. and Ooi, J.Y. (2006). Confined compression and rod penetration of a dense granular medium : discrete element modelling and validation. *Modern Trends in Geomechanics*: pp. 223–239, doi:10.1007/978-3-540-35724-7_14. (p. 203)

Chung, Y.C. and Ooi, J.Y. (2007). Influence of Discrete Element Model Parameters on Bulk Behavior of a Granular Solid under Confined Compression. *Particulate Science and Technology*, **26**(1): pp. 83–96, doi:10.1080/02726350701759381. (p. 94, 95, 152, 203)

Chung, Y.C. and Ooi, J.Y. (2011). Benchmark tests for verifying discrete element modelling codes at particle impact level. *Granular Matter*, **13**(5): pp. 643–656, doi:10.1007/s10035-011-0277-0. (p. 35)

Clark, W.C. and Mason, G. (1967). Tensile strength of wet granular materials. **91**: pp. 83–93. (p. 19)

Cleary, P.W. (2000). DEM simulation of industrial particle flows: case studies of dragline excavators, mixing in tumblers and centrifugal mills. *Powder Technology*, **109**: pp. 83–104. (p. 42, 143)

Cleary, P.W. and Sawley, M.L. (2002). DEM modelling of industrial granular flows: 3D case studies and the effect of particle shape on hopper discharge. *Applied Mathematical Modelling*, **26**: pp. 89–111. (p. 27, 29)

Coetzee, C.J. and Els, D.N.J. (2009). Calibration of granular material parameters for DEM modelling and numerical verification by blade-granular material interaction. *Journal of Terramechanics*, **46**(1): pp. 15–26, doi:10.1016/j.jterra.2008.12.004. (p. 33)

Cooper, K., Ohler, N., Gupta, A., and Beaudoin, S. (2000). Analysis of Contact Interactions between a Rough Deformable Colloid and a Smooth Substrate. *Journal of Colloid and Interface Science*, **222**(1): pp. 63–74, doi:10.1006/jcis.1999.6561. (p. 18)

Coulomb, C.A. (1776). Essai sur une application des regles des maximis et minimis a quelques problemes de statique relatifs a l'architecture. *Memoires de l'Academie Royale pres Divers Savants*, **7**. (p. 101)

Craig, R.F. (2004). *Craig's soil mechanics*. Spon Press, 7th edition, ISBN 0203494105. (p. 100, 101, 104)

Cundall, P.A. and Strack, O.D.L. (1979). A discrete numerical model for granular assemblies. *Géotechnique*, **29**(1): pp. 47–65. (p. 26, 37, 41, 47, 81)

Das, B.M. (2010). *Principles of Geotechnical Engineering*. Cengage Learning, 7th edition, ISBN 9780495411307, 683 pp. (p. 101)

DEM Solutions Ltd. (2010*a*). *EDEM 2.3 Programming Guide*. Edinburgh, UK, rev. 3c edition. (p. 39, 66)

DEM Solutions Ltd. (2010*b*). *EDEM 2.3 User Guide*. Edinburgh, UK, rev. 2c edition. (p. 41, 42, 43, 46, 52, 72, 78, 80, 81, 152)

DEM Solutions Ltd. (2011*a*). *EDEM 2.4 Hertz-Mindlin with JKR cohesion model*. DEM Solutions Ltd., Edinburgh, UK, 6 pp. (p. 51)

DEM Solutions Ltd. (2011*b*). *EDEM 2.4 Programming Guide*. Edinburgh, UK, rev. 1 edition. (p. 39, 66)

DEM Solutions Ltd. (2011*c*). *EDEM 2.4 Theory Reference Guide*. Edinburgh, UK. (p. 46, 49, 51, 52)

DEM Solutions Ltd. (2011*d*). *EDEM 2.4 User Guide*. Edinburgh, UK. (p. 41, 46, 49, 51, 52, 78, 80, 81)

DEM Solutions Ltd. (2012). *EDEM 2.4.3 User Guide*. Edinburgh, UK. (p. 42, 152)

Derjaguin, B.V., Muller, V.M., and Toporov, Y.P. (1975). Effect of contact deformations on the adhesion of particles. *Journal of Colloid and Interface Science*, **53**(2): pp. 314–326, doi:10.1016/0021-9797(75)90018-1. (p. 1, 18)

Ding, S. (2005). *Investigation of flow and pressure in silos during filling and discharging in presence of inserts*. Ph.d thesis, University of Edinburgh. (p. 24)

Donev, A., Cisse, I., Sachs, D., and Variano, E.A. (2004). Improving the density of jammed disordered packings using ellipsoids. *Science*. (p. 28)

Donev, A., Torquato, S., and Stillinger, F.H. (2005). Neighbor list collision-driven molecular dynamics simulation for nonspherical hard particles. *Journal of Computational Physics*, **202**(2): pp. 765–793, doi:10.1016/j.jcp.2004.08.025. (p. 28)

Dong, K., Yang, R.Y., Zou, R.P., and Yu, A.B. (2006). Role of Interparticle Forces in the Formation of Random Loose Packing. *Physical Review Letters*, **96**(14): pp. 1–4, doi:10.1103/PhysRevLett.96.145505. (p. 29, 157)

Dullien, F.A.L. (1991). *Porous media: fluid transport and pore structure*. 2nd edition, 574 pp., doi:10.1016/B978-0-12-223651-8.50001-8. (p. 153)

Durán, O., Kruyt, N.P., and Luding, S. (2010). Micro-mechanical analysis of deformation characteristics of three-dimensional granular materials. *International Journal of Solids and Structures*: pp. 1–35. (p. 204)

Ecke, S. and Butt, H.J. (2001). Friction between individual microcontacts. *Journal of Colloid and Interface Science*, **244**(2): pp. 432–435, doi:10.1006/jcis.2001.7959. (p. 78)

Enstad, G.G. and Ose, S. (2003). Uniaxial Testing and the Performance of a Pallet Press. *Chemical Engineering & Technology*, **26**(2): pp. 171–176, doi:10.1002/ceat.200390025. (p. 91)

European Federation of Chemical Engineers (1989). *Standard shear testing technique for particulate solids using the Jenike shear cell: a report of the EFCE Working Party on the Mechanics of Particulate Solids*. IChemE, 1–46 pp. (p. 92, 93)

Favier, J.F., Abbaspour-Fard, M.H., and Kremmer, M. (2001). Modeling nonspherical particles using multisphere discrete elements. *Journal of Engineering Mechanics*, **127**(October): pp. 971–977, doi:10.1061/(ASCE)0733-9399(2001)127:10(971). (p. 28)

Favier, J.F., Abbaspour-Fard, M.H., Kremmer, M., and Raji, A.O. (1999). Shape representation of axi-symmetrical, non-spherical particles in discrete element simulation using multi-element model particles. *Engineering Computations*, **16**(4): pp. 467–480, doi:10.1108/02644409910271894. (p. 28)

Feng, C.L. and Yu, A.B. (1998). Effect of liquid addition on the packing of mono-sized coarse spheres. *Powder technology*, **99**: pp. 22–28. (p. 29)

Ferellec, J.F. and McDowell, G.R. (2008). A simple method to create complex particle shapes for DEM. *Geomechanics and Geoengineering*, **3**(3): pp. 211–216, doi:10.1080/17486020802253992. (p. 28)

Ferellec, J.F. and McDowell, G.R. (2010). A method to model realistic particle shape and inertia in DEM. *Granular Matter*, **12**(5): pp. 459–467, doi:10.1007/s10035-010-0205-8. (p. 28)

Fischer-Cripps, A.C. (2007). *Introduction to contact mechanics*. Springer US, 2nd edition, ISBN 9780387681870, 1–221 pp. (p. 46)

Fisher, R.A. (1926). On the capillary forces in an ideal soil; correction of formulae given by W. B. Haines. *The Journal of Agricultural Science*, **16**(03): pp. 492–505, doi:10.1017/S0021859600007838. (p. 19, 56)

Fournier, Z., Geromichalos, D., Herminghaus, S., Kohonen, M.M., Mugele, F., Scheel, M., Schulz, M., Schulz, B., Schier, C.H., Seemann, R., and Skudelny, A. (2005). Mechanical properties of wet granular materials. *Journal of Physics: Condensed Matter*, **17**(9): pp. S477–S502, doi:10.1088/0953-8984/17/9/013. (p. 20)

Franklin, F.C. and Johanson, L.N. (1955). Flow of granular material through a circular orifice. *Chemical Engineering Science*, **4**: pp. 119–129. (p. 24)

Freeman, R.E. and Fu, X. (2011). The Development of a Compact Uniaxial Tester. In: *Particulate Systems Analysis 2011*, 2003, Edinburgh, UK, pp. 1–6. (p. 91)

Fu, P. and Harvey, J.T. (2008). A new polygon type discrete element model. *Granular Matter, submitted*: pp. 1–16. (p. 28)

GDR Midi (2004). On dense granular flows. *The European physical journal. E, Soft matter*, **14**(4): pp. 341–65, doi:10.1140/epje/i2003-10153-0. (p. 145)

Geng, J., Longhi, E., Behringer, R.P., and Howell, D. (2001). Memory in two-dimensional heap experiments. *Physical Review E*, **64**(6): p. 060301, doi:10.1103/PhysRevE.64.060301. (p. 11)

Goda, T.J. and Ebert, F. (2005). Three-dimensional discrete element simulations in hoppers and silos. *Powder Technology*, **158**(1-3): pp. 58–68, doi:10.1016/j.powtec.2005.04.019. (p. 31)

Goldenberg, C. and Goldhirsch, I. (2002). Force Chains, Microelasticity, and Macroelasticity. *Physical Review Letters*, **89**(8): pp. 1–4, doi:10.1103/PhysRevLett.89.084302. (p. 209, 213, 219)

Goldenberg, C. and Goldhirsch, I. (2004). Small and large scale granular statics. *Granular Matter*, **6**(2-3): pp. 87–96, doi:10.1007/s10035-004-0165-y. (p. 58)

Goldhirsch, I. (2010). Stress, stress asymmetry and couple stress: from discrete particles to continuous fields. *Granular Matter*, **12**(3): pp. 239–252, doi:10.1007/s10035-010-0181-z. (p. 58, 209, 213, 219)

Goldhirsch, I. and Goldenberg, C. (2002). On the microscopic foundations of elasticity. *The European Physical Journal. E, Soft matter*, **9**(3): pp. 245–51, doi:10.1140/epje/i2002-10073-5. (p. 58)

González-Montellano, C., Fuentes, J.M., Ayuga-Téllez, E., and Ayuga, F. (2012*a*). Determination of the mechanical properties of maize grains and olives required for use in DEM simulations. *Journal of Food Engineering*, **111**(4): pp. 553–562, doi:10.1016/j.jfoodeng.2012.03.017. (p. 33)

González-Montellano, C., Ramírez-Gómez, A., Fuentes, J.M., and Ayuga, F. (2012*b*). Numerical effects derived from en masse filling of agricultural silos in DEM simulations. *Computers and Electronics in Agriculture*, **81**: pp. 113–123, doi:10.1016/j.compag.2011.11.013. (p. 28, 33)

González-Montellano, C., Ramírez-Gómez, A., Gallego, E., and Ayuga, F. (2011). Validation and experimental calibration of 3D discrete element models for the simulation of the discharge flow in silos. *Chemical Engineering Science*, **66**(21): pp. 5116–5126, doi:10.1016/j.ces.2011.07.009. (p. 28, 33)

Greenwood, J.A. and Williamson, J.B.P. (1966). Contact of nominally flat surfaces. *Proceedings of the Royal Society A: Mathematical, Physical and Engineering Sciences*, **295**(1442): pp. 300–319. (p. 50)

Grima, A.P. and Wypych, P.W. (2009). On Improving the Calibration and Validation of Computer Simulations for Bulk Materials Handling Systems. *Australian Bulk Handling Review*, (October): pp. 84–91. (p. 31)

Grima, A.P. and Wypych, P.W. (2010). Development and validation of calibration methods for discrete element modelling. *Granular Matter*, **13**(2): pp. 127–132, doi:10.1007/s10035-010-0197-4. (p. 31)

Gröger, T., Tüzün, U., and Heyes, D.M. (2003). Modelling and measuring of cohesion in wet granular materials. *Powder Technology*, **133**(1-3): pp. 203–215, doi:10.1016/S0032-5910(03)00093-7. (p. 1, 29, 30, 157)

Haines, W.B. (1925). Studies in the physical properties of soils: II. A note on the cohesion developed by capillary forces in an ideal soil. *The Journal of Agricultural Science*, **15**(04): pp. 529–535. (p. 19)

Hamaker, H.C. (1937). The London-van der Waals attraction between spherical particles. *Physica IV*, **10**(1): pp. 1058–1072. (p. 18)

Härtl, J. (2008). *A study of granular solids in silos with and without an insert*. Ph.d. thesis, The University of Edinburgh. (p. 24, 28, 218, 235)

Härtl, J. and Ooi, J.Y. (2011). Numerical investigation of particle shape and particle friction on limiting bulk friction in direct shear tests and comparison with experiments. *Powder Technology*, **212**(1): pp. 231–239, doi:10.1016/j.powtec.2011.05.022. (p. 27, 35, 164, 166, 186)

Härtl, J., Ooi, J.Y., Rotter, J.M., Wójcik, M., Ding, S., and Enstad, G.G. (2008). The influence of a cone-in-cone insert on flow pattern and wall pressure in a full-scale silo. *Chemical Engineering Research and Design*, **86**(4): pp. 370–378, doi:10.1016/j.cherd.2007.07.001. (p. 24)

Hassanpour, A., Antony, S.J., and Ghadiri, M. (2008). Influence of interface energy of primary particles on the deformation and breakage behaviour of agglomerates sheared in a powder bed. *Chemical Engineering Science*, **63**(23): pp. 5593–5599, doi:10.1016/j.ces.2008.08.008. (p. 50)

Hassanpour, A. and Ghadiri, M. (2004). Distinct element analysis and experimental evaluation of the Heckel analysis of bulk powder compression. *Powder Technology*, **141**(3): pp. 251–261, doi:10.1016/j.powtec.2004.02.010. (p. 30)

Hassanpour, A. and Ghadiri, M. (2007). Characterisation of Flowability of Loosely Compacted Cohesive Powders by Indentation. *Particle & Particle Systems Characterization*, **24**(2): pp. 117–123, doi:10.1002/ppsc.200601111. (p. 30)

Heim, L.O., Farshchi, M., and Morgeneyer, M. (2005). Adhesion of carbonyl iron powder particles studied by atomic force microscopy by atomic force microscopy. *Journal of Adhesion Science and Technology*, (February 2013): pp. 37–41. (p. 65)

Herminghaus, S. (2005). Dynamics of wet granular matter. *Advances in Physics*, **54**(3): pp. 221–261, doi:10.1080/00018730500167855. (p. 18, 20)

Hertz, H. (1882). Uber die beruhrung fester elastischer korper (On the contact of elastic solids). *Journal für die reine und angewandte Mathematik*, **91**: pp. 156–171. (p. 47)

Hodges, C.S., Looi, L., Cleaver, J.A.S., and Ghadiri, M. (2004). Use of the JKR model for calculating adhesion between rough surfaces. *Langmuir : the ACS journal of surfaces and colloids*, **20**(22): pp. 9571–6, doi:10.1021/la035790f. (p. 50)

Holst, J.M.F.G., Rotter, J.M., Ooi, J.Y., and Rong, G.H. (1999). Numerical modeling of silo filling. II: discrete element analyses. *Journal of Engineering Mechanics*, (January), doi:10.1061/(ASCE)0733-9399(1999)125:1(104. (p. 34, 235, 236)

Hotta, K., Takeda, K., and Iinoya, K. (1974). The capillary binding force of a liquid bridge. *Powder Technology*, **10**: pp. 231–242. (p. 19, 20)

Hsiau, S.S. and Yang, S.C. (2003). Numerical simulation of self-diffusion and mixing in a vibrated granular bed with the cohesive effect of liquid bridges. *Chemical engineering science*, **58**(2003): pp. 339–351. (p. 33)

Hui, C.Y., Lin, Y.Y., Baney, J.M., and Kramer, E.J. (2001). The mechanics of contact and adhesion of periodically rough surfaces. *Journal of Polymer Science: Part B: Polymer Physics*, **39**: pp. 1195–1214, doi:10.1002/polb.1094/full. (p. 50)

Huntington, A.P. and Rooney, N.M. (1971). Chemical engineering tripos. Part 2. Research Project Report. Technical report, University of Cambridge. (p. 25)

Israelachvili, J.N. (2011). *Intermolecular and Surface Forces*. 3rd edition, ISBN 9780123919274, 704 pp. (p. 17, 18)

Itasca (2003). *PFC3D User Manual*. Itasca Consulting Group Inc., Minneapolis, USA. (p. 40, 43, 46, 47, 49, 152)

IUPAC (2009). *IUPAC Compendium of Chemical Terminology*. Blackwell Scientific Publications, Oxford, Research Triagle Park, NC, 2nd edition, ISBN 0-9678550-9-8, 1670 pp., doi:10.1351/goldbook. (p. 17)

Iveson, S.M., Litster, J.D., Hapgood, K., and Ennis, B.J. (2001). Nucleation, growth and breakage phenomena in agitated wet granulation processes: a review. *Powder Technology*. (p. 19, 20)

Iwashita, K. and Oda, M. (1998). Rolling Resistance at Contacts in Simulation of Shear Band Development by DEM. *Journal of Engineering Mechanics*, **124**(3): pp. 285–292, doi:10.1061/(ASCE)0733-9399(1998)124:3(285). (p. 43)

Jaky, J. (1944). The CoefiňĄcient of Earth Pressure at Rest. *Journal of the Hungarian Society of Engineers and Architects (Magyar Mernok es Epitesz-Egylet Kozlonye)*: pp. 355–388. (p. 99)

Jaky, J. (1948). Pressure in soils. In: *2nd ICSMFE, London*, volume 1, pp. 103–107. (p. 99)

Janssen, H.A. (1895). Versuche uber getreidedruck in Silozellen. *Zeitschrift des Vereins Deutscher Ingenieure*, (35): pp. 1045–1049. (p. 21)

Jenike, A.W. (1964). *Storage and Flow of Solids*. Bulletin of the Utah Engineering Experiment Station, University of Utah, revised edition, 198 pp. (p. 21, 23, 96, 97, 98)

Jensen, J.H. (2010). *Molecular Modeling Basics*. CRC Press, 189 pp. (p. 44)

Jensen, R.P., Bosscher, P.J., Plesha, M.E., and Edil, T.B. (1999). DEM simulation of granular media-structure interface: effects of surface roughness and particle shape. *International Journal for Numerical and Analytical Methods in Geomechanics*, **23**(June 1997): pp. 531–547, doi:10.1002/(SICI)1096-9853(199905)23:6. (p. 28)

Jensen, R.P., Edil, T.B., Bosscher, P.J., Plesha, M.E., and Kahla, N.B. (2001). Effect of Particle Shape on Interface Behavior of DEMâĂŘSimulated Granular Materials. *International Journal of Geomechanics*, **1**(1): pp. 1–19, doi:10.1061/(ASCE)1532-3641(2001)1:1(1). (p. 28)

Johnson, K.L. (1987). *Contact Mechanics*. Cambridge University Press, ISBN 0521347963, 468 pp. (p. 46)

Johnson, K.L. and Greenwood, J.A. (1997). An adhesion map for the contact of elastic spheres. *Journal of Colloid and Interface Science*, **333**(192): pp. 326–333. (p. 52)

Johnson, K.L., Kendall, K., and Roberts, A.D. (1971). Surface Energy and the Contact of Elastic Solids. *Proceedings of the Royal Society A: Mathematical, Physical and Engineering Sciences*, **324**(1558): pp. 301–313, doi:10.1098/rspa.1971.0141. (p. 1, 18, 49, 50, 53)

Johnstone, M.W. (2010). *Calibration of DEM models for granular materials using bulk physical tests*. Ph.d. thesis, University of Edinburgh. (p. 94, 96, 101)

Jones, J.E. (1924). On the Determination of Molecular Fields. II. From the Equation of State of a Gas. *Proceedings of the Royal Society A: Mathematical, Physical and Engineering Sciences*, **106**(738): pp. 463–477, doi:10.1098/rspa.1924.0082. (p. 30)

Jones, R. (2003). From Single Particle AFM Studies of Adhesion and Friction to Bulk Flow: Forging the Links. *Granular Matter*, **4**(4): pp. 191–204, doi:10.1007/s10035-002-0122-6. (p. 65, 66, 68)

Jones, R., Pollock, H.M., Geldart, D., and Verlinden-Luts, A. (2004). Frictional forces between cohesive powder particles studied by AFM. *Ultramicroscopy*, **100**(1-2): pp. 59–78, doi:10.1016/j.ultramic.2004.01.009. (p. 78)

Karlsson, T., Klisinski, M., and Runesson, K. (1998). Finite element simulation of granular material flow in plane silos with complicated geometry. *Powder Technology*, **99**: pp. 29–39. (p. 31)

Katagiri, J., Matsushima, T., and Yamada, Y. (2010). Simple shear simulation of 3D irregularly-shaped particles by image-based DEM. *Granular Matter*, **12**(5): pp. 491–497, doi:10.1007/s10035-010-0207-6. (p. 27)

Kendall, K. (1969). *Ph.D. Dissertation*. Ph.d. thesis, Cambridge University, England. (p. 49)

Ketterhagen, W.R. (2011). Modeling the motion and orientation of various pharmaceutical tablet shapes in a film coating pan using DEM. *International Journal of Pharmaceutics*, **409**(1-2): pp. 137–49, doi:10.1016/j.ijpharm.2011.02.045. (p. 11, 28)

Ketterhagen, W.R., Curtis, J.S., Wassgren, C.R., and Hancock, B.C. (2009). Predicting the flow mode from hoppers using the discrete element method. *Powder Technology*, **195**(1): pp. 1–10, doi:10.1016/j.powtec.2009.05.002. (p. 32, 218)

Ketterhagen, W.R., Curtis, J.S., Wassgren, C.R., Kong, A., Narayan, P.J., and Hancock, B.C. (2007). Granular segregation in discharging cylindrical hoppers: A discrete element and experimental study. *Chemical Engineering Science*, **62**(22): pp. 6423–6439, doi:10.1016/j.ces.2007.07.052. (p. 31)

Kock, I. and Huhn, K. (2007). Influence of particle shape on the frictional strength of sediments - A numerical case study. *Sedimentary Geology*, **196**(1-4): pp. 217–233, doi:10.1016/j.sedgeo.2006.07.011. (p. 28)

Kohonen, M.M., Geromichalos, D., Scheel, M., Schier, C., and Herminghaus, S. (2004). On capillary bridges in wet granular materials. *Physica A: Statistical Mechanics and its Applications*, **339**(1-2): pp. 7–15, doi:10.1016/j.physa.2004.03.047. (p. 20)

Labra, C., Ooi, J.Y., and Sun, J. (2013). Spatial and Temporal Coarse-Graining for DEM Analysis. In: *Powders & Grains 2013*, 3, Sydney, Australia, pp. 3–6. (p. 58, 59)

Langston, P.A., Ai, J., and Yu, H.S. (2013). Simple shear in 3D DEM polyhedral particles and in a simplified 2D continuum model. *Granular Matter*: pp. 13–15, doi:10.1007/s10035-013-0421-0. (p. 145)

Li, Q., Rudolph, V., and Peukert, W. (2006). London-van der Waals adhesiveness of rough particles. *Powder Technology*, **161**(3): pp. 248–255, doi:10.1016/j.powtec.2005.10.012. (p. 18)

Li, Q., Rudolph, V., Weigl, B., and Earl, A. (2004). Interparticle van der Waals force in powder flowability and compactibility. *International Journal of Pharmaceutics*, **280**(1-2): pp. 77–93, doi:10.1016/j.ijpharm.2004.05.001. (p. 18)

Lian, G., Thornton, C., and Adams, M.J. (1993). A theoretical study of the liquid bridge forces between two rigid spherical bodies. *Journal of Colloid and Interface Science*, (161): pp. 138–147. (p. 20, 56, 58)

Lim, W.L. and McDowell, G.R. (2005). Discrete element modelling of railway ballast. *Granular Matter*, **7**(1): pp. 19–29, doi:10.1007/s10035-004-0189-3. (p. 28)

Lin, X. and Ng, T.T. (1995). Contact detection algorithms for three-dimensional ellipsoids in discrete element modelling. *International Journal for Numerical and Analytical Methods in Geomechanics*, **19**(9): pp. 653–659, doi:10.1002/nag.1610190905. (p. 28)

Lu, M. and McDowell, G.R. (2006). The importance of modelling ballast particle shape in the discrete element method. *Granular Matter*, **9**(1-2): pp. 69–80, doi:10.1007/s10035-006-0021-3. (p. 28)

Luding, S. (2005*a*). Anisotropy in cohesive, frictional granular media. *Journal of Physics: Condensed Matter*, **17**(24): pp. S2623–S2640, doi:10.1088/0953-8984/17/24/017. (p. 54, 55, 68, 69, 79)

Luding, S. (2005*b*). Shear flow modeling of cohesive and frictional fine powder. *Powder Technology*, **158**(1-3): pp. 45–50, doi:10.1016/j.powtec.2005.04.018. (p. 54, 68, 69, 77)

Luding, S. (2006). About contact force-laws for cohesive frictional materials in 2D and 3D. *Behavior of granular media*. (p. 54)

Luding, S. (2007). Contact Models for Very Loose Granular Materials. In: *IUTAM Symposium on Multiscale Problems in Multibody System Contacts*, (ed.) P. Eberhard, chapter 14, Springer Netherlands, pp. 135–150, doi:10.1007/978-1-4020-5981-0_14. (p. 54)

Luding, S. (2008*a*). Cohesive, frictional powders: contact models for tension. *Granular Matter*, **10**(4): pp. 235–246, doi:10.1007/s10035-008-0099-x. (p. 54, 55, 64, 68, 69, 77, 79, 81)

Luding, S. (2008*b*). Introduction to discrete element methods. *European Journal of Environmental and Civil Engineering*, **12**(7-8): pp. 785–826, doi:10.1080/19648189.2008.9693050. (p. 31)

Luding, S., Manetsberger, K., and Müllers, J. (2005). A discrete model for long time sintering. *Journal of the Mechanics and Physics of Solids*, **53**(2): pp. 455–491, doi:10.1016/j.jmps.2004.07.001. (p. 79)

Luossavaara-Kiirunavaara AB (2009). Annual Report & Sustainability Report 2009. Technical report, Luleå, Sweden. (p. 5, 6)

Luossavaara-Kiirunavaara AB (2011). SILA: An important link in LKAB's logistics chain. *LKAB Magazine 1*: pp. 52–57. (p. 5, 6)

Luossavaara-Kiirunavaara AB (2012*a*). Future On The Urban Transformation In Kiruna. (p. 6)

Luossavaara-Kiirunavaara AB (2012*b*). Growth - LKAB. Available at: http://www.lkab.com/en/Future/LKAB-Strategy/Focus-areas/Grow/, date accessed: 12/10/2012. (p. 6)

Luossavaara-Kiirunavaara AB (2012*c*). Mining: How Ore Is Mined. Technical report. (p. 2, 4)

Luossavaara-Kiirunavaara AB (2012*d*). Narvik - LKAB. Available at: http://www.lkab.com/en/About-us/Overview/Operations-Areas/Narvik/, date accessed: 12/10/2012. (p. 2)

Luossavaara-Kiirunavaara AB (2012*e*). Processing: How ore is processed. Technical report. (p. 3)

Maltby, L.P. and Enstad, G.G. (1993). Uniaxial Tester for Quality Control and Flow Property Characterization of Powders. *Powder Handling and Processing*, **13**: pp. 135–139. (p. 91)

Mankoc, C., Janda, A., Arévalo, R., Pastor, J.M., Zuriguel, I., Garcimartín, A., Maza, D., and Arevalo, R. (2007). The flow rate of granular materials through an orifice. *Granular Matter*, **9**(6): pp. 407–414, doi:10.1007/s10035-007-0062-2. (p. 224)

Markauskas, D., Kačianauskas, R., Džiugys, A., and Navakas, R. (2009). Investigation of adequacy of multi-sphere approximation of elliptical particles for DEM simulations. *Granular Matter*, **12**(1): pp. 107–123, doi:10.1007/s10035-009-0158-y. (p. 28)

Martin, C.L., Bouvard, D., and Shima, S. (2003). Study of particle rearrangement during powder compaction by the discrete element method. *Journal of the Mechanics and Physic of Solids*, **51**: pp. 667–693. (p. 29)

Mason, G. and Clark, W.C. (1965). Liquid bridges between spheres. *Chemical Engineering Science*, **20**(March): pp. 859–866. (p. 19)

Masroor, S.A., Zachary, L.W., and Lohnes, R.A. (1987). A test apparatus for determining elastic constants of bulk solids. In: *SEM Spring Conference on Experimental Mechanics*, Houston, TX, USA, pp. 46–63. (p. 94, 95)

Masson, S. and Martinez, J. (2000). Effect of particle mechanical properties on silo flow and stresses from distinct element simulations. *Powder Technology*, (109): pp. 164–178. (p. 11, 29, 31)

Masuda, H., Higashitani, K., and Yoshida, H. (Eds.) (2010). *Powder Technology Handbook*. CRC Press, 3rd edition, ISBN 1439831882, 920 pp. (p. 96, 98)

Matsushima, T. and Katagiri, J. (2009). 3D shape characterization and image-based DEM simulation of the lunar soil simulant FJS-1. *Journal of Aerospace Engineering*, (January): pp. 15–23, doi:10.1061/(ASCE)0893-1321(2009)22:1(15. (p. 27)

Matsushima, T., Saomoto, H., Matsumoto, M., Toda, K., and Yamada, Y. (2003). Discrete Element Simulation of an Assembly of Irregularly-Shaped Grains: Quantitative Comparison with Experiments. In: *16th ASCE Engineering Mechanics Confeence*, Washington, Seattle, pp. 1–8. (p. 28)

Maugis, D. (1992). Adhesion of spheres: the JKR-DMT transition using a Dugdale model. *Journal of Colloid and Interface Science*, **150**(1). (p. 52)

Mayniel, K. (1808). *Traité expérimental, analytique et preatique de la poussée des terres et des murs de revêtement, Paris*. Bachelier librairie, 316 pp. (p. 101)

McGlinchey, D. (2008). *Bulk solids handling: equipment selection and operation*. Blackwell Pub., ISBN 9781405158251. (p. 96, 98)

McGlinchey, D. (2009). *Characterisation of Bulk Solids*. Wiley, ISBN 9781405143639. (p. 96, 98)

Mehrotra, A., Chaudhuri, B., Faqih, A., Tomassone, M.S., and Muzzio, F.J. (2009). A modeling approach for understanding effects of powder flow properties on tablet weight variability. *Powder Technology*, **188**(3): pp. 295–300, doi:10.1016/j.powtec.2008.05.016. (p. 29, 30)

Mikami, T., Kamiya, H., and Horio, M. (1998). Numerical simulation of cohesive powder behavior in a fluidized bed. *Chemical Engineering Science*, **53**(10): pp. 1927–1940, doi:10.1016/S0009-2509(97)00325-4. (p. 30, 33, 57, 58)

Mindlin, R.D. (1949). Compliance of elastic bodies in contact. *Journal of Applied Mechanics*, **16**(259): p. 16. (p. 81, 152)

Mindlin, R.D. and Deresiewicz, H. (1953). Elastic Spheres in Contact Under Varying Oblique Forces. *Journal of Applied Mechanics*, **20**: pp. 327–344. (p. 47, 48)

Mishra, B.K. and Thornton, C. (2001). Impact breakage of particle agglomerates. *International Journal of Mineral Processing*. (p. 50)

Mitarai, N. and Nakanishi, H. (2009). Simple model for wet granular materials with liquid clusters. *EPL (Europhysics Letters)*, **88**(6): p. 64001, doi:10.1209/0295-5075/88/64001. (p. 20)

Mitarai, N. and Nori, F. (2006). Wet granular materials. *Advances in Physics*, **55**(1-2): pp. 1–45, doi:10.1080/00018730600626065. (p. 18, 19, 20)

Modenese, C., Utili, S., and Houlsby, G.T. (2012). A Study of the Influence of Surface Energy on the Mechanical Properties of Lunar Soil Using DEM. In: *Discrete Element Modelling of Particulate Media*, (ed.) C.Y. Wu, chapter 9, RSC Publishing, ISBN 9781849735032, pp. 69–75, doi:10.1039/9781849735032-00069. (p. 50)

Moreno, R., Ghadiri, M., and Antony, S.J. (2003). Effect of the impact angle on the breakage of agglomerates: a numerical study using DEM. *Powder Technology*, **130**: pp. 132–137. (p. 50)

Moreno-Atanasio, R. (2012). Energy dissipation in agglomerates during normal impact. *Powder Technology*, **223**: pp. 12–18, doi:10.1016/j.powtec.2011.05.016. (p. 50)

Moreno-Atanasio, R., Antony, S.J., and Ghadiri, M. (2005). Analysis of flowability of cohesive powders using Distinct Element Method. *Powder Technology*, **158**(1-3): pp. 51–57, doi:10.1016/j.powtec.2005.04.029. (p. 30, 50)

Morrow, C., Lovell, M., and Ning, X. (2003). A JKR-DMT transition solution for adhesive rough surface contact. *Journal of Physics D: Applied Physics*, **36**: pp. 534–540. (p. 50)

Muite, B.K., Quinn, S.F., Sundaresan, S., and Kesava Rao, K. (2004). Silo music and silo quake: granular flow-induced vibration. *Powder Technology*, **145**(3): pp. 190–202, doi:10.1016/j.powtec.2004.07.003. (p. 24)

Muller, V.M., Yushchenko, V.S., and Derjaguin, B.V. (1980). On the influence of molecular forces on the deformation of an elastic sphere and its sticking to a rigid plane. *Journal of Colloid and Interface Science*, **77**(1): pp. 91–101, doi:10.1016/0021-9797(80)90419-1. (p. 52)

Müller-Breslau, H.F.B. (1906). *Erddruck Auf Stützmauern*. A. Kröner. (p. 101)

Munch-Andersen, J. (1986). The Boundary Layer in Rough Silos. *Second International Conference on Bulk Materials Storage, Handling and Transportation: 1986; Preprints of Papers*: p. 160. (p. 221)

Munch-Andersen, J., Askegaard, V., and Brink, A. (1992). *Silo model tests with sand. Bulletin No. 91*. Danish Building Research Institute., 1–39 pp. (p. 221, 222, 239)

Myers, M.E. and Sellers, M. (1971). Chemical engineering tripos. Part 2. Research Project Report. Technical report, University of Cambridge. (p. 25, 224)

Nedderman, R.M. (1992). *Statics and Kinematics of Granular Materials*. Cambridge University Press, paperback edition, ISBN 9780521404358, 368 pp. (p. 9, 21, 224)

Nedderman, R.M., Tüzün, U., Savage, S.B., and Houlsby, G.T. (1982). The flow of granular materials - I - Discharge rates from Hoppers. *Chemical Engineering Science*, **37**(11): pp. 1597–1609, doi:10.1016/0009-2509(82)80029-8. (p. 23, 26)

Ng, T.T. (2004). Shear strength of assemblies of ellipsoidal particles. *Géotechnique*, **54**(10): pp. 659–669. (p. 28)

Ng, T.T. and Lin, X. (1997). A three-dimensional discrete element model using arrays of ellipsoids. *Géotechnique*, **47**(2): pp. 319–329, doi:10.1680/geot.1997.47.2.319. (p. 28)

Nguyen, T.V., Brennen, C., and Sabersky, R.H. (1979). Gravity flow of granular materials in conical hoppers. *Journal of Applied Mechanics*, **46**(September): pp. 529–535. (p. 26)

Niiniskorpi, V. (2001). Phases and Microstructures in LKAB's Olivine and Dolmite fluxed pellets. In: *60th Ironmaking Conference Proceedings*, pp. 767–780. (p. 105)

Nowak, S., Samadani, A., and Kudrolli, A. (2005). Maximum angle of stability of a wet granular pile. *Nature physics*. (p. 18)

O' Sullivan, C. (2011). *Particulate Discrete Element Modelling: A Geomechanics Perspective*. Spon Press/Taylor & Francis, 1st edition, ISBN 0415490367, 576 pp. (p. 41, 46)

O' Sullivan, C. and Bray, J.D. (2003). Modified Shear Spring Formulation for Discontinuous Deformation Analysis of Particulate Media. *Journal of Engineering Mechanics*, **129**(7): pp. 830–834, doi:10.1061/(ASCE)0733-9399(2003)129:7(830). (p. 35)

O' Sullivan, C. and Bray, J.D. (2004). Selecting a suitable time step for discrete element simulations that use the central difference time integration scheme. *Engineering Computations*, **21**(2/3/4): pp. 278–303, doi:10.1108/02644400410519794. (p. 42, 143)

O' Sullivan, C., Bray, J.D., and Riemer, M.F. (2002). Influence of Particle Shape and Surface Friction Variability on Response of Rod-Shaped Particulate Media. *Journal of Engineering Mechanics*, **128**(11): pp. 1182–1192, doi:10.1061/(ASCE)0733-9399(2002)128:11(1182). (p. 10, 35)

O' Sullivan, C., Bray, J.D., and Riemer, M.F. (2004*a*). Examination of the Response of Regularly Packed Specimens of Spherical Particles Using Physical Tests and Discrete Element Simulations. *Journal of Engineering Mechanics*, **130**(10): pp. 1140–1150, doi:10.1061/(ASCE) 0733-9399(2004)130:10(1140). (p. 35)

O' Sullivan, C. and Cui, L. (2009). Micromechanics of granular material response during load reversals: Combined DEM and experimental study. *Powder Technology*, **193**(3): pp. 289–302, doi:10.1016/j.powtec.2009.03.003. (p. 29)

O' Sullivan, C., Cui, L., and Bray, J.D. (2004*b*). Three-dimensional discrete element simulations of direct shear tests. In: *Numerical Modeling in Micromechanics via Particle Methods - 2004: Proceedings of the 2nd International PFC Symposium*, pp. 373–382. (p. 35)

Ooi, J.Y., Chen, J.F., Lohnes, R.A., and Rotter, J.M. (1996). Prediction of static wall pressures in coal silos. *Construction and Building Materials*, **10**(2): pp. 109–116. (p. 24)

Ooi, J.Y., Chen, J.F., and Rotter, J.M. (1998). Measurement of solids flow patterns in a gypsum silo. *Powder Technology*, **99**: pp. 272–284. (p. 24)

Ooi, J.Y. and Rotter, J.M. (1990). Wall pressures in squat steel silos from simple finite element analysis. *Computers & Structures*, **37**(4): pp. 361–374. (p. 24, 31, 101)

Ooi, J.Y. and Rotter, J.M. (1991). Measured pressures in full scale silos: a new understanding. *Physical Review Letters*. (p. 24)

Ooi, J.Y. and She, K.M. (1997). Finite element analysis of wall pressure in imperfect silos. *International journal of solids and structures*, **34**(16): pp. 2061–2072. (p. 24, 31)

Ouadfel, H. and Rothenburg, L. (1999). An algorithm for detecting inter-ellipsoid contacts. *Computers and Geotechnics*, **24**(4): pp. 245–263, doi:10.1016/S0266-352X(99)00013-0. (p. 28)

Parisi, D.R., Masson, S., and Martinez, J. (2004). Partitioned Distinct Element Method Simulation of Granular Flow within Industrial Silos. *Journal of Engineering Mechanics*, **130**(7): pp. 771–779, doi:10.1061/(ASCE)0733-9399(2004)130:7(771). (p. 31)

Parker, R.S.R. and Taylor, P. (1966). *Adhesion and adhesives*. Pergamon Press, 142 pp. (p. 13)

Parrella, L., Barletta, D., Boerefijn, R., and Poletto, M. (2008). Comparison between a Uniaxial Compaction Tester and a Shear Tester for the Characterization of Powder Flowability. *KONA Powder and particle*, **26**(26): pp. 178–189. (p. 91)

Parsegian, V.A. (2006). *Van der Waals forces: a handbook for biologists, chemists, engineers, and physicists*. Cambridge University Press, ISBN 9780521839068, 1–394 pp. (p. 18)

Peña, A.A., Lind, P.G., and Herrmann, H.J. (2008). Modeling slow deformation of polygonal particles using DEM. *Particuology*, **6**(6): pp. 506–514, doi:10.1016/j.partic.2008.07.009. (p. 28)

Pierrat, P. and Caram, H.S. (1997). Tensile strength of wet granular materials. *Powder Technology*, **91**: pp. 83–93. (p. 20)

Pietsch, W. (2002). *Agglomeration Processes - Phenomena, Technologies, Equipment*. Wiley-VCH, Weinheim, 1486 pp. (p. 14)

Pietsch, W., Hoffman, E., and Rumpf, H. (1969). Tensile Strength of Moist Agglomerates. *Industrial & Engineering Chemistry Product Research and Development*, **8**(1): pp. 58–62, doi:10.1021/i360029a009. (p. 151)

Poncelet, J.V. (1840). *Mémoire sur la Stabilité des Revêtments et de seurs Fondations*. Bachelier, Paris. (p. 101)

Potyondy, D.O. and Cundall, P.A. (2004). A bonded-particle model for rock. *International Journal of Rock Mechanics and Mining Sciences*, **41**(8): pp. 1329–1364, doi:10.1016/j.ijrmms.2004.09.011. (p. 49)

Prokopovich, P. and Starov, V. (2011). Adhesion models: from single to multiple asperity contacts. *Advances in colloid and interface science*, **168**(1-2): pp. 210–22, doi:10.1016/j.cis.2011.03.004. (p. 18)

Rabinovich, Y.I., Adler, J.J., Ata, A., Singh, R.K., and Moudgil, B.M. (2000*a*). Adhesion between Nanoscale Rough Surfaces. *Journal of Colloid and Interface Science*, **232**(1): pp. 10–16, doi:10.1006/jcis.2000.7167. (p. 18)

Rabinovich, Y.I., Adler, J.J., Ata, A., Singh, R.K., and Moudgil, B.M. (2000*b*). Adhesion between Nanoscale Rough Surfaces - II. Measurement and Comparison with Theory. *Journal of Colloid and Interface Science*, **232**(1): pp. 17–24, doi:10.1006/jcis.2000.7168. (p. 18)

Ramm, E., Bischoff, M., and Schneider, B. (2010). On Some Features of a Polygonal Discrete Element Model. In: *Recent Developments and Innovative Applications in Computational Mechanics*, (eds.) D. Mueller-Hoeppe, S. Loehnert, and S. Reese, chapter Chapter 30, Springer, illustrated edition, pp. 265–273, doi:10.1007/252F978.3.642.17484.1.30. (p. 28)

Rankine, W.J.M. (1857). On the stability of loose earth. *Philosophical Transactions of the Royal Society of London*, **147**(May 2013): pp. 9–27, doi:10.2307/108608. (p. 99)

Rayleigh, J.W.S. (1885). On waves propagated along the plane surface of an elastic solid. *Proceedings of the London Mathematical ...*, **iv**(1): pp. 4–11, doi:10.1002/cbdv.200490137/abstract. (p. 42)

Reinke, S.K. (2011). *Comparison of measuring the lateral pressure ratio using confined compression test and lambdameter*. Masters thesis, TU Braunschweig. (p. 94, 96)

Remy, B., Khinast, J.G., and Glasser, B.J. (2012). Wet granular flows in a bladed mixer: Experiments and simulations of monodisperse spheres. *AIChE Journal*, **58**(11), doi:10.1002/aic.13743. (p. 1, 30)

Richefeu, V., El Youssoufi, M.S., and Radjaï, F. (2006*a*). Shear strength properties of wet granular materials. *Physical Review E*, **73**(5): pp. 1–11, doi:10.1103/PhysRevE.73.051304. (p. 19)

Richefeu, V., Radjaï, F., and El Youssoufi, M.S. (2006*b*). Stress transmission in wet granular materials. *The European Physical Journal. E, Soft matter*, **21**(4): pp. 359–69, doi:10.1140/epje/i2006-10077-1. (p. 19)

Rietema, K. (1991). *The Dynamics of Fine Powders*. Springer, ISBN 1851665943, 262 pp. (p. 17)

Ristow, G.H. (1997). Outflow rate and wall stress for two-dimensional hoppers. *Physica A: Statistical Mechanics and its Applications*, **235**: pp. 319–326. (p. 32)

Roberts, A.D. (1968). *Ph.D. Dissertation*. Ph.d. thesis, Cambridge University, England. (p. 49)

Roberts, A.W. and Wensrich, C.M. (2002). Flow dynamics or 'quaking'in gravity discharge from silos. *Chemical Engineering Science*, **57**: pp. 295–305. (p. 24)

Röck, M., Ostendorf, M., and Schwedes, J. (2006). Development of an Uniaxial Caking Tester. *Chemical Engineering & Technology*, **29**(6): pp. 679–685, doi:10.1002/ceat.200600068. (p. 91)

Rose, H. and Tanaka, T. (1959). Rate of discharge of granular materials from bins and hoppers. *Engineer*, **208**: pp. 465–469. (p. 23)

Rotter, J.M. (2001). *Guide for Economic Design of Circular Metal Silos*. Civil Engineering Series, Taylor & Francis, illustrated edition, ISBN 9780419234609, 235 pp. (p. 22, 23, 96, 98, 99, 234, 240)

Rotter, J.M., Holst, J.M.F.G., Ooi, J.Y., and Sanad, A.M. (1998). Silo pressure predictions using discrete-element and finite-element analyses. *Philosophical Transactions of the Royal Society A: Mathematical, Physical and Engineering Sciences*, **356**(1747): pp. 2685–2712, doi:10.1098/rsta.1998.0293. (p. 24, 31)

Rotter, J.M., Ooi, J.Y., Chen, J.F., Tiley, P.J., Mackintosh, I., and Bennett, F.R. (1995). Flow pattern measurement in full scale silos Final report on the BMHD/DTI Project. Technical report, British Materials Handling Board. (p. 24)

Rumpf, H. (1962). The Strength of Granules and Agglomerates. In: *Agglomeration*, (ed.) W. Knepper, Wiley Interscience, New York, NY, pp. 379–418. (p. 14, 151, 166)

Rusinek, R., Molenda, M., Sykut, J., Pits, N., and Tys, J. (2007). Uniaxial Compression of Rapeseed Using Apparatus with Cuboid Chamber. *Acta Agrophysica*, **10**(3): pp. 677–685. (p. 29)

Ruths, M., Alcantar, N.A., and Israelachvili, J.N. (2003). Boundary Friction of Aromatic Silane Self-Assembled Monolayers Measured with the Surface Forces Apparatus and Friction Force Microscopy. *The Journal of Physical Chemistry B*, **107**(40): pp. 11149–11157, doi:10.1021/jp0353946. (p. 78)

Sallam, A.M. and Ashmawy, A.K. (2009). Effect of particle shape and angularity on dilation of granular soils: a discrete element approach. In: *Proceedings of the 17th International Conference on Soil Mechanics and Geotechnical Engineering (ICSMGE 2009)*, p. 4, doi:10.3233/978-1-60750-031-5-417. (p. 28)

Samadani, A. and Kudrolli, A. (2000). Segregation transitions in wet granular matter. *Physical Review Letters*, **01610**(i): pp. 1–5, doi:10.1103/PhysRevLett.85.5102. (p. 20)

Samadani, A. and Kudrolli, A. (2001). Angle of repose and segregation in cohesive granular matter. *Physical Review E*, **01610**. (p. 20)

Samadani, A., Mahadevan, L., and Kudrolli, A. (2002). Shocks in sand flowing in a silo. *Journal of Fluid Mechanics*, **452**: pp. 293–301, doi:10.1017/S0022112001006991. (p. 20)

Sanad, A.M., Ooi, J.Y., Holst, J.M.F.G., and Rotter, J.M. (2001). Computations of Granular Flow and Pressures in a Flat-Bottomed Silo. *Journal of Engineering Mechanics*, **127**(10): pp. 1033–1043, doi:10.1061/(ASCE)0733-9399(2001)127:10(1033). (p. 24, 31)

Savkoor, A.R. and Briggs, G.A.D. (1977). The Effect of Tangential Force on the Contact of Elastic Solids in Adhesion. *Proceedings of the Royal Society A: Mathematical, Physical and Engineering Sciences*, **356**(1684): pp. 103–114, doi:10.1098/rspa.1977.0123. (p. 45)

Schulze, D. (2008*a*). *Powders and Bulk Solids: Behavior, Characterization, Storage and Flow*. Springer-Verlag Berlin Heidelberg, illustrated edition, ISBN 978-3-540-73767-4, 501 pp. (p. 14, 15, 18, 23, 24, 91, 96, 97, 98)

Schulze, D. (2008*b*). Silo quaking and silo honking. In: *Powders and Bulk Solids*, chapter Chapter 14, Springer Berlin Heidelberg, pp. 405–437, doi:10.1007/978-3-540-73768-1_14. (p. 24)

Schwarz, U.D., Zwörner, O., Köster, P., and Wiesendanger, R. (1997). Quantitative analysis of the frictional properties of solid materials at low loads. I. Carbon compounds. *Physical review B*, **56**(11): p. 6987. (p. 78)

Schwedes, J. (2003). Review on testers for measuring flow properties of bulk solids. *Granular Matter*, **5**(1): pp. 1–43, doi:10.1007/s10035-002-0124-4. (p. 91, 92)

Seville, J.P.K., Willett, C.D., and Knight, P.C. (2000). Interparticle forces in fluidisation: a review. *Powder Technology*: pp. 261–268. (p. 14, 15, 18)

Sheng, Y., Lawrence, C.J., Briscoe, B.J., and Thornton, C. (2004). Numerical studies of uniaxial powder compaction process by 3D DEM. *Engineering Computations*, **21**(2/3/4): pp. 304–317, doi:10.1108/02644400410519802. (p. 28, 42)

Shimizu, Y., Hart, R., and Cundall, P.A. (2004). *Numerical Modeling in Micromechanics via Particle Methods - 2004: Proceedings of the 2nd International PFC Symposium*. Taylor & Francis, Kyoto, Japan, ISBN 9789058096791, 448 pp. (p. 27)

Simons, S.J.R. (2007). Liquid bridges in granules. In: *Handbook of Powder Technology*, (eds.) A. Salman, M. Hounslow, and J. Seville, chapter Chapter 27, pp. 1257–1316, doi:10.1016/S0167-3785(07)80062-5. (p. 20)

Sitharam, T. and Nimbkar, M. (2000). Micromechanical modelling of granular materials: effect of particle size and gradation. *Geotechnical & Geological Engineering*, **18**: pp. 91–117, doi:10.1023/A:1008982027109. (p. 142)

Skinner, J. and Gane, N. (1972). Sliding friction under a negative load. *Journal of Physics D: Applied Physics*, **5**: pp. 2087–2095. (p. 78, 79)

Song, Y. and Turton, R. (2007). Study of the effect of liquid bridges on the dynamic behavior of two colliding tablets using DEM. *Powder Technology*, **178**(2): pp. 99–108, doi:10.1016/j.powtec.2007.04.010. (p. 28)

Sperl, M. (2005). Experiments on corn pressure in silo cells - translation and comment of Janssen's paper from 1895. *Granular Matter*, **8**(2): pp. 59–65, doi:10.1007/s10035-005-0224-z. (p. 21)

Sukumaran, B. and Ashmawy, A.K. (2003). Influence of inherent particle characteristics on hopper flow rate. *Powder Technology*, **138**(1): pp. 46–50, doi:10.1016/j.powtec.2003.08.039. (p. 23)

Sun, J. and Sundaresan, S. (2011). A constitutive model with microstructure evolution for flow of rate-independent granular materials. *Journal of Fluid Mechanics*, **682**(2011): pp. 590–616, doi:10.1017/jfm.2011.251. (p. 145)

Suzzi, D., Toschkoff, G., Radl, S., Machold, D., Fraser, S.D., Glasser, B.J., and Khinast, J.G. (2012). DEM simulation of continuous tablet coating: Effects of tablet shape and fill level on inter-tablet coating variability. *Chemical Engineering Science*, **69**(1): pp. 107–121, doi:10.1016/j.ces.2011.10.009. (p. 28)

Tabor, D. (1977). Surface forces and surface interactions. *Journal of Colloid and Interface Science*, **58**(1): pp. 2–13, doi:10.1016/0021-9797(77)90366-6. (p. 52)

Tao, H., Jin, B., Zhong, W., and Wang, X. (2010). Discrete element method modeling of corn-shaped particle flow in rectangular hopper. *Frontiers of Architecture and Civil Engineering in China*, **4**(2): pp. 267–275, doi:10.1007/s11709-010-0035-0. (p. 33)

Tegzes, P., Vicsek, T., and Schiffer, P. (2003). Development of correlations in the dynamics of wet granular avalanches. *Physical Review E*, **67**(5): p. 051303, doi:10.1103/PhysRevE.67.051303. (p. 20)

Thakur, S.C., Morrissey, J.P., Sun, J., Chen, J.F., and Ooi, J.Y. (2011). A DEM study of cohesive particulate solids: plasticity and stress- history dependency. In: *11th Particulate Systems Analysis Conference: PSA2011*, Edinburgh, UK, pp. 1–5. (p. 149, 150, 157, 191)

Thakur, S.C., Morrissey, J.P., Sun, J., Chen, J.F., and Ooi, J.Y. (2013). Micromechanical analysis of cohesive granular materials using discrete element method with an adhesive elasto-plastic contact model. *Granular Matter*. (p. 10, 143, 151, 157, 166, 172)

Thomas, P.A. and Bray, J.D. (1999). Capturing nonspherical shape of granular media with disk clusters. *Journal of Geotechnical and Geoenvironmental Engineering*, (March): pp. 169–178, doi:10.1061/(ASCE)1090-0241(1999)125:3(169. (p. 11, 27)

Thomson Reuters (2013). All Databases JKR Citation Report. Date accessed: 13/02/13. (p. 50)

Thornton, C. (1991). Interparticle sliding in the presence of adhesion. *Journal of Physics D: Applied Physics*, **24**: pp. 1942–1946. (p. 45)

Thornton, C. (1997). Coefficient of Restitution for Collinear Collisions of Elastic-Perfectly Plastic Spheres. *Journal of Applied Mechanics*, **64**(2): p. 383, doi:10.1115/1.2787319. (p. 48, 77)

Thornton, C. and Antony, S.J. (2000). Quasi-static shear deformation of a soft particle system. *Powder Technology*, **109**(1-3): pp. 179–191, doi:10.1016/S0032-5910(99)00235-1. (p. 10)

Thornton, C. and Ning, Z. (1998). A theoretical model for the stick/bounce behaviour of adhesive, elastic-plastic spheres. *Powder Technology*, **99**(2): pp. 154–162, doi:10.1016/S0032-5910(98)00099-0. (p. 53, 64)

Thornton, C. and Randall, C.W. (1988). Applications of theoretical contact mechanics to solid particle system simulation. In: *Micromechanics of granular materials*, (eds.) M. Satake and J. Jenkins, Elsevier, Amsterdam, pp. 133–142. (p. 42)

Tomas, J. (2003*a*). Flow properties of cohesive nanopowders. *China Particuology*, **1**(6): pp. 231–241. (p. 54)

Tomas, J. (2003*b*). Mechanics of nanoparticle adhesion-a continuum approach. In: *Particles on Surfaces 8: Detection, Adhesion and Removal*, (ed.) K. Mittal, VSP, pp. 1–47. (p. 54)

Tomas, J. (2004). Fundamentals of cohesive powder consolidation and flow. *Granular Matter*, **6**(2-3): pp. 75–86, doi:10.1007/s10035-004-0167-9. (p. 54)

Tomas, J. (2007*a*). Adhesion of ultrafine particles-A micromechanical approach. *Chemical Engineering Science*, **62**(7): pp. 1997–2010, doi:10.1016/j.ces.2006.12.055. (p. 45, 46, 54)

Tomas, J. (2007*b*). Adhesion of ultrafine particles-Energy absorption at contact. *Chemical Engineering Science*, **62**(7): pp. 1997–2010, doi:10.1016/j.ces.2006.12.055. (p. 54)

Tsuji, Y., Tanaka, T., and Ishida, T. (1992). Lagrangian numerical simulation of plug flow of cohesionless particles in a horizontal pipe. *Powder Technology*, **71**: pp. 239–250. (p. 47, 48)

Tüzün, U., Houlsby, G.T., Nedderman, R.M., and Savage, S.B. (1982). The flow of granular materials - 2 - Velocity Distributions in Slow Flow. *Chemical Engineering Science*, **37**(12): pp. 1691–1709. (p. 23)

Tüzün, U. and Nedderman, R.M. (1985*a*). Gravity flow of granular materials round obstacles-I. *Chemical Engineering Science*, **40**(3): pp. 325–336, doi:10.1016/0009-2509(85)85095-8. (p. 24)

Tüzün, U. and Nedderman, R.M. (1985*b*). Gravity flow of granular materials round obstacles-II. *Chemical Engineering Science*, **40**(3): pp. 337–351, doi:10.1016/0009-2509(85)85096-X. (p. 24)

Tykhoniuk, R., Tomas, J., Luding, S., Kappl, M., Heim, L.O., and Butt, H.J. (2007). Ultrafine cohesive powders: From interparticle contacts to continuum behaviour. *Chemical Engineering Science*, **62**(11): pp. 2843–2864, doi:10.1016/j.ces.2007.02.027. (p. 30, 54, 64)

van Honschoten, J.W., Tas, N.R., and Elwenspoek, M. (2010). The profile of a capillary liquid bridge between solid surfaces. *American Journal of Physics*, **78**(3): p. 277, doi:10.1119/1.3273854. (p. 19)

Vanel, L., Claudin, P., Bouchaud, J.P., Cates, M.E., Clément, E., and Wittmer, J.P. (2000). Stresses in silos: comparison between theoretical models and new experiments. *Physical Review Letters*, **84**(7): pp. 1439–42. (p. 23)

Vu-Quoc, L., Lesburg, L., and Zhang, X. (2004). An accurate tangential force-displacement model for granular-flow simulations: Contacting spheres with plastic deformation, force-driven formulation. *Journal of Computational Physics*, **196**(1): pp. 298–326, doi:10.1016/j.jcp.2003.10.025. (p. 45)

Vu-Quoc, L. and Zhang, X. (1999*a*). An accurate and efficient tangential force-displacement model for elastic frictional contact in particle-flow simulations. *Mechanics of Materials*, **31**: pp. 235–269. (p. 48)

Vu-Quoc, L. and Zhang, X. (1999*b*). An elastoplastic contact force-displacement model in the normal direction: displacement-driven version. *Proceedings of the Royal Society A: Mathematical, Physical and Engineering Sciences*, **455**(1991): pp. 4013–4044, doi:10.1098/rspa.1999.0488. (p. 48, 77)

Vu-Quoc, L., Zhang, X., and Lesburg, L. (2001). Normal and tangential force-displacement relations for frictional elasto-plastic contact of spheres. *International Journal of Solids and Structures*, **38**(36-37): pp. 6455–6489, doi:10.1016/S0020-7683(01)00065-8. (p. 48)

Walton, O.R. (1994*a*). Effects of interparticle friction and particle shape on dynamic angles of repose via particle-dynamics simulation. In: *Proceedinga of Workshop on Mechania and Statistical Physia of Particulate Materials*, (eds.) J. Jenkins and J. Goddard, LaJolla, California, USA. (p. 27)

Walton, O.R. (1994*b*). Force models for particle-dynamics simulations of granular materials. In: *North Amencan Treaty Organization Advanced Study Institute for Mobile Particulate Systems*, December, pp. 1–11. (p. 81, 152)

Walton, O.R. (2004). Potential discrete element simulation applications ranging from airborne fines to pellet beds. *SAE 2004 Transactions J. Aerospace*. (p. 55, 64, 68)

Walton, O.R. (2008). Review of Adhesion Fundamentals for Micron Scale Particles. *KONA Powder and Particle*, **26**(26): pp. 129–141. (p. 18)

Walton, O.R. and Braun, R.L. (1986). Viscosity, granular-temperature, and stress calculations for shearing assemblies of inelastic, frictional disks. *Journal of Rheology*, **30**(5): pp. 949–980. (p. 48, 49, 68)

Walton, O.R. and Braun, R.L. (1993). Simulation of rotary-drum and repose tests for frictional spheres and rigid sphere clusters. In: *DOE/NSF Workshop on Flow of Particulateand Fluids*, pp. 1–18. (p. 27)

Walton, O.R. and Johnson, S.M. (2009). Simulating the Effects of Interparticle Cohesion in Micron-Scale Powders. In: *AIP Conference Proceedings - Powders And Grains 2009: Proceedings Of The 6th International Conference On Micromechanics Of Granular Media*, (eds.) M. Nakagawa and S. Luding, AIP, Golden (Colorado), pp. 897–900, doi:10.1063/1.3180075. (p. 55, 56, 64, 68, 77, 79)

Wang, C., Hassanpour, A., and Ghadiri, M. (2008). Characterisation of flowability of cohesive powders by testing small quantities of weak compacts. *Particuology*, **6**(4): pp. 282–285, doi:10.1016/j.partic.2008.05.004. (p. 30)

Wang, C.Y., Wang, C.F., and Sheng, J. (1999). A packing generation scheme for the granular assemblies with 3D ellipsoidal particles. *International Journal For Numerical And Analytical Methods in Geomechanics*, **828**(October 1997): pp. 815–828, doi:10.1002/(SICI)1096-9853(199907)23:8. (p. 28)

Waters, J.F., Lee, S., and Guduru, P.R. (2009). Mechanics of axisymmetric wavy surface adhesion: JKR-DMT transition solution. *International Journal of Solids and Structures*, **46**(5): pp. 1033–1042, doi:10.1016/j.ijsolstr.2008.10.013. (p. 50)

Weinhart, T., Thornton, A.R., Luding, S., and Bokhove, O. (2012). Closure relations for shallow granular flows from particle simulations. *Granular Matter*, **14**(4): pp. 531–552, doi:10.1007/s10035-012-0355-y. (p. 58)

Weisstein, E.W. (2013). Sphere-Sphere Intersection. Available at: http://mathworld.wolfram.com/Sphere-SphereIntersection.html, date accessed: 19/4/2013. (p. 74)

Wensrich, C.M. (2002). Experimental behaviour of quaking in tall silos. *Powder Technology*, **127**: pp. 87–94. (p. 24)

Wensrich, C.M. (2003). Numerical modelling of quaking in tall silos. *International Journal of Mechanical Sciences*, **45**(3): pp. 541–551, doi:10.1016/S0020-7403(03)00057-2. (p. 24)

Wensrich, C.M. and Katterfeld, A. (2012). Rolling friction as a technique for modelling particle shape in DEM. *Powder Technology*, **217**: pp. 409–417, doi:10.1016/j.powtec.2011.10.057. (p. 35, 43)

Wiącek, J., Molenda, M., Horabik, J., and Ooi, J.Y. (2012*a*). Influence of grain shape and intergranular friction on material behavior in uniaxial compression: Experimental and DEM modeling. *Powder Technology*, **217**: pp. 435–442, doi:10.1016/j.powtec.2011.10.060. (p. 28, 170)

Wiącek, J., Molenda, M., Ooi, J.Y., and Favier, J.F. (2012*b*). Experimental and numerical determination of representative elementary volume for granular plant materials. *Granular Matter*, **14**(4): pp. 449–456, doi:10.1007/s10035-012-0351-2. (p. 28, 29)

Wilde, K., Rucka, M., and Tejchman, J. (2008). Silo music - Mechanism of dynamic flow and structure interaction. *Powder Technology*, **186**(2): pp. 113–129, doi:10.1016/j.powtec.2007.11.008. (p. 24)

Wilde, K., Tejchman, J., Rucka, M., and Niedostatkiewicz, M. (2010). Experimental and theoretical investigations of silo music. *Powder Technology*, **198**(1): pp. 38–48, doi:10.1016/j.powtec.2009.10.012. (p. 24)

Willett, C.D., Adams, M.J., Johnson, S.A., and Seville, J.P.K. (2000). Capillary bridges between two spherical bodies. *Langmuir*, (10): pp. 9396–9405, doi:10.1021/la000657y. (p. 19)

Williams, J.C., Birks, A.H., and Bhattacharya, D. (1971). The direct measurement of the failure function of a cohesive powder. *Powder Technology*, **4**(6): pp. 328–337, doi:10.1016/0032-5910(71)80058-X. (p. 91, 111)

Wójcik, M., Tejchman, J., and Enstad, G.G. (2012). Confined granular flow in silos with inserts - Full-scale experiments. *Powder Technology*, **222**: pp. 15–36, doi:10.1016/j.powtec.2012.01.031. (p. 24)

World Steel Association (2012). Sustainable Steel: At the core of a green economy. Technical report. (p. 2)

Xu, D., Liechti, K.M., and Ravi-Chandar, K. (2007). On the modified Tabor parameter for the JKR-DMT transition in the presence of a liquid meniscus. *Journal of Colloid and Interface Science*, **315**(2): pp. 772–85, doi:10.1016/j.jcis.2007.07.048. (p. 20)

Xu, J.Q., Zou, R.P., and Yu, A.B. (2004). Packing structure of cohesive spheres. *Physical Review E*, **69**(3): p. 032301, doi:10.1103/PhysRevE.69.032301. (p. 29, 157)

Xu, Y., Kafui, K.D., Thornton, C., and Lian, G. (2002). Effects of Material Properties on Granular Flow in a Silo Using DEM Simulation. *Particulate Science and Technology*, **20**(2): pp. 109–124, doi:10.1080/02726350215338. (p. 34)

Yan, Y. and Ji, S. (2010). Discrete element modeling of direct shear tests for a granular material. *International Journal for Numerical and Analytical Methods in Geomechanics*, (October 2009): pp. 978–990, doi:10.1002/nag. (p. 35)

Yang, R.Y., Zou, R.P., Dong, K.J., An, X.Z., and Yu, A.B. (2007). Simulation of the packing of cohesive particles. *Computer Physics Communications*, (January). (p. 29, 157)

Yang, R.Y., Zou, R.P., and Yu, A.B. (2000). Computer simulation of the packing of fine particles. *Physical review. E, Statistical physics, plasmas, fluids, and related interdisciplinary topics*, **62**(3 Pt B): pp. 3900–3908. (p. 29, 157)

Yang, R.Y., Zou, R.P., and Yu, A.B. (2003*a*). Effect of material properties on the packing of fine particles. *Journal of Applied Physics*, **94**(5): p. 3025, doi:10.1063/1.1598638. (p. 29, 157)

Yang, R.Y., Zou, R.P., and Yu, A.B. (2003*b*). Numerical study of the packing of wet coarse uniform spheres. *AIChE Journal*, **49**(7): pp. 1656–1666, doi:10.1002/aic.690490706. (p. 29, 157)

Yang, R.Y., Zou, R.P., Yu, A.B., and Choi, S. (2008). Characterization of interparticle forces in the packing of cohesive fine particles. *Physical Review E*, **78**(3): pp. 1–8, doi:10.1103/PhysRevE.78.031302. (p. 29, 157)

Yang, R.Y., Zou, R.P., Yu, A.B., and Choi, S.K. (2006). Pore structure of the packing of fine particles. *Journal of Colloid and Interface Science*, **299**(2): pp. 719–25, doi:10.1016/j.jcis.2006.02.041. (p. 29, 157)

Yang, S.C. and Hsiau, S.S. (2001). The simulation of powders with liquid bridges in a 2D vibrated bed. *Chemical engineering science*, **56**: pp. 6837–6849. (p. 24, 31)

Yao, H., Ciavarella, M., and Gao, H. (2007). Adhesion maps of spheres corrected for strength limit. *Journal of Colloid and Interface Science*, **315**(2): pp. 786–90, doi:10.1016/j.jcis.2007.07.021. (p. 52)

Zhang, K.F. and Ooi, J.Y. (1998). A kinematic model for solids flow in flat-bottomed silos. *Géotechnique*, **48**(1998): pp. 545–553. (p. 222, 232)

Zhong, Z., Ooi, J.Y., and Rotter, J.M. (2001). The sensitivity of silo flow and wall stresses to filling method. *Engineering Structures*, **23**: pp. 756–767. (p. 22, 23)

Zhou, C. (2010). *Investigation of micro- and macro-phenomena in densely packed granular media using the discrete element method*. Ph.d thesis, The University of Edinburgh. (p. 187, 204, 206, 207, 210)

Zhou, C. and Ooi, J.Y. (2009). Numerical investigation of progressive development of granular pile with spherical and non-spherical particles. *Mechanics of Materials*, **41**(6): pp. 707–714, doi:10.1016/j.mechmat.2009.01.017. (p. 11, 12)

Zhu, H.P., Zhou, Z.Y., Yang, R.Y., and Yu, A.B. (2007). Discrete particle simulation of particulate systems: Theoretical developments. *Chemical Engineering Science*, **62**(13): pp. 3378–3396, doi:10.1016/j.ces.2006.12.089. (p. 26)

Zhu, H.P., Zhou, Z.Y., Yang, R.Y., and Yu, A.B. (2008). Discrete particle simulation of particulate systems: A review of major applications and findings. *Chemical Engineering Science*, **63**(23): pp. 5728–5770, doi:10.1016/j.ces.2008.08.006. (p. 26)